AMES RESEARCH CENTER

RESEARCH AND TECHNOLOGY

1992

RESEARCH AND TECHNOLOGY 1992

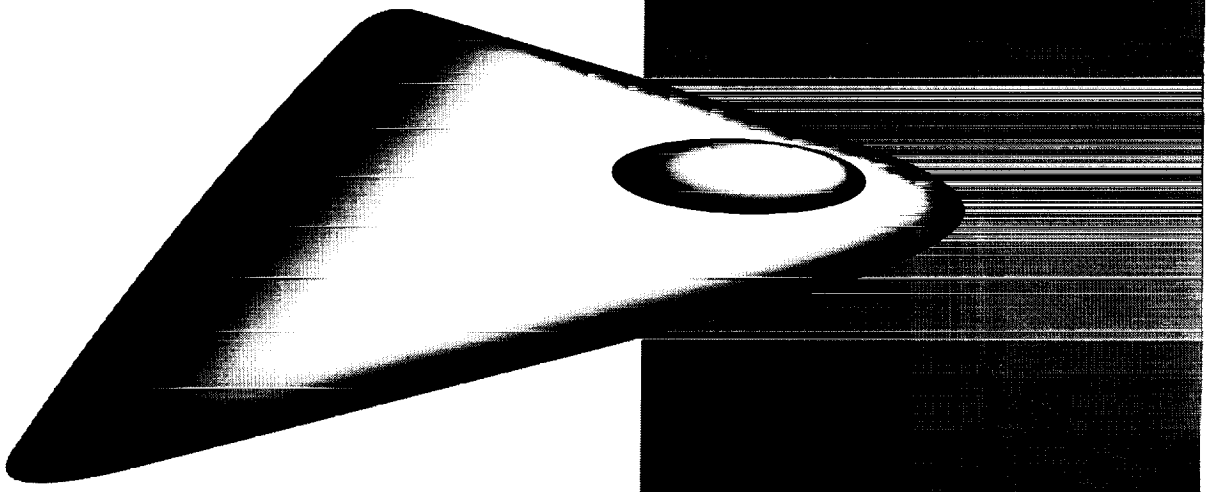

NATIONAL AERONAUTICS
AND SPACE ADMINISTRATION

AMES RESEARCH CENTER

Foreword

Each year, brief summaries of selected achievements at both the Ames-Moffett and Ames-Dryden sites of Ames Research Center are compiled as a NASA Technical Memorandum.

This year's report, Research and Technology 1992, presents some of the challenging work recently accomplished in the areas of Aerospace Systems, Flight Operations and Research, Aerophysics, and Space Research. Here, you can sample the scope and diversity of the research that is now being conducted and obtain a view of the stimulating research challenges of the future.

If you would like further information on any of the Ames research and technology programs, please call the contact person(s) at the end of each article.

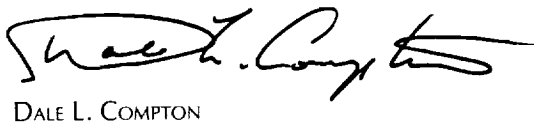

DALE L. COMPTON
Director

Aerospace Systems Directorate

Aircraft Technology Division

XV-15 Ground Vibration Test 1
C. W. Acree, Karen Studebaker

Hypersonic Waverider Vehicle Optimization 2
Jeffrey V. Bowles

Simplified Nose-to-Tail Scramjet Flow-Field Analysis 4
Jeffrey V. Bowles

Reduced Takeoff Roll Distance for Aircraft 6
Joseph C. Eppel, Paul C. Loschke

Assessment of Supersonic Oblique All-Wing Transports 7
Thomas L. Galloway, Mark H. Waters, Mark Moore

Low-Sonic-Boom Concept Analysis 9
Paul Gelhausen, Mark Moore, J. R. Gloudemans

Impact of Technology on Future Sea-Based Attack Aircraft 10
Andrew S. Hahn, Jeffrey J. Samuels

Enhanced Quasi-Procedural Aircraft Design Program 12
Hirokazu Miura, David Schleicher

High-Speed Rotorcraft Economic Optimization 14
David R. Schleicher, James D. Phillips, Kevin Carbajal

Investigation of High Lift Coefficients on Rotating Airfoils 15
Peter D. Talbot, Martin D. Maisel

Comprehensive Rotorcraft Analytical Methods 16
Joseph J. Totah

Small-Scale Investigation of Jet-Induced Effects 17
Douglas A. Wardwell, Craig E. Hange

Tiltrotor Aircraft/Vertiport Feasibility Studies Data Package 18
John Zuk

Full-Scale Aerodynamics Research Division

Optimum Airfoil Design Analysis 20
Fort Felker

Fighter Lift and Control Program 21
Scott Harris

Study of Aeroelastic Problems Using Active Controls 22
Stephen A. Jacklin

McDonnell Douglas Explorer Helicopter Test 23
Stephen A. Jacklin

Hub Loads Reduction: Blade Root Torsional Dampers 24
Sesi Kottapalli

Hub Loads Reduction: Sources of Inplane Shears 24
Sesi Kottapalli

Aerospace Systems Directorate (continued)

Full-Scale Aerodynamics Research Division (continued)

Full-Scale Higher Harmonic Control to Reduce Hub Loads and Noise 25
Sesi Kottapalli, Stephen Swanson

Rotor Design Optimization Using a Free-Wake Model 25
Jeffrey Light

Tiltrotor Download and Acoustics Research 26
Jeffrey Light, Marianne Mosher

Exact Domain Decomposition and Parallel Processing for Rotorcraft Computational Fluid Dynamics 27
Wayne O. Miller

Wind Tunnel Evaluation of a Sikorsky Bearingless Main Rotor 28
Thomas R. Norman

Full-Scale Rotor Wind Tunnel Test Techniques 29
Randy Peterson

Lift-Enhancing Tabs for High-Lift Systems 29
James Ross

Modern Four-Bladed Rotor Research in the 80- by 120-Foot Wind Tunnel 30
Patrick M. Shinoda, David B. Signor

Sikorsky S-76-C Blade Fold Test 32
David B. Signor, Steve Christensen

Flight Measurements of Blade–Vortex Interaction Noise 33
David B. Signor, Gloria K. Yamauchi, Michael E. Watts

High-Speed Research: High-lift/Engine Aeroacoustics Technology 34
Brian Smith34

Jet Noise Source Location Techniques 36
Paul Soderman

Two-Dimensional Tiltrotor Download 37
Paul Stremel

A Zonal Flow Analysis Method 38
Paul Stremel

Full-Scale Rotor Flow Visualization 39
Alexandra Swanson

Rotor Tip Vortex Core Study 40
Alexandra Swanson

NASA/McDonnell Douglas Canard Rotor/Wing Test 41
Stephen Swanson, Steve Christensen

Information Sciences Division

Bayesian Surface Reconstruction from Multiple Images 43
Peter Cheeseman

Integrated Planning, Scheduling, and Control for Automatic Telescopes 44
Mark Drummond, John Bresina, Keith Swanson

Aerospace Systems Directorate (continued)

Information Sciences Division (continued)

Space Shuttle Maine Engine Plume Analysis Using an Optical Processor 45
Charles Gary

Intelligent Dynamic Scheduling Algorithms for Automatic Telescopes 46
Butler Hine, Mark Drummond, Keith Swanson, William Borucki

Intelligent Mechanisms Laboratory 47
Butler Hine, Terry Fong, Michael Sims

Hypersonic Vehicle Takeoff and Climb 48
Charles Jorgensen, Paul Werbos, Robert Pap

Intelligent Procedure Development and Maintenance Project 49
Smadar Kedar

Intelligent Software Support for Scientific Model-Building 50
Richard Keller

Artificial-Intelligence-Based Planning for Data Analysis Tasks 51
Amy Lansky

Knowledge-Based Software Engineering (KBSE) 52
Michael Lowry

Computer Integrated Documentation 53
Nathalie Mathe, Bharathi Raghavan, Joshua Rabinowitz

Capturing Human Visuomotor Control Strategy in an Out-the-Window Flight Control Task 54
Anil Phatak, Charles Jorgensen

Telepresence and Autonomous Control of Undersea Vehicles 55
Daryl Rasmussen, Butler Hine, Terry Fong, Michael Sims

National Photonics Testbed 56
Max Reid

Parallel Systems Research 57
Catherine Schulbach, Jerry Yan

A Neural Learning Algorithm for Touch-Based Control of Mechanical Manipulation 58
Jay Steele

Temporal Prediction using Neural Networks 59
Eric Wan, Bernard Widrow, C. Schulbach, C. Jorgensen

Aerospace Human Factors Research Division

Electronic Chart Display Development 60
Vernol Battiste

Cognitive Complexity Assessment 60
Kevin M. Corker

Symbolic Operator Model 61
Kevin M. Corker, E. James Hartzell

Effect of Perspective Format Displays on Pilot Spatial Awareness 62
Nancy S. Dorighi, Stephen R. Ellis

Aerospace Systems Directorate (continued)

Aerospace Human Factors Research Division (continued)

Electronic Haploscope 63
Stephen R. Ellis

Attentional Fixation in Head-up Displays 65
David C. Foyle, Robert S. McCann

Crew Performance Assessment 66
Steven E. Gregorich, J. Victor Lebacqz

Cockpit Resource Management Training Assessment 67
Steven E. Gregorich, J. Victor Lebacqz

Displays for Optimal Planning of Rendezvous and Proximity Operations 68
Arthur J. Grunwald, Stephen R. Ellis

Distributed Cognition 69
Edwin Hutchins, Everett A. Palmer

Visual Cueing Aids for Rotorcraft Landings 70
Walter W. Johnson, Anthony D. Andre

Computationally Efficient Depth-from-Motion Displays 72
Mary K. Kaiser, Dennis R. Proffitt

Crew Factors in Aerospace Operations: Communication and Coordination 73
Barbara Kanki, Judith M. Orasanu

ViDEOS: Visual Display Engineering and Optimization System 74
James O. Larimer

Information Management and Transfer 75
Sandra Lozito, Kevin Corker

Presence and Virtual Presence in Planetary Exploration 76
Michael W. McGreevy, Lewis Hitchner, Cindy Ferguson, William Briggs

Pilot–Controller Communication 77
Daniel G. Morrow, Michelle A. Rodvold, Kevin Corker

Crew Factors in Aerospace Operations: Team Decision Making 78
Judith M. Orasanu, Barbara Kanki

Automated Checklists 79
Everett A. Palmer, Asaf Degani, Kathleen L. Mosier

Image-Based Sensor Fusion 80
Michel Pavel, Albert J. Ahumada, Jr., James O. Larimer

Aviation Safety Reporting System 81
William D. Reynard

Fatigue Education and Training Module 82
Mark R. Rosekind, Philippa Gander, J. Victor Lebacqz

Controlled Rest on the Flight Deck 83
Mark R. Rosekind, Philippa Gander, J. Victor Lebacqz

Age, Circadian Rhythms, and Sleep Loss in Flight Crews 83
Mark R. Rosekind, Philippa Gander, J. Victor Lebacqz

Aerospace Systems Directorate (continued)

Aerospace Human Factors Research Division (continued)

Pilot Interaction with Cockpit Automation 84
Nadine Sarter, David D. Woods, Everett A. Palmer

Research and Development of Glass Cockpit Technology 85
Robert J. Shiner

Man–Machine Integration Design and Analysis System (MIDAS) 86
Barry R. Smith, E. James Hartzell

Optimizing Image Compression for the Human Viewer 87
Andrew B. Watson, Albert J. Ahumada, Jr.

Motion-Contrast Sensitivity 88
Andrew B. Watson, Michael P. Eckert

Visual Display Optimization Tool 89
Andrew B. Watson, Jeffrey B. Mulligan, Albert J. Ahumada, Jr.

Intervention Strategies for the Management of Human Error 90
Earl L. Wiener, J. Victor Lebacqz

Flight Systems and Simulation Research Division

Divergence-Based Neural Network for Passive Ranging 91
Yair Barniv

Integrated Flight and Engine Controls for Rotorcraft 92
Robert T. N. Chen

Concepts for Pilot Interaction with an Automatic Nap-of-the-Earth Obstacle-Avoidance System 93
Victor H. L. Cheng, Richard Coppenbarger

Final Approach Spacing Tool 95
Tom Davis

Civil Tiltrotor Airworthiness Criteria 96
William A. Decker

RASCAL Research Helicopter 97
Michelle M. Eshow, Robert A. Jacobsen, Edwin W. Aiken

Control-System Design Criteria for STOVL Fighter Aircraft 98
James A. Franklin

CTAS/TSRV Trajectory Prediction Flight Test 99
Steve Green, D. Williams

Integrated Flight Dynamic and Propulsion System Model of the UH-60 101
Frederick D. Kim

Implementation Improvements for Simulator Motion Drive 102
Soren LaForce, John W. Bunnell

Flight Test Evaluation of Differential GPS—Precision Code Flight Test Results 103
B. David McNally

Motion Cueing in Simulation 104
Jeffery A. Schroeder

Aerospace Systems Directorate (continued)

Flight Systems and Simulation Research Division (continued)

Advanced Engine Control for Helicopters 105
Jeffery A. Schroeder

Validation of Multicamera Passive Ranging Algorithms 106
Phillip Smith, Banavar Sridhar

Object Segmentation for Helicopter Guidance 107
Banavar Sridhar

Parallel Multisensor Feature-Tracking Algorithm for Vision-Based Obstacle Detection 109
Raymond E. Suorsa, Banavar Sridhar

Computer Aiding for Low-Altitude Helicopter Flight 111
Harry N. Swenson, Richard E. Zelenka

Rotorcraft Flight Control Design Methods 112
Marc D. Takahashi

Frequency-Domain System Identification Methods 113
Mark B. Tischler, Mavis G. Cauffman

Rotorcraft Robust Flight-Control-System Design Using Quantitative Feedback Theory 114
Mark. B. Tischler

CTAS Field Development and Evaluation 115
Leonard Tobias, Arthur David Jones

Aerophysics Directorate

Aerodynamics Division

Nacelle Airframe Interference at Supersonic Mach Numbers 117
Gelsomina Cappuccio, Ronald C. Smith

Internal Flows Using Hybrid PNS/FNS Codes 118
William C. Rose, Michael D. Wong, Daniel P. Bencze

Fluid Dynamics Division

Dynamic Model for Large-Eddy Simulation 120
Knut Akselvoll, Parviz Moin

Visualization of Compressible Dynamic Stall 121
Lawrence W. Carr, Muguru S. Chandrasekhara

Navier–Stokes Prediction of Wing Rock 122
Neal Chaderjian

Enhancements of the Hyperbolic Grid Generator and User Interface 123
William M. Chan, Ing-Tsau Chiu

Numerical Simulation of High-Performance Aircraft Operations 125
Kalpana Chawla

Reynolds-Stress Modeling in Wall-Bounded Flow 126
Paul Durbin

Temperature and Density Measurements in a Turbulent, Mach 2 Boundary Layer 127
Douglas Fletcher

Pneumatic Forebody Flow Control 128
Kenneth Gee, Yehia Rizk, Lewis Schiff

3-D Laser Doppler Velocimeter Measurements 129
Dennis A. Johnson, Jeffrey D. Brown

Experimental Validation of the Direct Numerical Simulation of a Backstep Flow 131
Srboljub Jovic, David M. Driver

Computational Verification for the Laminar Flow Supersonic Wind Tunnel 132
Goetz H. Klopfer

Data Base Expansion Using Estimation Methods 133
Richard L. LeBoeuf, Rabindra D. Mehta

An Improved Two-Equation Turbulence Model 134
Florian Menter

Navier–Stokes Computations for Oscillating Control Surfaces 135
Shigeru Obayashi, Guru P. Guruswamy

Indication of Flow Direction by Liquid-Crystal Coatings 137
Daniel C. Reda, Joseph J. Muratore, Jr.

Computational Study of Vortex-Induced Tail Buffet 138
Yehia Rizk, Guru P. Guruswamy, Kenneth Gee

Numerical Simulation of a Self-Similar Turbulent Mixing Layer 139
Michael M. Rogers, Robert D. Moser

Faster Grid Generation 140
Reese L. Sorenson, Karen M. McCann

Aerophysics Directorate (continued)

Fluid Dynamics Division (continued)

Direct Numerical Simulation of Turbulent Combustion 142
Arnaud Trouvé, Luc Vervisch, Feng Gao, Jean-Michel Samaniego

Effect of Canard Vertical Position on Wing-Body Aerodynamics 143
Eugene L. Tu

Skin-Friction Measurements in a Three-Dimensional Supersonic Separated Flow 144
Jeffrey K. Wideman, James L. Brown

Unstructured Grid Generation 145
N. Lyn Wiltberger, Timothy J. Barth

Analytic Solutions for Computational Electromagnetics 147
Maurice Yarrow

Numerical Aerodynamic Simulation Systems Division

Concurrent Hybrid Computational Fluid Dynamics 148
Domingo A. Tavella, M. Jahed Djomehri, Katherine K. Kislitzin

An MIMD Implementation of a Parallel Euler Solver for Unstructured Grids 148
V. Venkatakrishnan, Horst D. Simon, Timothy J. Barth

Implementation of ENSAERO on the iPSC/860 149
Sisira Weeratunga, Eddy Promono

Thermosciences Division

Transient Flow Simulations in a Shock Tube 150
Jean-Luc Cambier, Susan Polsky

Direct Particle Simulation of Magellan Aerobraking 151
Brian L. Haas

Simulation of Polymer Properties 153
Richard L. Jaffe

Coated Composite Flexible Blanket Insulation 154
Demetrius A. Kourtides

Ab Initio Determination of Transport Properties 155
H. Partridge, J. R. Stallcop, E. Levin

Arc Jet Testing in Support of the Single-Stage-to-Orbit Vehicle 156
Salvatore R. Riccitiello

Vibrational Relaxation in Expanding Flows 157
Stephen Ruffin, Surendra Sharma

DuraTABI—A Durable, All-Weather Thermal Protection System 158
Paul M. Sawko

Hypersonic Nozzle/Afterbody Flow Field 159
Frank W. Spaid, Earl R. Keener

Advanced Aerogel Development 161
Susan M. White

Space Research Directorate

Advanced Life Support Division

Plasma Copolymerization of Ethylene and Tetrafluoroethylene 163
Morton Golub, Theodore Wydeven

Optimal Crop Selection for a Controlled Ecological Life Support System 164
Ann McCormack, Cory Finn, Betsy Dunsky

Sizing System for Pressurized Space Suits 165
Hubert Vykukal, Bruce Webbon

Performance of Lettuce in Gray-Water Streams 165
K. Wignarajah, David Bubenheim, Ted Wydeven, Jr.

Centrifuge Facility Project

Active Balancing of a Slowly Rotating Centrifuge 167
Michael J. Horkachuck

Dark-Cycle Video Monitoring 169
Arshad Mian, Sherry Chuang

Space Projects Division

Visual Observation of Compressible Oscillating Flow 171
Jeffrey M. Lee, Peter Kittel

Si:As Impurity Band Detector Arrays for Infrared Astronomy 172
Mark E. McKelvey, Robert E. McMurray, Jr., Craig R. McCreight

Earth System Science Division

Pilot Land Data System 174
Gary L. Angelici, Lidia Popovici, Jay Skiles

MODIS-N Airborne Simulator 174
James A. Brass, Jeffrey S. Myers

Airborne Infrared Disaster-Assessment System 175
James A. Brass, Leon Shameson

Fire Emissions and Biogeochemical Impacts in Brazil 176
James A. Brass, Chris Hlavka, Pam Matson, Bob Chatfield

Regional Ecosystem Simulation 177
Jennifer Dungan, David Peterson, Joseph Coughlan

Bidirectional Studies of Forest Canopy Reflectance 178
Lee Johnson

Investigations of Canopy Biochemical Composition 179
Lee Johnson, David Peterson

Carbon Emissions from Northern High-Latitude Ecosystems 179
Gerald P. Livingston, Leslie Morrissey, David Des Marais

Space Research Directorate (continued)

Earth System Science Division (continued)

Contributions of Tropical Forests and Tropical Land Use Change to Global Nitrous Oxide Emissions 181
Pamela A. Matson, Christine Billow, Jerri Mazzurco

ERS-1 SAR Investigations of High-Latitude Wetlands 182
Leslie A. Morrissey, Gerald P. Livingston

Advanced Chemical Monitoring System 183
Peter T. Palmer, Carla M. Wong

Oregon Transect Ecosystem Research Project 184
David L. Peterson

Evolution of Biological Carbon Fixation 185
Lynn J. Rothschild

Oxygen Evolution and Life on Mars 186
Lynn J. Rothschild

Global Monitoring and Human Health 187
Michael Spanner, Byron Wood, Louisa Beck

Hapex-II/Sahel Experiment 188
Michael Spanner, Robert Wrigley, Rudolf Pueschel

Biophysical Information in Asymmetric and Symmetric Diurnal Bidirectional Canopy Reflectance 188
Vern C. Vanderbilt

Studies of Stratospheric Trace Gases 189
James F. Vedder

ECOSAT Computational Facility for Biospherics and Terrestrial Ecosystems 190
Kenneth Weinstock, Mathias Ma, Rita Pettigrew

Computer Modeling of Clouds 190
Douglas L. Westphal

Prediction of Lyme Disease Risk: A Remote-Sensing Model Based on Landscape Epidemiology 192
Byron L. Wood, Louisa R. Beck, Sheri L. Dister

Search for Extraterrestrial Intelligence Office

High Resolution Microwave Survey Observations Begin 193
Peter R. Backus

Life Science Division

Urinary Calcium Excretion in Human Models for Spaceflight 195
Sara B. Arnaud, Meena Navidi, I. Wolinsky

Skeletal Asymmetry in Bending Stiffness of the Human Tibia 196
Sara B. Arnaud, Teresa M. Hutchinson

Intramuscular Pressure and Joint Torque During Concentric and Eccentric Exercise 197
Richard E. Ballard, Alan R. Hargens

Space Research Directorate (continued)

Life Science Division (continued)

Regional Microvascular Bloodflow During Gravitational and LBNP Stresses 198
Gregory A. Breit, Donald E. Watenpaugh, Richard E. Ballard, Gita Murthy, Alan R. Hargens

Bone Geometry, Structure and Mineral Distribution using Dual Energy X-Ray Absorptiometry 200
Tammy Cleek, Robert T. Whalen

Perceptual and Behavioral Adaptation to Altered Gravitational–Inertial Forces 202
Malcom M. Cohen

Effect of Spaceflight on Primary Rat Osteoblast Cultures 204
Charlotte M. Cone, Emily R. Morey-Holton, Stephen B. Doty

Chronic Exposure to Altered Gravity Affects Brainstem Neurochemistry in the Rat 205
Nancy G. Daunton, F. Tang, Robert A. Fox

CD4+/CD8+ T-Lymphocyte Ratio: Rehydration and Supine Exercise in Men 206
John E. Greenleaf, Catherine G. R. Jackson, DeSales Lawless

The Role of Muscle Function and Growth Factors in the Prevention of Muscle Atrophy in the Rat 207
Richard E. Grindeland

Gravitational Effects on Cell Biology 208
Rosalind A. Grymes

Back Pain during 6-Degree Head-Down Tilt is Similar to That during Actual Microgravity 209
Karen J. Hutchinson, Alan R. Hargens, Gita Murthy, Donald E. Watenpaugh, Victor A. Convertino, Peter C. Wing

Hypergravity Simulation on the Ames 20-G Centrifuge 210
Gerald M. Mulenburg

Exercise against Artificial Gravity Simulates Exercise against Normal Gravity 211
Gita Murthy, Donald Watenpaugh, Richard E. Ballard, Alan Hargens

Effects of Spaceflight on Gravity Sensors 213
Muriel D. Ross

The Role of Visual–Vestibular Interactions in the Perception of Motion 214
Leland S. Stone

Changes in the Proximal Femur During Spaceflight 215
Sharon Tanner, Emily R. Morey-Holton

Gravity Receptor Physiology After Exposure to Microgravity 216
David L. Tomko

Comparison of a Microgravity Experiment and a Hypergravity Equivalent 217
Marilyn Vasques

An Exercise Device that Uses Self-Generated Lower-Body Negative Pressure 218
Donald E. Watenpaugh

Adaptation to Rearranged Sensory Environments 220
Robert B. Welch

Monitoring the Ground Reaction Forces 221
Robert Whalen, Jason Quintana

Space Research Directorate (continued)

Space Life Sciences Payloads Office

Life Sciences Experiments Flown on STS-42 (IML-1) 223
Joellen Lashbrook, Charles M. Winget

Physiological Anatomical Rodent Experiments 224
Debra Reiss-Bubenheim

Frog Embryology and Autogenic Feedback Training Experiments on Spacelab-J 225
Greg Schmidt, Sally Ball

Space Science Division

The Astrophysical Simulation and Analysis Facility 227
Louis J. Allamandola, Farid Salama, Scott A. Sandford, William Schutte, Robert Walker

The Outer Heliosphere and Termination Shock 228
Aaron Barnes

The Venus Plasma Environment and the Inner Heliosphere 229
Aaron Barnes

Spectral Imaging of Astronomical Polycyclic Aromatic Hydrocarbon Sources 230
Jesse D. Bregman

Telepresence for Planetary Exploration 231
Geoffrey Briggs, Carol Stoker

Hypervelocity Impact Survivability Experiments for Carbonaceous Impactors 232
Ted E. Bunch

Particle–Gas Dynamics in the Protoplanetary Nebula 234
Jeffrey N. Cuzzi

Planetary Ring Dynamics and Morphology 235
Jeffrey N. Cuzzi

The Influence of Continental Evolution on the Rise of Oxygen in the Ancient Atmosphere 236
David J. Des Marais

A Gas Chromatographic Column for Storing Sample Profiles 237
Jean-Marie D. Dimandja, Jose R. Valentin, John B. Phillips

Exploring the Solar System through Stellar Occultations 239
Edward W. Dunham

Mars Site Selection for Exobiology Studies 240
Jack Farmer, David Des Marais

Gas-Grain Simulation Facility Conceptual Design 241
Mark L. Fonda, Judith L. Huntington

Particle Generation for the Gas-Grain Simulation Facility 243
Mark L. Fonda, Judith L. Huntington, Kenji Nishioka

Electrical Conductivity of Planetary Interiors 244
Friedemann Freund

Calculation of C_2 and C_2^- Opacity Sources 246
David Goorvitch

Space Research Directorate (continued)

Space Science Division (continued)

ATP Synthesis in the Extreme Halophiles 247
Lawrence I. Hochstein

The Center for Star Formation 248
David Hollenbach, Patrick Cassen

Facultative Anoxygenic Cyanobacteria 249
Linda L. Jahnke, Elaine Munoz

Prebiotic Polymerization Models 250
Anastassia Kanavarioti, Sherwood Chang

A GC–IMS for the In Situ Analysis of Extraterrestrial Environments 252
Daniel R. Kojiro, Glenn C. Carle

The Search for Interstellar Molecules in Carbonaceous Meteorites 254
Narcinda R. Lerner

Exobiology Experiments for the In Situ Analysis of the Martian Surface 255
Rocco Mancinelli, Lisa White

Structure of Simple Membrane–Water Interfaces 256
Andrzej Pohorille, Michael A. Wilson

A Titan Simulation Chamber 257
Shelly Pope

The New Ames Mid-Infrared Astronomical Camera 258
Thomas L. Roellig

Diode Laser Spectroscopy of $^{12}C/^{13}C$ and $^{16}O/^{18}O$ 259
Todd Sauke, Joe Becker

Analysis Techniques and the Search for Life on Mars 260
Debbie Schwartz, Rocco Mancinelli, Lisa White

Column Development for Gas Chromatographs 261
Thomas Shen

Computer Model of Microgravity Aerosols 262
David Stratton

Absolute Airborne Infrared Spectroscopy 263
Fred C. Witteborn, Martin Cohen, Diane H. Wooden

The Galileo Probe Mission to Jupiter 264
Richard E. Young

Gravity Waves in the Venus Atmosphere 265
Richard E. Young, Howard Houben

Simulation of the El Chichon and Mt. Pinatubo Volcanic Aerosol Clouds in the Stratosphere 266
Richard E. Young, Howard Houben, Brian Toon

The Tunguska Event of 1908 267
Kevin Zahnle

Dryden Flight Research Facility Directorate

Research Engineering Division

Post-Stall Envelope Expansion of the X-31 Enhanced Fighter Maneuverability Airplane 269
John T. Bosworth, Jeffrey E. Bauer, Patricia C. Seamount

Parameter Identification for Highly Augmented Aircraft 270
Albion H Bowers, Brent R. Cobleigh

Actuator Modeling for High-Angle-of-Attack Aeroservoelasticity 271
Martin J. Brenner

Landing Systems Research Aircraft Capabilities 272
Vincent Chacon, John Carter, Darlene Mosser-Kerner

Airborne Research System Architecture 274
Vince Chacon

Flying-Qualities Investigation of the Long-Period Dynamics of a Generic Hypersonic Vehicle 276
Timothy H. Cox

In-Flight Structural Deflection Measurement Technology Transferred to Industry 277
V. Michael DeAngelis, William A. Lokos

Engine Exhaust Characteristics in Support of Acoustic Testing 279
Kimberly Ennix, L. Dean Webb

F-18 Forebody Boundary-Layer Transition-Strip Study 281
David F. Fisher

Development of a Modal State Monitor 282
Lawrence C. Freudinger

Performance-Seeking Control Flight Results 283
John Orme

Real-Time Thrust Method for High Angle of Attack Engine Performance Evaluations 285
Ronald J. Ray, Andrew Yuhas

An Improved Task for Flying-Qualities Assessment of Aircraft 286
Mary F. Shafer

Spacecraft Autoland Project 287
Alex Sim, James Murray, Dale Reed

Flutter Excitation System Research and Flight-Test Results 289
Lura E. Vernon

A Novel Control-Surface Free-Play Measurement Technique and Its Application to the X-31 Aircraft 290
Leonard S. Voelker

Application of a Flush Airdata System to a Wing Leading Edge 291
Stephen A. Whitmore, Timothy R. Moes

Effects of Bleed-Air Extraction on Thrust Levels of the F404-GE-400 Turbofan Engine 293
Andrew Yuhas, Ronald J. Ray

Appendix

Color Plates 295

XV-15 Ground Vibration Test

C. W. Acree, Karen Studebaker

All existing analytical models of the XV-15 are known to have deficiencies in their input data. In particular, the accuracy of the wing/pylon structural-mode data is highly questionable. All such existing data are based on designs or analyses not directly verified by ground or flight tests.

The goal of the XV-15 Ground Vibration Test (Phase 1 Shake Test) was to directly measure zero-airspeed frequencies, damping, mode shapes, and modal masses for the XV-15 tiltrotor aircraft. The focus was on the wing and pylon, but the cockpit, fuselage, and tail were included. The data are important because whirl-flutter stability is a major concern for the advanced technology blades (ATB) being tested on the XV-15. Accurate determination of wing/pylon modes is required for prediction of XV-15 whirl-flutter margins.

NASTRAN analyses showed that a simple, inverted-vee bungee suspension would adequately approximate a free–free condition. The XV-15 was tested in essentially flightworthy condition, except that the rotor blades were replaced by dummy masses. Nearly all of the testing employed external, electrodynamic shakers to apply either vertical or chordwise loads at the wing/pylon junctions.

For Phase 1, both steel-blade and ATB configurations were tested with the pylons in airplane mode, which had the highest priority. Both swept-sine and random excitation were applied using single and dual shakers. Data were obtained for an array of over 130 accelerometers, including six-component linear+angular accelerometers at each hub, plus shaker force links and other transducers.

The Phase 1 test provided the first structural test data of any reliability for the XV-15; these data will significantly increase the confidence in subsequent predictions of XV-15 whirl-flutter margins. The success of the test also demonstrated a cost-effective means of acquiring such data within a restricted time schedule and demonstrated close cooperation between Ames and Dryden personnel.

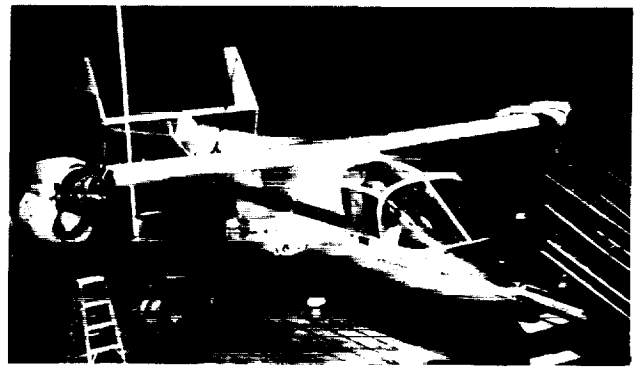

Fig. 1. XV-15 and suspension system.

The data are being analyzed while the XV-15 undergoes its 200-hour inspection. The results will be used to construct a full structural model of the XV-15, and then will be fed into the advanced rotorcraft codes CAMRAD and 2GCHAS for improved aeroelastic predictions. Phase 2 will test a greater variety of configurations of the modified aircraft.

Ames-Moffett contact: C. Acree/K. Studebaker
(415) 604-5423/4682
Headquarters program office: OA

Hypersonic Waverider Vehicle Optimization

Jeffrey V. Bowles

In support of hypersonic aircraft studies, the Systems Analysis Branch has developed a design synthesis tool for the design and optimization of hypersonic waverider configurations with integrated airbreathing propulsion systems. Waverider configurations utilize favorable aerodynamic interference effects to increase lift at supersonic or hypersonic speeds and hence offer the potential for improved high-speed lift-to-drag ratios. Propulsion system integration is also an important consideration for overall hypersonic vehicle performance. Included in the optimization process are several design constraints on the vehicle configuration.

The geometric definition of a hypersonic waverider configuration is computed by solving the differential equation for the streamlines for a real-gas axisymmetric flow field. A sixth-order polynomial is used to describe the surface geometry. Solution of the real-gas Taylor–Macoll equations gives the inviscid flow properties on the lower surface. A simplified compressible boundary layer reference enthalpy method is used to compute the local skin friction coefficient, which is used in turn to compute both skin friction drag and equilibrium radiation surface temperatures. Leading-edge temperatures are computed using a swept-cylinder model. Pressure lift and drag are computed by integration of the pressure coefficient over the surface of the vehicle. Base drag pressure coefficient is computed using 70% vacuum in the vehicle base region. The nose-to-tail propulsion flow field is solved using a real-gas shock/weak wave code coupled with a one-dimensional combustor

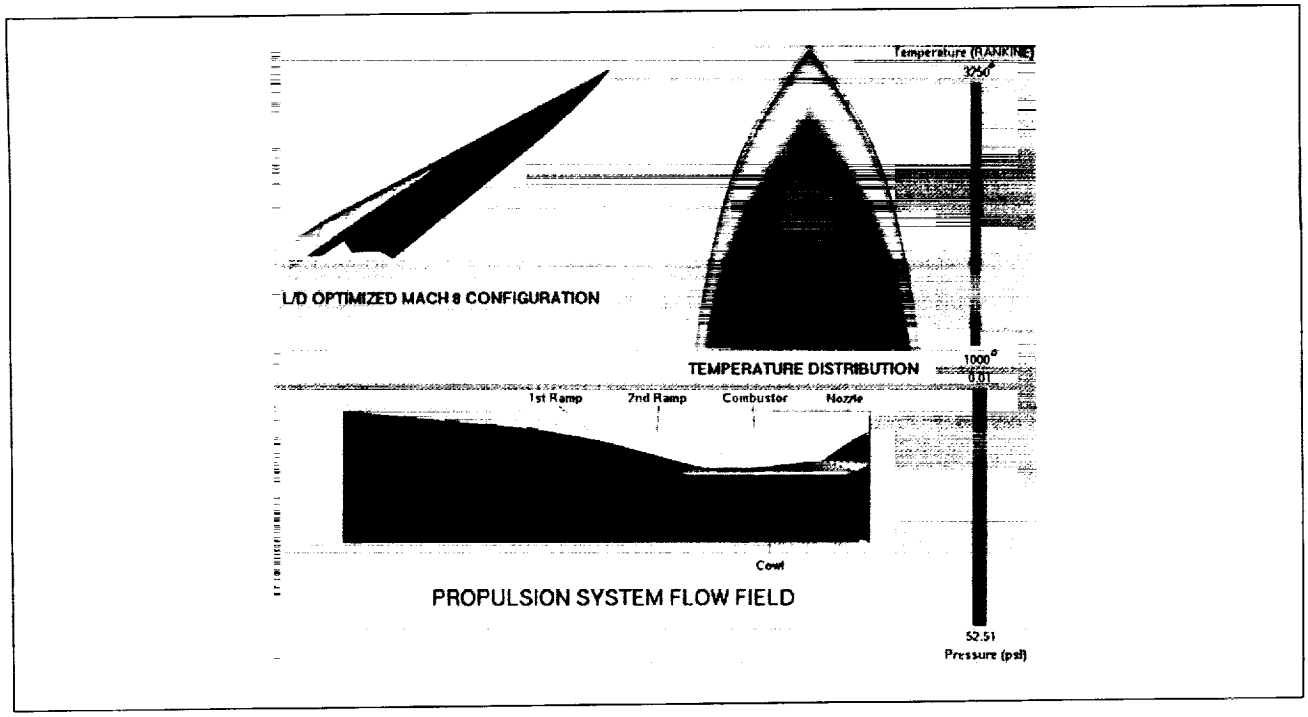

Fig. 1. Optimized Mach 8 waverider configuration, surface temperature distribution, and nose-to-tail flow field. (See color plate 1 in Appendix)

code to compute the inlet and nozzle flow field. The propulsion system selected for study was a hydrocarbon-fueled scramjet.

The waverider analysis code was coupled with a numerical optimization code (method of feasible directions) to determine the optimum configuration shape. As opposed to accelerator-type missions where the mass capture characteristics of the vehicle are most important, cruise configurations place an emphasis on the aerodynamic performance of the design. Hence vehicle lift-to-drag ratio (L/D), or, more importantly, the product of L/D and engine specific impulse (I_{sp}), becomes most important. The ratio of I_{sp} to L/D is proportional to the Breguet range factor, and maximizing its value results in optimum cruise range performance. The configuration, including engine installation details, was thus numerically optimized with this factor, using forebody shape, ramp angles, and cowl position as optimization parameters. The engine combustor geometry and operating parameters were held fixed during this optimization study.

Fifteen design parameters were used in the optimization process. Six parameters defined the waverider-generating surface (and thus the vehicle shape) and eight parameters defined the ramps, cowl, nozzle geometry, and leading-edge radius. The last design parameter was free-stream dynamic pressure. Eight constraints were used in the optimization process, including an engine throttle setting greater than or equal to the required cooling equivalence ratio, a leading-edge equilibrium radiation temperature limit of 3200°F, a wing-tip closure angle limit of 10 degrees, and a vehicle structural thickness limit at the vehicle end to account for nozzle integration. The volume was constrained to 1.7% of the cube of the vehicle length. Finally, the vehicle width-to-length ratio was constrained to be less than or equal to 0.75.

For the Mach 8 design, a generating shock angle of 12 degrees was selected. The waverider shape optimization process involved planform shape changes to sweep the leading edge in order to alleviate high heating rates at the higher free-stream dynamic pressures, traded off against a larger leading-edge radius and associated leading-edge bluntness drag. The design optimization process for the inlet (ramp positions and ramp angles) resulted in the two ramp shocks converging on the cowl lip (shock-on-lip), and then being reflected to the shoulder of the combustor entrance (shock-on-shoulder). The geometric contraction ratio was approximately 14, with a resulting pressure at the combustor inlet of about 1 atmosphere. The results show a required vehicle length of 23 feet and an overall vehicle body density of 20 pounds per cubic foot. An L/D of 4.3 was achieved, with a cowl-to-tail I_{sp} of 746 seconds at an equivalence ratio of 1.0, and a free-stream dynamic pressure of 900 pounds per square foot, resulting in an initial cruise altitude of 92,500 feet. The figure presents the optimized waverider configuration, the lower-surface temperature distribution, and the keel-line profile showing the nose-to-tail propulsion flow field.

Ames-Moffett contact: J. Bowles
(415) 604-6651
Headquarters program office: OAST

Simplified Nose-to-Tail Scramjet Flow-Field Analysis

Jeffrey V. Bowles

As part of the Hypersonic Research Program, an engineering analysis tool has been developed for computing the nose-to-tail flow field of a scramjet propulsion system. The simplified engineering model enables the rapid analysis of hypersonic propulsion systems for use in a conceptual vehicle synthesis code. A comparison of results obtained using the engineering analysis method with results obtained using a full computational fluid dynamics (CFD) analysis has been completed for (1) a hydrocarbon scramjet combustor with liquid oxygen preburning and (2) the external inlet and nozzle flow field of the engine integrated on a Mach 8 hypersonic cruise waverider research vehicle.

The slow reaction rates of a hydrocarbon/air mixture in a supersonic stream can have a significant impact on the inlet/combustor design. Because of the size limitation for an engine on a small research vehicle, a mechanism is required to provide sufficient fuel and air temperatures for burning within the combustor. One approach is to use a liquid-oxygen-augmented preburner located upstream of the main fuel injectors to promote burning in the combustor. Because liquid oxygen would be stored on board the research vehicle, the required preburning must be kept to a minimum to reduce the impact on the vehicle size and gross weight. For the relatively short cruise time of a hypersonic research mission (5 to 10 minutes) this additional on-board mass does not have a significant impact. The required preburner fuel and oxidizer flows were computed to ensure combustion of the hydrocarbon fuel injected at the main burner stations. To achieve a uniform mixed temperature at the main fuel-injector station equal to the auto-ignition temperature of the gaseous hydrocarbon fuel, approximately 2.5% of the overall stoichiometric engine fuel flow with an oxidizer/fuel ratio of 1.71 is required, which is twice the stoichiometric value for the preburner.

To predict the nose-to-tail flow-path characteristics for arbitrary hypersonic vehicle configurations, the propulsion analysis method consists of a planar, inviscid, two-dimensional (2-D), real-gas, weak-wave flow code coupled to a one-dimensional (1-D)

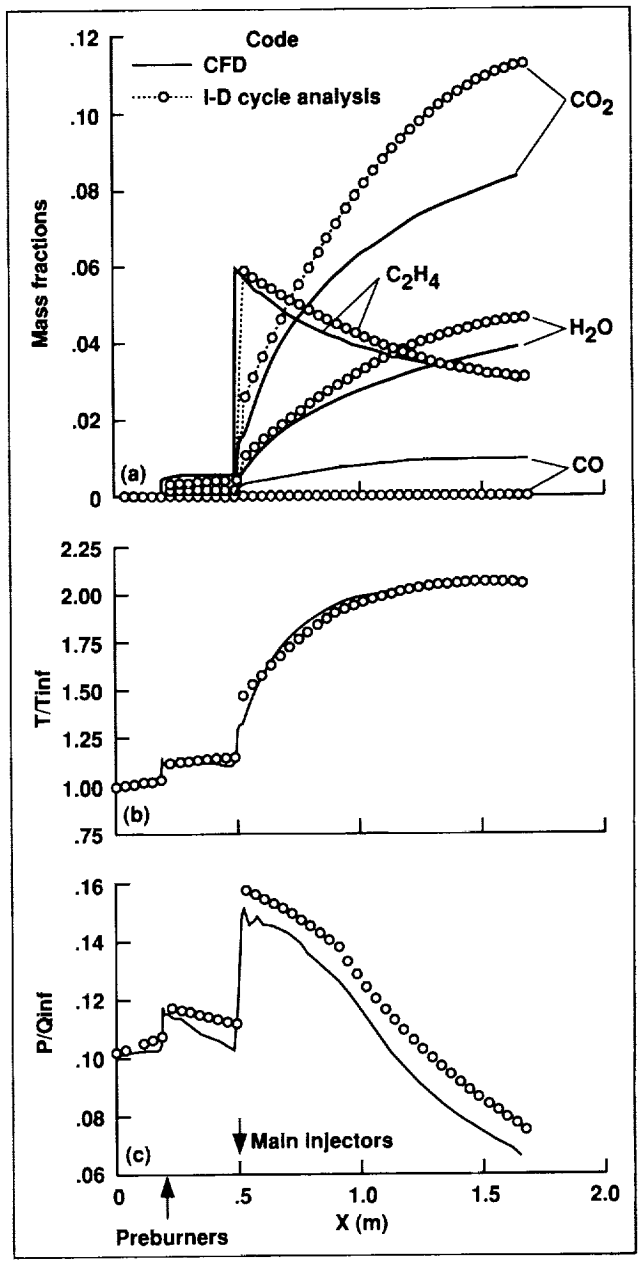

Fig. 1. Comparison of 1-D cycle analysis and CFD predictions for combustor flow field.

subsonic/supersonic combustor analysis code. The weak-wave code computes the inviscid inlet flow field as a function of the vehicle forebody/ramp geometry, including cowl position, angle of attack, and free-stream Mach number. The equivalent 1-D flow properties are then computed at the inlet throat, and the 1-D combustor mass, momentum, and energy equations (with wall skin friction and heat transfer) are solved stepwise through the burner. The nozzle flow field is then computed from the combustor exit solution using the real-gas, weak-wave 2-D code, including the nozzle and cowl flap geometry. The first-order estimates of the axial and normal forces and the pitching moment are computed as a function of vehicle geometry and flight condition. Overall propulsion system heat loads are then used to determine fuel inlet temperature or to compute the required engine cooling equivalence ratio. Modeling the combustion efficiency as a function of location in the combustor (i.e., providing a heat-release schedule) enables the 1-D code to predict the flow properties and engine performance using a multistep approach. The combustor efficiency model is developed from either experimental data or more detailed calculations. In the present analysis, a full Navier–Stokes three-dimensional (3-D) CFD analysis with finite rate chemistry and two-equation turbulence model was used to predict the combustor flow-field properties and to generate the combustor flow field and the equivalent heat-release schedule used in the 1-D analysis.

The first figure presents a comparison of the CFD results with those of a 1-D cycle analysis. The combustor efficiency computed by the CFD solution was implemented in the cycle code by curve-fitting the average fuel fraction schedule. Also shown in this figure is the predicted amount of carbon monoxide from both the CFD and 1-D cycle analyses. The CFD analysis predicts a greater amount than does the 1-D cycle code. This is because of the difference in the equilibrium mechanisms of the two codes and suggests an improvement to the simplified kinetics employed in the CFD solver for scramjet computations. Comparison of the average temperature and the momentum-averaged pressure shows general agreement (first figure). The differences can be attributed to the improved ability of the CFD method to account for detail and the difference in the equilibrium mechanisms. Verification of the 1-D cycle code results by the CFD analysis encourages further

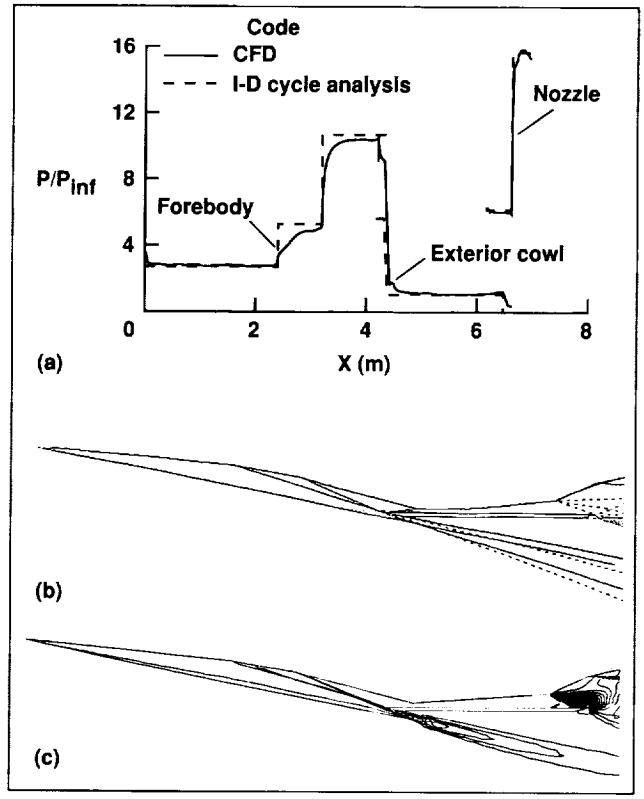

Fig. 2. Comparison of engineering and CFD codes for predicting the nose-to-tail propulsion system flow field.

application of the cycle code to a broader range of engine design parameters.

As a basis for a nose-to-tail comparison between the engineering and CFD codes, a Mach 8 conical flow-field-derived waverider was optimized to maximize the product of I_{sp} and L/D. The forebody geometry was defined as a two-ramp system with shock-on-lip/shock-on-shoulder. The second figure contains a plot of the surface pressure on the keel line of the vehicle (part (a)). Both the CFD and the cycle results are plotted. Agreement is excellent except in the vicinity of inviscid/viscous interactions. Agreement of the pressures on the waverider forebody are within 2% except at the leading edge, where CFD predicts a pressure spike resulting from boundary layer displacement. The ramp pressures also agree well except for the asymptotic behavior of the CFD results that is typical of shock/boundary layer interactions. Other reasons for the slight difference include

3-D effects. One such effect is encountered as the planar ramp emerges from the curved waverider forebody. The intersection line bends downstream from the vehicle symmetry plane. This 3-D effect reduces the pressure near the intersection region. The figure also shows very good agreement on the outer surface of the cowl and on the nozzle surface. Comparison of surface pressure on the upper surface showed that the CFD-predicted pressures were 3%–10% higher than the engineering predictions. This result is also explained by viscous/inviscid interactions.

Part (b) of the second figure shows the waverider nose-to-tail flow field predicted by the engineering method, with the flow regions bounded by waves (e.g., shocks and expansion waves). The pressure contours in part (c) show the shock and expansion waves that are predicted with CFD. The location and strength of these waves are in very good agreement with those predicted by the engineering code. The CFD results, however, predict that the ramp shocks lie slightly outside of the inlet instead of on the cowl lip. This difference is attributed to shock/boundary layer interactions and to 3-D effects.

Ames-Moffett contact: J. Bowles
(415) 604-6651
Headquarters program office: OAST

Reduced Takeoff Roll Distance for Aircraft

Joseph C. Eppel, Paul C. Loschke

The reduction in ground distance for aircraft takeoff that could be obtained with the use of an impulsively extendible nose gear strut (called the jump strut) is being investigated in a joint NASA/Air Force program. A reduced takeoff ground roll distance could enhance the utility of both civil and military aircraft where operations are required from short runways, aircraft carrier decks, or remote, unprepared sites. The Ames Quiet Short Haul Research Aircraft (QSRA) is being used because of its demonstrated low-speed flying qualities, which are desirable for safe operation during this investigation.

A key feature of the jump strut is that it can be implemented with a lightweight, low-cost, and low-complexity modification to a standard nose gear assembly. The QSRA jump strut assembly consists of the standard nose gear strut modified to accept high pneumatic pressure for the extension, a control valve/timing system, and a pneumatic reservoir and supply system (see first figure). In the past year, the installation and ground functional evaluation of the jump strut's mechanical, electrical, and pneumatic systems were completed and the flight evaluation was initiated.

This flight program is examining the effects of a wide array of variables including the pressure in the storage vessel, the duration of the valve opening, and the airspeed at the time of actuation of the jump strut

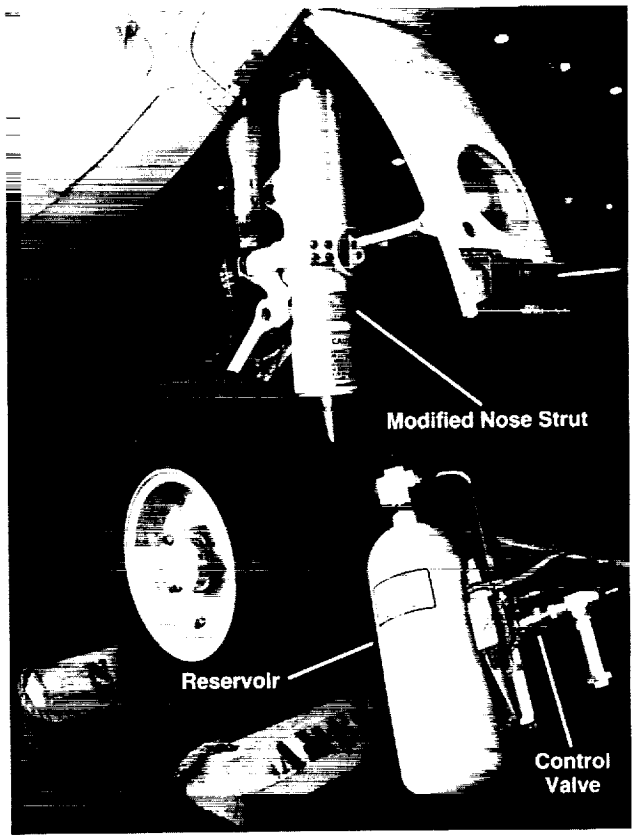

Fig. 1. Major components of the jump strut system.

system. Piloting techniques (i.e., elevator control) used during takeoff roll are being evaluated. In addition, the tests will investigate the influence of aircraft parameters such as thrust-to-weight ratio, wing loading, and center-of-gravity position on the takeoff ground roll distance. The results from this flight experiment are anticipated to show the overall quantitative reduction in takeoff distance as well as to identify the key system design and the operational procedures required to maximize these benefits.

Results from the initial flight tests show a ground roll distance reduction of 10%–15% (see second figure). Further flight tests will be conducted at the Ames Crows Landing Facility in the first quarter of 1993 to substantiate these early test results.

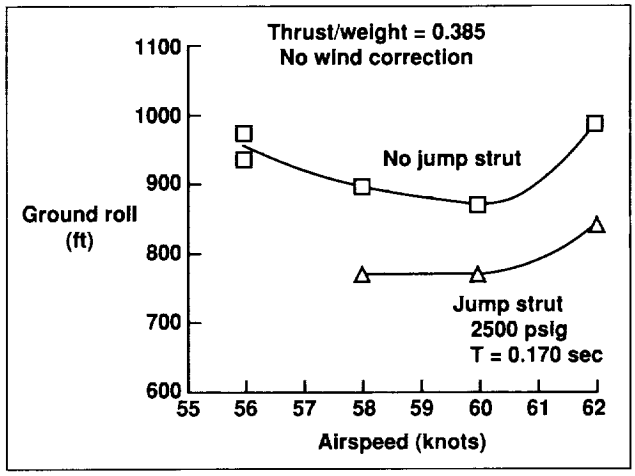

Fig. 2. Initial takeoff evaluation of the jump strut.

Ames-Moffett contact: J. Eppel
(415) 604-6276
Headquarters program office: OAST

Assessment of Supersonic Oblique All-Wing Transports

Thomas L. Galloway, Mark H. Waters, Mark Moore

Aircraft concepts using a wing that can be turned to different oblique angles as the forward-flight Mach number changes have been suggested by several researchers for transport applications. In the mid-1970s, Ames Research Center pursued wind tunnel and flight investigations of oblique-wing configurations based on theoretical developments by R. T. Jones. Recently, two approaches using the oblique-wing concept have received attention for passenger transport in supersonic flight. One configuration, identified as the oblique wing-body (OWB), carries passengers in a conventional cylindrical fuselage similar to subsonic aircraft. The other, known as the oblique all-wing (OAW), accommodates passengers within the wing structural box and requires adequate wing depth to meet passenger access, egress, and aisle requirements.

A study was performed by the Systems Analysis Branch to assess the economic potential of supersonic OWB and OAW designs compared to subsonic concepts with equivalent passenger capacity. The conceptual oblique-wing supersonic aircraft and the subsonic reference aircraft for this investigation were modeled using NASA's Aircraft Synthesis Program Institute (ACSYNT) aircraft design synthesis program. This computer-based design method estimates the aircraft performance and economics after sizing the configuration to meet the specified mission requirements. This study sized configurations for passenger loads of 300 to 500 and a design range of 5,000 nautical miles with standard international fuel reserves. The supersonic aircraft had design cruise Mach numbers of 1.6 or 2.0.

It was assumed that all concepts studied would use aluminum in the primary structure since the design Mach number did not exceed two. The subsonic designs incorporated a high-bypass turbofan

propulsion system currently in development. The engine for the Mach 1.6 oblique-wing designs was a bypass-ratio-1.5 turbofan design, whereas the Mach 2.0 OWB used a bypass-ratio-1.0 turbofan cycle. All of the aircraft were sized to perform the design mission with the best wing area, wing aspect ratio, and engine size. The mission cruise segments were flown at the altitude that maximized each segment's range.

Both supersonic design concepts exceed a million pounds gross weight at the 350- to 400-passenger size for the 5,000-nautical-mile design range. The gross weight of the largest subsonic design is less than 800,000 pounds. The OWB-design fuel fraction increases with design cruise speed and passenger size and results in a reduction in payload fraction. The payload fraction for the OAW increases as passenger size increases because there is only a small change in the concept's external geometry with passenger capacity.

Assessment of the economic viability of the concepts was based on the average passenger revenue, in cents per revenue-passenger mile (¢/RPM),

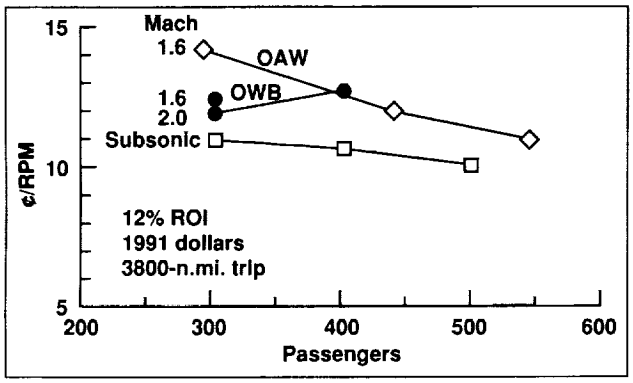

Fig. 1. Passenger revenue requirements.

required for the airline to make a 12% return on investment (ROI) when the aircraft is priced so that the manufacturer also makes a 12% ROI. Although the concepts were designed for a range of 5,000 nautical miles, the evaluations were done for an average trip distance of 3,800 nautical miles. This distance represents an average stage length when a fleet of aircraft with a 5,000-mile design range is scheduled to serve a typical airline system that has route distances greater than 2,500 nautical miles. The resulting revenue requirements for the study aircraft are shown in the accompanying figure.

The subsonic concepts show a required revenue level of 10 to 11 ¢/RPM, which is representative of current average yields reported by the airline industry. The estimated revenue level for the subsonic concepts is used as the reference for the economic viability of the supersonic concepts. At the 300-passenger size, the most attractive supersonic concept is the Mach 2 OWB. The higher productivity of the Mach 2 OWB offsets its higher price relative to the Mach 1.6 OWB. Both OWB concepts are substantially better than the large OAW at the 300-passenger size. As passenger capacity increases, the revenue requirement of the Mach 2 OWB increases whereas that of the Mach 1.6 OAW decreases. The requirements become the same at a passenger capacity of about 400. The Mach 1.6 OAW revenue requirement continues to decrease with increasing passenger size and is only 9% above the subsonic reference at the largest size in this study.

Ames-Moffett contact: T. Galloway
(415) 604-6181
Headquarters program office: OAST

Low-Sonic-Boom Concept Analysis

Paul Gelhausen, Mark Moore, J. R. Gloudemans

This study was performed to evaluate the size, performance, and economics of high-speed civil transport (HSCT) concepts designed to reduce the sonic-boom signature at the ground to an acceptable level in order to permit supersonic operation over land.

Several low-sonic-boom concepts designed to fly at Mach 2.0 over land and Mach 2.4 over water were initially sized using the conceptual design synthesis program ACSYNT for a 5,000-nautical-mile, 300-passenger mission. In cooperation with the Advanced Aerodynamic Concepts Branch and the Applied Computational Fluid Dynamics Branch at Ames, these concepts were analyzed and either

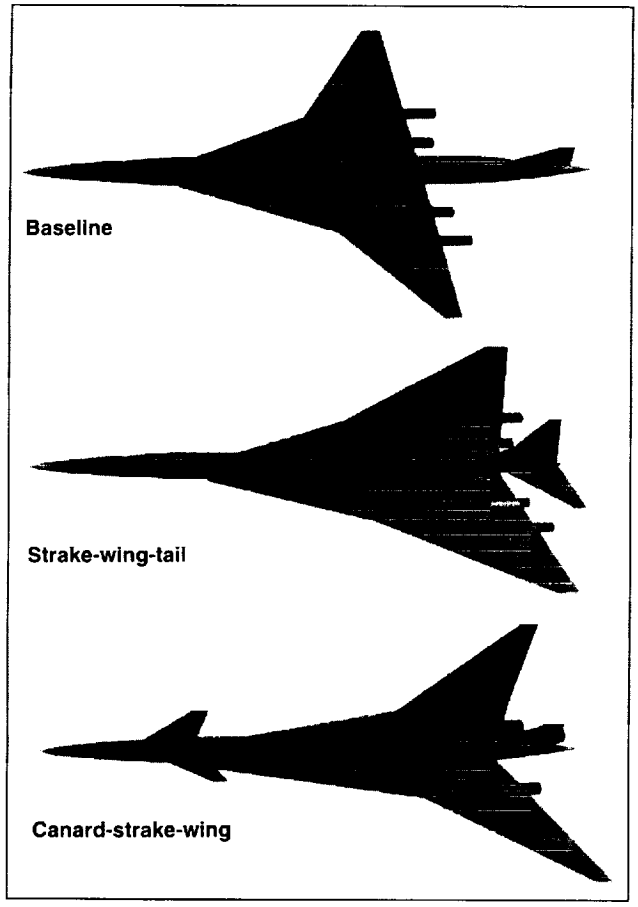

Fig. 1. Low-sonic-boom configurations.

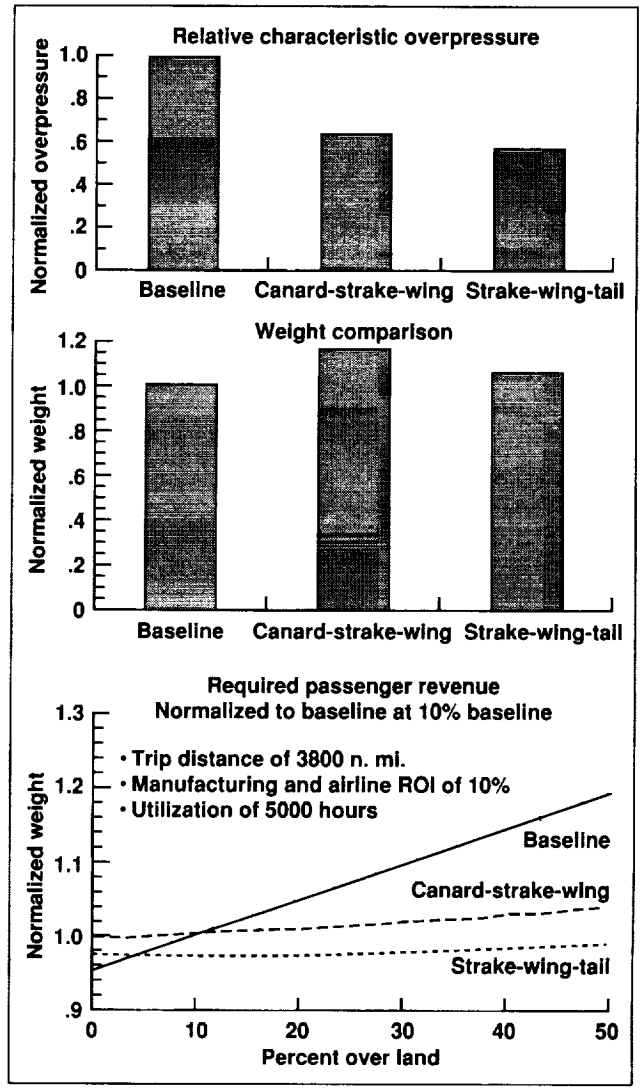

Fig. 2. Comparison of low-sonic-boom concepts.

modified or eliminated. The remaining configurations—aft-tail and canard-wing designs, each with a strake wing—were then compared to a performance-optimized baseline concept designed to fly the same mission except that it flies subsonically over land. The wing and engine of each aircraft was sized to minimize the gross weight, subject to FAA constraints. The economics were evaluated for an average flight

distance of 3,800 nautical miles and a 10% return on investment (ROI) for both the manufacturer and the operator. The three concepts that were studied in depth are shown in the first figure. The baseline and the wing-tail configurations have four engines. The canard-wing configuration was designed with three engines so the effect of two versus four underwing engines on the sonic-boom signature could be investigated.

The two low-sonic-boom configurations were determined to be the most promising approaches. The second figure shows three results of this study: (1) the sonic-boom overpressure levels predicted using the linear methods in ACSYNT, (2) the takeoff gross weight of each concept, and (3) the revenue required per passenger mile plotted against the percentage of the route that is over land, all expressed relative to the baseline values. The aft-tail design has slightly better overpressure characteristics than the canard design, but both have overpressure levels 40% below the baseline levels. The three-engine concept is somewhat heavier than the others, in part because of the larger engines that are required. The economic findings are that the reduced block time achieved by supersonic flight over land makes the required revenue dependent on route structure.

This study demonstrates the advantages of sonic-boom minimization for an integrated aircraft design, and indicates a need to maintain research in this area. The results show that if the performance estimates for the low-sonic boom configuration are realistic, the higher over-land speed will have a large effect on HSCT passenger ticket prices and, ultimately, market share. The selected concepts will be tested in a wind tunnel to verify the higher-order aerodynamic methods used to predict aerodynamic performance and sonic-boom signatures.

Ames-Moffett contact: P. Gelhausen
(415) 604-5701
Headquarters program office: OAST

Impact of Technology on Future Sea-Based Attack Aircraft

Andrew S. Hahn, Jeffrey J. Samuels

The objective of this study was to evaluate the effect of technology on future carrier-based, subsonic attack aircraft. The impact of technology and mission requirements on aircraft takeoff gross weight (TOGW) was highlighted. Two different technology levels were used for the designs. Contemporary-technology designs show what performance could be expected if the designs were started in the early 1990s, whereas the future-technology designs show what could be expected in the near future.

This study included an aircraft configuration matrix so that mission effectiveness trade-offs could be evaluated for different operational strategies. The matrix included aircraft with light and medium bomb loads, one- and two-person crews, internal and external bomb bays, and flying wing planforms. Changes were controlled so that each aircraft could be directly compared to its neighbors in the matrix. The Light Attack class carries a single crewperson, a moderate avionics weight appropriate for daylight missions, and two bombs. The Medium Attack class is similar but carries four bombs. The Medium All Weather class carries a second crewperson and substantially more avionics and electrical equipment to perform night and all-weather missions and handle higher-threat environments. The Medium Internal class carries four bombs internally. The Medium Flying Wing class carries four bombs and a crew of two but uses an A-12 planform for reduced detectability.

The Ames aircraft design and analysis code ACSYNT was used to perform constrained optimization to determine the wing area, wing sweep, wing aspect ratio, body length, body diameter, engine scale, and fuel usage that yielded the lowest-TOGW design. Use of common technology assumptions, engine-cycle simulation code, and design mission (i.e., the mission that determines the aircraft's configuration and sizing), and consistent application of

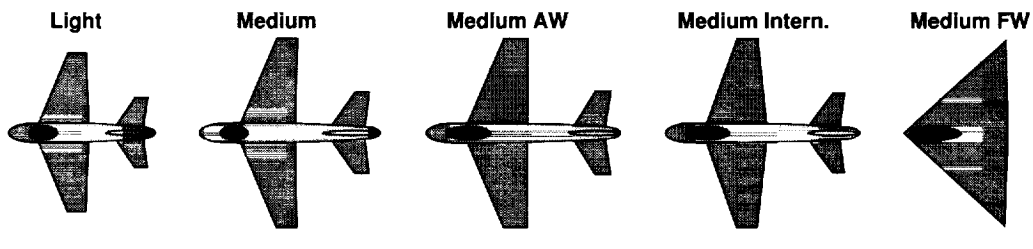

	Light	Medium	Medium AW	Medium Intern.	Medium FW
TOGW (lb)	24,777	33,438	37,573	34,486	26,392
Span (ft)	41.3	48.1	51.5	50.5	53.9
Length (ft)	38.2	45.2	48.2	49.8	30.8
Wing load	75.2	72.8	72.9	68.4	31.8
Thrust/weight	0.51	0.52	0.51	0.45	0.33

Fig. 1. Contemporary attack aircraft.

methods allows for direct comparison of the aircraft. The data generated include weights, dimensions, layout, maneuver performance, design constraints, and mission performance. The design mission was a modified version of the STOVL Strike Fighter Desired Operational Capabilities (SSF DOC) Interdiction mission. The gun model, number of rounds of ammunition, defensive missile type and carriage, armor weight, wing-fold weight, engine bypass ratio, tail volume coefficients, minimum body diameter, and maximum body length were all standardized.

Since the aircraft TOGWs were not sensitive to technology changes, and the same thrust and wing loading trends were noted in the future designs, only the contemporary-aircraft results are shown (see first figure). The second figure shows the ranges for the contemporary aircraft on the SSF DOC Close Air Support mission.

Findings for the different aircraft classes were compared. One Medium Attack aircraft weighs less than two Light Attack aircraft but has the same range and payload performance. This indicates that the additional load is beneficial from the range/payload standpoint, but this analysis does not address the cost or operational utility and flexibility of having twice as many light aircraft.

A second crewperson is less additional weight than two extra bombs, and provides additional capabilities.

The Medium Internal aircraft is lighter than the Medium All Weather. This indicates that internal weapons carriage actually saves weight. The TOGW of the Medium Attack class was reduced with internal weapons bays, primarily as a result of the reduced minimum drag. A sensitivity study of the internal-weapons-bay weight estimate showed that the TOGW of aircraft with internal weapons would be competitive with the external-weapons-carriage design even if the weapons-bay weight estimate were doubled. It is important to note that even without the bombs, the drag of external carriage typically increases zero-lift drag by 17%.

The Medium Flying Wing planform was the lightest and least sensitive of the designs and had the lowest thrust-to-weight ratio, the lowest fuel weight,

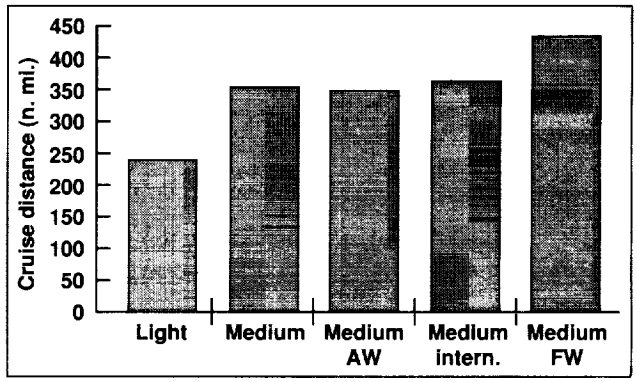

Fig. 2. Close Air Support mission cruise distances of contemporary aircraft.

and the best carrier waveoff capability of all the aircraft. This is largely due to the elimination of the vertical and horizontal tails. (The tail surfaces add weight, wetted area, and interference drag, but have little usable volume.) The Flying Wing trades these penalties for the additional cost and complexity of fly-by-wire and artificial stability. In addition, the Flying Wing was modeled with no interference and only half of the separation drag of a conventional fuselage-and-wing configuration. The clean zero-lift drag coefficient of the Flying Wing is about one third the drag of the other attack designs, and is due to the planform and not to the internal weapons carriage. The Flying Wing was also the only aircraft able to land with more than the design weapon load because the wing area was not constrained by the waveoff maneuver.

This study allowed a direct comparison between attack aircraft with different capabilities. Enough data were available to enable mission-effectiveness and cost analyses.

This work was presented at the AIAA Aircraft Designs Systems meeting in August 1992 and will be incorporated into a NASA technical memorandum.

Attack aircraft are difficult to compare because they have different capabilities. Results were normalized by the ratio of range times payload to gross weight, because an aircraft's cost is reflected by its TOGW. This figure of merit indicates the load-carrying capability of each aircraft with respect to its cost. As can be seen, all of the four-bomb aircraft have greater efficiency, which suggests that carrying more bombs may be more economical. The Medium Flying Wing is substantially more efficient than the others. The Flying Wing appears desirable from a capability-to-weight standpoint, but development costs may result in a higher cost per pound.

Ames-Moffett contact: A. Hahn
(415) 604-4235
Headquarters program office: OAST

Enhanced Quasi-Procedural Aircraft Design Program

Hirokazu Miura, David Schleicher

A new-generation conceptual aircraft design program based on quasi-procedural analysis was developed at Stanford University under the direction of Ilan Kroo. Conceptual-level aircraft design synthesis programs must interface with many analysis programs of diverse disciplines (which are composed of hundreds of subroutines), and share common data. Synergy among disciplines is critically important, but is often application dependent. Consequently, an aircraft synthesis program that uses the conventional rigid architecture is applicable only to specific types of aircraft and is difficult to modify or extend. Furthermore, such a program is likely to be inefficient when coupled with a design optimization program that requires a large number of analysis executions, because unnecessary calculations may be repeated and/or required responses are not calculated in the most convenient manner. Program efficiency is critical because aircraft synthesis programs must take advantage of advanced analysis tools that may require large amounts of time for automatic input data preparation as well as in execution of analyses.

The quasi-procedural method works with a set of compiled, procedural subroutines as the smallest program unit. In response to a request from the user or optimizer for evaluation of a dependent variable, the system determines which routine needs to be executed and then runs that routine. If the routine requires inputs from the data base, those inputs are provided to the routine by the executive module, which may require the execution of additional routines. This form of request-driven, backward-chaining execution is depicted in the first figure. Analysis routines communicate with the executive module and the data base in a simple fashion. Rather than passing data between the routines with global variables, each routine reads its input variables from the data base by calling the

utility routine GET, and sends computed results into the data base through the routine PUT.

Computational efficiency could be improved because the executive system keeps track of the variables that have been computed and only those parameters that affect them. When a request is made for the value of a dependent variable, the system recognizes whether that variable has been recently computed and is still valid or whether it must be recomputed. This aspect of the program architecture ensures consistency among the data in the data base and avoids unnecessary calculations. For example, consider the problem of calculating the lift coefficient ($C_{L)}$ of a high-aspect-ratio wing for variation of the twist angle at 20 spanwise stations, and the taper ratio. In calculating C_L, the most computationally intensive part is the assembly and factoring of the aerodynamic influence coefficient (AIC) matrix. Fortunately, this part of the calculation is independent of the twist variables and is only affected by the taper ratio. Thus, evaluation of the variation of C_L due to perturbation of any of the 20 twist variables will be a trivial operation. The second figure compares the total optimization times between the quasi-procedural and conventional methods. The figure indicates a significant savings obtained in the AIC calculation.

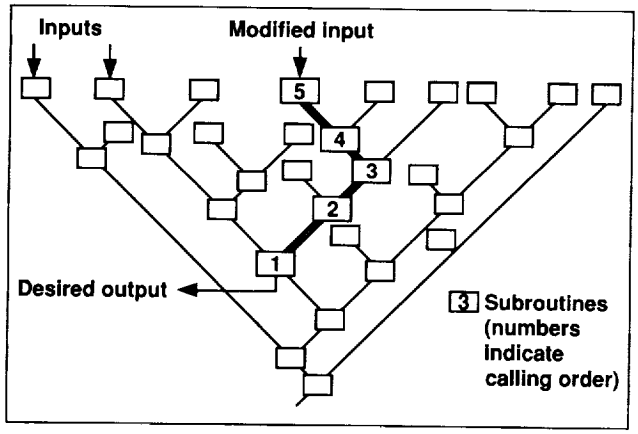

Fig. 1. Backward-chaining execution and consistency maintenance.

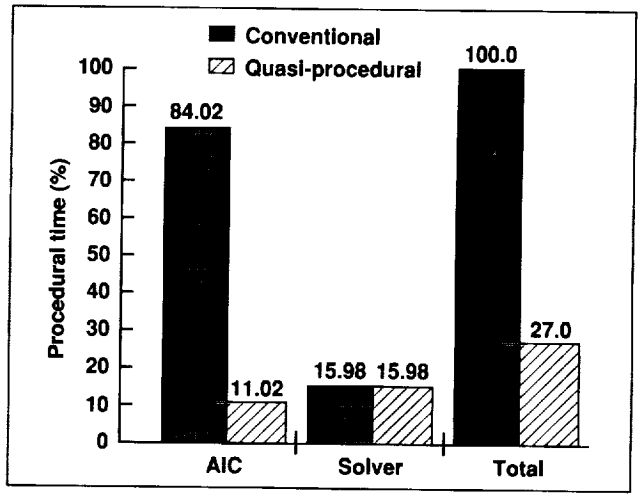

Fig. 2. Computational time distribution for quasi-procedural and conventional design methods.

Another significant innovation implemented in the new code is the efficient calculation of nonlinear system responses computed iteratively in the analysis modules. Such quantities frequently pose numerical problems for the optimization methods in achieving stable convergence. Problems of this type were shown to be alleviated by introducing carefully selected additional variables and constraints. This scheme again turned out to contribute significant improvement in the overall processing efficiency.

The program has been implemented on both engineering workstations and supercomputers. Not only is it currently applied to practical aircraft design problems at several U.S. aerospace companies, but some existing aircraft design codes are being rewritten as the results of successful demonstration of the quasi-procedural program architecture become known.

Ames-Moffett contact: D. Schleicher
(415) 604-5789
Headquarters program office: OAST

High-Speed Rotorcraft Economic Optimization

David R. Schleicher, James D. Phillips, Kevin Carbajal

The objective of NASA's high-speed rotorcraft study was to evaluate configurations and technologies that would allow the deployment of vehicles with both low-downwash characteristics and a forward-flight speed as high as 450 knots. An economic optimization study was conducted to assess the effect of cruise speed on the productivity and direct operating cost of a tiltrotor, a tiltwing, and a folding-tiltrotor aircraft.

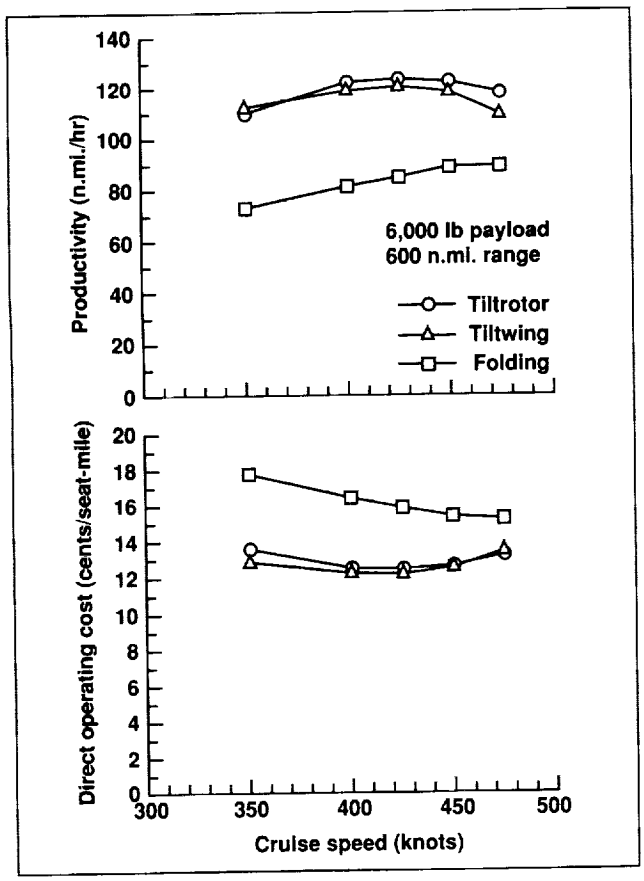

Fig. 1. High-speed rotorcraft: effect of cruise speed on productivity and direct operating cost.

Baseline models incorporating 1990 technology and using XV-15, V-22, CL-84, and XC-142A aircraft parameter values and performance trends were developed for a tiltrotor, a tiltwing, and a folding tiltrotor. Using the VASCOMP design synthesis program, the three concepts were sized for a civil transport mission with a 450-knot cruise speed, a 600-nautical-mile cruise distance, and a payload of 30 passengers plus baggage. A series of proposed advanced technologies were applied in combination to each of the current technology models. These advanced-technology configurations were then optimized for maximum productivity (payload weight × block speed/empty weight) and minimum direct operating cost for a range of cruise speeds between 350 and 475 knots. The effect of cruise speed on both vehicle productivity and direct operating cost for the three configurations is compared in the accompanying figure.

For the tiltrotor and the tiltwing, maximum productivity and minimum direct operating cost occur for a 425-knot cruise speed. Because the engine for these vehicles is primarily sized for cruise, these results show the tradeoff of decreasing block time and increasing engine power and vehicle empty weight. In the case of the folding tiltrotor, vehicle component weights stay relatively constant for the speeds under study because the rotor is uncoupled for the cruise mission segment and the resulting engine power is sized for hover. Thus, with increasing cruise speed, the folding tiltrotor productivity increases and direct operating cost decreases monotonically. This trend is primarily a function of the decreasing block time with increasing cruise speed.

The magnitude differences between the folding tiltrotor and the tiltrotor/tiltwing economic trends are a result of (1) the folding tiltrotor's significantly

heavier and less fuel-efficient convertible engine and (2) its large, low-disk-loading rotor which contains a heavy blade-folding mechanism. These two factors result in greater vehicle weight, lower productivity, and higher cost.

The results of this analysis show that advanced tiltrotors and tiltwings will be least costly for cruise speeds in the region of 425 knots. Advanced folding tiltrotors will be more costly to operate at all cruise speeds investigated. Future NASA high-speed rotorcraft research efforts will focus on technology to improve the economic viability of these vehicles.

Ames-Moffett contact: D. Schleicher
(415) 604-5789
Headquarters program office: OAST

Investigation of High Lift Coefficients on Rotating Airfoils

Peter D. Talbot, Martin D. Maisel

This research is aimed at understanding the source of unusually high lift coefficients (C_L) on rotating rotors and propeller blades under static thrust conditions. Experimental measurements made by Tung and Branum of the U.S. Army Aeroflightdynamics Directorate at Ames showed that locally measured C_L along the span of a three-bladed rotor continued to increase with increases in collective pitch. In many cases these C_Ls exceed expected values for the same type of airfoil tested under two-dimensional (2-D) conditions. No one has yet defined the variation of C_L with pitch for very high pitch angles (to 45 degrees) in a rotating environment. However, total propeller thrust measurements support the idea that stalling does not occur in the same way as on a wing. An interesting example is afforded by the data from a NASA report (CR-180848) which shows thrust versus pitch up to large (50-degree) angles for a seven-bladed swept-rotor propfan. There is no drop-off in thrust as pitch increases. A review of the literature has turned up other instances of this phenomenon but references to it are relatively rare. There seems to be little agreement about the underlying aerodynamic behavior. The objective of this research is to study this behavior analytically (using computational fluid dynamics codes) and experimentally to provide an understanding of its causes. A broader insight is expected from expanding the data of Tung and Branum to higher pitch angles in a hover facility.

Propellers and rotors were investigated using classical blade-element momentum theory models. Comparisons of predicted thrust, using modified airfoil characteristics and a blade-element model, required a lift variation beyond the point of stall quite different from that of a 2-D wing section. The results, shown in the figure, are a motivation for further model tests: 2-D airfoil data departs significantly from the test values at high pitch angles. There were two limitations to the original data set: maximum collective pitch was only 28 degrees, and no boundary layer information was available. It is intended to pursue the experiment of Tung and Branum to higher collective pitch angles so that the point of stall can actually be

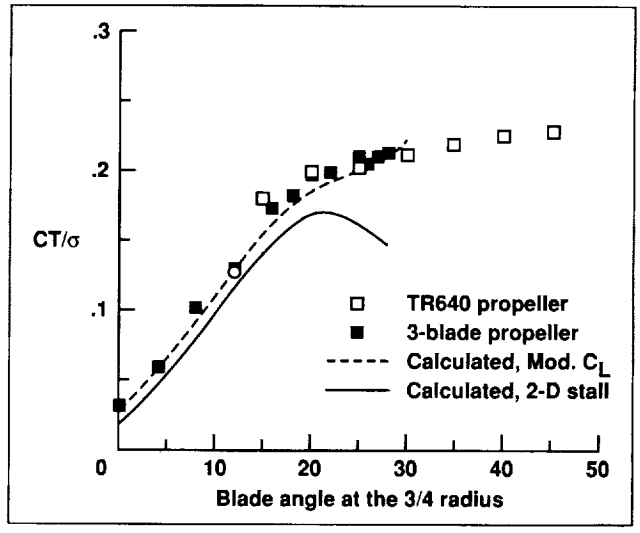

Fig. 1. Thrust behavior at high collective pitch compared to blade-element models.

seen and the performance can be measured. Also, a more controlled measure of lift versus pitch will be made for a known airfoil section. The calculations and a literature search have been completed. The propeller is to be tested in the Army anechoic chamber at Ames in mid-1993 after modifications to its blade section.

This research will be useful for a more precise prediction of the performance limits of tail rotors. It is necessary to know maximum thrust for handling qualities purposes and to accurately predict torque and thrust for loads and power during design. Also, any rotor or propeller mathematical models that use 2-D test data for airfoil characteristics would give improper results at the highest thrust levels. The results may be applicable to windmill aerodynamics at high thrust levels. An understanding of the phenomenon may lead to improved rotor designs.

Ames-Moffett contact: P. Talbot
(415) 604-5108
Headquarters program office: OAST

Comprehensive Rotorcraft Analytical Methods

Joseph J. Totah

The objective of this work is to develop and implement analytical tools that enhance the prediction of complex rotorcraft behavior.

The approach taken is to evaluate the accuracy of the state-of-the-art comprehensive rotorcraft analysis codes, such as CAMRAD/JA (Comprehensive Analytical Model of Rotorcraft Aerodynamics and Dynamics/Johnson Aeronautics), in the prediction of rotor system performance, loads, and stability, and to identify and address sources of inaccuracies in order to enhance the analysis and design of advanced rotor systems. It is important that accurate vehicle representations be established. A major effort was undertaken to assess the accuracy of the UH-60 main-rotor blade aerodynamics, which are a critical part of the CAMRAD/JA UH-60 model. An evaluation of several sets of airfoil data has been performed and the results have been published. The first figure illustrates the differences between accurate lift-curve-slope data and inaccurate data for the SC1095 airfoil section. This figure shows that accurate data exhibit a slightly different and less scattered trend than inaccurate data. Semiempirical expressions (shown by the solid line) were used to independently check the accurate data trends, and excellent correlation was obtained.

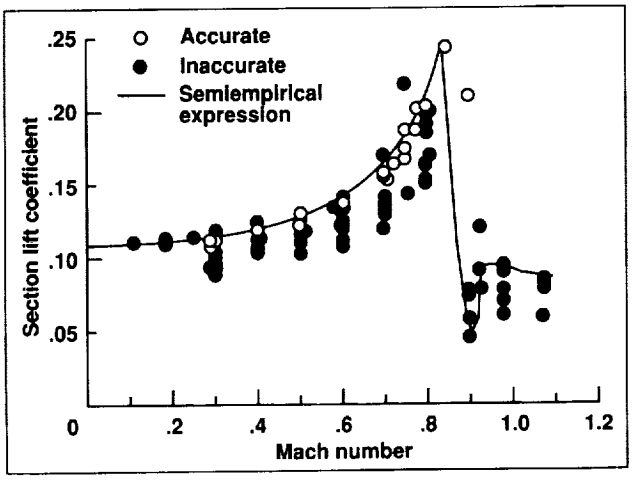

Fig. 1. SC1095 lift-curve slope versus Mach number.

CAMRAD/JA was modified in 1989 to allow for an option to use a 3 × 3 control-system-stiffness matrix to model control-system coupling resulting from structural flexibility that can occur in gimbaled rotor systems. Although this modification was an improvement, limitations were discovered in its implementation in CAMRAD/JA. These limitations were rectified this year through exhaustive correlative efforts using an XV-15 CAMRAD/JA model. The results presented in the second figure show a significant improvement in the prediction of 3/rev control loads in helicopter-mode forward flight of the XV-15 with advanced technology blades (ATB) than had been previously realized.

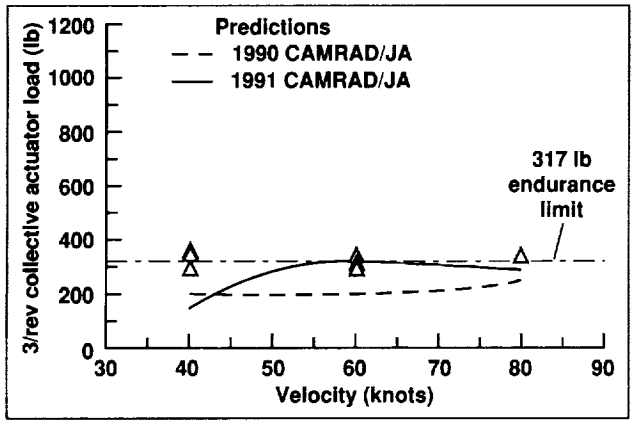

Fig. 2. Comparison of improved CAMRAD/JA predictions of XV-15/ATB 3/rev collective actuator loads.

New airfoil aerodynamics will be synthesized using the published results from the evaluation of UH-60 main-rotor blade airfoil data. The synthesized aerodynamics will be used in CAMRAD/JA in preparation for correlation with high-quality airloads data gathered from the UH-60 Phase II Program. Further performance and loads correlation efforts are planned for the XV-15/ATBs in order to document improvements realized by proper implementation of new and innovative methodologies in comprehensive analytical rotorcraft codes such as CAMRAD/JA.

Ames-Moffett contact: J. Totah
(415) 604-5057
Headquarters program office: OAST

Small-Scale Investigation of Jet-Induced Effects

Douglas A. Wardwell, Craig E. Hange

The objective of these small-scale investigations was to investigate the effects of jet flows during hover on the McDonnell Douglas mixed-flow vectored-thrust (MFVT) advanced short takeoff/vertical landing (ASTOVL) concept. Aerodynamic jet-induced and hot-gas ingestion characteristics were investigated.

A 5.3%-scale contoured model representing the two-jet MFVT ASTOVL configuration was built and instrumented to measure forces, pressures, and temperatures. The model was tested at the Jet Calibration and Hover Test (JCAHT) Facility at Ames. The first figure shows the model attached to the hover test rig. Nozzle thrust calibrations and exit flow surveys were also obtained at the JCAHT Facility. Nozzle sets tested were 0, 10, and 30 degrees from vertical. Although the model was fixed to the test rig, the 8-foot × 8-foot ground plane was movable so that changes in model pitch, roll, and altitude could be simulated. Aerodynamic forces on the model were measured with a six-component task balance. Pressures on the model undersurface were measured with mechanical scanivalves. Air temperatures on the model undersurface and at the inlets were measured with thermocouples. Maximum nozzle exit temperature during the test was 600°F. Some infrared images were

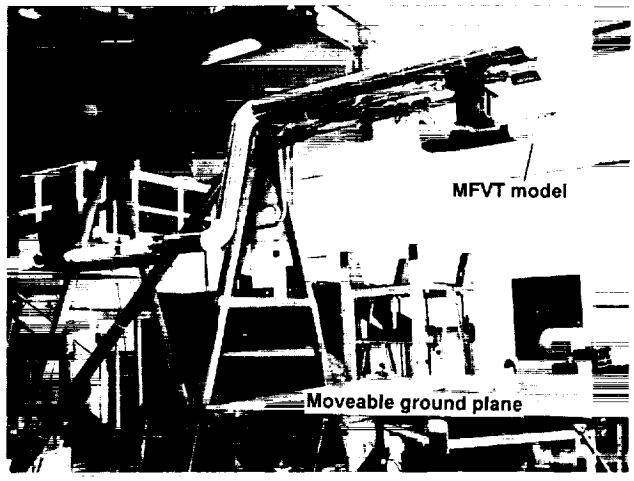

Fig. 1. MFVT model ready for testing on the hover test rig.

taken to investigate the possibility of using infrared for data acquisition and flow visualization.

The second figure shows lift loss (ΔL) data nondimensionalized by total thrust (T) as a function of height (H) nondimensionalized by equivalent jet diameter (D_e) as compared to predictions. Agreement

at the lower heights, where differences can be large, is encouraging.

Jet-induced lift and hot-gas ingestion characteristics for STOVL aircraft are very configuration dependent. The planform shape, nozzle layout, nozzle shape, and jet pressure ratio all contribute heavily to these characteristics. Data from this model will be added to the STOVL ground effects data base. This data base will be useful in the development of more accurate empirical/analytical prediction techniques for both aerodynamic force and hot-gas ingestion characteristics during hover. Current prediction routines give "order of magnitude" numbers and trends, but more accurate data are required for detailed aircraft design.

Any future small-scale ground effects tests are contingent on the needs of the Department of Defense for support of future STOVL programs.

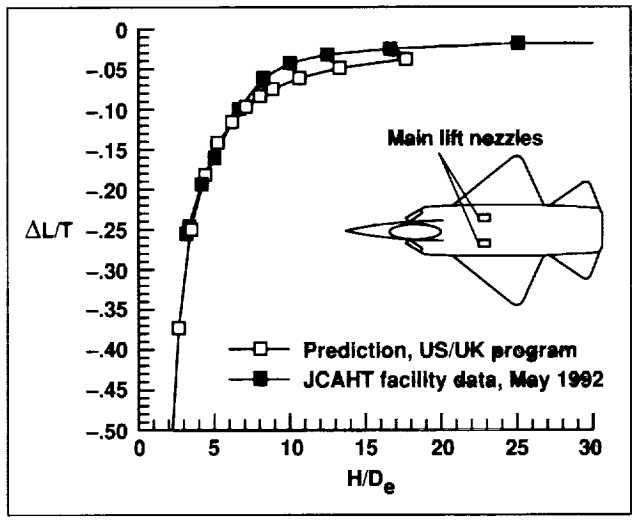

Fig. 2. Comparison of measured jet-induced lift to predictions for the MFVT configuration in horizontal hover (0-degree nozzles, level ground).

Ames-Moffett contact: D. Wardwell
(415) 604-6566
Headquarters program office: OAST

Tiltrotor Aircraft/Vertiport Feasibility Studies Data Package

John Zuk

The development and validation of tiltrotor technology by the United States government and industry in the past two decades has placed the United States in an international leadership position with respect to tiltrotor aircraft. The current military V-22 Osprey is the first tiltrotor production aircraft in the world. The implications for civil aviation are significant. A fleet of civil tiltrotor aircraft operating in a modernized national airspace system is expected to reduce current metropolitan air traffic congestion and to provide a practical alternative for meeting short-haul air transportation demands.

Tiltrotor aircraft could increase airport capacity by (1) bypassing existing airports altogether by operating from strategically located vertiports and (2) operating as hub-feeder commuter aircraft by replacing turboprops at airports and thus freeing turboprop runway slots for larger aircraft. Assessment of the feasibility of using tiltrotors in the national transportation system was undertaken in the FAA/NASA Civil Tiltrotor Missions and Applications Studies (Phases I and II). The studies were conducted jointly by the Boeing Commercial Airplane Group, Bell Helicopter Textron, and Boeing Helicopter. They found that the success of the civil tiltrotor will require (1) a market-responsive design, (2) changes to the airspace regulations that will allow the tiltrotor's unique operating capability to be fully utilized, and (3) development of vertiports. The FAA has formulated a vertical-flight program plan that addresses changes in the airspace regulations.

A tiltrotor-aircraft data package has been formulated by NASA to conduct the feasibility assessments. Configuration, performance, and operating data are provided for 8-, 19-, 31-, 40-, 52-, and 75-passenger aircraft. Two ways of obtaining cost data are included:

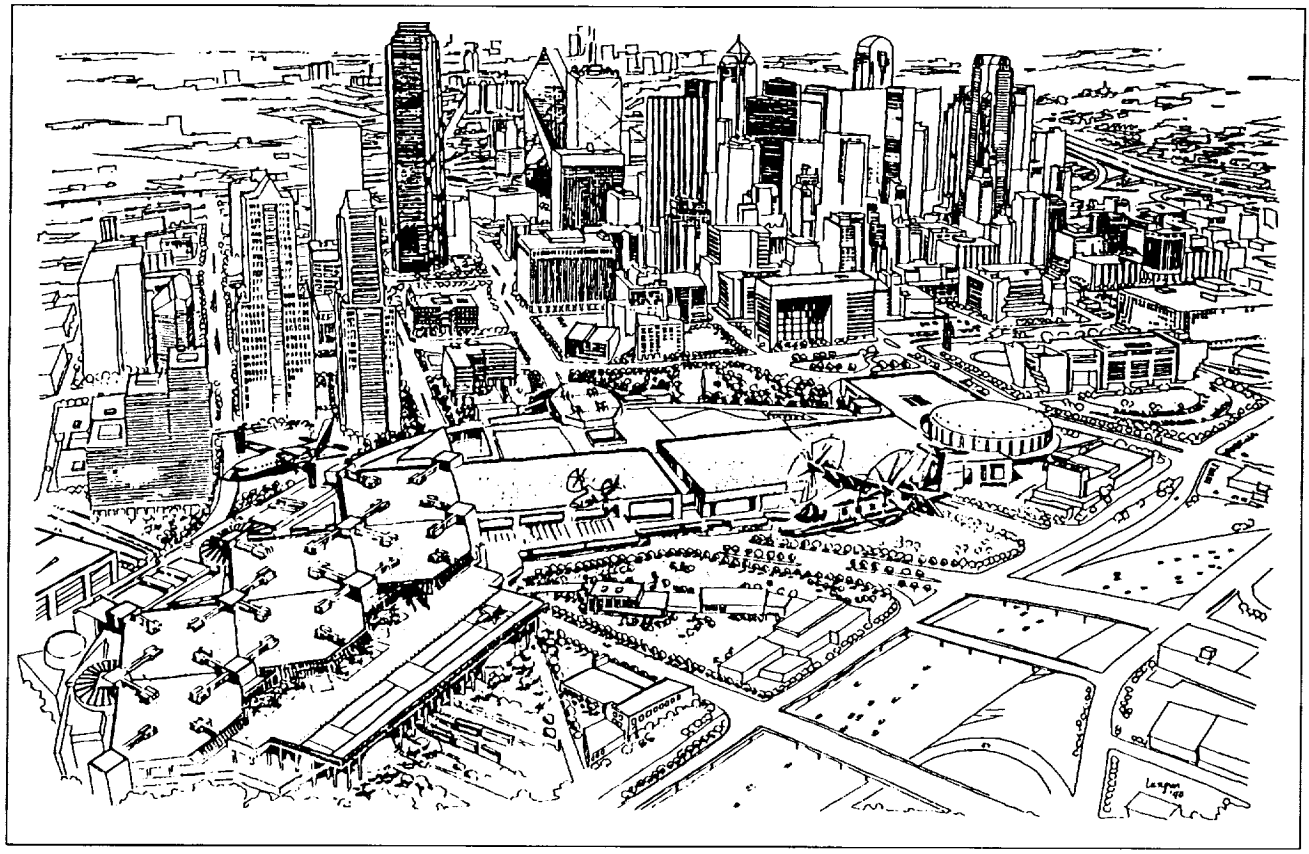

Fig. 1. Dallas Vertiport.

(1) tables for trip distances of 200, 300, and 500 nautical miles, and (2) generalized cost formulas in which size and trip distances are variables. Each size of tiltrotor aircraft is also compared with a turboprop aircraft of equivalent size.

The initial acquisition cost of a tiltrotor aircraft is 1.5 times greater than that of an equivalent turboprop. The total tiltrotor-aircraft trip cost for 200 nautical miles is 1.3 times greater than that for the equivalent turboprop, and the cash operating cost is 1.2 times greater.

This data package is especially useful for intermodal transportation studies such as those encouraged by the Intermodal Surface Transportation Act of 1991, and for the planning of intermodal terminals. Intermodal terminals will integrate ground transportation with vertical-flight air transportation. Tiltrotor aircraft will land on the roof of the intermodal terminals. The data package was used for the new intermodal transportation center at the Dallas Convention Center. As shown in the figure, the vertiport is part of its transportation system. In addition, more than 17 state, regional, and local vertiport studies using this data package are under way.

Ames-Moffett contact: J. Zuk
(415) 604-6568
Headquarters program office: OAST

Optimum Airfoil Design Analysis

Fort Felker

A new method has been developed for the design of optimum airfoils. The method uses the Navier–Stokes equations with a turbulence model as the governing equations for the fluid flow. A generalized-reduced-gradient method is used to find the optimum airfoil shape at a specified operating condition. The analysis is fast enough for implementation on any high-performance workstation.

Earlier airfoil optimization analyses used a limited set of shape functions to define the airfoil geometry. The airfoil shape found by these analyses was the best of the shapes that could be described using the arbitrarily chosen shape functions. The new analysis method overcomes this limitation by allowing the locations of all points that define the airfoil surface to be design variables. Also, the new method uses the Navier–Stokes equations to govern the flow instead of the full-potential equation used by earlier analyses.

This analysis method has been used to calculate the airfoil shape for minimum drag at transonic Mach numbers and zero lift. A NACA 0012 was used as the initial airfoil geometry, because its properties in transonic flow are well documented. The first figure shows the pressure distributions (C_p) on the NACA 0012 and final optimum airfoils. The shock developed by the NACA 0012 airfoil at this Mach number is eliminated on the optimum airfoil, resulting in lower drag. The second figure shows the convergence history for this case. The drag (C_d) is steadily reduced in the analysis, and the final drag is even lower than the subcritical drag of the NACA 0012.

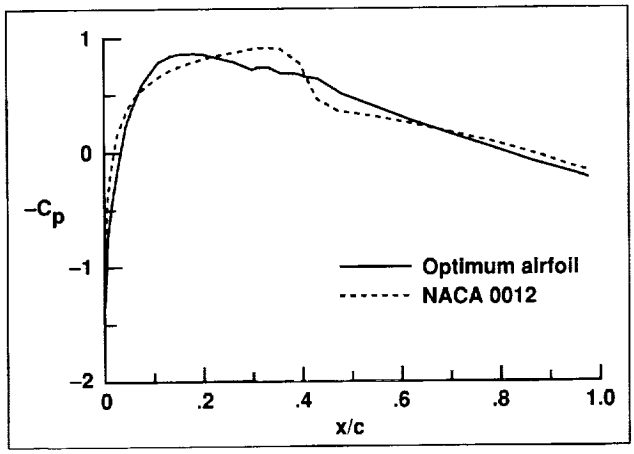

Fig. 1. Comparisons of surface pressure distributions on initial NACA 0012 and final optimum airfoils. Mach number = 0.78.

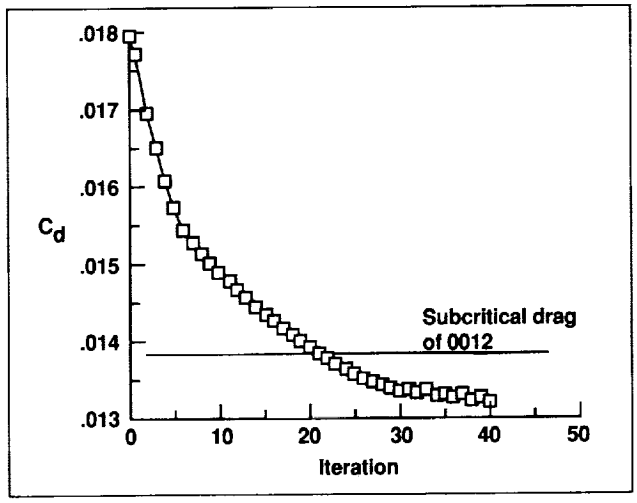

Fig. 2. Convergence history for optimum airfoil design analysis.

Work is under way to apply the analysis to lifting, nonsymmetric airfoils. Also, the Baldwin–Barth one-equation turbulence model will be used in subsequent versions of the analysis, instead of the Baldwin–Lomax turbulence model which is currently used.

Ames-Moffett contact: F. Felker
(415) 604-6096
Headquarters program office: OAST

Fighter Lift and Control Program

Scott Harris

The development of reduced-observability fighter aircraft presents a major challenge to the aerodynamicist charged with ensuring that aircraft maneuver levels are not compromised. The reduced-observability vehicle shapes and control concepts are fundamentally different from those of past air combat aircraft, and the drag of delta/diamond-planform wings at maneuver conditions is generally higher than that produced by the trapezoidal planforms used on aircraft such as the F-15 and F-16.

The Fighter Lift and Control (FLAC) program is a cooperative research effort between NASA Ames and the U.S. Air Force Wright Laboratory. It involves small- and large-scale wind tunnel tests and computational analysis of unique lift augmentation and control concepts on a realistic, low-observability fighter configuration. The goal of this program is to enhance the maneuver and control capability of future military aircraft.

The program includes several wind tunnel tests at Ames to determine the effectiveness of various high-lift, forebody vortex control, and leading-edge-extension vortex control concepts. The culmination of the program will be the testing of the most promising lift and control concepts on a 55%-scale model in the 40- by 80-Foot Wind Tunnel at full-scale Reynolds numbers. The configuration to be tested is shown in the first figure.

The first test in the FLAC program, of a 26%-scale semispan wing model, was conducted in the 7- by 10-Foot Wind Tunnel in the summer of 1992. Control surfaces consist of a three-section, full-span leading-edge flap and a two-section, partial-span trailing-edge flap. The airfoil is representative of that for a transonic fighter aircraft that has a sharp leading edge and a maximum thickness-to-chord ratio of 4.5%. Data obtained included wind-tunnel-scale system loads, test-section wall pressures, ground board pressures, total pressure surveys in the wing boundary layer, and flow visualization using surface oil, tufts, and off-body smoke.

The purpose of the semispan test was to improve the baseline aerodynamics of the FLAC wing in the angle-of-attack range typical of maneuver or combat. Passive and active boundary layer control devices were tested to determine their effectiveness at delaying separation and hence improving the maximum lift coefficient ($C_{L_{max}}$) and the lift-to-drag ratio. Various sizes and shapes of vortex generators, Gurney flaps, and other flow-control concepts were tested. In addition, the effectiveness of blowing streamwise and tangentially to the wing upper surface was explored at different mass flow coefficients.

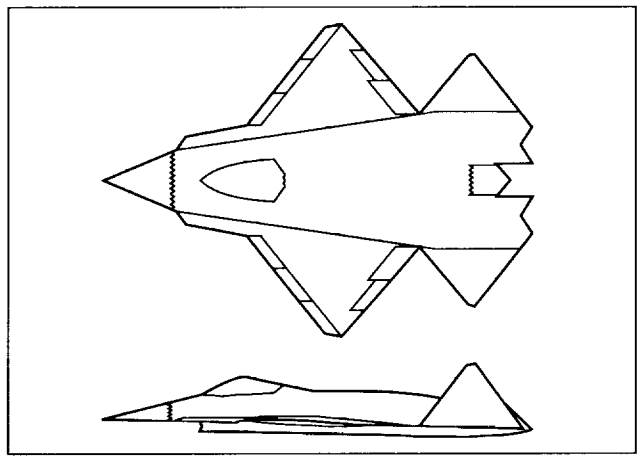

Fig. 1. Fighter Lift and Control program model configuration.

Wing blowing and the Gurney flap showed the most promise for improving the baseline aerodynamics. The blowing system consisted of partial-span slots placed at the leading-edge-flap hinge line. With wing blowing, $C_{L_{max}}$ was increased by as much as 10% and the maximum lift-to-drag ratio was increased by as much as 14%. A Gurney flap is a small (1%–3% of the wing chord) circulation control device placed on the lower surface near the trailing edge. With the Gurney flap, $C_{L_{max}}$ was increased by as much as 21%. In addition, the lift-to-drag ratio was consistently improved for higher lift coefficients by both devices.

The surface oil-flow pattern shown in the second figure demonstrates the complex flow field around

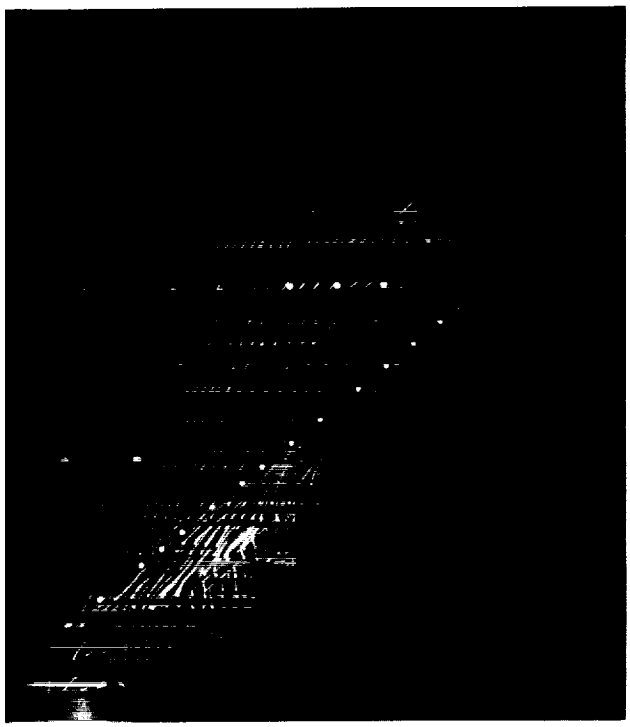

Fig. 2. Oil flow on the semispan wing model. (See color plate 2 in Appendix)

this wing. The presence of separation along the entire leading-edge flap complicates the use of vortex generators to increase wing performance. As a result of this test, modifications to the wing geometry will be made to improve the maneuver performance.

The second test in the FLAC program, of a full-configuration, 10%-scale model in the 7- by 10-Foot Wind Tunnel, is scheduled for February 1993. Forebody blowing, forebody strakes, and other vortex flow control devices will be tested. The goal is to determine the most effective concept for generating lateral control at angles of attack at which the rudders are ineffective. The large-scale model is currently in the design and fabrication stage and will include the best concepts for lateral control and maneuver-performance enhancement identified in the small-scale tests. The large-scale test is scheduled for the summer of 1994.

Ames-Moffett contact: L. Meyn
(415) 604-5038
Headquarters program office: OAST

Study of Aeroelastic Problems Using Active Controls

Stephen A. Jacklin

Two mechanisms have been considered for introducing higher harmonic control and individual blade control (IBC) to reduce rotor hub loads and vibrations. The first is to change the blade angle of attack through twisting of the blade root, as could be normally done by a helicopter swashplate. The second method is to induce changes in the blade pitch through movement of a servoflap placed on the outboard blade trailing edge (see figure). Thus far, only 4-per-rev higher harmonic control has been considered.

A major accomplishment of the past year's effort was to replace the spring-restrained, rigid rotor used previously. The new rotor model has a fully elastic blade representation with flap, lag, and torsional coupling. Tests of this new model with and without

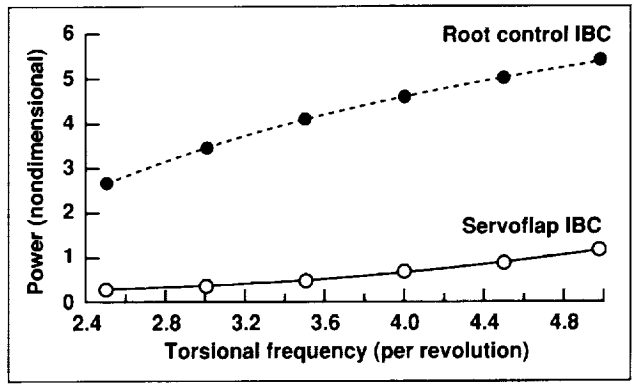

Fig. 1. Power reduction achievable through servoflap control.

the servoflaps have shown that with the servoflaps, about one-fifth as much power is required as when the whole rotor blade is moved from the root. The root control was estimated to take about 2% of the total rotor power. Although very encouraging, the results are considered preliminary and will be further investigated next year using an improved aerodynamic representation. The effect of additional harmonics will also be considered.

Ames-Moffett contact: Stephen A. Jacklin
(415) 604-4567
Headquarters program office: OAST

McDonnell Douglas Explorer Helicopter Test

Stephen A. Jacklin

The McDonnell Douglas Helicopter Company (MDHC) and Ames Research Center have jointly conducted a test of the MDHC Explorer rotor in the Ames 40- by 80-Foot Wind Tunnel (see figure). Test results showed that the control loads were low enough to make a hydraulically boosted control system unnecessary. Thus the MDX Explorer aircraft could be manufactured with a purely mechanical control system, which would make the aircraft lighter, more reliable, and less costly to maintain. The MDX Explorer will be the largest helicopter to fly without a hydraulically boosted control system. The information gained in this study is a valuable product of wind tunnel testing.

Another wind tunnel test will be performed in fiscal year 93. Pressure-instrumented rotor blades will be used to gain a better understanding of the sources of the rotor aerodynamic loading, both with and without higher harmonic control. A subsequent joint flight-test program is being discussed.

Ames-Moffett contact: Stephen A. Jacklin
(415) 604-4567
Headquarters program office: OAST

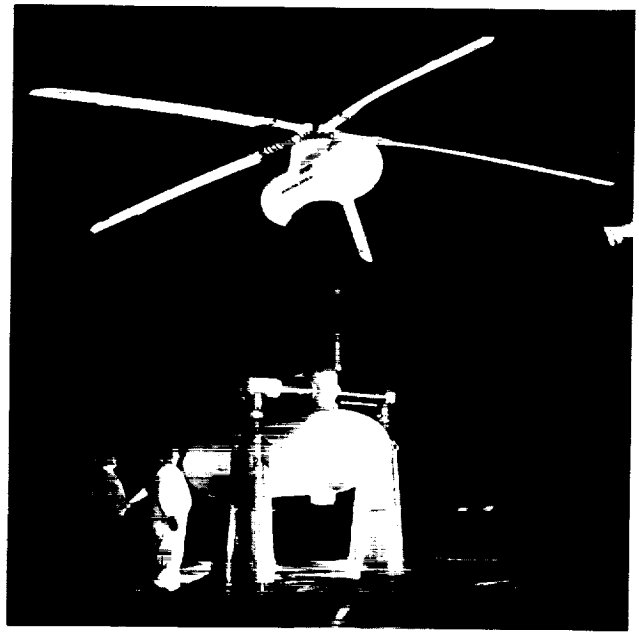

Fig. 1. MDX Explorer rotor in the Ames 40- by 80-Foot Wind Tunnel.

Hub Loads Reduction: Blade Root Torsional Dampers

Sesi Kottapalli

A new method of reducing helicopter rotor hub loads and marginally improving rotor performance by the introduction of large values of blade root torsional damping is presented. Theoretical considerations show that reduction of hub loads can come about by changes to the blade elastic torsional deflection. This basic theory was analytically verified by using a fully coupled aeroelastic rotorcraft analysis applied to a modern, articulated rotor blade, the Sikorsky S-76. From an implementation standpoint, a root-based torsional damping device may be more practical than one that involves a major portion of the blade span. Also, a root-based device may allow retrofitting of existing helicopter rotor blade/hub configurations.

Ames-Moffett contact: S. Kottapalli
(415) 604-3092
Headquarters program office: OAST

Hub Loads Reduction: Sources of Inplane Shears

Sesi Kottapalli

Recent analytical work performed at Ames has shown that at high airspeeds, for a moderate-thrust helicopter, the inplane vibratory shears that are produced at the rotor hub are much larger than the vertical vibratory shear. The present study identifies the sources that contribute to these inplane vibratory shears. One of the major approaches to helicopter vibration reduction is to reduce the shears through the addition of external mechanical devices. For example, Sikorsky Aircraft has added two sets of bifilars to its S-76 hub. A systematic approach is currently being followed that attacks the basic inplane hub shears and dissects them. The blade chordwise inplane shear is the important shear. It has three major components: the aerodynamic component, the inertial component, and the Coriolis contribution. From simplified equations and numerical estimations, it has been found that the chordwise inplane shear and, consequently, the hub inplane shears are strongly dependent on the out-of-plane response. The sources of helicopter rotor hub inplane shears lie not only in the inplane response but depend, perhaps strongly, on the flap and elastic flatwise responses or modes. This finding is based on the results obtained from a fully coupled rotorcraft aeroelastic analysis code wherein a modern, four-bladed, articulated rotor at 160 knots and 10,000 pounds thrust was analytically simulated.

Ames-Moffett contact: S. Kottapalli
(415) 604-3092
Headquarters program office: OAST

Full-Scale Higher Harmonic Control to Reduce Hub Loads and Noise

Sesi Kottapalli, Stephen Swanson

Open-loop higher harmonic control has been researched in the 40- by 80-Foot Wind Tunnel at Ames. The test involved the modern, five-bladed, moderate-thrust Sikorsky bearingless main rotor. Reductions in dynamic hub loads (1- and 5-per-rev) and, separately, reductions in noise that is caused by blade–vortex interaction (BVI) were obtained. A study was also made of the effect of 2-per-rev control on hub loads. During dynamics testing, the maximum airspeed was 160 knots and the thrust was kept constant at 14,000 pounds, with 1-per-rev and 5-per-rev control exercised separately. The full-scale BVI experiments were conducted at 12,000 pounds thrust and at 60 and 80 knots, with 5-per-rev control. In both hub-load and noise experiments, testing was conducted with all three modes of control: collective, lateral, and longitudinal. The amplitude and phase in each of these modes were varied to determine their optimum values. It was found that in cruise, at speeds from 120 to 160 knots, the 5-per-rev side force was reduced substantially by lateral control. A substantial reduction in the 1-per-rev normal force was achieved with 1-per-rev collective control. In the noise tests, at the BVI flight condition (descent, 60 and 80 knots), a reduction in BVI-related noise up to 5 decibels was consistently obtained. This was achieved by the application of lateral control. As reported earlier by others, noise and hub-load reductions require different modes of control, lateral versus collective, at this acoustic flight condition.

Ames-Moffett contact: S. Kottapalli
(415) 604-3092
Headquarters program office: OAST

Rotor Design Optimization Using a Free-Wake Model

Jeffrey Light

A Small Business Innovative Research (SBIR) Phase 2 contract was recently completed with Continuum Dynamics, Inc., of Princeton, N.J., to develop a rotor design optimization program. The resulting computer program, HERO (Helicopter Rotor Optimization), allows optimization of helicopter rotor hover performance. It couples state-of-the-art predictive techniques with an efficient optimization methodology.

The predictive portion of this program is based on the computer program EHPIC (Evaluation of Hover Performance using Influence Coefficients), which accurately predicts the aerodynamic performance of the rotor. EHPIC uses curved vortex elements and an influence coefficient relaxation technique to develop a force-free wake structure. In the current effort, improvements were made to the baseline EHPIC program, including the addition of a finite-element

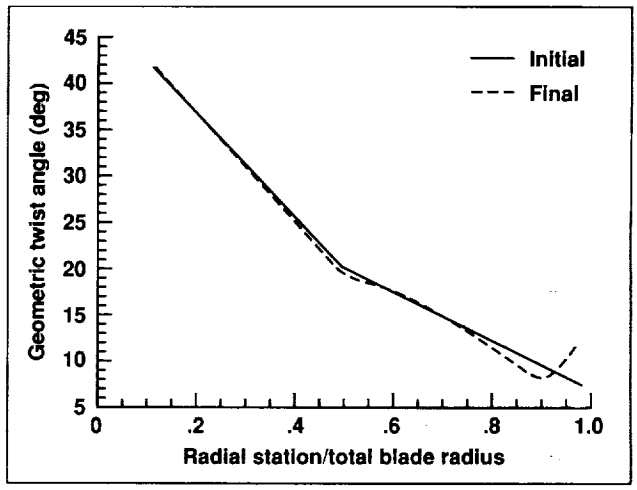

Fig. 1. Initial and final blade twist for optimized tiltrotor hover performance.

blade structural model, high-resolution rotor wake computations, and a lift limitation model.

The optimization methodology behind HERO is based on a general linear/quadratic programming algorithm. Computation time is minimized because many of the derivatives required by the optimization technique are routinely calculated during the wake relaxation in the EHPIC program. A variety of objective functions are available, including thrust, power, and propulsive efficiency. Design variables available include blade twist, chord, anhedral, and sweep.

In general, optimized designs were found to have a more uniform bound circulation distribution than the baseline cases. An XV-15 rotor was examined in one sample case. The design variables used were blade twist and tip sweep (outer 10% of radius). A reduction in power of 3% at a constant thrust was obtained. The principal change made by the analysis was the introduction of an up-twist near the blade tip (see figure). This characteristic was obtained for several optimization cases, and may be generally applicable to a variety of rotors.

Ames-Moffett contact: J. Light
(415) 604-4881
Headquarters program office: OAST

Tiltrotor Download and Acoustics Research

Jeffrey Light, Marianne Mosher

A small-scale test was completed that examined the download on a wing in the wake of a tiltrotor. A 7/38-scale V-22 rotor was mounted on the Ames Hover Test Rig (HTR), and two tiltrotor-type wings were tested (see figure). An image plane was used to represent the effect of the second rotor in a tiltrotor configuration. Measurements obtained included rotor performance and acoustics, wing loads, and wing surface pressures (static and dynamic).

A technique for reducing wing download using upper-surface blowing was examined. This technique uses spanwise jets of air to entrain the flow and reduce download. For a thrust coefficient representative of the V-22 aircraft in hover, the download was reduced from 9% to 8% of thrust. Various rotor/wing configuration changes were also examined, including wing sweep, rotor/wing separation distance, and wingspan.

Acoustic measurements were made to examine the impact of configuration changes and download reduction techniques. The microphones were located 5 rotor radii from the rotor centerline perpendicular to the wing, and 3 rotor radii below the rotor.

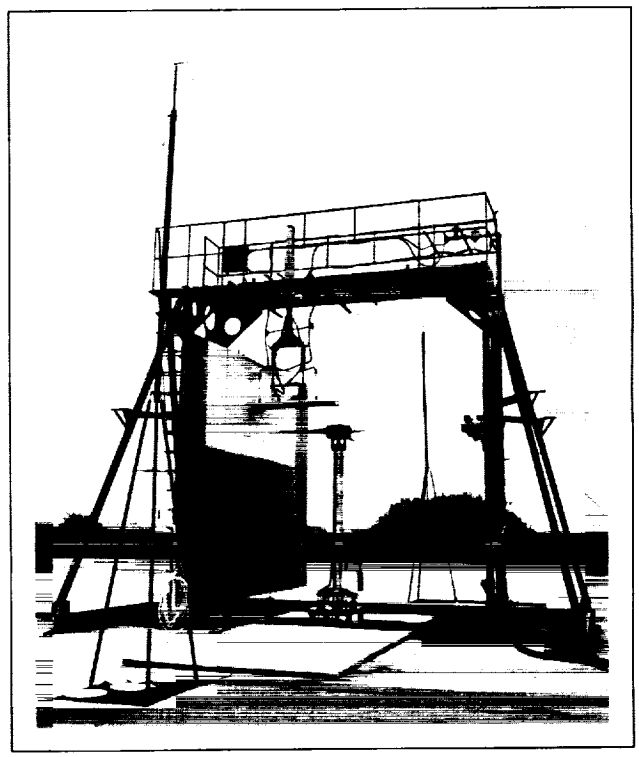

Fig. 1. Installation for tiltrotor hover download and acoustic testing.

Ames-Moffett contact: J. Light
(415) 604-4881
Headquarters program office: OAST

Exact Domain Decomposition and Parallel Processing for Rotorcraft Computational Fluid Dynamics

Wayne O. Miller

Computational fluid dynamics uses computer modeling for the prediction of fluid flows. A pertinent example is modeling of the airflow around helicopter rotor blades for the prediction of lift, drag, and noise. However, the computational requirements of such models have consistently challenged available computing resources, primarily because of the large problem sizes (domains) required for aerodynamic analyses. Rotorcraft analyses are especially demanding because of the wide range of phenomena that must be modeled, such as shock formation and boundary layer separation.

This research involves the application of domain decomposition and parallel processing to reduce the computational demands of such large analyses. Domain decomposition is the breaking up of one large problem into several smaller ones. This is obviously an advantage when the total effort spent in solving the several smaller problems is less than that required to solve the original large problem. It is not usually possible to completely separate, or decouple, the smaller problems from one another. Consequently, their solutions must be found repeatedly, using an iteration procedure, and the overall solution effort increases with the number of iterations required.

A unique aspect of the present research is that the smaller problems created by the decomposition process are decoupled in a mathematically exact sense. Therefore, only one solution of each smaller problem is required. The model problem currently being considered is the Poisson boundary value problem, which is a linear elliptic partial differential equation of importance to fluid dynamics. As shown in the figure, the problem domain is first discretized into a grid, and then is decomposed into several subdomains which pose smaller versions of the original problem. The exact information needed at the subdomain boundary nodes is found with the present approach, and the solution at the internal nodes is found using traditional means. Future research will extend the method to problems of rotorcraft aerodynamics.

Parallel computing is a natural extension of domain decomposition methods, because each subdomain problem represents an individual computational task. Consequently many processing units can be effectively used in parallel on the decomposed problem. The possible payoffs of using the present domain decomposition technique with loosely synchronous parallel computers are being examined. This would be an effective use of modern parallel computers, and should result in a further reduction of the computational resources needed for aerodynamic analyses.

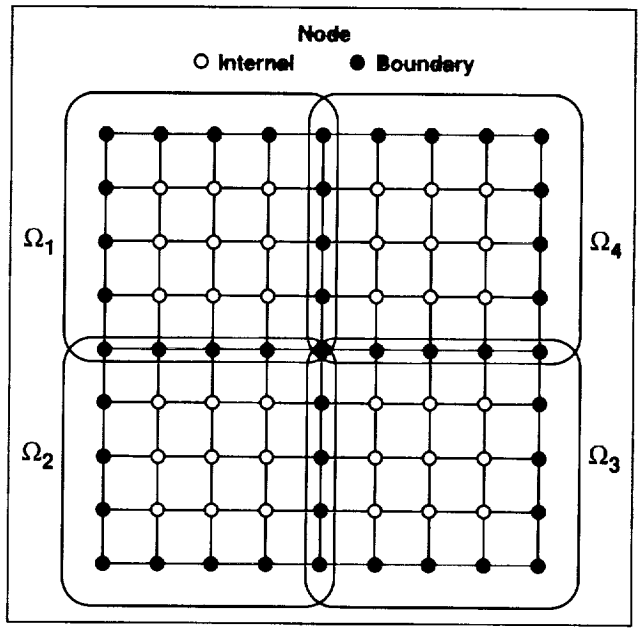

Fig. 1. Domain decomposition of a 9 × 9 grid into four 5 × 5 subdomains (subdomains share boundary nodes). Problem reduced from one domain with 7 × 7 = 49 unknown nodes to four with 3 × 3 = 9 unknown nodes each.

Ames-Moffett contact: W. Miller/F. Felker
(415) 604-6719/6096
Headquarters program office: OAST

Wind Tunnel Evaluation of a Sikorsky Bearingless Main Rotor

Thomas R. Norman

A Sikorsky Bearingless Main Rotor (SBMR) was successfully tested in the 40- by 80-foot test section of the Ames National Full-Scale Aerodynamics Complex (NFAC). This 44-foot-diameter demonstrator rotor system uses existing S-76 composite main rotor blades and a new five-bladed hub, employing design features similar to the rotor proposed for the RAH-66 Comanche. The rotor was first tested on the Sikorsky Main Rotor Whirl Stand, in 1991. A memorandum of agreement (MOA) was then signed to perform a wind tunnel test at Ames. Under the MOA, Sikorsky performed additional qualification testing and analysis to support the test program. NASA provided technical support during the pretest effort and then tested the rotor system for a 14-week period in 1992. The figure shows the Sikorsky rotor system mounted on Ames' Rotor Test Apparatus (RTA).

The primary objective of the wind tunnel test was to evaluate the SBMR in five areas: dynamics and stability, rotor structures and loads, handling qualities, aeroperformance, and acoustics. Data for each of these areas could then be correlated with analytical data to gain confidence in the analytical techniques used in the Comanche design, to improve modeling if needed, and to validate design concepts already selected. A secondary objective of this test was to evaluate the effects of active controls on rotor loads, performance, and acoustics.

Three new wind tunnel test methodologies were developed which proved useful in meeting the SBMR test objectives. The first, dynamic calibration of the rotor balance, allowed for determination of dynamic hub loads. The second, an automated fatigue monitoring system, allowed on-line tracking of component fatigue damage. The third involved the use of frequency-response methodology for conducting handling-qualities and dynamics research.

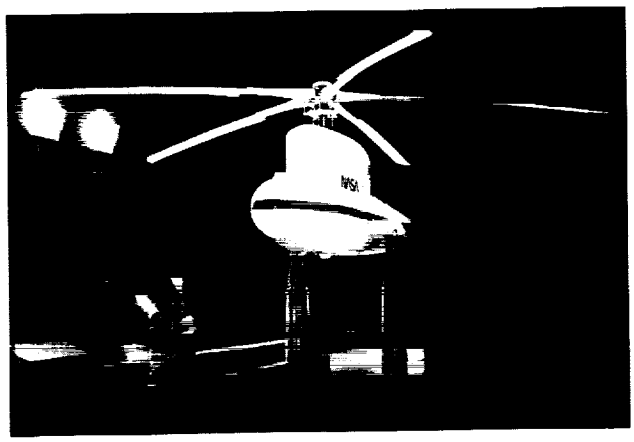

Fig. 1. Sikorsky bearingless rotor mounted in the Ames 40- by 80-Foot Wind Tunnel.

The rotor was tested at thrust levels of up to 19,000 pounds, rotor speeds of up to 346 rpm, tunnel velocities of up to 200 knots, pitching moments up to RTA shaft-bending limits, shaft angles of up to ±10 deg, and yaw angles of up to ±5 deg. Approximately 1800 data points, including 220 stability points and 460 acoustic points, were recorded.

Results have been published in three joint NASA/Sikorsky papers prepared for the 1993 American Helicopter Society National Forum.

Ames-Moffett contact: T. Norman
(415) 604-6653
Headquarters program office: OAST

Full-Scale Rotor Wind Tunnel Test Techniques

Randy Peterson

A comprehensive research program has been initiated in a joint program with the Deutsche Forshungsanstalt für Luft- und Raumfahrt (DLR) to develop and validate techniques for wind tunnel testing of helicopter rotor performance, loads, and dynamics.

In 1992 a BO-105 helicopter was flight tested in Germany. The isolated rotor system and the helicopter were heavily instrumented to acquire high-quality data on blade loads, trim-control positions, and flight conditions.

A subsequent test of a full-scale BO-105 rotor system has been completed in the Ames 40- by 80-Foot Wind Tunnel on the Ames Rotor Test Apparatus (RTA). In addition to extensive rotor instrumentation, the RTA has an accurate rotor balance to measure rotor trim forces and moments. The balance can also measure the vibratory hub loads of the rotor. The BO-105 rotor was tested throughout the helicopter's flight envelope and to very high speeds (greater than 170 knots).

Data from a separate 40%-scale test planned for 1994 in the Deutsch–Niederlandischer Windkanal with a BO-105 rotor will complement the full-scale test results.

Ames-Moffett contact: R. Peterson
(415) 604-5044
Headquarters program office: OAST

Lift-Enhancing Tabs for High-Lift Systems

James Ross

The objective of this study was to develop technology to increase the efficiency of the high-lift systems of modern subsonic transports. By increasing lift during the approach and takeoff flight regimes, a greater payload and range can be achieved and community noise can be reduced. Furthermore, by reducing the complexity of the standard multielement high-lift systems, significant weight savings can be realized.

The lift-enhancing tab is typically a flat plate, on the order of 1% of the airfoil chord in height, deployed near the trailing edge perpendicular to the pressure side of the airfoil (see figure). When it is incorporated into a multielement airfoil, the lift-enhancing tab serves to turn the flow onto the following element, delay flow separation, and increase lift.

A combined computational and experimental program is being pursued. A Navier–Stokes analysis

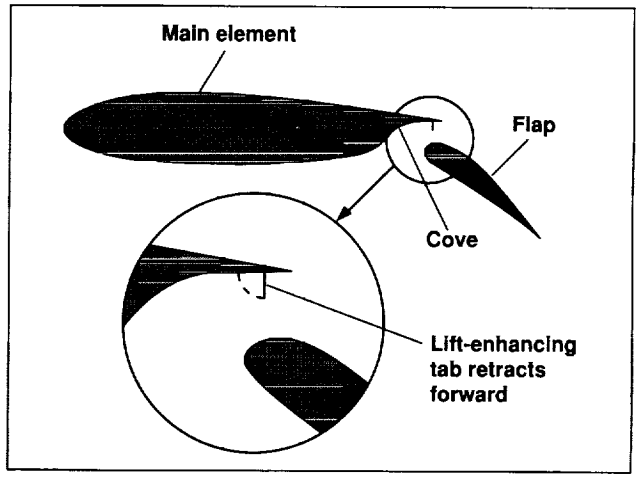

Fig. 1. Lift-enhancing tab for a high-lift system.

first indicated the potential of this device when it is applied to the cove of a two-element airfoil as shown in the figure. The computations predicted that it would produce a significant lift increment by reducing the flow separation on the flap. However, empirical results were needed for validation of these calculations.

A two-dimensional airfoil test was subsequently conducted in the 7- by 10-Foot Wind Tunnel. The two-element airfoil was instrumented to measure the resulting pressure distributions and wake profiles. Several configurations were tested with various flap settings to investigate the performance of the lift-enhancing tab. The results indicated substantial lift enhancement and validated the previous computations.

A full-scale test of a small subsonic transport is now being planned for study of the three-dimensional effects on tab performance. A retired Air Force T-39 was converted into a wind-tunnel model for testing in the 80- by 120-Foot Wind Tunnel and will serve as a test bed for future high-lift studies.

Ames-Moffett contact: J. Ross
(415) 604-6722
Headquarters program office: OAST

Modern Four-Bladed Rotor Research in the 80- by 120-Foot Wind Tunnel

Patrick M. Shinoda, David B. Signor

The first (full-scale) rotor test in the Ames 80- by 120-Foot Wind Tunnel, of a Sikorsky S-76 rotor hub/blades system mounted on the recently modified Rotor Test Apparatus (RTA), was completed. The rotor system was acquired to provide an opportunity to study aerodynamic, dynamic, and acoustic phenomena of a modern four-bladed rotor system. The accomplishments were as follows:

1. The first successful operation of the newly modified RTA with the steady/dynamic rotor balance was completed.
2. Wind-tunnel-wall pressure data were acquired to establish new methodologies for wall corrections at low speeds.
3. Rotor performance, controls, and loads were documented from hover to 100 knots for validation of theoretical predictions.
4. Dynamic hub loads (up to 10 per rev) were measured, providing insight into airframe vibration sources.

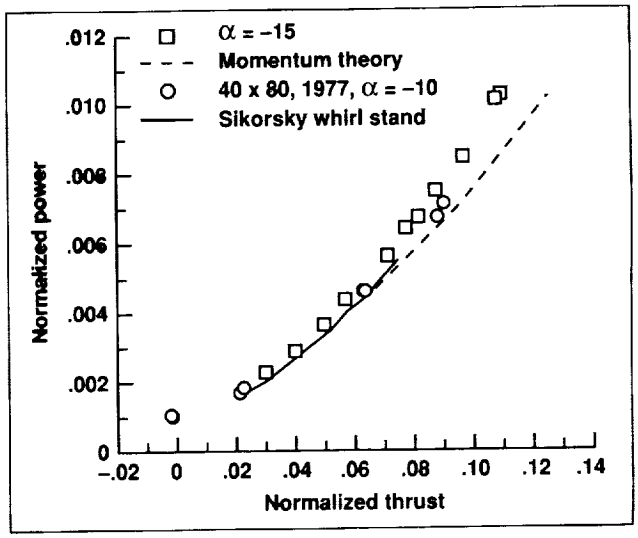

Fig. 1. Comparison of S-76 hover test data with CAMRAD/JA model predictions.

5. A comprehensive rotor data base was obtained for a low-speed/high-thrust envelope, in order to establish rotor limits in maneuvering flight and rotor power requirements.

6. The wide-field shadowgraph technique was demonstrated with a full-scale rotor system for quantitative wake geometry measurements in forward flight.

A sample of rotor performance data is shown in the figures. The first figure shows a correlation of S-76 rotor hover performance data from (1) the 1977 test in the Ames 40- by 80-Foot Wind Tunnel, (2) a test at the Sikorsky whirltower facility in Stratford, Connecticut, (3) CAMRAD/JA model predictions, and (4) a test in the Ames 80- by 120-Foot Wind Tunnel. The second figure presents thrust sweep comparisons of CAMRAD/JA predictions with the 80-by-120 data at an advance ratio of 0.20 at different angles of attack.

A comparison of in-flight acoustics with an S-76 helicopter will be made later this year. A second wind tunnel test in the Ames 40- by 80-Foot Wind Tunnel with the S-76 rotor system is planned for 1994. The research program will continue the assessment of the capabilities of the two wind tunnels for rotor performance testing and acoustic testing, development of improved wind tunnel wall correction methods, studies of the effects of higher harmonic rotor controls on rotor loads, and a comparison study of S-76 rotor blades to modified S-76 reduced-noise blades for possible blade–vortex-interaction noise reduction.

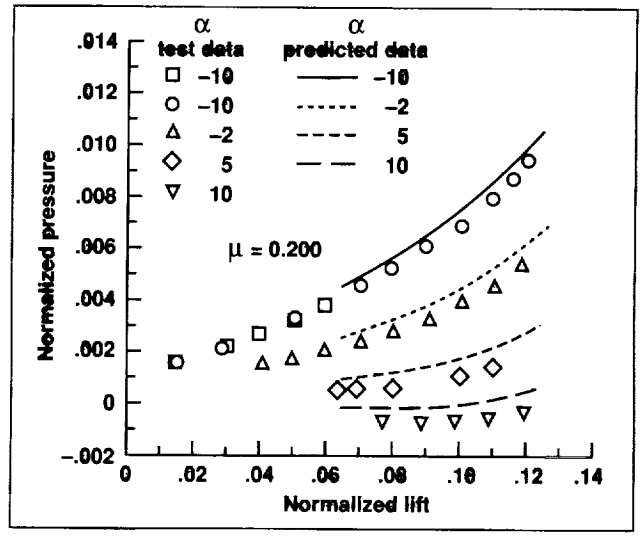

Fig. 2. Comparison of S-76 80-by-120 thrust sweep data with CAMRAD/JA model predictions.

Ames-Moffett contact: P. Shinoda
(415) 604-6732
Headquarters program office: OAST

Sikorsky S-76-C Blade Fold Test

David B. Signor, Steve Christensen

A test was conducted to validate manual blade fold capability on a Sikorsky S-76-C helicopter at wind speeds of up to 45 knots. The test was done in the National Full-Scale Aerodynamics Complex (NFAC) 80- by 120-Foot Wind Tunnel. The manual blade fold capability was demonstrated with the S-76-C oriented at five azimuth angles ranging from nose into the wind to tail into the wind. Wind speed was varied from 20 to 45 knots at each azimuth. A crew of five was required to complete the blade fold evolutions. The evolutions were documented on videotape, with fixed cameras and a mobile video camera operator in the test section. A series of blade

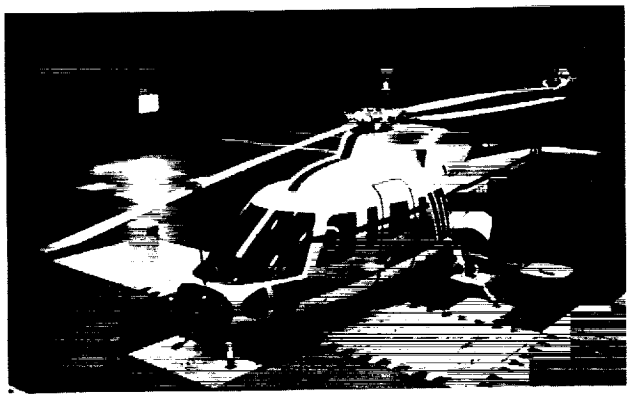

Fig. 1. Forward view of S-76-C with folded blades.

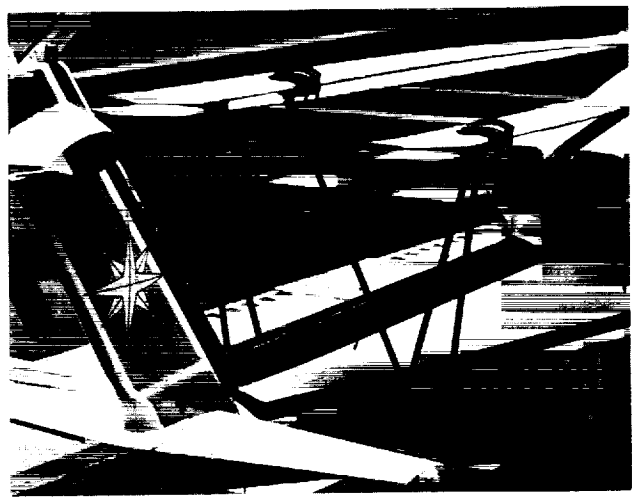

Fig. 2. Aft close-up view of S-76-C blade fold hardware.

fold and unfold evolutions was conducted which successfully proved the manual blade fold capability. The S-76-C in the folded configuration is shown in the figures.

Ames-Moffett contact: D. Signor
(415) 604-4562
Headquarters program office: OAST

Flight Measurements of Blade–Vortex Interaction Noise

David B. Signor, Gloria K. Yamauchi, Michael E. Watts

Acoustic measurements of a Sikorsky S-76-C helicopter in flight were acquired using the NASA Ames YO-3A research aircraft. The investigation was designed to further the understanding of the blade–vortex interaction noise generated by the S-76 rotor. Time-accurate separation distances between the S-76-C and YO-3A were achieved using a portable laser rangefinder. These results provide the first comparison of in-flight acoustic measurements with full-scale wind tunnel data and will allow a preliminary determination of the validity of using the Ames 80- by 120-Foot Wind Tunnel as an acoustic facility for full-scale rotors.

The technique of acquiring acoustic measurements of helicopters in forward flight was developed more than 15 years ago by Schmitz and Boxwell, who provided comparisons between flight and small-scale wind tunnel data for two-bladed rotor systems. The concern about scaling of aerodynamic and acoustical phenomena is always present when flight data are compared with small-scale data, however.

Full-scale rotor data are needed for the ultimate comparison of wind tunnel measurements and theoretical predictions. Recently, the In-Flight Rotorcraft Acoustics Program was established at Ames. The objective of the program is to use the capabilities of the YO-3A to measure noise from helicopters whose full-scale main rotors were tested or will be tested in the National Full-Scale Aerodynamics Complex.

The YO-3A has a microphone mounted on each wingtip and on the top of the vertical tail. The data acquisition system on board the YO-3A records the signals from the three microphones, along with airspeed, altitude, outside air temperature, angle of attack and sideslip angle, 1-per-rev signal from the helicopter, an IRIG-B time code, and voice channel. In addition, in this investigation, the helicopter attitude and main rotor speed were recorded once during the 30-second time record. The weight of the helicopter was calculated by measuring the fuel burn rate. When the two aircraft were stabilized at specified test conditions, data were recorded continuously for 30 seconds. During this 30-second time period, the distance between the helicopter and the YO-3A was also continuously recorded on board the helicopter. A portable, eye-safe laser was used as a rangefinder and was operated from the back seat of the helicopter. A small section of the YO-3A starboard wing was used as a target for the laser. The distances were viewed by means of the head-up display on the laser, and the values were downloaded to a lap-top computer. The values were synchronized through the time code with the acoustic data recorded by the YO-3A data system. The capability of recording a time-accurate separation distance is a much desired refinement of the previous in-flight testing technique.

Flight conditions were selected from within the flight envelope of the two aircraft and as close as possible to conditions tested with the full-scale rotor in the 80- by 120-Foot Wind Tunnel. The S-76-C helicopter was positioned so that the tail microphone on the YO-3A was located 25 degrees below the rotor hub at a rotor azimuth of 150 degrees. The distance between the rotor hub and the tail microphone was nominally two rotor diameters (88 feet). The angular alignment of the two aircraft was established visually by the pilot, who aligned the top of the YO-3A tail with a target on the right wing of the YO-3A. The flight formation viewed from the side is shown in the first figure.

Fig. 1. S-76-C and YO-3A formation, side view.

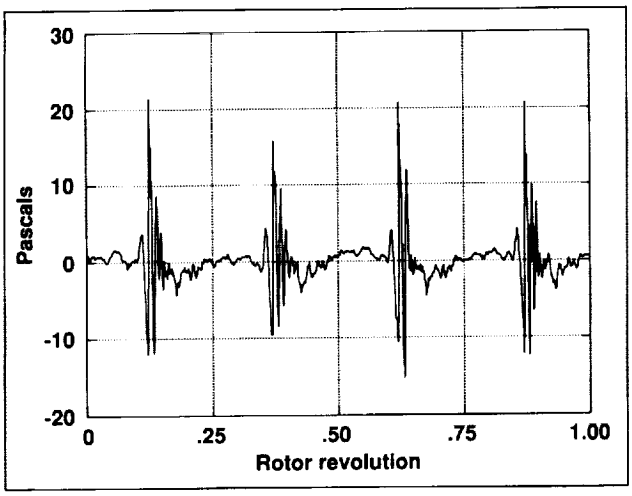

Fig. 2. S-76-C blade–vortex interaction noise acoustic signature.

One rotor revolution of averaged data from the tail microphone digitized using a 2.5-kilohertz filter is shown in the second figure. The blade–vortex interaction events are clearly evident. The flight parameter values for the figure are as follows: true airspeed = 66 knots, descent speed = 748 feet/minute, hover tip Mach number = 0.603, advance ratio = 0.164, and rotor coefficient of thrust = 0.00778.

Ames-Moffett contact: D. Signor
(415) 604-4562
Headquarters program office: OAST

High-Speed Research: High-Lift/Engine Aeroacoustics Technology

Brian Smith

The Ames High-Lift/Engine Aeroacoustics Technology (HEAT) program is documenting the significance of the interactions of the high-lift systems and noise suppressor nozzles that will be incorporated into the high-speed civil transport (HSCT). The effects of the suction flows generated by the ejector nozzle inlets on the high-lift performance of the wing during takeoff and climb are measured, and the effects of the HSCT wing flow field on the acoustic performance of the suppressor nozzles are determined. The ejector nozzles, which are required to meet community noise-limitation requirements, are designed to entrain large quantities of ambient air to cool and slow the exhaust jet. This research is being conducted jointly with Boeing Commercial Airplane Group as part of the NASA High-Speed Research program.

In support of this effort, computational studies and a small-scale experiment have been performed to predict the behavior of the large half-span model/symmetry plane to be used in a large-scale tunnel investigation scheduled for 1994 in the Ames 40- by 80-Foot Wind Tunnel. The HSCT model, which is

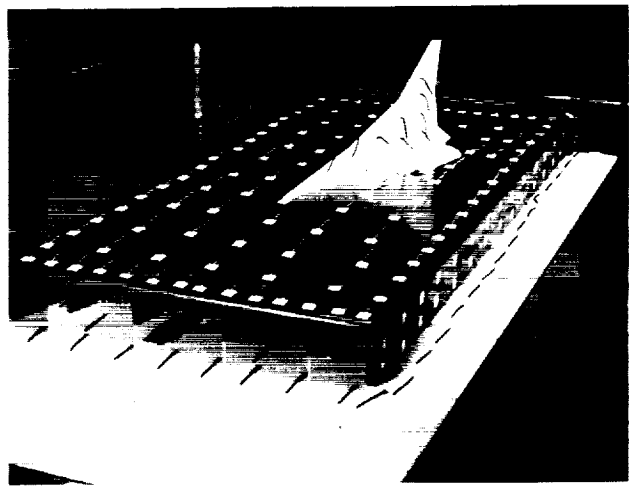

Fig.1. Small-scale HEAT symmetry plane prototype in the Ames 7- by 10-Foot Wind Tunnel.

over 42 feet long, will be mounted on an acoustically treated symmetry plane situated above the boundary layer on the floor of the wind tunnel. A small-scale wind tunnel study of the aeroacoustic characteristics of the proposed symmetry-plane design was carried out in the Ames 7- by 10-Foot Wind Tunnel to reduce the technical risk of testing a full-scale symmetry plane with dimensions of approximately 22 by 55 feet. The first figure shows the scale model of the symmetry plane installed in the wind tunnel. With only minor modifications, the small-scale prototype was found to have highly satisfactory off-body and surface flow characteristics. The second figure illustrates the predicted perturbation in the static pressure field at the location of the symmetry plane which is due to the presence of the HSCT wing operating at the takeoff lift coefficient of 0.55. These results are being used to design the large-scale test hardware.

The test also documented the acoustic characteristics of the symmetry-plane/wing combination. In order to resolve the noise generated by the exhaust plume of the large-scale jet simulator, the symmetry-plane structure must not generate excessive flow

Fig. 2. PMARC code predictions of the static pressures on the HEAT symmetry plane. (See color plate 3 in Appendix)

noise. The third figure illustrates the noise spectrum obtained with and without the wing. The tunnel background noise spectrum is shown for comparison. The noise generated by the symmetry plane is only slightly greater than the background noise, and the

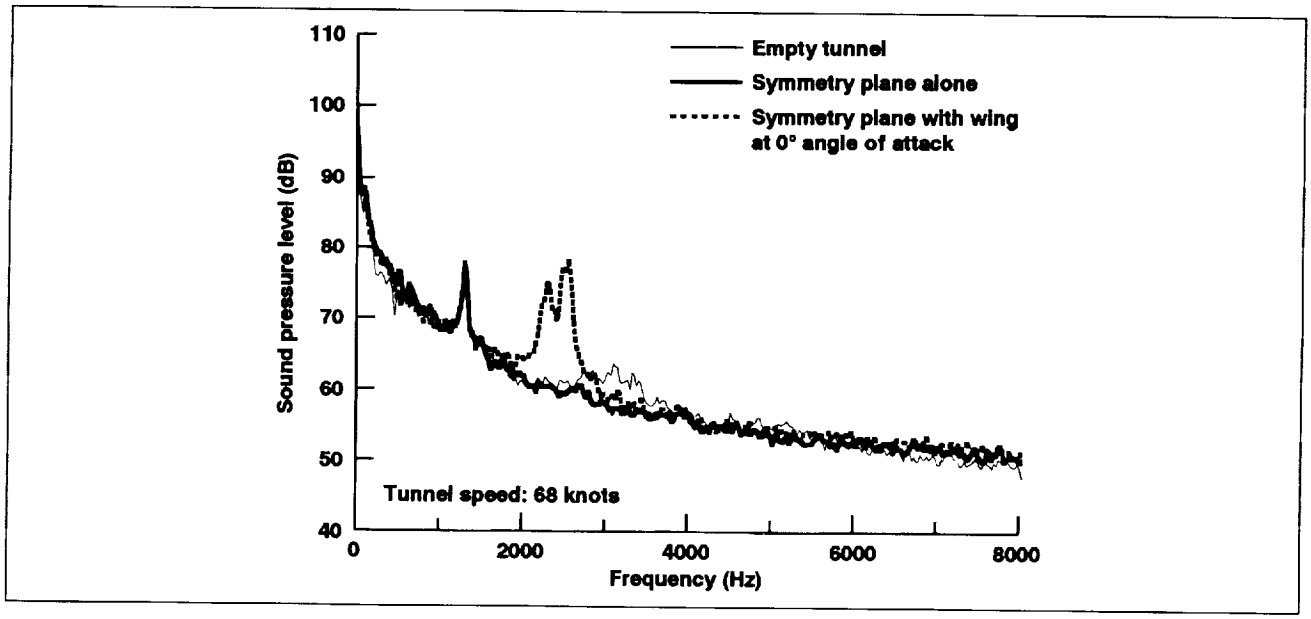

Fig. 3. Acoustic characteristics of the HEAT symmetry plane with and without the wing.

combination of symmetry plane and wing produces noise peaks that are significantly greater than the symmetry-plane-only increment. When the dominant peak at around 2500 hertz is scaled down to the frequencies expected for the large-scale test, it has been determined that the flow noise from the test hardware will not prevent resolution of the noise generated by the ejector/suppressor.

Ames-Moffett contact: B. Smith
(415) 604-6669
Headquarters program office: OAST

Jet Noise Source Location Techniques

Paul Soderman

Two experimental techniques have been developed to locate jet noise sources in exhaust plumes and to determine the radiation direction of those sources. This technology is needed for wind tunnel studies of jet noise so that the data can be correctly extrapolated to far field. Improper assumptions of source location or radiation direction can cause large errors in far-field directivity patterns.

The first technique involves measurement of acoustic intensity in two planes near the jet. Acoustic intensity is a vector quantity that defines the sound amplitude and propagation direction. By judicious mapping of the sound field, it was shown that source regions in the jet could be identified along with the radiation directions. Both quantities change with frequency and jet condition. The second method is based on correlation of near-field microphone signals with those measured in the far field. The information is consistent with that obtained with the intensity method, but it takes longer to acquire. On the other hand, the correlation method may work when there is wind over the microphones; it is not likely that the intensity method would work in that circumstance. Hence both methods have advantages depending on the conditions of the experiment.

The figure shows the identification of a 500-hertz noise source in a Mach-0.6 jet using the acoustic intensity device moved along a sideline 20 nozzle diameters away. The apparent target measured at each instrument position is consistent from one position to the next. Thus the data measured at that frequency can be extrapolated to far field in any direction with confidence.

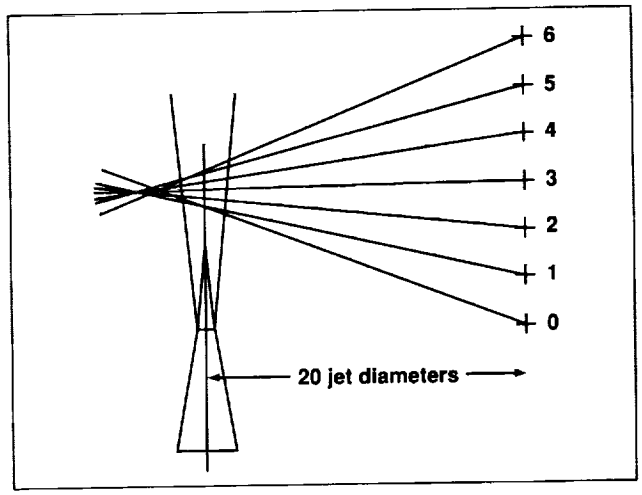

Fig. 1. Jet noise source identification using acoustic intensity microphone.

Ames-Moffett contact: P. Soderman
(415) 604-6675
Headquarters program office: OAST

Two-Dimensional Tiltrotor Download

Paul Stremel

The numerical prediction of download, the vertical drag on a rotorcraft during hover, is important in the design analysis of rotorcraft. Download limits helicopter performance in hover and is a significant problem in the design of tiltrotor configurations, where the lifting wing is immersed in the rotor wake.

Limited success in correlating analytical with experimental results for two-dimensional (2-D) download has been achieved. The loading on the airfoil was significantly overestimated in the calculations. In addition, the base pressure—the surface pressure on the lower surface of the airfoil—was not closely predicted by previous methods.

Because of the limited ability to predict 2-D download, a method was developed to calculate the flow about bluff bodies, and this method was applied to the 2-D download flow field. The results were then correlated with experimental data. The agreement between predicted and measured values was good, although the average download was still overestimated. To further evaluate the method, the prediction

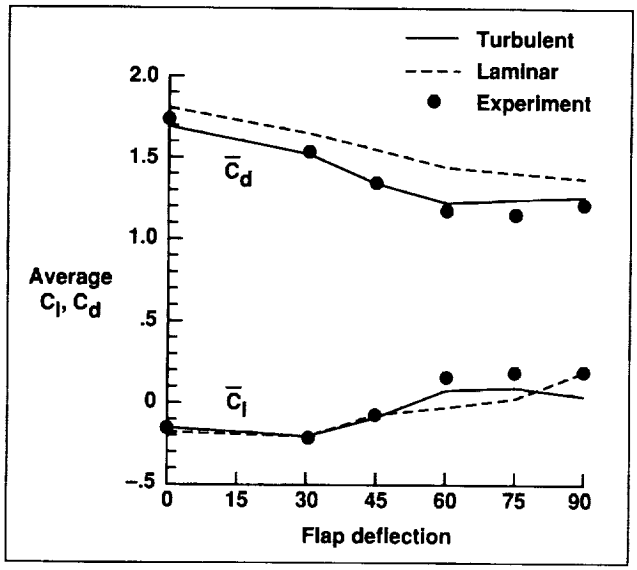

Fig. 1. Comparison of predicted average airfoil lift (C_l) and drag (C_d) with experimental values: Re = 1 × 10^6, laminar and turbulent boundary layer models, α = –90 deg.

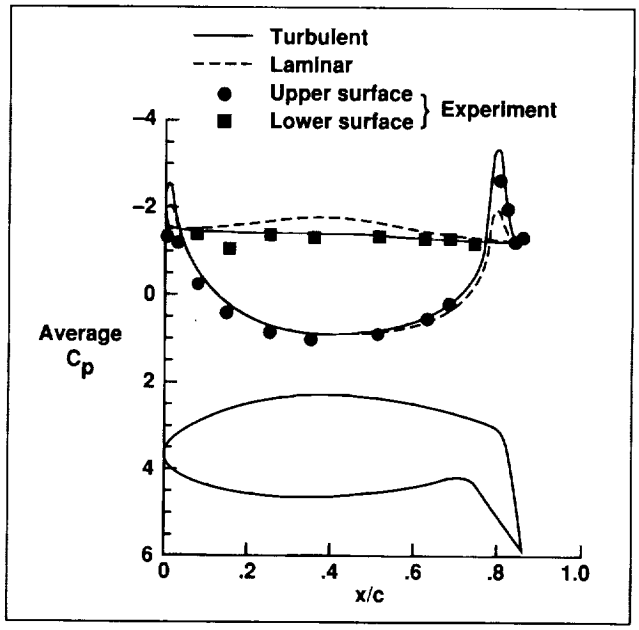

Fig. 2. Comparison of predicted average surface pressure coefficient (C_p) with experimental results (as a function of airfoil chordlength): α = –90 deg, δ_f = 60 deg, Re = 1 × 10^6; laminar and turbulent boundary layer models.

of flow at high Reynolds numbers and also turbulence modeling must be included.

The present results demonstrate the ability of the analytical method to predict the flow about an airfoil at –90 degrees incidence. The flow was calculated for a Reynolds number of 1 million and for laminar and turbulent boundary layer models. The effect of the turbulent boundary layer model on the predicted airfoil lift and drag, shown in the first figure, was found to be significant. The average drag predicted by a laminar flow model was significantly overestimated compared to the experimental results and results obtained with the turbulent flow model. This overestimation was most apparent at flap deflections between 45 and 75 degrees, and is due to the differences in the prediction of upper-surface flow separation and to differences in the convection and diffusion of the

vorticity in the wake of the airfoil. The results for the turbulent boundary layer model are shown to be in excellent agreement with the experimental values.

A comparison of the average surface pressure on the airfoil for a flap deflection of 60 degrees is shown in the second figure. The results for the laminar and turbulent boundary layer models and the experimental values are presented. The base pressure predicted by the turbulent boundary layer model is in better correlation with the experimental values than that predicted by the laminar boundary layer model. In addition, the results for the turbulent boundary layer model demonstrate a significant increase in the suction peak on the upper surface at the flap hinge location. This decrease in the pressure is shown from the upper surface of the flap to the trailing edge of the airfoil and represents a significant improvement in the correlation with experimental data.

Ames-Moffett contact: P. Stremel
(415) 604-4563
Headquarters program office: OAST

A Zonal Flow Analysis Method

Paul Stremel

A zonal method has been developed to predict the aerodynamics of rotors in hover and vertical climb. The new procedure uses overlapping zones for the potential and viscous flow regions. Closed-loop coupling at an intermediate boundary within the flow domain allows for a reduction of the outer domain size. The accuracy of the three-dimensional zonal method, ZAP3D, has been assessed in comparisons with ARC3D simulations for a rectangular wing with a NACA 0012 airfoil section. Calculations have shown that reductions of the outer domain size to approximately one chordlength can be achieved without loss of accuracy.

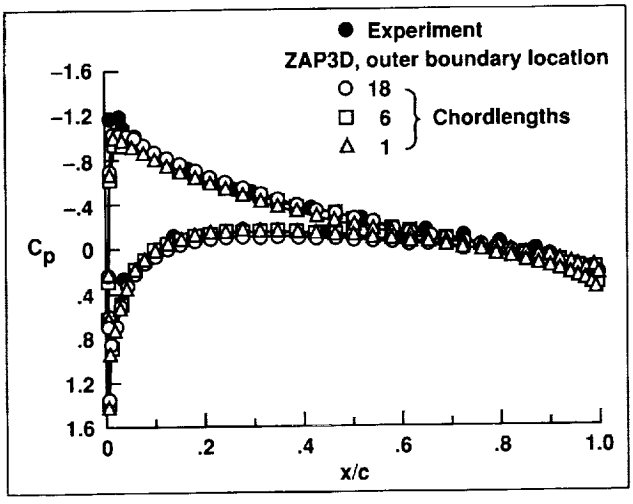

Fig. 1. Comparison of computed pressure distribution for a hovering two-bladed rotor at the 89% spanwise location.

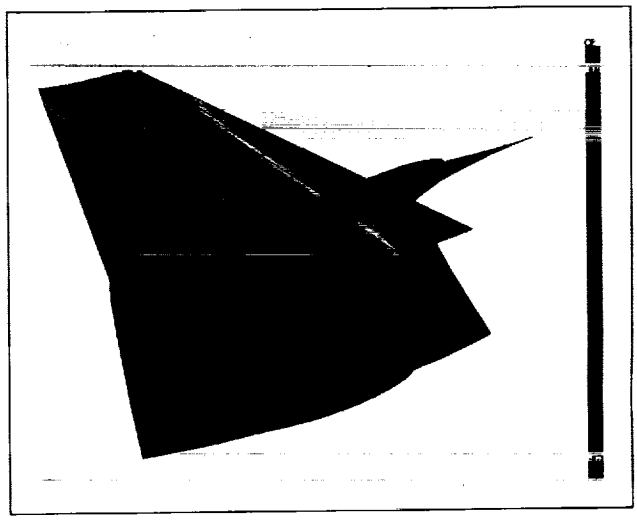

Fig. 2. Computed pressure contours for the flow field of a hovering two-bladed rotor. (See color plate 4 in Appendix)

With this baseline work complete, ZAP3D is being applied to simulate a helicopter rotor in hover and climb. The detailed rotor wake effects from outside the ZAP3D domain are included through the

potential flow module. A comparison of the computed and experimentally measured blade surface pressures for varying outer boundary locations is shown in the first figure. The results were calculated for a hover simulation at a Reynolds number of 1.92 million, a tip Mach number of 0.44, and a blade angle of attack of 8 degrees. A comparison of the computed pressure distributions indicates that the ZAP3D solution is independent of the outer boundary location and is in close agreement with the experimental pressure distribution. The pressure contours on a rotor blade, shown in the second figure, demonstrate the ability of the method to predict the full three-dimensional flow field for a hovering helicopter rotor.

Ames-Moffett contact: P. Stremel
(415) 604-4563
Headquarters program office: OAST

Full-Scale Rotor Flow Visualization

Alexandra Swanson

The feasibility of conducting full-scale rotorcraft flow-visualization research was demonstrated in 1992. This was the first time the wide-field shadowgraph technique was applied to flow visualization of a full-scale helicopter rotor system. Flow-visualization data was obtained from a 13.4-meter-diameter S-76 rotor mounted on the rotor test apparatus (RTA) in the 24- by 37-Meter Wind Tunnel. The first figure shows how two simultaneous views (top and side) of selected regions of the rotor wake were obtained in an attempt to resolve three-dimensional tip vortex coordinates. Images of blade–vortex interactions were also acquired in support of rotor aeroacoustics

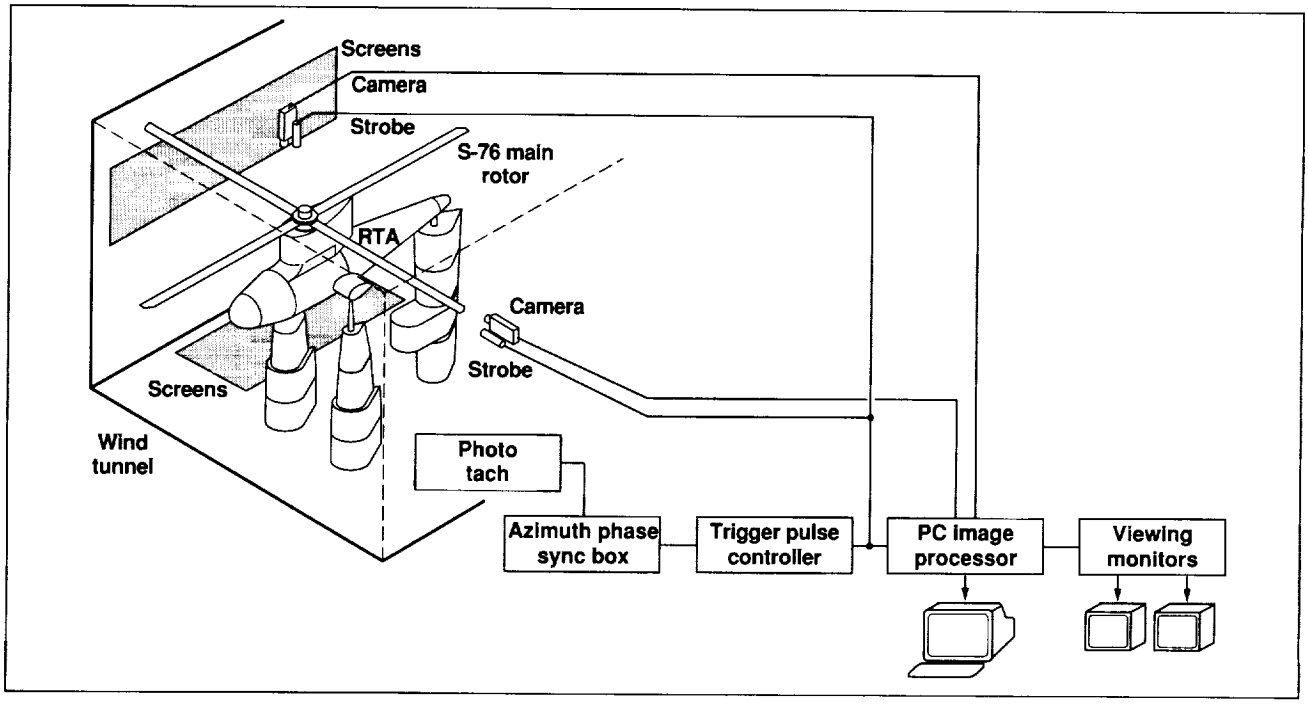

Fig. 1. Experimental setup.

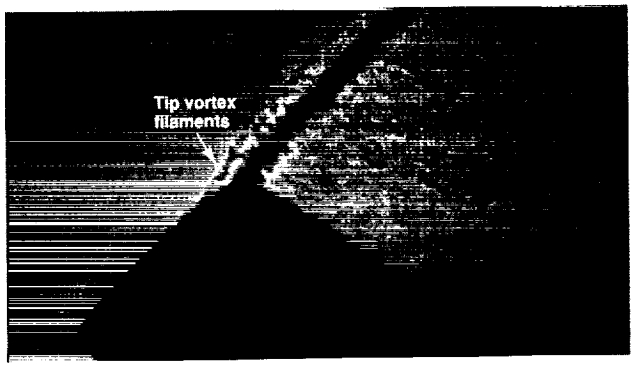

Fig. 2. Shadowgraph of tip vortex rollup.

research. Details of tip vortex rollup, double tip vortex features, and the inboard vortex sheet were revealed. The second figure is a typical shadowgraph, taken from above the rotor, which shows individual strands coalescing into one primary tip vortex. The versatility of the wide-field shadowgraph technique was demonstrated in high-quality flow-visualization images and data for an extensive range of test operating conditions (hover, forward flight, descent) at advance ratios of up to 0.25. Full-scale flow visualization using the wide-field shadowgraph technique is relatively straightforward. The major tasks include implementing a reliable high-resolution real-time digital imaging system, installing large retroreflective screens, and ensuring adequate protection of the screen surface quality.

Ames-Moffett contact: A. Swanson
(415) 604-6856
Headquarters program office: OAST

Rotor Tip Vortex Core Study

Alexandra Swanson

Flow visualization was conducted on a 2.1-meter-diameter, small-scale V-22 tiltrotor. Wake geometry was acquired for various tiltrotor models, which included download reduction devices and high-wing-sweep configurations. Of special significance was an investigation of the use of the shadowgraph technique as a nonintrusive means of obtaining measurements of the tip vortex core size. Previous experimental results showed that shadowgraphs of the vortex core are highly sensitive to changes in thrust and wake age. The first figure illustrates how both shadowgraph and hot-wire techniques were used to acquire spatial measurements and velocity profiles of the vortex core. The second figure presents a sample of hot-wire results. Core size measurements were based on the background convection velocity and the

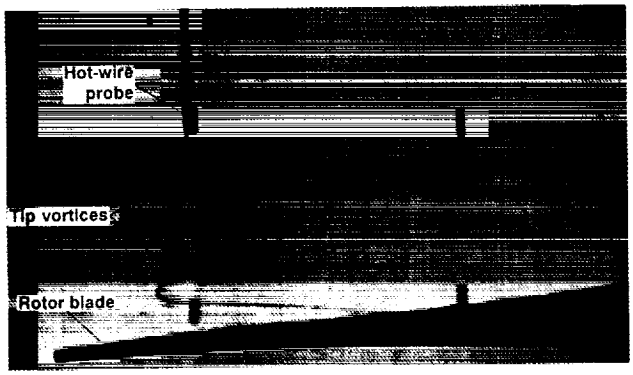

Fig. 1. Simultaneous shadowgraph and hot-wire data acquisition.

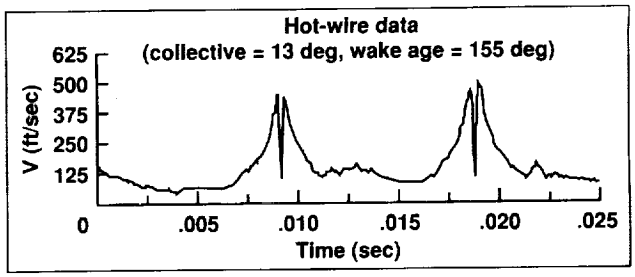

Fig. 2. Hot-wire measurements of vortex core size.

time it took for the hot wire to slice through the core. The background convection velocity data from the hot-wire technique were in good agreement with velocities derived from shadowgraph wake geometry measurements. Preliminary examination of the hot-wire data indicates that the core radius lies somewhere between the dark inner nucleus of the vortex core and the outermost ring feature of the vortex core. More thorough examination of the data is required in order to determine whether shadowgraph measurements can provide an accurate means of estimating core size.

Ames-Moffett contact: A. Swanson
(415) 604-6856
Headquarters program office: OAST

NASA/McDonnell Douglas Canard Rotor/Wing Test

Stephen Swanson, Steve Christensen

NASA Ames Research Center and McDonnell Douglas Helicopter Company have conducted a joint program to evaluate the aerodynamic characteristics of a new high-speed rotorcraft concept called the Canard Rotor/Wing (CRW). The CRW is a stoppable-rotor concept which can hover and fly at low speeds like a conventional helicopter but also, in its stopped-rotor mode, fly at high speeds comparable to those of commercial aircraft. For helicopter mode flight, the CRW uses a two-bladed, teetering rotor which is driven by reaction jets located at the rotor tips. Cross sections of the rotor airfoil are symmetric ellipses unaugmented by mechanical flaps or circulation control. The reaction jets provide the required rotor power to generate lift, without the weight of a transmission or the addition of a tail rotor to counteract rotor torque. Conventional turbofan engines are used to supply high-pressure air to the rotor reaction jets as well as to supply thrust for forward flight. After a vertical takeoff, forward flight speed is increased and the aircraft's lift is transferred from the rotor to the canard and horizontal tail lifting surfaces. At the conversion speed, with the lift completely transferred from the rotor to the lifting surfaces, rotor rotation is stopped and the rotor is locked into a fixed-wing configuration for high-speed flight. Stopping a nonlifting rotor minimizes (1) the stresses placed on the rotor, (2) the control requirements of the rotor, and (3) the aircraft vibrations produced when the rotor rotation is being stopped. This helps to reduce the design challenge of developing the stoppable-rotor system.

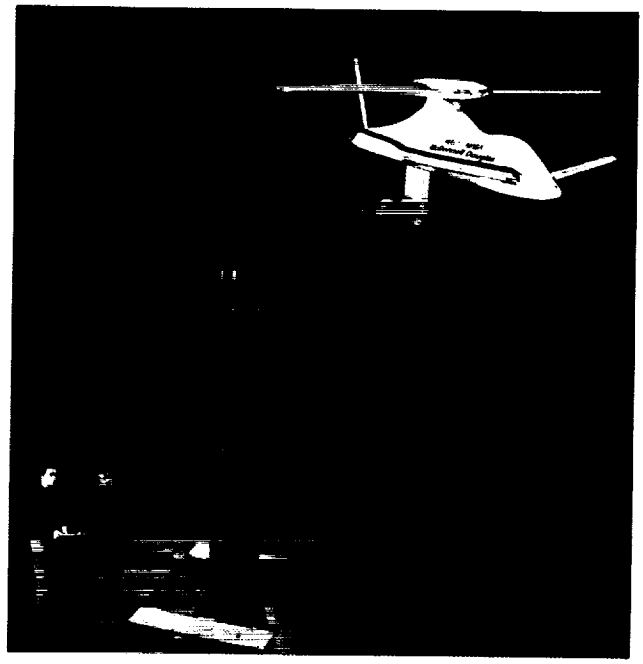

Fig. 1. Canard rotor/wing test model mounted in the Ames 40- by 80-Foot Wind Tunnel.

To determine the feasibility of the concept, a low-speed, fixed-wing test was completed in the Ames 40- by 80-Foot Wind Tunnel. This test identified the fixed-wing aerodynamic characteristics of the CRW concept in its conversion configuration and at the higher speeds in cruise configuration. The first figure shows the test model mounted in the wind

tunnel in its cruise configuration. The major findings of the test included

1. The CRW concept was capable of generating the required amount of lift at the conversion speed and obtained an acceptable lift-to-drag ratio in the cruise configuration.

2. A major source of drag on the CRW was interference between the three lifting surfaces—the canard, the rotor, and the tail.

3. A comparison of an H-tail configuration and a T-tail configuration showed the H tail to be more stable.

The second figure shows trends in pitching moment for the two tails as a function of angle of attack. Much of the degradation of the T tail was due to interference from the rotor.

Ames-Moffett contact: S. Swanson
(415) 604-4565
Headquarters program office: OAST

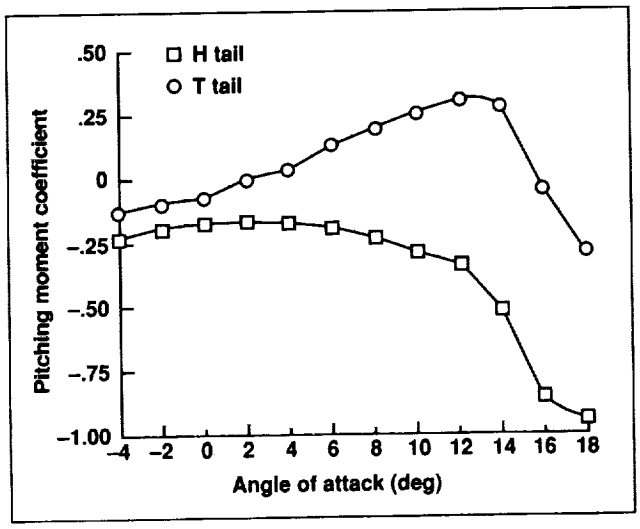

Fig. 2. Pitching moment of H-tail and T-tail cruise configurations.

Bayesian Surface Reconstruction from Multiple Images

Peter Cheeseman

A number of research efforts are under way to explore the use of Bayesian (statistical) methods to solve complex inference problems for noisy data. Such problems frequently arise in NASA applications. In 1992, we began a project to take multiple images of a particular area and to use the information in these images to build a high-resolution composite image that represents the best estimate of what the true surface must be (see figure). We initially used multiple images of the surface of Mars (taken by the Viking Orbiter) and constructed a high-resolution composite image that shows features that are not visible in any of the contributing images. We are currently extending this technique to more complicated images, such as the Voyager images of Ganymede, in which the

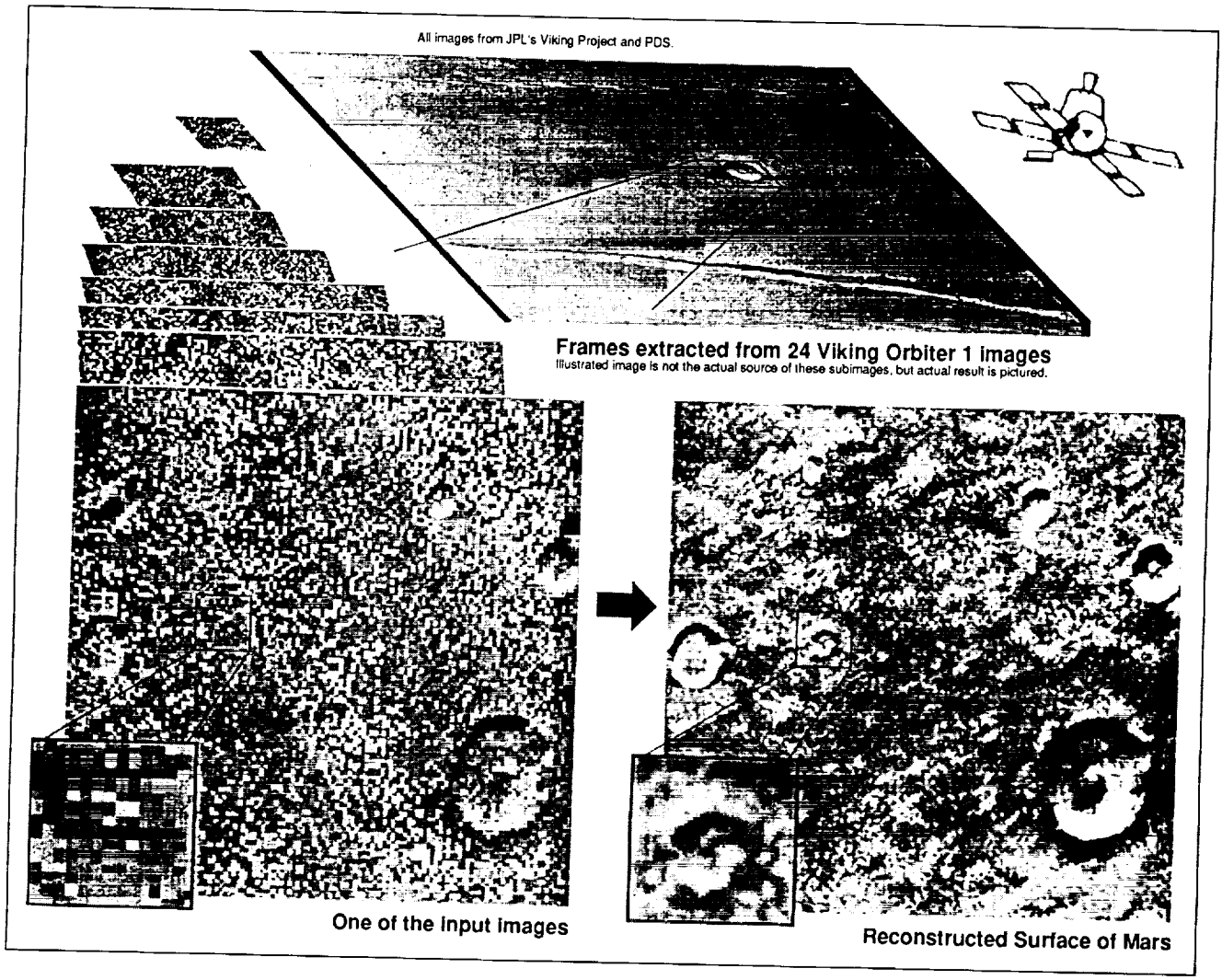

Fig. 1. An example of Bayesian surface reconstruction from multiple images.

curvature of the planetary surface must be taken into account.

The development of a procedure for combining multiple-image information required the solution of a number of problems. We had to find accurate registrations of the individual images for the composite, correct for nonuniform gain in the camera, learn and correct for the point-speed function within the camera, and make other corrections related to noisy pixels. We found algorithms for solving these problems and for taking into account the neighbor correlations.

Ames-Moffett contact: P. Cheeseman
(415) 604-4946
Headquarters program office: OAST

Integrated Planning, Scheduling, and Control for Automatic Telescopes

Mark Drummond, John Bresina, Keith Swanson

The immediate goal of this project is to design and implement a practical planning and scheduling system for the fully automatic management of remotely located telescopes. Although the system, called CERES, is specific to the telescope management problem, the principles by which it operates have general applicability. We have sought generality in the design of CERES because our ultimate goal is to better understand the basic principles of general-purpose planning and scheduling systems. We hope to eventually build a planning and scheduling software tool kit.

An "automatic" telescope is controlled by a dedicated computer. The computer directs the operation of the telescope and its observatory enclosure in response to sets of commands it receives over an electronic network. Currently, the sets of commands are sent by a human principal astronomer (PA). The PA receives requests for telescope observations from astronomers located around the country. The PA has little influence on how these requests are executed at the telescope. The PA collects the requests, checks them for syntactic validity, packages them into a set of commands, and sends the set over the network to the telescope. The telescope selects and executes commands from this set by "heuristic dispatch," a simple technique that performs no look-ahead scheduling.

Our project is providing tools to make the PA's job easier and to improve the process of request execution at the remotely located telescope. CERES is a more sophisticated scheduling system that resides at the PA's site and interacts in real time with the telescope over the electronic network, commanding it to execute the astronomers' requests more efficiently than by heuristic dispatch. Additionally, we are developing a higher-level language to allow astronomers to more easily express their requests to the PA. We are collaborating with astronomers in the design of the CERES scheduler and the request-specification language. Initial results obtained via detailed telescope simulation have been encouraging. We are actively seeking time on a real telescope to better demonstrate the utility of the CERES system.

Ames-Moffett contact: M. Drummond
(415) 604-4710
Headquarters program office: OAST

Space Shuttle Main Engine Plume Analysis Using an Optical Processor

Charles Gary

Optical processing of plume spectra could provide a means of observing the functioning of an engine in real time. Real-time matrix analysis of the space shuttle main engine plume requires as many as one billion operations per second from a processor that is light enough and efficient enough to be flown into space. These requirements can be met by an optical matrix-vector processor (OMVP).

Many different methods are currently used to monitor space propulsion engines, including temperature and stress gauges as well as spectrometers which look at the exhaust plume of the engine. Whereas instruments such as temperature and stress gauges provide useful "red lines" for the detection of catastrophic real-time failures, they do not give detailed information about the functioning of the engine. The spectrum of the engine's plume can provide information on what materials are being burned and thus how well the engine is functioning.

Unfortunately, the analysis of the plume spectra is computationally intensive; minutes to hours are now required to analyze a single spectrum. The analysis must therefore be done off-line. However, the high throughput of OMVPs will allow the spectral analysis to be done in real time. The critical parameters that will determine the success of OVMPs are (1) the applicability of linear (matrix-vector) analyses for finding the components of the fuel being burned and (2) the processing power and efficiency of the OMVPs.

Research in the Ames Photonics Laboratory has shown that a linear analysis of plume spectra does provide an accurate estimate of the elements being burned. A computational accuracy of 8 bits was used because it reflects the achievable accuracy of an optical processor. Actual spectra (with 4,096 points) from the NASA Stennis Space Center engine test stand in normal burn and failure conditions were analyzed using a matrix to determine the contents of the fuel. The resulting estimates were accurate to within 5% for all but one of the elements, which shows that a linear analysis consisting of a matrix-vector multiplication can provide useful real-time knowledge of an engine's health.

Ames-Moffett contact: C. Gary
(415) 604-3590
Headquarters program office: OAST

Intelligent Dynamic Scheduling Algorithms for Automatic Telescopes

Butler Hine, Mark Drummond, Keith Swanson, William Borucki

There are many NASA mission scenarios in which the unattended operation of a scientific instrument is desired because of the high cost of a human operator. This is especially true for astronomical observations, in which the method of data acquisition is well suited to automatic operation. Ground-based robotic telescopes (see figure) currently perform unattended photometric measurements of stars for periods of weeks to months, scheduling their observations using lists of subjects (i.e., stars) and priorities provided ahead of time by astronomers. The telescopes are not sophisticated with respect to efficient observation scheduling, system monitoring, or self-maintenance. These capabilities are critical for operation in space or at other inaccessible sites. This project is an attempt to transfer state-of-the-art technology in the areas of intelligent scheduling and system monitoring to the operation of automated telescopes. The application of artificial intelligence techniques can increase the performance and flexibility of automated telescopes. In addition to the simple quantitative increase in the performance of the system, there is a qualitative increase in its capabilities. This is especially true when these techniques are applied to complex networks of scientific instruments. A cooperating network of astronomical telescopes, differing in wavelength sensitivity or geographical location, can perform a new type of observational science that is difficult or impossible to do with classical telescopes and observing techniques.

A high-fidelity automatic photometric telescope (APT) simulator was designed to allow the development and testing of advanced planning and scheduling control software. A prototype interactive scheduling tool was developed and put to immediate use in preparing the fall 1991 observing schedule for an operating APT. A cooperative control system was then developed which makes use of optimum schedules when available from the scheduler, without entirely abandoning the default heuristic technique. The increase in performance obtained using new scheduling algorithms in existing simulated control systems was measured, and a group of automatic-telescope users was formed in the United States who are dedicated to implementing and testing distributed network control concepts. A workshop was held on the application of a prototype autonomous telescope to a proposed lunar mission.

Fig. 1. Fully robotic ground-based telescope.

Future plans include using the scheduling algorithms in the field and measuring their performance, acquiring an automatic telescope locally for fault diagnosis and system-monitoring research, and, eventually, implementing an Antarctic-based robotic telescope as a lunar mission precursor.

Ames-Moffett contact: B. Hine
(415) 604-4379
Headquarters program office: ARC DDF

Intelligent Mechanisms Laboratory

Butler Hine, Terry Fong, Michael Sims

In fiscal year 92, a new Intelligent Mechanisms Laboratory was developed in the Automation Sciences Research Facility. The objective of researchers in this laboratory is the *systems* investigation of intelligent mechanisms. The research is focused on the task of building intelligent mechanisms, rather than being driven by a particular technological bias. We have concentrated on architectures for intelligent mechanisms, including software, computer processors, machine learning, sensing (i.e., robotic vision, contact, and proximity sensors), and user interfaces.

This technology is important to NASA missions in three specific areas: (1) the safe and fault-tolerant movement of robotic devices near the Space Station or shuttle; (2) construction and exploration on planetary surfaces; and (3) the use of undersea vehicles as analogs of space vehicles.

Laboratory facilities include a PUMA 560 robot mounted on a rail (7 degrees of freedom); mobile platforms; an airbearing table; a two-dimensional zero-gravity facility; various end-effectors (i.e., grippers) and sensors; various computing environments (iWarp systolic array parallel processor, Sun Microsystems and Macintosh computers, Silicon Graphics workstations, and embedded real-time architectures running VxWorks); camera systems; and image-processing capabilities. We also have access to undersea vehicles and a virtual environment facility.

The laboratory is connected by ethernet and Fiber Distributed Data Interface to collaborative facilities using a uniform communication environment, developed at Carnegie Mellon University, called the Task Control Architecture. We have also incorporated the TelRIP communications protocol, developed at Johnson Space Center and Rice University, into our simulator visualization tasks.

The intelligent mechanisms group has developed a fully functional mobile land vehicle to test state-of-the-art software control and communications architectures in an operational environment. The vehicle is capable of untethered operation indoors and out, and has a capable on-board processor, high-bandwidth communications channels connecting it with the control station, and a multitude of environmental sensors. The platform design is highly modular, and represents an attempt to unify the hardware architectures in use in the Intelligent Mechanisms Laboratory. The vehicle is not intended to resemble a flight-qualified version, but it is a fully functional mobile platform upon which to perform technology demonstrations.

Ames-Moffett contact: B. Hine
(415) 604-4379
Headquarters program office: OAST/DARPA

Hypersonic Vehicle Takeoff and Climb

Charles Jorgensen, Paul Werbos, Robert Pap

This work supported fundamental technology needs of the National Aerospace Plane Program (NASP). In 1991, the National Science Foundation (NSF) and Accurate Automation, Inc., supported the development of a graphic simulation environment in which the Generic Hypersonic Aerodynamic Model Example (GHAME) was incorporated into a modified version of a flight simulator. This model, developed at Dryden Flight Research Center, was based on aerothermodynamic data gathered from the space shuttle, the X-24B, and the SB-70. A human control interface was connected to the simulator which then implemented commands using a neural network to control a simplified NASP design during take-off and climb to 40,000 feet. The neural controller works by combining a robust linear controller with a trained neural controller that has learned a transfer function from nonlinear residuals not modeled by the linearized equation, i.e., information which would normally be considered to be errors. When a command is exercised by the pilot, the linear and neural components are combined to produce the correct control signal.

In 1992, the same approach was used to control a simulated PUMA robot arm. In this demonstration, a nonoptimal linear controller, an optimal controller, and a neural controller were compared as they attempted to compensate for the forces and torques caused by a heavy payload dropped suddenly by the arm during payload relocation. The error curves demonstrate superior performance relative to both of the other methods in the control of the torque error for the arm, and comparable performance for the position error.

Ames-Moffett contact: C. Jorgensen
(415) 604-6725
Headquarters program office: NSF

Intelligent Procedure Development and Maintenance Project

Smadar Kedar

Specific procedures for controlling complex operations such as in-orbit shuttle activities, ground processing, and shuttle monitoring are widely used at NASA. Currently, most development and maintenance of such procedures is done on paper, consuming large amounts of time, money, manpower, and storage space.

The Intelligent Procedure Development and Maintenance Project at Ames produces prototype tools to assist in developing and maintaining complex procedures in electronic rather than paper form. These tools reduce the cost, time, and effort in procedure development and maintenance, while increasing the accessibility and accuracy of the procedures.

This year we designed and developed two prototype systems. In collaboration with Nathalie Mathe (with a grant from the European Space Agency), we began developing a procedure refinement assistant for control of a dynamic system. This system provides a range of increasingly automated levels of assistance, from structured editors to algorithms that suggest the most likely refinements to be made, and that can revise their suggestions based on user feedback. Second, we continued development of a rule-debugging assistant integrated with an artificial-intelligence planning system. We have shown, as a separate result, that the rule-debugging assistant improves the correctness of planning over time, but with some loss of efficiency.

Next year we plan to provide computerized tools to apply the principles of procedure development and maintenance to NASA operations. We have submitted a joint proposal for a collaboration with Mission Operations at Johnson Space Center. The first step is to produce an electronic procedures system—a networked system for simply viewing flight procedures and related documents in electronic rather than paper form. This will be a networked system for document production and viewing at mission control. Offices at Johnson and other centers will be able to access the documents remotely by personal computer. Future plans include creation of an "intelligent electronic library" which will use hypermedia tools to retrieve and browse procedures and related documents in various forms (text, schematics, video, animation, voice). We also plan to create "intelligent revision control tools" to electronically track and control procedure review and revision. In addition, we will investigate a cooperative procedure-development environment, which would provide tools for team procedure design and revision.

Ames-Moffett contact: N. Mathe
(415) 604-3515
Headquarters program office: OAST

Intelligent Software Support for Scientific Model-Building

Richard Keller

We are building a software environment that makes it easier for scientists to construct, modify, and share scientific models. The SIGMA (Scientists' Intelligent Graphical Modeling Assistant) system functions as an intelligent assistant to the scientist. In constructing this system, we are using a variety of advanced software techniques, including knowledge representation and automatic programming techniques from artificial intelligence, as well as techniques from object-oriented programming, graphical interfaces, and visualization. SIGMA is being developed in collaboration with scientists in the Space Science Division's Theoretical Studies Branch and the Earth System Science Division's Ecosystem Science and Technology Branch.

During 1992, we enhanced SIGMA's ability to handle array-structured data, to numerically integrate certain types of ordinary differential equations, and to make program calls to external subroutines provided by the scientist. As a result of these enhancements, we were able to use SIGMA to reconstruct a model that analyzes Voyager 1 observations to determine a temperature profile for Titan's atmosphere. By executing the model created with SIGMA, we successfully reproduced a table of data that had been published in a scientific journal. Also during this year, we extended our knowledge base to support modeling activities associated with the Forest-BGC ecosystem model. A third accomplishment was the design and implementation of a graphical user interface for our system (see figure). This new interface, which replaces our old text-based interface to SIGMA, allows users to view models as graphical objects, and greatly facilitates scientist interaction with the system.

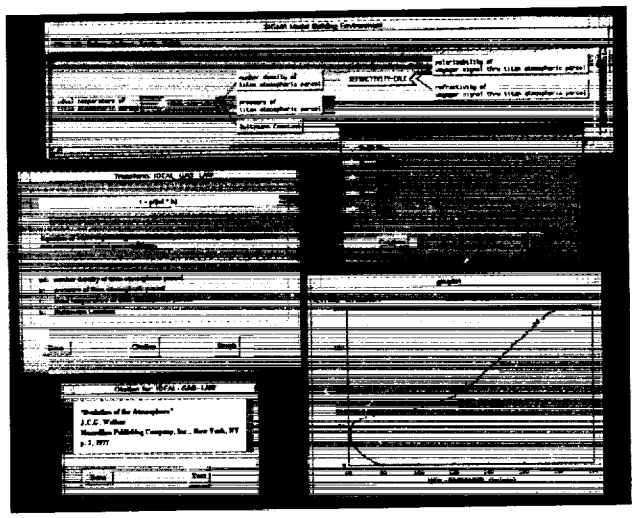

Fig. 1. SIGMA graphical interface displaying a portion of a Titan atmospheric model.

Ames-Moffett contact: R. Keller
(415) 604-3388
Headquarters program office: OSSA/OAST

Artificial-Intelligence-Based Planning for Data Analysis Tasks

Amy Lansky

The focus of our research is planning—the process of creating coordinated plans of action that meet required constraints. Artificial-intelligence-based (AI-based) planning techniques include methods for determining what actions must be performed, ordering the actions so that they obey relevant domain constraints, allocating required resources to actions, and then, during plan execution, modifying the plan as situations warrant. We are developing a domain-independent planner, COLLAGE, that is flexible enough to allow experimentation with several different approaches to cost-effective planning.

COLLAGE is being applied to the task of planning data-retrieval and data-preparation steps commonly performed by earth scientists. Over the next decade, NASA will launch several satellites containing instruments for studying the Earth's ecosystems. The Earth Observing System (EOS) will provide a qualitative leap in data volume and availability for the earth-science community. Whereas their primary goal is to analyze and interpret data (typically by ecosystem modeling and simulation), earth scientists spend much of their time—perhaps over 50%—on selecting and preparing data for analysis and interpretation. The task is complex because of the enormous range of data sets to choose from, the complexity and interdependency of constraints that define the suitability of specific data-preparation choices, and the possibility for several forms of failure during data preparation.

All of these characteristics also make the data-selection-and-registration problem amenable to automation using AI-based planning techniques, which explore a wide range of plan choices while also satisfying domain constraints. Such automation can speed up this otherwise tedious and time-consuming task. Automated reasoning allows the exploration of a more complete range of possibilities for data selection and preparation, and more thorough constraint and integrity testing. AI-based planning solutions to this problem will also enable data selection and preparation choices to be documented and justified, allowing data distortions to be diagnosed and corrected and the option of plan reuse. COLLAGE has two features that make it uniquely suited to this task. First, many different kinds of plan-construction methods can be employed. COLLAGE contains a broad repertoire of domain-independent plan-construction algorithms. The system is easily extended to include new planning methods, including domain-specific methods. For the data analysis domain, the ability to use tailorable methods of plan construction is important for achieving natural, flexible, and cost-effective planning. Second, COLLAGE uses localized search, a technique for partitioning potentially intractable planning search spaces into smaller, more manageable search spaces. The primary benefit of localized reasoning is search cost reduction. Also, since expensive algorithms are applied to much smaller, localized plans, the cost of the plan-construction process is reduced. Another potential advantage of localization for data analysis is that it facilitates plan reuse and modification via localization and containment of plan interdependencies.

Work is nearly finished on extending the COLLAGE constraint repertoire. We are working with Ames earth scientists to build a domain theory and a wide range of problem instances that require data selection and preparation for various data analysis applications, including the ecosystem model Forest-BGC. We hope to integrate our work with other AI-based systems being developed at Ames. Ultimately, we hope to hook up COLLAGE and SIGMA (Scientists' Intelligent Graphical Modeling Assistant) as part of a larger "scientific workbench" that will enable earth scientists to conduct modeling and data preparation in a unified computational framework.

Ames-Moffett contact: A. Lansky
(415) 604-4431
Headquarters program office: OAST

Knowledge-Based Software Engineering (KBSE)

Michael Lowry

The goal of this project is to develop the technology to assist end users in developing their own software systems out of components from existing libraries of code. NASA has a large number of software libraries, but it is often difficult for scientists who did not develop a particular software library to use it effectively. Even when a library is well designed and extensively documented, end users often lack the time or expertise to become knowledgeable about the myriad choices of subroutines, parameters, and other options. The result is poor use of the capabilities of a software library, and, too often, outright errors.

To address these problems, the knowledge-based software engineering (KBSE) project seeks to automate the development of software systems from high-level specifications that are acquired interactively from an end user. Software development, maintenance, and reuse will be raised from the code level to the specification level, resulting in greatly improved productivity and quality. By targeting systems built from existing software components, the KBSE project will leverage the considerable investment NASA has already made in its software libraries.

This project draws on artificial intelligence (AI) and formal methods. AI techniques are well suited to assist in the early stages of software development, when the objective is to understand the requirements of a problem and to specify the high-level behavior of a software system that can solve the problem. The discipline of formal methods applies mathematical logic to the development of verifiably correct software. Formal methods are well suited for automating the later stages of software development, when the objective is to develop a correct implementation from a specification of the desired behavior of a software system.

In the summer of 1992, research began on automating software development for the domain of solar system geometry. This domain includes analysis of geometric information needed to interpret data gathered by interplanetary spacecraft, ground- and space-based astronomy, and radio astronomy. This domain is also used for planning interplanetary missions and astronomical observations. NASA's Jet Propulsion Laboratory has developed the SPICE software library of over 500 FORTRAN routines for this domain. SPICE currently has more than 600 registered users.

The KBSE project has developed a high-level specification language for solar system geometry. A prototype graphical user interface has been developed that will enable space scientists to enter specifications through diagrams. A method was developed for deriving programs from specifications. The derived programs consist of calls to subroutines in a software library, based on Waldinger's deductive tableau formalism. As expected, the straightforward application of this method led to a combinatorial explosion in the search space. Tactics were developed that control the growth of the search space, and were successfully tested on examples. One tactic consists of guiding the theorem prover to construct a data-flow graph. Another tactic, which is currently undergoing implementation, entails decomposing a specification into a hierarchy of abstraction spaces.

Research in calendar year 1993 will first focus on completing the prototype system and testing it with end-users in the scientific community. We will then extend the system's capabilities to provide users with interactive debugging at the specification level. The KBSE project will explore methods for determining whether a specification is complete and unambiguous and for giving suitable feedback to an end user. We will also investigate means for semiautomatically choosing approximations of end-user specifications, making trade-offs between accuracy and computational performance. We expect that the research we do for the domain of solar system geometry can be generalized in future years to other domains.

Ames-Moffett contact: M. Lowry
(415) 604-3369
Headquarters program office: OAST

Computer Integrated Documentation

Nathalie Mathe, Bharathi Raghavan, Joshua Rabinowitz

The objective of the Computer Integrated Documentation (CID) project is to facilitate intelligent interaction between humans and computers in computerized information indexing and retrieval tasks through the integration of hypermedia and knowledge-based systems capabilities. Rapid and effective access to information in large documentation systems is needed at NASA. Accessing and using information stored in such systems has become increasingly difficult because of the growing volume of documentation, the diversity of information sources, and the frequent rate of change of such documentation. A major problem in managing large documentation systems is the lack of capability for efficient contextual information retrieval and revision. As conversion of large volumes of paper documents and technical manuals into electronic format continues, the need for accurate indexing becomes increasingly important. Typically such documents are indexed manually at great expense, and search methods are crude. Improved indexing and retrieval methods are needed. These methods will also facilitate the frequent revision of documents.

Particular needs for solutions have been identified at the Space Station Freedom Level I (SSF Level I) Engineering Office at NASA Headquarters (NASA HQ), and at the Combined Mission Control Center for the Space Transport System (STS) and Space Station Freedom (SSF) at Johnson Space Center (JSC). The CID project addresses these needs with (1) new techniques for acquiring appropriate retrieval strategies; (2) new techniques for retrieving context-dependent information; (3) hypermedia techniques for interconnecting documents, including text and graphics; and (4) intelligent interface design including user modeling and relevance feedback.

A CID prototype system has been developed to help SSF Level I personnel manage the Program Requirement Document for SSF. The CID system enables integration of various technical documents in a hypermedia framework and includes an intelligent context-sensitive browsing tool that interacts with and learns from the user. CID's knowledge-based indexing mechanism allows case-based knowledge acquisition through experimentation.

Research was conducted this year on the extension of the context-sensitive information retrieval technique to take into account previous users' actions, and on the development of a more sophisticated query language. To help navigate in large documentation systems, we developed two new graphical tools: a graphical table-of-contents browser, which displays the hierarchical organization of the whole document, and a graphical semantic browser, which lets the user browse hyperlinks between descriptors and referents in a document by using various search modes and context-sensitive filters.

During the past year, we developed a fully working prototype of the CID system. A first evaluation was conducted at NASA HQ in June 1992, and new user requirements were included in this prototype. A second evaluation was performed in December 1992. The context-sensitive information retrieval and indexing mechanism has proved to be useful for rapid retrieval of previously accessed information, as have the graphical browsers for visualizing information without having to actually read a document. A larger-scale evaluation will be conducted in 1993 with SSF Level I personnel at NASA HQ. We also started a collaboration with JSC to define a joint project on the design of an electronic documentation system for a Combined Mission Control Center for STS and SSF at JSC. The CID software package has been distributed to several NASA users, universities, and corporations.

Ames-Moffett contact: N. Mathe
(415) 604-3515
Headquarters program office: OAST

Capturing Human Visuomotor Control Strategy in an Out-the-Window Flight Control Task

Anil Phatak, Charles Jorgensen

Numerous mathematical models have been developed that emulate human performance after measuring the input–output behavior of humans in closed-loop tasks. These models are based on control and estimation theory, incorporating what is known about human visual perception, information processing or cognition, and motor control. Existing modeling methods usually fall short because they describe what an ideal human *should* do rather than what he or she actually does. To understand actual human control strategy in vision-directed vehicular control tasks, a more direct, bottom-up, observation-based approach is needed.

Neural-network modeling has been used successfully to describe behaviors too complex for detailed mathematical or physical models. In particular, neural networks have been trained to replicate observed input–output data using a combination of autonomous (unsupervised) and guided (supervised) learning algorithms.

In 1991, experimental helicopter out-the-window hover-control-task data were analyzed using Adaline and sigmoid backpropagation algorithms. A reasonable fit was obtained, but it appeared that a two-layer feed-forward network would be required to gain a more accurate solution. In 1992, the real source of many problems in pilot model fitting was clarified by the finding that a multilevel-hysteresis neural network followed by a time-delayed nonlinear second-order dynamic model for the human motor-control system was successful in duplicating the actual pulsatile nature of human-pilot stick responses. This success confirmed that at least one major source of error in earlier pilot models was that they were not taking into account perceptual and motor time delays when calculating which input stimuli the pilots were actually responding to during hover.

Ames-Moffett contact: C. Jorgensen
(415) 604-6725
Headquarters program office: OAST

Telepresence and Autonomous Control of Undersea Vehicles

Daryl Rasmussen, Butler Hine, Terry Fong, Michael Sims

Since the earliest days of NASA it has been recognized that the undersea environment offers an accessible and, in many ways, realistic analog for space environments. The undersea environment is hostile and relatively inaccessible to humans, but is scientifically attractive for a number of reasons. Because of the similarities of operations in space and those under the sea, the latter can provide real-world experience in testing and proving technology in preparation for its use in space.

This project comprises research in remote human and autonomous operation of undersea vehicles. These vehicles are test platforms for the development and validation of hardware and software technologies for future space applications. The work is focused on machine vision, virtual reality used for teleoperation, and advanced data analysis. This project is a collaborative effort between the Intelligent Mechanisms Group, the Photonics Group, the Human Factors division, the Aerospace Robotics Lab (ARL) at Stanford, the Monterey Bay Aquarium Research Institute (MBARI), the Naval Postgraduate School, and the Telepresence Science Working Group (an element of Ames Research Center's Center for Mars Exploration).

In 1991, collaboration was initiated with ARL and MBARI on applied machine vision, and work began on force feedback control in a virtual environment. In 1992, researchers began implementing virtual-environment-based teleoperation of an undersea vehicle. In November, we accomplished the first teleoperation from Ames of an underwater remotely operated vehicle (ROV) in the Antarctic using a head tracking display to control a slaved camera system. Future plans include performing complete teleoperation of an Antarctic ROV under the ice during a data-gathering mission using a virtual-reality control interface from Ames. We will also apply advanced data-analysis techniques to real-time sensor flow from Monterey Bay. One technique being investigated is sensor overlay for telepresence. Operational and prototype platforms have been built and operated in which the pilot of the vehicle uses navigational displays and images from on-board cameras displayed on television monitors. These camera displays are sufficient for navigation, tracking, and some scientific purposes, but there is often a wealth of auxiliary sensor data available from the vehicle to the pilot or scientists which could be incorporated into the visual display to aid in the operations. This is a pilot project in which auxiliary sensor data is superimposed on the camera view of the scene so that an operator is able to identify scientifically interesting regions.

Ames-Moffett contact: D. Rasmussen
(415) 604-6603
Headquarters program office: OAST

National Photonics Testbed

Max Reid

The coordination of optical processing research efforts that are currently being conducted by NASA, other government laboratories, industry, and academia will greatly enhance the technological benefit gained from all of the programs.

A National Photonics Testbed has been established at NASA Ames Research Center which will bring the developers of optical processing devices and systems together with potential users of these systems. Technologies developed by the Department of Defense, industry, and academic laboratories, as well as devices, materials, and systems developed in-house, are combined and evaluated in systems demonstrated in the testbed laboratory environment.

User requirements are defined and refined through close consultation between Ames photonics researchers and NASA systems developers, such as guidance-and-navigation personnel at Johnson Space Center, Space-Shuttle-main-engine test personnel at Marshall Space Flight Center and Stennis Space Center, and space structures control system developers at Langley Research Center.

National technology resources are combined with user requirements to develop and demonstrate prototype laboratory optical processing systems. The devices, systems, and user-requirements data base will be maintained in operational status for use by industry, government, and academia. New concepts may be quickly compared to the existing system without expensive and time consuming redevelopment of the hardware and data base infrastructure.

The ultimate product of the photonics testbed will be fully developed systems that are ready for flight qualification and use in specific NASA missions.

Ames-Moffett contact: M. Reid
(415) 604-4378
Headquarters program office: OAST

Parallel Systems Research

Catherine Schulbach, Jerry Yan

Parallel computer systems hold the promise of providing the order-of-magnitude increases in speed that will be needed to meet the requirements of future NASA missions. Many aspects of parallel computer systems are not well understood, so research is needed in several areas. This year our work focused on architectural scalability and tools for instrumentation, performance evaluation, and visualization.

To understand the architectural approaches suitable for future generations of computing systems, and to develop and evaluate multiprocessor prototypes suitable for the NASA High Performance Computing and Communication Program (HPCCP), the issue of scalability was addressed using AXE—a rapid prototyping/modeling environment developed at NASA Ames. In 1992, ARC2D, a representative application for the Computational Aerosciences (CAS) project (in HPCCP), was modeled using AXE. We were able to predict its execution time on the Intel "Gamma" computer to within 7%, in most cases. We intend to project the performance of our ARC2D model on thousands of processors (connected as hypercubes as well as two-dimensional meshes). From the results, we hope to be able to identify software and hardware bottlenecks and to determine how hardware parameters affect performance.

Because the debugging of program performance on parallel systems is significantly more difficult than on sequential systems, research was undertaken to develop new techniques for instrumenting, monitoring, and presenting the state of concurrent program execution in a coherent and user-friendly manner. In past years, a prototype software tool for monitoring program execution was developed to illustrate these concepts. The tool, called the Ames instrumentation system (AIMS), automatically instruments FORTRAN programs, monitors their execution, and displays performance data graphically on workstations that support X-Windows. An important feature provided by AIMS is source code click-back. This year, AIMS was incorporated into run-time environments to increase user productivity. Resource-utilization monitoring techniques were studied to identify load imbalances and facilitate the development of dynamic resource management strategies. In 1992, AIMS was distributed to Langley Research Center, Lewis Research Center, the Numerical Aerodynamic Simulation Division at NASA Ames, the University of Michigan, and the University of Illinois for teaching and evaluation. In addition, a beta-version of AIMS was developed which accepts C programs and runs on the 512-node iPSC/Delta at Caltech. An intrusion compensation algorithm was included to compensate for the overhead caused by the instrumentation software.

AIMS will be extended by working closely with CAS application specialists at various NASA centers to identify the features most useful for their work. Instead of taking the (unscalable) approach of "using 5 minutes to examine 5 milliseconds of execution," we will develop monitoring and visualization methodologies and systems that will be more selective about which data are to be collected and displayed. Although software instrumentation is much more flexible than hardware monitors are, it disrupts the application it is trying to monitor. Therefore, we will be exploring the use of hardware monitors on future HPCCP testbeds.

Ames-Moffett contact: C. Schulbach
(415) 604-3180
Headquarters program office: OAST

A Neural Learning Algorithm for Touch-Based Control of Mechanical Manipulation

Jay Steele

A fundamental goal of NASA is to again put humans on the Moon and establish a lunar base. Automated vehicles and manipulators for accomplishing tasks in the lunar environment will be essential. The purpose of this study is to develop a system capable of handling the control problem of safely moving these vehicles and manipulators around perceived, potentially dynamic obstacles in a cluttered work space. The system must be capable of learning and storing information about the world in addition to controlling a physical robot with a real-time control loop.

A distributed control system was developed that consists of a Puma 562 robot arm mounted on a linear track. Using the Task Control Architecture system from Carnegie Mellon University, a computer is set up with one process running the central host module and another process running a neural learning/control module. On another computer (a single-board computer using VxWorks, a real-time UNIX operating system) runs another process that is the robot control module. This module controls the robot testbed using a 35-Hz control loop. It collects information from sensors that indicate obstacles in the robot's path, and stops the robot's motion when necessary in order to prevent collisions.

The system allows the neural learning/control module to move the robot arm to specific joint positions and determine whether the move was successful. If the specific move has failed because of a sensor-detected collision with an obstacle, the neural learning/control module learns that this is not a good move to make and, ideally, selects another move to achieve its long-term goal. We have developed a reinforcement-learning system that uses an evaluation function for each goal position which indicates the most appropriate action for a given state. This evaluation function is reinforced both by short-term success (in this case, getting closer to the specified goal) and long-term success (actually reaching the goal). This reinforcement changes values assigned to all the possible actions at each state, and the action with the highest value for the current state is the action commanded to the robot controller.

The next step is to fully integrate this reinforcement-learning system with the robot controller and to modify the system to allow better continuity between different evaluation functions for different goal positions.

Ames-Moffett contact: J. Steele
(415) 604-6081
Headquarters program office: ARC DDF

Temporal Prediction using Neural Networks

Eric Wan, Bernard Widrow, C. Schulbach, C. Jorgensen

For certain problems in time series prediction, classical approaches have shown only limited success. For complicated time series, difficulty may arise from high-dimensional nonlinear dynamic or chaotic processes. Long-term prediction, such as for the stock market, where errors in linear models tend to geometrically accumulate with time, is especially difficult.

Our objective was to develop an improved neural-network technique for performing time-series prediction, for application in the analysis and prediction of complex data streams. Prediction-performance evaluations were made using the Wolf sunspot data series, astrophysical data, sleep apnea responses, and data on NH3-laser-focusing behavior obtained during the international Time Series Prediction Competition sponsored in January 1992 by the Santa Fe Institute. A new type of nonlinear neural network was used to extract a model of the underlying dynamics that gives rise to a particular time series. This architecture used a multilayered network that embedded time delays into the structure by modeling individual synapses as finite impulse response filters.

Training of the neural network was performed by multiple presentations of specific time series. Evaluation was then done of the actual prediction of a portion of the time series the network had not observed. Evaluations of short-term (one time step ahead) and long-term prediction were done. The new network proved to be the most successful in the competition with regard to relative mean-squared error prediction.

Ames-Moffett contact: C. Schulbach
(415) 604-3180
Headquarters program office: OAST

Electronic Chart Display Development

Vernol Battiste

A prototype electronic-chart display (ECD) system coupled with a global positioning system (GPS) receiver was flight-tested during a snow and ice study conducted by the NASA C-130 Earth Resources aircraft over Glacier and Yellowstone National Parks in February 1992. To aid the navigator/photographer in maintaining geographical orientation and to reduce the workload, the ECD system was temporarily installed at the navigator station. The ECD system was compared to the inertial navigation system (INS)/ paper-map system normally used by the navigator. A post-flight questionnaire was designed to provide a subjective assessment of the capabilities and functionality of the system.

GPS and INS data were synchronized for comparison. GPS data were less variable (distance in meters = (minimum/maximum) 18/52, standard deviation (SD) = 9.27) and more accurate than INS data (distance in meters = 1.8/555, SD = 132.89). The informal responses by all crew members to the ECD system were favorable, given its single-map-page format (8.5- by 13-inch scanned pages) and limited display size (4 by 4 inches). The responses from the navigator/photographer indicated an equivalent rating for the ECD system and the paper chart/INS method, despite the display limitations of the former and the respondent's greater experience with the latter. He also indicated that the ECD system afforded greater flexibility than the paper maps currently used. The ECD system will be installed in the C-130 aircraft in early 1993. Through a project funded by the Technology Utilization office, the system will also be tested in a California Highway Patrol vehicle.

Ames-Moffett contact: V. Battiste
(415) 604-3666
Headquarters program office: OAST

Cognitive Complexity Assessment

Kevin M. Corker

The myriad of dedicated controls and displays that were spread throughout aircraft cockpits have been replaced with integrated multifunction devices that encapsulate a wide range of information display and control within a single cathode ray tube or control pad. While providing a "cleaner-looking" crew station, such multifunction, multimode instruments impose significant memory and decision-making requirements on the operators.

Yufik at the Institute for Medical Cybernetics (IMC) is developing a network representation technique to explore measures of cognitive complexity quantitatively under a Phase II U.S. Army Small Business Innovative Research (SBIR) contract. A weighted directed graph makes explicit the information content and control relationships between detailed operator activities and the associated equipment. This prototype software tool will provide one of the first objective measures of cognitive complexity.

The IMC has produced a display-comprehension model focused on the organization of associative memory structures that are exercised when a display is used. Some indication of the relative amount of processing effort, or "cognitive complexity," can be found by measuring the degree of organization in such structures and how well they match the operator interface. In addition, to the extent that these associative structures capture regularity patterns in the

procedures for using the equipment, they can be used to predict when cohesive clusters of control sequences, or "chunking," will occur—an important consideration in training potential operators.

Under this SBIR contract, Yufik's theoretical approach will be refined, a PC-based software tool will be developed, and empirical testing of the results will begin.

Ames-Moffett contact: K. Corker
(415) 604-0055
Headquarters program office: U.S. Army

Symbolic Operator Model

Kevin M. Corker, E. James Hartzell

The analysis of system performance through simulation requires efficient and effective representation of significant parameters of human–system interaction. The user/analyst must be able to examine and manipulate component models. These models must include descriptions of the mission that is being performed, the operators performing it, and the equipment being used in its performance. The Symbolic Operator Model (SOM) of the A^3I Man–Machine Integration Design and Analysis System (MIDAS) is an inclusive structure that holds component representations of functional processes that are required to account for and predict human-operator behavior. These components, implemented by means of an integrated object-oriented architecture, are as follows:

1. *Updatable world representation (UWR):* The UWR is the operator's memory store (long term, but modifiable). It is implemented as a network of objects that are linked to each other by relations. The organizing structure of those relations is that they are part of more general systems. Knowledge of the current state of the objects held in the UWR can be degraded as a function of time since last information update. The decay function for working memory is a variable exponential function that is calculated using the time since an activity or object entered the store. Questions such as whether the operator could have known a particular fact and, if that fact was known, was it known in sufficient time or detail to guide behavior, can be addressed through manipulation of the operator's world knowledge.

2. *Perceptual processes:* Visual-information processing is used to update information held in the UWR. General visual scanning, directed visual processing, scanning patterns, and fixation points and times support predictions of what is and is not available to the visual system.

3. *Attention filters:* A model of visual attention, specified by Remington and Johnston of the Human Interface Research Branch, acts as a filter for information streaming in from the vision and perceptual models, allowing separate control of attention and vision. Pre-attentive filters also exist, modeling attention "capture" by salient environmental stimuli.

4. *Activity/procedural representation:* Activities are the methods through which action is effected in MIDAS. The activity organization is based on the spawning and completion logic of activities decomposed from high-level mission goals to individual flight and switch actions. In addition to physical action (in control and communication), behavior of the human operator is modeled to include information processing.

5. *Cognitive processes:* The cognitive processes currently supported in the SOM take the form of contingent responses to changing environmental states. These contingent behaviors are guided by a set of rules and a set of decision algorithms that are invoked with consideration of the state of knowledge (the UWR state) and the state of the world (time available to decide on a particular response). Information recall and local scheduling of actions are also represented as cognitive processes that take both time and effort.

6. *Scheduling:* Scheduling of a set of activities is performed in the SOM by a set of functional components: the Scheduler, the Goal Decomposer, and the

Task Loading Model. The scheduling takes place in service of a goal through the iterative application of constraints. Constraints inherent in the activity being performed and constraints imposed by the inherent limitations of humans are considered and met by means of a blackboard structure and constraint-satisfaction heuristics.

7. *Task loading:* Performance of activities imposes loads on the human operator. These loads are calculated as a function of the tasks being performed, and are measured in the context of the set of actions performed by the human. Task loads guide scheduling according to strategies of load management, and serve as indicators of the difficulty of mission-imposed activity requirements.

8. *Response/effector processes:* Human psychomotor responses are modeled within the constraints of the aircraft equipment suites. This model provides limited description of human neuromotor response and verbal communication protocols.

The SOM will integrate these and other functional components into a unit that can model the behavior of human operators as they interact with the equipment suite of a specific vehicle in the performance of a set of goals describing a mission.

Ames-Moffett contact: K. Corker
(415) 604-0055
Headquarters program office: U.S. Army

Effect of Perspective Format Displays on Pilot Spatial Awareness

Nancy S. Dorighi, Stephen R. Ellis

The anticipated increase in commercial air traffic in the next century will require a system that allows closer spacing between aircraft, trajectories that are more fuel efficient, and fewer schedule disruptions caused by poor visibility. Pilots may be challenged to manage narrower error tolerances, even in adverse weather conditions, and to navigate new curved approaches to runways made possible by microwave landing system technology. Perspective displays may help pilots maintain optimum spatial awareness, and thereby maximize the efficient use of available airspace and airport facilities, yet also ensure safety.

Pilots rely on out-the-window vision, their vestibular sense, and cockpit instruments to perceive their location, motion, and attitude. Spatial orientation can be seriously affected when vision or vestibular cues are degraded. Poor visibility and high levels of distraction or fatigue are examples of conditions in which spatial awareness may be temporarily degraded. Also, in coordinated turns ordinarily encountered during airline flights, the pilot after a time loses the physical sense of turning, because of the absence of significantly varying lateral forces or angular accelerations on the body. Distraction may cause the pilot to lose track of how far through a turn the aircraft may have come, adding uncertainty to directional judgment. A study is in progress to determine whether a perspective pathway display format integrated with a display of basic ground references provides a significant improvement in pilot spatial awareness. In this work, the Tunnel-in-the-Sky pathway display developed by Arthur Grunwald of the Technion, Israel Institute of Technology is compared to a conventional primary flight display (attitude direction indicator), in the framework of a basic set of cockpit instruments (horizontal map, heading, altimeter, and others), with special emphasis on spatial awareness during turns.

The Tunnel-in-the-Sky is a two-dimensional perspective display that functions much like a flight director but provides additional information. This display format makes up for the loss of visual cues by providing predictive information, look-ahead capability, and basic ground-reference elements, all in an inside-out (egocentric) frame of reference. The Tunnel-in-the-Sky may make the approach to landing easier by providing greater preparation time for control inputs. If the information is presented in a body-referenced manner as it would appear out the window, it may be more readily comprehended.

Thus, with less attention required for navigation, more attention can be given to maintaining spatial awareness.

In contrast, conventional flight instruments provide only flat, two-dimensional "snapshots" of the aircraft state, with minimal future-trend information. Furthermore, the individual status displays must be integrated to produce a perceived spatial orientation.

An initial part-task experiment has been conducted to determine the conditions under which spatial awareness may be increased by use of the Tunnel-in-the-Sky display that was integrated into a 757-type suite of primary flight displays. The primary flight-display software was provided by Langley Research Center and runs on IRIS-4D-series computers made by Silicon Graphics. Curved approach scenarios were used to compare a conventional attitude direction indicator with the Tunnel-in-the-Sky display in the flight-deck instrument suite of a modern glass cockpit of a commercial airliner. Spatial awareness was measured by the accuracy of the pilot's judgment of the visual direction of a set of targets representing actual terrain features along or near the approach path. Preliminary findings show that pilots locate the targets more precisely when manually flying approaches with the help of tunnel displays as opposed to conventional symbology. In general, with both types of displays pilots are found to regularly underestimate the magnitude of the azimuth angle to targets.

Ames-Moffett contact: N. Dorighi
(415) 604-3258
Headquarters program office: OAST

Electronic Haploscope

Stephen R. Ellis

An electronic haploscope has been built in order to gain a better understanding of the components of binocular stimuli that determine external location, orientation, and shape of virtual images viewed in head-mounted, stereoscopic, virtual-image displays. Such displays may be used to present "immersing" virtual environments or, in a see-through mode, to superimpose stereoscopic computer imagery on real scenes, as in stereoscopic head-up displays.

A haploscope is a particular type of stereoscope that allows independent control of the accommodative and vergence demands for fused, clear binocular vision. Most classical versions of the haploscope accomplish this independent control with pairs of viewing optics pivoted independently about the centers of rotation of the user's eyes. Thus, the accommodative demands for viewing targets along each optical channel can be varied by movement of the target along the optical axis of each channel. The vergence demand is controlled by rotating the entire optical system. In the electronic haploscope, the vergence demand is varied by a combination of electronic shifts of the graphics viewport and prisms introduced into the optical system. The use of computer-driven CRT displays as image sources allows unique flexibility and control of the stereo image.

The existing see-through system uses specially modified Citizen monochrome high-definition television monitors that display a video signal that provides at least 500 lines of vertical resolution and 700 pixels of horizontal resolution. The maximum monocular horizontal field of view is 30 degrees. Binocular overlap can be varied from 0% to 100%. Optical distortion is minimized through the use of a corrected-lens system for most of the power. Accommodative demand can be brought in from infinity by the addition of standard trial lenses. Maximum luminance is in the low-to-medium photopic range and can be varied by the selection of different characteristics of the partially silvered combining lens.

Studies of the interaction of stereo virtual images and physical backgrounds at different depths have been conducted. The apparent depth of the stereo virtual images appears to be influenced by their

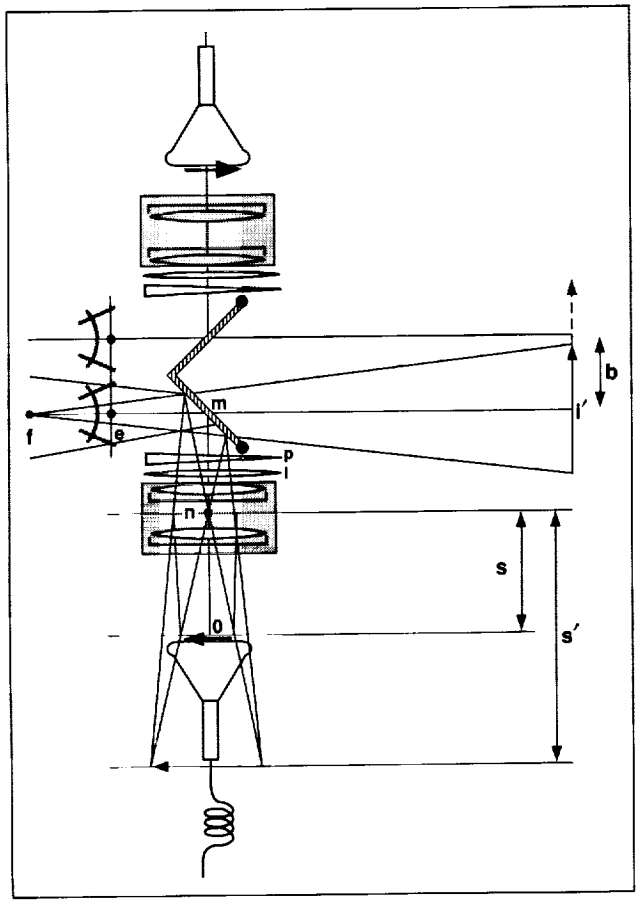

Fig. 1. Electronic haploscope (explanation in text).

superposition upon different surfaces, but this influence appears to be highly variable for different subjects. Current studies will investigate the roles of visual and oculomotor variables that determine the apparent depth of the superimposed stereo image. Understanding of the factors influencing the apparent depth, size, and shape will assist in the design of physically unrealizable virtual environments to be used for improved communication and control in manufacturing, telemanipulation, and telerobotics.

The figure is a schematic design of an electronic haploscope. The viewer's right eye is located at e, looking through a partially silvered mirror, m. The accommodative relief is provided by an Erfel eyepiece with a nodal point located at n. The virtual image, i, is generated on the CRT at o but is seen at i because of the mirror. Supplementary prisms may be introduced at p and trial lenses at l. The region of binocular overlap, b, can be varied.

Ames-Moffett contact: S. Ellis
(415) 604-6147
Headquarters program office: OAST

Attentional Fixation in Head-up Displays

David C. Foyle, Robert S. McCann

The head-up display (HUD) uses the technique of placing symbology collimated at infinity in the pilot's field of view in order to allow pilots to see the out-the-window view of the world as well as the onboard aircraft displays. A flight simulation task (see first figure) was used to evaluate the influence of superimposed symbology location on information integration. In this part-task simulation, pilot subjects were simultaneously required to follow a ground track and to maintain an altitude of 100 feet. Altitude information was available from either (1) out-the-window (terrain) visual cues only, or (2) out-the-window visual cues supplemented by a superimposed digital altitude indicator (i.e., simulated HUD symbology). The HUD symbology was presented at three distances from flight-relevant, terrain-path information, from three HUD locations: lower (directly superimposed), center, and upper (farthest distance). Root mean squared error (RMSE) altitude and RMSE heading were measured.

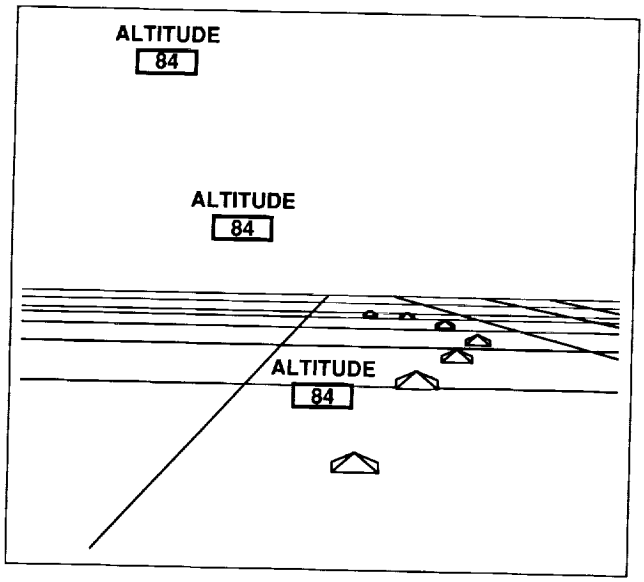

Fig. 1. Stylized schematic of superimposed flight symbology (showing the three tested locations) overlaid on an out-the-window view from the part-task mission simulation.

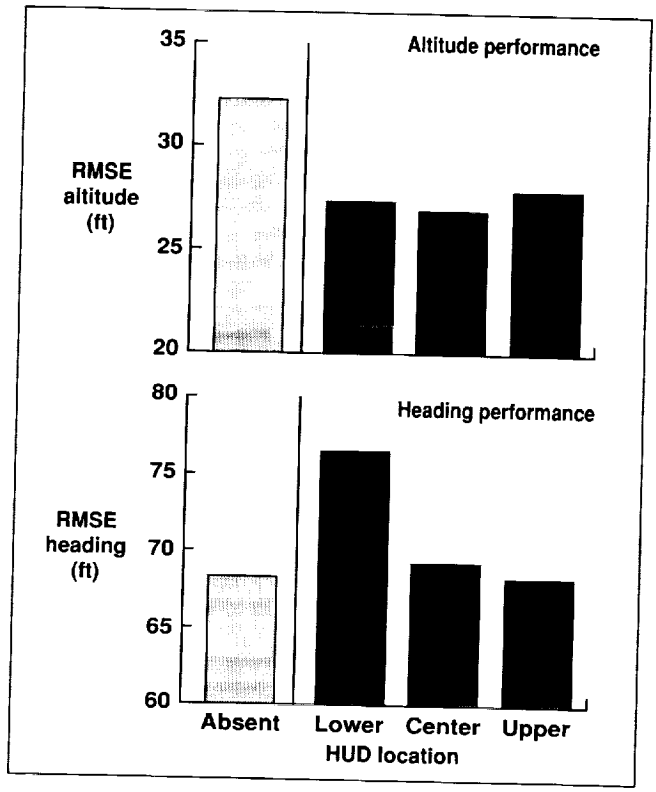

Fig. 2. Performance results from the simulation: altitude maintenance performance (top graph) and ground track (path) error (bottom graph).

Not surprisingly, altitude performance (second figure, top graph) improved when digital altitude information was presented on the HUD. The HUD information was equally beneficial at all three HUD locations. As shown in the bottom graph, use of the HUD had no adverse effect on subjects' ability to follow the path when the HUD was located in the center or upper position. When the HUD was in the

lower position, however (when the HUD was closest to or directly superimposed on the flight-relevant terrain-path information), the HUD-related improvement in altitude maintenance was achieved at the expense of poorer path performance.

The results of this simulation study indicate that pilots were not able to attend to both the HUD information and the outside world terrain when the two were directly superimposed. Directly superimposed placement did not result in information integration, and in fact, encouraged attentional fixation. Simultaneous processing of the HUD information and the outside world information was best in conditions that encouraged attentional or visual scanning.

Ames-Moffett contact: D. Foyle
(415) 604-3053
Headquarters program office: OAST

Crew Performance Assessment

Steven E. Gregorich, J. Victor Lebacqz

Aeronautical operators that use multipilot aircraft have placed an emphasis on the performance of crews as teams that goes beyond the traditional emphasis on individual technical proficiency. Technologies for the measurement of crew performance have been developed mostly in field settings (i.e., in airline training departments and line operations). Field development has some advantages but offers limited empirical control. A laboratory-based research program dedicated to the conceptualization and measurement of crew performance has been initiated. The goals of this program include the development of objective measurement techniques that can be administered reliably and are empirically valid. These techniques will be useful to researchers exploring the determinants of crew performance as well as in training programs designed to disseminate their findings.

The research focuses on expert-observer evaluations of global crew performance, categories of operational errors, and related crew behaviors observed during videotaped simulated flight segments. This effort has developed (1) a philosophy that aids in the identification of operational errors and their temporal location, (2) a classification of errors according to their behavioral manifestation, and (3) strategies for classifying crew responses to the errors. Throughout, an attempt has been made to distinguish between errors and recovery strategies attributable to individual aviators and those attributable to two or more crewmembers. Future research efforts will use global observations of experts and measures of specific crew behaviors as sources of data about crew performance. These data, in combination with the data describing operational errors, will be used to develop and validate models of crew performance and methodologies for its accurate measurement.

Ames-Moffett contact: V. Lebacqz/S. Gregorich
(415) 604-5792/0031
Headquarters program office: OSSA/FAA

Cockpit Resource Management Training Assessment

Steven E. Gregorich, J. Victor Lebacqz

As a result of increased emphasis on the performance of aeronautical crews as teams, training programs designed to enhance crew effectiveness have become common among military and commercial air-transport operators. The training typically takes place both in classroom settings and in full-mission-simulator training exercises. Training departments seek guidance in the design, implementation, and evaluation of training programs. A data-based system of assessment can complement informal assessments by providing information that is not otherwise available. Through formal data collection, information can be systematically compiled in common metric, and thus disseminated across fleets and organizations.

The program is focused on providing assessments of training outcomes, instructional techniques and preferences, curriculum content, and background characteristics of individuals and organizations that affect outcomes. Recent advances include refinement and validation of two self-report instruments that are completed by trainees. One instrument is completed both before and after the classroom portion of training. The other instrument is completed after simulator-training exercises. A general philosophy and framework for training-program assessment was developed. This framework provides guidance for developing an integrated system of training and assessment. It also lends insight into the strengths and weaknesses of current assessment efforts. With this framework in mind, efforts are under way to expand assessment efforts, especially the examination of the effects of training curricula.

Ames-Moffett contact: S. Gregorich
(415) 604-0031
Headquarters program office: OSSA/FAA

Displays for Optimal Planning of Rendezvous and Proximity Operations

Arthur J. Grunwald, Stephen R. Ellis

Concepts have been developed and evaluated for space-station-proximity-operations displays or other generic displays of relative orbital position. The original display concept emphasized the use of metrical computer graphics to present spatial information to astronauts. An interactive proximity-operations-planning system was developed which allowed on-site designing of fuel-efficient, multiburn maneuvers in a multispacecraft environment. Maneuvering took place in, as well as out of, the orbital plane. The difficulty in the informal planning of such missions that arises from higher-order control dynamics was solved by visualizing the relative trajectories and the relevant constraints in an easily interpretable graphic format to provide operators with immediate feedback on their design actions.

The newest display version not only uses inverse dynamics to remove control nonlinearities associated with orbital maneuvering, but has been integrated with a multiburn optimizer that can be interactively adjusted to adapt an automatic path-planning routine to a specific constraint environment that reflects plume, structure, and velocity constraints on orbital trajectory planning.

The visualization that provides this feedback shows a perspective bird's-eye view of a space station and co-orbiting spacecraft referenced to the station's orbital plane. The operator has control over two modes of operation: (1) a viewing system mode, which enables exploration of the spatial situation about the space station and (2) a trajectory design mode, which allows the interactive "editing" of waypoints and maneuvering burns to obtain a trajectory that complies with all operational constraints and with the optimization routine. Thus, through a graphic-aided interactive process, the operator can continue to improve his design until all constraints are met and an optimal path for maneuvering has been identified.

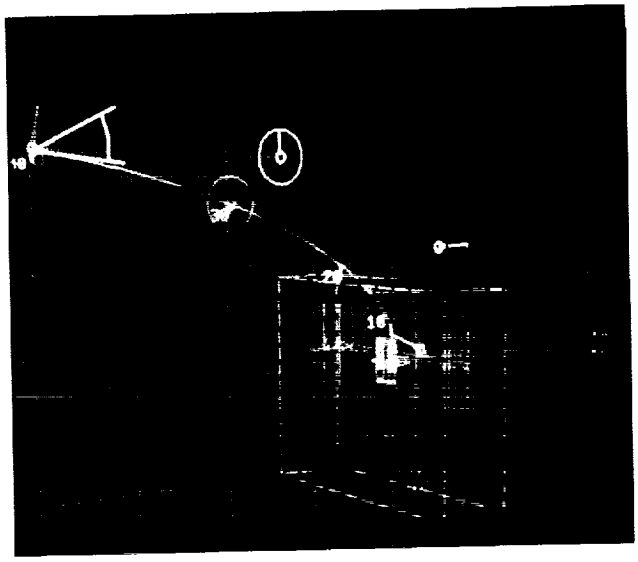

Fig. 1. Display for optimal planning of rendezvous and proximity operations.

An experimental program in which operators design a series of missions that vary in complexity and constraints has been implemented. Operator actions (i.e., viewing-system operations or trajectory design) have been recorded for manual planning and will be recorded for planning that is done with the automatic optimizer. Review of the trajectory design characteristics is used to identify the heuristic design rules that can be used in improved automated orbital-planning systems.

This work is conducted jointly by Ames Research Center, the Israel Institute of Technology (Technion), and the University of California, Berkeley.

Ames-Moffett contact: A. Grunwald
(415) 604-0104
Headquarters program office: OAST

Distributed Cognition

Edwin Hutchins, Everett A. Palmer

Automation in the cockpits of commercial transports is rapidly changing both the cognitive tasks faced by individual pilots and the cognitive properties of the cockpit itself as a system. The information-processing capabilities of the cockpit system result from a complex set of interactions distributed among pilots and representational media. Cockpit behavior is viewed from multiple perspectives. First the trajectories of task-relevant information are traced as the cockpit system accomplishes a set of tasks. This level of analysis deals with the movement of directly observable task-relevant information (i.e., pilot actions, pilot verbal communications, and machine responses). At a second level, these observable representations provide specifications for the cognitive tasks that must be performed by the pilots for the system to function.

This project (undertaken through a collaborative agreement between Ames and the University of California, San Diego) is investigating how pilots use the autopilot, the autothrottle, and the flight management system to solve flightpath-control problems. One problem with the current autoflight interface that the distributed cognition perspective brings into focus is that the locations for taking action and evaluating the consequences of action are spread throughout the cockpit. Actions are taken in one place (the mode control panel) and evaluated in another place (the flight mode annunciators and the primary flight displays). Extra mental work is required to compose actions, evaluate results, and know when different representations of flightpath "say the same thing." It is not sufficient that all the information be present. It is also necessary that the information be represented in a way that facilitates the cognitive tasks required of the pilots in order to compose actions and evaluate their consequences. There are also important conceptual regularities in the behavior of the autoflight system that the current interface masks. It is possible to build physical regularities into the behaviors of the displays that correspond to conceptual regularities in the system being managed. Building these kinds or correspondences of display behavior and conceptual structure into the display is a good way to lower the cognitive costs of interaction with the system. With minimal training, a pilot can learn to "see" the conceptual structure directly in the display rather than have to do mental computations to reconstruct it. An interface constructed with representations that require less mental work will reduce the need for error-prone mental processing and increase the likelihood that necessary checking tasks will be accomplished. A graphic autoflight-mode control panel has been designed according to these concepts and will be evaluated in the Advanced Concepts Flight Simulator.

Ames-Moffett contact: E. Palmer
(415) 604-6073
Headquarters program office: OAST

Visual Cueing Aids for Rotorcraft Landings

Walter W. Johnson, Anthony D. Andre

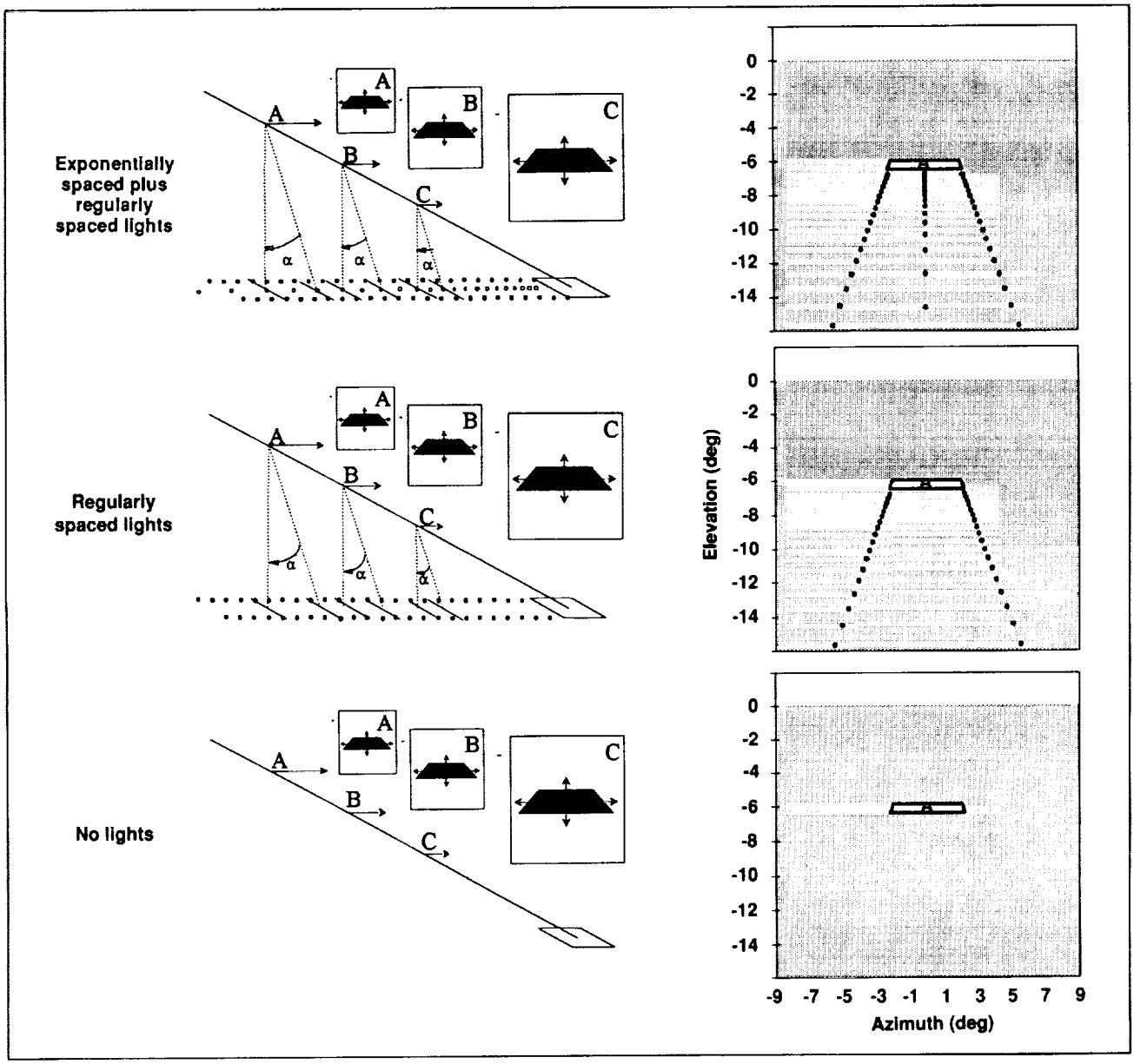

Fig. 1. Perspective view of approach lights and landing pad at glideslope intercept for the three approach lighting conditions (right) and associated visual cue analyses at three trajectory locations (A, B, and C) for constant closure rate approaches (left). Cue analyses depict constant relative expansion rate (percent/second) of pad image in all conditions (dark expanding polygons), constant flow rate (α/second) for both conditions in which approach lights were used, and a constant edge rate (lights/second) for the middle row of lights in the exponential-plus-regular approach lighting condition.

Rotorcraft landings in physically constrained environments, such as urban vertiports, present potential hazards not commonly faced in fixed-wing or rotorcraft landings at conventional airports. One major hazard is the presence of buildings or other obstructions beneath the glideslope or directly behind the landing pad. In such environments it is necessary for pilots to accurately maintain their assigned glideslope and also to reliably regulate their speed in order to achieve zero velocity at the landing pad.

Investigators in the Rotorcraft Human Factors Research Branch and the Flight Dynamics and Controls Branch addressed this problem in a study designed to examine approach lighting configurations that make three types of vehicle speed information visually available through rotorcraft windows.

The study, conducted in the Ames Vertical Motion Simulator, examined three approach lighting options over a range of initial speeds and ranges from the landing pad. In one condition, only the landing pad itself, together with the horizon line, was visible (first figure, bottom). This made relative-closure-rate (speed/remaining distance) information available in the form of the landing pad's *relative optical expansion rate* (percent change in optical size per second). Military rotorcraft pilots are instructed to maintain the closure rate during descents to hover. By regulating this value a pilot can regulate deceleration rate and ensure that the vehicle will arrive at the landing pad with zero final velocity.

A second condition added two rows of regularly spaced approach lights that extended out from the edges of the landing pad (first figure, middle). Now, in addition to the optical expansion mentioned above, the lights passing beneath the simulated vehicle provide two other forms of potentially useful optical information, *optical flow rate* and *optical edge rate.* Like the relative optical expansion rate, the optical flow rate of the approach lights provides relative closure information, this time in the form of the angular speed of the lights as they pass through the field of view. Because the optical flow rate is proportional to the vehicle speed divided by the vehicle altitude, the pilot can regulate the relative closure rate by regulating the flow rate. On the other hand, the optical edge rate of the approach lights (the frequency with which the approach lights pass through the visual field) is proportional to the vehicle speed

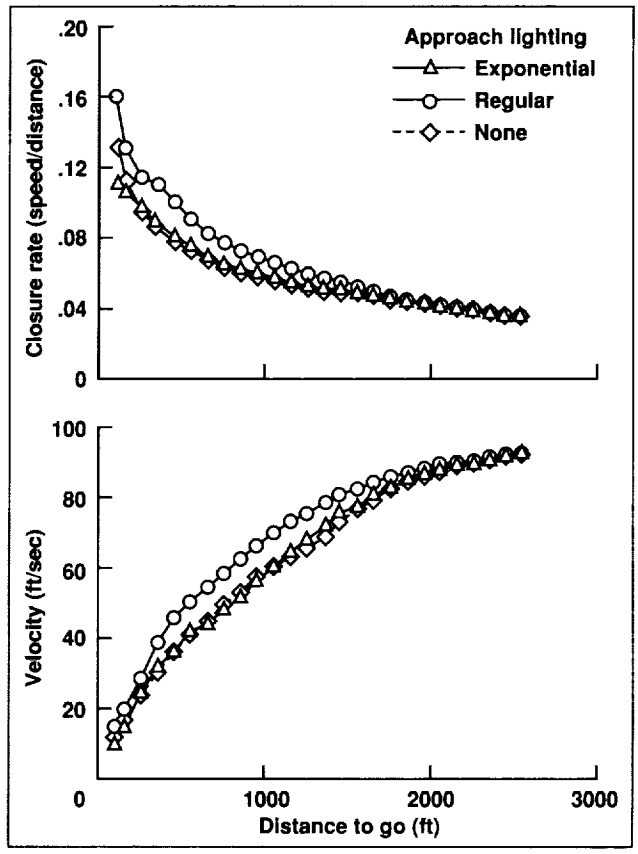

Fig. 2. Closure rate and velocity as functions of distance from the landing pad and the approach lighting condition for an initial velocity of 92 feet/second and a glideslope intercept at 2,645 feet.

divided by the approach-light spacing. Whereas evenly spaced lights yield good edge rate information about speed, a pilot must actively extract and take into account the rate of change in the edge rate, and also the distance to the pad, in order to use the edge rate to effectively regulate closure rate deceleration.

A third condition provided an additional row of lights in which the light spacing increased linearly with distance from the pad (first figure, top). Now, regulating the rate of passage of these lights through the visual field would regulate the relative closure rate, and any edge rate would yield a continuously decreasing velocity.

The results of the study showed that (1) closure rates were slower in the final portion of the approach

when the exponential lights were provided (second figure, top) and (2) the presence of the evenly spaced lights caused pilots to initially generate milder decelerations than in the cases where no approach lighting (pad only) or exponential approach lighting was provided (second figure, bottom). Thus the presence of a strong visual cue (edge rate) that was not linked to closure rate led to delayed decelerations.

These results indicate that the tailoring of approach-light spacing is an important and effective aid to pilots in their attempt to regulate decelerations to hover.

Ames-Moffett contact: W. Johnson
(415) 604-3667
Headquarters program office: OAST

Computationally Efficient Depth-from-Motion Displays

Mary K. Kaiser, Dennis R. Proffitt

Recent developments in microelectronics have encouraged the use of three-dimensional data bases to create accurate volumetric renderings of graphical objects for visual displays. However, even with the computational capabilities of current-generation graphical systems, real-time display of such objects is difficult, particularly when dynamic spatial transformations are involved and when there are cost, space, or other constraints on the sophistication of the systems that can be used. Thus, computational simplifications are beneficial as long as the required visual effects are maintained.

One such computational simplification involves the use of fractal geometry. A relatively simple propagation algorithm is used to create scenes of seemingly complex texture and structure by exploiting the insensitivity of the observer to the underlying mathematical regularities. We are examining the possibility of using analogous simplifications to produce depth-from-motion displays. Motion algorithms can be used that are far less complex than those required to produce the proper motion transformation of a three-dimensional data base. As with fractal rendering, our techniques create visual effects that are often perceptually indistinguishable from true transformations.

An example technique is based on a phenomenon known as the stereokinetic effect (SKE). As shown in the first figure, an SKE display preserves a subset of the image transformations that an object (here, a cone) undergoes when it is moved relative to an observer. In this example, the SKE version of a

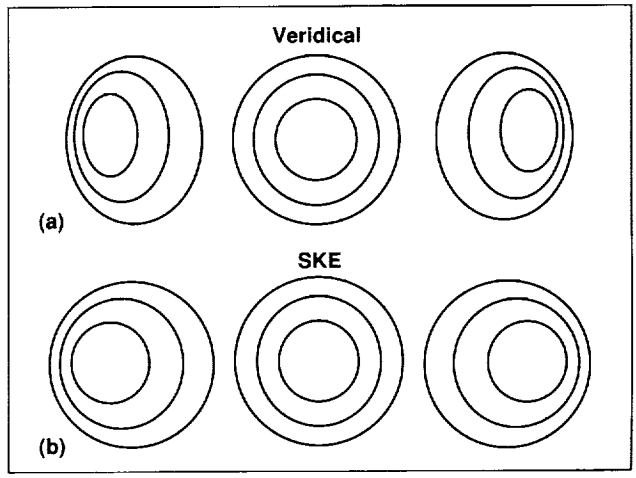

Fig. 1. Three frames of (a) a true (veridical) y-axis rotation of a cone, depicting –50, 0, and 50 degrees, and (b) the corresponding frames of an stereokinetic effect (SKE) display. Note that the transformations in (a) consist of both between-contour and within-contour motions, whereas only between-contour motions occur in (b).

Y-axis rotation preserves the between-contour transformations, but not the within-contour changes (i.e., the contours do not change aspect ratios as they do in the true rotation display). Deleting the transformations to which observers are insensitive can greatly reduce the computational complexity of the display, yet a sense of depth is preserved, as shown in the second

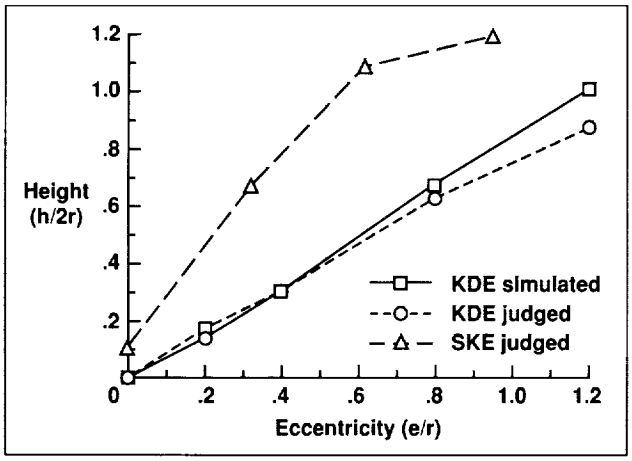

Fig. 2. Mean perceived heights (expressed in terms of the diameter of the cone's base) for the SKE and veridical displays as a function of display eccentricity (i.e., the distance that the contours shift in an oscillation, e, relative to the cone's base radius, r).

figure. We have created SKE-enhanced demonstrations for both contour map and air traffic control displays.

We are currently identifying other limits of human sensitivity to depth-from-motion information. Whereas some transformations are imperceptible because of their small magnitude (as in the above example), some transformations simply do not appear to be utilized in depth perception processes. This insensitivity is not currently instantiated in computational ideal-observer models. By exploiting this insensitivity, we can make spatial displays more computationally efficient while retaining their perceptual effectiveness.

Ames-Moffett contact: M. Kaiser
(415) 604-4448
Headquarters program office: OAST

Crew Factors in Aerospace Operations: Communication and Coordination

Barbara Kanki, Judith M. Orasanu

Crew Factors researchers are studying communication strategies that facilitate effective information flow both within teams and between interfacing teams during mission sequence tests conducted by payload engineers in the operations and checkout facility at Kennedy Space Center. We have systematically tracked the ways in which multiple, highly diverse teams cope with procedural deviations and other online delays and anomalies. In addition to developing an online coding methodology for classifying communications, we have made detailed analyses from the audiotapes produced during test days. Results have highlighted the test conductor's role in coordinating multiple teams in the face of ongoing disruptions to procedures and real-time troubleshooting. A final report will be generated in FY93. We plan to extend the general methodology to shuttle maintenance operations in the Orbiter Processing Facility and to the payload integration operations that will be conducted in the Space Station Processing Facility.

The relationship between automation and crew communication and coordination is far from direct or uncomplicated. For example, many varieties and combinations of automated systems may coexist in a single aircraft. The use of these systems (and subsystems) varies according to flight conditions, conditions on the ground, and other participants in the aviation system. In principle, advanced-technology aircraft should yield rewarding payoffs for flight operations, but we are concerned about unanticipated costs to the crew under some conditions.

Crew Factors researchers have also begun research on nonverbal communication in advanced-technology aircraft. There may be important information conveyed through actions as well as through speech. Particularly in the advanced-technology aircraft, where one cannot assume that all crewmembers are sharing the same information resources, actions such as computer input, gesturing

and pointing to information on a CRT, and simple gaze direction may become critical cues in maintaining a shared perception of a situation. Recent work has used data from a high-fidelity simulation study in which the automation context focused on electronic versus manual checklist use. The role of nonverbal communication is expected to have implications for training (e.g., the identification of effective strategies), as well as for workstation design.

Ames-Moffett contact: B. Kanki
(415) 604-5785
Headquarters program office: OSSA

ViDEOS: Visual Display Engineering and Optimization System

James O. Larimer

A joint effort between the Defense Advanced Research Projects Agency (DARPA), the U.S. Army, and NASA, supported primarily by DARPA's High Resolution Systems Program, is producing a computer-aided design (CAD) tool for designing and using flat panel displays wherein performance "figures of merit" are provided in image-quality units, as determined by a model of human visual processes. For example, a designer may wish to use a liquid-crystal (LC) flat panel display as a visual-control interface in a tank or aircraft. In this case, the important design issues would include contrast, color, the effect of ambient illumination, viewing-angle performance, and legibility. The Visual Display Engineering and Optimization System (ViDEOS) is being developed to help the systems engineer to evaluate the performance of a particular LC, flat panel display in this conceptual crew-station environment. ViDEOS can also be used to optimize design trade-offs in LC-display engineering development or component engineering. It is a common language that supports a dialog between the systems engineer and the component engineer.

The current focus is on developing an end-to-end tool for designing active-matrix LC displays. Later versions will include other flat panel display types. The system has several modules that are integrated through a software interface running in the X-Windows and UNIX environment. The entire system is written to be used on a standard UNIX-workstation platform. ViDEOS consists of the following modules: (1) a circuit-analysis and modeling module for modeling the thin-film transistor pixel matrix and drive circuits, (2) an optical-modeling module for determining the configuration of the LC layer and modeling the optical performance of the LC shutters, including the light source and all optical layers, (3) a device-modeling module for configuring the pixel-tiling geometry, (4) an image-rendering module for pixelating arbitrary input images, (5) a biological-vision-model module for modeling image quality, and (6) an interface-shell module for integrating all of the modules and for inputting, displaying, and archiving data. In addition to the software effort, an empirical research effort is under way to validate the model predictions. This effort includes construction of actual LC cells and extensive psychophysical research to validate image-quality predictions.

We know of no display-modeling effort anywhere in the world with the end-to-end scope of ViDEOS. American companies participating in or associated with this program include InFocus, Rockwell, Honeywell, GE, IBM, OIS Optical Imaging Systems, Hughes, and the SRI/David Sarnoff Research Lab.

Ames-Moffett contact: J. Larimer
(415) 604-5185
Headquarters program office: U.S. Army

Information Management and Transfer

Sandra Lozito, Kevin Corker

Efficient and safe operations in the National Airspace System depend on the accurate and timely transfer of information between air traffic controllers and pilots. There is increasing use of digitized information transfer (data link) methods for air–ground communication in order to reduce voice communication errors and radio frequency congestion. Furthermore, increased use of automation in air traffic control (ATC) is likely to result in more complex clearance messages. The potential of this strategic airspace-and-trajectory control can be more fully exploited by using a digitized air–ground link. As the implementation of data-link technologies emerges, it is clear that research in this area must emphasize human factors to ensure that these changes in air–ground communication do not introduce more problems than they solve.

The Flight Human Factors Branch is involved in ongoing research on human factors issues of data link. This effort is focused on human/system integration both on the flight deck and in the ground-side control stations. A series of experiments has been initiated to investigate the following:

1. Content and format of data-link messages
2. Integration of data-link implementation with other developing technology, such as ATC automation concepts
3. Development and use of system-analytic models for ATC procedures (in collaboration with Honeywell, Inc.)
4. Situation awareness associated with frequency monitoring in general and military aviation (undertaken by the Massachusetts Institute of Technology).

Our approach to the exploration of these issues includes part-task simulation, full-mission simulation, and the use of modeling techniques. The subjects in our studies are line pilots and/or trained controllers.

Differences in data-link textual formats were examined in part-task simulation. A primary task of flight and clearance tracking was associated with a secondary task involving visual monitoring. Secondary-task performance was used as a primary measure between the two formats. Data-link acknowledgment-times-to-clearance messages were also measured. Our data revealed no significant differences on secondary-task performance or acknowledgment time as a function of the two clearance formats studied.

A full-mission simulation, using the Advanced Concepts Flight Simulator (ACFS), was designed and is under development. This experiment is intended to explore the integration of data-link technology and ATC automation. Specifically, the ACFS has been enhanced through the development of the Flight Management System, adding vertical navigation automation and data-link implementation capabilities. To complement these flight-deck enhancements, the Man-Vehicle Systems Research Facility has also integrated the Center/TRACON Automation System, an ATC advisory tool developed at Ames. These increases in cockpit and ATC capabilities will support an air–ground compatibility study scheduled to begin in spring 1993.

Ames-Moffett contact: S. Lozito
(415) 604-0008
Headquarters program office: OAST/FAA

Presence and Virtual Presence in Planetary Exploration

Michael W. McGreevy, Lewis Hitchner, Cindy Ferguson, William Briggs

The most visible schism among planetary explorers is over the question of whether or not human presence is important for exploration. This controversy tends to obscure the fact that all exploration missions ultimately include humans. The missions require close working relationships between the exploring humans, the exploration systems, and the environments to be explored. Systems of one sort or another always mediate between planetary explorers and the environment, enabling and constraining the actions they may take, and conveying and limiting the information about the environment that is available as a basis for action. Thus the design of these mediating systems is central to planetary exploration both with and without human presence.

A new kind of mediating system, one that provides virtual presence, is emerging from over 30 years of experience in planetary exploration. On one hand, data gathering associated with planetary exploration has evolved from the taking of photographs to the point where entire planets are digitized. On the other hand, explorers have been creating advanced but generally ad hoc visualization and interaction techniques for planetary exploration. These include the Surveyor Mosaic Spheres; Apollo surface panoramas and stereo pairs; Mariner mosaicked globes; Viking panoramas, stereo pairs, and synthetic perspectives; and Voyager and Magellan animations. The common goal of each of these techniques was spatial integration and more natural terrain visualization.

Over the last several years, improvements in computer graphics hardware, software, algorithms, and peripherals have made it possible for researchers at NASA Ames to implement virtual, interactive environments from digital-terrain models and digital-image models of Mars and Earth. Such virtual-planetary-exploration (VPE) systems recreate, to a useful extent, the experience of actual presence within the displayed environment. In the future, by combining detailed digital models of the planets with advanced VPE systems, planetary environments can be reintegrated from their data, even as that data is acquired in real time, enabling virtual planetary exploration and model-based telepresence. Such a capability will be able to provide an integrating medium for interactions between distributed explorers, exploration systems, and planetary environments.

Research is being conducted in the field and in the laboratory to understand and characterize the factors that enable and constrain useful interactions between explorers, planetary environments, and VPE systems. The central objective is to achieve an understanding of the nature of human presence in natural environments, particularly the presence of scientific explorers, and to embody that understanding in a theory of presence. The ongoing analyses that are contributing to the theory are based on ethnographic field methodology and object-oriented analysis. Designs and guidelines for virtual-presence systems are being derived from the analyses. In addition, prototypes are being developed from these designs in order to investigate their applicability, probe the limits of implementation, and provide feedback for the field work, analyses, and designs.

Recent accomplishments include a published review of NASA's evolutionary development of virtual planetary exploration; field investigations of the work of planetary geologists; development of the necessary components of a continuity theory of presence; development of algorithms for user-based complexity management of digital terrain models; development of gesture recognition algorithms and subsystems; elaboration of an ethnographic and object-oriented analysis methodology for the application of field observations to design; and continually improving implementations of virtual environment prototypes. Most important, the work is persuading mission planners, such as those developing the Artemis lunar mission, of the practical value of virtual-planetary-exploration technology.

Ames-Moffett contact: M. McGreevy
(415) 604-5784
Headquarters program office: OAST

Pilot–Controller Communication

Daniel G. Morrow, Michelle A. Rodvold, Kevin Corker

Pilot–controller communication is critical for safe and efficient flight. It is often a challenging component of piloting, and is reflected in the number of incidents and accidents involving miscommunication. A previous field study identified communication problems that disrupt routine communication between pilots and controllers. The present part-task simulation study followed up the field results with a more controlled investigation of communication problems. Pilots flew in a minimal simulation in which they were frequently vectored by air traffic control (ATC), which required intensive communication. We examined the influence of message length (one message with four commands versus two messages with two commands each) and noncommunication workload on communication accuracy and length. Longer ATC messages appeared to overload pilot memory, which resulted in incorrect or partial readbacks, as well as requests for repetition of the message. The timing of the two short messages also influenced communication; the second message interfered with memory of or response to the first short message when the second message followed too soon after the first message. Performing the noncommunication monitoring task did not influence communication. Instead, communication reduced monitoring accuracy. These results indicate that controllers should take pilot memory limits into account when formulating and delivering messages.

In addition to the part-task study, we further analyzed problems of understanding, using data from the previous field study in an effort to obtain a multidimensional problem "profile." For instance, some problems may be more frequent than others but can always be repaired when they do occur. Other problems may be less frequent but may be likely to go unrepaired or take a long time to repair. We also explored the possible composite or summary scores that provide a single index of "severity" for each problem. For example, a "severe" problem would occur frequently, take several communication interchanges to indicate and repair, and would be less likely to be repaired than other problems.

Problems of understanding were generally infrequent (469 out of 7,685 transactions), and those that occurred were usually repaired; the lowest rate of repair was 76%, which occurred for repeating unacknowledged previous messages. Whereas pilots and controllers often resolved problems of understanding, this process increased communication time and thus reduced efficiency. There was some evidence that controllers and pilots have different kinds of problems, which may reflect their different roles in ATC communication. Controllers were more likely than pilots to repeat unacknowledged messages or to correct readbacks, and they tended to miss, or not hear, pilot messages. Pilots, on the other hand, were more likely to—at least partly—misunderstand controller messages. The results of these studies will lead to a better understanding of pilot–controller communication in general, and will be used to improve aviation communication and training procedures.

Ames-Moffett contact: K. Corker/D. Morrow
(415) 604-0055/0009
Headquarters program office: OAST

Crew Factors in Aerospace Operations: Team Decision Making

Judith M. Orasanu, Barbara Kanki

Team problem solving in aircraft crews occurs under high-risk and stressful conditions. Both crew productivity and flight safety depend critically on the effective and efficient coordination of the crews' problem-solving efforts. However, we have little hard evidence of what constitutes effective problem-solving and decision-making behavior when crews face different kinds of problems.

We have addressed this issue by analyzing the problem-solving behavior of professional air-transport crews during simulated in-flight emergencies. We studied whether optimal task-management behavior is sensitive to crew size (two- versus three-member crews) and problem type. We found that effective crews, irrespective of crew size, showed higher situational awareness and requested more task-relevant information. Their decision making was more sensitive to situational constraints, and tended to be conservative: high-performing crews were less likely to commit themselves to preliminary decisions. Instead, they tended to postpone any decisions until sufficient information was gathered, reducing the risk of having to revise them. High-performing crews also employed more effective task management strategies. They generally initiated critical tasks as soon as possible, and could thus finish them in an orderly and timely fashion. Other effective strategies reflect crew size. Since two-member crews had fewer cognitive resources available than three-member crews, an optimal two-member strategy was to "stay ahead of the game." Effective captains used low-work-load periods to prepare for anticipated emergencies. In three-member crews, on the other hand, effective captains had their first officers fly the plane and devoted themselves to managing and monitoring the crews' problem-solving efforts. The effects of problem type on decision making and task-management strategies are currently being analyzed, and will provide useful information for crew training applications.

Certain classes of flight problems require joint solutions by pilots and dispatchers. Little is known about how working together influences the strategies used to solve problems or how it influences the quality of solutions, or about differences associated with each role or perspective. These differences include how each participant views the problem and what information each considers relevant. We have begun a study of pilots and dispatchers who work either singly or in concert; we are examining their approach to solving a problem that involves a placarded flight system on the aircraft. The problem can manifest itself on landing if weather conditions deteriorate, but does not affect takeoff or cruise.

From videotapes and interviews, we are examining the information structure and strategies exhibited by the pilots and the dispatchers as they respond to the problem working alone or together via telephone (as they normally would in such a situation). In addition, we are examining strategies evident when the pairs work together: How explicitly do they communicate their view of the problem and their rationale for a particular solution? Are more options considered or more information used when two work together? We are investigating the contributions made by each participant, how they signal their understanding or lack thereof, and whether they seek greater explicitness as they work on the problem.

Ames-Moffett contact: J. Orasanu
(415) 604-3404
Headquarters program office: OSSA

Automated Checklists

Everett A. Palmer, Asaf Degani, Kathleen L. Mosier

Automated checklists can remedy a number of the problems that arise with paper checklists. Automated checklists can graphically highlight pending, completed, and skipped steps. If the automated checklist can "sense" and display the state of aircraft subsystems, it can provide a redundant check of the completion of many cockpit tasks. It may also guard against automaticity in pilot behavior, in which a pilot sees the expected value of a display instead of its actual value. A touch-operated checklist can also use direct-manipulation graphic techniques to aid the pilot in switching from one checklist to another without losing track of partially completed checklists and without getting lost in a bulky paper procedures manual.

Two versions of an automated checklist have been implemented in the Advanced Concepts Flight Simulator. The two designs differ in the degree of pilot involvement in conducting the checklists. One version requires the crew to manually acknowledge the completion of each checklist item. The other version automatically indicates completed items without requiring pilot acknowledgment. These two designs and a paper checklist were evaluated in line-oriented simulation. Twelve crews from one major air carrier flew a routine four-leg, short-haul trip.

Design features of the automated checklists influenced crew behavior in a number of ways. For example, crews with paper checklists were more likely to wait for an externally controlled checklist item like "DOORS" to be completed rather than skip and later return to the item. Pilots skipped three times as many items with the automated checklist as they did using the paper checklist. When a normal checklist was resumed after being interrupted by the need to run an irregular checklist, pilots were more likely to restart the paper checklist than the automated checklist. In each case, the difference in pilot behavior can be explained as their taking advantage of the new feature of the automated checklist that provides a graphic display of completed and skipped checklist items. Results also suggest that making checklist procedures more automatic, either by asking crews to accomplish steps from memory or by providing checklists that encourage crews to rely on system state *as indicated by the checklist*, rather than as indicated by the system itself, tended to discourage information gathering, and had the potential of promoting dangerous operational errors.

Ames-Moffett contact: E. Palmer
(415) 604-6073
Headquarters program office: OAST

Image-Based Sensor Fusion

Michel Pavel, Albert J. Ahumada, Jr., James O. Larimer

Sensor-fusion algorithms combine information from different sources into a single display to reduce the work load of pilots who must rapidly integrate the information. Although our approach can be generalized to other sensors and tasks, we focus on the pilot's task of deciding whether to land in low visibility. The pilot's decision is based on (1) the image from an active or passive millimeter-wave radar and (2) an image of the scene rendered from a graphical data base of information on the terminal environment together with position information. The combining rule will be based on properties of the images that can be computed in real time using known methods and available hardware.

Each kind of image has limitations. Radar images have limited spatial resolution as a result of limited antenna size, and they have noise problems caused by limited signal power in conjunction with intrinsic sensor noise. The major limitation of the position-based (data-base-rendered) image is that it does not include new obstacles such as other aircraft or ground vehicles that may be on or near the runway. Our approach to these problems uses two principles—multiresolution analysis and noise analysis.

Multiresolution image analysis

Multiresolution image analysis has been successful in fusing visual and infrared imagery. In this approach, the image is first decomposed into bandpassed images in a manner analogous to the generation of separate bandpassed audio signals by a stereo-system graphic equalizer. The fusion algorithm combines two corresponding bandpass images, one from each source, and then the fused-bandpass images are recombined.

There are two major benefits in this approach. One is that the high-spatial-resolution-image component of the position-based image is not subjected to the fusion algorithm at all. Only the low-resolution part of the position-based image, which is represented by the same small number of image values as the low-spatial-resolution radar image, participates in the combination. This results in a large computational savings. The ability of the multiresolution approach to match images of different resolutions also allows it to work easily with variable-resolution-sensor data.

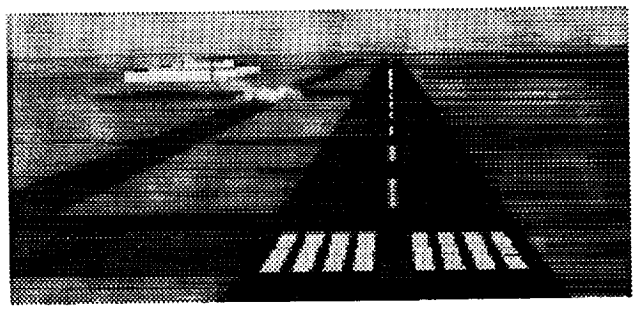

Fig. 1. Image-based sensor fusion.

A second advantage of multiresolution image analysis is that combination of images in the different spatial frequency bands results in little cross masking between the different bands. Information in one band can be seen relatively easily through the other bands. This may explain, in part, the success of the fusion of visual and infrared imagery despite mismatches of contrast polarity.

Noise analysis

Much of the radar image is noise. A running estimate of the noise level at each sensor region and resolution allows only the statistically significant components of the noisy image to be selected for output. If the energy of a region of a bandpass image is in the noise level, the corresponding component of the position-based image is selected. Since the radar image has no signal energy at high spatial frequencies, these bands are determined only by the position-based image.

The figure shows the result of fusing a simulated passive radar image with the corresponding graphical-data-base image. The passive radar sensor has rendered the scene with an aircraft taxiing toward the runway during approach. The position-based image has the same scene information without the obstacle. In the fused image the intruding aircraft is essentially as visible as it was in the original sensor image, although it lacks the detail of objects that are also in the data base.

Ames-Moffett contact: M. Kaiser
(415) 604-4448
Headquarters program office: OAST

C-2.

Aviation Safety Reporting System

William D. Reynard

The Aviation Safety Reporting System (ASRS), managed by NASA at the request of and with funding from the Federal Aviation Administration (FAA), was established in 1976. The ASRS has received, processed, and analyzed over 232,000 voluntarily submitted aviation incident reports from pilots, air traffic controllers, and others.

These incident reports describe unsafe occurrences and hazardous situations. ASRS offers confidentiality, and the FAA provides limited immunity for unintentional aviation safety transgressions the incident reporters may have committed. In exchange, the program receives safety information that can be used to remedy reported hazards, to provide data for planning and improving the National Airspace System, and to conduct research on pressing safety problems. The particular concern of the ASRS is the quality of human performance in the aviation system.

The ASRS is unique among aviation reporting systems. Its special qualities include the following:

1. Proof of the concept to acquire, analyze, and utilize incident data
2. Unique methods to capture otherwise inaccessible human-performance data
3. One-of-a-kind data base of actual incident information as reported by the events' participants
4. World's largest repository of human performance information
5. Consistent support and utilization of the program by government and industry
6. Proven capability for diverse applications to both research and operations
7. Ability to actively monitor the aviation system
8. Capability for effective technology transfer as evidenced by ASRS-type systems in other countries and disciplines.

In addition to screening and processing incident reports for entry into a data base, the ASRS maintains the data base and its supporting computer hardware and software, and interrogates the data base to satisfy the information requirements of government and industry organizations. Report receipts can be statistically analyzed for trends and problem concentrations, although there are important theoretical limitations on the use of ASRS data for this purpose.

The ASRS has published more than 42 research reports that are based on its data. These reports cover the full spectrum of aviation activity. In addition, the program has issued over 1,370 alerting messages and responded to more than 3,000 special data requests from the aviation community and the public. The ASRS also publishes a monthly safety bulletin, *CALLBACK*, and a quarterly safety and training publication, *DIRECTLINE*.

The ASRS operates under an Interagency Agreement with the FAA that is effective until March 1994. It has achieved a rapport with FAA operational and research organizations, and is used by NASA, the National Transportation Safety Board, the Department of Defense, and the aviation community. The ASRS has an active research program that encompasses both in-house investigations and support for independent users of ASRS data. A large and growing report volume continues to challenge ASRS resources; however, with increased FAA and NASA support, the program has the potential to significantly increase its operational and research activities.

The concept of a national program of voluntary, confidential incident reporting has proved to be so productive and well received that similar programs have been established in the United Kingdom, Canada, Australia, New Zealand, and Germany.

Ames-Moffett contact: W. Reynard
(415) 604-6467
Headquarters program office: FAA

Fatigue Education and Training Module

Mark R. Rosekind, Philippa Gander, J. Victor Lebacqz

The NASA Ames Fatigue Countermeasures Program investigates the extent of fatigue, sleep loss, and circadian rhythm disruption in different flight environments and the impact of these factors on pilot performance. A program is under way to identify, develop, and scientifically evaluate countermeasures to reduce the adverse effects of these factors. The countermeasures can involve personal strategies, operational guidelines, and education and training to help pilots maintain optimal levels of performance and alertness during flight operations. Investigations include field studies to obtain information and to test countermeasures in actual flight conditions. Laboratory studies are used to evaluate the potential usefulness of countermeasures before they are implemented on the flight deck.

Since its inception, a primary goal of the Fatigue Countermeasures Program has been to return information obtained through research and other activities to the operational community. Enough scientific data have been collected to create the first education-and-training module on fatigue in flight operations. The module is entitled, "Strategies for Alertness Management in Flight Operations," and includes basic information about fatigue, sleep, sleepiness, and circadian rhythms. It describes how flight operations affect these physiological factors, identifies some of the misconceptions about fatigue in aviation, and offers recommendations for countermeasures. The approximately 1.5-hour live presentation includes an opportunity for discussion to provide critical examples of how to apply the information to specific types of flight environments. The interactive presentation is complemented by a NASA technical memorandum that includes the visual materials from the presentation along with appendices that provide information on sleep disorders, sleeping pills and relaxation strategies, recommended reading, and operational summaries from other NASA technical memoranda. The module is intended for everyone in the aerospace industry—line pilots, flight attendants, schedulers, airline managers, federal regulators, and safety investigators.

The module has been field tested at five sites, by commercial airlines and overnight cargo operators. Every carrier that has tested the module has expressed interest in using the information for training of personnel, especially pilots and flight attendants. Some companies will offer the training on a daily basis at their headquarters; others will incorporate it into annual training programs or in special areas such as International Ground School. The Ames Fatigue Countermeasures Program will provide workshops on implementing the education and training module.

Ames-Moffett contact: M. Rosekind
(415) 604-3921
Headquarters program office: OAST/FAA

Controlled Rest on the Flight Deck

Mark R. Rosekind, Philippa Gander, J. Victor Lebacqz

A previous NASA study demonstrated that a planned rest period for pilots during the cruise portion of nonaugmented, three-pilot long-haul flights improved subsequent performance and alertness. Following a prearranged rotation, pilots were allowed, one at a time, to take a brief (40-minute) rest period, during which they could nap if they chose. Most were able to fall asleep, and slept for about 26 minutes. They later demonstrated better performance and greater alertness than crews that were not allowed a rest period. A NASA technical memorandum reporting these findings has been published. Based partly on the results of this study, an industry/government work group drafted an Advisory Circular (AC) for the Federal Aviation Administration. The AC provides guidelines for the development of a program that would sanction the use of controlled rest on the flight deck as an acute in-flight fatigue countermeasure. Controlled rest is one of many potential countermeasures to reduce fatigue and maximize pilot performance and alertness.

Ames-Moffett contact: M. Rosekind
(415) 604-3921
Headquarters program office: OAST/FAA

Age, Circadian Rhythms, and Sleep Loss in Flight Crews

Mark R. Rosekind, Philippa Gander, J. Victor Lebacqz

Previous field research has resulted in the world's largest data base on fatigue, sleep, and circadian factors in flight crews. An analysis of this extensive data base examined the relationship between age, sleep, and circadian rhythms in flight operations. The data from 205 pilots in six different flight operations were examined. These pilots were physiologically monitored to record core body temperature. They recorded their sleep and fatigue levels in self-report logbooks and they completed a questionnaire that included a variety of standardized inventories.

Older crewmembers flying long-haul operations had significantly greater daily sleep loss during trips than younger crewmembers. The sleep loss reported by long-haul pilots aged 50–60 years averaged 3.5 times that reported by pilots aged 20–30 years. Also, the daily low point of the body temperature (a marker of the circadian (24-hour) rhythm) occurred later in pilots aged 30–50 years than in those aged 20–30 years. The peak in the daily temperature was lower in pilots over 40 years than that in pilots aged 20–30 years.

Age-related changes in sleep and circadian patterns are known to occur. The findings in this study suggest that the development and implementation of fatigue countermeasures should take into consideration the age-related changes that occur.

Ames-Moffett contact: M. Rosekind
(415) 604-3921
Headquarters program office: OAST/FAA

Pilot Interaction with Cockpit Automation

Nadine Sarter, David D. Woods, Everett A. Palmer

In a questionnaire study of pilot attitudes toward cockpit automation, a majority of the pilots agreed with the statement, "There are still things in the automation that happen that surprise me." The pilots also stated that there were parts of the autoflight system that they still did not understand. More recently, 20 experienced airline pilots flew a scenario in a part-task simulator and were confronted with situations and tasks that tested the completeness and accuracy of their knowledge of one of the core systems of cockpit automation, the Flight Management System (FMS). The FMS supports the pilot in a variety of tasks such as flight planning, navigation, performance management, flight progress monitoring, and automatic flightpath control. An important characteristic of automatic flightpath control is the high frequency of mode switching. (Transitions between modes of control occur in response both to pilot input and to changes in flight status that are sometimes unknown to the pilot.) Both the flexibility of the FMS and the mode switching of flightpath control impose cognitive demands on the pilot. The pilot must decide which level and mode of automatic control to use in a given set of circumstances, know how to engage the mode, and then track the status and behavior of the automation and the mode it is in at the moment.

An experimental scenario was designed to address predefined phenomena of interest—for example, the pilot's awareness of the automation mode and its behavior. The scenario tasks were incorporated into a 60-minute flight from Los Angeles to San Francisco that the 20 airline pilots flew in a fixed-base B-737-300 part-task trainer. In one task, the pilots were asked to set up the FMS to use the automatic APPROACH mode. They had to remember that a lower altitude had to be entered in the mode control panel before they engaged the APPROACH mode. Later, in the final descent, they were asked to describe how they would disengage the APPROACH mode if air traffic control told them to change their heading and altitude to avoid another aircraft. Eight of the pilots engaged the APPROACH mode without lowering the altitude first and were surprised when the aircraft did not start the descent. When asked how to disengage the APPROACH mode after electronic guidance has been initiated, most of the pilots knew one way to comply, but 14 of the pilots suggested at least one ineffective approach.

The underlying reason for many of the problems observed in this study seems to be related to a lack of mode awareness and to gaps in pilots' mental models of the functional structure of the automation. The results indicate a need for more pilot training and for more effective interfaces between pilots and cockpit automation.

This work was accomplished in collaboration with the Department of Industrial and Systems Engineering at Ohio State University.

Ames-Moffett contact: K. Corker/E. Palmer
(415) 604-0055/6073
Headquarters program office: OAST

Research and Development of Glass Cockpit Technology

Robert J. Shiner

In order to study the effects of modern technology in transport aircraft operations, the Full-Mission Simulation Branch has contracted to develop and acquire a current-technology "glass cockpit" flight simulator modeled after the Boeing 747-400 aircraft that can perform full-mission simulation. Special features will permit normal interactions with air traffic controllers in a fully simulated air traffic environment. The simulator also includes enhanced capabilities to monitor crew and aircraft performance to support reliable and precise measurement of crew behavior in the simulated man–system environment.

The new simulator and the Advanced Concepts Flight Simulator already in operation will be used for research on ways to reduce aircraft accidents and flight delays. Such issues as reducing pilot workload, improving communication among system elements, and reducing crew fatigue will be studied.

The new simulator incorporates all aircraft system features, and can realistically model a wide variety of operating environments and equipment malfunctions. These capabilities provide the researcher with the opportunity to compare air-crew performance in routine, high-workload, and emergency circumstances. The system's high fidelity will allow generalization of research findings to the real world of flight operations.

The Boeing 747-400 (glass cockpit) aircraft represents the new generation of transport aircraft in which computer-driven, on-board systems have great authority. Modern aircraft computers control aircraft movement, sequentially implement a programmed flight plan, and have the ability to gather and process information from other systems to optimize performance in meeting secondary goals such as fuel efficiency. The glass cockpit features computer-created video displays of aircraft flight and system status information that reduce the number of gages and other information displays within view of the cockpit crew.

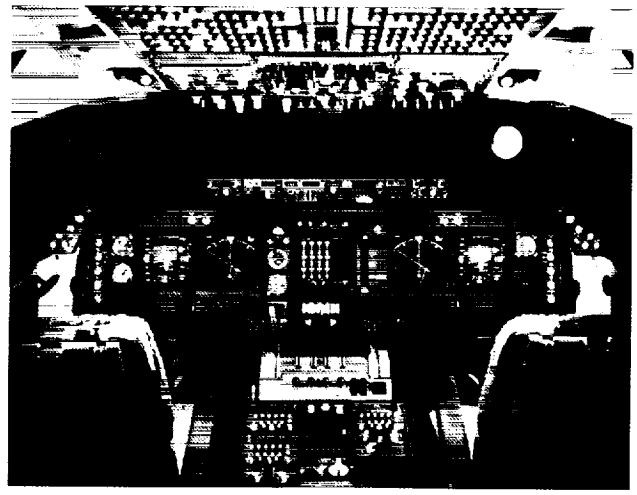

Fig. 1. Interior of the Boeing 747-400 glass cockpit.

One of the first experiments planned for the new simulator will study the effect of using computer data-link communications instead of voice communications between pilots and air traffic controllers. The simulator will also be used for research programs that are part of the National Plan for Aviation Human Factors and other programs appropriate for the 747 simulator.

Ames-Moffett contact: R. Shiner
(415) 604-0257
Headquarters program office: OAST

Man–Machine Integration Design and Analysis System (MIDAS)

Barry R. Smith, E. James Hartzell

The Man–Machine Integration Design and Analysis System (MIDAS) program is a major product of the joint Army–NASA Aircrew/Aircraft Integration (A^3I) Program. It has been under way since 1985 within the NASA Aerospace Human Factors Research Division and the Army Aeroflightdynamics Directorate. MIDAS is an integrated suite of software components to aid analysts in applying human factors principles and human performance models to the design of complex human–machine systems. MIDAS is intended to be used at the early stages of conceptual design, as an environment wherein designers can use computational representations of the crew station and operator, instead of hardware simulators and man-in-the-loop studies, to discover first-order problems and ask "what if" questions regarding the projected operator tasks, equipment, and environment for advanced vehicles. Consisting of over 450,000 lines of C, C++, and Lisp code on Silicon Graphics workstations, MIDAS serves as the framework in which research findings and models are incorporated.

MIDAS contains tools to describe the operating environment, equipment, and procedures of crewed systems, with models of human performance/behavior used in static and dynamic modes to evaluate aspects of the crew-station design and operator task performance. Specifically, models of visual perception, attention, memory function, rule-based and algorithmic decision making, task loading, and scheduling behavior are included. These models are encoded in an object-oriented architecture in which the individual models (as well as the system under study) are represented as interdependent agents that communicate with each other. The modular structure and strict communication protocol of this architecture allows MIDAS to support multiple representations of human performance at varied levels of detail. The results are typically presented graphically and visually to the research psychologist or design engineer, often as a computer simulation of crewed flight. In this sense, MIDAS is similar in concept to computational tools such as finite-element analysis and computational fluid dynamics, which are used to improve designs and reduce costs. The resultant MIDAS testbed then serves to support further research on human performance models, as well as aid designers with predictive data on operability, levels of automation, and function allocation issues for human–machine systems.

Although MIDAS is currently focused on helicopters, it can be generalized to other vehicles. In fact, interest in MIDAS has arisen from applications as diverse as the layout of nuclear-power-plant control consoles and the design of emergency response vehicles and dispatch stations. Recently the A^3I group provided MIDAS software tools and models to Boeing in exchange for applications data, a practical evaluation of their utility, and collaboration on future modifications. Boeing supplied computer-aided design files, equipment specifications, and procedure manuals for a special-operations-forces Chinook variant, the MH-47E; these were used during the last development phase of MIDAS. Through MIDAS, the group was able to replicate a number of human engineering issues in legibility, reach accommodation, and display formatting that arose during the actual preliminary airworthiness evaluation for the MH-47E.

The target date for a full-prototype system is 1995. Five major phases of development have been completed. The current phase involves empirical testing of embedded models, a software port to improve computational speed, and revised methods for activity representation guided by planning research in the Artificial Intelligence Research Branch. In addition, application-oriented work continues under Technical Exchange Agreements and with the Aviation Safety/Automation Program.

Ames-Moffett contact: B. Smith
(415) 604-4264
Headquarters program office: U.S. Army

Optimizing Image Compression for the Human Viewer

Andrew B. Watson, Albert J. Ahumada, Jr.

The next era of space exploration, especially the "Mission to Planet Earth," will generate immense quantities of image data. For example, the Earth Observing System (EOS) is expected to generate in excess of one terabyte per day. NASA faces a major technical challenge in managing this great flow of imagery: in collecting, pre-processing, transmitting to Earth, and archiving the data, and distributing the information to scientists at remote locations. Expected requirements in most of these areas exceed current technology. Part of the solution to this problem lies in efficient image-compression techniques.

For much of this imagery, the ultimate consumer is the human eye. Image compression should therefore be designed to match human visual capacities. We have developed two techniques for optimizing image compression for the human viewer. The first consists of a formula based on psychophysical measurements, developed jointly with IBM, that computes a discrete cosine transform (DCT) quantization matrix for any specified combination of viewing distance, display resolution, and display brightness (see figure). This DCT quantization matrix is used in most recent standards for digital image compression

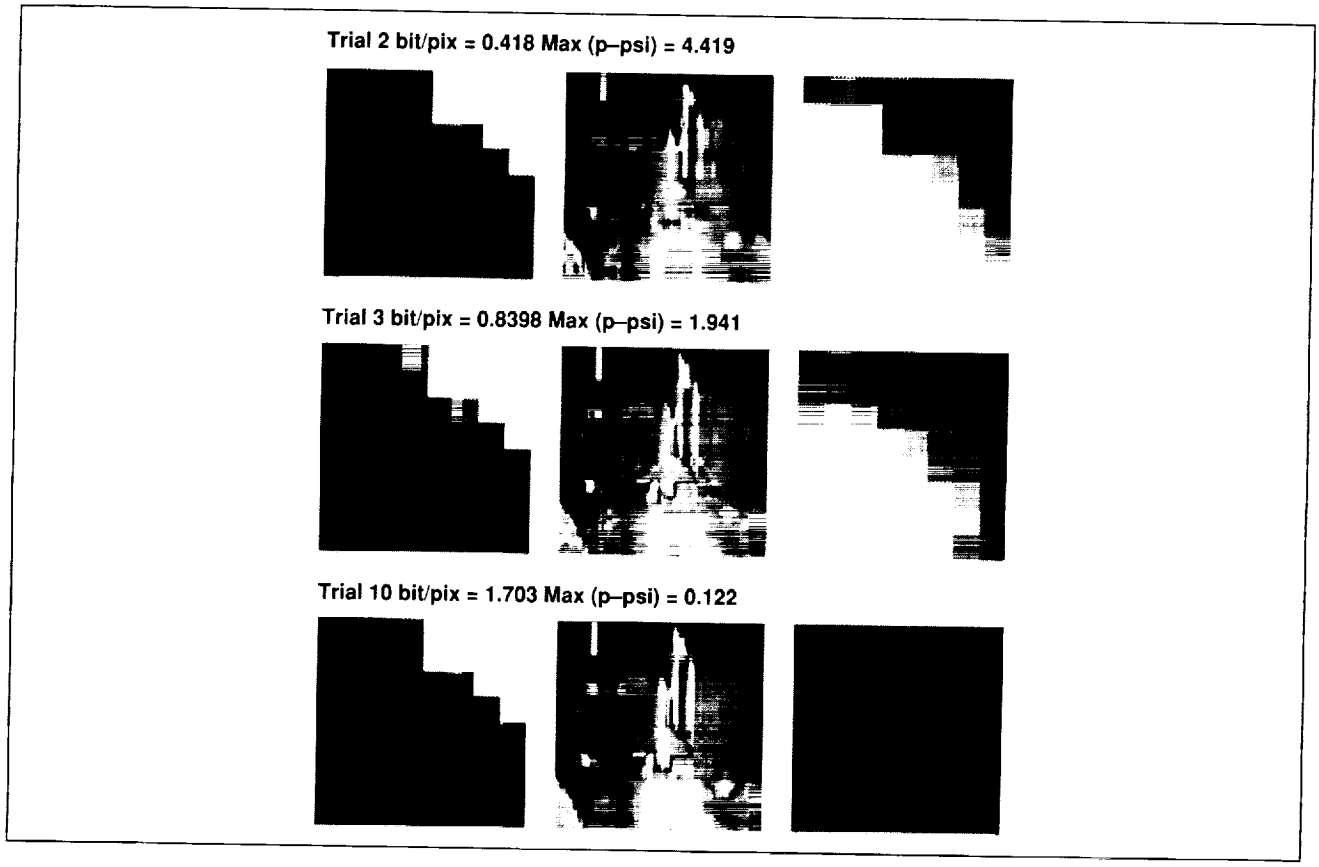

Fig. 1. The figure shows several steps in the progressive optimization of an image. Each row shows the quantization matrix (left), the compressed image (middle), and the matrix of perceptual errors (right). The optimization seeks a uniform perceptual error matrix.

(Joint Photographic Experts Group, Motion Photographic Experts Group). The second technique optimizes the DCT quantization matrix for each individual image, according to the contents of the image. This is accomplished by means of a model of visual sensitivity to compression artifacts. Together, these two techniques will allow systematic perceptual optimization of image compression in NASA imaging systems.

Ames-Moffett contact: A. Watson
(415) 604-5419
Headquarters program office: OAST

Motion-Contrast Sensitivity

Andrew B. Watson, Michael P. Eckert

Understanding human motion perception is critical for predicting human performance in visually guided flight, in designing effective robotic vision systems, and in designing efficient high-resolution image-communication systems. We have been studying the human ability to discern differences in velocity from one part of an image to another. Such motion discontinuities (or motion "edges") occur whenever one object moves in front of another, and are highly informative regarding relative velocity and relative depth.

Observers were presented with a display in which two noise images moved over one another in upward and downward directions. The luminance contrast of each image was varied sinusoidally over the screen, with the two sinusoids in antiphase. The appearance was of alternating stripes of upward and downward motion. By varying the amplitude of the sinusoids, a threshold for detection of the spatial variation in velocity could be measured. The inverse of this threshold is the *motion-contrast sensitivity*. By varying the spatial frequency of the sinusoid, the spatial resolution of this sensitivity could be determined.

The results (see figure) were compared to a model in which local velocity estimates are both integrated and differentiated. Differentiation would be diagnostic

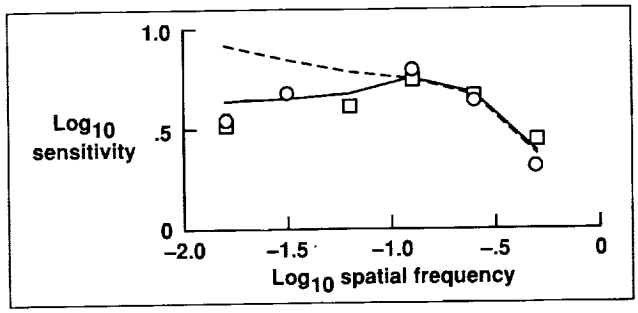

Fig. 1. Motion-contrast sensitivity measurements (symbols) and model simulations. The horizontal axis is the spatial frequency of the sinusoidal modulation of the motion stimulus. The curves are for models with (solid curve) and without (dashed curve) motion-edge detectors.

of a mechanism expressly designed to detect motion edges. The data support the existence of motion-edge detectors.

Ames-Moffett contact: A. Watson
(415) 604-5419
Headquarters program office: OAST

Visual Display Optimization Tool

Andrew B. Watson, Jeffrey B. Mulligan, Albert J. Ahumada, Jr.

High-resolution visual display systems are complex and expensive to design. The ultimate goal is high visual quality, but the quality cannot be evaluated until a prototype display is constructed. There is a need for design tools that will allow prediction of display quality from a symbolic description of a hypothetical design. These tools must incorporate models of human vision.

Since its inception, the Vision Group at Ames has had the goal of developing mathematical and computational models of human vision, and applying these models to visual human factors and visual technology. One facet of this work is the application of vision models to the design of visual displays. We are developing a visual display optimization tool (see figure) that will be used by display designers to

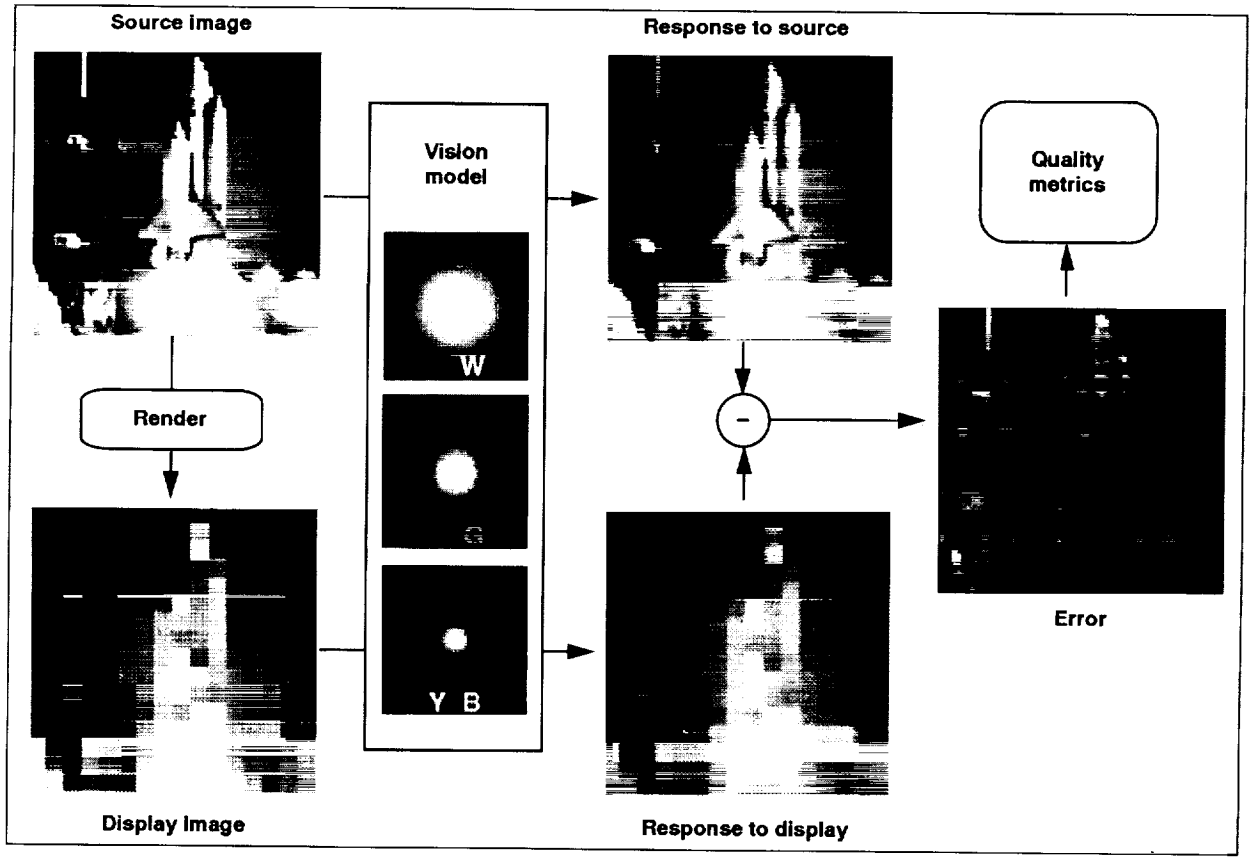

Fig. 1. Schematic of the visual display optimization tool. An ideal source image is rendered into a display image. Source and display images are passed through a vision model that contains black/white, red/green, and yellow/blue channels, each with a different spatial resolution. The responses to source and display images are subtracted, to reveal the visible display error. This in turn can be transformed into various display-quality metrics.

ensure, before a prototype is built, that optimal visual quality is obtained. We have developed a prototype system for specifying, rendering, and evaluating a candidate display. The prototype incorporates the following vision model elements: color transformation, contrast sensitivity, filtering by channels tuned for spatial frequency and orientation, within-channel contrast masking, and pooling of perceptual error over space, orientation, and frequency. The prototype is implemented in the language *Mathematica*.™ In this language, the code is compact and high level, but only demonstrations of limited size and resolution can be attempted. A technical memorandum describing the prototype is in preparation.

Future plans include the determination of optimal parameters for each stage of the model, the addition of local contrast gain control and local luminance gain control, selection between feed-forward and feed-back implementations of contrast gain control, and design of psychophysical experiments to test this and other display-quality models.

Ames-Moffett contact: A. Watson
(415) 604-5419
Headquarters program office: OAST

Intervention Strategies for the Management of Human Error

Earl L. Wiener, J. Victor Lebacqz

This study examined the management of human error in the cockpit. The principles may apply as well to other applications in the aviation realm (e.g., air traffic control, dispatch, weather) and to other high-risk systems outside of aviation (e.g., shipping, high-technology medical procedures, military operations, nuclear power production).

Management of human error is to be distinguished from error prevention. It is a more encompassing term, which includes not only the prevention of error, but also preventing errors, once made, from adversely affecting the system. Management techniques and tools include

1. Traditional human-factors engineering
2. Improvement of feed-back and feed-forward of information from system to crew
3. "Error-evident" displays that make erroneous input more obvious to the crew
4. Trapping of errors within a system
5. Goal-sharing between humans and machines (also called "intent-driven" systems)
6. Paperwork management
7. Behavior-based approaches, including procedures, standardization, checklist design, training, and cockpit resource management
8. Error-tolerant designs

"Intervention strategies"—means of error management by intervention in the system—are stressed. A distinction is made between two models of intervention: those directed toward a very specific and well defined human error (e.g., wrong-runway landings); and those directed toward less defined, often vague sources of error (e.g., complacency, fatigue).

Ames-Moffett contact: V. Lebacqz
(415) 604-5792
Headquarters program office: OAST

Divergence-Based Neural Network for Passive Ranging

Yair Barniv

Helicopters in covert nap-of-the-Earth operations require passive ranging for obstacle avoidance. A forward-looking camera can be used to produce a stream of images. The velocity vectors of all points in the image plane, as obtained from this imagery stream, constitute the optical flow (OF). Ranges to these points can be calculated directly from the OF.

There are many methods of deriving range from the OF. One way, independent of the image plane location and the vehicle's maneuvers, is based on calculating the divergence, which is a measure of the local expansion at any given point. This method relies on the objects being textured.

Neural networks (NNets), consisting of highly parallel, multiply connected processing units, are potentially suitable for such a task, as has been demonstrated in other NASA applications. Our goal is to develop an NNet that will respond to divergence while disregarding all other motions in the image plane. This NNet will be trained to derive divergence by examples.

A simplified diagram of the NNet-based divergence detector is shown in the figure. Initially, we intend to process only two consecutive images at a time. The pixel values of these images inside some square window serve as input to the first layer of neurons. The hidden layer enables the creation (through training) of internal data representation such that the single output will represent "time to go," i.e., distance divided by forward speed. Our main effort is concentrated on the problem of practical input-data representation or preprocessing.

Other areas of investigation are (1) choosing training samples and procedures, (2) simulating the scenario needed to generate the samples, (3) specifying the testing procedure, and (4) specifying the number of hidden layers and the number of neurons in each layer.

The following algorithms have been completed: flight and imagery-generation simulation, NNet's sample generation, and the NNet training and testing routines.

Ames-Moffett contact: Y. Barniv
(415) 604-5451
Headquarters program office: OAST

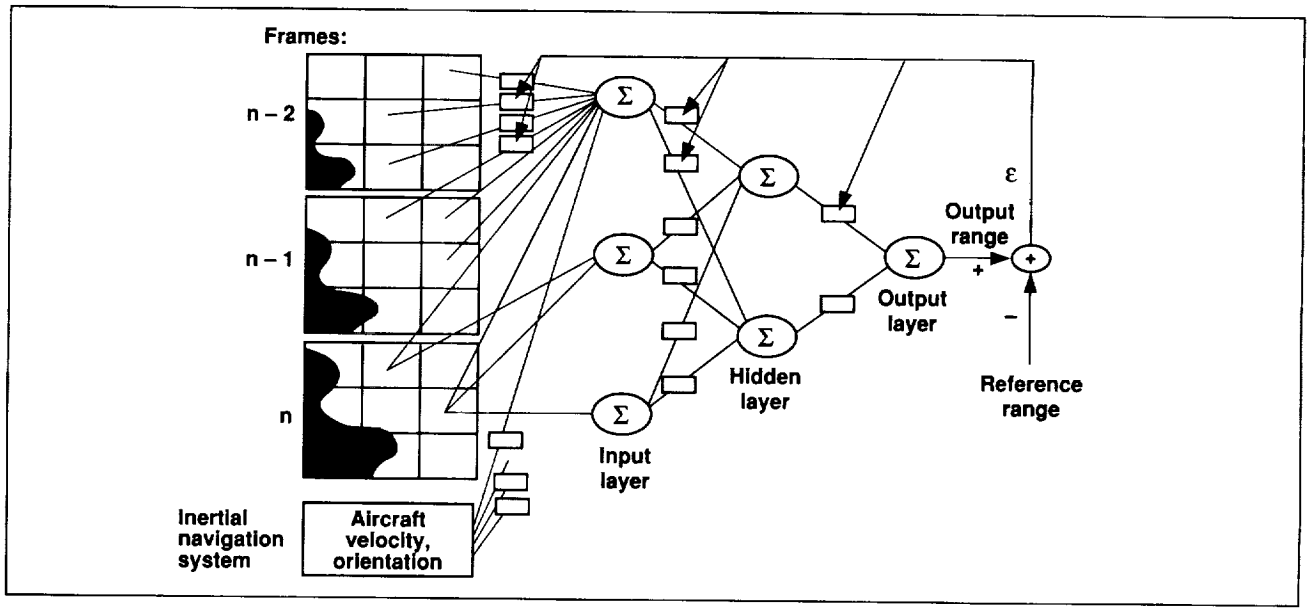

Fig. 1. NNet passive ranging.

Integrated Flight and Engine Controls for Rotorcraft

Robert T. N. Chen

Engine/fuel control and rotor/drive-train/airframe dynamic interface problems have often been encountered in the ground or flight testing of helicopters. These problems are exacerbated by the recent need for enhanced agility and maneuverability, especially for military helicopters. A highly responsive engine and rotor speed governor can introduce strong couplings with the dynamic modes of the rotor and drive-train systems, and compromise the stability margin. An analytical study was conducted to investigate these dynamic interface problems. The influence of the rotor speed variations on the flight dynamics of the helicopter in hover, and the potential benefits of using rotor states as additional feedback signals in the flight control system were also investigated. A parametric high-order helicopter hover model was developed that included heave/yaw body motion, the rotor speed degree of freedom, rotor blade motion in flapping and lead–lag modes, inflow dynamics, a drive-train model with a flexible rotor shaft, and an engine/rpm governor.

The model was first used to gain insight into the engine/drive-train/rotor system dynamics and to obtain a simple formula for estimation of the dominant first torsional mode, which is important in the dynamic integration of the engine and airframe system. Then a linearized version of the model was used to investigate the effects of rotor speed variations and rotor state feedback on helicopter flight dynamics. Results show that, when rotor speed variations are included, the effective vertical damping decreases significantly from that calculated with a constant speed assumption, and thus correlates better with flight test data. Higher closed-loop bandwidths appear to be more readily achievable with rotor state feedback. Both aircraft and rotor flapping responses to gust disturbances are significantly attenuated when rotor state feedback is used. Detailed results of the study have been documented in a NASA technical memorandum.

Ames-Moffett contact: R. Chen
(415) 604-5008
Headquarters program office: OAST

Concepts for Pilot Interaction with an Automatic Nap-of-the-Earth Obstacle-Avoidance System

Victor H. L. Cheng, Richard Coppenbarger

The first version of a full three-dimensional obstacle-avoidance guidance and control system for automated nap-of-the-Earth (NOE) helicopter flight was successfully evaluated in a computer simulation environment. This evaluation was followed by a systematic study on how the automatic guidance and control modules could be meaningfully replaced or modified by manual pilot input. Candidate pilot interface concepts were identified, including detail designs of pilot input and display. The concepts were to be implemented on computer simulations with interactive graphics for pilot-in-the-loop evaluation.

The study produced three candidate interface concepts. The first figure shows the basic automatic obstacle-avoidance guidance and control modules, in which the controller is a specialized autopilot. The figure shows where the pilot input for the three separate concepts would enter the automatic system. The first concept, pilot-directed guidance (PDG), uses the pilot input to replace the nominal trajectory, which in a fully automatic system would represent a desired trajectory in the absence of obstacles and with perfect terrain information stored on board. The PDG concept behaves like a velocity command in the horizontal plane. It provides the same clobber-protection capability available from the automatic system, but it trades the hands-off capability of an automatic system for more direct pilot coupling.

The second concept, pilot-corrected guidance (PCG), does not replace the nominal trajectory but instead allows the pilot to modify it incrementally. This concept resembles control-wheel steering in the horizontal plane. It maintains the clobber-protection capability, as well as allows hands-off operation wherein the system defaults to automatic flight.

In the third concept, pilot-corrected control (PCC), the pilot input enters the autopilot controller module instead of the guidance module. Here the autopilot issues a velocity command in three-dimensional space and the pilot input incrementally adjusts this velocity command. Here again, the pilot can fly hands-off, but nonzero pilot input will disable clobber protection.

The PDG concept has been implemented in a workstation-based helicopter simulation, and data fed back by test pilots have been used to improve the

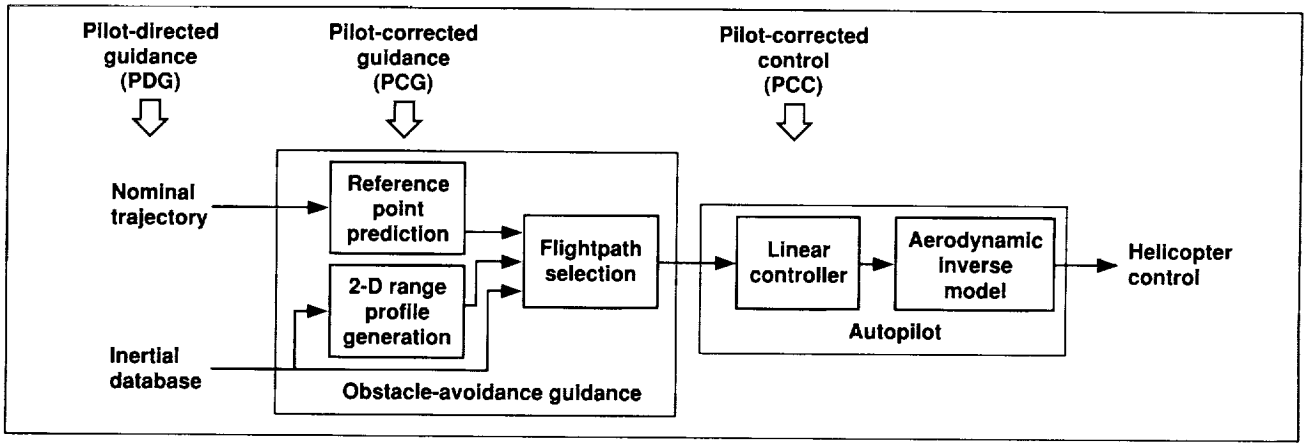

Fig. 1. Automatic nap-of-the-Earth guidance and control system overlaid with pilot input entry points for three pilot-interaction concepts.

pilot control and display interfaces. The implementation depicted in the second figure involves displaying nominal trajectory information to the pilot, who provides speed and lateral acceleration commands to the automatic guidance and control system using the control stick. The automatic system tries to track pilot commands but, if necessary, will provide overriding obstacle avoidance according to sensor information. Vertical terrain following, also based on sensor information, is provided automatically, with the clearance altitude controlled by the pilot. The head-up symbology, designed to prevent display clutter, included a white "post" to represent the pilot-controlled reference point location (reference input to the automatic system), and a series of yellow posts to designate the nominal trajectory. Numerous flights were conducted at low airspeed to determine an acceptable range of look-ahead time and lateral-maneuver search window, which the pilot can control in addition to the general velocity vector. The evaluation was carried out by two NASA research pilots, who flew three courses that involved different obstacle configurations. This simulation demonstrated the capability of pilots to interface successfully with the automated NOE guidance and control technology developed at Ames. This technology has significant potential for reducing pilot workload.

The resulting PDG implementation will be evaluated on the Vertical Motion Simulator. The other two concepts will be similarly implemented on the workstation-based simulation for evaluation.

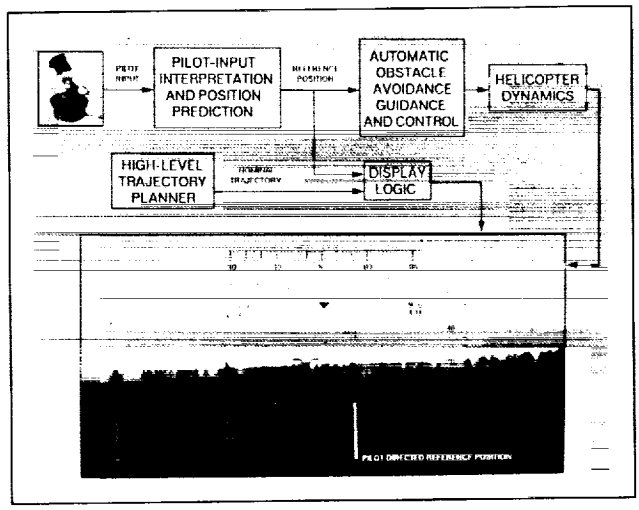

Fig. 2. PDG control-stick interface and head-up display symbology, overlaid with computer-generated cockpit view.

Ames-Moffett contact: V. Cheng
(415) 604-5424
Headquarters program office: OAST

Final Approach Spacing Tool

Tom Davis

The Final Approach Spacing Tool (FAST) is an element of the integrated Center/TRACON (terminal radar approach control facilities) Automation System (CTAS) designed at NASA Ames. It is in its final phase of development in preparation for field development and testing at the Dallas/Fort Worth TRACON. The FAST system is undergoing simulation evaluations with the FAA's Air Traffic Requirements System Development Team. Controllers participating in the simulation are representatives from air traffic control facilities throughout the United States.

The FAST system monitors each aircraft's current state (position, airspeed, and heading) and predicts arrival times to all possible runways according to the local TRACON's standard arrival operations, the controller's inputs, the aircraft's performance characteristics, and the current weather conditions. For a particular runway assignment and scheduled arrival time at the assigned runway, an efficient path to the runway is synthesized using speed-control and path modifications. The system checks for horizontal conflicts along each aircraft's path and resolves those which are procedurally necessary (e.g., merges separate streams of aircraft). The runway assignment, relative sequence at the runway, and suggested vector and speed commands are displayed to the controller automatically or by trackball-based functions.

Fig. 1. Air traffic controllers using the FAST system on full digital ARTS displays.

All major software components of the FAST have been designed and implemented. These include a route analysis program that generates sets of efficient paths according to facility procedures, a trajectory synthesis algorithm that makes predictions of aircraft arrival times according to aircraft performance and weather conditions, a profile selector program that selects the most appropriate path for an aircraft according to controller preferences and conflict resolution, an interactive controller graphical interface, and communications links to the Traffic Management Advisor and the Center Descent Advisor automation tools.

In a real-time simulation evaluation that has been ongoing since November, 1990, operational controllers from the FAA have been exposed to a variety of traffic conditions that includes runway-capacity-limited arrival rates for instrument-flight-rules (IFR) conditions, over-capacity arrival rates, multiple missed approaches, and a mix of IFR and visual-flight-rules traffic. Recent testing included evaluation of FAST on the intended hardware at the Dallas/Fort Worth TRACON. This hardware included an interface between the air traffic control computers in the Dallas/Fort Worth TRACON and the FAST workstation. In addition, two full digital automated-radar-tracking-system (ARTS) displays, which will be used to display the FAST advisories, were used for the first time during the simulation (see figure). The evaluations have demonstrated a perceived decrease in workload during difficult traffic scenarios, and a decrease in arrival spacing at the runway for the automation-assisted runs over the manual or baseline runs. The controllers voiced strong support for implementation and field testing of the FAST system. Field development of the system in Dallas/Fort Worth is scheduled to begin in 1993.

Ames-Moffett contact: T. Davis
(415) 604-5452
Headquarters program office: OAST

Civil Tiltrotor Airworthiness Criteria

William A. Decker

Piloted simulation experiments conducted in the Ames Vertical Motion Simulator have contributed to government and industry efforts to determine airworthiness certification criteria and develop design and operations guidelines for the civil tiltrotor aircraft.

The simulation results guided a recent effort by industry, sponsored by the FAA, to formulate a plan to develop an initial set of terminal procedures for a civil tiltrotor transport. The VERTAPS (vertical flight instrument flight rules terminal area procedures) plan provides a road map for development of the airway and ground infrastructure for a vertical-flight (principally tiltrotor) transportation system. Selection of the candidate glideslope angle and minimum level of aircraft equipment to be evaluated in the VERTAPS effort was directly influenced by the Ames simulation results.

Results of the most recent pair of simulations, reported in a paper presented at the National Forum of the American Helicopter Society in June 1992, showed that instrument approaches using only approach guidance angular error ("raw data") should be limited to glideslopes of 6 degrees or less because of handling-qualities and tracking performance considerations. The addition of a flight director to the cockpit instrumentation expanded the range of acceptable approaches to 15-degree glideslopes.

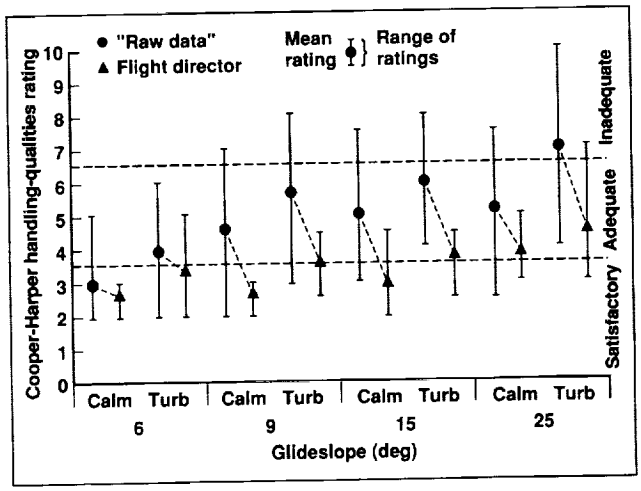

Fig. 1. Handling-qualities ratings for glideslope tracking by means of either angular error ("raw data") guidance or a flight director. Satisfactory instrument approaches are possible on glideslopes of up to 15 degrees when a flight director is used.

These handling-qualities results are summarized in the figure.

Ames-Moffett contact: W. Decker
(415) 604-5362
Headquarters program office: OAST

RASCAL Research Helicopter

Michelle M. Eshow, Robert A. Jacobsen, Edwin W. Aiken

The NASA/Army Rotorcraft Aircrew Systems Concepts Airborne Laboratory (RASCAL) is being developed using a UH-60A Black Hawk helicopter at Ames Research Center. The RASCAL will be a flying laboratory capable of supporting the research requirements of major NASA and Army guidance, control, and display research programs. It will also be a research platform available to customers such as the FAA and industry.

The RASCAL facility is being developed incrementally to support the progressive phases of the research programs; flight test programs are being conducted as each new capability is added to the vehicle. Two flight test experiments were completed this year. The first experiment was aimed at developing improved mathematical models of the UH-60A for use in piloted simulation and control law design. The experiment made use of the newly installed precision instrumentation and data acquisition system, which records pilot control inputs and aircraft motion. It also used the precision laser tracking capability of the Crows Landing flight test facility. The second experiment was part of a research program in image processing for obstacle detection. A stereo pair of video cameras was mounted in the nose of the aircraft, and data were collected to validate image-processing algorithms.

A global positioning system was installed in the aircraft that will be used in a differential mode to investigate helicopter approach and landing tasks. This work, supported by the FAA, contributes to the development of requirements for civil terminal area operations.

Milestones were also met this year for some longer-term aircraft installations—the fly-by-wire research flight control system (RFCS) and the helmet-mounted display. A preliminary design of the RFCS, which will be a full-authority, fail-safe system with a mechanical backup, was completed. A detailed statement of work was completed in preparation for procuring the RFCS. Procurement was also initiated for the helmet-mounted display, which will have biocular optics, extensive image generation processing power, and some color capability.

The research system preliminary design and the phased development approach were documented in two conference papers this year.

Ames-Moffett contact: M. Eshow
(415) 604-5272
Headquarters program office: OAST/Army

Control-System Design Criteria for STOVL Fighter Aircraft

James A. Franklin

As part of NASA's program to develop technology for short takeoff and vertical landing (STOVL) fighter aircraft, control-system designs have been developed for a conceptual STOVL aircraft. The control-system designs have been evaluated throughout the powered-lift flight envelope on Ames Research Center's Vertical Motion Simulator. Items assessed in the control-system evaluation were maximum control power used in transition and vertical flight, control-system dynamic response associated with thrust transfer for attitude control, thrust margin in the presence of ground effect and hot-gas ingestion, and dynamic-thrust response for the engine core. Effects of wind, turbulence, and ship airwake disturbances are incorporated in the evaluation. Results provide the basis for a reassessment of existing flying-qualities design criteria applied to STOVL aircraft.

Pitch control power used in transition is in general accord with existing criteria, whereas that used for hover and vertical landing is somewhat lower. When a translational velocity command system that uses deflected thrust for longitudinal force control is employed, pitch control use is considerably less than criteria suggest. No criteria, except for hover, exist for shipboard recovery. Within the range of control bandwidth that provides satisfactory flying qualities, the control designer has considerable latitude in closed-loop system design to achieve reasonable control activity and disturbance rejection.

In the roll axis, control power recommended by current design criteria is insufficient to cover demands for transition and hover point acquisition. Agreement with criteria is good for vertical landing. Again, no criteria are available for shipboard operations. For these operations, lateral velocity command through bank-angle control typically used greater control power than did an attitude command system alone. There is merit in reducing roll control bandwidth, up to the point of deterioration in pilot ratings, to reduce control usage.

For transition, hover, and vertical landing, the existing criteria are more than adequate for yaw control use. As before, shipboard operations are not covered by the existing criteria.

Thrust transfer rates for pitch and roll control were observed to be greatest for shipboard operations. The decelerating transition placed the next greatest demand. Control mode did not have a strong influence on these results. Control bandwidth, however, was a factor in pitch control rate for vertical landing. The designer has considerable latitude in choice of bandwidth for the closed-loop control system to achieve satisfactory flying qualities while avoiding excessive control use or actuation rates.

Thrust margins for vertical landing in the presence of ground effect and hot-gas ingestion were defined according to results from simulation of the YAV-8B Harrier. The shapes of the boundaries depend on height control out of ground effect for positive ground effect, on abort capability at decision height for neutral to moderately negative ground effect and ingestion, and on control of sink rate and hover position to touchdown for larger negative ground effect. The boundary correlates with an analytical prediction of the trend of thrust-to-weight ratio with mean ground effect that is required to arrest a nominal sink rate with an application of maximum thrust at decision height. The employment of a vertical velocity command control does not alter the thrust margin requirement.

An engine core thrust response bandwidth of 4–5 radians/second is sufficient to achieve satisfactory ratings for height and sink rate control. For bandwidths below 3 radians/second, the control task deteriorates rapidly. Vertical velocity command systems can tolerate somewhat slower engine response (if the overall airframe response is not altered) than can be accepted by the pilot for manual control of thrust. Up to a point, the vertical landing is insensitive to the maximum rate of change of core thrust; however, a loss of control appears at the lowest thrust transfer rates. Vertical velocity command does not seem to alter these results.

Ames-Moffett contact: J. Franklin
(415) 604-6004
Headquarters program office: OAST

CTAS/TSRV Trajectory Prediction Flight Test

Steve Green, D. Williams

Simulation studies of the Center TRACON (terminal radar approach control facilities) Automation System (CTAS), a set of automation tools designed to assist controllers in decision making, have demonstrated a strong potential for air traffic control (ATC) system-wide benefits including fuel savings, reduced delays, and increased controller productivity. The fundamental benefit of CTAS is the ability to predict and control aircraft trajectories in the ATC environment. Flight test evaluations of the CTAS trajectory-prediction algorithms are being used to validate simulation results as well as to determine the type and magnitude of real-world effects that influence the accuracy of CTAS trajectory predictions. These flight tests are a joint activity of the Ames and Langley Research Centers. Preliminary results from the first flight test (completed in October 1992) are presented here.

The purpose of the first flight test was to evaluate CTAS trajectory-prediction accuracy for constant-course enroute descents into the terminal area. The figure illustrates the test airspace and routings. The Langley Transport System Research Vehicle (TSRV) Boeing 737 was used as the test airplane. The TSRV, operating from Denver Stapleton International Airport, conducted test runs over a closed circuit. The aircraft climbed outbound from Denver, and leveled off before turning inbound. The test run was initiated at PONNY intersection (see figure), and was completed at KEANN (the metering fix or gate into the terminal area). The descent runs were initiated at cruise altitude (Flight Level 350) and ended when the aircraft met the metering fix crossing condition (17,000 feet mean sea level and 250 knots indicated airspeed). The CTAS field system at the Denver Air Route Traffic Control Center provided real-time CTAS advisories to the TSRV. A total of 26 descent runs were completed; ten runs were conducted during two night flights (low-traffic environment), and the remainder were conducted during three daytime flights.

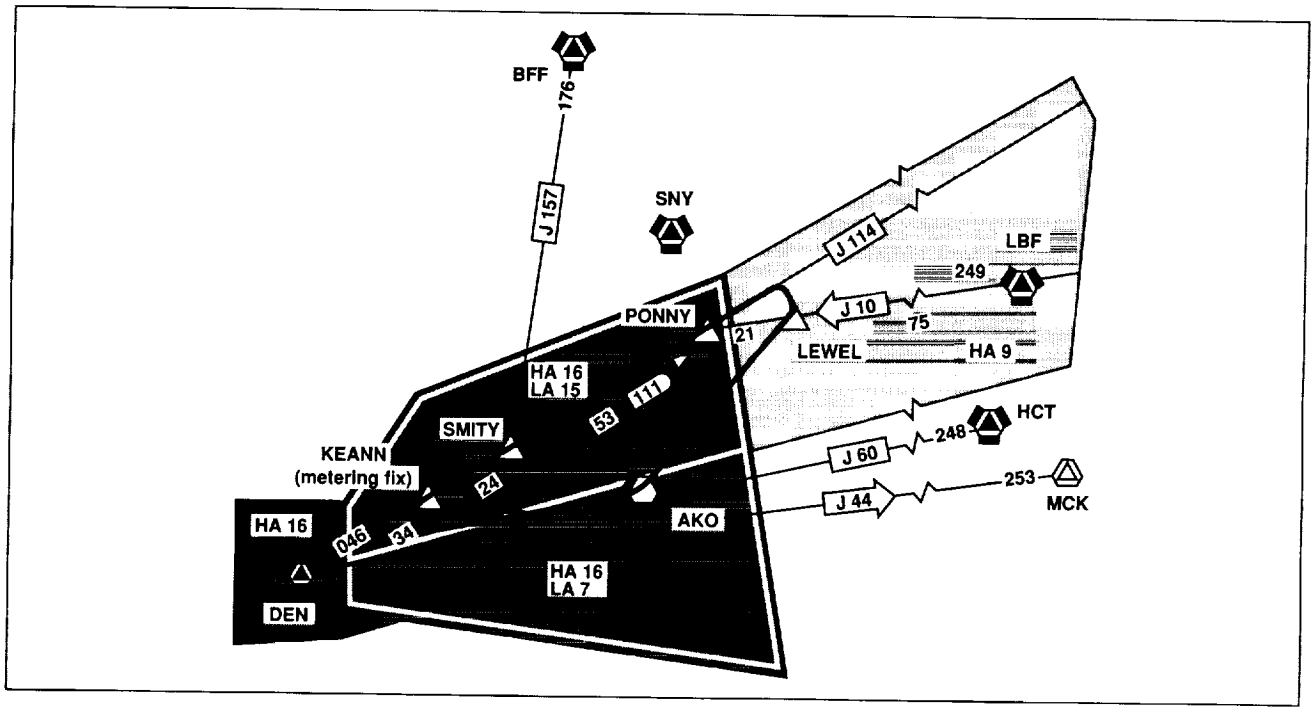

Fig. 1. Denver area flight test routing.

Test conditions evaluated trajectory prediction for a variety of cruise- and descent-speed profiles spanning the envelope of the aircraft. The pilots were issued the top-of-descent position according to CTAS trajectory prediction. Runs were divided into idle and constrained descents. Idle runs (no thrust/drag variations allowed by the pilot) were designed for the study of aircraft performance and atmospheric effects, whereas constrained runs (pilots used controls to meet ATC restrictions) were designed to study pilot procedure modeling. The flight-management-system-equipped research flight deck and the conventionally equipped forward flight deck were used to simulate the systems and procedures of differently equipped aircraft. Special procedures and a descent calculator were developed for use by the flight crew. Atmospheric characteristics were wide ranging and included maximum observed wind magnitudes of 20 to 80 knots as well as significant altitude gradients in wind magnitude (10 knots/1,000 feet spanning 5,000 feet) and direction (20 degrees/1,000 feet spanning 6,000 feet).

Preliminary results of the accuracy of CTAS predictions of arrival time at the metering fix (bottom of descent) have been analyzed. The data indicate that arrival-time predictions are highly accurate, with mean errors on the order of 12 seconds with a standard deviation of 13 seconds even in the presence of significant atmospheric modeling errors. The constrained runs showed a marked improvement in achievement of the crossing conditions (altitude and speed as well as time) at the metering fix. Flight-Management-System (FMS) automation was clearly superior to the non-FMS case with regard to improved accuracy and reduced pilot workload. However, pilot comments indicate a need for some refinement of descent procedures for both FMS and non-FMS cases. In summary, these results meet the accuracy criteria set for the initial CTAS deployment.

Significant modeling errors, which contributed to prediction errors, were observed in three main areas: atmospheric characteristics, pilot procedures, and aircraft performance. Analysis of the data is under way at Ames and Langley as well as at the National Oceanic and Atmospheric Administration (the contributors of the atmospheric modeling data). Initial analysis has uncovered a CTAS modeling error which contributed a 10%–25% error in descent rate prediction. Future flight tests will focus on the study of curved-path descents and the development of operational pilot/ATC procedures.

Ames-Moffett contact: S. Green
(415) 604-5431
Headquarters program office: OAST

Integrated Flight Dynamic and Propulsion System Model of the UH-60

Frederick D. Kim

A nonlinear mathematical model of a UH-60 Black Hawk has been expanded to include the dynamics of the propulsion system. The components of the propulsion system—fuel controller, gas generator, and power turbine—have dynamics that are well within the frequency range of modern flight control systems. A high-order state space model is extracted from this nonlinear model through finite-difference approximation and is used in developing advanced control-law methodologies. The linear model also supports integrated flight and engine control-law design studies that take advantage of the additional degrees of freedom from the propulsion system. This advanced model is important in developing control concepts to enhance helicopter agility and maneuverability and in developing methods to assist the pilot in energy management and envelope limiting.

The propulsion system is modeled for the General Electric T700-GE-700 turboshaft engine. The mathematical model uses a component-type simulation in which thermodynamic and kinematic models of the different engine components are combined to represent the dynamics of the whole engine. The time-varying elements of the propulsion system include the power turbine speed, the gas generator speed, three pressure states, and the fuel flow. The fuel control that governs the rotor speed is modeled as a proportional-integral-derivative (PID) controller. It was determined that a PID model of the fuel control could adequately represent the closed-loop dynamics of the controller at the frequency of interest for handling qualities and control-system designs. The underlying assumption is that the complex dynamics of the engine's electrical control unit, which includes numerous time delays, feedback loops, and hysteresis effects, can be lumped into a PID model of the controller. State space parameter identification techniques were applied to identify the coefficients of the PID-type fuel controller using a combination of frequency responses obtained from flight tests and a state space model of the plant extracted from the nonlinear model of the helicopter.

A validation study of the high-order state space model was conducted in the frequency domain through comparisons of the frequency responses predicted by the linearized state space model with flight test data. The study was conducted for the UH-60 Black Hawk at hover and at forward speeds of 80 and 120 knots. In general, predictions of the on-axis frequency responses were good to excellent whereas those of the off-axis responses were poorer. Models with and without the propulsion system dynamics were also compared. They revealed that the propulsion system dynamics influence mainly the mid-frequency dynamics of the aircraft with the effect predominant in the heave and yaw degrees of freedom. As a consequence, flight control designs that neglect propulsion system dynamics could suffer from poor handling qualities in the heave and yaw degrees of freedom.

Ames-Moffett contact: F. Kim
(415) 604-5272
Headquarters program office: OAST

Implementation Improvements for Simulator Motion Drive

Soren LaForce, John W. Bunnell

Contemporary simulator motion drive algorithms are typically designed in an analog (continuous) environment but implemented in a digital (discrete) environment. The intended continuous system, specified as frequency domain (Laplace transform) transfer functions, may not be properly represented by the algorithms used for digital implementation. The motion drive software in use with the Vertical Motion Simulator (VMS) at Ames Research Center was recently investigated; the original algorithms (Euler integration method) were changed to the state transition matrix method. Comparison of the frequency responses of the original and new implementations showed that the state transition matrix method more closely approximates the desired analog responses. In addition, test pilots who evaluated both implementations preferred the motions generated with the state transition matrix method over those generated with the Euler integration method.

The main difference between the two implementation methods is that the Euler integration method advances time and the integrator output is actually the integral predicted to occur at a time one-half time step in the future. The state transition matrix method may be implemented to provide no time advance during integration.

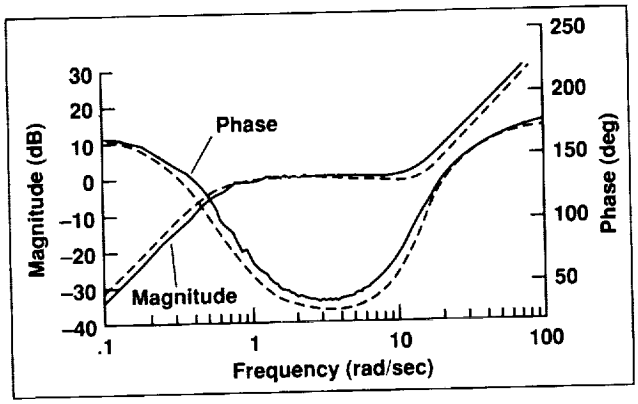

Fig. 1. Frequency response obtained with the Euler integration method.

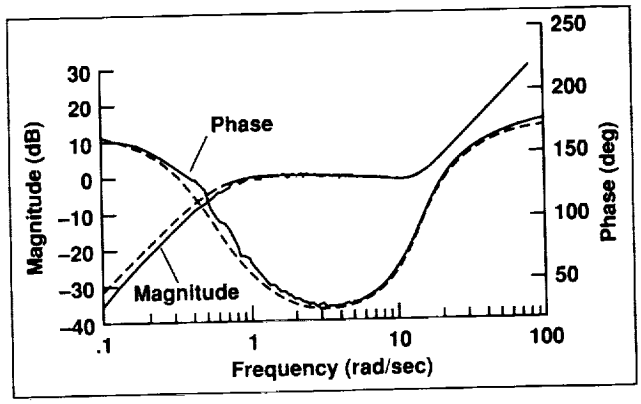

Fig. 2. Frequency response obtained with the state transition matrix method.

For this study, the implementation improvements were made only in the motion drive software. The motion drive software determines the appropriate simulator commands from inputs from the pilot and the mathematical model of the aircraft being simulated. No changes were made in any other part of the simulation or the simulation facility.

The frequency responses of the software both for the Euler integration method and for the state transition matrix method were measured (see figures).

In addition, a brief study was done in which four NASA test pilots were asked to perform several tasks, using the same aircraft model, with the different sets of motion drive software. Three of the pilots felt that the state transition matrix software produced more appropriate motion cues. Typical comments were that the Euler integration software produced motion cues that were "abrupt" or "jerky" when compared to motion cues produced by the state transition matrix software. These impressions are supported by the frequency response measurements. Sharp commands, such as step inputs to the controls, contain a large amount of high-frequency information. The first figure shows the measured response to be approximately

3 decibels (about 40%) larger than the theoretical response for frequencies between 10 and 80 radians per second when the Euler integration method is used. The second figure shows that no gain amplification occurs with the state transition matrix method. The high-frequency gain amplification can be expected to produce motion cues that are more abrupt and/or jerky than desired.

Ames-Moffett contact: S. LaForce
(415) 604-3892
Headquarters program office: OAST

Flight Test Evaluation of Differential GPS—Precision Code Flight Test Results

B. David McNally

The Ames Research Center is evaluating use of the Global Positioning System (GPS) to support fixed-wing aircraft and rotorcraft during phases of flight that require high positioning accuracy. The GPS is a constellation of 24 satellites that provide 16-meter Precision Military Code (P-Code) positioning accuracy, and 100-meter Coarse Acquisition Code (C/A-Code), or civil code, accuracy. Local corrections to satellite range measurements, data-linked to the aircraft, are the basis of Differential GPS (DGPS), which provides an even more accurate solution. Three-meter or better accuracy is expected with current P-Code and C/A-Code GPS receivers operating in the differential mode. NASA has a joint program with the Department of Defense and the Federal Aviation Administration to evaluate DGPS positioning accuracy through flight testing, and to determine operational procedures for making effective use of DGPS capability.

The program is divided into two phases. Phase 1 evaluated the ability of P-Code DGPS to provide precise three-dimensional positioning information in terminal approach and landing operations. Phase 2 is evaluating DGPS carrier tracking methods for precision guidance, i.e., guidance required for low visibility approach and landing. The integration of DGPS with an Inertial Navigation Unit (INU) is of particular interest.

A P-Code Differential GPS system was installed and flight tested in a NASA King Air aircraft (NASA 701). The airborne system included a P-Code GPS receiver and an INU. Differential corrections to satellite range measurements were computed in a stationary ground reference station, data-linked to the aircraft, and applied to corresponding satellite measurements. A simple scheme for integrating DGPS and INU measurements was implemented in flight, and the resulting solution was used to drive standard approach guidance instruments in the cockpit. The aircraft was tracked with a laser for measurement of true position.

The flight data were analyzed postflight to determine if positioning accuracy could be improved with higher levels of DGPS/INU integration. Several integration schemes were evaluated and it was found that all levels of integration provided about the same positioning accuracy. Accuracy was measured in terms of cross-track and vertical position error, as determined by the laser, as the aircraft descended in a standard 3-degree approach to the runway. The DGPS/INU system provides about 1-meter cross-track accuracy and about 2.8-meter vertical accuracy, compared to 2.7 meters and 10.7 meters with the GPS. Development and flight testing of the Phase-2 system involving DGPS carrier tracking is under way.

Ames-Moffett contact: B. McNally
(415) 604-5440
Headquarters program office: OAST

Motion Cueing in Simulation

Jeffery A. Schroeder

Motion cueing requirements for flight simulation are ill-defined and controversial. The Federal Aviation Administration, the military, and industry would like to know how much motion and what quality of motion is necessary to train pilots and to develop aircraft systems with confidence.

This experiment tested a motion fidelity hypothesis that suggests quantified levels of motion fidelity using a combination of two parameters. The first parameter is the ratio of the acceleration obtained by simulator measurements to the acceleration calculated by a mathematical model. The second parameter is the phase error between the simulator acceleration and the calculated acceleration (essentially how far ahead in time one acceleration is relative to the other). The hypothesis indicates whether the motion fidelity is high, medium, or low. A high level of motion fidelity was defined as "motion sensations similar to those of visual flight." Ten combinations of the two parameters, from full motion to no motion, were tested on the Ames Vertical Motion Simulator. Pilots practiced repeatedly with the full-motion condition, and this condition was thus considered the "baseline aircraft" for comparison with the other motion conditions. For each combination, a set of quantitative performance data was collected, and the pilots were asked to rate subjectively the motion fidelity relative to the baseline aircraft.

The figure shows time histories of the same pilots' collective input and the resulting aircraft altitude for two different parameter combinations: full motion and no motion. The pilot was asked to translate vertically in 10-foot increments as precisely and as quickly as possible. For the full-motion case, with which the pilot had practiced repeatedly, precise translations were accomplished rapidly. When the parameters were changed to the no-motion case without the pilot's knowledge, increased collective was used initially, which resulted in the inability of the pilot to control altitude changes precisely. However, the pilot gradually readjusted the strategy and was able to improve performance toward the end of the run by mentally processing the available (although degraded) cueing differently. This readjustment increased pilot workload and illustrated the effect of the motion cues. Several evaluation pilots were surprised at how much the motion affected their ability to perform what they had thought was a purely visual task.

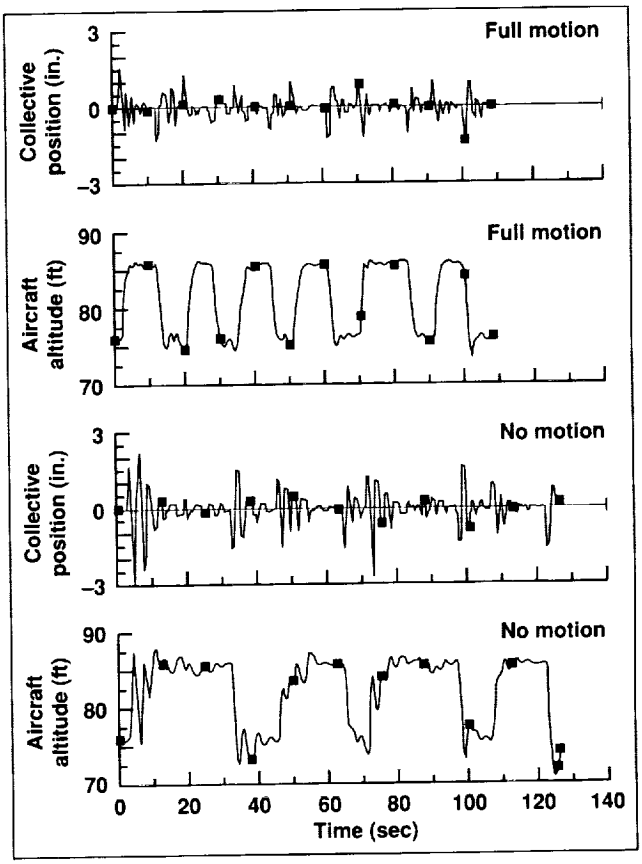

Fig. 1. Simulator motion effects—vertical translation.

Another complete set of data was obtained with the pilots tracking a target that was flying a random trajectory. Both tasks provided validation data for the development of pilot–vehicle motion and visual cueing models.

Ames-Moffett contact: J. Schroeder
(415) 604-4037
Headquarters program office: OAST

Advanced Engine Control for Helicopters

Jeffery A. Schroeder

Full-authority digital engine control (FADEC) allows more advanced control of helicopter engines because (1) the control unit is electronic, which allows for complex logic between its inputs and its calculated outputs; (2) it has the capability of easily using as many aircraft state inputs as are necessary; and (3) its effect on engine control is not limited by the presence of a direct mechanical link that could potentially override or modify its outputs.

The figure shows how the proposed FADEC interfaces with the existing UH-60A engine control system. The latter consists principally of an electronic control unit (ECU) and a hydromechanical unit (HMU). The existing engine control, although adequate for operational use, does not easily allow investigation of potential improvements to the control of the engine. Substantial changes to the existing system are hampered by the direct mechanical link between the pilot's load demand spindle setting, which is essentially the collective control position. This direct-link input may be supplemented by advanced logic in the ECU, but the ECU is currently designed to have only a limited impact on the control of the engine.

A study to examine the feasibility of modifying a NASA/Army UH-60A helicopter with a programmable (FADEC) system has been completed by Sikorsky Aircraft, with General Electric and Chandler-Evans as subcontractors.

Development of a flexible and safe programmable FADEC for the research environment was required to enable FADEC'S control laws to be changed frequently. The figure shows that to ensure safe operation, the existing engine control system will be retained, and the FADEC will be switched on through a fuel-transfer valve during research operations. This

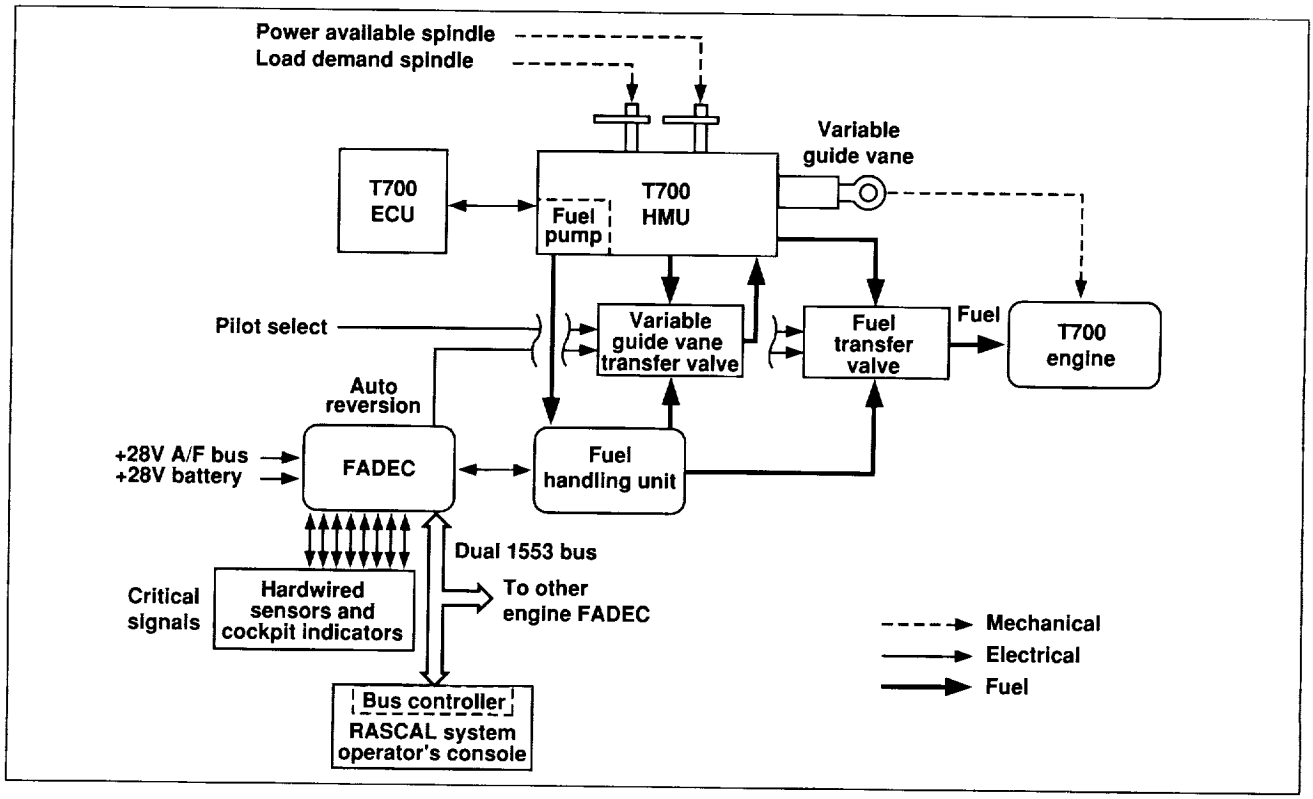

Fig. 1. Proposed FADEC architecture.

implementation will allow for a back-to-back comparison between the improved engine control laws and the existing ones.

The results of the contract indicate that this method is feasible. A preliminary design was completed that included a safety analysis, which indicated possible flight safety problems in switching back and forth between the FADEC and the existing system. The existing system will need to have knowledge of what the FADEC is commanding in order to handle sudden changes in fuel flow. Finally, a program was developed to outline the remaining steps in installing such a FADEC in the aircraft.

Ames-Moffett contact: J. Schroeder
(415) 604-4037
Headquarters program office: OAST

Validation of Multicamera Passive Ranging Algorithms

Phillip Smith, Banavar Sridhar

A data base has been developed using NASA's RASCAL UH-60 helicopter for validation of multicamera computer vision obstacle-detection and passive-range-estimation algorithms for aiding pilots during rotorcraft nap-of-the-Earth (NOE) flight. Earlier work, using helicopter flight data, demonstrated the validity of single-camera passive ranging algorithms. However, single-camera passive ranging is subject to certain limitations independent of the algorithm used. Further research and laboratory testing have shown that many of these limitations can be overcome through the use of multiple cameras.

The multicamera data base comprises four major elements: (1) video imagery data from two video cameras, (2) camera motion state information, (3) camera calibration parameters, and (4) true range measurements. The first three elements are required in passive ranging. The fourth element, true range information, provides an independent check on the accuracy of range estimates.

Fig. 1. Camera installation on nose of RASCAL UH-60.

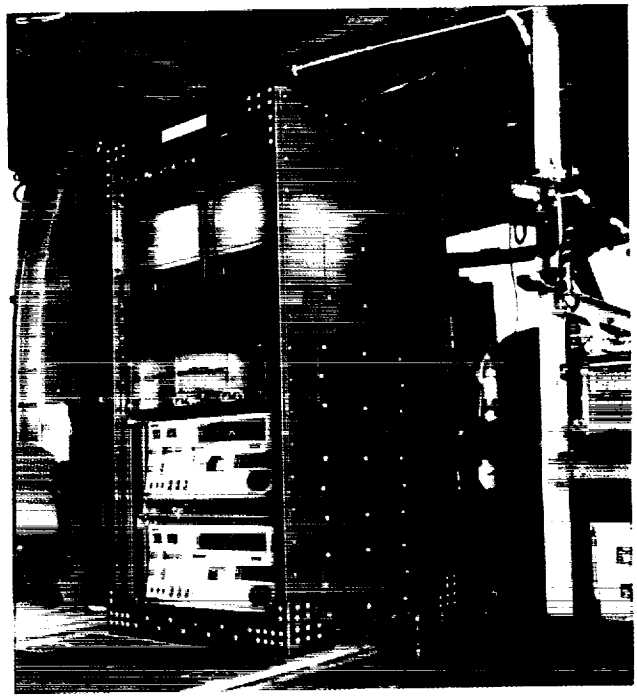

Fig. 2. Research system installed in helicopter fuselage.

The camera installation on the nose of the UH-60 helicopter is shown in the first figure. Systems for recording the video information and measuring the camera motion state are installed in the helicopter cabin as shown in the second figure. True range

measurements are obtained with a ground-based laser tracker that measures the location of the helicopter and the location of designated (stationary) obstacles.

Camera calibration parameters describe the relationship between the position of an object and its location in an image taken by the camera. For calibration of the camera system, positions of several visual targets were measured using surveying techniques. Images taken with the cameras provide the corresponding image locations for the visual targets. Solution of a nonlinear minimization problem relating the two sets of measurements yields the required camera calibration parameters.

Flight tests have been performed at low altitudes over both man-made and natural terrain, allowing validation of multicamera ranging algorithms designed for general unstructured environments as well as those designed to take advantage of structure to simplify the ranging calculations and thereby reduce computational requirements.

Ames-Moffett contact: P. Smith
(415) 604-5469
Headquarters program office: OAST

Object Segmentation for Helicopter Guidance

Banavar Sridhar

It is desirable in some missions to fly helicopters at altitudes so low that objects such as trees become obstacles in the flight path. Electro-optical sensors can be used to compute the distance to these objects. The computation is based on the optical flow at different points in the image. The motion algorithms provide a sparse set of ranges to discrete features in the image sequence as a function of azimuth and elevation. The first figure shows the 45th image in a sequence of 240 images in which the helicopter is flying above the runway. The objects in the view of the imaging sensor are labeled A, B, . . ., H. Objects A, B, C, D, and E are trucks on the runway; F is the time stamp; G is the runway; and H is the rotorcraft nose boom. In the second figure, the bright dots indicate the objects for which discrete ranges have been produced by the motion algorithms. For obstacle-avoidance guidance and display purposes, this discrete set of a few hundred to several thousand ranges needs to be grouped into subsets that correspond to objects in the real world. This research presents a new method for object segmentation that is based on clustering the sparse range information provided by motion algorithms and the spatial relation provided by the static image.

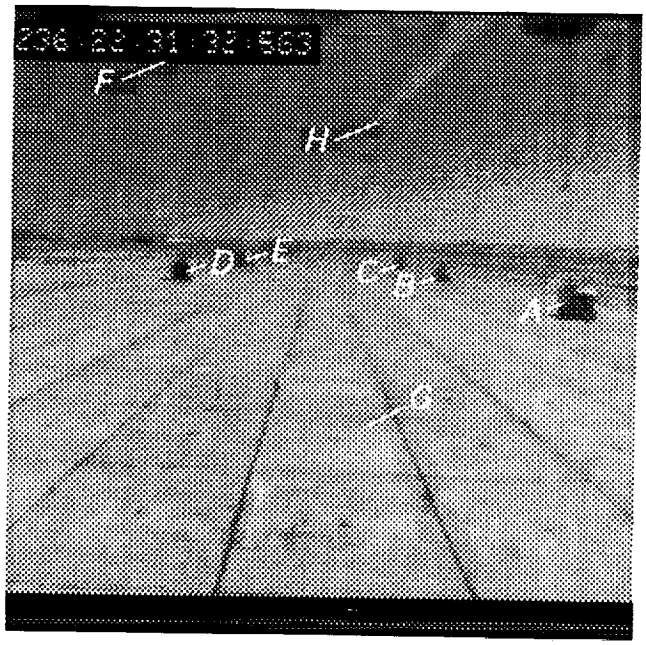

Fig. 1. 45th image in a sequence of images taken from a helicopter.

Fig. 2. 60th image in a sequence of images taken from a helicopter.

The segmentation of the range map into groups, each group corresponding to an object, is a combinatorial optimization problem. A hierarchical approach that allows the problem to be solved as a series of subproblems with problem-dependent constraints is used to reduce the amount of computation.

First, the range is divided into groups according only to the distance of the objects from the vehicle along a horizontal line directly in front of the vehicle.

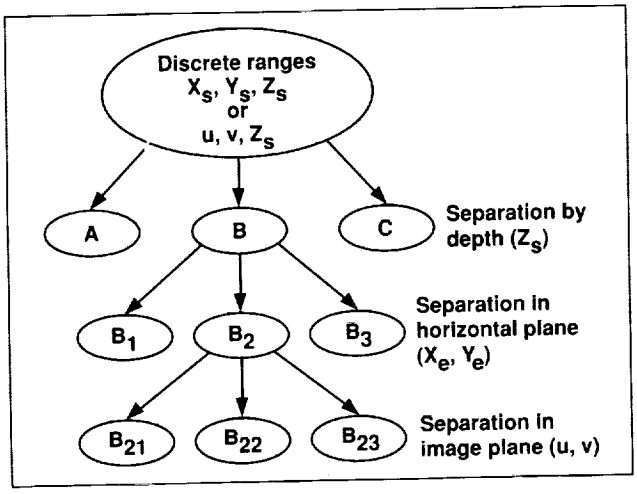

Fig. 3. The hierarchical clustering method.

It is assumed that the viewed physical objects are separable from one another in depth. The depth values of the features of each of these objects are expected to have a distribution. For convenience, these distributions are assumed to be Gaussian. The grouping process involves the construction of a depth histogram and its approximation by a number of Gaussian distributions. The features are assigned to the groups defined by these distributions.

Next, starting with the grouping that is based on depth, each group is split further according to the separation of the objects in the horizontal plane. The rationale for this separation is twofold. First, low-altitude helicopter maneuvers, which are limited to flying around the objects, are preferred. Second, objects that are at the same depth may be far apart in the horizontal plane. In such a situation a Euclidean distance may separate these objects in the horizontal plane. From a rotorcraft guidance point of view, if the separation between two objects is greater than the rotor diameter, a path between the objects is of interest. If the separation is not sufficient, then the two objects form a single obstacle (single object) in the flight path.

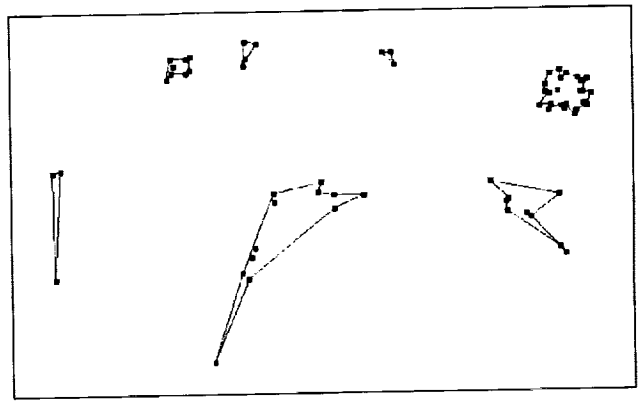

Fig. 4. Final object groups resulting from the clustering method.

The next level of grouping takes place in the image plane. The computation of range in the optical flow algorithms is usually done locally to reduce the amount of computation. Thus the range computation does not take into account the interpixel relationships between ranges that belong to the same group. The groups are examined for consistency in the image plane and any groups with inconsistent members are subdivided. We use the minimum spanning tree

algorithm to achieve grouping in the image plane. The hierarchical steps are summarized in the third figure.

The last figure shows the object grouping that results from the application of the clustering methodology. The figures show that the methodology is able to group most objects correctly and that it can be used as a starting point in the creation of object models for display and guidance.

Ames-Moffett contact: B. Sridhar
(415) 604-5450
Headquarters program office: OAST

Parallel Multisensor Feature-Tracking Algorithm for Vision-Based Obstacle Detection

Raymond E. Suorsa, Banavar Sridhar

Intelligent low-altitude guidance systems for helicopters require information about objects in the vicinity of the flightpath of the vehicles. Several techniques have been proposed for distance determination using electro-optical sensors. The distance to various objects in a scene is computed from the optical flow that results from the relative motion between the sensor and objects on the ground together with information on the helicopter state obtained from an inertial navigation system. One algorithm can detect, track, and estimate the distance to image features (i.e., patches of an image with common statistics or spatial structure) over time from a multisensor system mounted on a vehicle moving with six degrees of freedom. This algorithm has been parallelized to run on either distributed-memory computers or multithreaded shared-memory computers.

Low-level feature tracking is a highly parallel process. Each detected feature is assigned an autonomous tracking unit (ATU). The ATU can be implemented in software as a separate process or thread. The tracking unit can track a feature in a single sensor over time. The feature-tracking mechanism begins with the process of feature selection, which is done by partitioning the master image using a cell grid. Once a feature is detected within the cell grid, an ATU is spawned to track the feature. If a feature leaves the image plane or otherwise becomes untrackable, the ATU dies. As motion imagery evolves, ATUs track the optical flow within the image. Thus an ATU generally flows from the center of the image toward an edge (assuming forward motion).

Over time, the ATUs spread out from the originating cell and could potentially cover much of the image. To overcome the data locality requirements, a higher-level abstraction is introduced (above the level of the ATU). This abstraction, the virtual processor region, adds spatial locality restrictions to each ATU within the image space.

The first figure illustrates the idea behind virtual processor regions (VPRs). The textured squares represent the location of ATUs within a master sensor image plane. The ATUs are arranged to simulate the tracking of two trees and several ground features. The image is divided into 8×8 VPRs (heavy lines). Each VPR is responsible for maintaining a rectangular arrangement of grid cells. In this example, each VPR is allocated 5×5 grid cells (thin lines). The boundaries for the VPRs are the same as those for the underlying grid cells—the maximum number of VPRs is equal to the number of grid cells.

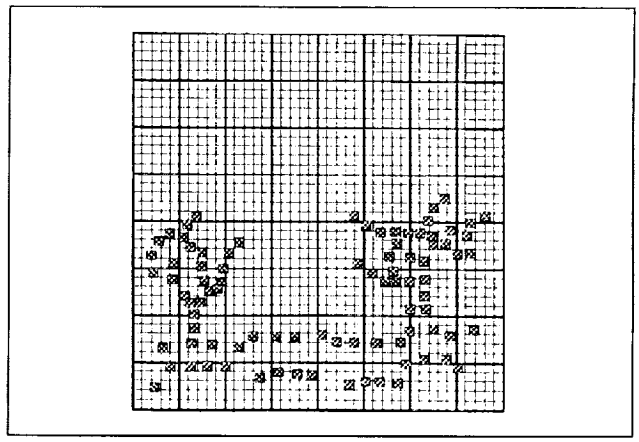

Fig. 1. Image plane partitioning.

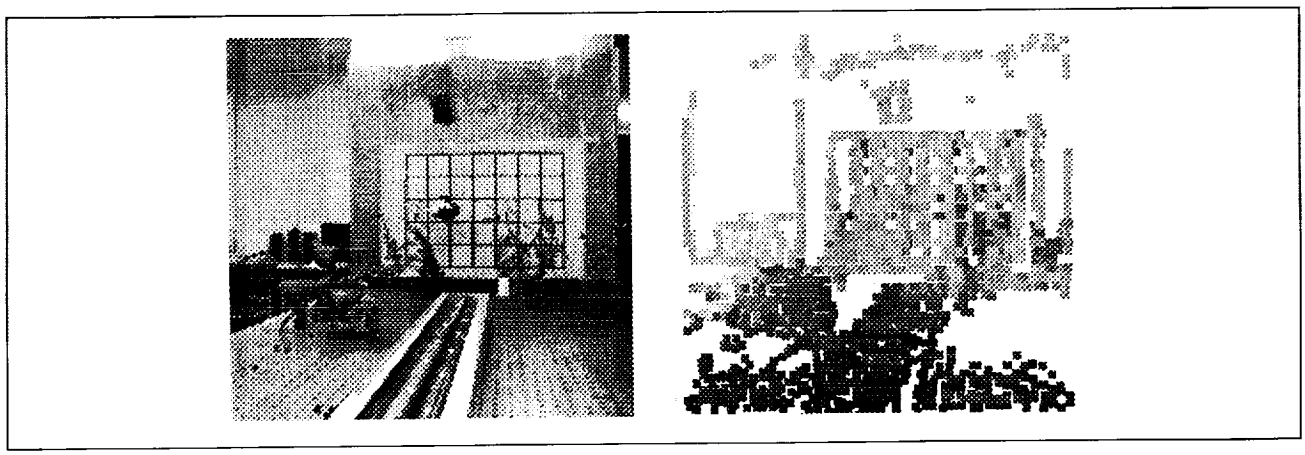

Fig. 2. Sensor image with corresponding intensity-coded range map.

The VPRs represent separate regions within the image plane that can be allocated to a processing element. In the example in the first figure, there are 64 VPRs which can be distributed among up to 64 processing elements in a task/data parallel fashion. Each element processes the ATUs (textured squares) and performs feature detection in untracked grid cells (white squares) which are contained within its assigned VPR. Because the VPRs are spatially allocated, their image data requirements are fixed.

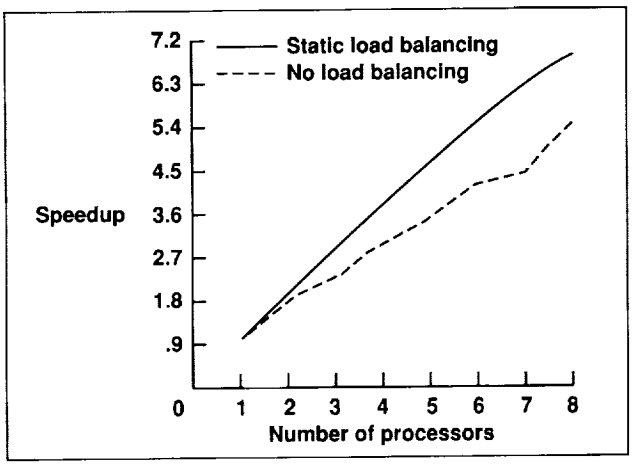

Fig. 3. Effect of load balancing and number of processing elements on speedup for shared memory.

Each VPR is task and data independent. The computational load represented by each VPR is proportional to the number of ATUs being managed by that VPR. If the feature distribution in a scene is nonuniform, the number of ATUs per VPR may vary greatly over the set of VPRs. If this occurs, a load-balancing technique is needed to most effectively utilize every processing element in a parallel system.

The second figure shows the 20th master sensor image along with its corresponding range map. The range map, composed of 1,450 tracked features, has been projected onto the master image plane with the range coded by intensity. The cumulative execution time to process the first 20 image pairs of the sequence was used as the basis of comparison for each of the computer load balancing schemes tested. The third figure shows the speedup graph for a multithreaded shared-memory computer as the number of computed nodes is increased.

Ames-Moffett contact: R. Suorsa
(415) 604-6334
Headquarters program office: OAST

Computer Aiding for Low-Altitude Helicopter Flight

Harry N. Swenson, Richard E. Zelenka

As an element of the Automated Nap-of-the-Earth Program, a system has been developed that uses stored terrain information for helicopter flight control automation. The system is referred to as the Computer Aiding for Low-Altitude Helicopter Flight guidance system. The system significantly enhances the capability of helicopters to operate safely and effectively in adverse conditions. A joint NASA–Army flight evaluation of this near-terrain guidance and display system is currently being conducted on the Army's NUH-60 Systems Testbed for Avionics Research (STAR) helicopter. The system integrates precision navigation, digital terrain maps, automated mission planning, and modern onboard computer systems to define a valley-seeking trajectory for covert maneuvering penetration in hostile conditions. The trajectory is manually flown by the pilot tracking the head-up/eyes-out helmet-mounted display symbology developed for the system. The display presentation is a pathway-in-the-sky coupled with a phantom-aircraft, flightpath vector/predictor pursuit tracking guidance symbology (see first figure). The current flight test follows two highly successful simulations on the Ames Vertical Motion Simulator (VMS). The flight test has three phases: (1) functional flight evaluation, to verify the system installation in the STAR helicopter, (2) engineering flight evaluation, to determine the system's performance and the flight envelope, and (3) operational flight evaluation, to demonstrate the system to Army line pilots.

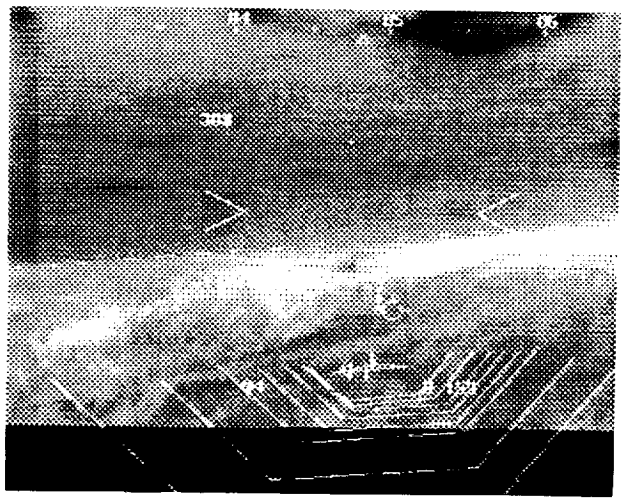

Fig. 1. Helmet-mounted display guidance with FLIR background.

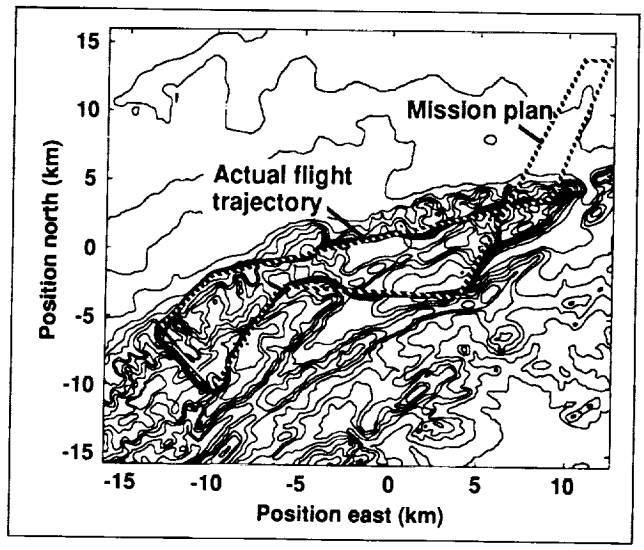

Fig. 2. Example horizontal ground track and mission plan from flight test.

Army and NASA research pilots have flown the NUH-60 STAR helicopter through the functional and engineering flight evaluations. The functional test included (1) verification of the helicopter hardware installations of the Precision Navigation System and helmet-mounted display, (2) validation of the Ames near-terrain guidance system software, and (3) the Army system installation and communication software. After several flights and system modifications, the NASA research pilots verified the system as functionally equivalent to the system tested on the Ames VMS. The engineering evaluations include 12 variations in flight conditions, terrain-masking performance, and display parameters, 50% of which have been completed by the Army and NASA research pilots. The evaluations have been based on a 30-nautical-mile multiwaypoint mission flown at 80–100 knots in rugged mountainous terrain at 125 feet above the ground. An example mission plan

with the actual flight trajectory is shown in the second figure, superimposed on a contour map of the flight test area. The third figure shows the aircraft and terrain altitudes as the pilot is tracking his guidance symbology over the example mission. The flight evaluations are the first successful attempt to bring digital terrain information into the piloted control of a helicopter. The flight test validates research designs for near-terrain helicopter flight control automation. This research has been recognized by the Army as a cornerstone of their Aided Pilotage program.

Ames-Moffett contact: H. Swenson
(415) 604-5469
Headquarters program office: OAST

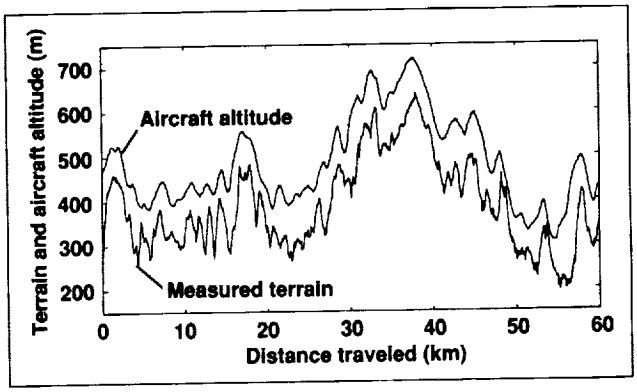

Fig. 3. Example aircraft and terrain altitude from flight test.

Rotorcraft Flight Control Design Methods

Marc D. Takahashi

The increasing demands for performance and a desire for multimode capabilities in future rotorcraft has placed a great burden on flight control systems. These systems have great potential for increasing levels of agility and maneuverability as well as increasing system stability and wind gust disturbance rejection. The flexibility of digital full-authority systems can fill the need for multimode capabilities for day-and-night operations. Achieving these higher levels of performance from the flight control system is inhibited by the rotor dynamics. In the past, the rotor dynamics were considered to be of a high enough frequency that they could be ignored. Future demands have made this assumption untenable.

Possible means of overcoming these performance limits are to use measurements from the rotor or to estimate rotor states from the fuselage motions. A recent analysis was completed of the use of the rotor states in the feedback in the pitch and roll axes. There were three main results. (1) It was found that the rotor-state feedbacks are functional in the pitch and roll feedback loops. This functionality has been largely ignored in the literature, and thus design and tuning of the control laws was difficult. Using the interpretation developed in this study, one can easily see how flapping feedback can be used to introduce phase lead and thereby remove the time delay of the rotor. (2) A control-law structure was developed to facilitate use of the body and rotor-state gains to comply with a modern helicopter handling-qualities design specification (ADS-33C). The structure divides the feedbacks into high-frequency attitude feedbacks and low-frequency translational mode feedbacks. This division allows the designer to manage the attitude modes (pitch and roll angular motion) separately from the translational modes (fore–aft and sideward motion). (3) The ideas developed in this study can be applied to a realistic helicopter flight-control design problem. An example design using the feedback structure and the rotor-state gains was developed that meets the Section-3 hover requirements of ADS-33C. This example used a configuration of a medium-weight utility helicopter with an articulated rotor with realistic sensor and actuator time delays. The rotor model included flap and lead–lag dynamics, and inflow dynamics to capture unsteady wake effects.

Ames-Moffett contact: M. Takahashi
(415) 604-5271
Headquarters program office: OAST

Frequency-Domain System Identification Methods

Mark B. Tischler, Mavis G. Cauffman

System identification refers to the technique by which mathematical models of vehicle and subsystem dynamics are extracted from input-to-output response data. These models are useful for the validation of analytical predictions and piloted simulations, for checking for compliance with handling-qualities specifications, and for updating control-system designs after first flight. Special tools are being developed that are specifically suited to the difficult problem of modern coupled, unstable airframe rotorcraft dynamics. The Army, NASA, and Sterling Federal Systems have jointly developed an integrated facility for system identification that is based on a comprehensive frequency-response approach that is uniquely suited to the difficult problems associated with flight-test data analysis. The overall concept is to (1) extract a complete set of nonparametric input-to-output frequency responses that fully characterizes the coupled characteristics of the system without a priori assumptions; (2) conduct a nonlinear search for a state-space model that matches the input/output frequency-response data set; and (3) verify the accuracy of the extracted models by comparing the predicted and actual response time histories.

The identification procedure described above has been implemented in a comprehensive set of user-oriented programs and graphics-intensive utilities within the facility referred to as CIFER—comprehensive identification from frequency responses. Extensive improvements in the facility's capability were implemented this year. The CIFER package was used extensively on a number of aircraft projects within the government (e.g., AH-64 and UH-60 flight tests) and in the aerospace community (V-22, Longbow, Georgia Tech manned simulator). An example of the CIFER-identified models is shown in the figure for the lateral response of the AH-64 helicopter in hover. It can be seen that the identified model closely predicts the aircraft responses, especially in the off-axis (pitch), as compared to the simulation model. In a first-of-its-kind application, CIFER was also used to extract the dynamic characteristics of the Sikorsky Bearingless Main Rotor (SBMR) from full-scale wind tunnel tests in the Ames 40- by 80-Foot Wind Tunnel. The extensive

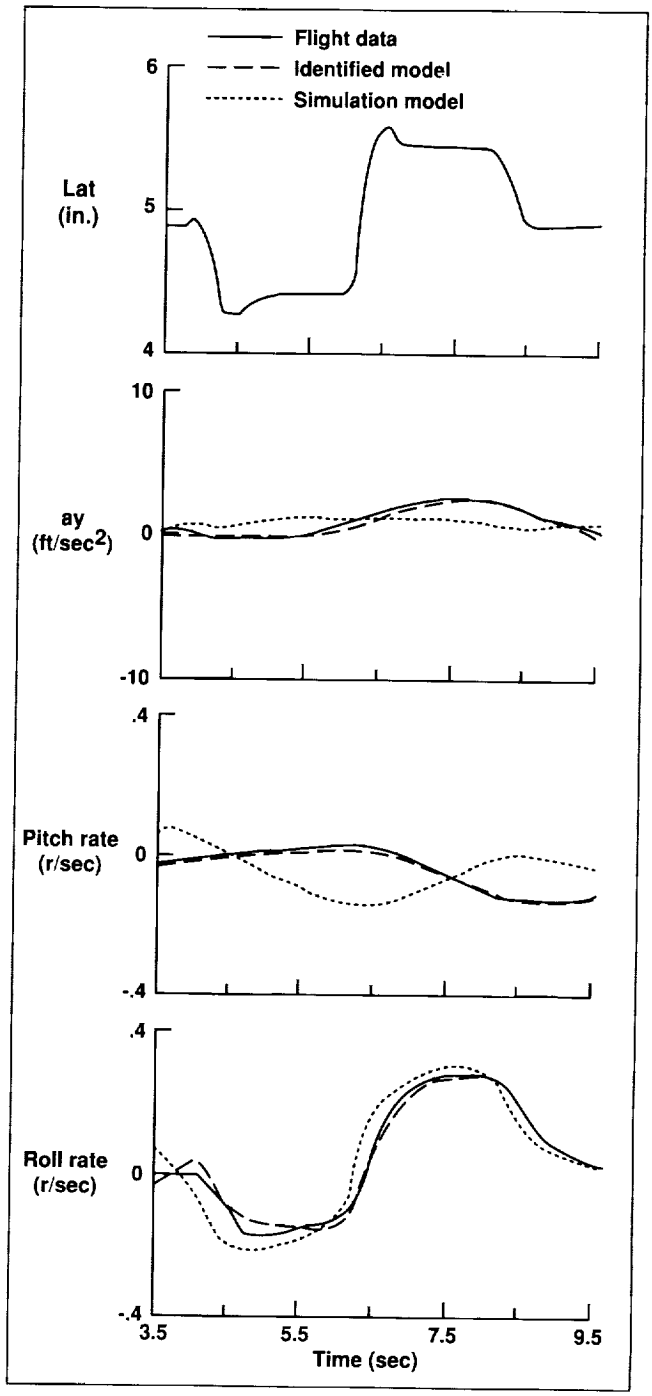

Fig. 1. Predictive capability of CIFER-identified model of the AH-64 in hover.

data base developed from this test will support industry, academic, and government research in the rotor dynamics, flight control, and simulation disciplines. Sikorsky Aircraft is using CIFER analysis of the data to validate the rotor dynamics models used in the synthesis of the Comanche control-system design.

A second major achievement this year was the licensing and release of CIFER version 2.0. Seven site licenses were sold to the aerospace community under the Technology Transfer Act. Eighteen research organizations participated in a comprehensive hands-on CIFER short course developed and conducted at the Ames Research Center in April. The CIFER system is now used by many research centers.

Current efforts focus on use of CIFER in the identification of models of the UH-60. These results will be used for simulation model validation and in the development of an advanced flight control system for the UH-60 RASCAL helicopter.

Ames-Moffett contact: M. Tischler
(415) 604-5563
Headquarters program office: OAST

Rotorcraft Robust Flight-Control-System Design Using Quantitative Feedback Theory

Mark B. Tischler

Design techniques are needed that can successfully realize high-bandwidth decoupled response specifications for modern rotorcraft configurations. Advanced frequency-domain techniques have been developed that are well suited to the rotorcraft problem. These methods are based on quantitative feedback theory (QFT), which is an extension of classical control theory. A comprehensive study of the QFT methodology and its application to rotorcraft flight control was completed this year. This study has led to a significantly improved understanding of the relationship between QFT and other classical and modern multi-input, multi-output (MIMO) techniques. Specifications for QFT design were based on an evaluation of the Army's handling-qualities specification (ADS-33) and UH-60 RASCAL requirements. In-house, high-order linear models (UMGENHEL) were heavily used to provide the needed aircraft characteristics as a function of flight condition. Air Force QFT design software was integrated into Aeroflightdynamics Directorate modeling and design tools.

A new low-order matching method was developed to design robust crossfeed compensators for MIMO QFT control systems. The technique minimizes cross coupling given an anticipated set of parameter variations for the range of flight conditions of concern. Results were summarized in a paper presented this year concerning an analysis of the pitch/roll coupling of the UH-60 Black Hawk helicopter in near-hovering flight. A robust crossfeed is designed that shows significant improvement in decoupling performance and robustness over the fixed-gain or single-point dynamic compensators (see figure). The design

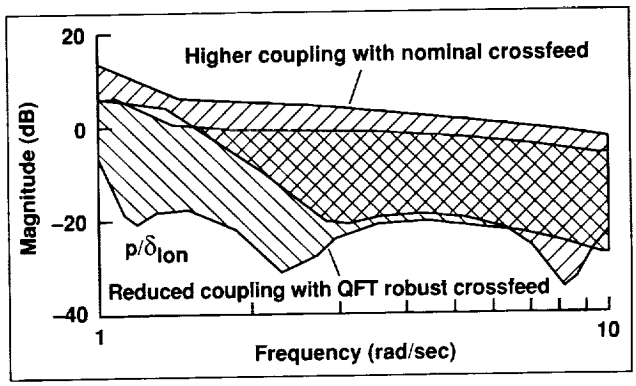

Fig. 1. Design of robust crossfeeds for decoupling.

method and results are presented in an easy-to-use graphical format that lends significant physical insight to the design procedure. This plant precompensation technique is an appropriate preliminary step in the design of robust feedback control laws for rotorcraft via QFT or other classical methods. Current efforts are focused on the refinement of the crossfeed design using the higher-order models of the UH-60, and the completion of the QFT feedback design.

Ames-Moffett contact: M. Tischler
(415) 604-5563
Headquarters program office: OAST/Army

CTAS Field Development and Evaluation

Leonard Tobias, Arthur David Jones

The Center/TRACON (terminal radar approach control facilities) Automation System (CTAS) is an integrated set of automation tools used for planning traffic arrival into major terminal areas. The system was developed and evaluated in thousands of hours of real-time simulations involving air traffic controllers as subjects. These evaluations demonstrated a strong potential for system-wide air traffic control (ATC) benefits including increased controller productivity, fuel savings, and reduced delays. However, before a decision is made to implement these tools nationwide, another step is required: field evaluations must be conducted at selected Federal Aviation Administration (FAA) enroute control centers and TRACONs. The FAA has agreed to conduct these evaluations jointly with NASA and has designated two centers and two TRACONs (Denver and Dallas/Fort Worth) for initial field testing. The evaluations will be used at selected field sites in order to expose the tools to a broad spectrum of users and to continue the development process.

Traffic Management Advisor (TMA)

The first tool to be brought to a field site was the Traffic Management Advisor (TMA), which was installed in the operational area of the Traffic Management Unit (TMU) at the Denver Center and TRACON. The TMA is the sequence and schedule tool for CTAS and is developed for use by the traffic planners at the site rather than by the radar controllers who are in direct contact with the aircraft. The figure shows the TMA workstations situated in the TMU at the Denver Center.

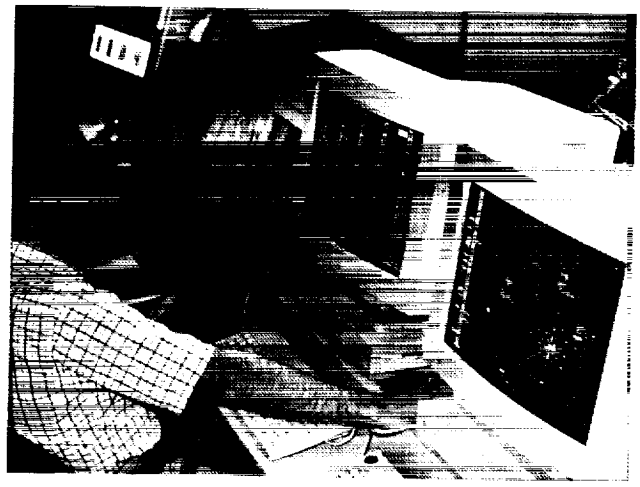

Fig. 1. Traffic Management Advisor installation in the Traffic Management Unit located in the Denver FAA Enroute Control Center.

Site hardware and software were installed in early 1992. After a cadre of TMU controllers was selected by the FAA, training on the use of the TMA was conducted. Initial assessments were conducted in late 1992, and a second assessment period is scheduled for 1993.

This assessment validated the field development and evaluation process. In addition, a number of near-term benefits and products have been identified. The most significant are (1) increased communication and coordination between the Center and the TRACON

because of the enhanced information available in the TMA displays and (2) identification of several auxiliary aids for data collection by TMU personnel using the TMA workstations.

As a result of these findings, the FAA has scheduled a 60-day limited operational evaluation of these tools for late 1993.

Final Approach Spacing Tool (FAST)

This second CTAS tool provides active advisories to controllers operating in TRACON airspace. After extensive development of software by Ames researchers and hardware by the FAA and its contractors, the tool should be ready for initial deployment to the Dallas/Fort Worth TRACON in mid-1993. In the Ames Aerospace Automation Laboratory, operational FAA hardware has been integrated with modern workstations and the NASA-developed CTAS software. Extensive simulations are under way, which will be followed by formal release of software to the FAA in mid-1993. Planned milestones for this year include (1) FAA certification of the special hardware and software required for the interface of CTAS with existing FAA ATC equipment and (2) identification and initial training of the TRACON controllers. These activities will initially be limited to the TRACON training area and operational use is planned for 1994.

Ames-Moffett contact: L. Tobias
(415) 604-5430
Headquarters program office: OAST

Nacelle Airframe Interference at Supersonic Mach Numbers

Gelsomina Cappuccio, Ronald C. Smith

A wind tunnel test of a nacelle airframe interference model was conducted in 1992 to assess the installed performance characteristics of candidate nacelles over the operating Mach number range, for various nacelle positions and mass flow ratios. The test was conducted in the Ames 9- by 7-Foot Supersonic Wind Tunnel at Mach numbers of 1.6, 2.0, and 2.4, using existing hardware. The overall model, shown in the first figure, consisted of a 0.024-scale model of Boeing's supersonic transport configuration (circa 1970) and a nacelle support system that remotely positions the nacelles independently of the wing-body model in the axial, lateral, and vertical directions, and allows for variable mass flow ratio through the nacelles. Four basic configurations were tested: the combination of the wing-body and nacelles, the four nacelles as a unit, an isolated nacelle, and the isolated wing-body. The nacelles were also tested with and without centerbodies to assess supersonic spillage effects. The nacelles with centerbodies are shown in the first figure.

The wing-body model has an overall length of 62.2 inches and a wingspan of 40.8 inches. The delta wing has a leading-edge sweep of 50.5 degrees and an inboard leading-edge extension with a sweep of 75.0 degrees. The left-hand wing contains 130 pressure orifices on the lower and upper wing surfaces. The wing-body model was supported with a six-component internal strain-gage balance for measuring lift, drag, and pitching moment.

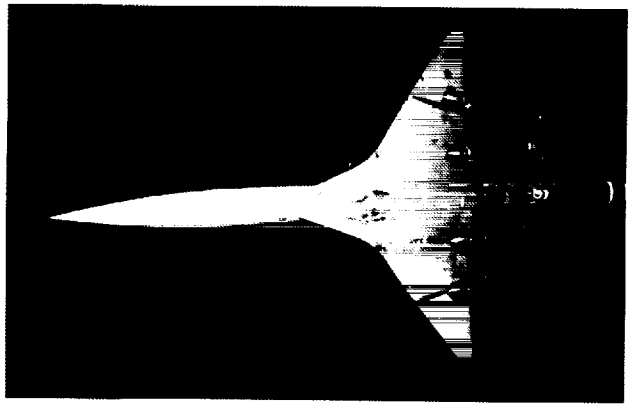

Fig. 1. Wing-body/nacelle combination installed in the Ames 9- by 7-Foot Supersonic Wind Tunnel.

Fig. 2. Florescent oil photograph, Mach number = 2.5.

The existing nacelles were axisymmetric and were designed for subsonic and low-supersonic Mach number operations with high-bypass-ratio engines. The two left-hand nacelles were pressure instrumented, and the two right-hand nacelles were mounted individually on separate flow-through, six-component strain-gage balances. Each of the pressure nacelles had 48 static pressure orifices located in four rows equally spaced around the nacelles. The nacelle force balances were housed in the wall thickness of each nacelle and were used to measure the aerodynamic forces on the external surface of the nacelle.

The extensive force and pressure data acquired in this test will allow NASA and industry to assess their capability to predict the interference characteristics of candidate nacelle geometries. Such interference characteristics can play a dominant role in the selection of the inlet concept and the nacelle shape. Another important aspect of the test program is the acquisition of flow-visualization data in the form of

florescent oil flows that can be used to establish boundary layer separation criteria. An example of such a flow-visualization picture is shown in the second figure. The flow separation on the wing inboard of the outer nacelle can clearly be seen.

A second phase of the test assessed the effects of pylons and diverters. The wing-body was tested with two different nacelle designs attached to the model via diverters and pylons. These nacelle designs are the ones being considered by Boeing and McDonnell Douglas for their high-speed transport configurations. Boeing's nacelle design was tested with four different diverter geometries, and McDonnell Douglas's was tested with a pylon and a diverter. This phase of the test will provide the drag increments that result from various pylon/diverter heights and shapes.

Ames-Moffett contact: G. Cappuccio
(415) 604-1313
Headquarters program office: OAST

Internal Flows Using Hybrid PNS/FNS Codes

William C. Rose, Michael D. Wong, Daniel P. Bencze

A space-marched parabolized Navier–Stokes (PNS) code (STUFF, written by Greg Molvik at Ames) has been combined with an established, time-marched full Navier–Stokes (FNS) code (SCRAM2D) to produce a rapid analysis of a hypersonic vehicle forebody and engine inlet. The space-marched code is used when the flow is parabolic (with no significant upstream influences), whereas the time-marched code is used when the flow is elliptical (with possible upstream influences, including separation). This effort has developed the "patching" techniques required for moving from one code to another easily and accurately. Typically, the STUFF code is used upstream of any strong shock-wave boundary layer interactions, and then SCRAM2D is used for the remainder of the inlet flow.

This newly developed technology has been applied to the designing and analysis of a representative forebody and inlet system. The forebody is modeled as a simple cone, and the inlet consists of a multiramp, dual-flow-path system intended to simultaneously feed both a turbojet and a ramjet propulsion module. The computation was performed for a flight condition in which both propulsion paths are operating.

The first figure shows the Mach number contours from the two-dimensional solution for the forebody and inlet flows. The design Mach number of the system is 5.0, but the solution is for the off-design condition of Mach 3.0. At this condition, there is substantial spillage over the cowl. The second figure

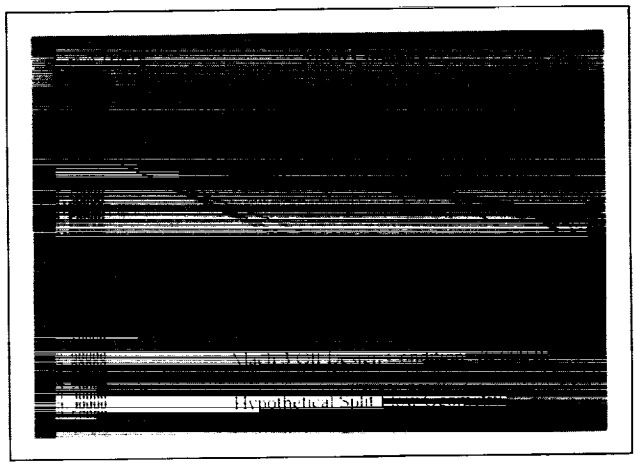

Fig. 1. Mach number contours for the entire forebody/inlet flow field. (See color plate 5 in Appendix)

shows the Mach number contours calculated within the dual flow path of the inlet system. The turbojet path uses the SCRAM2D code entirely whereas the ramjet path uses both the STUFF and the SCRAM2D codes. Both solutions are started from the forebody solution obtained with STUFF.

In this computation, the turbojet duct was back pressured to create a terminal normal shock, whereas the ramjet duct was allowed to flow freely. However, in both cases, the strong shocks in the ducts created shock-wave boundary layer interactions that had to be

stabilized with boundary layer bleed. The solution shown in both figures is a steady-state solution. But when the back pressure in the turbojet duct was increased, the turbojet inlet unstarted. This unstart process was analyzed with the SCRAM2D code in its time-accurate mode. The results indicated that flow will ultimately be spilled from the turbojet to the ramjet path, resulting in an unstart of the ramjet duct. A video of this time-dependent behavior has been produced.

The use of the combined STUFF and SCRAM2D codes reduces the required computation time and increases the resolution near the wall. Computational time for this typical problem is reduced from about 20 hours to about 2 hours for the steady-state solution with an attendant increase in flow-field resolution.

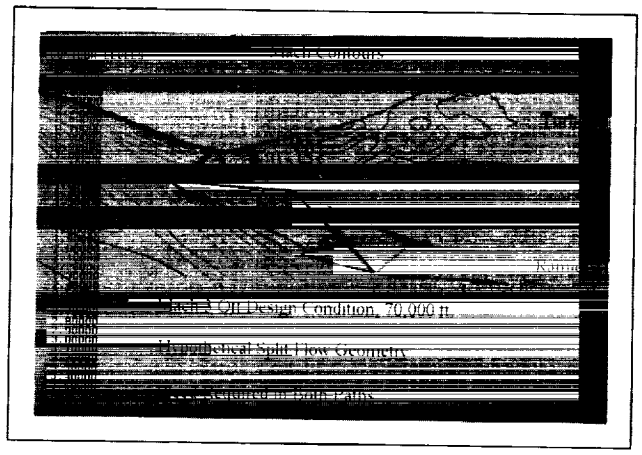

Fig. 2. Detailed Mach number contours in the turbojet and ramjet ducts. (See color plate 6 in Appendix)

Ames-Moffett contact: D. Bencze
(415) 604-6618
Headquarters program office: OAST

Dynamic Model for Large-Eddy Simulation

Knut Akselvoll, Parviz Moin

The dynamic model for large-eddy simulation (LES) of turbulent flows determines model coefficients by sampling the smallest scales resolved in the simulation. This procedure is done locally at each time step and thus the model coefficients are functions of space and time. The dynamic model procedure has the distinct advantage that no a priori calibration of model constants is necessary; the coefficients are determined automatically during the computation. Furthermore, the coefficients vary as necessary in space and time, thereby adjusting to additional "physics" or geometrical complexity when required. One example of this adaptability is that damping functions are not needed near solid boundaries because the model coefficient is reduced near the wall in such a way that the subgrid-scale model develops the correct near-wall behavior. Another example is that no ad hoc adjustments are necessary in the computation of laminar/turbulent flow transition.

Before this year, the dynamic model had been tested only in homogeneous turbulence and in turbulent channel flow. Although these simulations in simple geometries were quite successful, the model had not yet been tested in a more challenging setting. Accordingly, a simulation of the flow over a backward-facing step was performed. The distinguishing features of this flow are a massive separation zone behind the step, an adverse pressure gradient, and a recovery zone. Accurate prediction of the reattachment point as well as of the skin friction within the separated region are critical tests for any turbulence model. The figures show the computed skin friction and mean velocity profiles for the dynamic model LES and the corresponding direct simulation. The results are compared with a fully resolved direct numerical simulation (DNS). The agreement is excellent. The LES results were obtained using about 1% of the computer resources required for DNS. Both the LES and DNS results are in excellent agreement with experimental data obtained at the same flow conditions at Ames.

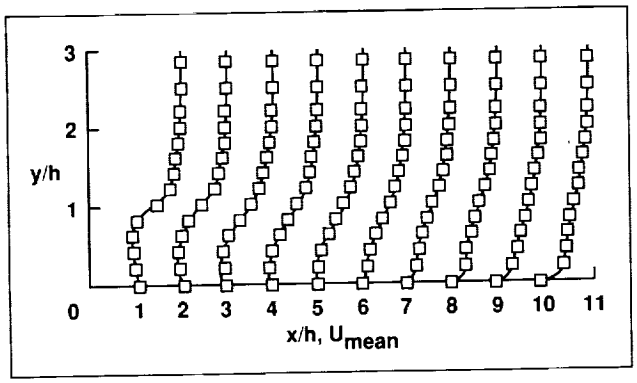

Fig. 1. Mean velocity profiles at various streamwise locations. Symbols are from direct numerical simulation; continuous lines symbolize large-eddy simulation; h is the step height.

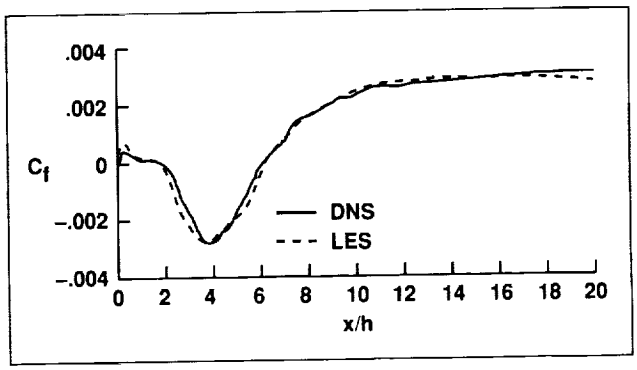

Fig. 2. Skin friction (C_f) as a function of distance from the step. Negative skin friction indicates reversed flow (separated region). The downstream zero crossing marks the reattachment point.

Ames-Moffett contact: P. Moin
(415) 604-5127
Headquarters program office: OAST

Visualization of Compressible Dynamic Stall

Lawrence W. Carr, Muguru S. Chandrasekhara

Dynamic stall significantly limits the speed and maneuverability of helicopters. Predicting dynamic stall effects has been especially difficult in the compressible flow environment that occurs on helicopter airfoils. In order to better understand the dynamic-stall process, a new technique was developed for quantitative visualization of the dynamic-stall flow field in compressible flow. This technique dramatically increases the information available to the scientist, as can be seen in the comparison of flow field information from various visualization techniques presented in the figure.

The photo on the left shows hydrogen-bubble visualization of dynamic stall obtained in a water tunnel. The image shows the character of the flow during the early stages of dynamic stall but presents only a qualitative description of the flow: the bubble patterns are particle path lines and do not actually represent the instantaneous character of the flow. This was the state of the art in 1978 for imaging unsteady flow away from the surface of airfoils.

The center photo presents a stroboscopic schlieren image of dynamic stall and is the result of the first phase of an ongoing study of compressibility effects on dynamic stall. This photo shows actual instantaneous flow characteristics, including the presence of dynamic stall. This is the first documentation of the dynamic-stall vortex in compressible flow, although the image is based on flow gradients and does not actually show the details of the flow.

The photo on the right shows a real-time interferogram of dynamic stall obtained by a recently developed interferometry technique. In contrast to the other photos, this photo is a completely *quantitative* image of the dynamically stalling flow field. Each alternating dark/light line in the photo is a quantitative demarcation of density and can be considered to be a line of constant Mach number as well. Thus, for the first time, the flow away from the airfoil can be fully documented during compressible dynamic stall while the test is still in progress.

The availability of real-time interferograms on a continuous basis has allowed scientists to explore the physics of unsteady separation and dynamic stall in compressible flow, and has revealed critical new elements of dynamic stall—elements that will be crucial in any attempt to control and use unsteady flow control for improved performance of aircraft.

Ames-Moffett contact: L. Carr
(415) 604-4143
Headquarters program office: OAST, U.S. Air Force, U.S. Army

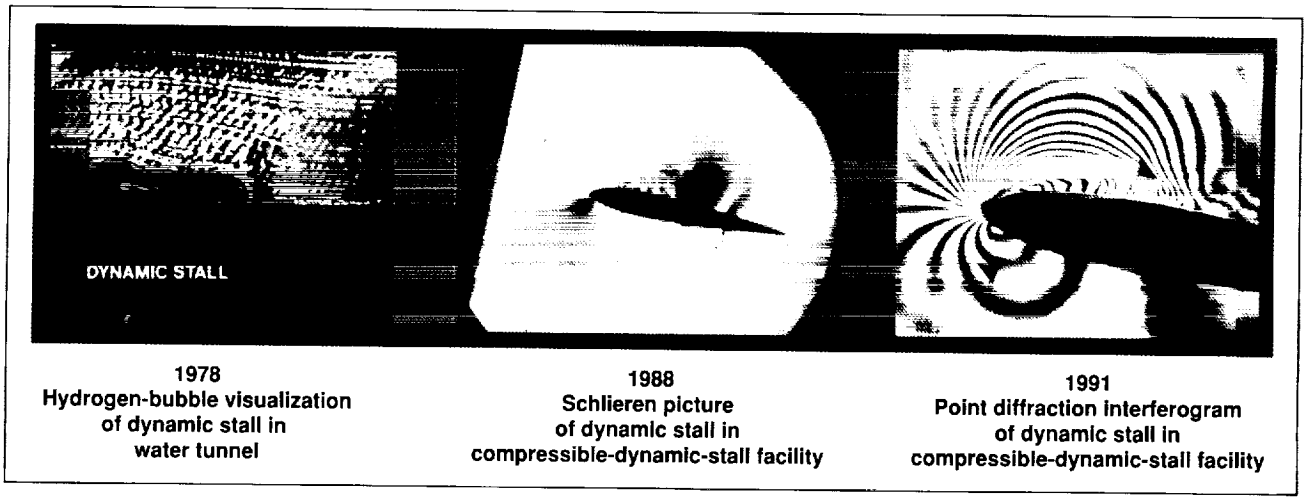

Fig. 1. Comparison of visualization techniques for unsteady flow.

Navier–Stokes Prediction of Wing Rock

Neal Chaderjian

A landing High-Speed Civil Transport or National Aerospace Plane, or a maneuvering tactical fighter, operates in high-angle-of-attack flight conditions. Because of the slender bodies and highly swept wings of these aircraft, vortices can form on the leeward (top) sides. These vortices can provide additional nonlinear lift, improved maneuverability, and improved agility. Although certain performance gains can be realized at high angles of attack, the vortices can also produce adverse side effects. For example, vortex asymmetries interacting with an aircraft's motion can lead to wing rock, a sustained periodic motion in roll and yaw. This motion can lead to departure from controlled flight, endangering both the pilot and the aircraft.

As a first step toward the viscous flow simulation of wing rock, the Navier–Stokes simulation code is used to predict vortical flow about a 65-degree-sweep delta wing mounted on a sting. The sting allows one degree of freedom in roll about the wing's longitudinal axis. The free-stream Mach number is 0.27, the angle of attack is 15 degrees, and the Reynolds number based on the wing root chord is 3.67 million.

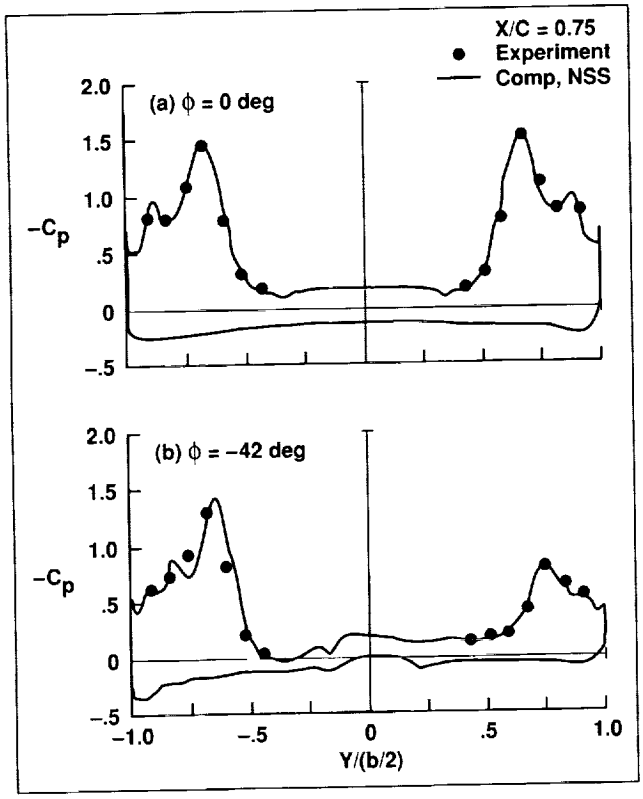

Fig. 1. Comparison of static roll (ϕ) surface-pressure coefficients.

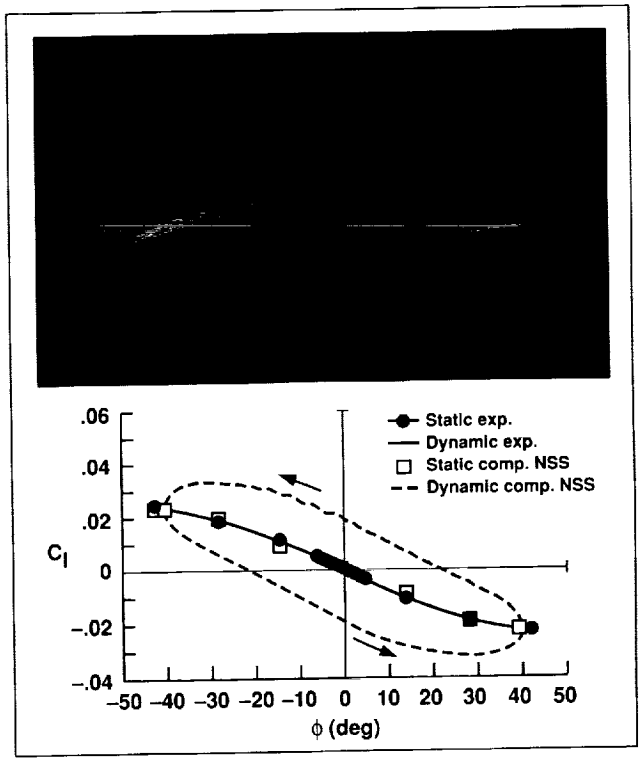

Fig. 2. Visualization of dynamic roll vortices and comparison of static and dynamic rolling moment coefficients. (See color plate 7 in Appendix)

Static cases were computed through 42 degrees of roll. The first figure shows a comparison between computational and experimental surface-pressure coefficients (plotted against the spanwise coordinate). Results are shown at the 75% root chord position for zero and 42 degrees of roll. The agreement of computational and experimental values is excellent. This same level of accuracy is obtained at several intermediate roll positions.

A forced dynamic roll oscillation was also simulated. The same Mach number, angle of attack,

and Reynolds number were used. The results for this large-amplitude (40 degrees), high-rate-of-roll (7 cycles per second) motion are summarized in the second figure. The leeward-side vortices are visualized using helicity-density contours at 10% chord intervals along the longitudinal axis. The figure corresponds to an instant in time when the wing is at –40 degrees of roll. Green contours indicate a clockwise rotation of the vortices; red contours indicate a counterclockwise rotation. Secondary and tertiary flows can also be seen by a change of color in the body-normal direction. This figure indicates that there is no vortex breakdown at this angle of attack, which is confirmed by experiment.

Also shown in the second figure is a comparison between dynamic computational (dashed line) and experimental (solid line) rolling moment coefficients (C_l). The agreement is very good. The loops trace a counterclockwise movement in time. The area enclosed by these loops represents the energy of the wing motion. The counterclockwise direction indicates that the motion is damped, and the computational and experimental damping energies agree within 3%. The static computational and experimental rolling moment coefficients are also shown in the figure and are in very good agreement. Differences between static and dynamic values indicate significant rate effects.

The Reynolds-averaged Navier–Stokes approach looks promising. The next step is to carry out a similar study at 30 degrees angle of attack, at which vortex breakdown does occur, and then compute wing rock.

Ames-Moffett contact: N. Chaderjian
(415) 604-4472
Headquarters program office: OAST

Enhancements of the Hyperbolic Grid Generator and User Interface

William M. Chan, Ing-Tsau Chiu

The accuracy of flow simulations using computational fluid dynamics (CFD) methods is highly dependent on the quality of the computational grids used. In aerodynamics applications that involve complex geometries, the process of grid generation is typically time consuming and requires much user effort. The objectives of this project are to enhance the robustness and user friendliness of the hyperbolic volume grid generator, HYPGEN, to reduce the required user effort with the aid of a graphical user interface, UI, and to provide support for the users.

The robustness of earlier versions of the hyperbolic grid generation algorithm has been significantly enhanced in HYPGEN such that general and complex geometries can be treated. Recent improvements include the implementation of various optimization techniques, which have resulted in a 10% speedup of the code. Feedback from users was used to improve the capabilities of the code in order to treat more complex cases and to enhance user friendliness.

The design of UI consists of graphical objects commonly found in graphical user interfaces, e.g., buttons and sliders, that allow users intuitive ways of changing options and selecting parameters. Default values of various options are automatically selected by UI, thereby reducing the initial learning effort of new users. Viewing of the grid within UI is also easily achieved with automatic viewpoint setup.

HYPGEN can be used independently or it can be driven by UI. HYPGEN and UI can be run on the same machine or on separate machines depending on the user's needs. For example, one might want to generate large grids (using HYPGEN) on supercomputers and have the UI running on workstations. The speed (more than 100,000 grid points per CPU second on the CRAY Y-MP) and the ease of use of the code for a wide variety of complex geometries have made it a useful tool in the grid-generation process.

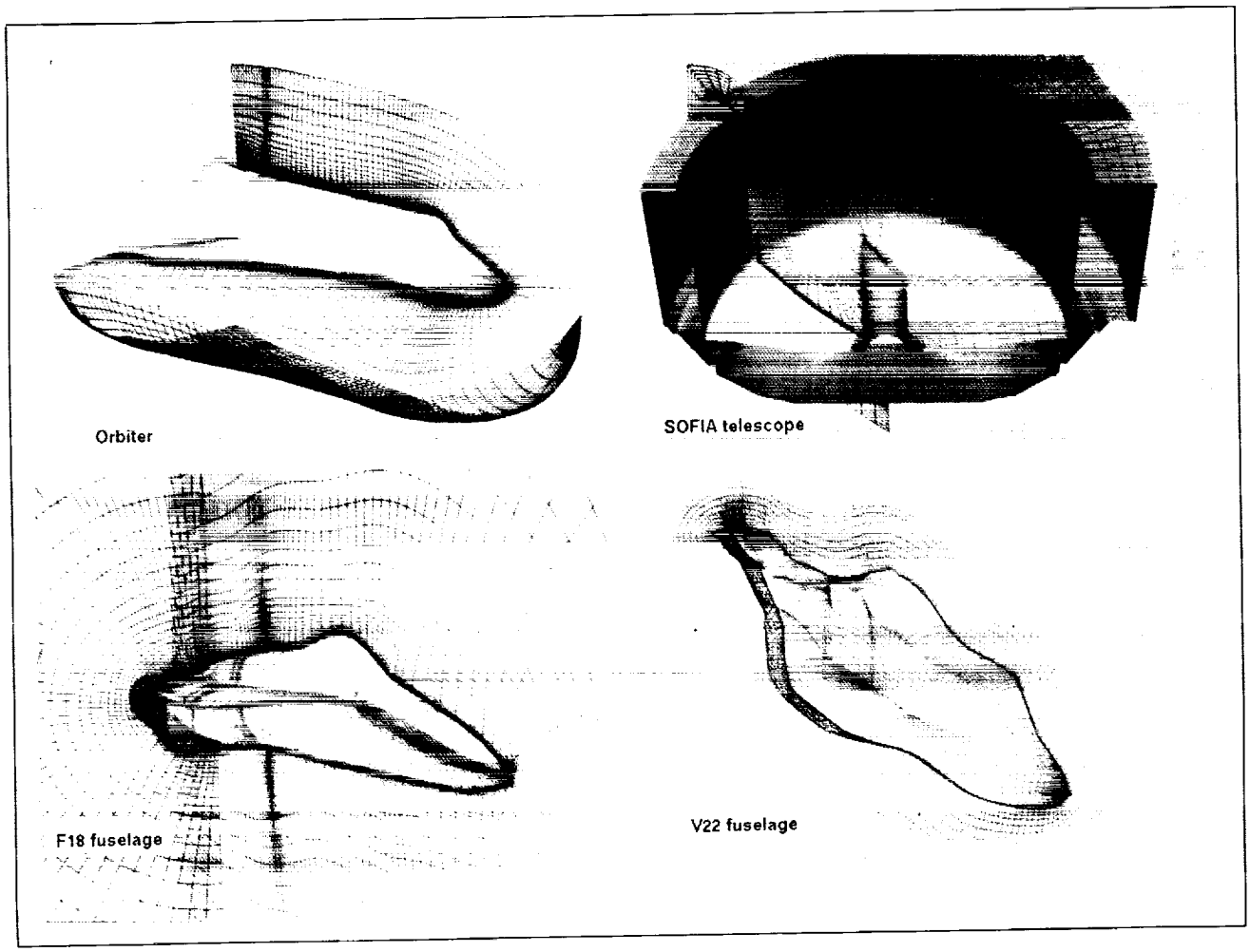

Fig. 1. A sample of volume grids produced by HYPGEN.

The figure shows a sample of volume grids that were produced at Ames by HYPGEN. The code has also been distributed to various government and industry groups and universities including NASA Johnson Space Center, the Air Force, Wright Laboratory, Boeing, Douglas Aircraft, Rockwell International, the University of California at Davis, and Penn State University.

Ames-Moffett contact: W. Chan
(415) 604-6607
Headquarters program office: OAST

Numerical Simulation of High-Performance Aircraft Operations

Kalpana Chawla

Thrust vectoring can be used to improve short-field, up-and-away, and post-stall maneuvering performance of high-performance aircraft. When vectored thrust is used to meet short-runway requirements, as in the case of the Harrier AV-8B, a complex fluid dynamics interaction between the vectored jets, the ground, and the airframe is encountered. This flow field can put the aircraft at risk as a result of lift loss and hot-gas and debris ingestion. As a result of these risks, performance and operational flexibility may be reduced.

A computational study has been carried out to predict the lift loss experienced by aircraft that use thrust vectoring in ground effect, by computing flow past a delta wing with thrust reverser jets in the straight-and-level and descent flight profiles. Results are compared with experimental data from Paulson and Kemmerly's Vortex Research Facility at NASA Langley, where a similar setup was used. The time-accurate computations for the straight-and-level flight were performed for a number of heights (h/b = 1.0, 0.5, 0.35, and 0.25, where h is the height and b is the wingspan) above the ground. The computations overestimate the lift coefficient; however, the flow physics of the lift loss with increased ground proximity is captured. The time-accurate simulation of the descent from h/b = 1.0 to h/b = 0.25 captures the initial increased lift that results from the conventional ground cushion effect as the delta wing approaches the ground. The figure shows the averaged lift coefficient for the straight-and-level flight cases and the lift coefficient at the experimental sampling rate for the descent case. The raw experimental data for the descent case show oscillations very similar to those observed in the computations. However, the raw data were modified by the experiment team by subtracting body inertias and averaging.

Both the straight-and-level flight and the descent simulations exhibit high levels of unsteadiness in the computed lift coefficient. Spectra of the lift histories indicate preferred frequencies in the narrow Strouhal-number range of 0.015 to 0.03 for the straight-and-level flight for all computed heights. The same range of frequencies is preferred when spectra are computed

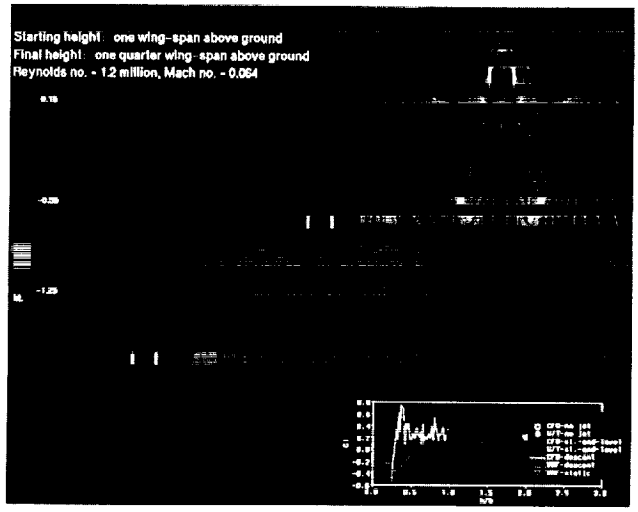

Fig. 1. A delta-wing aircraft descent simulation. (See color plate 8 in Appendix)

over segments of descent. Efforts were made to understand the unsteady flow structures that produce the lift oscillations. It was shown that the ring vortex shedding frequencies are too high to cause the lift oscillations. Ground vortex puffing was ruled out as the cause of lift oscillations because it appears only at lower heights. Lift oscillations, however, over the same range of preferred frequencies appear even at greater heights (e.g., h/b = 1.0).

The presence of a "wave-like" pressure field in the vicinity of the jet indicates that the jet oscillations result in moving pressure waves. It was shown that the lift oscillation frequency is related to the frequency of these waves. Analysis of temporal variations of pressure at various locations on the ground indicates frequencies within the range of the lift oscillation frequencies. It is conjectured that a ground-vortex-puffing type of flow physics occurs in the vortex formed behind the jet, causing its size to oscillate and resulting in jet oscillations. It was concluded that the lift oscillations are due to large-scale motions of the jet and the jet-induced flow structures.

Ames-Moffett contact: T. Holst
(415) 604-6032
Headquarters program office: OAST

Reynolds-Stress Modeling in Wall-Bounded Flow

Paul Durbin

The simplest turbulence model is the scalar eddy viscosity model. This type of model draws an analogy between molecular, viscous friction, and turbulent mixing of momentum. Actually, turbulent mixing is not analogous to molecular transport; the turbulent eddies that stir a fluid are affected by forces that act on the flow and the geometry within which the flow is confined, whereas molecular processes are not so affected. Thus in many cases the eddy viscosity model is inadequate. Reynolds-stress closure, the subject of this research, is a more elaborate model that attempts to represent mathematically many of the forces that affect turbulent eddies.

Turbulent mixing in flows of engineering interest is "anisotropic," which means that the effectiveness of turbulent stirring varies with direction. For instance, a wall suppresses the component of turbulent velocity that is perpendicular to its surface, so the mixing intensity is greater parallel to the wall than perpendicular to it. A convex, curved wall causes a stabilizing centrifugal force that suppresses flow to and from the surface. The first figure illustrates this effect. It shows the heat transfer coefficient on a wall that starts out flat, then goes around a 90 degree bend. The bend begins at x = 0 and ends at x = 0.7 meter. Within the curved section, it can be seen that the heat transfer is suppressed by the curvature. As a point of reference, the dashed line in the figure shows the heat transfer coefficient that would be measured on a flat wall.

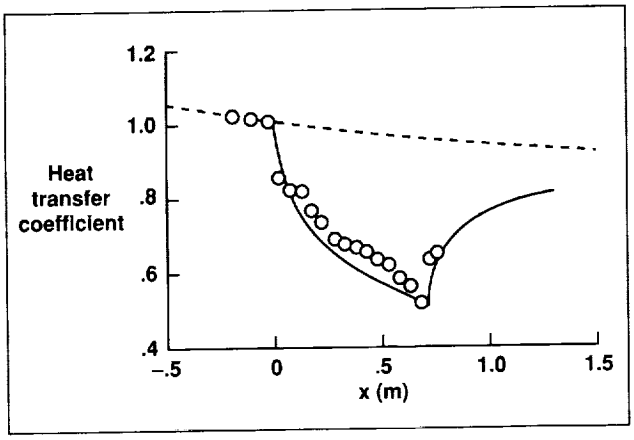

Fig. 1. Heat transfer coefficient determined by the Reynolds stress model (the solid line represents a surface containing a 90-degree bend, beginning at x = 0 and ending at x = 0.7 meter; the dashed line represents a flat surface) and by experimental data (symbols).

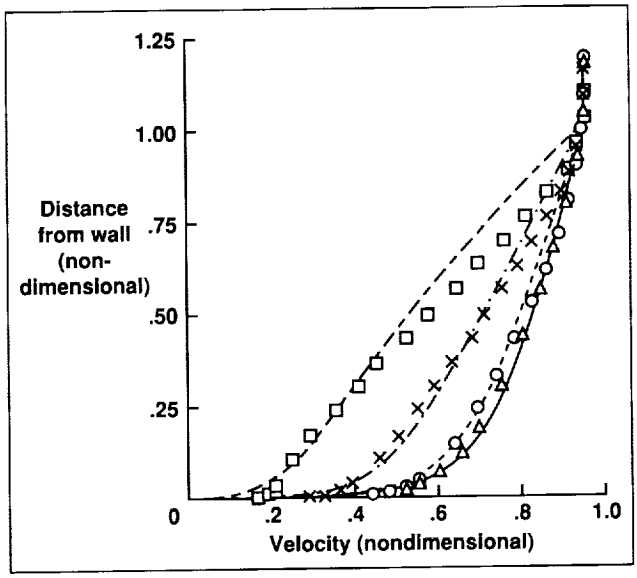

Fig. 2. Profiles of averaged velocity at various downstream positions in a decelerating flow (solid line, x = 0; dashed line, x = 1 meter; chain dot, x = 2 meters; chain dashed, x = 3 meters). The symbols represent experimental data.

When the flow near a wall is subjected to a decelerating pressure gradient, the region of shear thickens rapidly, and the averaged velocity increases more gradually away from the wall. These alterations to the averaged velocity influence the distribution and scale of the turbulent eddies. The present mathematical model can account for many of these effects of pressure gradients. The second figure shows profiles of the average velocity as the flow progresses through a decelerating pressure gradient. The ordinate is the distance from the wall, scaled by the thickness of the shear layer. This scaling was done for the purpose of presentation; the model predicts the layer thickness. The abscissa is the average velocity, scaled by the velocity far from the wall. The latter prescribes the

pressure gradient. The first profile, represented by the solid line, is very full; the turbulent eddies stir the fluid efficiently and the velocity remains high through most of the layer, then drops to zero abruptly as the wall is approached. The later profiles are less full. As the flow slows, the turbulent mixing is unable to keep up with the deceleration, and the velocity profile is eaten into by the pressure gradient.

Ames-Moffett contact: P. Durbin
(415) 604-4726
Headquarters program office: OAST

Temperature and Density Measurements in a Turbulent, Mach 2 Boundary Layer

Douglas Fletcher

A new laser-spectroscopic technique that was developed at Ames Research Center has been used to measure the temperature and density fluctuations in a turbulent, supersonic boundary layer. The technique uses a tunable, pulsed ultraviolet laser to induce fluorescence from oxygen molecules and to produce Raman-scattered light from nitrogen and oxygen during the same laser pulse. By obtaining light signals from the wind tunnel air flow constituents directly, uncertainties that result from spatial and temporal nonuniformity of special seed material are avoided. The laser-induced fluorescence (LIF) signal level depends on the density and temperature at the measurement location, whereas the Raman signal level depends only on density. Density can thus be measured directly from the Raman signal variation. Temperature is determined from the LIF signal variation after correction for density by the Raman signal. Precise focusing of the laser beam allows a spatial resolution of 1 millimeter or better for the single-pulse temperature and density measurements.

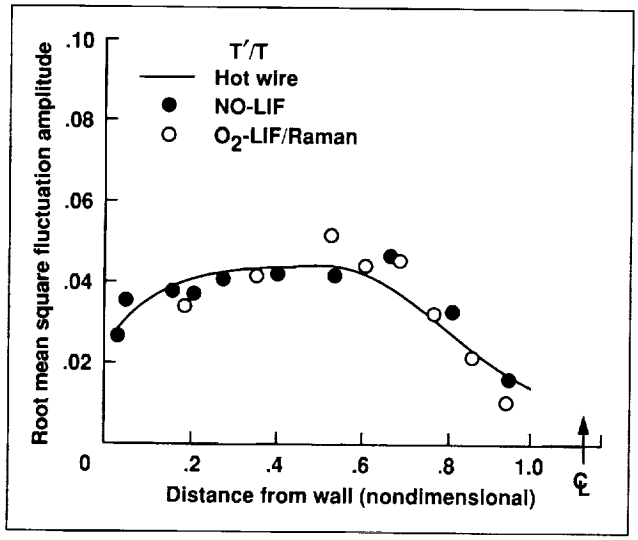

Fig. 1. Comparison of the LIF/Raman-measured temperature fluctuations with earlier measurements in the Mach 2 boundary layer.

The LIF/Raman technique has now been used to measure the variations of mean and fluctuating thermodynamic properties in a turbulent, Mach 2 boundary layer. At the measurement location the boundary layer thickness was 12.1 millimeters and the free-stream density and temperature were typically 0.55 amagat and 157 kelvin for a Mach number of 2.06. Previous flow surveys were performed with thermocouple and pitot probes and a hot-wire anemometer to verify and document the turbulent nature of the boundary layer. An earlier spectroscopic technique based on the LIF of nitric oxide (NO) seeded into a nitrogen flow provided an additional set of temperature and density fluctuation amplitude measurements.

The measured values obtained with the LIF/Raman spectroscopic technique are in good agreement with results from the earlier flow surveys. As shown in the first figure, the measured temperature fluctuation amplitudes in the boundary layer agree very well with earlier hot-wire-anemometer and spectroscopic (NO-LIF) surveys. In the second figure, the density fluctuation amplitudes measured with the LIF/Raman technique are seen to agree well with the NO-LIF measurements; both spectroscopic techniques measure an increase in density fluctuation level that is a result of the intermittent movement of a weak shock.

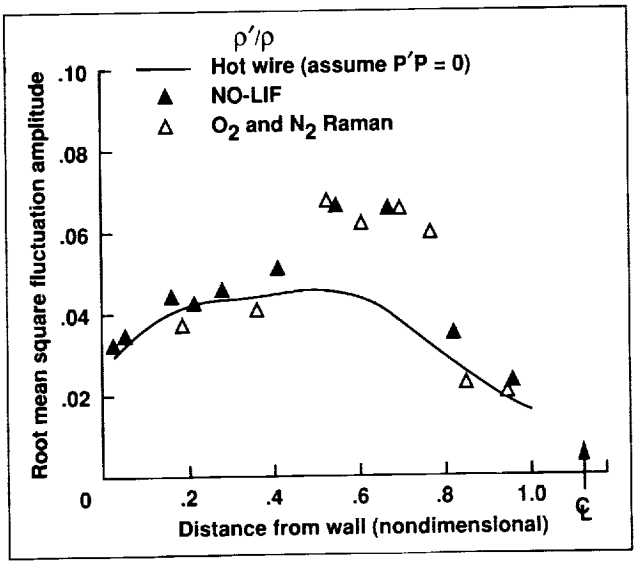

Fig. 2. Comparison of the LIF/Raman-measured density fluctuations with earlier measurements in the Mach 2 boundary layer.

The weak shock influences the density fluctuations most strongly in the region near 60% of the boundary layer thickness. Density fluctuation amplitudes were derived from the hot-wire measurements of temperature fluctuations by assuming negligible pressure fluctuations. Because pressure fluctuations accompany the weak shock movement, this assumption is invalid and the hot-wire anemometer missed an important flow feature that was detected by the spectroscopic technique.

These temperature and density fluctuation measurements represent the first application of the LIF/Raman technique in a turbulent, supersonic flow. The results demonstrate the ability of the spectroscopic technique to obtain turbulent fluctuation amplitudes in high-speed, compressible airflows without relying on an intrusive probe or special flow-seeding material. Information gained from the application of the LIF/Raman approach will provide insight into the effects of turbulence in supersonic and hypersonic flows.

Ames-Moffett contact: D. Fletcher
(415) 604-6457
Headquarters program office: OAST

Pneumatic Forebody Flow Control

Kenneth Gee, Yehia Rizk, Lewis Schiff

Pneumatic forebody flow control by means of tangential slot blowing was analyzed using computational fluid dynamics. Blowing was applied to a full aircraft geometry flying at a high angle of attack. The effect of blowing on the flow field about the aircraft, and the side force and yawing moments produced by this method, were obtained.

The flow about the F-18 aircraft during tangential slot blowing was computed using a multizone, thin-layer Navier–Stokes code called F3D/Chimera. The slot geometry used in full-scale wind tunnel tests was modeled in the computations. The jet conditions were introduced as boundary conditions in the grid that modeled the slot. A computation for the isolated forebody was obtained under wind tunnel test conditions. A computation for the full aircraft geometry was obtained using flight test conditions.

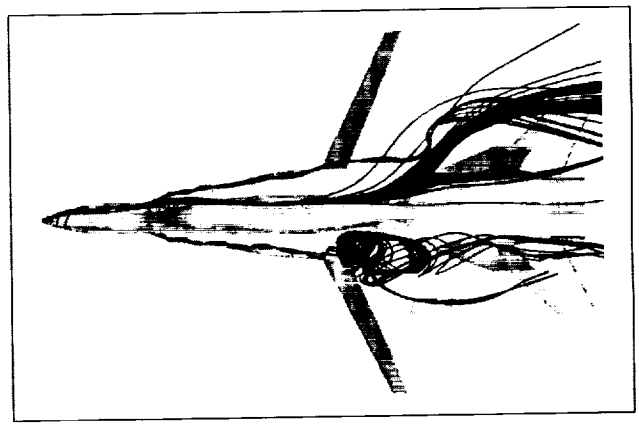

Fig. 1. Off-surface particle traces showing the effect of blowing on the flow field about the F-18.

A comparison of the computations with experimental data from a full-scale wind tunnel test of the F-18 with tangential slot blowing was made. The full aircraft computation showed the qualitative effects of blowing on the flow field (see first figure). The forebody vortex was dominated by the slot blowing. The interaction of the forebody vortex with the leading-edge-extension (LEX) vortices causes a delay in the burst of the nonblowing-side LEX vortex. There was an indication of a strong interaction between the forebody vortex that resulted from blowing and the vertical tails. Surface pressure coefficient (C_p) agreement between the computational and the experimental data was excellent (second figure). Slight discrepancies occurred in the separation region of the jet, but the computation matched the pressure drop resulting from the attached jet quite well. The side force and yawing moment were produced by the pressure drop on the nose that resulted from blowing and, to a greater extent, by the asymmetry in the vortex burst point over the LEX and wing. The interaction of the vortices with the vertical tails also generated a side force and yawing moment, although the direction and magnitude of the force and moment appeared to fluctuate because of the unsteadiness of the flow in this region.

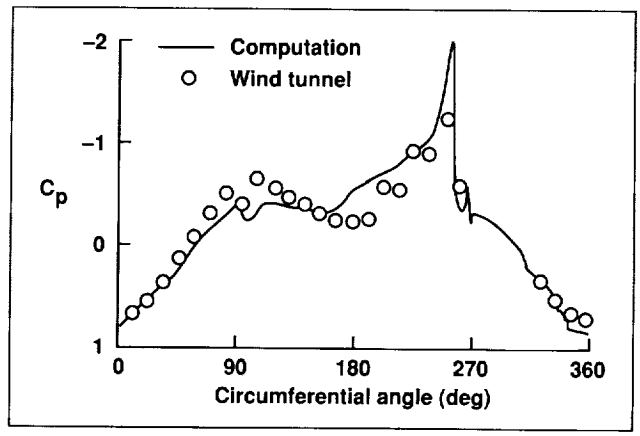

Fig. 2. Comparison of surface pressure data at a pressure station on the nose of the F-18.

Ames-Moffett contact: K. Gee
(415) 604-4491
Headquarters program office: OAST

3-D Laser Doppler Velocimeter Measurements

Dennis A. Johnson, Jeffrey D. Brown

As a result of the advances that have taken place in computational fluid dynamics (CFD), there is an increasing need for near-surface turbulence Reynolds stress data to aid in the development and validation of turbulence models for Reynolds-averaged Navier–Stokes (RANS) solution methods. Reynolds stresses are correlations of velocity fluctuations that represent added momentum transfer in turbulent flows. In RANS solution methods, these stresses are estimated via a turbulence model.

The development of Reynolds stresses near a solid surface is not particularly well understood for flows that are three-dimensional (3-D) and that have regions of separation. It is believed that a better understanding of how these stresses develop under such conditions would have a significant impact on CFD as applied to commercial-transport wing design.

Currently, a laboratory study of the flow about a wedge is being conducted in the Thermal Sciences Division at Stanford University. The flow develops a 3-D boundary-layer flow much like that which occurs on aircraft wings. The first figure shows a plan view of this flow. The boundary layer is the thin viscous layer that develops along a solid surface as a result of friction. In the figure, velocity vectors are shown to illustrate the turning of the flow near the surface.

Reynolds stress data are obtained extremely close to the surface by means of a specially designed laser Doppler velocimeter (LDV). The LDV uses a beam-turning probe to directly measure the illusive third (i.e., crossflow) velocity component, W. This small beam-turning probe, which is inserted into the flow, also gives excellent spatial resolution (diameter = 0.04 millimeter, length = 0.08 millimeter).

Shown in the second figure are LDV measurements of the Reynolds stresses, $-\overline{uv}$ and $-\overline{vw}$, plotted as a function of distance from the surface, y. These happen to be the most important stresses for this particular flow because the spatial gradients are largest in the direction normal to the surface. The measurement location relative to the wedge is indicated in the first figure. The stress $-\overline{vw}$, which is produced as a result of mean crossflow velocities, is difficult to measure even far from solid surfaces with hot-wire anemometry or conventional LDV. In the present experiment, $-\overline{vw}$ measurements to within

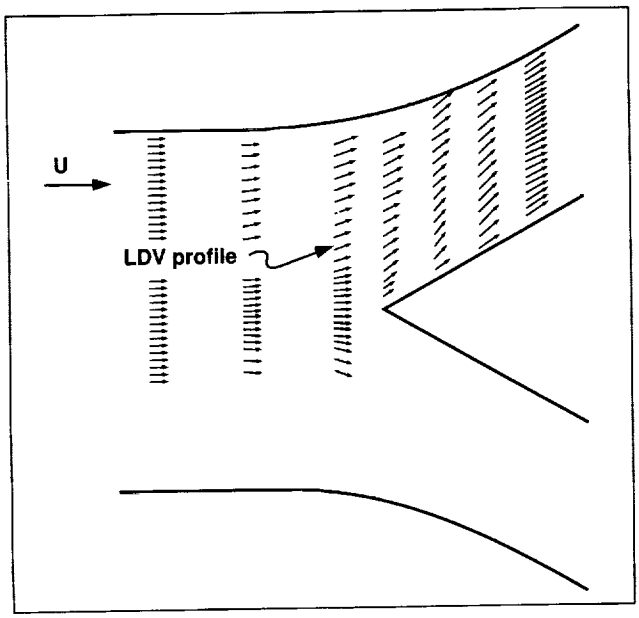

Fig. 1. Plan view of 3-D wedge flow.

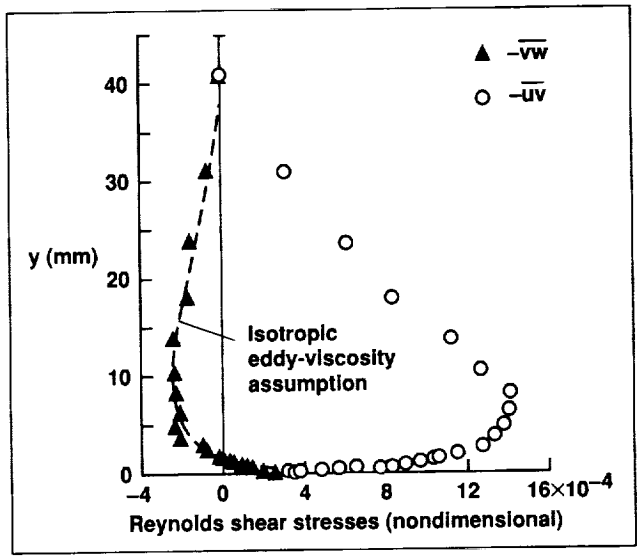

Fig. 2. Near-surface Reynolds shear stress measurements.

0.06 millimeter of the surface are being accomplished. This distance corresponds to a viscous wall distance, y^+, of only 2 in the present experiment. At this particular location, the popular isotropic eddy-viscosity assumption appears valid, as seen from the comparison in the second figure. Departures from theory are expected to occur at locations closer to the wedge, where more flow skewing occurs.

Ames-Moffett contact: D. Johnson
(415) 604-5399
Headquarters program office: OAST

Experimental Validation of the Direct Numerical Simulation of a Backstep Flow

Srboljub Jovic, David M. Driver

This experiment was motivated by a recent cooperative project on separated flows, undertaken by the Modeling and Experimental Validation Branch at NASA Ames and the NASA/Stanford Center for Turbulence Research, in which a backward-facing step configuration was chosen as the simplest geometry to generate a flow with separation that is equally suitable for an experiment and for direct numerical simulation (DNS). This pioneering computational effort in numerical fluid dynamics requires direct verification by experiments that are designed to directly match computational efforts. Therefore, the Reynolds number of the DNS is limited by the available computer memory and speed. The DNS predictions were thus confined to a step height Reynolds number of 5100, for which there were no experimental data. Consequently, an experiment was devised to match the conditions of the DNS. The experiment was carried out in a wind tunnel with a double-sided, symmetrical, abrupt expansion to simulate the single-sided expansion with a top wall slip condition.

The general conclusion that can be drawn from the figures is that the agreement of the experimental results and the DNS computations is excellent. The distributions of pressure shown in part (a) of the figure, measured on the top and the bottom walls of the wind tunnel (square and triangle symbols, respectively), show that the flow was symmetrical and that the top- and bottom-wall reattachment lengths were approximately equal. The reattachment length was deduced in two independent ways and was found to be at a location 6 ± 0.15 step heights (h) downstream of the step. The reattachment length obtained by DNS was 6 h.

Time-averaged skin friction was measured using a laser-oil interferometer technique. The results are shown in part (b) of the figure. The computations are seen to agree well with the data to within the experimental uncertainty.

Flow field and structure characteristics were measured at three typical streamwise locations and these results are presented in parts (c) and (d) of the

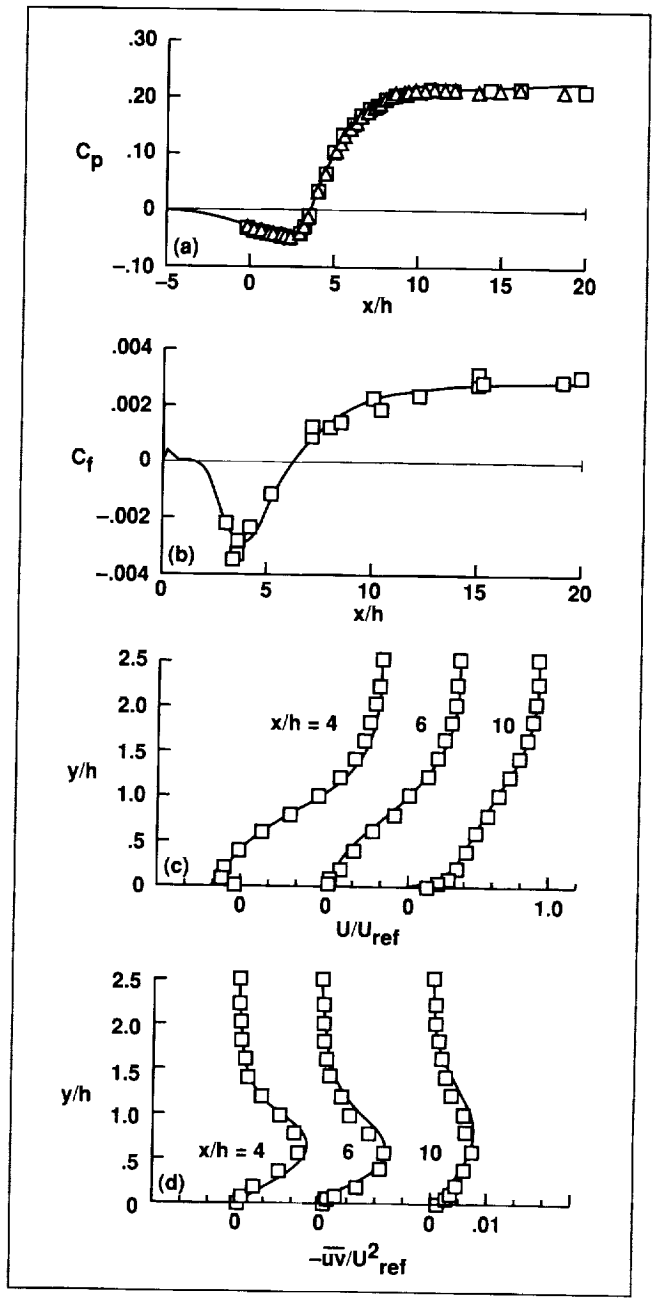

Fig. 1. Measured and computed (a) pressure, (b) skin friction, (c) velocity, and (d) Reynolds shear stress in a backward-facing step flow.

figure. The minimum skin friction and the maximum Reynolds stresses occur at approximately x/h = 4. The flow reattaches at location x/h = 6. Again, the agreement of the measured and computed mean streamwise velocities and shear stresses is excellent at all three locations.

The excellent agreement between the experimental and simulation values provides confidence in the DNS prediction of this complex flow. Numerous problems in the area of turbulence modeling and flow structure can now be extensively tested using this DNS data base.

Ames-Moffett contact: S. Jovic
(415) 604-6211
Headquarters program office: OAST

Computational Verification for the Laminar Flow Supersonic Wind Tunnel

Goetz H. Klopfer

Computational tools were developed so that the design of a test model and its placement within the test section of the Laminar Flow Supersonic Wind Tunnel (LFSWT) could be verified by numerical simulation of the Navier–Stokes equations before the model is constructed. For studies of transition from laminar to turbulent flow in the supersonic Mach regime it is important to know the extent of clean and undisturbed flow over the model.

Modified versions of the upwind parabolized Navier–Stokes (UPS) and the compressible Navier–Stokes finite volume (CNSFV) codes were used to solve the thin-layer Navier–Stokes equations for the laminar flow about the test model in the LFSWT. The faster UPS code was used for the higher Mach numbers investigated, and the multizonal CNSFV was used for the lower supersonic Mach regime.

Computations have been performed for a NACA 64A010 wing with a 70-degree leading-edge sweep mounted on the top wall of the LFSWT at Mach 1.6, for inviscid and viscous flows with the UPS and CNSFV codes, respectively. Various other model locations were studied to verify that the top-wall-mounted position provides the largest extent of undisturbed flow on the model. The accompanying figure shows the inviscid shock pattern obtained with the UPS code. The impinging shocks on the tunnel walls as well as on the model itself can be seen. The undisturbed region on the model is the triangular region in front of the reflected shock wave impinging on the model. The flow field behind the impinging shock wave is no longer undisturbed, hence the part

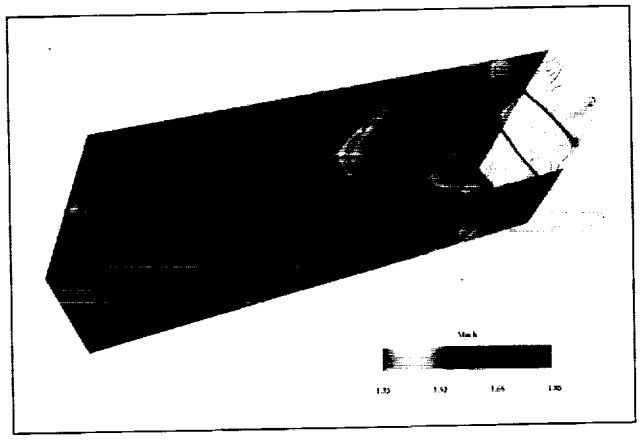

Fig. 1. Computed shock waves on a test model at Mach 1.6 in the Laminar Flow Supersonic Wind Tunnel. (See color plate 9 in Appendix)

of the model behind the shock is not useful for any natural transition study.

The accurate prediction of the flow field inside the LFSWT for various test models is important for maximizing the usefulness of the tunnel, especially when relatively small test sections are considered. Numerical simulation can also be used for designing tunnel modifications and innovative passive and active tunnel devices to minimize the impact of reflected shock waves on the test model. This is a cost-effective means of increasing the usable size of the LFSWT.

Ames-Moffett contact: E. Tu
(415) 604-4486
Headquarters program office: OAST

Data Base Expansion Using Estimation Methods

Richard L. LeBoeuf, Rabindra D. Mehta

Simultaneous multipoint velocity information is essential for a complete understanding of turbulent flow structure. Effective modification of the flow structure can often lead to the control of important phenomena such as lift, drag, noise, and mixing.

Hot-wire and laser Doppler anemometry are two popular flow-measurement devices. Unfortunately, simultaneous multipoint measurements are not easily obtained with either of these techniques, in spite of their rather large hardware costs. Another option is to use particle image velocimetry (PIV), which yields velocity measurements at several random field points in a plane. However, PIV has its own limitations, especially in high-Reynolds-number flows. An alternative approach, which has been explored recently in mixing-layer flows, is the estimation of simultaneous multipoint measurements using a single pair of hot-wire probes.

This estimation method entails modeling the velocity at one location with reference to the velocity at other locations in the flow. Choosing this relationship has an effect on the accuracy and on the ease and speed of evaluating the model constants and calculating the estimated field. The simplest choice is to model the velocity at one location as a linear combination of measured reference velocities. The estimation coefficients of this relationship are traditionally determined by minimizing the mean-square (MS) error of the estimate. However, this approach severely underestimates the energy of the fluctuations. A new scheme was devised whereby the correlation coefficient of the estimate with respect to the true signal at the estimation location is maximized. For one-point, two-component estimates, the result is independent of the estimated energy. Therefore, the energy of the estimates can be set equal to the measured data, and the correspondence between the estimate and its measured counterpart can be maximized. This scheme results in more realistic estimated velocity fluctuations than those obtained using the traditional MS estimation. The information required for the linear estimation coefficient determination are the reference/estimate and reference/reference two-point cross-correlation measurements, and the covariance of the velocity signals at the estimation locations. After the estimation coefficients have been found, it is a simple matter to determine the estimated field using a set of simultaneous measurements at the chosen reference locations.

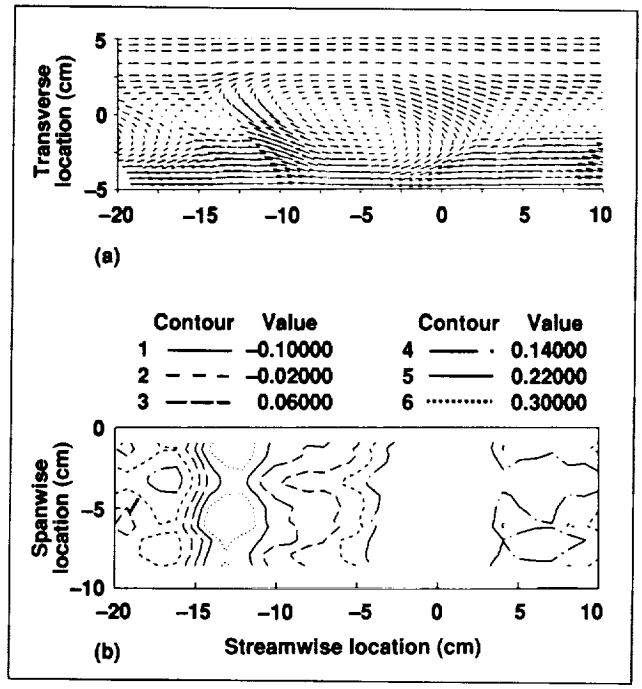

Fig. 1. Estimated velocity profiles. (a) Transverse profile of secondary velocity vectors; (b) spanwise profile of the transverse velocity.

Linear multipoint estimation was applied to a plane mixing layer in which the streamwise vorticity kinematics were of interest. Measurements using two cross-wire probes (and a single reference velocity) permitted the estimation of simultaneous transverse and spanwise velocity profiles in time, as shown in the figure. Part (a) of the figure shows 23 estimated secondary velocity vectors across the mixing layer. The presence of a spanwise vortex is clearly indicated near the center of the graph. Part (b) of the figure shows estimates, at 18 spanwise locations, of the

velocity normal to the mixing layer. In this graph, the streamwise vorticity produces a signature indicated by the sets of islands between streamwise locations −18 and −12 cm. The islands appear synchronously with the spanwise vortices identified in part (a). The lack of structure-to-structure spanwise motion of these signatures in longer records supports the conjecture that the streamwise vorticity has little spanwise meander relative to a fixed probe.

These techniques can be used in a variety of experiments designed to validate numerical simulations.

Ames-Moffett contact: R. LeBoeuf
(415) 604-6925
Headquarters program office: OAST

An Improved Two-Equation Turbulence Model

Florian Menter

One of the main obstacles in the development of reliable numerical methods for aerodynamic applications is the limited accuracy and limited generality of available turbulence and transition models. The most widely used turbulence models (Cebeci–Smith, Baldwin–Lomax, and k-epsilon models) overestimate the turbulent shear stress in adverse-pressure-gradient boundary layers. As a result, either the predicted location of separation of the flow from the surface of the body is too far downstream or the separation is missed altogether. Because the onset and size of the separation limit the effectiveness of the aerodynamic

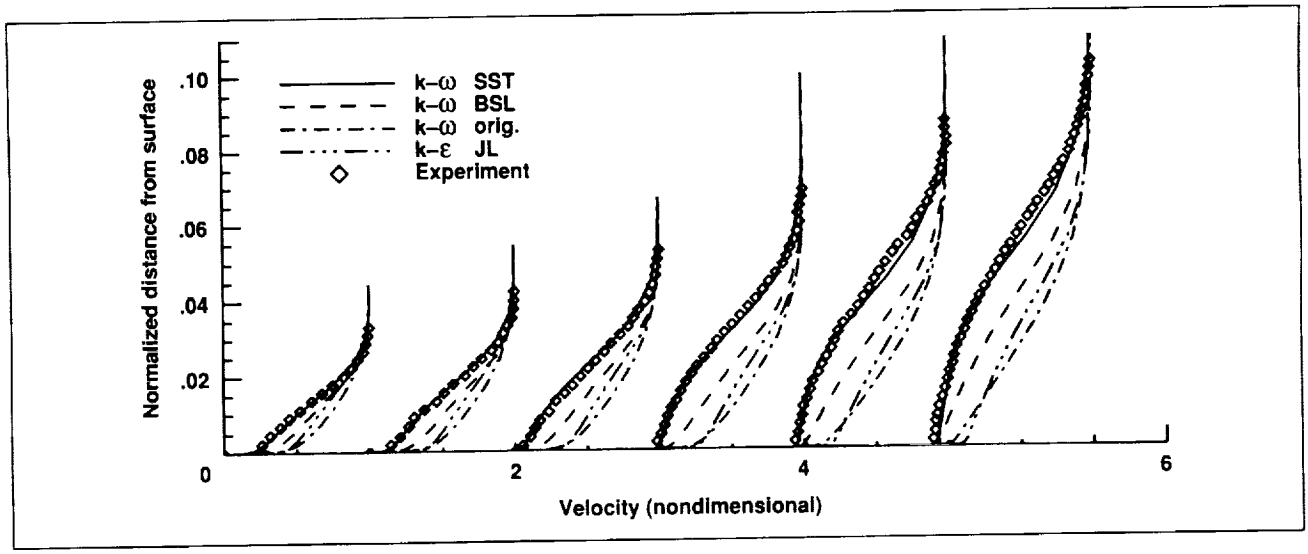

Fig. 1. Velocity profiles on the upper surface of a NACA 4412 airfoil at an angle of attack of 13.87 degrees for different streamwise stations.

device, computations based on the cited turbulence models may lead to overly optimistic predictions and are, therefore, of limited value in a design process.

Another turbulence model that is gaining popularity, known as the Johnson–King model, has provided a significant improvement in the accuracy of prediction of separated flows. A large number of airfoil and wing computations using the Johnson–King model have demonstrated the ability of this model to accurately predict flow separation and shock locations. However, the algebraic nature of the model necessitates the specification of an algebraic length scale, which can become ambiguous for flows around complex geometries and/or flows involving multiple length scales.

A new two-equation model has been designed that is based on the k-omega model of Wilcox but that has additional features that largely improve its performance. A zonal modeling approach is introduced that uses blending functions that can distinguish between boundary layers and free shear layers. This feature allows the use of different constants in the different flow regions. It also eliminates the free-stream dependency which was a major shortcoming of the original k-omega model. In regions of adverse pressure gradients, the model automatically introduces the assumption that the turbulent shear stress is proportional to the turbulent kinetic energy, and thereby accounts for the transport of the former in much the same way as the Johnson–King model does. The resulting model is called the shear-stress transport (SST) model and has been calibrated for a large number of research flows. The zonal modeling approach allows the accurate calibration of the model for a significantly larger number of flows than is usually possible with a single set of constants. The figure shows a comparison of velocity profiles computed with four different turbulence models for a NACA 4412 airfoil at a 13.87-degree angle of attack. The SST model clearly generates significantly better results than the other models, mainly because of its inherent sensitivity to adverse pressure gradients.

Ames-Moffett contact: F. Menter
(415) 604-6229
Headquarters program office: OAST

Navier–Stokes Computations for Oscillating Control Surfaces

Shigeru Obayashi, Guru P. Guruswamy

The general objective is to continue the development of the aeroelasticity computer code, ENSAERO, to complement expensive wind-tunnel and flight tests. In this work, the geometric capability of the code is extended to simulate oscillating control surfaces.

The code computes aeroelastic responses by simultaneously integrating the Reynolds-averaged Navier–Stokes equations and the modal structural equations of motion using aeroelastically adaptive dynamic grids. The computational grid moves with every time step to follow the deflection of the control surface. A zonal grid technique is used to handle large deflections of the control surfaces.

The resulting code has been applied to simulate transonic flows over rigid wings with oscillating control surfaces. The figure shows the instantaneous flow field and the comparison of computed unsteady pressures with experiment over a clipped delta wing. The wing has a leading-edge sweep angle of 50.4 degrees and a 6%-thick circular-arc airfoil section. At a Mach number of 0.9 and an angle of attack of 3 degrees, both a leading-edge vortex and a shock wave are present on the upper surface of the wing. The trailing-edge control surface oscillates at a frequency of 8 hertz and an amplitude of

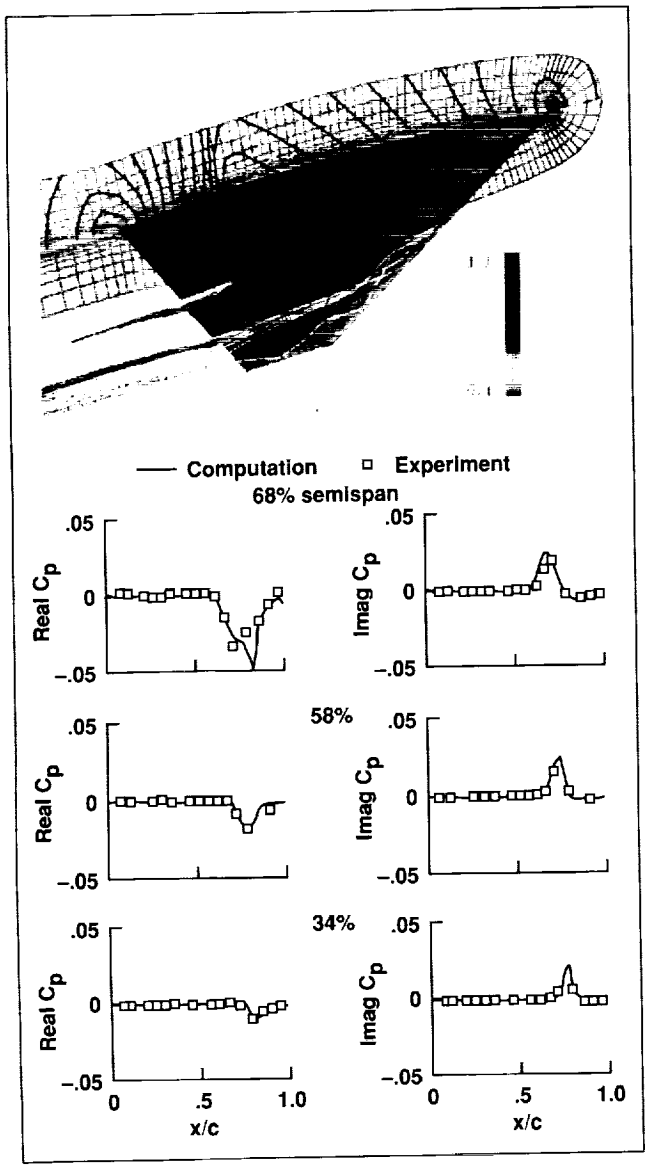

Fig. 1. Navier–Stokes computation on a clipped delta wing with oscillating control surface. Left: Pressure contours and instantaneous streamlines. Right: Comparison of unsteady pressures. (See color plate 10 in Appendix)

6.65 degrees. The response of the upper surface pressure to the control surface motion is represented in terms of the real and imaginary parts of the first component of the Fourier coefficients of the unsteady pressures at three spanwise sections. At the 68% section, the computed result shows a negative peak at the 80% chord in the real part. This corresponds to the control-surface hinge line. Peaks in other plots are due to the shock wave motion and coincide with experimental data.

The computed unsteady pressures successfully predict the response characteristics of the control surface motions measured in the experiments. This is the first time that the unsteady three-dimensional Navier–Stokes simulation has been performed with a moving grid for oscillating control surfaces.

The wing version of the code is available for distribution, and several requests from industry have been received. The code is currently being extended to wing-body control configurations. Implementation of active controls is also considered.

Ames-Moffett contact: G. Guruswamy
(415) 604-6329
Headquarters program office: OAST

Indication of Flow Direction by Liquid-Crystal Coatings

Daniel C. Reda, Joseph J. Muratore, Jr.

In aerodynamics research, valuable information can be gained from visualization of dynamic surface shear stress ("flow friction") patterns created by airflows over solid bodies (for example, flows over an airfoil). The liquid-crystal coating method is a diagnostic technique that can make such friction patterns visible in color with a response that is rapid (to one millisecond), continuous (over entire test surfaces), and reversible (results are valid for dynamically changing flow conditions that encompass both increasing and decreasing frictional forces).

The liquid-crystal phase of matter is a highly nonuniform, fluid-like state that exists between the solid and uniform-liquid phases of some organic compounds. Such materials can exhibit optical properties that are characteristic of solid, crystalline materials. If a thin film of liquid crystals is applied to a surface and the molecules within the coating are aligned by frictional forces into the required planar state, then this molecular structure selectively scatters incident white light as a spectrum of colors, each color being oriented at a discrete angle relative to the surface. The first figure shows this effect schematically. When a flow is introduced over the coated surface, the "reflected" spectrum rotates. Until now, color changes seen by a fixed observer were thought to be only a function of the strength (or magnitude) of the frictional force. Recent results obtained at NASA Ames have conclusively shown that this reflected spectrum rotates in opposite angular directions

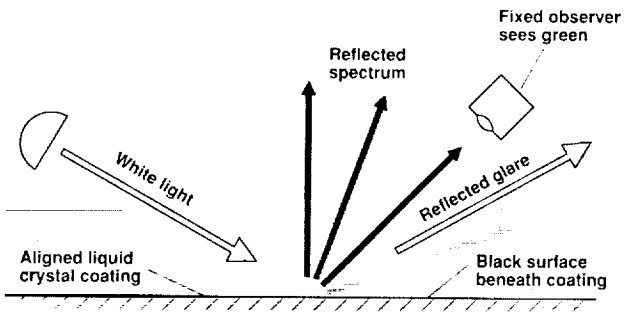

Fig. 1. Liquid-crystal reflected spectrum. (See color plate 11 in Appendix)

Fig. 2. Color patterns induced by equal-strength, opposite-direction tangential jets flowing side by side. (See color plate 12 in Appendix)

depending on the direction of the frictional force applied to the coating.

Results of an experiment conducted to illustrate this finding are shown in the second figure. Two equal-strength jets of air were blown tangentially across a planar test surface coated with aligned liquid crystals. The surface was obliquely illuminated by white light from a direction perpendicular to the plane of the jets.

Simultaneous images of the coating's color response were recorded from matching offset angles on either side of the light plane. Flow away from the observer was seen to be blue in both views, whereas flow toward the observer was a reddish brown. Opposite flow directions thus appeared as different colors to each observer.

With this new technique, dynamic flow reversals or flow divergences can now be made visible over an entire test surface at image-recording rates as high as 1000 frames/second. Extension of the technique to visualization of relatively small changes in surface shear stress direction appears feasible.

Ames-Moffett contact: D. Reda
(415) 604-6034
Headquarters program office: OAST

Computational Study of Vortex-Induced Tail Buffet

Yehia Rizk, Guru P. Guruswamy, Kenneth Gee

The objective of this research is to use computational fluid dynamics (CFD) to provide better understanding of the vortex-induced tail buffet phenomenon. Tail buffet has been observed on twin-tail aircraft like the F-18, which rely on vortex lift in the high-angle-of-attack flow regime.

CFD was used to simulate the unsteady flow field around the F-18 aircraft, including the flow about a flexible vertical tail. A weak coupling between the aerodynamics and the structures was used. A time-accurate Navier–Stokes solver combined with a generalized structured-grid zonal scheme was used for the aerodynamics part. A time history of the computed airloads for the baseline F-18 and the modified F-18 (with leading-edge extension (LEX) fence) is shown in the first figure. These airloads were used as a forcing function to compute the structural response of the flexible vertical tail using modal analysis. Time-accurate computations at an angle of attack of 30 degrees show that the buffet frequency is proportional to the airspeed (second figure). At flight speed, tail buffet is observed because the airloads frequency is very close to the tail's first natural frequency of bending. Computations also show that installing the LEX fence introduces an unsteady vortex interaction that results in reduction of the airloads frequency compared to the tail natural frequency.

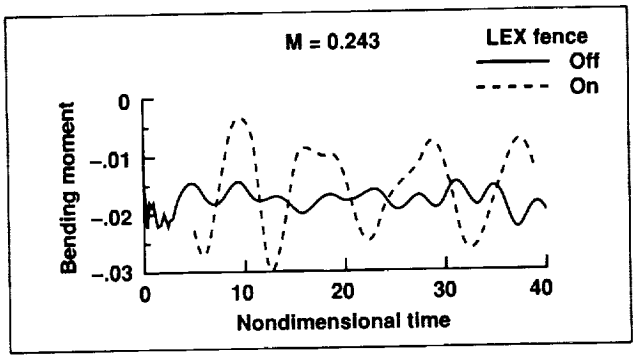

Fig. 1. Effect of LEX fence on vertical-tail airload fluctuations.

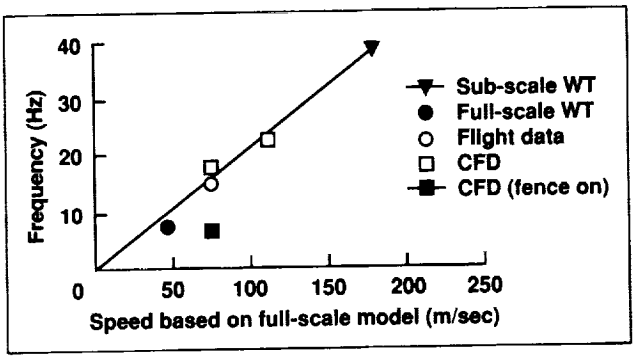

Fig. 2. Comparison between computed and measured buffet frequency.

A better understanding from CFD and wind tunnel and flight testing of the vortex/tail interaction should lead to more effective means of controlling or alleviating the buffet and preventing premature tail structural fatigue for current and future high-performance aircraft.

Ames-Moffett contact: Y. Rizk
(415) 604-4466
Headquarters program office: OAST

Numerical Simulation of a Self-Similar Turbulent Mixing Layer

Michael M. Rogers, Robert D. Moser

When two fluid streams of different velocity come into contact, a "mixing layer" is formed. Such layers are efficient at mixing fluid from the two streams and are frequently employed in situations where molecular mixing is required for a chemical reaction.

Turbulent mixing layers evolve "self-similarly" once they reach a developed state; mean profiles at different points in the layer evolution will collapse when scaled by the appropriate length and velocity scales. For the plane (two-dimensional in the mean) mixing layer examined here, the appropriate scales are the constant velocity difference across the layer and the linearly growing layer thickness.

Experimental mixing layers typically result when two streams come into contact after leaving the tip of a "splitter plate." If the boundary layers on the splitter plate are laminar, then a transition to turbulence occurs somewhere downstream and will eventually be followed by self-similar growth. Alternatively, the splitter-plate boundary layers may be turbulent, again resulting in self-similar layer growth somewhere downstream. We have generated a direct numerical simulation (resolving all scales of turbulent motion) of such a turbulent plane mixing layer begun from turbulent boundary layers. The initial boundary layer turbulence was obtained from previous direct numerical simulations generated by Spalart.

Previous numerical simulations of three-dimensional turbulent mixing layers have not been able to achieve self-similarity because of either insufficiently high Reynolds numbers or an insufficient sample of eddies in the computational domain. We have overcome both of these limitations by considering visual-layer-thickness Reynolds numbers of up to 18,500 in a very large streamwise domain. Note that experimental mixing layers begun from laminar boundary layers have typically completed their transition to turbulence before the Reynolds number reaches this value. The computation requires up to $512 \times 210 \times 192$ modes to accurately resolve this flow and uses 1100 hours of Cray Y-MP time.

After going through a transitional period in which the layer evolves from turbulence with boundary layer characteristics to turbulence that is typical of mixing

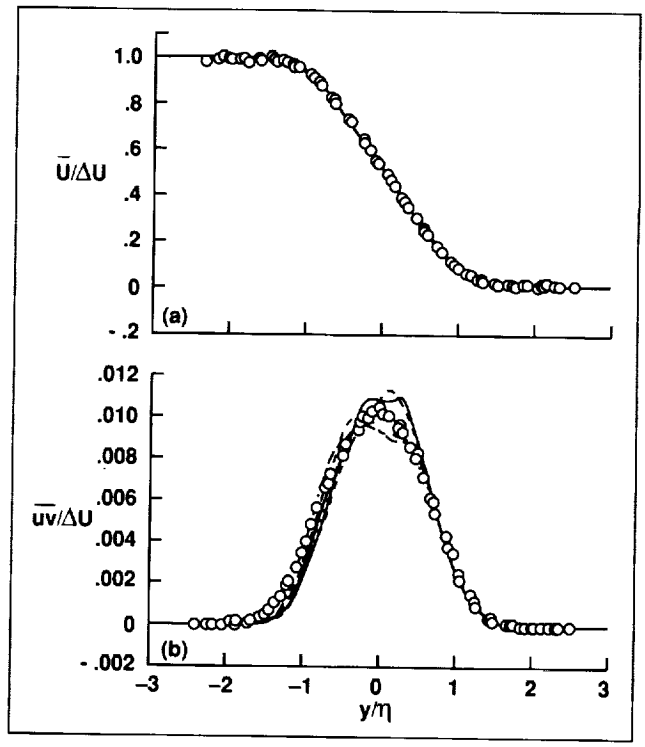

Fig. 1. Scaled cross-stream average profiles of (a) mean velocity and (b) Reynolds shear stress at five stations in the self-similar region, compared with the experimental data of Bell and Mehta at Ames (symbols).

layers, a self-similar period is indeed obtained. During this period, integrated statistics scale as they should for a self-similar layer, and scaled mean velocity, Reynolds stress, and root mean square vorticity profiles collapse. The layer grows linearly at a rate that is in good agreement with experimental values. The scaled mean velocity profiles and Reynolds shear stress profiles at five stations are shown in the first figure, along with experimental data obtained by Bell and Mehta in a plane mixing layer begun from turbulent boundary layers. The agreement between computation and experiment is good, as is the collapse of the data from the five stations. Root-mean-square vorticity profiles also exhibit good collapse at the five stations. We are in the process of comparing

Fig. 2. Spanwise vorticity contours (solid = negative, dotted = positive) at a point in the self-similar region. The free-stream flow direction is to the right on the top and to the left on the bottom.

these profiles with experimental profiles obtained by Wallace and coworkers at the University of Maryland using a "vorticity" probe.

The structure of the vorticity field in the self-similar layer is complex; it contains many small-scale eddies of both signs, of all three vorticity components. A contour plot of the spanwise vorticity at a point in the self-similar period is shown in the second figure. The flow appears much more complicated, with less large-scale "coherent structure" than many researchers have thought.

In addition to simulating the hydrodynamic flow field, the concentration of a passive chemical species (one that leaves the velocity field unaffected) was tracked in order to directly address mixing in the flow. The resulting concentration fields are used for flow visualization, for testing turbulent flux models, and for modeling simple chemical reactions.

Ames-Moffett contact: M. Rogers
(415) 604-4732
Headquarters program office: OAST

Faster Grid Generation

Reese L. Sorenson, Karen M. McCann

Computational fluid dynamics (CFD) has been accepted as a useful tool for certain parts of the aircraft design process, but a major impediment to its increased application is the time required to generate computational grids about real aerodynamic shapes. Grids are collections of points (typically illustrated as the intersections of lines connecting them) on and about an aircraft (see figure). The CFD simulation gives numerical values for quantities that describe the flow (velocity, pressure, temperature, etc.) at grid points. The locations of grid points, i.e., the design of the grid, have a profound influence on the speed and accuracy of the CFD simulation. However, the generation of a good grid about a real airplane can take months, and for many design projects this is unacceptable.

This research has produced three computer programs that greatly accelerate the process of grid generation. The first is GRAPEVINE ("grids about anything by Poisson's equation in a visually interactive networking environment"). A proven batch-mode structured elliptic grid generator has been improved by the creation of a modern graphical user interface (GUI) running on a workstation (illustrated in the figure). The user watches the grid as it is iteratively generated. The GUI allows the user to better understand the grid-generation process and to control it more efficiently.

Small grids are created entirely on the workstation. For large grids, which require more computing power than is available on most workstations,

GRAPEVINE allows a supercomputer to be connected to the GUI. Large grids are then generated with the supercomputer operating as a "slave," with the GUI on the workstation as the "master." The ability to watch the grid as it converges is retained.

GRAPEVINE has accelerated the process of grid generation by as much as a factor of ten. A typical case that illustrates the acceleration is the generation of an H-H-type grid about an isolated wing. This exercise formerly required a week; with GRAPEVINE, the generation of the grid required 4 hours. This research, in addition to creating the GUI, has improved the numerical method for elliptic grid generation, making the solution process more stable and improving the quality of the resultant grids. Two other programs have been produced, both of which also have modern GUIs. The first, 3DPREP, assists the user in preparing input data for GRAPEVINE. The other is 3DECANT, a general-purpose grid display program.

Ames-Moffett contact: R. Sorenson
(415) 604-4471
Headquarters program office: OAST

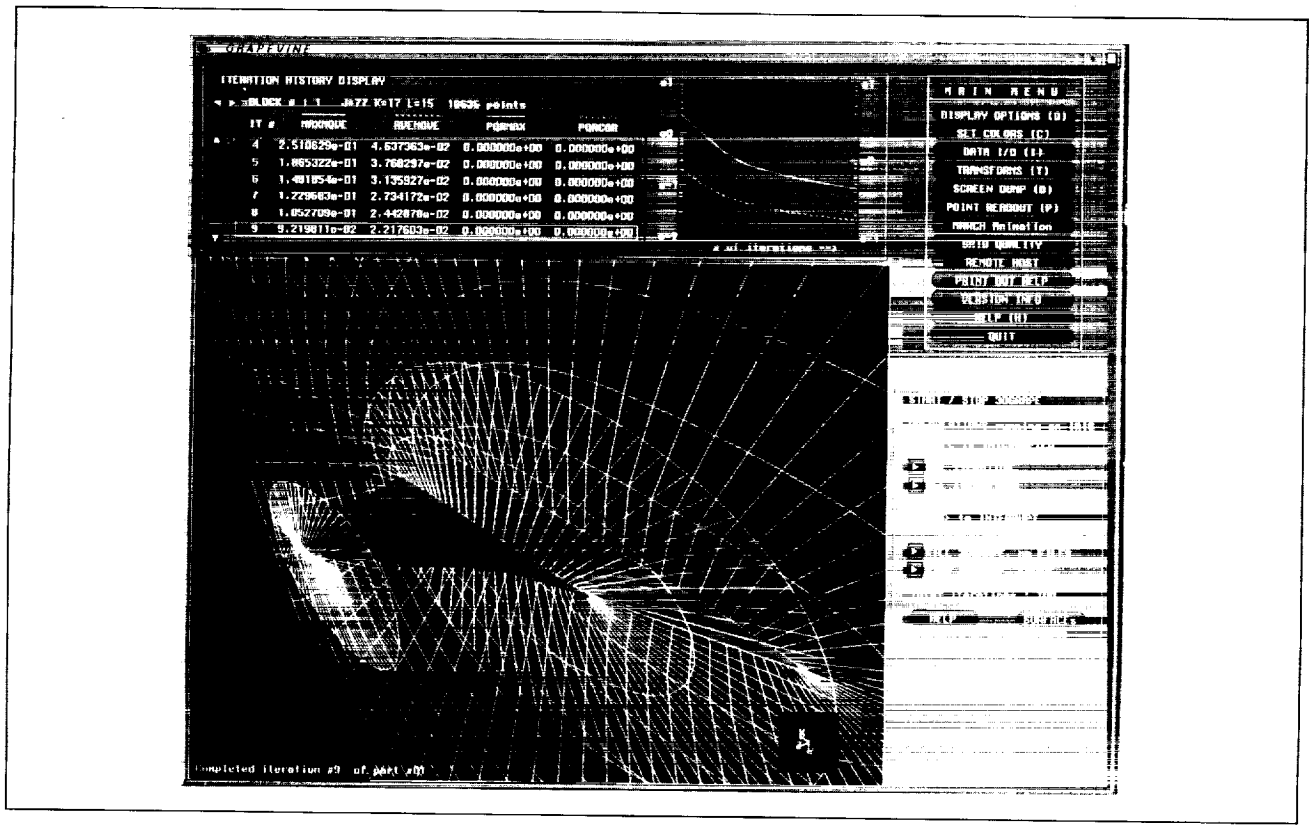

Fig. 1. The program GRAPEVINE generating a grid about a wing.

Direct Numerical Simulation of Turbulent Combustion

Arnaud Trouvé, Luc Vervisch, Feng Gao, Jean-Michel Samaniego

Turbulent combustion is encountered in many practical systems such as jet engine afterburners, ramjets, rocket motors, industrial burners, power plants, and internal combustion engines. Typical practical problems include inefficiency of the combustion system, the growth of combustion instabilities, and the production of pollutants. Turbulent combustion is also a challenging problem for basic research in areas in which the fluid mechanics and the chemistry are strongly coupled. Our objectives are to use direct numerical simulation methods to increase our basic understanding of flame–turbulence interactions and to test and develop models for engineering calculations of turbulent combustion.

Direct numerical simulation uses numerical methods with high resolution both in space and time that fully resolve all the relevant scales of the turbulent flow field. When it is applied to turbulent combustion, direct numerical simulation is limited by computational expense to simplified reaction schemes. Instead of a complete analysis of the combustion process, a reduced, finite-rate chemistry model is required. In our work, the chemical model is a single- or two-step finite-rate chemical reaction. The numerical codes are three-dimensional, high-order finite difference codes developed at the NASA Ames/Stanford University Center for Turbulence Research. An important feature of these codes is that they can treat nonperiodic domains. The codes fully account for compressibility effects and thermal expansion of the reacting flow that results from heat release. The computations are performed on Cray Y-MPs at NASA Ames Research Center.

Simulations of premixed or nonpremixed combustion have been used in the following ways: (1) in qualitative studies aimed at describing the topology of the turbulent flames. The main question here is to determine where the reaction takes place, i.e., in fronts, pockets, or large volumes. Our studies indicate that in practical situations, the flame is a front; (2) in qualitative or quantitative studies aimed at classifying the different modes of flame–flow coupling according to their relative importance in the overall picture. For instance, a typical question is whether the effects of molecular transport can be neglected in a turbulent reaction zone. Simulations of Lewis number effects show that molecular transport plays a dominant role in the determination of the mean turbulent reaction rate, and cannot be neglected; and (3) in quantitative studies aimed at providing detailed comparisons with model predictions. The following are typical questions: Are the model assumptions soundly based, and what is their domain of validity? Are the model predictions accurate? If they are not accurate, where do the shortcomings lie? Can the current formulations be improved, and how? Our studies indicate, for example, that current flamelet models are soundly based but improvements are required to account for Lewis number effects.

The recent development of both efficient numerical methods and new, nonintrusive experimental techniques has led to significant progress over the last five years in understanding and modeling turbulent combustion. Until last year, however, direct numerical simulation of turbulent combustion was, like most experimental investigations, limited to qualitative studies, and direct quantitative comparisons with models were not possible. Direct numerical simulation of turbulent combustion has now made possible direct, detailed comparisons with models. These latest developments are likely to ensure an increasingly important role for direct numerical simulation in the validation, development, and production of models for engineering calculations.

Ames-Moffett contact: P. Moin
(415) 604-5127
Headquarters program office: OAST

Effect of Canard Vertical Position on Wing-Body Aerodynamics

Eugene L. Tu

The objective of the current work is to validate computational methods, improve understanding of complex canard–wing-body aerodynamics, and study the effects of canard vertical position by accurately simulating the flow field about a close-coupled canard–wing-body configuration. Results from this study validate the capability of using computational fluid dynamics (CFD) to improve the aerodynamic performance of canard-configured aircraft.

Using the transonic Navier–Stokes (TNS) flow solver, the Reynolds-averaged thin-layer Navier–Stokes equations are solved for the flow about a canard–wing-body configuration with various canard vertical positions. A patched multizoned grid scheme is used that allows for mismatched zonal interfacing between the close-coupled canard and wing regions. The effects of turbulence are modeled using the Baldwin–Lomax algebraic eddy-viscosity model.

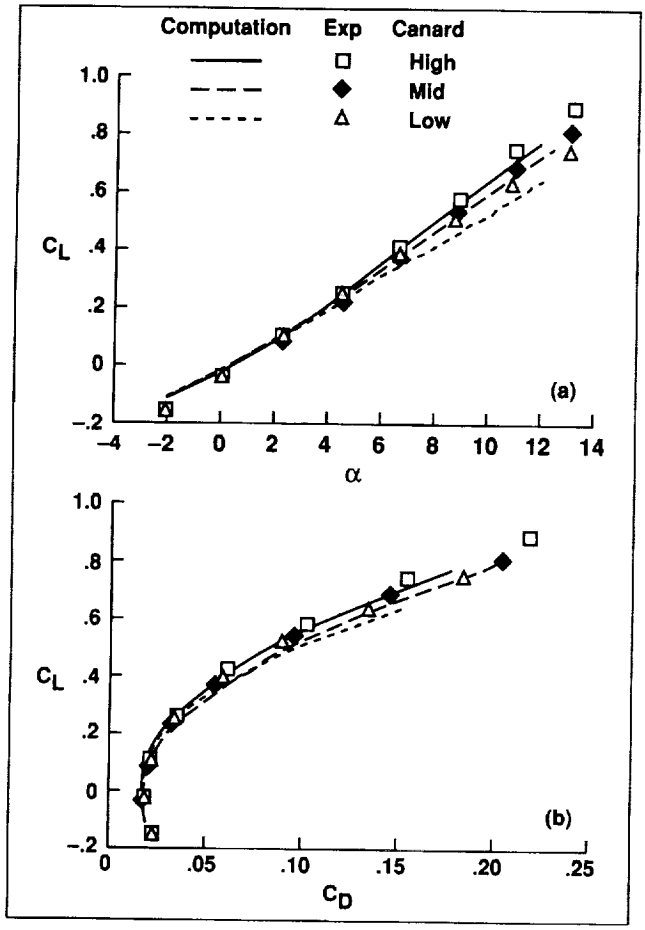

Fig. 1. Comparison of computed and experimental forces for the high-, mid-, and low-canard configurations. (a) Lift; (b) drag.

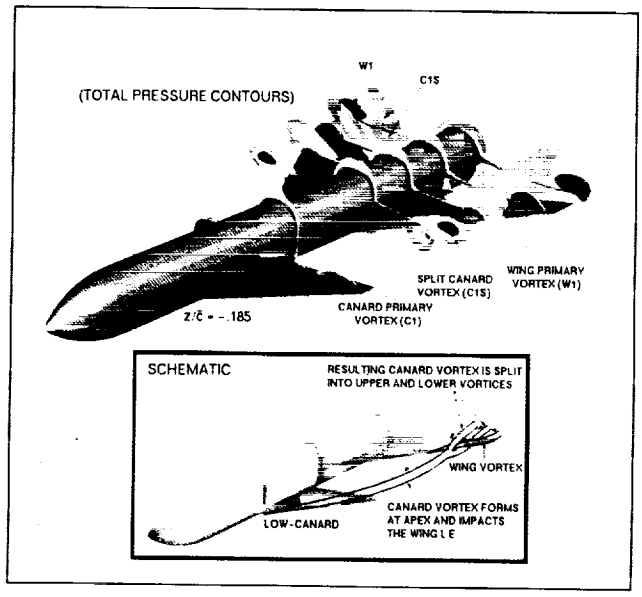

Fig. 2. Perspective view of crossflow total pressure contours and schematic of canard/wing vortex trajectories for the low-canard configuration.

Computations are made at a transonic Mach number of 0.90, angles of attack from –2 to 12 degrees, a Reynolds number based on mean aerodynamic chord of 1.52 million, and canard vertical positions of –0.185, 0.0 and +0.185 (low-, mid-, and high-canard configuration). The first figure illustrates the comparison of computed lift and drag curves with experimental results. Both computed and experimental lift curves show significant differences in lift coefficients between the low-, mid-, and high-canard configurations at higher angles of attack. As angle of attack is increased, the low-canard results clearly indicate unfavorable canard–wing interaction. Computed and experimental drag polars also indicate unfavorable effects of the low canard. The characteristics of the low-canard case are further illustrated in the second figure, which shows the cross-flow visualization of

total pressure contours and a schematic of the vortex–wing interaction. The cross-flow total pressure contours show that at the given flow conditions, the low-canard vortex impacts the wing leading edge and is split into two (upper and lower) vortices. The split canard vortex that passes under the wing can induce an undesirable low-pressure region on the wing lower surface. Further complicating the flow field is the wing vortex that forms on the upper surface of the outboard portion of the wing. These results are used to explain the significant effects that subtle differences in canard vertical positioning can exhibit on the aerodynamic performance of the configuration.

The accurate prediction of the effects of canard positioning on canard–wing-body aerodynamics is critical to the design and optimization of canard-configured aircraft. Analysis has resulted in a better understanding of a complex flow field that was the source of experimentally observed aerodynamic performance characteristics.

Ames-Moffett contact: E. Tu
(415) 604-4486
Headquarters program office: OAST

Skin-Friction Measurements in a Three-Dimensional Supersonic Separated Flow

Jeffrey K. Wideman, James L. Brown

A study has been conducted of a three-dimensional, supersonic shock-wave/turbulent boundary layer interaction (SW/BLI) in order to obtain accurate experimental data for turbulence and code validation. The experimental model consisted of a sting-supported cylinder upon which a turbulent boundary layer developed and encountered a conical flare that was offset 0.5 inch from the cylinder centerline. The experiment was performed at a Mach number of 2.89 and a Reynolds number of 18 million/meter in the High Reynolds Channel I facility at Ames. The highlight of the study was the acquisition of skin friction data by an oil-flow laser interferometer. Surface pressure measurements were obtained in 15-degree intervals around the cylinder and flare. Additional measurements included surface oil flow, schlieren, and laser light sheet illumination which were used to document the flow topology.

The laser skin-friction interferometry technique measures the rate of change in thickness of a flowing oil film on the model surface. The surface shear stress can then be deduced from this information. This technique is advantageous compared to other skin-friction measurement techniques for application in the flow field studied because it is nonintrusive and allows the taking of measurements in shear- and pressure-gradient flows.

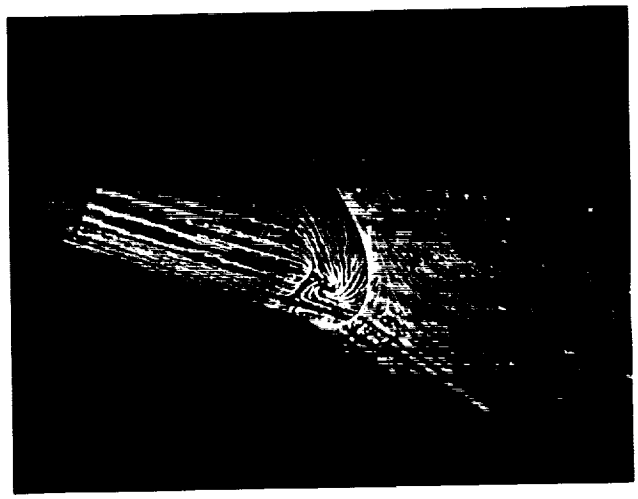

Fig. 1. Oil-flow topology near the bottom line of symmetry of the cylinder–flare model.

The undisturbed turbulent boundary layer on the cylinder initially encounters the influence of the shock wave–boundary layer interaction along the top line of symmetry, and separates. The three-dimensional separated zone proceeds along the cylinder–flare

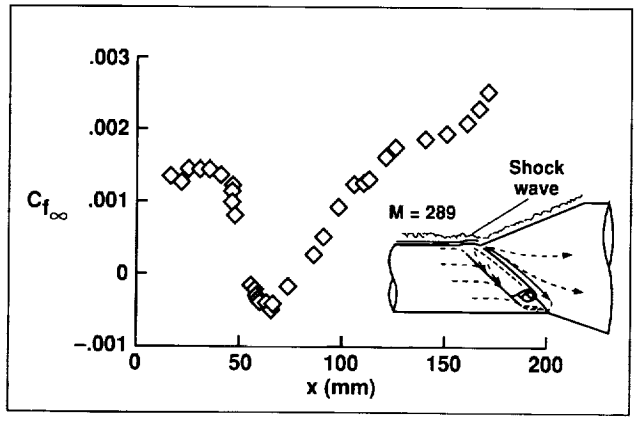

Fig. 2. Skin friction results along bottom line of symmetry.

junction toward the bottom of the model. A view from beneath the model, shown in the first figure, reveals the flow topology near the bottom line of symmetry. Some obvious aspects of the topology are the upstream separation line, which is perpendicular to the free-stream flow direction, and the focus indicating a vortical structure of fluid leaving the surface.

The skin friction data collected along the bottom line of symmetry are shown in the second figure. Upstream, the skin friction decreased quickly as the flow showed the initial effects of the interaction. Measurements in the separated region were repeatable. The extent of the separated region is evidenced in the figure by negative values for the skin friction. The flow reattaches on the flare, and the skin friction reverts to positive values. The magnitude of the skin friction continues to increase along the length of the flare to values that are much larger than the undisturbed boundary layer values upstream of the interaction.

Ames-Moffett contact: J. Wideman
(415) 604-6192
Headquarters program office: OAST

Unstructured Grid Generation

N. Lyn Wiltberger, Timothy J. Barth

The objective of this research is to develop a unique unstructured grid-generation and adaptation algorithm for complex geometries in two dimensions and for geometric surfaces in three dimensions, and to create a flexible grid-generation algorithm in which the user can construct different triangulations by specifying various grid quality measures.

An incremental triangulation algorithm called HARLEY that is based on point insertion and local edge swapping is used. One of the advantages of this method over preexisting triangulation methods such as Watson's algorithm is that edge swapping can be used to optimize user-specified grid quality measures. For example, local edge swapping can be used to minimize the maximum cell angle (a MinMax triangulation) or to maximize the minimum cell angle (a MaxMin or Delaunay triangulation). In addition, Steiner triangulations can be produced by inserting new sites at triangle circumcenters followed by edge swapping according to the MaxMin criteria. Incremental insertion of sites also provides flexibility in choosing cell refinement criteria. For instance, by choosing a refinement criterion based on solution error, the method can be used for solution-adaptive grid generation. The algorithm has been extended to three-dimensional surfaces by locally projecting three-dimensional surface patches into two-dimensional space for purposes of the surface triangulation. The implementation of a dynamic heap structure coupled with recursive programming results in a code with modest run times on an engineering workstation.

The edge-swapping algorithm provides a coherent basis for unstructured grid generation and adaptation about complex geometries by utilizing various user-defined grid quality measures. The adaptation feature of the algorithm is particularly advantageous for three-dimensional surface triangulation, because adaptive

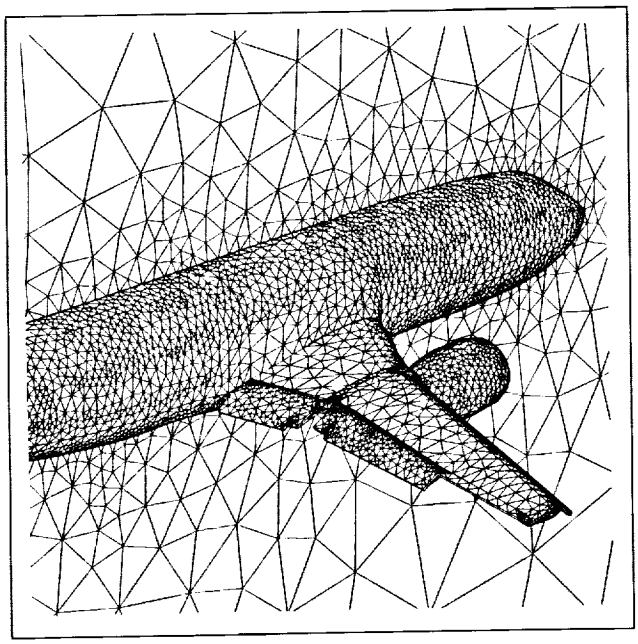

Fig. 1. Steiner surface triangulation of Boeing 737 with flaps deployed.

surface clustering can be performed according to surface characteristics. In contrast, the lack of direct control of surface clustering is a weakness of the advancing-front method for surface grid generation. Independently, the data structure used in the edge-swapping algorithm suggests a new procedure for multigrid acceleration of current flow solvers on unstructured grids. The figure shows a Steiner surface triangulation of a Boeing 737 with its flaps deployed.

The code is currently being made available for distribution, and several requests from industry and academia have been received. The creation of a theory and application manual is in progress and will be published as a NASA technical report.

Ames-Moffett contact: N. Wiltberger
(415) 604-4474
Headquarters program office: OAST

Analytic Solutions for Computational Electromagnetics

Maurice Yarrow

The objective of this research is to develop an extensive analytical data base of electromagnetic scattering from generic objects of pulsed plane waveforms and to use these data for the testing and validation of a high-order-accurate, explicit finite-difference method that solves Maxwell's equations in the time domain.

Generic shapes are subjected to pulsed plane waves of arbitrary shape. The resulting scattered electromagnetic fields are determined analytically by superposition of the scattered fields from monochromatic plane waves. These fields are then computed efficiently at field locations for which numerically determined electromagnetic fields are required. Of particular interest are the pulsed waveform shapes typically used by radar systems. The results can be used to validate the accuracy of finite-difference time-domain Maxwell equation solvers. A two-dimensional solver that is second- and fourth-order accurate in space and fourth-order accurate in time is examined. Dielectric media properties are modeled by a ramping technique that simplifies the associated gridding of body shapes. The attributes of the ramping technique are evaluated by comparison with the analytic solutions.

We have found, first, that using analytic solutions for the scattering of pulsed plane waveforms from generic shapes is immensely useful in the development and validation of electromagnetic numerical methods. Analytically generated data can be used in a variety of ways for comparison with numerical results. Particularly useful is a spectral approach, in which the character of propagated waveforms is seen in terms of the Fourier transform of the waveform, and information about code performance is elicited on a frequency by frequency basis.

Second, we have found that dielectric media properties may be imposed by a media ramping technique. This approach avoids the difficulties associated with the use of body-fitted coordinates and requires no special algorithm to account for media-interface jump discontinuity conditions.

The results will be extended to additional generic shapes for a variety of pulse waveforms. These will be used extensively in the ongoing Maxwell-equation-solver development efforts.

Ames-Moffett contact: M. Yarrow
(415) 604-5708
Headquarters program office: OAST

Concurrent Hybrid Computational Fluid Dynamics

Domingo A. Tavella, M. Jahed Djomehri, Katherine K. Kislitzin

Structured grids can resolve boundary layers well, but are relatively rigid. Unstructured approaches are flexible, but face difficulties in regions with boundary layers. The goal of this study is to create a methodology that exploits the relative advantages of each approach by combining them as independent computational processes that can be executed concurrently on different platforms, communicating through a computer network.

An implicit structured Navier–Stokes solver is applied in a thin region near the surface of the configuration, and an explicit unstructured Euler solver is applied in the exterior of the flow domain. The two solvers are independent processes running on separate supercomputers. They solve a coupled viscous–inviscid flow field by communicating data across the network that connects the machines. The implementation of the project will be done in two stages. In the first stage, the methodology is developed with two structured Navier–Stokes and Euler codes; in the second stage, the structured Euler code is replaced by an unstructured code.

The first stage was concluded successfully. The boundary layer regions were resolved with a structured Navier–Stokes code, and the outer field was computed with a structured Euler solver. The methodology was applied to a missile at an angle of attack of 30 degrees. The heterogeneous computation was achieved by running one of the solvers on the Cray-2 and the other on the Cray Y-MP. The results were compared with full Navier–Stokes computations run on a single machine. Data communication represents only a small fraction of the time spent in computation.

This work demonstrates that complex flow fields can be resolved by the concurrent heterogeneous solution of Navier–Stokes and Euler codes. By exploiting the strongest features of each solver in the appropriate flow regions, the hybrid approach is both flexible and robust.

The second phase of the project is in progress.

Ames-Moffett contact: D. Tavella
(415) 604-4344
Headquarters program office: OAST

An MIMD Implementation of a Parallel Euler Solver for Unstructured Grids

V. Venkatakrishnan, Horst D. Simon, Timothy J. Barth

Unstructured grids are used increasingly often in the area of computational fluid dynamics because they offer flexibility in handling complex geometries and in adapting to flow features. The goal of this study is to assess the performance of an explicit, unstructured, finite-volume solver on a multiple-instruction, multiple-data-stream (MIMD) computer.

The explicit finite-volume solver solves the Euler equations by using an upwind discretization and a multistage Runge–Kutta time integration procedure. The unstructured grid is statically partitioned and distributed across multiple processors. The processors communicate through shared interior boundary vertices.

The unstructured grid solver has been successfully implemented on the Intel iPSC/860 parallel computer. The code has been optimized to yield good performance.

Several partitioning strategies have been investigated. It has been found that recursive bisection using the spectral partitioning technique gives the best

performance. Efficient data structures have been derived to handle communication in a general manner. A scheduling algorithm has also been derived and implemented for efficient communication. The resulting code is quite efficient; for a problem with 15,606 vertices, we achieve 306 megaflops on 128 processors (about twice the speed of a Cray Y-MP/1). If the problem were larger, we would achieve three to four times the speed of a Cray Y-MP/1.

This work demonstrates that unstructured grid codes can perform well on MIMD computers. Implicit schemes and extensions to three-dimensional applications are planned.

Ames-Moffett contact: V. Venkatakrishnan
(415) 604-3960
Headquarters program office: OAST

Implementation of ENSAERO on the iPSC/860

Sisira Weeratunga, Eddy Promono

The goal of this work is the implementation of an existing multidisciplinary application on the Intel parallel computer. The code ENSAERO by G. Guruswamy of the Computational Aerosciences Branch was selected for the implementation. This code couples a computational fluid dynamics (CFD) code with a modal structures code in order to study aeroelasticity. ENSAERO has been extensively tested on the Cray Y-MP and will be heavily used in high-performance computing and communications/ Computational Aerosciences efforts.

First, two separate codes to do the CFD calculations and the modal analysis were developed and tested on the Intel. The interaction between the CFD and modal codes was handled by special software developed by E. Barszcz of the Numerical Aerodynamic Simulation Systems Applied Research Branch which allows communication between groups of Intel processors. At present, 32 nodes are used for the CFD and one node is used for the modal analysis. The combined applications were tested with static (infinite damping) and dynamic (no damping) cases for a delta wing.

This is the first multidisciplinary computational aerodynamic application to run on the Intel at Ames Research Center.

Guruswamy's group is using this code on the Intel to determine the flutter envelope of a wing. Promono will replace the structure modal analysis code with a finite-element version that will use multiple computer nodes on the Intel. In addition, algorithms for concurrent coupling of the structure and fluid codes will be studied. Long-term research will examine issues of grid deformation that results from the flexing of elastic structures.

Ames-Moffett contact: S. Weeratunga
(415) 604-3963
Headquarters program office: OAST

Transient Flow Simulations in a Shock Tube

Jean-Luc Cambier, Susan Polsky

The Ames Electric Arc Shock Tube (EAST) Facility provides a high-enthalpy flow for testing components of hypersonic aerospace vehicles. In this facility, gas at high pressure in a reservoir (the driver tube) is put in contact with a test gas in another reservoir (the driven tube), by opening a diaphragm between the two reservoirs. A strong shock followed by a contact discontinuity (CD)—the interface between the "driver" gas and "driven" gas—propagates rapidly down the tube. At the end of the driven tube, the shock is reflected and heats the test gas to a high temperature. This superheated test gas then expands into the nozzle and test chamber. The reflected shock eventually interacts with the incoming CD and, in the ideal case, comes to rest. This creates a reservoir of test gas at steady, uniform pressure and temperature. In reality, deviations from the ideal condition can be expected and reflected shock waves that are generated during the shock–CD interaction may affect the steadiness of the reservoir pressure. Shock–boundary layer interactions may have similar effects, and may cause an early contamination of the reservoir region by the driver gas, thereby reducing the available test time. Insight into these phenomena can be obtained with the help of computational fluid dynamics, which allows us to examine the effect of several parameters (nozzle shape, shock velocity, initial pressure, etc.) on the flow fields. By comparing the computed flow variables with experimental measurements, we can also explain some of the observed experimental features. Finally, the numerical simulations can be used to verify some design modifications.

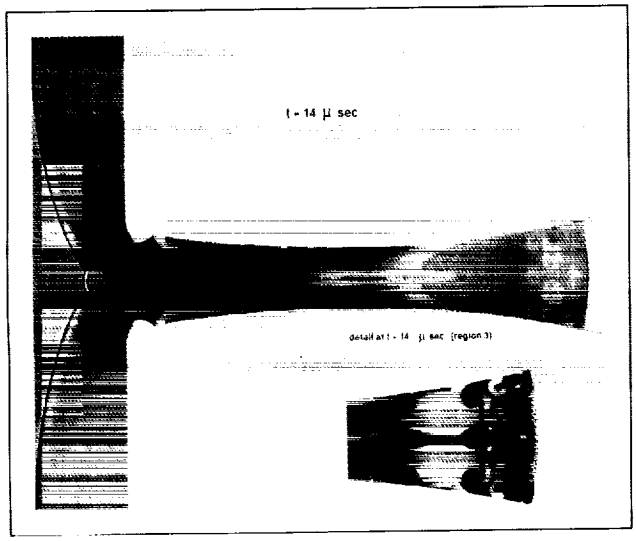

Fig. 1. Logarithmic density contours of the transient flow field in the driven tube and nozzle section of EAST facility, at 14 microseconds after the shock reflection at the end of the driven tube.

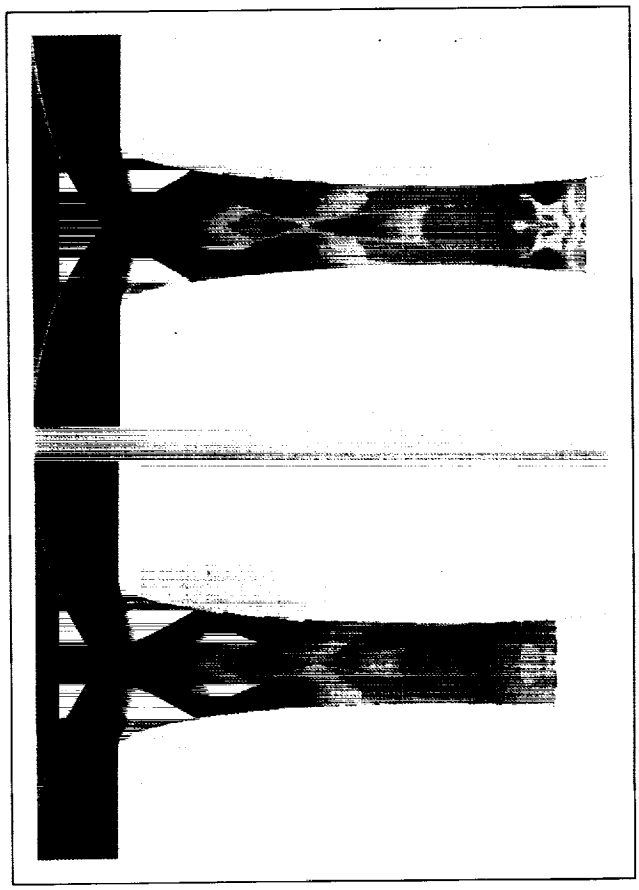

Fig. 2. Logarithmic density contours at an earlier time (comparison between inviscid calculation (top) and viscous calculation (bottom).

In the first figure, we show the shock structure at the end of the driven tube and the beginning of the supersonic nozzle. The reflected shock is on the left,

and the main shock is propagating down the nozzle, on the right-hand side. The contours of the density field (in logarithm scale) are taken at 14 microseconds after the arrival of the shock at the end of the driven tube. The multiple shock reflections on the sides of the nozzle are resolved to high accuracy. In order to compute this transient flow, we have used a technique of multiple grids, with subscale, moving grids. In this case, a grid of very high resolution is superimposed on the background grid in the nozzle region. This high-resolution grid is allowed to slide along with the main shock structure, in order to keep a high level of spatial accuracy in that region. The details of the shock structure are well reproduced in that grid (region 3 at the bottom of the figure). In particular, the roll-up of the interface (Richtmyer–Meshkov instability) is clearly evident.

This calculation was performed by solving the inviscid equations of motion coupled with the chemical kinetics. Since the main shock propagates into a low-density flow, the viscous effects are expected to be important near the shock. This is demonstrated in the second figure, in which the inviscid density contours are shown in the top portion of the figure and the viscous results are shown in the lower portion. The instabilities at the interface have disappeared, and the main shock has been slowed down.

Ames-Moffett contact: G. Deiwert
(415) 604-6198
Headquarters program office: OAST

Direct Particle Simulation of Magellan Aerobraking

Brian L. Haas

A direct Monte Carlo particle method was used to simulate aerobraking of the Magellan spacecraft through the outer reaches of the Venus atmosphere. The spacecraft has been mapping the surface of Venus from a highly elliptic orbit since September 1990. Mission planners at NASA's Jet Propulsion Laboratory (JPL) would like to circularize the orbit to improve mapping but the maneuver cannot be performed through thruster activity alone because of the limited amount of propellant remaining on board. The orbital maneuver could be achieved, however, through a series of about 1,600 grazing passes through the planet's atmosphere. These maneuvers would provide valuable data on atmospheric entry of satellite spacecraft.

The Magellan satellite was not designed for aerobraking. Two issues of great concern to mission planners are (1) the aerodynamic heating on the fragile solar panels and (2) the stability of the spacecraft when it enters at off-design attitudes. Techniques that are normally used to analyze spacecraft dynamics at extremely high altitudes are based on the assumption that the flow about the vehicle is "free molecular," which means that the gas molecules may collide with the spacecraft but not with one another. This assumption does not apply, however, at lower altitudes where molecules do collide significantly as a result of increased gas density. The nominal altitude proposed for Magellan aerobraking is 140 kilometers, where the flow is not entirely free molecular but remains sufficiently rarefied that continuum flow calculations, which are based on the Navier–Stokes equations, do not apply either. The only computational technique suited to this flow is the direct Monte Carlo particle method in which the motion and interaction of thousands of particles are used to simulate gas dynamics on a computer.

As depicted in the first figure, the particles flow through a simulated wind tunnel and around the spacecraft, the surfaces of which are modeled by planar facets. The temperature of each surface facet is assessed directly in the simulation by recording the net heat flux and assuming radiative equilibrium with deep space. In the figure, the flow is directed at a 30-degree pitch angle to the central body axis of the

spacecraft. Particles are reflected very slowly from the cool spacecraft body such that the gas density builds up near each exposed surface. This buildup promotes intermolecular collisions in these flow regions, which alter gas–surface interaction and reduce heat transfer to the body.

The resulting aerodynamic forces on each body facet are computed in order to assess the net pitching moments on the vehicle. Repetition of this simulation for several entry pitch attitudes yields the moment coefficients plotted in the second figure. Results for the rarefied simulation are compared to results from a free molecular flow simulation in which particles are artificially prevented from colliding. The latter results

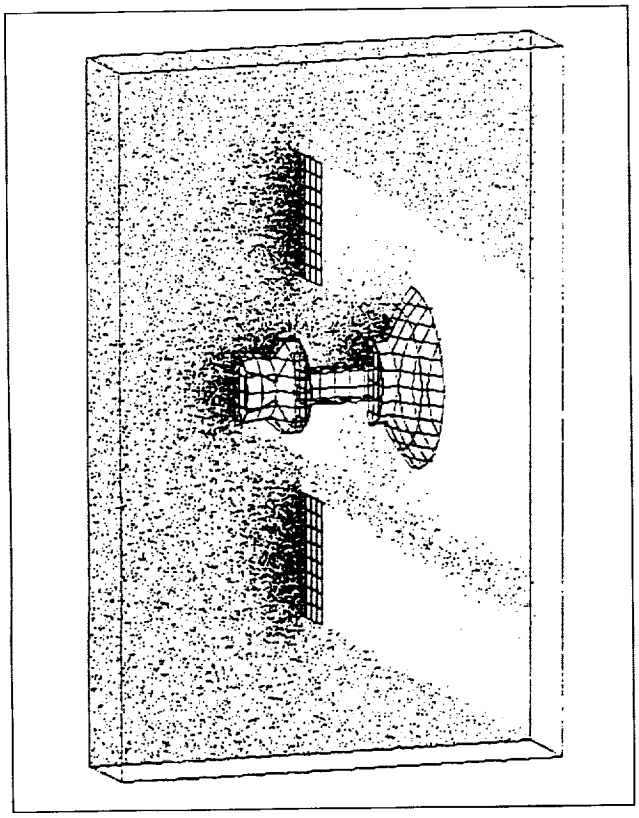

Fig. 1. Computational particles plotted at the symmetry plane for flow (from left to right) at a 30-degree pitch attitude about the Magellan spacecraft in the simulated wind tunnel. The spacecraft configuration is dominated by two large solar panels above and below, the high-gain antenna aft, and the central body core.

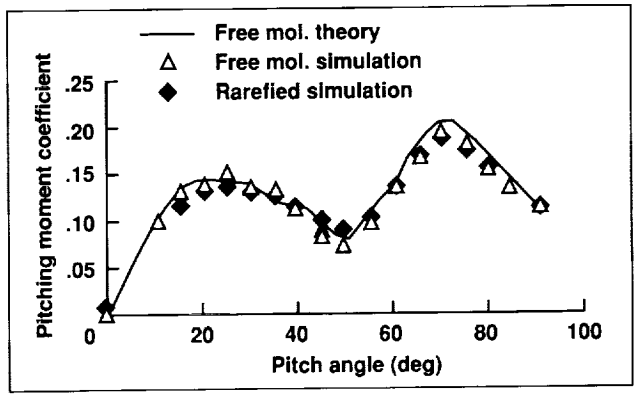

Fig. 2. Pitching moment coefficients for Magellan aerobraking at several entry pitch angles. Results are from the realistic rarefied simulation, a free molecular simulation, and free molecular theory.

agree with free molecular theory, and thus provide some validation of the simulation method. More important, the realistic rarefied results are nearly identical to the others, which indicates that molecular collisions are sufficiently rare in this flow that we can conclude that the free molecular assumption is appropriate. For all entry attitudes, the aerodynamic moment acts to reduce the pitch angle and promote spacecraft stability. Similar results are observed for spacecraft yaw characteristics.

Aerodynamic drag and solar panel heating were also computed at the nominal attitude (zero pitch and yaw angles) for atmospheric entries at altitudes from 125 to 140 kilometers. Differences between rarefied and free molecular results proved that molecular collisions are significant below 130 kilometers altitude. Computed surface temperatures remained safely below the 120°C limit of the panels only for entry altitudes that exceeded 138 kilometers. These results were important for JPL and the Magellan contractor, Martin-Marietta Astronautics, in winning approval for the aerobraking mission proposal.

Ames-Moffett contact: W. Feiereisen
(415) 604-6198
Headquarters program office: OAST

Simulation of Polymer Properties

Richard L. Jaffe

Computational chemistry methods have been used to improve the accuracy of material simulations of the morphological and mechanical properties of high-performance polymers for aerospace applications.

The development of new high-performance polymeric materials has been marked by attempts to synthesize materials with specific properties. An example is LARC-TPI, a polyimide resin developed at Langley Research Center, which maintains its insulating and structural properties at higher temperatures than other polyimides do. This polymer is used in various composite systems.

In recent years, materials simulation methods have been developed that permit calculations of structural and mechanical properties for a wide range of polymers, provided that the intrachain and interchain forces are known. These forces are usually expressed mathematically as a potential energy force field that is made up of stretching, bending, and torsional terms, which represent molecular vibrations, and pairwise nonbonded terms, which represent van der Waals and electrostatic interactions.

In the present study, standard ab initio quantum chemistry methods are being used to determine these parameters. Appropriate model compounds are used to represent short segments of the polymer chain. For example, 2,4-dichloropentane is used to represent polyvinyl chloride, and compounds like phthalimide and diphenyl ether are used to represent parts of a typical polyimide repeat unit. The molecular geometry, relative energy, and vibrational frequencies for each conformer are computed. To efficiently obtain the equilibrium geometry of each conformer, gradient methods are used in which the energy and its first and second derivatives with respect to the atomic displacements are calculated. The calculations are carried out at the Hartree–Fock level of theory using an expansion of Gaussian functions to represent the atomic orbitals. These basis sets generally have two functions for each atomic valence orbital augmented with polarization functions (e.g., d-type orbitals for C, O, etc.). For most chemical systems, relative conformer energies are determined to within 0.25 kilocalorie per mole.

Calculations have been completed for many of the components commonly found in polyimides. From this work, the effect of chemical composition on chain stiffness and interchain packing can be estimated. We find that deformation of the polyimide chain occurs most easily at the imide nitrogen. In order to make higher-modulus chains, the molecular geometry must be such that pyramidization of the nitrogen atom bonds cannot contribute to chain lengthening. Meta-linked polyimides generally exhibit higher moduli for this reason.

Another application of this research has been the study of the structure and vibrational spectra of polymeric precursors for high-temperature ceramic materials for use in thermal protection systems. An experimental program is under way in the Thermal Protection Materials Branch at Ames Research Center to use silicon–boron–carbon polymers as precursors for preparing silicon boride ceramics. These novel chemical compounds were difficult to characterize by standard methods. Calculations of the geometries and vibrational spectra of numerous model compounds were used to determine likely chemical structures and to develop an infrared spectroscopy diagnostic to easily estimate the amount of oxygen impurities in sample polymers.

These computational methods are being used to study polyethers and perfluoropolyethers. Members of the latter class of polymers are used as lubricants for jet turbines because their properties are retained at high temperatures.

Ames-Moffett contact: R. Jaffe
(415) 604-6458
Headquarters program office: OAST

Coated Composite Flexible Blanket Insulation

Demetrius A. Kourtides

A ceramic coating has been developed that enhances the heat tolerance of flexible ceramic insulations. This coating, called protective ceramic coating (PCC), is applied to ceramic flexible insulations used in the thermal protection systems of aerospace vehicles that are subjected to very high convective heating rates. The coating lowers the surface temperature of the insulation and prevents heat transfer through the fabric surface so that the underlying materials are protected from degradation. The surface temperature is lowered as a result of an increase in the total hemispherical emittance of the coated insulation.

A higher surface emissivity is desirable because it increases the ability of the system to radiate energy compared to that of a black body at the same conditions. A typical formulation of the PCC contains silicon hexaboride powder, silica powder, and colloidal silica particles in deionized water. The colloidal particles hold the coating together and bind it to the fabric. The coating is applied either by brushing or, preferably, by spraying, and is air dried for 24 hours.

The first figure shows a comparison of the emittance of three ceramic fabrics: an uncoated silicon carbide (SiC) fabric, a similar fabric coated with the PCC, and a similar fabric coated with a C-9 coating. The C-9 coating is currently used to coat the flexible insulation called advanced flexible reusable insulation

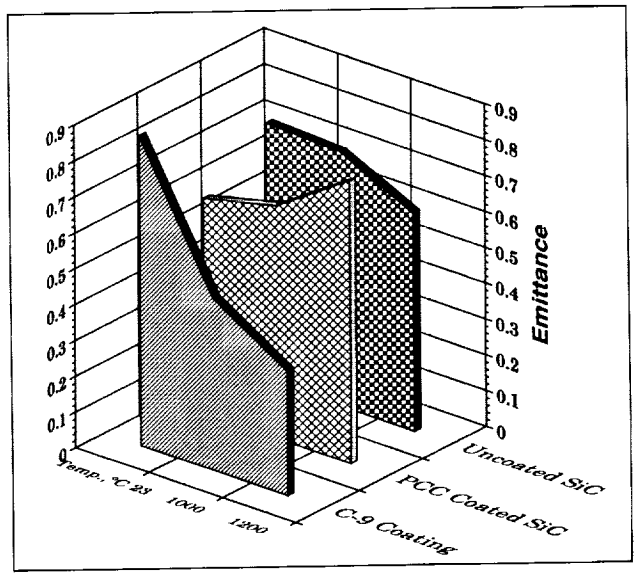

Fig. 1. Effect of temperature on the emittance of ceramic fabrics.

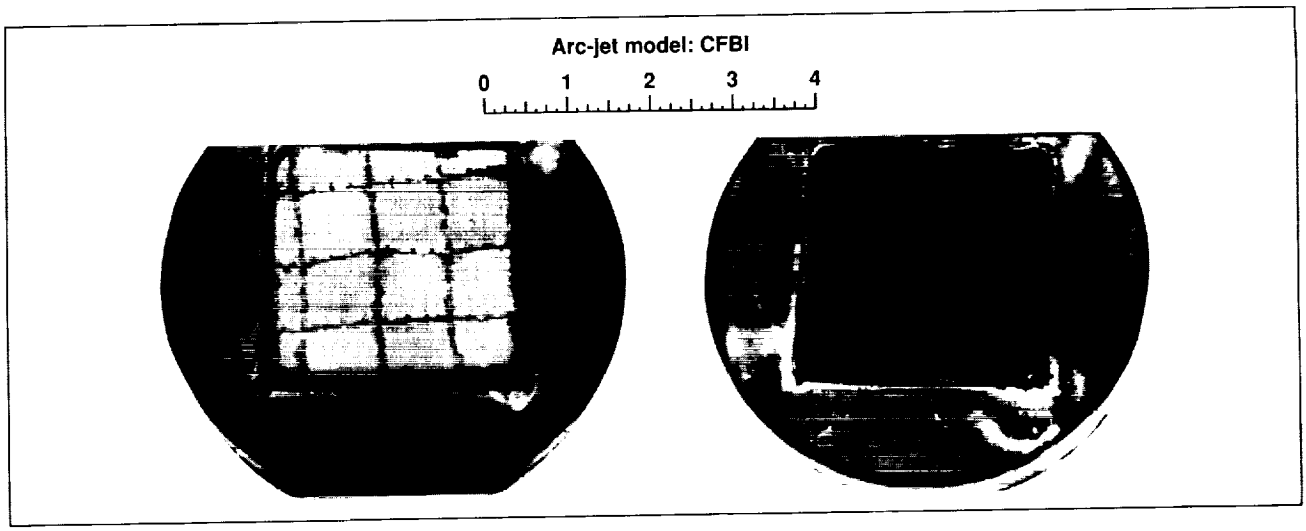

Fig. 2. PCC-coated composite flexible blanket insulation before and after heating test.

(AFRSI) that is used on the exterior of the Shuttle Orbiter. The emittance of the PCC-coated fabric increases at higher temperatures, whereas the emittance of the C-9-coated and the uncoated fabrics decreases. This comparison indicates the effectiveness of the PCC in radiating energy at high temperatures.

The coating has been applied to flexible insulations such as the composite flexible blanket insulation (CFBI). These coated insulations were tested in the Ames 20-Megawatt Panel Test Facility, which simulates an aeroconvective heating environment.

The second figure shows the PCC-coated CFBI before and after heating for 2 minutes at 39 watts per square centimeter. The insulation was inserted in a ceramic model holder to avoid edge effects. As shown in the figure, there was no visible damage to the outer fabric of the insulation after this severe exposure. Without the coating, the insulation would have been destroyed. There was a change in the color of the insulation, and this is attributed to the high emissivity of the coated fabric at high temperatures.

The coated CFBI insulation has potential application as a low-cost thermal protection system for reentry vehicles for Mars and other planetary probes.

Ames-Moffett contact: D. Kourtides
(415) 604-4784
Headquarters program office: OAST

Ab Initio Determination of Transport Properties

H. Partridge, J. R. Stallcop, E. Levin

The objective of this work is to accurately determine transport properties that are required for studies of nonequilibrium flow fields for air at high temperatures. These flow fields occur in front of vehicles such as the aeroassisted space transfer vehicle (ASTV) and in hydrogen-burning combustion processes such as in scramjets that are being designed for the National Aero-Space Plane.

The transport properties, such as thermal conductivity, viscosity, and thermal diffusion, are basic parameters required in flow-field calculations whenever viscous and heat-transfer effects are important. The previously available tabulations of transport properties have been based on incomplete knowledge of the required interaction potentials. For example, the high-spin atom–atom potentials have frequently not been characterized experimentally, and crude models were used to estimate the potentials. Likewise, molecule–molecule interactions are quite complex, but the transport properties have been generally estimated from simple exponential potentials. Whereas the resulting transport properties agree with the experimental data within about 5%, measurements have been performed primarily for temperatures below about 2,000 K. For the temperature range of interest for ASTV studies (5,000 to 20,000 K), the molecular internal energy modes dominate the energy transfer, hence a realistic potential energy surface is required to compute the thermal conductivity.

Two principal steps are required. The first step is the determination of the potential energy surfaces required to describe the interacting systems. Available experimental results are applied to determine some potential data. State-of-the-art quantum-mechanics procedures are employed to compute the unknown potentials. These computational procedures have been verified extensively; they reproduce the experimentally derived potentials, and also yield the correct asymptotic behavior of the interaction energy. The second step of the calculation involves the determination of the collision integrals from the scattering phase shifts. (According to the kinetic theory of gases, the transport properties of an arbitrary gas/plasma mixture can be determined from these binary collision integrals.) A semiclassical formulation is used to determine the phase shifts; it has been found that this procedure accurately reproduces the results of quantum mechanics calculations for temperatures greater than 300 K.

Tabulations of transport data have been published for the interactions of nitrogen and oxygen atoms and their ions, the interactions of hydrogen atoms with nitrogen atoms, nitrogen (N_2), hydrogen (H_2), water, and inert-gas atoms (e.g., helium and argon), and the interactions of H_2 with H_2 and N_2. The tabulations are being extended to include interactions between electrons and oxygen.

Ames-Moffett contact: H. Partridge
(415) 604-5236
Headquarters program office: OAST

Arc Jet Testing in Support of the Single-Stage-to-Orbit Vehicle

Salvatore R. Riccitiello

As part of a cooperative agreement between NASA and McDonnell Douglas Corporation, the Thermal Protection Materials Branch was asked to provide technical guidance in the designing and development of the thermal protection system (TPS) for the single-stage-to-orbit (SSTO) vehicle, the Delta Clipper.

After reviewing prior NASA results on the aeroconvective heating performance of a number of continuous-fiber-reinforced ceramic matrix composites (CFCMC), McDonnell Douglas selected carbon/silicon carbide CFCMC as the baseline high-temperature material for the Delta Clipper TPS for areas where the surface temperature exceeds 2,200°F. Pursuant to the previous NASA studies, several improved versions of this composite have become available, as well as new sources for it. Carbon/silicon carbide has been selected as a baseline material for the TPS for the National Aero-Space Plane (NASP).

McDonnell Douglas requested that an advanced coated carbon/carbon material developed during the NASP program also be evaluated. Evaluation of a modified carbon/silicon carbide produced by DuPont, Inc., showed that this material performed even better, with regard to mass loss, than the previously evaluated material, which was superior to other materials considered for this temperature range (see figure). The advanced carbon/carbon material gave a mixed performance. In the first test, coating spallation occurred in the initial exposure and further tests were canceled. A second model was tested and performed well. The mass loss rate was low and the coating did not spall. However, the residual physical properties have not been measured. With all coated carbon/carbon materials, the material is only as good as the coating for applications where oxidation may be an issue.

Fig. 1. Arc jet test.

A carbon/silicon carbide ceramic matrix composite produced by a vendor other than DuPont survived the test sequence; however, it experienced subsurface oxidation and residual property degradation.

A second phase of the test program was the evaluation of a metallic thermal protection system fabricated by Rohr Industries for Langley Research Center and supplied to Ames Research Center via McDonnell Douglas. The model, a 12-inch-square metallic TPS, was mounted in a holder and evaluated at conditions that generated surface temperatures of 1600°F–1650°F and 1406°F–1450°F. Results are currently being analyzed.

Arc-jet testing of other thermal protection systems is scheduled for 1993.

Ames-Moffett contact: S. Riccitiello
(415) 604-6080
Headquarters program office: OAST

Vibrational Relaxation in Expanding Flows

Stephen Ruffin, Surendra Sharma

Accurate predictions of flow fields around high-speed reentry vehicles such as the proposed aero-assisted space transfer vehicle and planetary entry probes depend on an understanding of the thermo-chemical, nonequilibrium state of the gas. At temperatures that are typical for the shock layers surrounding these hypersonic vehicles, significant vibrational excitation occurs. This excitation reduces the gas translational temperature and thus affects the pressure and heat transfer experienced during flight. The vibrational excitation process and the relaxation process that occurs on the shoulder and wake of high-speed vehicles also affects the rates of chemical dissociation and recombination of the gas species. Accurate predictions of vibrational processes are therefore essential in designing heat shields to protect these vehicles.

The widely used vibrational relaxation models fail to predict population inversion, which often occurs in expanding flows, and may fail to accurately predict the overall relaxation rate. The objective of this work is to develop a vibrational rate model that accurately predicts the vibrational relaxation process in hypersonic expanding flows. Computational studies and the development of relaxation and coupling models must rely on data from experimental facilities on the ground. The Electric Arc Shock Tube (EAST) Facility at Ames Research Center is used to generate data that simulate high-altitude, high-speed flight.

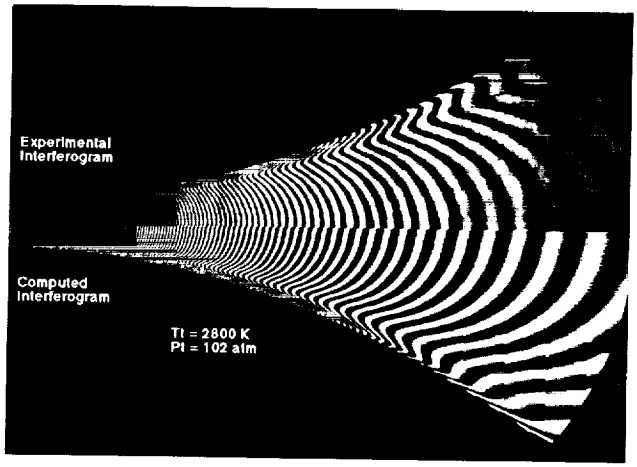

Fig. 1. Experimental and 2-D computed interferograms of expanding nitrogen in the EAST Facility nozzle.

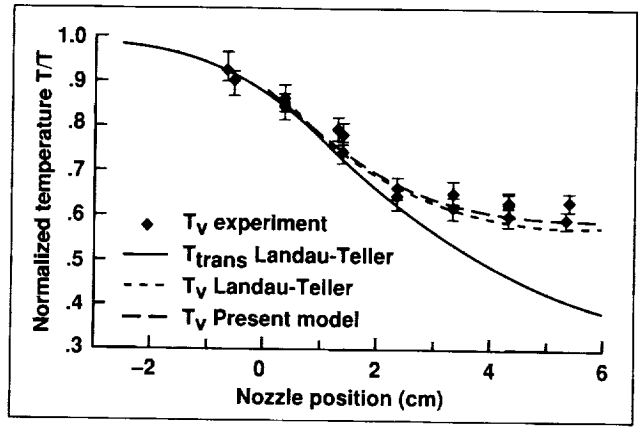

Fig. 2. Comparison of vibrational relaxation models and experimentally observed vibrational temperature in the EAST Facility nozzle.

The equations that describe the detailed vibrational process are called vibrational master equations. In this study the vibrational master equations are solved simultaneously with quasi-one-dimensional (1-D) fluid-dynamics and chemical-rate equations to study nozzle flows. The thermochemical predictions are then compared to data obtained in the EAST Facility and other experimental facilities. These comparisons are used to develop and validate accurate models that are also efficient enough to be used in multidimensional flow solvers.

The first figure shows a comparison of experimental and computed interferograms in the EAST Facility nozzle. Each light and each dark band corresponds to a constant-density contour. The two-dimensional (2-D) computed results are in good agreement with experimental data. This 2-D prediction is used to define an effective quasi-1-D nozzle geometry for use in quasi-1-D code which computes detailed vibrational energy transfer. Vibrational temperature for the first few quantum levels is determined experimentally by a technique called Raman scattering. The second figure shows experimental and computed temperatures along the nozzle centerline. The vibrational

relaxation model is found to give accurate predictions of vibrational temperature. The predicted and observed rates, which are believed to be more realistic, are slower than those inferred from older experiments which used indirect measurement techniques and impure test gases.

This work provides a significant contribution to model development and code validation that is relevant to reentry aerothermodynamics. The next step is to conduct further validations of the vibrational model for other conditions and to incorporate the model into multidimensional flow codes for studies of reentry flow shoulder and wake regions.

Ames-Moffett contact: G. Deiwert
(415) 604-6198
Headquarters program office: OAST

DuraTABI—A Durable, All-Weather Thermal Protection System

Paul M. Sawko

The need for both lightweight and durable thermal protection systems has evolved from the various program demands associated with the Space Shuttle, the National Aero-Space Plane, aerobraking vehicles, and, most recently, the revived single-stage-to-orbit (SSTO) vehicles. One flexible ceramic thermal protection system (TPS), called tailorable advanced blanket insulation (TABI), provides high thermal insulative efficiency that results in low backface temperatures, which allows direct bonding of the insulation to vehicle substructures. However, TABI lacks the durability and weatherability demanded for SSTO missions. The operation of the SSTO vehicles should be similar to that of commercial airplanes; they should require little maintenance and be capable of rapid turnaround under adverse weather conditions. The performance of the current TABI system must therefore be augmented.

DuraTABI is a TPS that is based on the attachment of a thin (3 to 5 mil), high-temperature metal foil (e.g., titanium, Inconel, Haynes, niobium) to the TABI fabric surface by means of a ceramic-to-metal brazing technique. This is shown schematically in the figure. The objective is to provide a metal-covered flexible ceramic insulation system that possesses superior resistance to weather hazards and the physical abuse of handling and maintenance yet is thermally efficient and lightweight.

Some preliminary results of tests conducted in a mini-wind-tunnel test facility (MWTF) and the

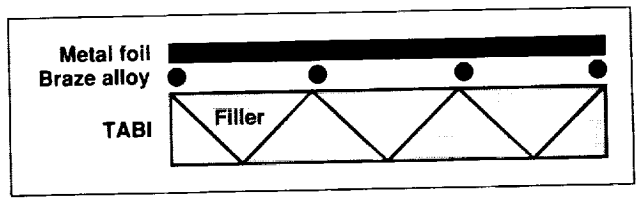

Fig. 1. Schematic of DuraTABI thermal protection system.

20-Megawatt Panel Test Facility are discussed. In these tests, a one-inch-thick silicon carbide woven TABI insulated with alumina filler had a 5-mil-thick Inconel 625 foil attached to the fabric surface by means of a copper/silver braze alloy. The test article was exposed to a dynamic pressure of 400 pounds per square foot, an overall sound pressure level of 166 decibels, and a fluctuating pressure of 1.5 pounds per square inch. The MWTF test showed no change after 300 seconds. An identical panel was tested in the arc-jet test facility using argon as the test gas. A Mach number of 7.8, a Reynolds number of 11,600, and a heat flux of 1.4 British thermal units per square foot·second were measured. The results showed no foil delamination after an exposure time of 94 seconds at a maximum temperature of 1,300°F.

Ames-Moffett contact: P. Sawko
(415) 604-6079
Headquarters program office: OAST

Hypersonic Nozzle/Afterbody Flow Field

Frank W. Spaid, Earl R. Keener

A study was conducted to experimentally characterize the flow field created by the interaction of a single-expansion-ramp-nozzle flow with a hypersonic external stream. Data were obtained from experiments with a generic nozzle/afterbody model in the Ames 3.5-Foot Hypersonic Wind Tunnel. The data are intended for use in computational fluid dynamics (CFD) code validation.

The first figure includes a shadowgraph of the interaction flow field and a schematic diagram which includes a portion of the flow within the model. The free-stream Mach number is 7.3. The model has a

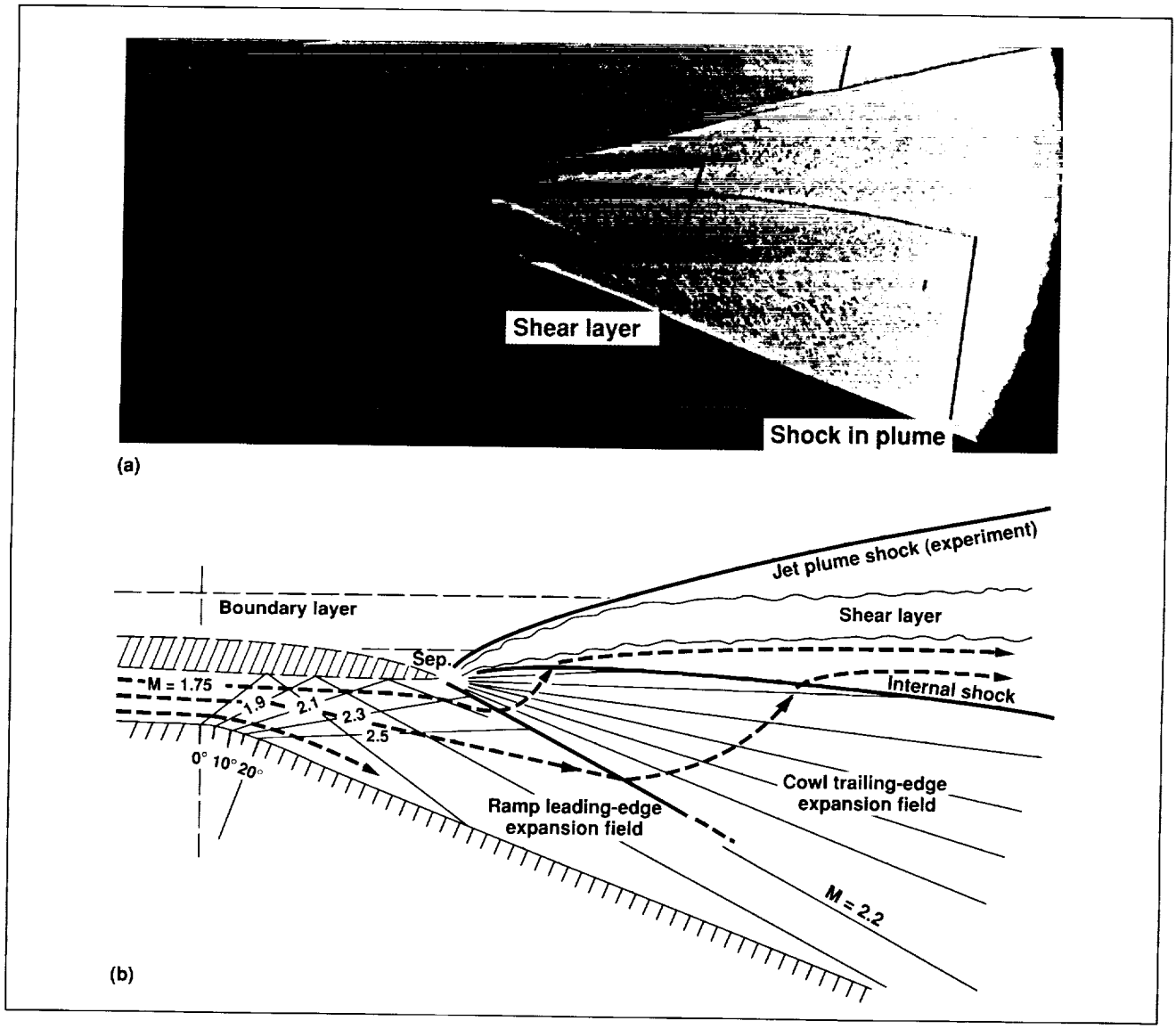

Fig. 1. Side view of jet-plume flow from model nozzle: (a) shadowgraph photograph and (b) schematic drawing.

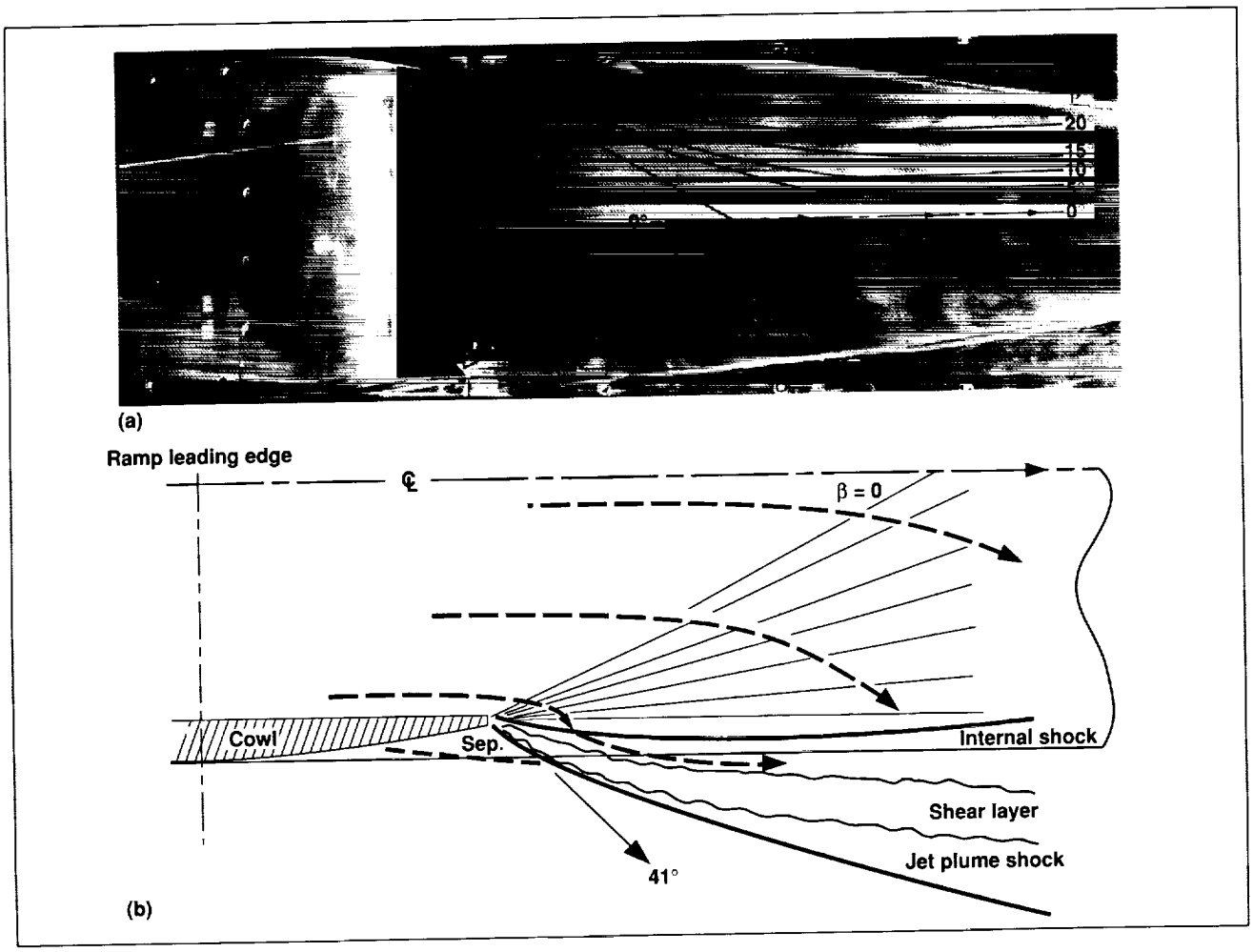

Fig. 2. Top view of jet-plume flow from model nozzle: (a) photograph of oil flow on ramp with flow angles and (b) schematic of horizontal cross section (planform) and wave diagram of cowl and jet plume.

wedge-shaped forebody, the leading edge of which is outside the field of view to the left. Room-temperature compressed air is supplied to a plenum within the model, which is then expanded in an internal nozzle to a Mach number of 1.75, and is further expanded by flowing over a 20-degree ramp. The static pressure at the cowl exit, where the jet exhausts into the external stream, is greater than the test-section static pressure, and this results in a further expansion of the jet. The interaction between the two flows results in the curved shocks and shear layer shown in the photograph and in the schematic diagram. These flow-field features are representative of scramjet exhaust nozzle flow.

A variety of data were obtained during this experiment. Flow-visualization data include shadowgraphs and surface oil-flow-visualization photographs (see second figure). The model was extensively instrumented with static-pressure gages, and static-pressure distributions on the ramp and the forebody were obtained. Forebody and ramp boundary layer profiles were measured with fixed boundary layer rakes. Skin friction on the ramp was measured at one location with Preston tubes. Measurements of local static pressure and tube impact pressure allowed the local surface shear stress to be determined.

The interaction flow field was extensively surveyed by means of five-hole and thermocouple probes. The five-hole probe data consist of distributions of impact pressure and pitch- and yaw-plane flow inclination angles. The thermocouple probe data

are used to determine distributions of total temperature which give the shear-layer locations directly.

Several composite views of the interaction flow field have been constructed from the probe data, in both streamwise, planform, and cross-stream planes. These data were useful in the construction of schematic diagrams such as those shown in the figures. Detailed comparisons among these data can be used to validate CFD codes.

Ames-Moffett contact: W. Lockman/G. Deiwert
(415) 604-5235/6198
Headquarters program office: OAST

Advanced Aerogel Development

Susan M. White

Aerogels, also known as "solid smoke," have the potential of being a breakthrough material for space vehicle insulation because of their extremely light weight, low thermal conductivity, and other unique properties. Aerogels are currently made of a wide variety of oxides and polymers. The solid framework is composed of precipitates that are only nanometers thick, whereas Shuttle tiles are composed of fibers that are microns in thickness. The transparency of the materials, shown in the first figure, can be tailored to suit the application.

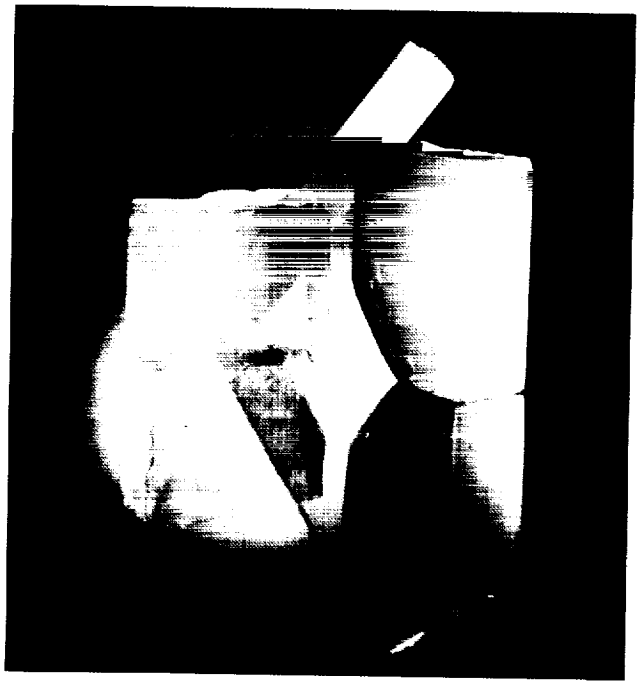

Fig. 1. Aerogels showing different degrees of transparency.

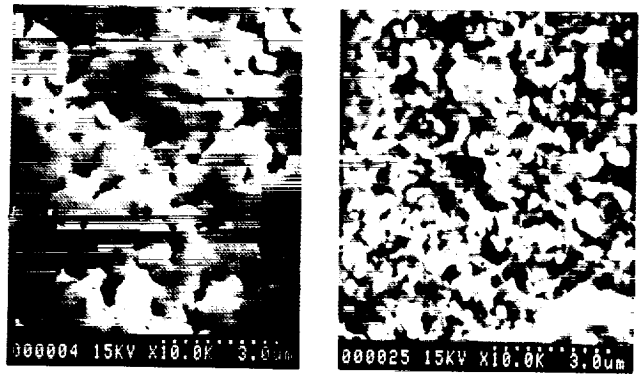

Fig. 2. Scanning electron micrographs of aerogels showing the effect of fiber loading after extreme heating.

For space applications, aerogels have two important weaknesses: structural problems and high surface activity. The most important structural problem of the material is its tendency to sinter to a full-density solid at a temperature below its melting temperature. A set of fiber-loaded stabilized aerogel samples was produced to test the concept of loading the aerogels with heat-resistant fibers to preserve the low-density structure of the aerogel when it is sintered. Surface activity was reduced by chemically bonding extra atoms to the hydroxyl groups on the aerogel itself.

Progress to date includes the production of the first fiber-reinforced aerogels; the final density of the samples was successfully reduced. Stabilized zirconia was chosen for a fast and relatively inexpensive test of this new concept, because the necessary fibers and chemical precursors are commercially available. In the second figure, scanning electron micrographs

show the material after extreme heating. The image on the left shows the unloaded aerogel which is almost fully sintered. The image on the right shows the fiber-loaded sample, which maintained a relatively low-density microstructure compared to the unloaded sample even after extreme heating. To solve the problem of the high surface activity that is characteristic of aerogels, silica aerogels were used as a testbed because their chemistry is already well understood. Extra atoms were chemically bonded to the aerogel structure itself. Samples have been successfully produced, and testing is in progress.

The goal of the first year of this project was to create two new classes of lightweight materials—reduced-surface-activity aerogels and fiber-loaded refractory aerogels—in order to explore their potential for space applications. This goal was successfully met. These approaches for reducing the surface activity and for fiber-loading aerogels should be applicable to aerogels made of materials that can withstand much higher temperatures than those used to test the concepts. This project was done in collaboration with Lawrence Livermore National Laboratory and TRW.

Ames-Moffett contact: S. White
(415) 604-6617
Headquarters program office: OAST

Plasma Copolymerization of Ethylene and Tetrafluoroethylene

Morton Golub, Theodore Wydeven

An extensive literature exists on plasma polymerization, i.e., the formation or deposition of organic solids or films under the influence of a plasma or partially ionized gas. Relatively little work has been reported, however, on plasma copolymerization of organic monomers that may be homo- or copolymerized by nonplasma techniques, i.e., by free radical, ionic, or rearrangement mechanisms. In the few plasma copolymerization studies that have involved polymerizable monomers, the following monomer pairs were notable: hexamethyldisiloxane (HMDSO) and methyl methacrylate (MMA), vinyl acetate (VA) and styrene (ST), and HMDSO and tetrafluoroethylene (TFE). For the vapor pair HMDSO/MMA, Urrutia and coworkers reported in 1988 that the deposition rate varied linearly with monomer composition, indicating that copolymer formation from each of the vapors was unaffected by the presence of the other polymerizing species. In contrast, they found an inhibiting effect in the plasma copolymerization of the vapor pair VA/ST. The plot of deposition rate versus monomer composition was concave upward and located *below* the straight line joining the deposition rates for the separate monomers VA and ST. An inhibiting effect analogous to that of VA/ST was also reported by Sakata and coworkers in 1988 for the monomer pair HMDSO/TFE.

Because neither the HMDSO/MMA pair nor the VA/ST pair was considered to be polymerizable by conventional copolymerization procedures, nor, presumably, was the HMDSO/TFE pair, we investigated, by means of infrared and X-ray photoelectron (XPS) spectroscopies, the plasma copolymerization of ethylene and TFE. Ethylene (ET) and TFE are a monomer pair that not only undergoes free-radical copolymerization but can yield the commercially important alternating ET/TFE copolymer (Tefzel). In the course of this work, we observed still another effect. There was a positive interaction between the monomers such that the rate of plasma deposition of ET/TFE versus mole % TFE in the feed gas gave a concave-downward plot situated *above* the straight line joining the deposition rates for the separate monomers ET and TFE, with a maximum rate occurring at about 70–80 mole % TFE. Moreover, the plasma copolymerization of ET/TFE, which apparently followed a predominantly "atomic" polymerization, resulted in clustering of carbon–fluorine moieties in the overall "polymer" microstructures and/or the appearance of fluorine atoms in highly fluorinated environments. These results were noted in connection with the observation that the mean binding energies of the XPS fluorine F_{1s} peaks for the ET/TFE plasma copolymers, which increased monotonically with percent fluorine (% F), were consistently higher than those for several commercial polymers of partially or fully fluorinated mono-olefins at comparable values of % F.

After this study was in progress, we came across a 1982 paper by Tsujimoto and coworkers, who, in the course of studying graded density coatings, found that the rates of deposition of ET/TFE copolymers using an argon-ET-TFE plasma showed a similar positive interaction between the monomers, with a maximum rate at an ET/TFE partial pressure ratio of about 40/60. However, those workers provided no data on the microstructures of their plasma copolymers, whereas we focused on the microstructural characterization of the ET/TFE plasma copolymers. Another relevant study, by Wang and Chen in 1988, demonstrated unambiguously by means of mass spectroscopic analyses of the *oligomers* formed in the plasma treatment of 1:1 blends of hexafluoropropylene and ET that these monomers indeed undergo plasma copolymerization and not merely simultaneous plasma homopolymerization of the respective monomers. It followed, then, that the plasma treatment of ET/TFE blends likewise yielded polymeric products in which fragments of ET and TFE were covalently interlinked.

An important reason for undertaking this study was to explore the potential for creating Tefzel- or Teflon-like coatings on various substrates for use in advanced life support systems. Such coatings may be useful in the development of biofilm-resistant polymeric surfaces.

Ames-Moffett contact: M. Golub
(415) 604-3200
Headquarters program office: OAST

Optimal Crop Selection for a Controlled Ecological Life Support System

Ann McCormack, Cory Finn, Betsy Dunsky

A controlled ecological life support system (CELSS) uses the natural ability of plants to regenerate air and water and to supply food in order to provide life support for long-duration manned missions. Current plant research is directed toward obtaining quantitative empirical data on the regenerative capacity of each species of plant and obtaining system volume and power requirements. Ames researchers have developed two analytical techniques for optimizing crop species selection so that system volume and power requirements are minimized. The first technique uses decision analysis in the form of a spreadsheet. The second method uses standard design optimization techniques. Each technique allows the researcher to specify the level of life support supplied by the plants, as well as other system parameters. Simple models of plant processes are used in the development of these methods.

Although current life support technology is based solely on physical and chemical processes, for long-duration missions, such as a trip to Mars or long-term habitation on the Moon or on Mars, a CELSS has the potential to provide human life support with significant cost savings and safety benefits over currently envisioned physical/chemical systems. In particular, the amount of food that would need to be resupplied from Earth may be significantly diminished. In addition, higher plants can provide both air revitalization (through release of oxygen and uptake of carbon dioxide) and water processing (through transpiration) capabilities. Also, some waste disposal can be carried out biologically. The figure shows an example of an integrated biological and physical/chemical CELSS.

Most research in the use of plants for life support has concentrated on productivity levels and the effects of environmental parameters on productivity. Little work has been done on evaluating the air- and water-regeneration and waste-management capabilities. Evaluation of these capabilities is the next logical step

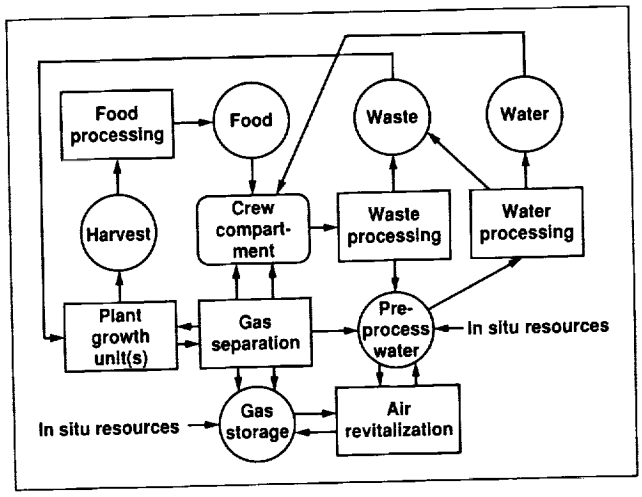

Fig. 1. Example integrated CELSS.

in developing an integrated life support system. The two techniques described above transform newly acquired plant performance data into parameters that describe a CELSS for use in "trade" studies, and thus provide a link between data generation and development of an optimal CELSS design.

Trade studies are generally conducted to determine the advantages and disadvantages of various design options. Trade study techniques such as decision analysis and design optimization can be developed in parallel with research on basic plant performance so that the studies can be performed as soon as reliable data become available. Analysis tools such as these will become increasingly important as we begin to address the complexities involved in integrating biological components with physical/chemical life support system components.

Ames-Moffett contact: A. McCormack
(415) 604-0087
Headquarters program office: OAST

Sizing System for Pressurized Space Suits

Hubert Vykukal, Bruce Webbon

Extravehicular activity (EVA) by space-suited astronauts will be an integral part of all future crewed spaceflight missions. Advanced robots and tele-operated machines will certainly be used to conduct increasingly complex operations, and they will be integral elements of space exploration. However, the capabilities of machines will not equal those of the human brain, senses, and hands in the foreseeable future. Therefore, all crewed missions will require a robust EVA capability.

Space suits are needed to protect the EVA astronauts from the hazards of the environment and to contain an atmosphere around their bodies at a pressure sufficiently high that they are able to breathe. The suits must be rugged and highly mobile so the astronauts can work productively without fatigue. The suits must fit properly both for comfort and to allow the required mobility. Space suits are currently sized to fit the EVA astronauts by selection of the appropriate sizes of suit elements from a large inventory of parts. These elements are then assembled to form a "custom fit" suit for each astronaut. The suits cannot be easily resized during a mission either to correct a comfort problem or to fit a different astronaut. This approach will not be practical on future long-duration missions in which, for example, the EVA equipment may be part of a permanent space base and the same suit must be used by different astronauts. Therefore, a method is required that will allow a pressure suit to be easily and accurately adjusted to fit different-sized users.

A design concept was recently developed that allows adjustment of the length of the suit arms and legs. The adjustment can be done by the astronaut while the suit is pressurized, to allow a precise fit that maximizes both comfort and function. The concept was designed to be retrofitted into the arms of the current suit used on the space shuttle. If the design is adopted by the shuttle program, it should greatly improve EVA productivity as well as provide substantial cost savings by reducing the inventory of different-sized parts.

Ames-Moffett contact: H. Vykukal
(415) 604-5386
Headquarters program office: OAST

Performance of Lettuce in Gray-Water Streams

Kanapathipillai Wignarajah, David Bubenheim, Ted Wydeven, Jr.

Water is a major component of any crewed space mission. After use, water ends up as shower water, laundry water, dish-wash water, urine, fecal water, sweat, or respired water. The wash waters are contaminated mainly with soaps, surfactants, and other cleansing agents, and can constitute as much as 75%–80% of the used water. Using this water to grow crops for consumption by humans has been long viewed as important in developing a regenerative life support system. In addition to production of food, the benefits of growing crops include removal of carbon dioxide and generation of oxygen, potential removal of noxious pollutants, and regeneration of potable water.

Igepon, an anionic surfactant, constitutes 98.5% of the handwash/shower detergent formulation selected by NASA. It is produced from a natural coconut oil extract. Researchers at Johnson Space Center found that test subjects used approximately

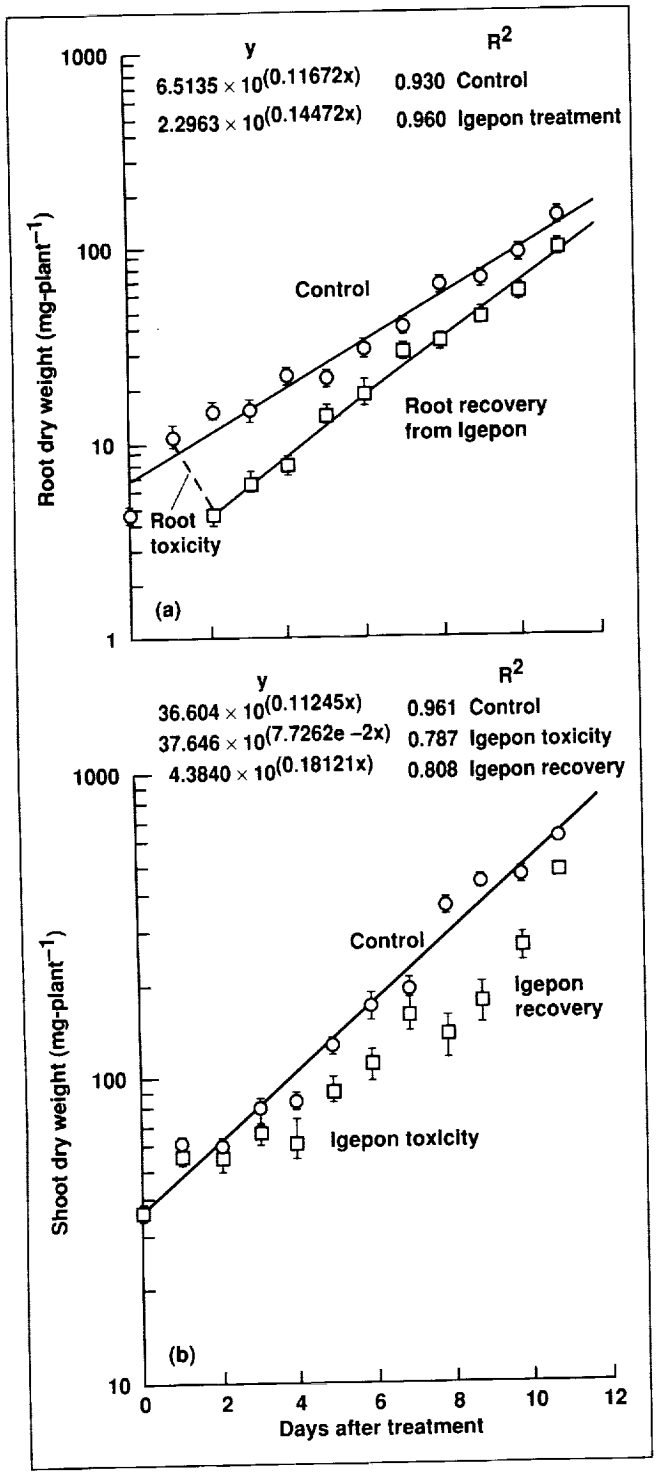

Fig. 1. Recovery of roots (first graph) and shoots (second graph) after exposure to a toxic level of Igepon (250 mg · ℓ^{-1}).

1000 mg · ℓ^{-1} of the Igepon-based soap per shower in a microgravity shower system.

At Ames Research Center, lettuce (a candidate crop for controlled ecological life support systems (CELSSs)) was grown in hydroponic units, under greenhouse conditions, in nutrient solutions that contained a range of Igepon concentrations. Concentrations of 125 mg · ℓ^{-1} or higher of Igepon in nutrient solutions were toxic to lettuce. Toxicity symptoms included browning of the roots within 4–6 hours, followed by death of the roots. At moderate concentrations (250 mg · ℓ^{-1} Igepon), plants showed the potential for recovery from the initial toxicity. The recovery response involved the development of new roots after 2 days (see figure) and resumption of leaf growth after 9 days in the Igepon solution.

Most surfactants, and in particular those of animal or plant origin, are known to be readily biodegradable, and often the products of biodegradation are nontoxic substances. A number of microorganisms as well as vascular plants are known to degrade surfactants. Our investigations confirmed that the phytotoxic effects of Igepon on lettuce can be mitigated rapidly (within 3 days). Lettuce offers some promise for the recycling of gray water and bioremediation processes in CELSSs. The results of these investigations are being used to develop strategies for growing lettuce and other candidate crops for an efficient bioregenerative life support system.

Ames-Moffett contact: K. Wignarajah
(415) 604-5201
Headquarters program office: OSSA

Active Balancing of a Slowly Rotating Centrifuge

Michael J. Horkachuck

In the past, life sciences requirements for a 2.5-meter centrifuge (to provide artificial gravity) have been perceived to be in conflict with the materials sciences requirements. Materials sciences calls for an environment on the space station that is as near zero gravity as possible. Analytical predictions indicate that the steady-state background accelerations on the space station may be approximately one millionth of Earth surface gravity, i.e., 10^{-6} gravitational unit. Rotating equipment is seen as a potential disturbance to this environment. NASA structural analysis models of Space Station Freedom predict the need to balance the centrifuge, so that forces seen at the centrifuge-to-space-station interface are on the order of 0.1 pound force. The centrifuge, when it contains live animals and plants, will certainly become unbalanced as these specimens grow during 90-day missions. Compensation for these mass-distribution changes at the source is seen as the most direct possible countermeasure.

Analysis and prototyping at Ames Research Center have provided insight into the usefulness of mechanical actuators to slew weights on a centrifuge rotor to compensate for unbalances.

As shown in the first figure, force transducers (as well as accelerometers) have been used to sense the phase and magnitude of the unbalance. This information is then used by a program in a Macintosh II computer that calculates the position to which balance weights need to be moved. Individual motors can then reposition the balance weights while the centrifuge continues to rotate. In tests, the system has been rebalanced in approximately 30 seconds after it was intentionally unbalanced. The time needed depends on the accuracy required (signal-averaging time), the noise in the sensor signals, a buffer in the signal analyzer that must be filled, and the computer algorithm. The majority of the 30 seconds is used to

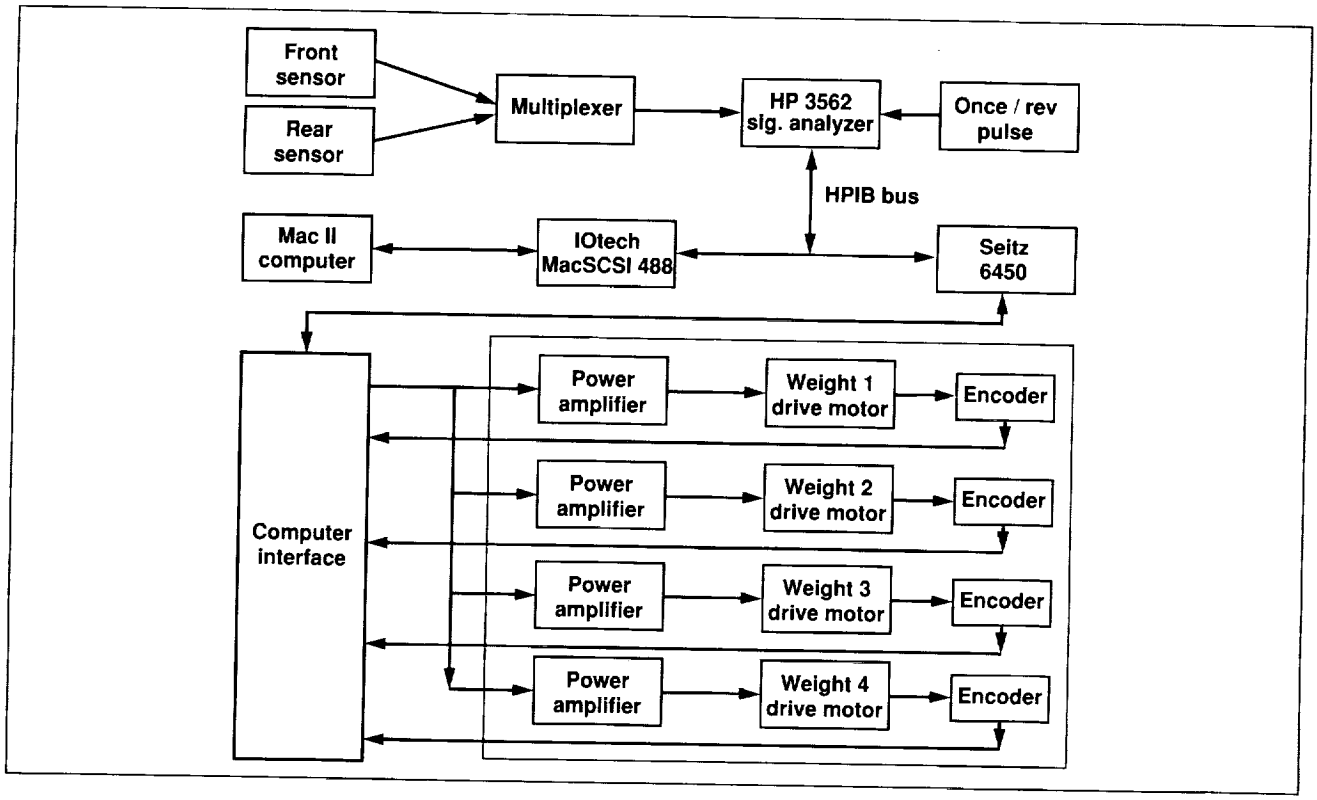

Fig. 1. The centrifuge active balancing system.

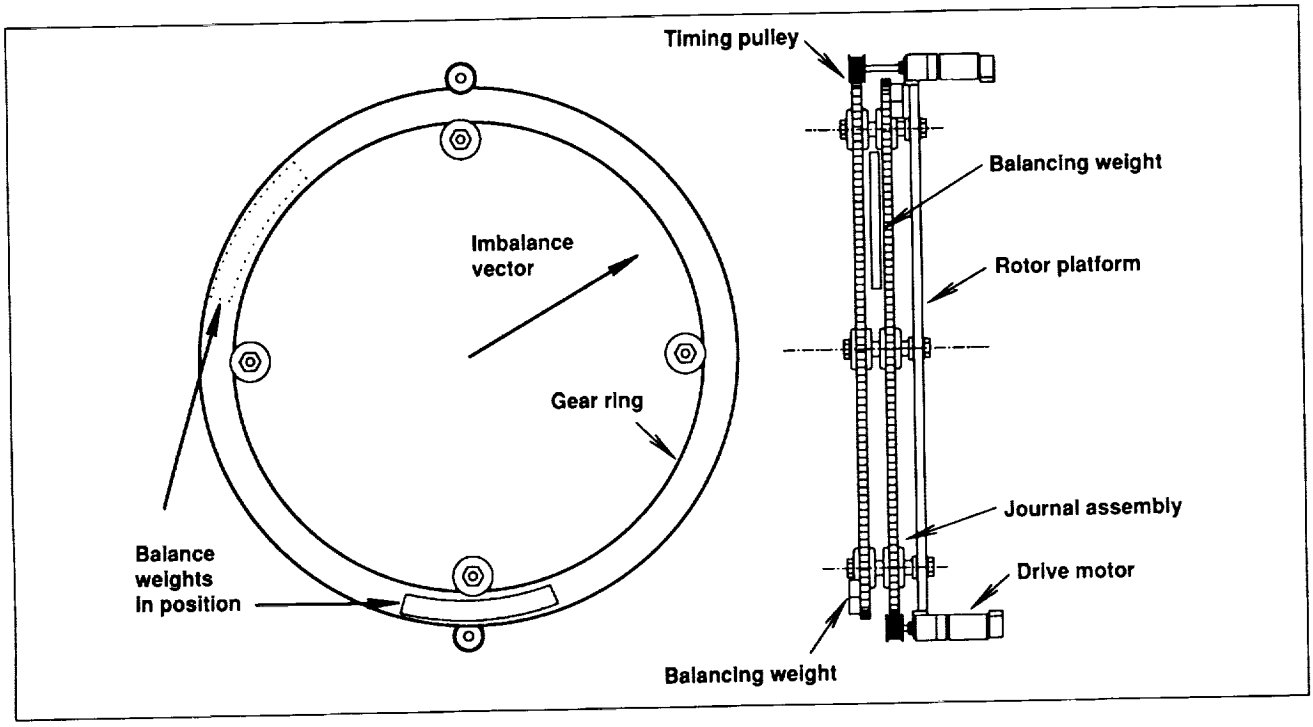

Fig. 2. Actuator configuration for single-plane balancing.

signal average the unbalance reading. Currently, load cells with signal-averaging techniques have allowed automated balancing to less that 0.1 pound-force (output at the attachment to ground) in one rotational plane. This corresponds well with the force limits predicted by analysis done on the finite-element models that are being used to anticipate the microgravity environment of the space station.

The second figure shows that the actuators in this system are motor-driven gear rings that each contain a balancing weight. This configuration was preferred over linear actuators in early centrifuge design studies because it could be designed to be at the very perimeter of the rotor, and thus provide the most balance compensation per pound of balance weight. It allows greater flexibility in packaging of equipment for experiments throughout the center of the rotor. Multiplane balancing is achieved by the use of two sets of actuators, a pair of rings in the front of the centrifuge and a second pair at the rear. Work is progressing on multiplane balancing and electronics to replace the signal analyzer (to allow more flexibility in signal averaging). Other ongoing work includes development of a real-time, multi-input–multi-output controller that might compensate for animal motion.

Ames-Moffett contact: M. Horkachuck/A. Harbury
(415) 604-3823/1108
Headquarters program office: OSSA

Dark-Cycle Video Monitoring

Arshad Mian, Sherry Chuang

Space Station Freedom will include a life sciences laboratory known as the Centrifuge Facility which will incorporate a large number of cameras distributed in various animal and plant habitat chambers. Video-monitoring capability during the dark portion of the circadian cycle is required for observing the animals and plants. The scientific requirements precluded the use of red light for simulating dark conditions, so we investigated the use of infrared (IR) cameras and a charged coupled device (CCD) monochrome camera with a near-IR light source. The objectives were to achieve acceptable imagery and minimize the weight, volume, and power requirements. In addition, for the CCD camera, the effects of near-IR illumination on animal specimens were to be studied.

Infrared cameras use a variety of detector technologies that are sensitive in several regions from 1 to 200 microns, as shown in the first figure. Detector cooling is generally required. It is performed by either a large cryogenic cooling unit or a small thermoelectric cooler. These cooled cameras provide sharper images than uncooled cameras. However, the weight, volume, and power requirements tend to preclude the use of cooled IR cameras in Centrifuge Facility animal and plant habitats.

As an alternative to the IR cameras, a miniature black and white CCD camera with the IR filter removed was evaluated. Near-IR illumination from light-emitting diodes with a wavelength centered at 0.88 micron provided excellent imagery. The second figure shows a comparison of images from a CCD camera and a noncooled IR camera that operated in the 8–12-micron range. The CCD camera offered the best option with minimum weight, volume, and power and excellent imagery, but the effects of near-IR lighting on rodents still needed to be understood.

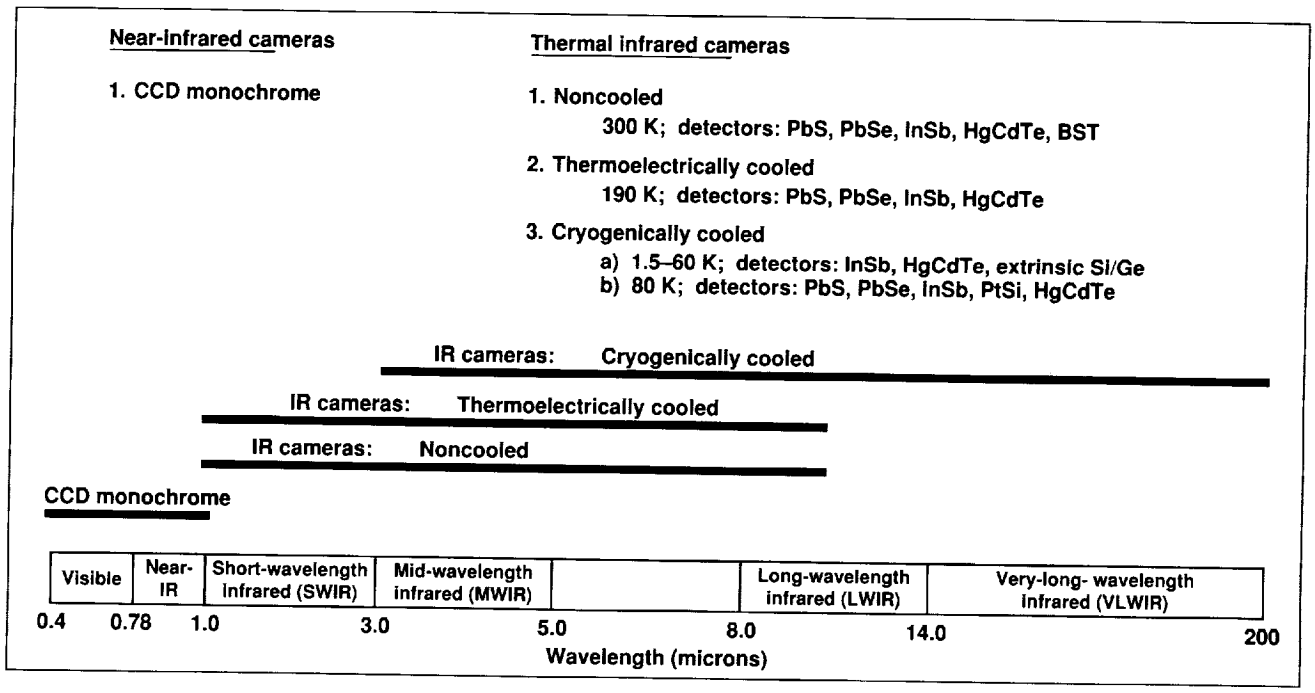

Fig. 1. Infrared detector characteristics.

An experiment was designed to quantify the effects of near-IR light stimulus on rodent circadian rhythms. The indicator used for this investigation was the melatonin level in the pineal glands. The experiment indicated that a 0.88-micron light source emitting up to 33.8 microwatts per square centimeter could be used without affecting the circadian rhythms of rodents in the dark cycle. This experiment, however, examined only one possible effect of illumination on rodents; extrapolation to other specimens and other physiological effects will require more studies.

As a result of these studies, the Centrifuge Facility has excluded IR cameras from its specifications, a change which should result in cost savings and allow a simpler video implementation with excellent imagery.

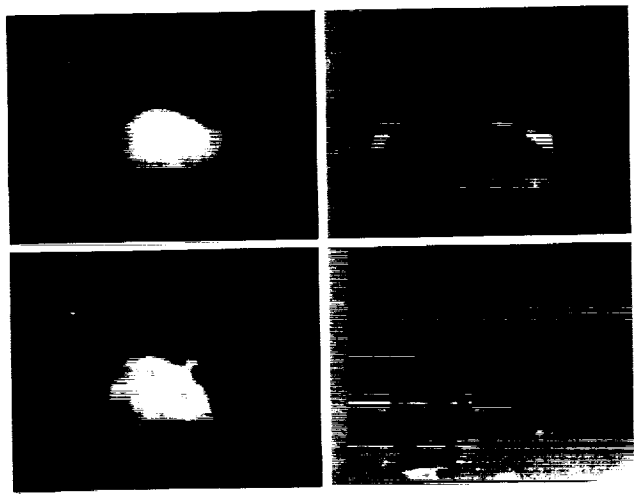

Fig. 2. Comparison of CCD (left) and IR (right) camera images for rodent observation.

Ames-Moffett contact: A. Mian
(415) 604-3450
Headquarters program office: OSSA

Visual Observation of Compressible Oscillating Flow

Jeffrey M. Lee, Peter Kittel

We have developed a flow-visualization system to examine the fundamental nature of compressible oscillating flows for the pulse-tube refrigerator (PTR). The PTR is an advanced long-life, low-vibration cryogenic cooler. It is ideal for use in space-based missions such as the Earth Observing System (EOS), in which reliability and microphonics are of primary concern. An understanding of compressible oscillating flow and the associated energy transport mechanism is pivotal in the designing of efficient, high-performance PTRs.

Our flow-visualization system allows direct visual observation of a gas undergoing a compressible oscillating flow. The gas is enclosed in a clear tube. Attached to each end of the tube is a reciprocating piston. The relative motion of the two pistons subjects the gas to different compressible oscillating flows. To make the various flows visible, oil vapor is used as "smoke" (the gas itself is transparent). The flows are first recorded with a videotape recorder and then compared to flows obtained by periodic solutions of the compressible Navier–Stokes equations of motion. Energy-loss mechanisms resulting from nonideal flows are identified so that these loss mechanisms can be minimized.

Three different components of oscillating flow have been observed (see figure). The first component is an *axial oscillating flow*. The second component is a *radial oscillating flow* that is in phase with the axial component. Both the axial and the radial components are first-order dependent on the oscillation frequency. They are coupled through mass conservation and represent the linear nature of the flow. The third flow component is a *steady secondary streaming*. It is second-order dependent on the frequency and is observed over the entire tube length. It represents the nonlinear nature of the flow. The three flow components combine to form a laminar flow that is axisymmetric. This simple laminar flow is complicated by the fact that it appears to be hydrodynamically unstable. We also observe complex three-dimensional "mixing." Both the mixing and the steady streaming flows represent energy-loss mechanisms. In previous models, the viscous, nonlinear nature of the equations of motion which give rise to these undesirable flows has not been considered. The results of our flow-visualization system constitute the first definitive proof of the existence of these nonideal flows for PTR-configured systems.

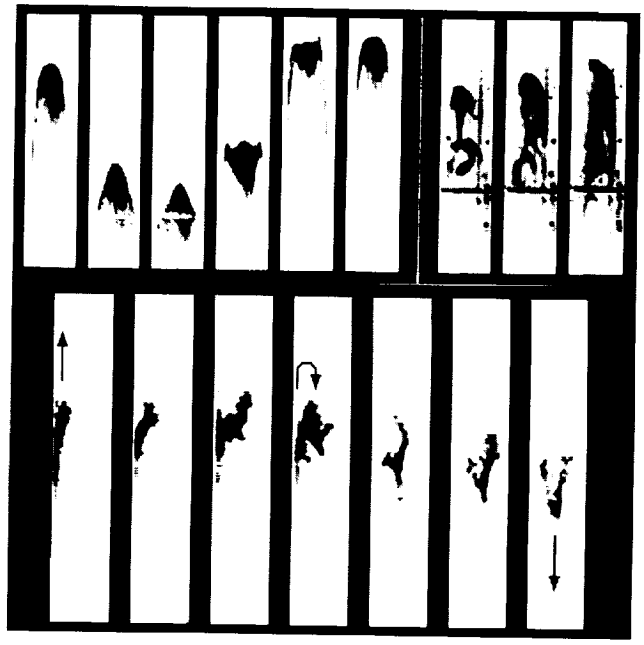

Fig. 1. Sequence of video frames showing different components of compressible oscillating flow: top left, viscous laminar axial flow; top right, axial and radial "mixing" flow; bottom, steady streaming flow.

The results will be used to design PTRs that minimize energy transport losses. The losses associated with streaming can be minimized by reducing the velocity amplitude difference between the tube ends. The losses associated with mixing can be reduced by increasing the dynamic Reynolds number. Increasing the dynamic Reynolds number confines mixing losses to thin regions near the tube wall. The success of our flow-visualization system has enabled us to identify PTR energy-loss mechanisms and will lead to improved design models.

Ames-Moffett contact: J. Lee
(415) 604-5693
Headquarters program office: OAST

Si:As Impurity Band Detector Arrays for Infrared Astronomy

Mark E. McKelvey, Robert E. McMurray, Jr., Craig R. McCreight

Infrared (IR) astronomy from space-based platforms requires the development of detector technologies that can operate reliably in the radiation environment found in Earth orbit. The impurity band conduction (IBC) detector, invented by Rockwell International, shows promise to address this need for NASA astronomy applications. IBC detectors rely on a thin, highly doped IR-active layer to provide high quantum efficiency from a small detector volume, minimizing the ionization cross section for cosmic ray events. A high-purity blocking layer keeps the high doping levels in the IR-active layer from resulting in excessive dark current. In ionizing radiation environments, IBC detectors are found to exhibit much smaller shifts in response characteristics than other detectors. They also exhibit wider spectral response than alternative photo-conductor (PC) architectures, without many of the anomalous response quirks associated with PC devices. IBC architectures are well suited to modern epitaxial fabrication methods, and the technology has progressed to the point where large-format hybrid focal plane arrays (FPAs) sensitive to IR wavelengths as long as 28 micrometers can be reliably produced by several manufacturers. The figure shows an example of a typical readout integrated circuit for these large-format arrays.

A team at Ames is evaluating the performance of a number of IBC FPAs fabricated in arsenic-doped silicon (Si:As) for suitability in IR astronomy applications in the 5–30 micrometer wavelength range. 10- by 50- and 20- by 64-element arrays from Rockwell International, 58- by 62- and 256- by 256-element arrays from Hughes Aircraft Company, and 128- by 128-element arrays using Rockwell detector material on NASA-developed Valley Oak Semiconductor readouts have all been tested over the past year, with encouraging results. Quantum efficiencies of over 50% have been measured with virtually zero response shift after sizable doses (several rads) of gamma radiation. Dark-current levels

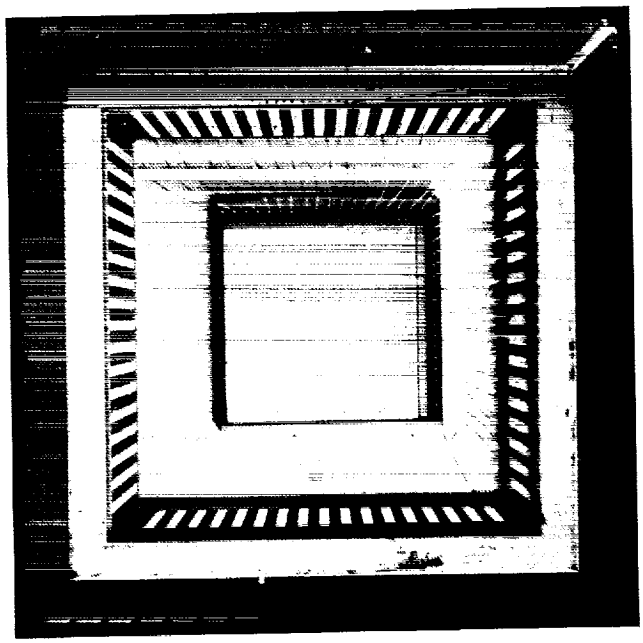

Fig. 1. Photograph of Valley Oak Semiconductor 256- by 256-element cryogenic readout. The pixel size is 30 μm, and the array is fully multiplexed through one output lead.

below 10 equivalent electrons per second have been measured. Read noise levels below 150 equivalent electrons have been measured. While this noise level is higher than we had hoped, it is likely that the problems are associated with the readouts or the test apparatus rather than the detectors themselves. Developing readouts with superior low-temperature noise performance is a continuing objective of our research program.

Hughes 58 by 62 IBC arrays have been used in a new mid-infrared camera for ground-based astronomy in collaboration with another group at Ames (see the report by T. Roellig in this volume). In addition to its scientific value, this camera serves as a testbed for

examining and demonstrating the usefulness of these IBC detector arrays in actual astronomical observations. The first astronomical observations with the new camera took place in November 1992 with the NASA 60-inch telescope on Mt. Lemmon, near Tucson. High-quality 10-micrometer images of several objects were obtained, and the performance of the Hughes array was excellent.

Further experimentation and optimization will continue in the next year, with emphasis on refining IBC technology and improving readouts to enhance overall IR focal plane performance in NASA space- and ground-based astronomy applications.

Ames-Moffett contact: M. McKelvey
(415) 604-3196
Headquarters program office: OAST

Pilot Land Data System

Gary L. Angelici, Lidia Popovici, Jay Skiles

The Pilot Land Data System (PLDS) is a limited-scale distributed information system that serves the data management needs of NASA's land science research community. The PLDS is managed by Goddard Space Flight Center, with Ames Research Center, the Jet Propulsion Laboratory (JPL), and the academic community participating. Data management services provided by the PLDS include an on-line data inventory accessible on major networks, data and information verification, data distribution, active science project support, and data publication.

A major accomplishment of the PLDS at Ames during the past year, in collaboration with a group of Ames researchers who are studying ozone depletion, was the establishment of a CD-ROM data publication capability. PLDS staff members can properly prepare a wide variety of earth sciences remote sensing data, field data, and model data in accordance with the rigorous standards of the earth sciences community. With commercial premastering software on the PLDS computer system, these data can then be written in CD-ROM image format to magnetic tape from which the master CD-ROM is produced at the JPL. To date, one CD-ROM disk, comprising 575 megabytes of satellite, aircraft, and field data, has been generated for the Oregon Transect Ecosystem Research project. This new capability is now available to assist in preserving unique suites of data for use by future researchers.

Ames-Moffett contact: G. Angelici
(415) 604-5947
Headquarters program office: OSSA

MODIS-N Airborne Simulator

James A. Brass, Jeffrey S. Myers

Ames Research Center and Goddard Space Flight Center are currently developing an airborne simulator for the planned MODIS-N imaging instrument on board the Earth Observing System (EOS) satellite. Because the MODIS-N instrument has become one of the primary sensors planned for the first EOS launch (in the middle to late 1990s), it is important that a system be developed to simulate the data (spatial and spectral) expected to be obtained from the spaceborne system.

The advantages of simulating data from the MODIS-N instrument are many. Simulation studies will allow design criteria to be examined, evaluated, and potentially changed before the instrument is launched. Data quality can be assessed, data management issues can be dealt with, and a constituency of researchers and applications engineers can be developed to use the satellite once it is in orbit. Research can be initiated before launch, to allow hypothesis testing and modification of channel placement and width before development of the satellite system. More important, researchers and applications engineers will not have to wait to use data from the MODIS-N instrument, producing hyperspectral data from the visible through thermal portion of the spectrum. Applications and uses of the data will have been developed prior to launch.

The simulation system is based on a modified 50-channel spectrometer built by Daedalus Enterprises for the AADS-1268 scanner. It uses four detector arrays to simultaneously acquire data in the 0.53- to 14.5-micron range, with bandwidths from 40 nanometers to 0.5 micron. It is currently interfaced to a 12-channel digitizer with 8- and 10-bit resolution for flight testing purposes; however, a state-of-the-art

50-channel, 16-bit digitizer is under development. The system has been successfully flown on over 15 flights on the NASA ER-2 aircraft to date. In addition, when flown together with the thermal infrared multispectral scanner instrument, it can be used to spectrally approximate the proposed Advanced Spaceborne Thermal Emission and Reflection Radiometer instrument.

Ames-Moffett contact: J. Myers
(415) 604-6252
Headquarters program office: OSSA

Airborne Infrared Disaster-Assessment System

James A. Brass, Leon Shameson

A low-cost, flexible multispectral scanner was built by NASA Ames under a grant from the Director's Discretionary Fund. The scanner was built primarily to fill the need of researchers to understand and measure the effects of fire on ecosystem and atmospheric processes. However, it also has applications in disaster monitoring and assessment.

There are 130,000 wildland fires each year in the United States. These fires burn 10 million hectares of land and produce 25 million metric tons of particulates. In addition, trace gases such as carbon monoxide, methane, carbon dioxide, nitrogen oxide, and nitrous oxide are generated from burning biomass and are injected into the troposphere at exceedingly high rates. Soil erosion and nutrient loss are triggered by fires that clear the vegetative cover and destroy the flora and fauna over large areas. In the Mediterranean ecosystems of southern California, the increased runoff after fires has been found to contain nitrate concentrations ten times higher than EPA acceptable standards.

Digital infrared scanning systems have been used to "look" at fires since the early 1970s. These systems have major flaws in their ability to characterize flame temperature and fire intensity. Problems with saturation of the sensor and with calibration at high temperatures still exist, preventing quantifiable measurement of flame characteristics or fire energy release, which are important factors in the impact of fires on ecosystem dynamics and trace-gas production.

The new multispectral system has four important attributes:

1. It can be flown on different types of aircraft;
2. It can obtain quantifiable, unsaturated data from active fires;
3. It allows high-temperature calibration for accurate measurement of flame temperature; and
4. It is telemetry-compatible for real-time analysis.

From a research standpoint, the system produces unique data sets in which the flame front is discriminated from superheated soils and from fire intensity or amount of energy being produced by the fire. These measurements were difficult to obtain before the development of this scanner; they are critically important in modeling the impact of fire on the biosphere.

This scanning system can be used to support disaster monitoring and assessment. The high-resolution optical system coupled with a four-detector array allows high-resolution visible and infrared products to be produced for fire detection, landslide assessment, earthquake damage assessment, and pollution monitoring. A first major mission using this system, supported by a multiagency team from NASA Ames, the U.S. Forest Service, and the Los Angeles County Fire Department, has been completed in Brazil. Flying in a twin-engine aircraft over the tropical forests and savannas of Brazil, the system collected data from 70 major wildland fires and for the first time provided data that characterized the flaming front and the fire intensity. Coupled with trace-gas measurements from other instruments on board the aircraft, the data obtained constitute one of the most complete data sets on fire impact in Brazil.

Ames-Moffett contact: J. Brass
(415) 604-3329
Headquarters program office: DDF

Fire Emissions and Biogeochemical Impacts in Brazil

James A. Brass, Chris Hlavka, Pam Matson, Bob Chatfield

The Brazil/United States Fire Initiative was signed in 1992 as a means of cooperative research to reduce the extent and environmental impact of widespread burning in the tropical savannas and forests of Brazil. This integrated program combines assessment of fire environmental impacts, scientific exchange, management support, and fire management demonstration in priority conservation areas. The Initiative is authorized by an implementing arrangement constituted under the Memorandum of Understanding for Forestry cooperation between the U.S. Department of Agriculture (USDA) Forest Service and the Instituto Brasileiro do Meio Ambiente e dos Recursos Naturais Renovaveis (IBAMA), and the science and technology agreement between the United States and Brazil. Agencies currently participating include

- Instituto Brasileiro do Meio Ambiente e dos Recursos Naturais Renovaveis
- USDA Forest Service
- Instituto Brasileiro de Geografia e Estatistica
- National Aeronautics and Space Administration
- Instituto Nacional de Pesquisas Espaciais
- Agency for International Development
- Conselho Nacional de Desenvolvimento Cientifico e Technologico
- National Center for Atmospheric Research
- Corpo de Bombeiros Militar do Distrito Federal
- University of Washington
- Universidade de Brasilia
- Universidade de Sao Paulo
- Centro de Pequisa Agropecuaria dos Cerrados
- USDA Office of International Cooperation and Development
- World Wildlife Fund

Fire is pervasive in central Brazil, but its consequences are known only in broad outline. Fire is used to clear broad expanses of tropical forest for shifting agriculture and cattle ranching. In the Atlantic forests of the southeast, fires threaten the dwindling native forests and established plantations of pine and eucalyptus. Across the 200 million hectares of the cerrado or tropical savanna, fires recur at intervals of two to four years, threatening wildlife and the biodiversity of the ecosystem. Together, agricultural and wildland fires are likely a major source of greenhouse gases that may be altering global climate.

A core project of this initiative is the "assessment of fire emissions and biogeochemical impacts in tropical savanna and forests of central Brazil." Under this project, measurements were taken during September 1992 to determine fire extent, energy release, and emissions of carbon monoxide, carbon dioxide, and particulates into the atmosphere. Measurements from a National Center for Atmospheric Research King Air aircraft were made over extended regions of the cerrado, including samples of fires in dry scrub, moist forest, and agricultural areas. Remotely sensed data on fire characteristics were derived from a four-channel multispectral scanner. Concurrently, air samples within the outside smoke plumes were taken for carbon monoxide, carbon dioxide, particulates, and water vapor measurements. In addition, grab samples were taken at various altitudes for analysis in the United States. Three well-instrumented prescribed burns were also completed during the field campaign. Differing vegetation types were burned to determine the impact of species and fire intensity on trace gas generation. The controlled burns allowed the measurement of other important characteristics such as above-ground biomass and burning efficiency which help determine trace gas and particulate production.

The field campaign lasted one month and sampled over 70 fires. This campaign has produced the most extensive sampling of fires in Brazil. Infrared imagery and gas samples have coincidentally been collected. Initial results have shown a large variability in fire behavior, from large, intense fires to very-slow-moving line fires. This fire variability is also evident in the measurement of trace gas flux, with concentrations of carbon monoxide and carbon dioxide varying with smoldering and flaming stages.

Ames-Moffett contact: J. Brass
(415) 604-3329
Headquarters program office: OSSA

Regional Ecosystem Simulation

Jennifer Dungan, David Peterson, Joseph Coughlan

The goal of this research is to test the extent to which stand-level models of forest evapotranspiration and net primary production can be extrapolated to the regional level. The approach is to use process-based models developed to represent fluxes over small areas and run them using spatially distributed input data over large regions. Environmental variables important in the models, such as surface temperature, precipitation, soil type, and leaf area index, are derived from maps or remotely sensed data. The ecosystem model at the core of this work is based on Forest-BGC, developed by S. Running and J. Coughlan (University of Montana) and MTN-CLIM, a meteorological model developed for mountainous terrain, also developed at Montana. The output fields generated by the model include photosynthetic production, transpiration, evaporation, and outflow. The simulation system, including the process model and the means of analyzing inputs to them and outputs from them, is called the Regional Hydroecological Simulation System (RHESSYS).

Work proceeded with other Ames researchers in the development of a software tool called SIGMA (Scientists' Intelligent Graphical Modeling Assistant) for model building and modification. The domain objects, which are the fundamental units of the ecosystem model (such as leaves, canopy, soil, and atmosphere), and the equations that relate the fluxes between them were entered into the system. Using a new interface developed for SIGMA, the first execution of the parts of the model was accomplished. In the future, SIGMA will provide a means of flexibly changing the models that form the basis of RHESSYS.

A new method for combining "ground truth" data, or measurements on the ground, and remotely sensed data was tested using a data set contributed by the U.S. Forest Service. The method is designed to produce the spatial distribution of a surface variable by taking into account the ground data, any remotely sensed data that are believed to be related to those ground data, and the spatial correlation of both sets of data. The variable used in the first test was stem basal area of conifer stands at 300 locations throughout the Flathead National Forest in western Montana. Results showed much greater variance than typically found with interpolation or remote sensing extrapolations.

Ames-Moffett contact: J. Dungan
(415) 604-3618
Headquarters program office: OSSA

Bidirectional Studies of Forest Canopy Reflectance

Lee Johnson

The goal of this research is to determine how forest canopies reflect solar radiation as a function of view and illumination angle, and to determine if this information can be used to discern ecologically meaningful information about the target. The advanced solid-state array spectroradiometer (ASAS), flown aboard the NASA C-130 research aircraft, was used to collect radiance data over several forest canopies from seven discrete view angles in 29 channels throughout the 450–850-nanometer spectral region.

During 1991, an atmospheric radiative transfer model (called LOWTRAN7 by the U.S. Air Force) was used to remove atmospheric effects from nadir-view (downward looking) and solar-backscatter-view (sun behind sensor) ASAS observations at all sites for both the June and August dates. For selected ASAS scenes, all view angles were corrected. Good agreement was shown between retrieved ASAS reflectance and field-measured reflectance.

Reflectance of a given forest canopy varied as a function of view angle, with forescatter observations lower than backscatter observations. In the red spectral region (near 650 nanometers), sparse canopies were more reflective than dense canopies (with similar soil and understory) at all view angles, with a constant difference in reflectance attributable to soil background effects. In the near-infrared spectral region (near 780 nanometers), sparse and dense canopies were approximately equal in the forescatter direction, with reflectance from the dense canopy becoming relatively greater in the backscatter views. This phenomenon may be related to the "hotspot effect," which has been shown in theory to be greater for more dense canopies. The normalized-difference vegetation index (NDVI), which has been shown in other studies to be related to the canopy leaf area index (amount of leaf area per unit ground area) was fairly independent of view angle for the sparse canopy. However, the dense canopy showed a strong dependency of the NDVI on view angle, with larger NDVI in the forescatter than in the backscatter directions.

The NDVI was calculated for both the nadir and backscatter data acquired at several sites in both June and August 1990. On each date, curvilinear relationships were found that explained more than 90% of the variation between both nadir and backscatter NDVI and field-measured canopy leaf area index, which was constant between dates. No appreciable difference in the strength of these relationships was found as a function of view angle. However, the regression equation coefficients were more stable between dates for the backscatter views than for the nadir views. This is probably because less soil and understory is visible in the off-nadir views than at nadir, and the off-nadir views were thus less influenced by background changes that occurred between the two observation dates.

These findings address the potential scientific return from planned directional-viewing sensors, and are applicable to correction of scan-angle effects encountered by current-generation scanning instruments, such as those on Landsat.

Ames-Moffett contact: L. Johnson
(415) 604-3331
Headquarters program office: OSSA

Investigations of Canopy Biochemical Composition

Lee Johnson, David Peterson

The goal of this research project is to determine if the biochemical composition of forest leaves and canopies can be estimated from analysis of high-spectral-resolution remote sensing data. During 1991, several Advanced Visible and Infrared Imaging Spectrometer (AVIRIS) forest canopy observations were corrected for atmospheric influence by use of the atmospheric radiative transfer model (called LOWTRAN7 by the U.S. Air Force), using atmospheric transmission measurements acquired at the time of overflight. Regression equations were formed to relate AVIRIS reflectance data to field-measured concentrations of several foliar chemical constituents: total nitrogen, total phosphorus, amino acids, lignin, cellulose, starch, sugars, and total chlorophyll. Strong relationships were found for all chemicals. Generally good agreement was found between wavelength selections for nitrogen-bearing constituents and known locations of absorption features that are due to nitrogen–hydrogen molecular bonds. This study suggests that AVIRIS data may be used to generate regional-scale estimates of foliar chemical composition from remotely sensed data, which in turn may be used to develop estimates of ecosystem flux rates and biogeochemical cycling rates.

Ames-Moffett contact: L. Johnson
(415) 604-3331
Headquarters program office: OSSA

Carbon Emissions from Northern High-Latitude Ecosystems

Gerald P. Livingston, Leslie Morrissey, David Des Marais

The role of northern wetlands in global atmosphere–biosphere interactions remains an unresolved but key factor in projecting climatic change that will occur in response to increasing atmospheric concentrations of greenhouse gases such as carbon dioxide and methane. Wetlands north of 45°N constitute areally over half of the Earth's total wetlands, and the amount of organic carbon stored in the peats and soils beneath these ecosystems exceeds that in any other biome on Earth. Because climatic change will be first and most dramatic in northern high latitudes, microbial decomposition processes acting on these carbon stores will almost certainly lead to increased atmospheric loading of carbon dioxide and methane, and thus potentially enhance the greenhouse phenomenon.

This project has focused on quantifying regional rates of exchange of methane from these northern wetlands, and their controlling factors. The global warming potential of methane and its decomposition products is estimated at nearly 15% of the total radiative forcing under current atmospheric conditions. The atmospheric concentration of methane has more than doubled over the past century and is continuing to increase at a rate of about 1% per year. Uncertainties in current estimates of boreal methane sources are high, attributable to the limited measurements of emissions and to inappropriate techniques for quantifying the uncertainties on global and annual scales. The observed seasonally variable interhemispheric gradient in atmospheric methane concentrations suggests that northern wetlands may account for as much as 35% of all natural sources.

Supported by NASA's Interdisciplinary Research in Earth System Science, Polar Land and Oceans Programs, and the U.S. Geological Survey Global Change Initiative, efforts are under way within the Earth System Science Division to quantify regional and seasonal methane emissions from selected

northern ecosystems and to address the potential of increased emissions from these ecosystems should climatic warming be realized. In situ observations established that the factors that regulate local methane exchange rates, e.g., hydrology, vegetation type and quantity, and substrate temperature, are consistent across a wide diversity of wetlands and environmental conditions in Arctic and boreal regions. Moreover, it was demonstrated that surface inundation and vegetation type and quantity in these regions could be regionally characterized using Earth observational satellites. Surface and satellite observations were then integrated using classical sampling theory to yield regional estimates of emissions and uncertainty. These results suggested not only that published estimates of methane emissions from northern ecosystems were overestimated by a factor of 3 to 5, but also the hypothesis that as much as 90% of net methane emissions from northern ecosystems may come from as little as 10% of the total high-latitude land area. The figure shows a schematic elevation cross section that is representative of central Alaska. Note that microbial processes in the well drained upland environments seasonally consume atmospheric methane at low rates per unit area; low-productivity wetlands represent low-magnitude sources, and productive herbaceous wetlands represent significant sources. Calculation of regional/seasonal exchange rates is still pending completion of satellite characterizations based on Landsat Thematic Mapper and European Remote Sensing (ERS-1) synthetic aperture radar data (see L. Morrissey, "ERS-1 SAR Investigations...," in this report). Preliminary results to date, however, based on a geographic information system derived from high-altitude aerial photography over

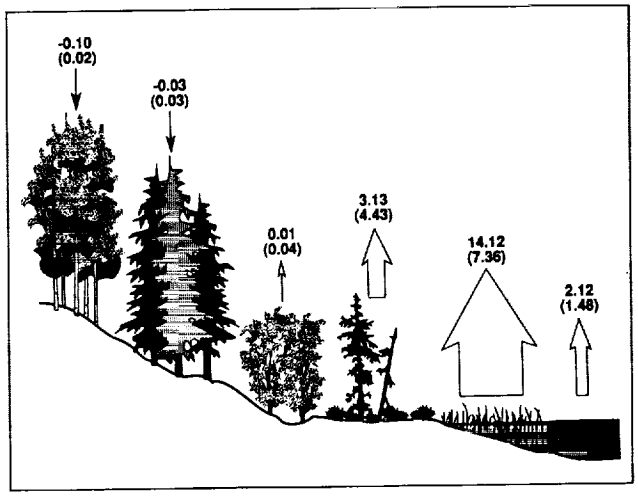

Fig. 1. Methane exchange rates along an elevational cross section representative of boreal ecosystems in central Alaska. Methane exchange rates (mean ± SE) are in milligrams per square meter per hour.

much of a 2500-square-mile area, clearly substantiate the hypothesis that significant methane sources represent a very small proportion of the total area of the boreal ecosystem. Ongoing Monte Carlo simulation studies pertaining to the propagation of error in regional estimates and to environmental factors such as soil temperature that cannot be measured from space will aid interpretation of these results and provide evidence to support the extension of these findings to other regions of study.

Ames-Moffett contact: G. Livingston
(415) 604-3232
Headquarters program office: OSSA

Contributions of Tropical Forests and Tropical Land Use Change to Global Nitrous Oxide Emissions

Pamela A. Matson, Christine Billow, Jerri Mazzurco

Nitrous oxide, a trace gas whose atmospheric concentrations have increased 0.2%–0.3% per year for the last 20–30 years, is one of several important greenhouse gases. In addition to absorbing infrared radiation released from Earth's surface, nitrous oxide also catalyzes the breakdown of ozone in the stratosphere. Because of these roles, considerable attention has been directed to understanding the changing sources and sinks of this gas. Our research has elucidated the importance of tropical ecosystems and tropical land use change as sources of the global increase.

Results from studies at a range of sites selected along gradients of soil fertility and climate suggest that 2.4 teragrams per year of nitrous oxide is emitted from humid and wet tropical forests, and that another 1 teragram per year is emitted from seasonally dry tropical forests. Thus, undisturbed tropical forests represent the largest background source of nitrous oxide globally.

Tropical forests are being disturbed at a very rapid rate: 8–10 million hectares are cleared and permanently converted to other uses each year. Our research on cattle pastures in Brazil indicates that conversion of rainforest to pasture results in a threefold increase in annual nitrous oxide flux over that in undisturbed forest; thus, clearing in these humid tropical environments may account for up to 25% of the annual global increase in nitrous oxide in the atmosphere. Studies of land conversion in the dry tropics suggest that upland pastures there may not have elevated fluxes; land use change in those environments may not result in increased emissions. Current research in Hawaii and Brazil is focusing on the importance of tropical agriculture as a source of nitrous oxide, nitric oxide, carbon dioxide, and methane. Early results show elevated fluxes of nitrous oxide, and nitrogen trace gases are associated with nitrogen fertilization. We estimate that over 50% of nitrogen gases lost from agricultural systems are lost within one-week periods following fertilization. Further work will examine the mechanisms that control trace gas fluxes in intensively managed tropical ecosystems, and this work will be incorporated into simulation models.

Ames-Moffett contact: P. Matson/C. Billow
(415) 604-6884/3223
Headquarters program office: OSSA

ERS-1 SAR Investigations of High-Latitude Wetlands

Leslie A. Morrissey, Gerald P. Livingston

The predominance of methane-producing wetlands in the tundra and taiga (boreal forest) makes these ecosystems important contributors to the global methane budget. European Remote Sensing (ERS-1) satellite synthetic aperture radar (SAR), launched in July 1991, provides the first spaceborne SAR system for multiyear, multitemporal assessment of high-latitude ecosystems. Analysis of ERS-1 C-band SAR data is under way to determine the type and extent of wetlands (methane source areas), the extent and timing of inundation (anaerobic substrates required for methane production), and vegetation community type and amount (methane transport pathway). This research is being conducted in collaboration with the Jet Propulsion Laboratory and the NASA Ames methane project with funding from NASA's Polar and Interdisciplinary Programs.

Initiated in April 1991, ERS-1 project activities have concentrated on the acquisition and analysis of ERS-1 SAR data for Barrow, Prudhoe Bay, and Minto, Alaska, during the growing seasons of 1991 and 1992. Results from ERS-1 data collected over northern Alaska have shown that methane emissions are positively related to the position of the local water table relative to the ground surface and radar backscatter. As shown in the figure, rates of methane emissions from Arctic tundra are highest for inundated sites, and decrease dramatically for comparable sites where the water table is either at the surface or 5 centimeters or more below the surface. Similarly, ERS-1 SAR backscatter is directly related to the position of the local water table: the strongest return is from herbaceous sites with standing water.

Results from the analysis of SAR data collected by a DC-8 aircraft in Alaska in May 1991 document the successful discrimination (89% accuracy) of methane exchange in boreal vegetation communities. Backscatter for methane-consuming upland deciduous and coniferous forests and tall shrublands was well separated from that of methane source areas. Even within methane source areas, communities that have high exchange rates (i.e., fens) are separable from bogs and open water, which have low exchange rates. Vegetation communities underlain by water had substantially higher radar cross sections, a result of double bounce scattering, than all other communities.

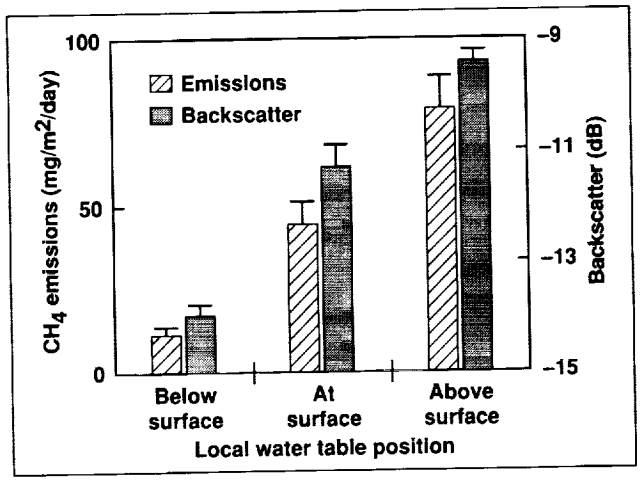

Fig. 1. Methane emissions and ERS-1 SAR backscatter related to the position of the local water table for herbaceous tundra sites (mean ± standard error).

Ames-Moffett contact: L. Morrissey
(415) 604-3617
Headquarters program office: OSSA

Advanced Chemical Monitoring System

Peter T. Palmer, Carla M. Wong

Advanced chemical monitoring systems are essential for a wide variety of applications. These systems may range from advanced life support systems for future NASA missions such as the space station and the lunar base to more routine applications in the environmental, toxicological, clinical, biochemical, and pharmaceutical industries. However, the monitoring systems currently available are inappropriate for in situ analysis and unattended operation. Efforts on this project have focused on the development of an artificial-intelligence-based ion trap system for life support and ecosystem monitoring applications.

Monitoring air quality for long-term space missions is a formidable task. Analytical requirements include monitoring major or critically important constituents as well as contaminants expected to be present at trace levels. Thus a sensitive and versatile instrument is needed. The monitoring system should be able to control and optimize itself, process large quantities of multidimensional data, combine data from different experiments, use intelligent feedback to enable real-time decision making, and interact with users in a facile manner. The complexity and heuristic nature of these tasks implies the need for a knowledge-based system to "run" the chemical analysis and operate the instrument.

An expert-system/ion-trap-mass-spectrometer system has been developed at Ames to meet these needs, and is diagrammed in the figure. The ion trap instrument can detect compounds present at concentrations as low as one part per billion, can run a variety of complementary experiments, and has excellent potential for miniaturization. New technology has been developed for this instrument that enables the execution of tandem mass spectrometry (MS/MS) experiments. This technique provides a faster, more sensitive, more direct solution to many monitoring applications. The expert system provides real-time, on-line, and autonomous execution of a "user-designed" analysis strategy. It provides specialized knowledge for decision making, integrated processing software for mass spectral data, and intelligent feedback for formulating new analysis goals.

This system is currently configured for air monitoring applications. The new technology represented by the MS/MS capability has been successfully demonstrated for direct monitoring of specific toxic compounds and greenhouse gases. The system is also being used to monitor individual contaminants in a closed environment, to explore the effects of various trace-level contaminants on plant growth, and to study anthropomorphic and biogenic emissions of hydrocarbons into the atmosphere.

Ames-Moffett contact: P. Palmer
(415) 604-3615
Headquarters program office: OAST

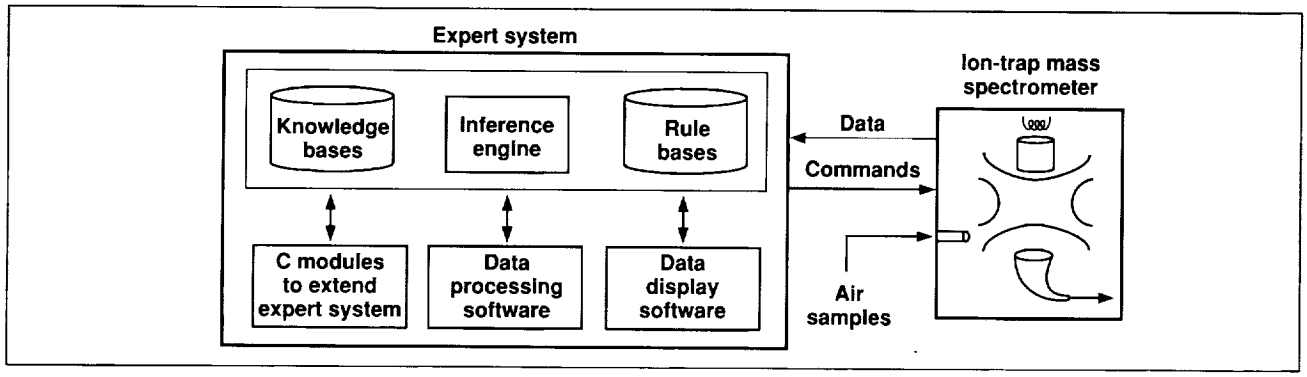

Fig. 1. Advanced chemical monitoring system based on an ion-trap mass spectrometer and an expert system for autonomous air monitoring applications.

Oregon Transect Ecosystem Research Project

David L. Peterson

The Oregon Transect Ecosystem Research (OTTER) project was a NASA effort to study ecosystem structure and function using remote sensing and computer simulation of a broad span of coniferous forests in west-central Oregon. The project's main goals were to predict the major fluxes of carbon, nitrogen, and water through forest ecosystems across a transect of six research sites from the coastal forests of central Oregon to the dry, desert forests of the interior. This 300-kilometer transect covers virtually the entire range of forest processes and tree sizes one encounters in coniferous forests worldwide. The project was brought to a successful conclusion in 1992 with special editions of two journals, the *Journal of Ecological Applications* and *Remote Sensing of Environment*, and the publication of a series of CD-ROM disks to provide copies of the OTTER data from the six sites for further scientific study.

The OTTER project used a combination of computer simulation models, radiative transfer models, field data collection, and remote sensing to accomplish its goals. In earlier research, a mechanistic ecosystem process model driven by parameters extracted from remotely sensed data of all types was developed. In OTTER, a multidisciplinary team of scientists from the United States and Canada sought to validate this model for the six sites studied. A large, multiyear campaign was conducted to acquire data during the four principal seasons that affect plant growth processes in Oregon: the dormant period in winter before the outbreak of new leaf buds (February and March), the period of wet soils and full leaf development (May to June), the period of seasonal drought (August), and the period of leaf senescence (October). During each period, for two years, an extensive set of remote sensing data were collected by sensors flying aboard most of NASA's fleet of aircraft for Earth observations (two ER-2s, a C-130, and a DC-8) and also from aircraft of cooperators—an ultralight aircraft from Oregon State University and light aircraft from Canada and the United States. Satellite data from the National Oceanic and Atmospheric Administration's Advanced Very High Resolution Radiometer were also used. These sensors included synthetic aperture radar, thematic mapper simulators, high- and very-high-spectral-resolution optical imagers, thermal infrared scanners, bidirectional multispectral imagers, and various other instruments. This effort resulted in a digital data base of over 15 gigabytes of ground, meteorological, remote sensing, and simulation data.

The OTTER Project involved many scientists and was coordinated by Ames and Oregon State University. Reports of specific accomplishments from OTTER appear elsewhere in this report. The project showed that through a combination of field observations, remote sensing, and modeling, each of the principal controls on ecosystem processes, such as net photosynthesis, respiration, and evapotranspiration, could be successfully measured.

Ames-Moffett contact: D. Peterson
(415) 604-5899
Headquarters program office: OSSA

Evolution of Biological Carbon Fixation

Lynn J. Rothschild

Biological carbon fixation (primary production) was a crucial innovation in early evolution because it liberated life from abiotically produced organic carbon. Biological carbon fixation permitted the development of the biogeochemical carbon cycle, the evolution of a complex community structure among living organisms, and, indirectly, the formation of an aerobic environment on Earth through oxygenic photosynthesis. Both morphological fossils and the stable carbon isotope record suggest that biological carbon fixation arose very early in the evolution of life, at least by 3.5 billion years ago. Oxygenic photoautotrophy (performed by organisms that do photosynthesis), the subject of this research, may have evolved as early as 2.9 billion or possibly even 3.5 billion years ago.

The goal of this research is to reconstruct patterns of photosynthesis that were present in ancient microbial systems. This is accomplished by studying photosynthesis in extant microbes under modern conditions as well as in the presence of elevated levels of carbon dioxide. Models of the atmosphere of early Earth suggest that atmospheric carbon dioxide levels were several orders of magnitude higher than they are at present, and atmospheric carbon dioxide levels are currently rising.

Two types of model systems are under study. Microbial mats are thought to be modern analogs for fossil stromatolites. The mats are found in a hypersaline pond in the marine intertidal (Baja California), and in acidic springs (Yellowstone National Park). The composition of the mats studied ranged from prokaryotic to eukaryotic. Studies in fiscal year 1992 supported our previous work showing that in these mats, the diurnal pattern of carbon fixation is influenced primarily by the availability of light and inorganic carbon, and secondarily by the availability of nitrogen. Total daily carbon fixation is strongly influenced by both the availability of carbon and the average temperature.

Work on a second type of model system involved laboratory cultures of eukaryotic algae. Several species of marine phytoplankton, including red algae, cryptomonads and coccolithophores, were cultured under elevated levels of carbon dioxide. In all cases, growth rate was enhanced by raising the level of carbon dioxide above average oceanic levels. If other nutrients are not limiting in nature, this work implies that carbon dioxide at levels higher than now present would enhance the primary productivity of phytoplankton.

Ames-Moffett contact: L. Rothschild
(415) 604-6525
Headquarters program office: OSSA

Oxygen Evolution and Life on Mars

Lynn J. Rothschild

One of NASA's missions is to look for evidence of life elsewhere in the solar system. Mars is considered the most promising planet. Because of the hypothesized similarities in the environments of Earth and Mars in their early histories, a Martian biota probably would be based on organic carbon.

The major by-product of most types of carbon fixation on Earth is oxygen. As a result of photosynthesis, the most widespread type of biological carbon fixation, the Earth became aerobic. The ultimate goal of this project is to map the concentration of oxygen over the surface of Mars in order to understand the subsurface. We expect that such a map would be useful for Mars exploration in several respects. Relatively high levels of oxygen may be indicative of biological activity. Oxygen is a vital resource for human exploration; thus, the results of the oxygen survey of Mars would be useful in selection of sites for human exploration. The Viking Gas Exchange Experiment showed that humidifying the Martian regolith at the Viking lander sites released oxygen. In an indirect way, local concentrations of near-surface oxygen could be indicative of increased humidity. Water is also of interest for exobiological and human explorations of Mars. Finally, data on carbon fixation under Martian conditions, especially in Martian concentrations of carbon dioxide, will be of importance in food and oxygen production on Mars in conjunction with human exploration.

In fiscal year 1992, studies were completed on this project. We identified two partial model systems for extant life on Mars; we showed that carbon fixation increased in these systems under conditions of elevated carbon dioxide such as would be encountered on the surface of Mars, and that oxygen evolution as an indicator of photosynthetic activity can be easily detected in the gas near plants.

If life were present on Mars today, it would face potentially lethal environmental conditions such as a lack of water, frigid temperatures, ultraviolet radiation, and soil oxidants. In addition, the Viking missions did not detect any near-surface organic carbon for assimilation. Autotrophic organisms that lived under a protective layer of sand or gravel would be able to circumvent the ultraviolet radiation and lack of fixed carbon. Two photosynthetic near-surface microbial communities were identified, one in the inter- and supertidal of Laguna Ojo de Liebre (Baja California Sur, Mexico) and one in the acidic gravel near several small geysers in Yellowstone National Park. Both communities were studied with respect to their ability to fix carbon, including in the presence of elevated levels of inorganic carbon. Carbon fixation was much less than what would be expected from a similar area of grass, but was, nonetheless, significant. There was an immediate and dramatic increase in carbon fixation rate when supplemental inorganic carbon was added at midday. Whereas these sand communities were not exposed to the entire suite of Martian environmental conditions simultaneously, such communities can provide a useful model ecosystem for a potential extant Martian biota.

Oxygen evolution was measured directly for two photosynthetic organisms. The author and student Jeff Mulatto were able to easily detect oxygen evolution over grasses by using a hand-held oxygen probe. Next, samples were preincubated in the dark for one to several hours, during which time oxygen was consumed, thus increasing the signal-to-noise ratio.

The results show that carbon fixation, and thus oxygen evolution, can occur in subsurface (sand) communities in the absence of standing water. This suggests that the levels of oxygen at the surface of these communities may be higher than ambient levels. We found that oxygen evolution by photosynthetic organisms can be easily monitored. The signal was greatly enhanced by a short preincubation in the dark. These results are important for both exobiology and future human exploration of Mars.

Ames-Moffett contact: L. Rothschild
(415) 604-6525
Headquarters program office: OSSA

Global Monitoring and Human Health

Michael Spanner, Byron Wood, Louisa Beck

In 1982, there were an estimated 250 million malaria cases globally. Nearly half of the world's population lives in areas where ongoing antimalaria activities are being conducted. According to the World Health Organization, global malaria has increased significantly over the past 15 years, and factors that have influenced this increase include reduced funding and manpower for control, increased resistance of the mosquito vector to insecticides, and the appearance of drug-resistant forms of malaria. Near-real-time data on the temporal and spatial dynamics of the vector populations are required for effective disease control.

The Global Monitoring and Human Health Program at Ames Research Center consists of three projects: Di-Mod, Flight Opportunities, and Outreach. Di-Mod, a phased, multiyear research project, was initiated by NASA to develop predictive models of vector population dynamics and malaria transmission risk using remotely sensed data and geographic information systems (GIS). The first phase of Di-Mod, completed three years ago, focused on identifying high-mosquito-producing rice fields in California; the second phase centers on malaria transmission risk in southern Chiapas, Mexico. As part of the current research, a land-cover map of Chiapas was produced from Landsat Thematic Mapper data. The land covers identified are those associated with various stages of the life cycle of the malaria vector, the mosquito *Anopheles albimanus*: pastures, where mosquitoes acquire blood meals from cattle; floodable pastures, which provide larval habitat; and trees, which offer resting sites for the blood-engorged mosquitoes. Spatial modeling techniques are being used to evaluate the relationship between land cover and mosquito abundance. The temporal aspect of mosquito abundance with respect to rainfall patterns is also being analyzed, using current rainfall data.

The goal of the Flight Opportunities project is to develop design criteria for a remote sensing system (Medsat) dedicated to disease surveillance, and to prepare a strategy for identifying, equipping, and training people in developing countries to use remote sensing data for disease surveillance. During the past year, Ames has supported engineering studies at the University of Michigan to design a small, light-weight, synthetic-aperture radar for Medsat. Also, the University of Texas, El Paso, has received a grant from NASA's Office of Minority Programs to support research on sensor fusion that can be applied to the processing, analysis, and modeling of large multispectral data sets.

The major goal of the Outreach project is to promote the use of remote sensing and GIS in monitoring and predicting the spatial patterns of vector-borne diseases. Several collaborative studies are under way. Ames is working with investigators at the University of California, Davis, to extend Di-Mod Phase I results to other rice-growing regions. Ames is also collaborating with researchers from the New York Medical College to develop a predictive model of Lyme disease transmission risk in suburban New York. In addition to these studies, Ames investigators are participating in International Space Year activities to promote the use of remote sensing in environmental assessment and global change studies. Finally, a National Research Council fellowship for disease modeling is being established at Ames.

Ames-Moffett contact: M. Spanner
(415) 604-3620
Headquarters program office: OSSA

Hapex-II/Sahel Experiment

Michael Spanner, Robert Wrigley, Rudolf Pueschel

The goal of the Hydrological Atmospheric Pilot Experiment (Hapex)-II/Sahel Experiment is to understand the interactions between the land surface and the atmosphere. The study area for this research is the Sahel region of the country of Niger, in the western sub-Sahara. The Sahel region is a transitional zone between the arid Sahara desert in the north and the tropical rainforest in the south. The major focus of the Hapex-II/Sahel Experiment is to study the effect of climate on vegetation and the effect of vegetation on climate, and to monitor these effects using remotely sensed data. The intensive observation period began in mid-August and ended at the end of September in 1992.

Ames' participation in the experiment involved the Airborne Tracking Sun Photometer on the NASA C-130 aircraft and a field-portable Sun Photometer deployed at several of the study sites. The Sun Photometers measured solar radiation in the visible through near infrared wavelengths. The measurements will be used to calculate the amount and properties of aerosols that were in the atmosphere during the experiment. Specifically, the aerosol optical depth, the single-scattering albedo, and the phase function of the aerosols will be calculated. This information is important because the amount and properties of the aerosols have an influence on the climate of the Earth and they also affect remotely sensed data acquired from aircraft and spacecraft platforms. The aerosol data will be used in a radiative transfer model to atmospherically correct remotely sensed data collected during the experiment.

Ames-Moffett contact: M. Spanner
(415) 604-3620
Headquarters program office: OSSA

Biophysical Information in Asymmetric and Symmetric Diurnal Bidirectional Canopy Reflectance

Vern C. Vanderbilt

We developed a new theory for partitioning the information content in diurnal measurements of the bidirectional reflectance of the vegetation canopy in order to detect differences that may be related to biophysical variables. The theory, which divides the canopy reflectance into asymmetric and symmetric functions of solar azimuth angle, attributes asymmetric variation to diurnal changes in the biophysical properties of the canopy.

Conversely, the symmetric function is attributed to the effects of sunlight interacting with a hypothetical "average canopy" which would display the average diurnal properties of the actual canopy—the average canopy architecture and the average spectral scattering properties of the foliage and soil. Although the theory can be applied to many types of canopies, the analysis described here requires that the canopy architecture be symmetrical or mirror symmetrical about a vertical north–south plane.

As a first application of the theory, we analyzed radiometer data collected diurnally in the Thematic Mapper wavelength bands from two walnut canopies that received differing irrigation treatments. The reflectance of the canopies varied with sun and view angles and across seven bands in the visible, near-infrared, and middle-infrared wavelength regions.

Even though one of the canopies was permanently water stressed and the other was stressed in mid-afternoon each day, no water stress "signature" was unambiguously evident in the reflectance data. The observed diurnal reflectance changes appeared to be primarily, but not exclusively, attributable to the changing angle of solar illumination interacting with the canopy, an architecturally rough surface.

Ames-Moffett contact: V. Vanderbilt
(415) 604-4254
Headquarters program office: OSSA

Studies of Stratospheric Trace Gases

James F. Vedder

This work is part of a joint effort of Ames Research Center and the National Center for Atmospheric Research (NCAR). The NCAR is funded separately by NASA Headquarters. Since its participation in the Airborne Arctic Stratospheric Expedition (AASE) in 1989, the Whole-Air Sampler for the ER-2 research aircraft has been modified to carry 29 sampling canisters (the original instrument carried 14 canisters). This year, the Whole-Air Sampler was one of the instruments on the ER-2 aircraft during the missions of the AASE II. The missions were based at Eielson Air Force Base, Alaska, in October 1991, and at Bangor, Maine, from November 1991 through March 1992. In contrast to the previous polar missions, the Airborne Antarctic Stratospheric Experiment (AAOE) and the AASE, which made measurements during single seven-week periods, the AASE II missions made measurements over the lifetime of the polar vortex, from formation to dissipation. As many as 29 pressurized samples of air were collected on each flight. In addition to the flights northward into the vortex, there were ferry flights and flights southward. Thus samples were obtained from inside and outside the vortex as it developed and from middle and low latitudes. The canisters with the air samples from each flight were shipped immediately to NCAR for analysis of about 30 trace gases by gas chromatography.

The results from the previous missions (AAOE and AASE) are being used in a number of ways. The age of the air inside the vortex relative to that outside and relative to the time of entry into the stratosphere from the tropical troposphere has been determined from the measurements of trace gases such as carbon dioxide and chlorofluorocarbon-115 (CFC-115), which have very long stratospheric lifetimes and known annual rates of increase in the troposphere. The results indicate an age of about four years for air within the vortex. Additional analyses and inclusion of the recent measurements are providing ages as a function of altitude and time. Knowledge of the age of the air is important for evaluating the accuracy of the predictions of the models of the atmosphere and for determining the potentials of anthropogenic gases for depletion of stratospheric ozone. Relative to this depletion, some of the new constituents replacing the damaging CFCs are appearing in measurable amounts in the air samples from the stratosphere. Accurate prediction of their effects requires knowledge of the age of the air.

The amount of chlorine and bromine in various chemical states in the stratosphere is a key factor in the depletion of ozone. The data from the Whole-Air Sampler include measurements of trace gases carrying about 99% of the organic chlorine and about 99% of the organic bromine into the stratosphere. There, these gases are photolyzed and the chlorine and bromine are freed to catalytically destroy ozone. The amounts of chlorine and bromine available for the destruction of ozone are determined from the total amounts of these elements in the gases entering the stratosphere at the time indicated by the age of the air less the amount in the organic constituents measured by the air sampler.

Ames-Moffett contact: S. Wegener
(415) 604-6278
Headquarters program office: OSSA

ECOSAT Computational Facility for Biospherics and Terrestrial Ecosystems

Kenneth Weinstock, Mathias Ma, Rita Pettigrew

The capabilities of the Ecosystem Science and Technology (ECOSAT) Branch's Computational Facility (ECF) for Biospherics and Terrestrial Ecosystems were upgraded during 1992. A major acquisition was ERDAS software (IMAGINE 8.0.1 and ERDAS 7.5) to provide image processing and raster-based geographic information system (GIS) functionality on five of the UNIX-based workstations. This new software should facilitate the transition of image processing functions to the UNIX workstations from the present VAX/IDIMS system, which is scheduled for retirement at the end of 1993.

A Silicon Graphics IRIS Crimson Elan system was acquired for visualization and high-end graphics applications (funded by the U.S. Geological Survey). An additional 8 gigabytes of disk storage was added to the Sun SPARCstation systems devoted to image processing. A CD-ROM reader was installed on the ECF 486/PC which now allows compact discs to be read on most ECF systems, including Macintosh, SPARCstation, SGI and PC-compatible systems. An exabyte 8500 8-millimeter tape drive and a 150-megabyte, 1/4-inch cartridge tape drive were acquired for system backup and data archiving on the SPARCstations.

Software packages added to the ECF include the GRID module for raster-based GIS processing within the ARC/INFO software environment. Major upgrades include ARC/INFO GIS software to version 6.0, PV WAVE visualization and data analysis to version 4.0, and KHOROS image-processing software to patch level 5.

Ames-Moffett contact: K. Weinstock
(415) 604-3327
Headquarters program office: OSSA

Computer Modeling of Clouds

Douglas L. Westphal

In November and December 1991, NASA conducted a field program called the First International Satellite Cloud Climatology Project Regional Experiment, Phase II (FIRE-II) in Kansas and Oklahoma with a goal of obtaining a better understanding of the life cycle of the high-tropospheric clouds called cirrus clouds. These clouds are widespread and play an important role in the Earth's climate system by modulating the radiation balance. Relatively small changes in the clouds' morphology can determine whether the atmospheric column containing a cloud experiences heating or cooling. This sensitivity is very important in considerations of the possibility of greenhouse warming. The FIRE-II field program was needed because cirrus clouds are poorly understood, difficult to detect by satellite, and difficult to model with computers.

During the past year, we have used the data collected from the ground, aircraft, and satellites during the FIRE-II field program to develop better computer models of cirrus clouds. Despite advances in supercomputers, climate modelers cannot model individual clouds but instead must rely on simplified treatments of clouds in the computer models. One set of data from the field program is used as a guide in developing these treatments, or parameterizations, and another independent set of data is used to verify the accuracy of the parameterization. At present we are studying three different cloud parameterizations

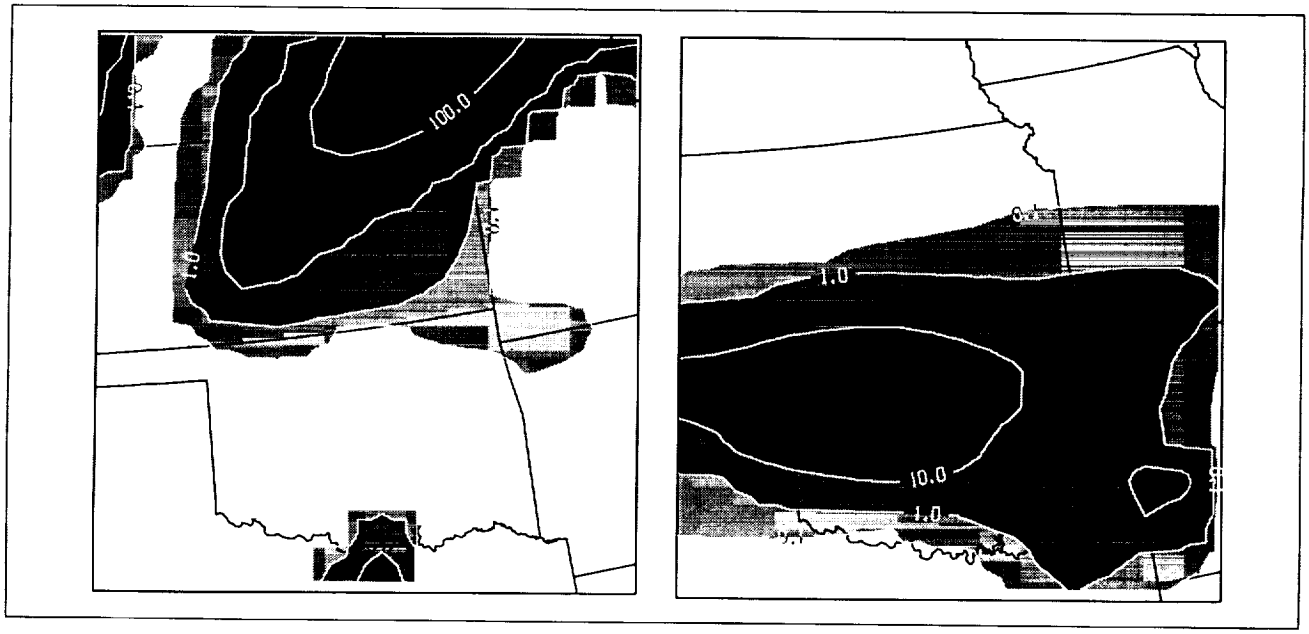

Fig. 1. Computer simulations of cirrus clouds over the southern Great Plains, of mid-latitude origin (left, 10:00 a.m. CST, November 26, 1991) and subtropical origin (right, 1:00 a.m. CST, December 16, 1991).

within the same weather forecast model and intercomparing the cloud simulations from the different versions of the forecast model.

During FIRE-II the cirrus clouds observed over Kansas were generated as far away as Washington and Mexico, or as nearby as western Kansas. The dynamical forcing, morphology, and climatic impact of the cirrus clouds for these cases are vastly different. This diversity is invaluable in verifying the robustness of the cloud parameterizations.

As an example of the diversity, the figure shows the predicted cloud fields over the southern Great Plains during a case of local generation of mid-latitude cirrus clouds (left figure) and during an occurrence of subtropical cirrus clouds originating in Mexico (right figure). The plotted variable is the clouds' visible optical depth, which is a radiative measure of the amount of cloud that is present. We see that the mid-latitude cirrus clouds are ten times thicker (radiatively) than the subtropical cirrus clouds. The altitudes of the clouds (not shown) are also quite different; the subtropical cirrus clouds are more than a kilometer higher than the mid-latitude clouds. The two types of cirrus clouds will have vastly different effects on climate. Using measurements made during FIRE-II we are evaluating the ability of the models to reproduce the observed properties of these subtropical and mid-latitude cirrus clouds.

Ames-Moffett contact: D. Westphal
(415) 604-3522
Headquarters program office: OSSA/DOE

Prediction of Lyme Disease Risk: A Remote-Sensing Model Based on Landscape Epidemiology

Byron L. Wood, Louisa R. Beck, Sheri L. Dister

Lyme disease, a spirochetal infection transmitted by *Ixodes* ticks, is currently the most prevalent, widely distributed, and rapidly increasing vector-borne disease affecting human health in the United States and the north temperate regions of the world. The disease was first recognized in Lyme, Connecticut, in 1972 and is now reported in 43 states, although more than 80% of the cases are concentrated in suburban areas along the Northeastern coast. The degree of contact between humans and ticks influences the patterns of transmission risk. Currently, the landscape of many Northeastern suburban areas is characterized by an urban-to-rural gradient which facilitates various degrees of contact. Remote-sensing and geographic-information-system (GIS) technologies provide efficient means of identifying, monitoring, and modeling environmental or landscape features associated with human–tick contact.

The goal of our research is to combine remote-sensing characterizations of landscape elements with field and laboratory measurements to spatially predict Lyme disease transmission risk in Westchester County, New York. The results of field studies suggest that canine exposure to the Lyme disease spirochete is a sensitive method for assessing human risk. Canine exposure was not uniform in these studies, but increased by municipality from south to north along an urban-to-rural gradient. Our study used remote-sensing data to quantify this gradient, and then related land cover by municipality along the gradient to positive canine seroprevalence.

The key landscape elements in the urban-to-rural gradient were deciduous forest; residential sparse, medium, and high vegetation; and urban elements. These landscape elements demonstrated the largest percent differences in area, by municipality, between the northern and southern portions of the county. Our results indicate that, of the land covers studied, the proportion of deciduous forest in an area in this suburban environment is the most powerful indicator of Lyme disease transmission risk at the municipality level, as measured by canine seroprevalence rates. The lowest canine seroprevalence rates occurred where residential sparse and medium vegetation classes had replaced deciduous forest or reduced it to small isolated patches in the southern part of the county. The highest canine seroprevalence rates occurred in the northern part of the county, where residential areas were interspersed throughout the deciduous forest. An analysis of edges between the residential high vegetation and deciduous forest classes followed the spatial pattern of the increasing canine seroprevalence data along the urban-to-rural gradient. Linear regression analysis of the residential high vegetation proportions (with more than seven contiguous deciduous pixels) versus canine seroprevalence showed a high correlation ($r = 0.84$). The results of this investigation have demonstrated that remote sensing and epidemiological data can be integrated in a GIS to determine correlations between land cover and canine infection rates and therefore to predict Lyme disease transmission risk along an urban-to-rural gradient.

This research is supported by the NASA Ames Director's Discretionary Fund. Durland Fish of the New York Medical College, Valhalla, New York, is a co-investigator in the project.

Ames-Moffett contact: B. Wood
(415) 604-4187
Headquarters program office: DDF

High-Resolution Microwave Survey Observations

Peter R. Backus

The High-Resolution Microwave Survey (HRMS) is a search for radio signals produced by technological civilizations that may exist on distant planets. The HRMS is part of the Toward Other Planetary Systems (TOPS) Program in the Solar System Exploration Division. Over the past 32 years there have been more than 50 attempts to find evidence of such signals. The HRMS is the most advanced and comprehensive search of its kind ever conducted. In the first few minutes of operation on October 12, 1992, the HRMS surpassed the combined efforts of all previous searches.

The HRMS is divided into two complementary search strategies, the Sky Survey and the Targeted Search. The Sky Survey, operated by the Jet Propulsion Laboratory, scans the entire sky for strong signals in the range of frequencies from 1 to 10 gigahertz. The Targeted Search achieves high sensitivity to continuous wave (CW) and pulse signals that may drift in frequency by as much as 1 hertz per second by searching a narrower range of frequencies, from 1 to 3 gigahertz, and focusing on about 1000 nearby sun-like stars. The Targeted Search is operated by Ames Research Center, which also is the lead center for the HRMS. On October 12, both search modes began their observational phase. The Sky Survey began at the new 34-meter "Venus" antenna at NASA's Goldstone Deep Space Communications Complex in the Mojave desert. Simultaneously, the Targeted Search inaugurated observations at the world's largest radio telescope, the 305-meter antenna of the Arecibo Observatory in Puerto Rico.

During the past year, the Targeted Search team worked on completing and integrating the special-purpose computers and electronics that make up the Targeted Search System (TSS). The TSS can be thought of as a supercomputer designed to automatically detect faint signals. As deployed to Arecibo, it performs about 30 billion floating point operations per second. This capability will be increased.

At Arecibo, the TSS converted a 10-megahertz-wide portion of the output of the observatory's receivers in two polarizations into a form needed by the Multichannel Spectrum Analyzer (MCSA). The MCSA divided the input bandwidth into more than 14 million simultaneous channels, each 1 hertz wide, measuring the power in all channels every 0.7 second. The 28 million power measurements were then sent to the CW signal detector which searched for continuous signals within the range of possible frequency drift rates. At the same time, the MCSA processed the same data into channels with resolutions of 7 and 28 hertz. The power values in the channels for all resolutions were compared to a "threshold" value. Channels with power greater than the threshold were sent to the Pulse Detector which searched for regularly spaced pulses within the drift limits. The entire TSS was controlled by a system of communicating software processes running on a powerful workstation, which configured the TSS, pointed the telescope, and evaluated signals reported by the detectors.

In order to take advantage of the largest available radio telescopes (e.g., Arecibo), the TSS is packaged in a Mobile Research Facility (MRF). The MRF is a radio-frequency-shielded, air conditioned container on a special flatbed trailer. The MRF has features that allow it to be transported on military cargo aircraft. On September 15, the MRF was loaded onto a C-141 Starlifter and flown to Puerto Rico. Observations at Arecibo focused on a list of 25 stars within 100 light years. The observatory's receivers provided four frequency bands covering a total of about 300 megahertz (MHz) within the range of 1300 to 2400 MHz. Each "observation" of a star in a 10-MHz bandwidth consisted of three steps: pointing the antenna at the star, then pointing it away from the star, and then pointing it back at the star. Each observation step lasted either 92 or 299 seconds. Signals detected only when the telescope was pointed at the star were considered potential extraterrestrial signals and were subjected to further tests. Signals detected both "on" and "off" the star were deemed to be terrestrial interference. A total of 436 observations were conducted during the 200 hours of assigned telescope time. A large number of interference signals

were detected and cataloged. A few signals required further tests, but all proved to be intermittent terrestrial signals. No signals from beyond our solar system have been detected yet.

The first spinoff from the HRMS is well under way. The concept of life in the universe is being used as the central theme for supplementary science curriculum materials for grades three through nine. These materials, developed in summer workshops by local teachers, are now being tested in schools around the country, and reports are encouraging. Full nationwide distribution will occur next year, with international distribution to follow. This million-dollar, three-year program is funded by the National Science Foundation (70%) and NASA (30%).

Ames-Moffett contact: D. Brocker/L. Webster
(415) 604-3650/6726
Headquarters program office: OSSA

Urinary Calcium Excretion in Human Models for Spaceflight

Sara B. Arnaud, Meena Navidi, I. Wolinsky

An increase in the excretion of calcium in the urine occurs regularly during spaceflight and in human bed-rest models. There are a number of explanations for this. One is that more calcium is released from bone when the bone is subjected to reduced biomechanical loads. The kidney is then required to filter an increased amount of calcium. Almost all of this bone mineral is normally returned to the general circulation by reabsorption in the renal tubules. Renal calcium reabsorption is regulated by parathyroid hormone, primarily. The release of calcium from bone suppresses this hormone and its action on the kidney. Less calcium reabsorbed means more calcium excreted. This process, referred to as bone-resorptive calciuria, is very sensitive to changes in the calcium endocrine system.

A second potential cause of calciuria is a large amount of salt in the diet. It has been recognized for many years that high dietary salt intake is associated with increased excretion of calcium, which is transported through the kidney in an obligatory fashion with the excess sodium. For 7 days, we analyzed 24-hour urine specimens from eight adult male bed-rest subjects on diets containing high normal levels of sodium (190 millequivalents per day). Urinary excretion levels of calcium and sodium were parallel in the first few days of bed rest, when fluid shifts occur in the head-down-tilt model. Calcium excretion remained elevated and sodium excretion returned to pre-bed-rest level at the end of the week. A second bed-rest study, lasting 30 days, in which the amount of dietary salt consumed by 11 male volunteers was restricted to 110 millequivalents per day, revealed no significant increase in the excretion of urinary calcium. Dietary calcium in both bed-rest studies was the same. Concentrations of parathyroid hormone in the blood were depressed in the 7-day study, promoting calciuria, and were unchanged in the 30-day study, preventing increases in urinary calcium.

A third explanation for increased urinary calcium excretion during spaceflight is an increase in the level and activity of adrenal hormones as a result of endocrine or physiologic stress. This phenomenon was reflected by the increase in cortisol in the urine of astronauts during the Skylab missions. Steroid-induced increase in urinary calcium is thought to be related primarily to increased bone resorption, a mechanism similar to the first described above. However, the endocrine regulator of urinary calcium excretion, parathyroid hormone, is more likely to be elevated than suppressed when the adrenal gland is overactive.

The likelihood that all three mechanisms for calciuria are actively promoting calcium loss in the same individuals during spaceflight is high. To determine the interaction of these mechanisms, their effect on bone, and their manifestations and prevention, the hind-limb-suspension flight simulation model in the rat is being used.

Ames-Moffett contact: S. Arnaud
(415) 604-6561
Headquarters program office: OSSA

Skeletal Asymmetry in Bending Stiffness of the Human Tibia

Sara B. Arnaud, Teresa M. Hutchinson

Highly localized decreases in mineral concentrations in the weight-bearing bones of astronauts and animals are found after spaceflight. The extent to which mineral deficits in leg bones affect the support function of the bone and impose a risk for fracture is uncertain. A newly designed instrument that has been successfully used to determine the bending stiffness (EI) of the ulna has been used to measure the material properties of the tibia. For bone, E is a reflection of its chemical composition, primarily its mineral content, and I, the bending moment of inertia, its geometry.

The Mechanical Response Tissue Analyzer (MRTA) was originally developed by D. Young of Ames and C. Steele of Stanford University. The noninvasive instrument, designed for clinical testing by Gait Scan, Inc., of Ridgewood, New Jersey, was used to test the tibias and ulnas of healthy men to acquire normative data as a base for post-flight measurements. We studied 48 men, aged 38.3 ± 7 years, who weighed 78.7 ± 8 kilograms. Thirty-nine were right-handed and nine were left-handed. Each subject rested the proximal and distal ends of the limb to be tested (forearm or lower leg) on comfortable supports. A low-frequency vibratory stimulus lasting a few seconds was delivered, through a probe, to the skin surface at the center of the long bone. The resonant response was detected at the same site and analyzed by a seven-parameter algorithm. The mineral density in the ulna was determined, in the proximal third of the bone, by a densitometer (Norland), and the density of the tibia (the entire area) by dual photon absorptiometry (Hologic, Inc.).

The results (mean ± SD) for mineral density and bending stiffness in the ulnas and tibias are given in the table.

We found significantly higher values for EI in the right than in the left ulna and higher stiffness in the left than in the right tibia. It is significant that this measurement picked up differences in the physical properties of bones with the same mineral density. These observations illustrate the importance of bone geometry as well as mineral content in evaluating stiffness, a measure of bone strength. It is clear that chronic under-use of the left arm in right-handed men accounts for its lower bending stiffness. Higher bending stiffness in the left tibia may be related to the common practice in bipeds of supporting body weight on one side rather than equally. To our knowledge, skeletal asymmetry in bone material properties of the human tibia has not been previously documented.

Ames-Moffett contact: S. Arnaud
(415) 604-6561
Headquarters program office: OSSA

Table 1. Mineral density and bending stiffness of the ulna and tibia

	Tibia		Ulna	
	R	L	R	L
Stiffness (EI), Nm^2	159 ± 5	174 ± 6*	48 ± 11	42 ± 9**
Mineral density, g/cm^2	1.415 ± 0.15	1.393 ± 0.13	0.882 ± 0.08	0.876 ± 0.08

*$p < 0.05$
**$p < 0.01$

Intramuscular Pressure and Joint Torque During Concentric and Eccentric Exercise

Richard E. Ballard, Alan R. Hargens

It is well known that eccentric muscular activity (lengthening of muscle fibers during activation) generates higher tensile force than concentric muscular activity does and consequently may be important for prevention of muscle atrophy in space. However, the mechanism responsible for this higher eccentric force is not known. Investigators have proposed various biomechanical, biochemical, and neurophysiological mechanisms to explain the force-generation differences between the two muscular activities. Intramuscular pressure (IMP), the fluid pressure created as a muscle contracts within its fascial compartment, correlates linearly with contraction force; this correlation may provide valuable insights into the mechanisms of these dynamic muscle actions. This study was undertaken to relate joint torque and IMP to joint angle (muscle length) during concentric and eccentric exercise of the soleus (SOL) and tibialis anterior (TA) muscles of humans.

Pressures in the SOL and TA were continuously recorded during maximum voluntary concentric and eccentric isokinetic contractions in nine healthy male volunteers (aged 28–54). The IMP was measured using a small saline-filled catheter inserted into the muscle under local anesthesia. A Lido Active isokinetic dynamometer provided resistance for exercise while ankle joint position and torque were measured.

In the SOL muscle (first figure), the angle at which peak torque was achieved during concentric activity (11 ± 1 degrees (mean ± SE)) was significantly different than the angle of peak torque during eccentric activity (18 ± 2 degrees). In all nine subjects, during eccentric contraction, peak torque and IMP occurred at the end of the contraction, when the muscle was fully stretched. During concentric SOL contractions, peak IMP occurred at a lower joint angle (3 ± 1 degrees) than peak torque. No significant joint angle differences at peak torque were observed between concentric and eccentric contractions of the TA.

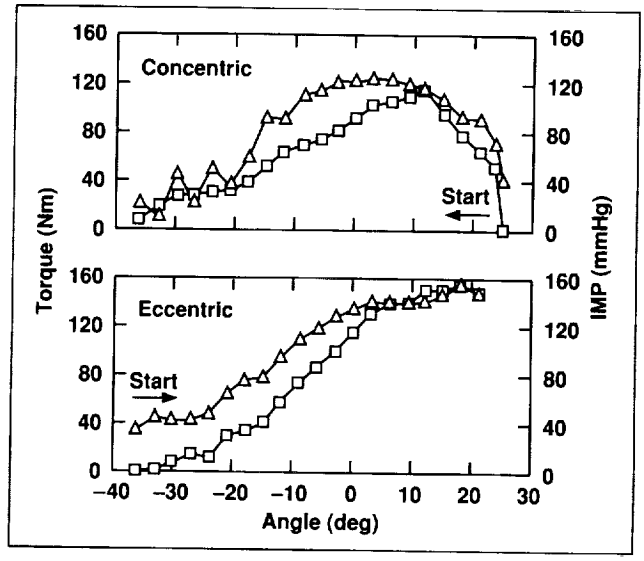

Fig. 1. Torque (squares) and IMP (triangles) during concentric and eccentric SOL activity. Positive joint angles represent dorsiflexion, negative joint angles indicate plantarflexion, and zero is defined as a 90-degree angle between the foot and the tibia.

Why did peak eccentric forces occur at a greater muscle length than peak concentric forces in the SOL but not in the TA? One possible explanation is that full dorsiflexion of the foot (as occurs at the end of eccentric SOL action) is limited primarily by passive tension of the SOL and gastrocnemius muscles. This increased passive tension leads to greater force late in the contraction, when fiber pennation angle is acute. Full plantarflexion, as occurs at the end of eccentric TA action, however, may be limited not by TA stretch but by calcaneus, tibia, and surrounding soft-tissue compression. Other possible explanations may relate to morphological and architectural differences between the two muscles.

At short muscle lengths, IMP per unit torque is generally greater than it is for long muscle lengths. The increased tensile forces and lower IMPs may be

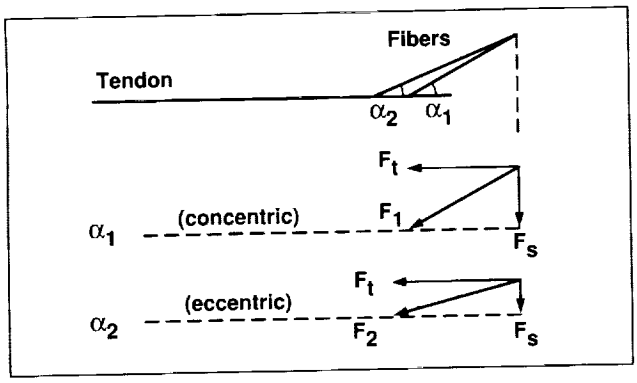

Fig. 2. The angle α_1 represents the fiber pennation angle in a shortened muscle, and α_2 is the pennation angle in a lengthened muscle. The tensile force (F_t) is transmitted to the muscle tendon during muscular activity. Theoretically, the stress (F_s) within each muscle fiber generates intramuscular pressure. F_1 and F_2 are the total tensions on the fibers.

explained, at least in part, by differences in fiber pennation angle (second figure). Because of the relatively low pennation angle (α_2) in the fully lengthened muscle, tensile force is transmitted to the tendon more effectively than it is in a shortened muscle. This mechanism of transmitting stress to the tendon is possibly required in order to avoid damage to joints and soft tissue as a result of the higher forces found in eccentric activation of the soleus. A more complete understanding of the mechanism of eccentric-force generation will aid in the development of exercise countermeasure hardware and protocols for spaceflight.

Ames-Moffett contact: R. Ballard/A. Hargens
(415) 604-5747/5746
Headquarters program office: OSSA

Regional Microvascular Bloodflow During Gravitational and LBNP Stresses

Gregory A. Breit, Donald E. Watenpaugh, Richard E. Ballard, Gita Murthy, Alan R. Hargens

In astronauts, the most significant cardiovascular event during the transition to microgravity is a major redistribution of blood pressure along the length of the body. We are investigating lower-body negative pressure (LBNP) as a means of restoring the blood pressure distribution and musculoskeletal loads to levels normal for upright activity on Earth. Because the regional regulation of microcirculatory bloodflow is highly sensitive to changes in local blood pressure, we compared the relative effects of LBNP and whole-body tilting on the distribution of microvascular bloodflow along the length of the body. Nine human subjects underwent corresponding tilting and LBNP protocols. For whole-body tilting, subjects were initially placed in a supine position (0 degrees) on an electric motorized tilt table. At 30-second intervals, subjects were tilted to 12, 24, 37, 54, 90, 54, 37, 24, 12 degrees, and back to 0 degrees. For negative-pressure sessions, subjects were placed in a supine position in the LBNP chamber, which was sealed at the subject's waist. At 30-second intervals, subjects underwent 20, 40, 60, 80, 100, 80, 60, 40, 20, and 0 mmHg negative pressure, to achieve loading and blood pressure at the foot equivalent to those experienced during upright posture. In both sessions, subjects opposed the footward force by pushing against a footplate. Both protocols ended with 5 minutes of supine recovery. Microvascular bloodflow was measured by three laser Doppler flowmeters, placed at the neck, thigh, and shin. This noninvasive optical technique provides an indication of bloodflow in arterioles, capillaries, and venules within a 1-cubic-millimeter volume of skin.

Normalized (baseline = 1.0) microvascular bloodflow during tilting and LBNP are shown in the figure. Microvascular flow at the level of the neck increased significantly during head-up tilt (HUT), but not during LBNP. Microvascular flows in the lower leg and thigh were reduced significantly during low levels of each stress and remained reduced at up to 90 degrees HUT in both measurement sites and at up to 100 mmHg LBNP in the thigh. At 40 to 100 mmHg LBNP, flow in the lower leg increased significantly

from 35.0% ± 5.6% of baseline to 75.0% ± 13.6% at 100 mmHg LBNP, and abruptly fell to 34.7% ± 6.6% on the return to 80 mmHg. Throughout the HUT protocol, relative flow in the lower leg was significantly lower than that in the thigh. This was not the case during LBNP.

The pressure across blood vessel walls at foot level is approximately equivalent in upright standing posture and with 100 mmHg LBNP. However, LBNP exerts a uniform increase in pressure across vessels of the lower body, in contrast to the linearly increasing pressure profile present during upright posture. Microvascular bloodflow is under the strong influence of local mechanisms that cause constriction of blood vessels in response to increases in local pressure. Because of the importance of these local reactions, we believe that the effects of tilting and LBNP differ with respect to both the magnitude and the distribution of microvascular flows. The results of this study demonstrate that microvascular responses to gravitational stress vary significantly along the length of the body, and suggest that local microvascular autoregulation plays an important role in these responses. The distinction between LBNP and exposure to Earth gravity is potentially crucial when LBNP is considered as an alternative gravitational stress for use as a cardiovascular countermeasure for long-duration spaceflight. For example, external compression may be necessary during LBNP to provide a distribution of blood pressures similar to that of upright standing posture.

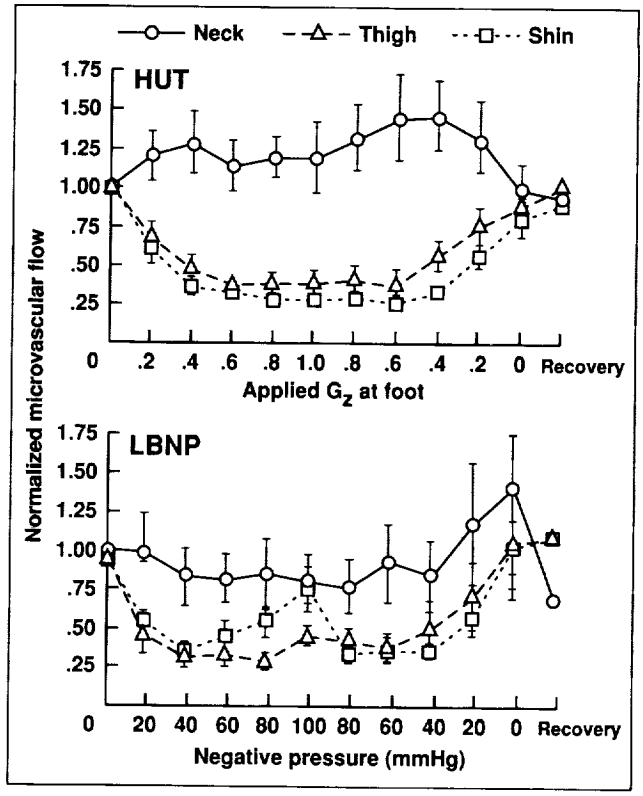

Fig. 1. Relative levels of cutaneous microvascular bloodflow at the neck, thigh, and shin during HUT (top, n = 7) and LBNP (bottom, n = 6). Four subjects are common between the two groups. Bars denote standard errors.

Ames-Moffett contact: A. Hargens
(415) 604-5746
Headquarters program office: OSSA

Bone Geometry, Structure, and Mineral Distribution using Dual-Energy X-Ray Absorptiometry

Tammy Cleek, Robert T. Whalen

Long bones like the human femur can be thought of as beams with irregular cross sections and curvatures. The strength of a beam is measured by its ability to carry loads. For any beam or femur cross section, there exist a maximum and a minimum principal moment of inertia with particular orientations orthogonal to each other (first figure, part (a)). The torsional strength and stiffness of the femur is determined by these moments of inertia along with bone material properties. Part (b) of the first figure depicts a typical femur and midshaft cross section with principal moments of inertia indicated. To a large extent, the irregular cross-sectional geometry is a result of the mechanical forces applied to the bone by daily activities. We have developed a noninvasive method that uses dual-energy x-ray absorptiometry (DXA) to compute the principal moments of inertia along the length of a bone in order to get a measure of bone strength. By computing moments of inertia and determining cross-sectional geometries for long bones, the changes in bone structural properties with growth and different loading patterns can be investigated.

Dual-energy x-ray absorptiometry is currently the most widely used method of analyzing regional and whole-body changes in bone mineral content (BMC) and areal bone mineral density (BMD) (grams/cm^2). With a measurement precision of 1%–2%, DXA provides a useful means of detecting small changes in bone mineral content and mineral distribution. These types of measurements have been used in the diagnosis of osteoporosis and to study changes in bone that are related to age, spinal cord injury, exercise, and spaceflight. However, BMC and BMD values only provide a measure of the *total* amount of mineral in a region. Severe compression of scan data discards valuable information about the structure and distribution of bone mass. The data do not provide direct measures of long-bone geometry, structure, or strength, nor do regional measurements detect localized changes in other regions of the same bone.

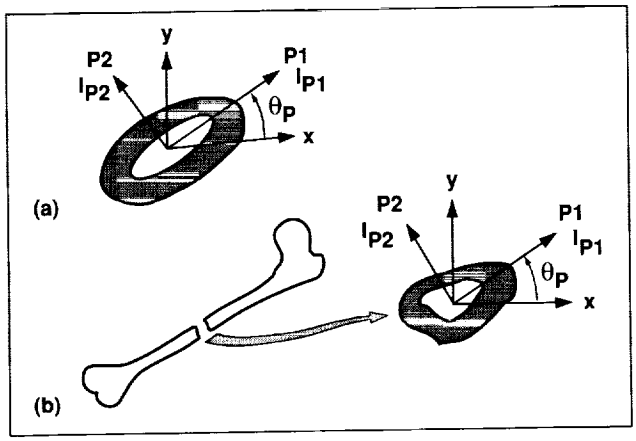

Fig. 1. Principal axes (P1 and P2) and orientations, θ_P, of (a) elliptical cross section and (b) midshaft cross section of a typical femur. I_{P1} and I_{P2} are the principal moments of inertia.

The capabilities of DXA can be enhanced significantly by special processing of pixel BMC data which yields cross-sectional geometric and structural information. We have extended this method of analysis in order to develop nonuniform structural-beam models of long bones. Cross-sectional area, area centroid, and the moment of inertia in the plane of the x-ray beam can be computed by integrating pixel BMC across the scan width. Principal moments of inertia and orientation of the principal axes at each scan cross section can also be determined by combining the information from the independent analyses of three noncoplanar scans. Structural-beam models are generated by combining the section properties from each cross section.

Our initial efforts have concentrated on validating our approach and algorithms by using models, or phantoms, with known material properties and geometries. Aluminum phantoms were designed and machined for investigation of the influence of different phantom shapes and angular positions on the accuracy of computed section properties (second figure).

Expected or "true" values were computed from micrometer measurements of the aluminum phantoms or were set by the machining operation used to create the piece. Multiple scans were taken on each piece

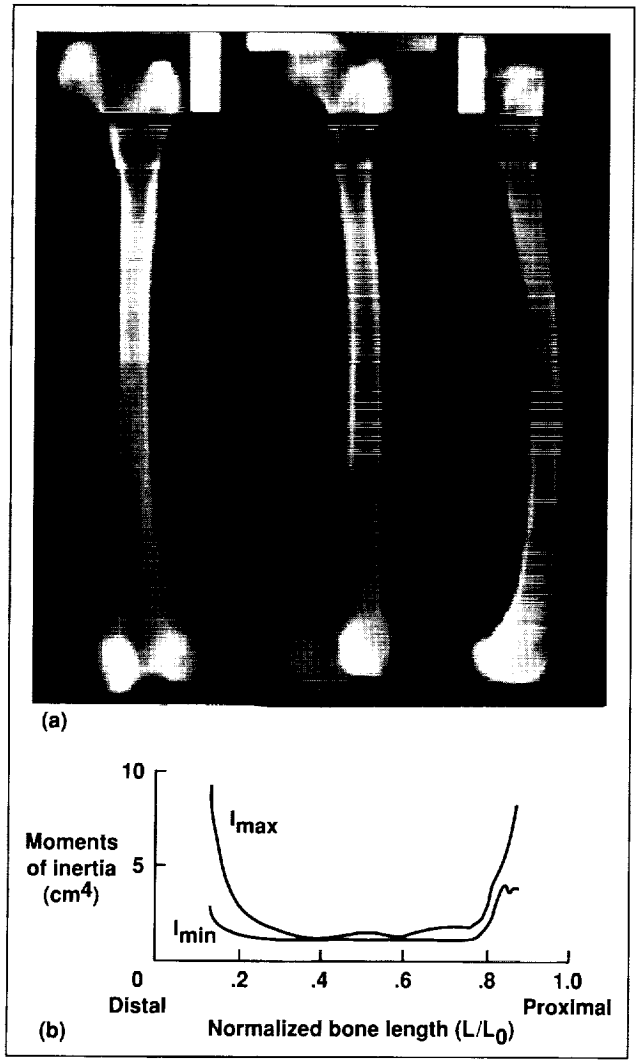

Fig. 2. (a) DXA scans of femur in three planes, (b) principal moments of inertia along the femur. Values are calibrated to the aluminum phantoms.

along its entire length, and axial rotations were done with an indexer. Computer programs accessed raw attenuation data and computed section properties from single and multiple noncoplanar scans. Excellent agreement was found between experimentally determined and "true" section properties of axisymmetric and nonaxisymmetric phantoms. Orientation of principal moments of inertia computed from DXA data were within 2 degrees of expected values for all cases. Moments of inertia were calculated to within 3% or 4% of expected values.

We have also done some preliminary work on applying our methods to bone by analyzing a femur from a cadaver. The femur was scanned in three planes in 45-degree increments. Early results show that, as expected, the principal moments of inertia are larger at the proximal and distal ends with the major axis oriented in the mediolateral plane. The principal major axis rotates 90 degrees to the anteroposterior plane in the mid-diaphysis, although the bone cross section is nearly isotropic in this region since the minimum and maximum moments of inertia are nearly equal to each other.

Whether a single scan or multiple scans are used, we believe this method of analysis will provide a useful link between changes in local loss and reorganization of bone mineral and changes in long-bone strength which occur with changes in daily activity patterns, spaceflight, or spinal cord injury.

Ames-Moffett contact: T. Cleek
(415) 604-0518
Headquarters program office: OSSA

Perceptual and Behavioral Adaptation to Altered Gravitational–Inertial Forces

Malcom M. Cohen

Perceptual illusions involving the mislocalization of visual objects have been reported during and immediately following exposure to the altered gravitational–inertial forces (GIFs) that are encountered during launch into orbit, orbital insertion, orbital flight, and reentry. One of the most dramatic of these illusions is the elevator illusion, which causes a visible target to appear above its true location when the target is viewed in hypergravity, and below its true location when viewed in hypogravity. The elevator illusion has been attributed to changes in oculomotor control that result from atypical stimulation of the otolith organs under altered gravitational–inertial conditions. Because the illusion is of significant theoretical and practical interest, we have undertaken a comprehensive investigation to increase our understanding of it.

The study described here is the most recent of a series in which we have examined changes in perception and perceptual-motor behavior that result from exposure to altered GIFs. Our studies all use a particular research strategy: systematic alteration of the gravitational–inertial field in which perception and behavior take place. We explicitly assume that, by carefully observing how perception and behavior are altered by controlled perturbations of GIFs, we will be able to delineate the range over which normal perception and behavior remain unaffected by specific gravitational–inertial inputs, and we will be able to describe and predict quantitatively how various parameters of perception and behavior are altered by systematic changes in gravitational–inertial conditions.

In general, we regard hypogravity or hypergravity environments as arbitrarily selected points along a gravitational–inertial continuum. In our studies, we select specific values for these points to evaluate their effects.

Since the classical observations by Helmholtz more than 100 years ago, it has generally been accepted that the apparent location of a visual target depends on both retinal and extraretinal information. The retinal information is derived from the image of the target on the retina, its location on the retina, and the presence or absence of images from other objects in the visual field. The extraretinal information is derived from the position of the eyes relative to the head, and of the head relative to an external frame of reference, such as gravity.

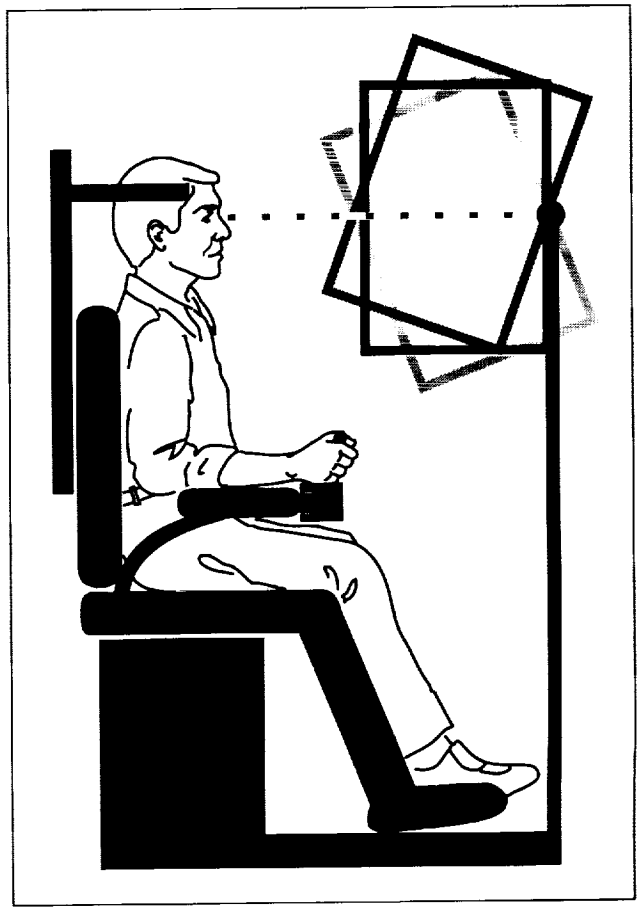

Fig. 1. Subject viewing target on posterior wall of pitch box. All three orientations of pitch box are shown.

To evaluate the relative contributions of retinal and extraretinal information on localizing a visual target in the current study, we systematically altered the orientation of an optical array with respect to GIFs by having each of 18 subjects look into a pitchbox (first figure), and set a target so that it appeared to be at "eye level horizontal." In earlier studies, we demonstrated that targets viewed on the back wall of a pitchbox appear to be displaced from their actual positions. When the pitchbox is pitched up, a target at eye level horizontal appears to be below its true position; when the pitchbox is pitched down, the same target appears to be above its true position.

The subject adjusted the position of the target with a toggle switch, which controlled an electric motor that drove the target up or down on the back wall of the box. The experimenter set the box at each of three orientations: (1) pitched up 20 degrees, (2) level, and (3) pitched down 20 degrees. Three illumination conditions were also used: (1) full illumination; (2) only the edges of the box faintly visible, by means of electroluminescent strips; and (3) total darkness, in which only the target could be seen. Each illumination and box pitch condition was

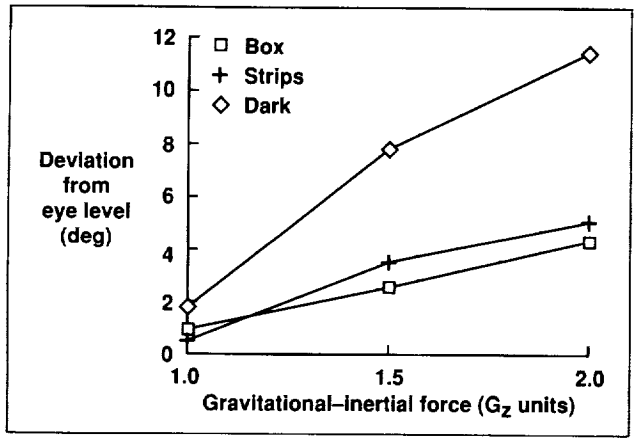

Fig. 2. Apparent target location as a function of illumination and gravitational–inertial force.

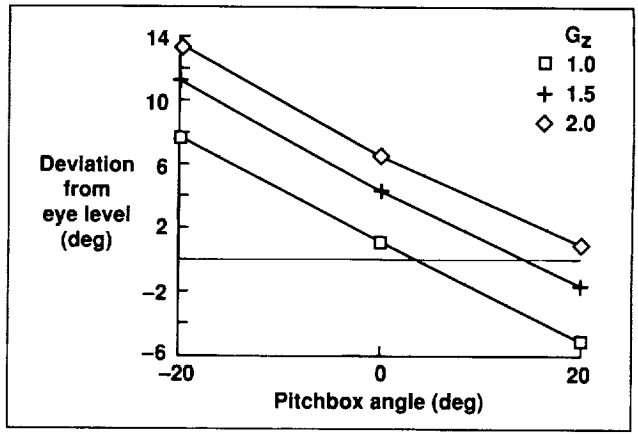

Fig. 3. Apparent target location as a function of pitchbox angle and gravitational–inertial force.

combined with three conditions of GIFs: (1) 1.0 G_z, (2) 1.5 G_z, and (3) 2.0 G_z, as produced by the Ames 20-G human centrifuge.

The results were as follows:

1. The elevator illusion, which increased with increasing magnitudes of GIFs, was attenuated in the presence of the pitchbox when the pitchbox was fully illuminated and when it consisted of dimly lit electroluminescent strips, as compared to the illusion obtained in total darkness (second figure).
2. The orientation of the pitchbox caused the target to appear displaced from its true position by a fixed amount; the slope of this effect was essentially the same at all GIFs (third figure).

These results suggest a simple linear model to account for the combined effects of gravity and optical stimulation on the ability of humans to localize visual targets with respect to elevation.

Ames-Moffett contact: M. Cohen
(415) 604-6441
Headquarters program office: OSSA

Effect of Spaceflight on Primary Rat Osteoblast Cultures

Charlotte M. Cone, Emily R. Morey-Holton, Stephen B. Doty

Spaceflight alters bone mineralization in young rats. To study this defect at the cellular level, we developed a culture system in which fetal rat calvarial osteoblasts (OBs) are grown on collagen-coated dextran microbeads in tissue dishes with Minimal Essential Medium (MEM) supplemented with 10% fetal bovine serum and 0.3 millimolar ascorbic acid (MEM+). Osteoblasts cultured in this system exhibit typical *in vivo* morphology, and spontaneously mineralize within 3 weeks. A modification of the culture system was flown on STS-45. Ten days before flight, approximately 7×10^6 cells with microbeads were introduced into each of four Cellco bioreactor chambers. MEM+ was pumped continuously through the hollow fibers of the bioreactor. At loading, the glucose concentration of the MEM+ was increased to 4 grams/liter to accommodate the low-volume (300-milliliter) allowance for four chambers. The postflight glucose concentration in the used medium bag was 1.6 grams/liter, indicating good cellular metabolism during the 9-day flight in the Space Tissue Loss culture system. Electron micrographs of attached flight cells showed (1) well differentiated bone cells and normal collagen fibrils, (2) no demonstrable alkaline phosphatase activity, and (3) dense collagen aggregates without mineral. High-glucose MEM+ caused increased glycogen storage in Earth and space osteoblasts. Floating cells from the space chamber medium were dead, which suggests that cell attachment/reattachment and cell survival may change during spaceflight. Attached spaceflight cells were healthy and were actively synthesizing matrix that was not yet mineralized. These preliminary data suggest that spaceflight may alter the bone mineralization process at the cellular level.

Ames-Moffett contact: E. Morey-Holton
(415) 604-5471
Headquarters program office: OSSA

Chronic Exposure to Altered Gravity Affects Brainstem Neurochemistry in the Rat

Nancy G. Daunton, F. Tang, Robert A. Fox

A number of investigations are being conducted on changes in the structure, biochemistry, and physiology of the nervous system associated with behavioral adaptation to altered gravitational environments. A study of the effects of chronic exposure to hypergravity on neuropeptides in various brain areas was recently completed. The study was undertaken in collaboration with investigators in the Department of Physiology at the University of Hong Kong.

Rats were exposed to hypergravity (2 G) for either 4 or 14 days, with centrifugation used to generate the chronic altered gravitational conditions. It has been shown previously that such exposures cause changes in vestibular function and in the structure of the gravity receptors in the vestibular end organs. Immediately after hypergravity exposure, the levels of several neuropeptides (thyrotropin-releasing hormone (TRH), substance P, metenkephalin, somatostatin, cholecystokinin) in various areas of the brain (brainstem, hypothalamus, cerebral cortex, striatum) that might play a role in the process of adaptation were determined by radioimmunoassay.

After chronic exposure to hypergravity the levels of both TRH and substance P were altered in the brainstem. As shown in the figure, the levels of TRH were increased after both 4 and 14 days of exposure, whereas levels of substance P were increased only after 4 days of exposure. Levels of the other neuropeptides in the brainstem did not change, and no major changes were found in any neuropeptides in the other brain areas. Animals exposed to the rotational but not the hypergravity component of centrifugation showed no changes in neuropeptide levels in the brainstem or elsewhere. Thus it seems likely that the changes seen in TRH and substance P in the brainstem are related specifically to the process of adaptation to hypergravity. The fact that both of these neuropeptides have been shown to play a role in adaptation to unilateral loss of vestibular function supports this suggestion.

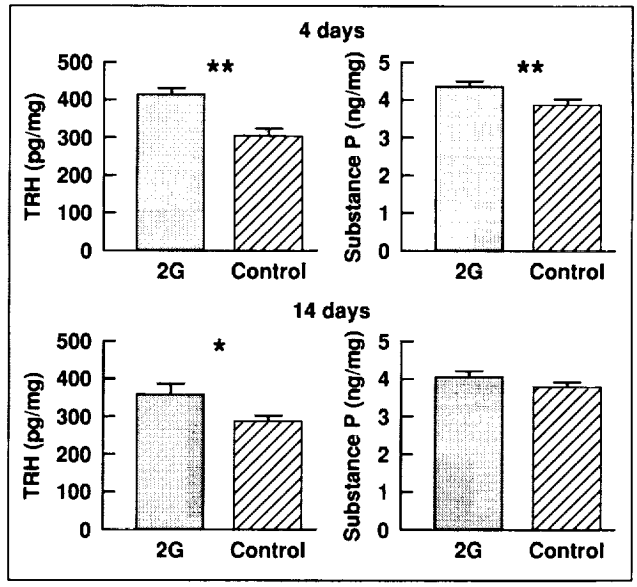

Fig. 1. Levels of brainstem TRH and substance P in rats after exposure to hypergravity (2 G) for 4 or 14 days, compared with levels in control animals housed in the same room (= $p \leq 0.05$; ** = $p \leq 0.01$).*

We will evaluate the effects of agonists and antagonists of these two neuropeptides on the time course of adaptation to hypergravity. In addition, we will determine the specific brainstem nuclei in which the changes occur, so that the specific role of each of these neuropeptides in the adaptation process can be understood. This information will be used in the development and refinement of methods, both pharmacological and behavioral, for facilitating adaptation to altered gravitational conditions.

Ames-Moffett contact: N. Daunton
(415) 604-4818
Headquarters program office: OSSA

CD4+/CD8+ T-Lymphocyte Ratio: Rehydration and Supine Exercise in Men

John E. Greenleaf, Catherine G. R. Jackson, DeSales Lawless

Optimal functioning of the immune system is essential for the astronauts' health and performance on long-duration space missions. Some immune-system parameters (e.g., T-lymphocyte function) appear to be depressed during flight, but the exact nature of the defect and its long-term consequences have not been elucidated. Physical exercise training programs are being developed as countermeasures for spaceflight deconditioning; the optimal mode, frequency, intensity, and duration of exercise are still being investigated. Performance of moderate submaximal exercise and moderate exercise training on Earth stimulates immune function, whereas intensive exercise and hard exercise training diminish immune function. Exercise training regimes performed during spaceflight could similarly affect immune function.

Reduced total body water with accompanying decreased plasma volume (hypovolemia) occurs in astronauts during flight. Additional hypovolemia occurs during exercise and is proportional to exercise intensity. Astronauts attempt voluntary rehydration with sodium chloride (NaCl) tablets and water prior to reentry. The effects of rehydration on the immune function of dehydrated subjects are unknown, especially in conjunction with exercise. This study investigated the effects of prior dehydration and immediate pre-exercise rehydration on the CD4+/CD8+ T-lymphocyte ratio during exercise in four men (aged 30–46 years) during supine submaximal exercise for 70 minutes at 71% ± 1% of their estimated peak oxygen uptake. Six rehydration fluid formulations were used: (1) water + aspartame (a noncaloric sweetener); (2) 19.6 milliequivalents per liter (mEq/l) NaCl + aspartame; (3) 157 mEq/l NaCl–Na citrate + aspartame; (4) 19.6 mEq/l NaCl + 9.7% glucose; and two commercial drinks: (5) Performance, and (6) Power Surge.

All pre-exercise post-rehydration CD4+/CD8+ ratios (mean ± SE) were below 1.2, the upper limit of the pathological range. Mean post-exercise ratios were greater for all six rehydration fluids than the respective pre-exercise ratios, and four of them increased into or beyond the normal range. The largest percent increase (172%) was with drink (3), followed by increases with drinks (6) and (5) of 125% and 120%, respectively. The mean (± SE) of the six post-exercise ratios (1.38 ± 0.16), was significantly higher ($P < 0.05$) than the mean pre-exercise ratio of 0.77 ± 0.12. The interaction of dehydration and exercise on immune function requires further study.

Ames-Moffett contact: J. Greenleaf
(415) 604-6604
Headquarters program office: OSSA

The Role of Muscle Function and Growth Factors in the Prevention of Muscle Atrophy in the Rat

Richard E. Grindeland

Skeletal muscles—especially antigravity, postural muscles—sustain losses of mass and function during exposure to actual or simulated microgravity. These losses of strength and function can readily compromise astronauts' ability to rapidly emerge from a space vehicle, their performance on the surface of another planet, and their physiology on return to Earth. Moreover, atrophic muscles are significantly more susceptible to injury such as tearing. It is therefore important to prevent or minimize muscle degradative changes in space. Changes in systemic endocrine function as well as decreased exertion of the muscles themselves appear to contribute to muscle atrophy during space travel. The overall goal of our research is to prevent muscle atrophy in microgravity by use of hormone–exercise regimens. Treatment with hormones or exercise alone has been only partially effective in previous studies.

Effects of Growth Hormone (GH), Insulin-like Growth Factor-I (IGF-1), and Exercise on Muscle Atrophy and Bone Growth in Hindlimb-Suspended (HS) Rats

Male rats without pituitary glands (hypophysectomized) were suspended for 10 days. They were given GH, IGF-I, and/or exercise. The exercise consisted of three daily bouts of climbing a 1-meter ladder, inclined at 85 degrees, five times while carrying a load equal to 50% of the rat's body weight. Eleven hindlimb muscles with different functions were studied. In the muscles that atrophy during HS, the GH + exercise countermeasure increased muscle weights by 34%, restoring them to normal weights. Non-atrophic muscles grew in direct proportion to body weight. With IGF-I + exercise, atrophic muscles grew 18%, twice as fast as body weights, but were not restored to normal levels.

During HS, the growth of long bones was reduced; the growth of the tibia was stimulated equally well by IGF-I in ambulatory, HS, and HS + exercise rats, showing no interactive effect of exercise and IGF-1. GH stimulated growth, but less in HS than in ambulatory rats, indicating some tissue resistance to the hormone in the HS rat. Again, however, exercise and GH had a synergistic effect on bone growth, returning growth to normal levels.

Work Capacity of HS Rats

The work capacity of astronauts is decreased in space, but the cause(s) of this diminished capacity is unknown. A previous study revealed that HS rats also sustain a reduced work capacity. As expected, hypophysectomized rats started at a lower work capacity than intact rats, but they showed no decrement after exposure to simulated microgravity (HS), whereas intact rats did. Thus, some systemic factor is apparently involved in the reduced work capacity; identification of this factor is being pursued.

Muscle Protein Synthesis in HS Rats

After discovering that exercise (ladder climbing) together with GH treatment reversed muscle atrophy in HS, hypophysectomized rats, we sought to determine if this regimen would also forestall atrophy in intact (nonhypophysectomized) rats. Daily injections of GH had no effect on muscle mass. Ladder climbing attenuated soleus and gastrocnemius muscle atrophy by 35% and 28%, respectively. Addition of GH to the exercise regimen attenuated gastrocnemius atrophy by 43%, but had no additional effect on the soleus. Muscle protein synthesis was decreased 67% and 43% by HS in soleus and gastrocnemius muscles, respectively. Exercise and/or GH stimulated total protein synthesis in atrophic muscles of HS rats only slightly. In contrast, contractile (myofibrillar) protein synthesis was markedly stimulated by the hormone–exercise treatment.

Our initial studies indicate that regimens that are effective in the hypophysectomized animal are also effective in the intact animal and that the GH–exercise treatment stimulates protein synthesis in atrophic muscles.

Ames-Moffett contact: R. Grindeland
(415) 604-5756
Headquarters program office: OSSA

Gravitational Effects on Cell Biology

Rosalind A. Grymes

In a multicellular organism, each cell in a tissue contributes to the normal interplay of functions. Each performs a set of behaviors as a result of genetic memory, current environmental inputs, and preprogrammed destiny. One environmental input is gravity, an external physical stressor. Its effects are inescapable –on Earth, its impact on cellular activities cannot be isolated. We are investigating the contribution of gravitational force to both static and induced cellular behaviors.

New behaviors result from new environmental inputs, as in the recognition of cytokine growth factors by membrane receptors. Growth factor binding at the cell membrane initiates a cascade of intracellular communication molecules which transmit a signal to the nucleus. The communication pathways consist of two related networks: (1) the chemical mediators of signal transfer and (2) the cytoskeleton. The cytoskeleton provides three-dimensional structure to the cell, distributing forces through tensional elements.

Our laboratory examines the interaction between dermal fibroblast cells and one cytokine growth factor, platelet-derived growth factor (PDGF). We use a spectrum of cells representing different states of development, including those of Werner's syndrome (WS), a human disease of accelerated aging. Changes in replicative potential and gene expression, and a relative insusceptibility to induced proliferation, are characteristic both of aged cells and of cells exposed to microgravity. We have pinpointed an altered pattern of expression in the genes whose products are required for appropriate induction of the enzyme interstitial collagenase, or collagenase type I, a matrix metalloprotease.

In the past year, we have established in-house cell-culture and molecular biology facilities. Our experiments encompass both chemical and structural signaling pathways. We are examining the modification of cell behavior by applied external stress (mechanical stretch) and by the absence of unidirectional gravity (through constant gravity vector rotation). We have focused on very early responses to PDGF binding. Using specific antibodies, we observe the course of early signal transduction in WS and normal-control cells (young and old). We can also visualize the cytoskeleton and study the movement of molecules in several signaling pathways along this network.

Two novel methods are applied to our cells in these investigations. In the first, we add to the gravitational constant a range of externally applied, manipulable tensional stresses. This is achieved with a Flexercell® unit, which uses deformable membranes and microprocessor-controlled vacuum suction to create a mechanically active environment. Individual and colony morphologies of dermal fibroblasts cultured in a Flexercell® unit are unique. Second, to nullify the unidirectional field of 1 G experienced on Earth, we use a rotating-assembly incubator. We have found that even simple inversion of cell cultures results in an apparent randomization of culture morphology compared to controls. Constant vectorial averaging of the direction of perceived gravity is hypothesized to generate similar growth alterations.

Living organisms respond to the demands of an environment where external stimuli are essentially unbounded and unpredictable. Cellular responses, although adaptable, are bound by each cell's genetic capability for change. Understanding the cell/environment interface with respect to information acquisition and genetic response is a broad goal of cellular and molecular biology. Cytoskeletal architectures have evolved under the influence of gravity, and are clearly tension/compression systems responsive to mechanical stresses and physical forces. Gravity-related research in cellular signal transduction is a unique opportunity for revealing the importance of gravity.

Ames-Moffett contact: R. Grymes
(415) 604-3239
Headquarters program office: OSSA

Back Pain during 6-Degree Head-Down Tilt is Similar to That During Actual Microgravity

Karen J. Hutchinson, Alan R. Hargens, Gita Murthy,
Donald E. Watenpaugh, Victor A. Convertino, Peter C. Wing

Back pain is one of the most common problems experienced by astronauts early during exposure to microgravity. In a recent retrospective study, 13 of 19 Shuttle crew members complained of back pain during microgravity. Their pain was localized in the lower back (50%), and consisted of dull pain (62%) with an average intensity of 2 on the five-point McGill Questionnaire scale. This pain may be of sufficient degree to adversely affect the well-being and performance of astronauts. Spaceflight data indicate that the spine lengthens 4–7 centimeters in microgravity. Our objective in this study was to compare data on back pain and spinal lengthening (height increase) obtained during simulated microgravity (6-degree head-down tilt (HDT)) with data obtained during actual microgravity.

After informed written consent was obtained, eight healthy male volunteers (aged 38 ± 2 years (mean ± SE); weight 80.8 ± 3.7 kilograms), were admitted to the Human Research Facility at NASA Ames for a 16-day, 6-degree HDT (microgravity simulation) study. All subjects completed the McGill Questionnaire, in which pain intensity is graded from 0 (no pain) to 5 (intense and incapacitating pain), each day at 7:00 p.m. during pre-tilt control, HDT, and post-tilt recovery periods. The subjects' heights were measured each day while they were in a supine (control and recovery) or HDT position.

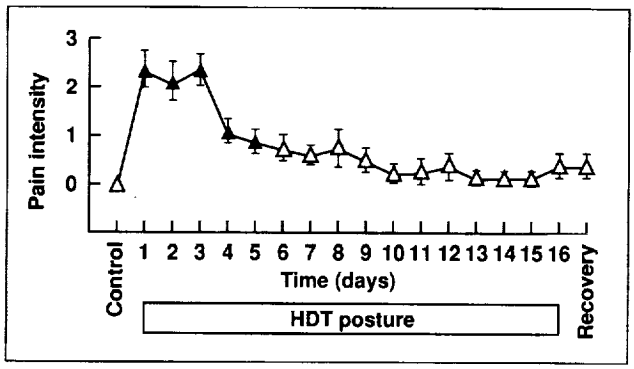

Fig. 1. Intensity of back pain during pretilt control period, 16 days of HDT, and post-tilt recovery. Pain was rated on a five-point scale (0—no pain; 1—very low level; 2—pain can be ignored; 3—painful, can continue work; 4—severe, makes concentration difficult; and 5—intense, incapacitating). Δ indicates significantly higher than pretilt control ($p \leq 0.01$).

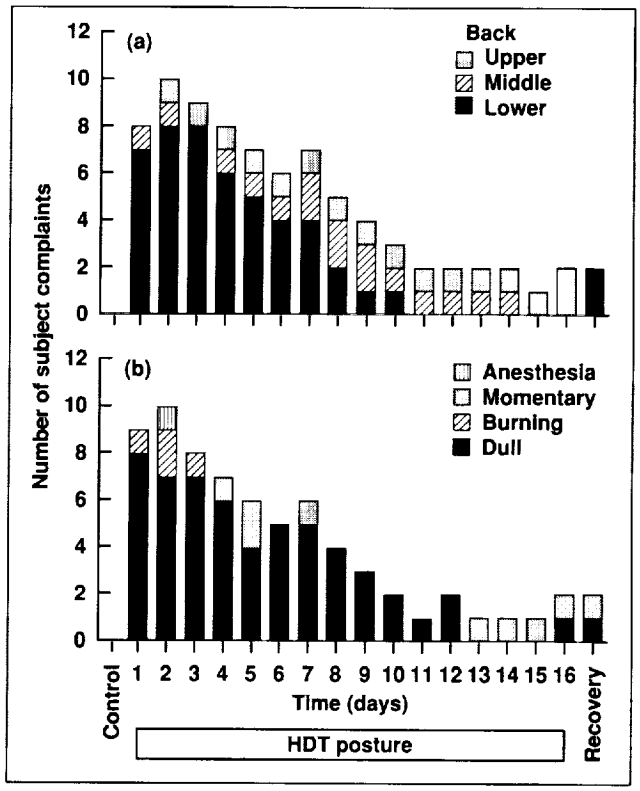

Fig. 2. Distribution and type of back pain. (a) Location of back pain during pretilt control, 16 days of HDT, and post-tilt recovery (some subjects reported more than one pain location). (b) Type of back pain during pretilt control, 16 days of HDT, and post-tilt recovery (some subjects reported more than one type of pain).

Back pain increased significantly from zero (baseline control period) to 2.3 ± 0.4 at days 1–3 of HDT (first figure). During this time, all of the subjects experienced lower-back pain and categorized this as dull and/or burning (second figure). By day 4 of HDT, the pain level decreased to 1.1 ± 0.2 with 88% of the subjects (seven of eight) still experiencing pain. Only two subjects reported any pain at the end of HDT and during recovery. Subjects' heights increased by

2–3 centimeters by day 3 of HDT and remained at that level until recovery (third figure).

Although spinal lengthening in space is twice that during HDT, the HDT model of microgravity provides a good simulation of the type, level, distribution, and time course of back pain associated with actual microgravity. Lower-back pain in simulated microgravity may be related to a combination of 6-degree HDT and spinal lengthening; most people do not experience back pain during a normal night's sleep in a horizontal position. In the HDT model, pain subsides in intensity when spinal lengthening stops. Thus back pain in actual and simulated microgravity may result from the stretching of paraspinal ligaments and musculature until a new resting spinal length is reached.

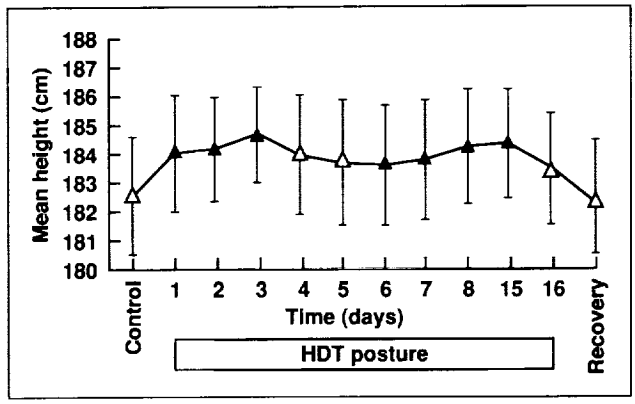

Fig. 3. Subject heights during pretilt control, 16 days of HDT, and post-tilt recovery. Δ indicates significantly higher than pretilt control ($p \leq 0.01$).

Ames-Moffett contact: K. Hutchinson/A. Hargens
(415) 604-5747/5746
Headquarters program office: OSSA

Hypergravity Simulation on the Ames 20-G Centrifuge

Gerald M. Mulenburg

Centrifugation is the standard method for simulating hypergravity to evaluate the effects of launch into and reentry from space. Hypergravity simulation can also be used to study the effects of gravity on living organisms, from single cells to humans. This capability is particularly important in developing an understanding of how humans can effectively operate in other than Earth gravity such as on the moon (1/6 Earth gravity), on Mars (3/8 Earth gravity), and during long spaceflight missions at zero gravity.

The Ames Life Science Division has a unique suite of six research centrifuges ranging in diameter from 8 feet to 56 feet. The largest, the Ames 20-G Centrifuge facility (see figure), is currently NASA's

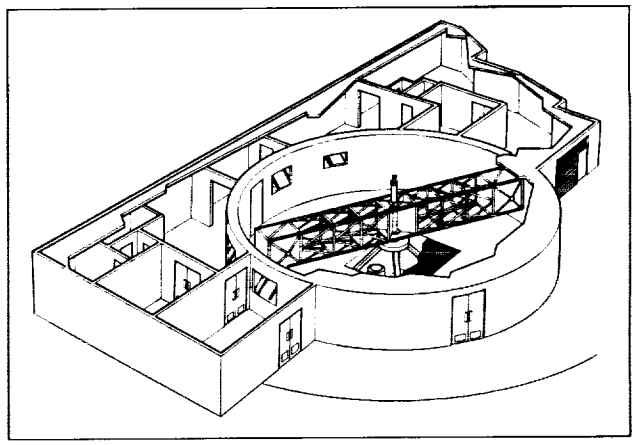

Fig. 1. The Ames 20-G Centrifuge.

only human-rated centrifuge. The open truss arm of the 20-G has three large cabs (7 feet long by 7 feet high by 6 feet wide), one on each end and one near the center. The three cabs permit concurrent experiments with widely varying operational requirements. Cab B has a swing chair for accurate G_z loading of human subjects and has been used extensively for psychophysical studies and tolerance testing of humans before and after bed-rest simulations of microgravity conditions. Cab A is available for other experiments, including an evaluation of an exercise treadmill installation. Cab A was also recently used in conjunction with Cab C for a study of cutaneous bloodflow and blood volume changes in supine subjects under 1-G centripital force at the foot. Cab C can be used for low-G studies, and provides an opportunity to evaluate different gravitational gradients when used in conjunction with one of the outer cabs, as in the cutaneous bloodflow experiment.

A unique feature of Cab C is that it can be used for examining the coupling effect of rotation rate and G level. By running identical-G-level experiments in Cab C and one of the outer cabs, which would therefore be moving at widely different rotation rates, any differences in results could be attributed to the different rotation rates.

After replacement installation of a state-of-the-art drive control system and a general overhaul and upgrade of the 20-G in 1993, several new experiments are planned. These include evaluation of exercise under hypergravity, a study of eye movement tracking of a target, and a test of a solar array panel under launch conditions prior to launch into space.

Ames-Moffett contact: G. Mulenburg
(415) 604-3279
Headquarters program office: OSSA

Exercise against Artificial Gravity Simulates Exercise against Normal Gravity

Gita Murthy, Donald Watenpaugh, Richard E. Ballard, Alan Hargens

Prolonged existence in microgravity reduces lower-body muscle strength and bone mineral density, neuromuscular coordination, and the capacity to stand or exercise in Earth gravity. Exposure to microgravity may also increase bloodflow and blood pressure in the head and decrease these parameters in the lower body. These effects are largely due to loss of weight-bearing, loss of gravitational pressure gradients throughout the circulatory system, and the resultant headward fluid shifts. Thus, microgravity-induced musculoskeletal and cardiovascular responses may necessitate exercise and other appropriate countermeasures during spaceflight in order for the integrity of both systems to be maintained. Previously, we documented that exposure to 100 millimeters of mercury of lower-body negative pressure (LBNP) generates a force of about one body weight at the feet, which is equivalent to standing upright in Earth gravity (1 G). We propose that exercise against such artificial gravity as LBNP provides simultaneous musculoskeletal and cardiovascular loading that is similar to exercise against 1 G.

To test our hypothesis, nine healthy male subjects performed toe/heel raises at 25 cycles/minute for 5 minutes under two conditions: upright against normal gravity and supine against LBNP. Footward force, intramuscular pressure (IMP) in the soleus muscle, arterial blood pressure, and heart rate were measured. Mean footward forces produced during upright 1-G exercise and supine LBNP exercise were not different. The IMP response to exercise was also similar between the two conditions (see figure). Mean arterial blood pressure was not different between the

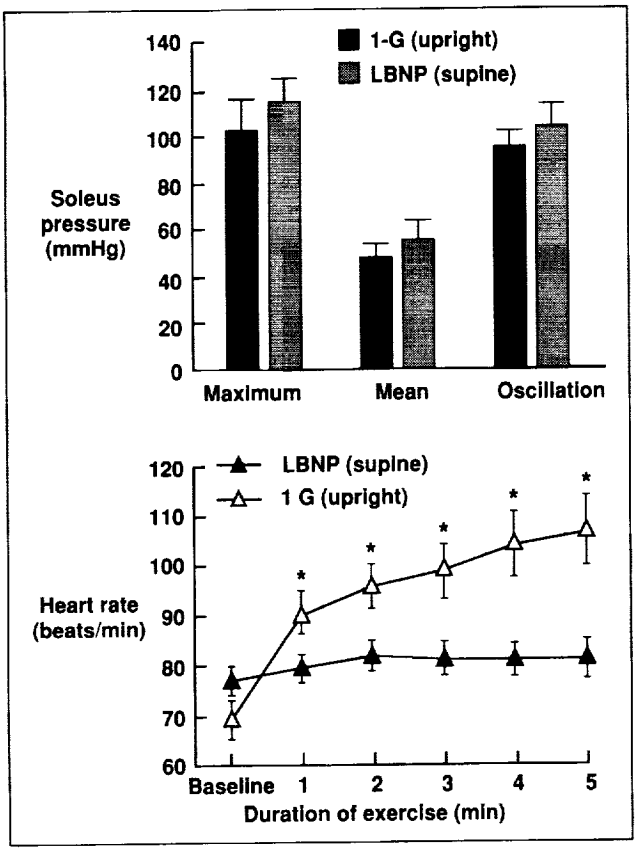

Fig. 1. Soleus intramuscular pressure (top) and heart rate (bottom) during exercise against 100 mmHg LBNP and against normal gravity (1 G) (= $p \leq 0.05$).*

two conditions of exercise, yet heart rate was considerably elevated during exercise against LBNP compared to exercise against 1 G.

These results indicate that exercise in microgravity against the artificial gravity of LBNP will produce musculoskeletal responses similar to exercise performed upright against normal gravity. Cardiovascular effects, however, are dissimilar between these conditions because of blood pooling and tissue swelling in the lower body during LBNP. Recent pilot studies indicate that a compression suit around the lower body counteracts this LBNP-induced pooling and consequently reduces cardiovascular stress. The LBNP concept of artificial gravity may provide a cheaper, faster, and smaller-scale alternative to rotating artificial gravity for protecting crew members exposed to long-duration spaceflight.

Ames-Moffett contact: G. Murthy/A. Hargens
(415) 604-5747/5746
Headquarters program office: OSSA

Effects of Spaceflight on Gravity Sensors

Muriel D. Ross

Our previous ultrastructural research indicated that vestibular gravity sensors (maculas) are organized for weighted parallel distributed processing of information. There are two main interacting circuits: highly channeled and distributed modifying. Type I macular sensory hair cells are part of the highly channeled circuit. Type II macular sensory hair cells sense, distribute, and modify information flowing through the system and are part of the distributed modifying circuit. In an altered gravitational environment, type II cells should show more synapse changes than type I cells because of their many functions in the neural network. (Synapses are sites of communication between neurons.)

This concept has now been tested by statistical analysis of more than 6,000 synapses, called ribbons, in over 1,000 sensory cells of maculas of rats flown on SLS-1 and of other rats used as ground controls. Data were obtained from four sets of 50 serial sections from right maculas of each of the following groups: three flight and three control rats euthanized on the day of shuttle landing (recovery day + zero, R + 0); and three flight and three control rats euthanized nine days later (recovery day + mission length, R + ML). Two consecutive series of 50 sections were obtained from maculas of one animal in each group to determine whether results would vary between the two sites, and no significant differences in counts were observed.

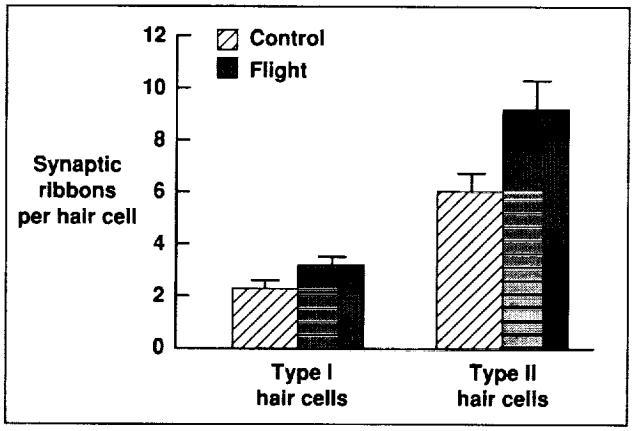

Fig. 1. The mean number of synaptic ribbons in receptor cells (type I and type II) in gravity sensors of flight rats compared to controls on the day of shuttle landing.

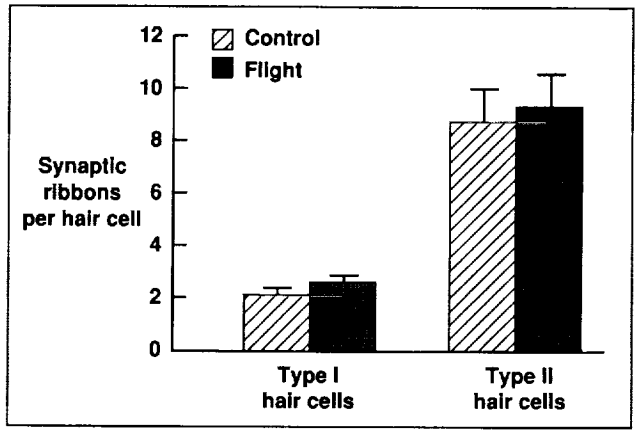

Fig. 2. The mean number of synaptic ribbons in type I and type II hair cells of flight rats compared to controls, nine days postflight.

The chief results are illustrated in the figures, which compare the average (mean) number of synapses in type I and type II sensory cells of flight animals with those of their controls. At R + 0, besides the increments in synaptic ribbons shown in the first figure, there was a doubling of pairs of synaptic ribbons and a ten-fold increase in groups of synaptic ribbons in type II hair cells of flight rats. All of these differences were significant to the $p \leq 0.0001$ level. At R + ML (second figure), the mean number of ribbons in type I hair cells of R + ML controls was almost exactly that of controls at R + 0. However, mean counts in type I hair cells of flight animals, although lower than those recorded at R + 0, had not returned to a normal level. The difference in mean counts between type I cells of flight and ground control rats was statistically significant ($p \leq 0.0163$). More surprising were results for type II hair cells, in which the mean ribbon count from R + ML flight animals was not reduced compared to that obtained at R + 0. (Compare bars at extreme right in the figures.) Additionally, the mean count in type II hair cells of

control animals had increased so that there was now no significant difference between R + ML flight and ground control groups.

The findings at R + 0 indicate that spaceflight results in a reweighting of gravity sensor synapses to adapt the maculas to their new, altered environment in which gravity is diminished. The increments in pairs and groups of synaptic ribbons probably increase the likelihood that a particular synaptic site will release its transmitter substance in microgravity.

The findings at R + ML are thought to be attributable to the stress of numerous manipulations of the rats, both control and flight, carried out in pursuit of research goals of other investigators sharing the SLS-1 rats. In support of this hypothesis was the presence of porphyria, a red discoloration about the eyes that is an external sign of stress. The findings strongly suggest that stress can change synaptic structure in vestibular maculas, and that it does so selectively by acting on neural elements of the distributed modifying circuitry.

The current findings support the original thesis that the distributed modifying circuit is the more dynamic and exhibits more changes during an adaptive response. Shuttle flight appears to retune vestibular gravity sensors so that they can function in microgravity. The results suggest that the maculas of astronauts become adapted to weightlessness, and upon the astronauts' reentry into Earth's atmosphere, this adaptation may impair balance and make rapid egress from a burning shuttle difficult.

Ames-Moffett contact: M. Ross/T. Chimento
(415) 604-4804/4825
Headquarters program office: OSSA

The Role of Visual–Vestibular Interactions in the Perception of Motion

Leland S. Stone

The perception of motion is critical for the performance of visually guided navigation and movement. Motion information may be perceived by visual, vestibular, and oculomotor systems. A clear understanding of how motion information is processed within each of these systems and how the three systems interact is crucial for modeling human performance in tasks that require motion processing, and for anticipating how altered-gravity environments may adversely affect perception.

Recent research has focused on the visual contribution to motion perception—specifically, on how the accuracy of human visual motion perception depends on the stimulus parameters. Contrast, in particular, has been found to have a profound effect: a lower-contrast pattern appears to move more slowly than a comparable higher-contrast reference pattern. This suggests that fog or shadows or other low-contrast viewing conditions (e.g., wearing night goggles) might adversely affect motion perception and, therefore, navigation. We are examining whether this contrast-induced difference in perception is sustained when comparisons are made across time rather than across space.

We have also studied the visual perception of heading (direction of forward translation) within a simulated three-dimensional (3-D) environment. We have refuted the dominant model of heading estimation by showing that accurate performance does not require local differential motion (the motion parallax produced when two nearby points are at different depths) and by showing that actual human performance is different than simulations of the dominant model. Our psychophysical results are also being used to develop and refine a biologically plausible template model of heading perception which has recently been expanded to include depth estimation and to consider the role of eye movements. With a new image display system and a versatile 3-D display software package that continues to be developed, we will examine the role of motion and other visual cues (disparity, shading, perspective) in depth estimation during navigation. With a newly acquired eye tracker,

we will simultaneously measure human eye-movement responses during visually simulated self-motion to determine their potential contribution to heading and depth perception.

Using the linear sled at the Ames Vestibular Research Facility, we have begun a study of the vestibular contribution to motion perception. By measuring heading perception during forward translation in total darkness, we have found preliminary evidence that whereas the visual system can resolve heading differences of about 1–2 degrees, the vestibular system is not nearly as discerning (uncertainty > 10 degrees) in the task.

The long-term goal of this project is to use combined visual/vestibular stimulation to examine how all of these factors (visual motion, otolith stimulation, eye movements) interact in the perception of self-motion. This information is critical for an understanding of human performance in altered-gravity environments (i.e., for anticipating human error from altered otolith function), for designing preflight training paradigms as countermeasures to spaceflight-induced sensorimotor performance deficits (based on a clearer understanding of the interactions of multiple sensory inputs and eye movements), and for designing effective and efficient virtual-reality devices both as tools for future neuroscience research and as performance enhancers for aerospace applications.

Ames-Moffett contact: L. Stone
(415) 604-3240
Headquarters program office: OSSA

Changes in the Proximal Femur During Spaceflight

Sharon Tanner, Emily R. Morey-Holton

The rat frequently functions as a biped during such activities as playing, grooming, and eating. The hip joint, particularly the ball and neck of the femur, bears increased mechanical loads during bipedal activities. This region may require high strain for the maintenance of bone mass, and may thus be especially responsive to decreased loading. This study examined the effect of a nine-day spaceflight on mineralized tissue in the neck of the femur. Proximal femurs collected from individually housed, young, growing male Sprague–Dawley rats flown on SLS-1 were demineralized, cut into thin sections, and stained for bone and cartilage. The site of analysis consisted of four adjacent fields (0.37 square millimeter each), beginning 0.5 millimeter below the growth plate. The fields were configured in a 2-1-1 (T-shaped) arrangement, representing three different regions of the metaphysis. Bone and cartilage areas were measured using the National Institutes of Health program Image. Values for the first two fields were averaged since they were the same distance from the growth plate. Controls had 32% ± 6% (mean ± SD), 29% ± 7%, 27% ± 5% bone and 8% ± 2%, 6% ± 3%, and 5% ± 2% cartilage in fields 1 + 2, 3, and 4, respectively. Flight rats had 26% ± 5%, 24% ± 9%, 26% ± 10% bone and 7% ± 2%, 5% ± 3%, and 5% ± 3% cartilage in fields 1 + 2, 3, and 4. The percentage of cartilage at these sampling sites was not affected by spaceflight. Only the amount of bone in fields 1 + 2 (where the bone had formed most recently) was significantly decreased in the flight rats compared to controls ($p < 0.005$). This study demonstrated the ease of analyzing mineralized tissue in the proximal femur and that the femur neck is an appropriate sampling site for investigating the response of bone to changes in mechanical load.

Ames-Moffett contact: E. Morey-Holton
(415) 604-5471
Headquarters program office: OSSA

Gravity Receptor Physiology After Exposure to Microgravity

David L. Tomko

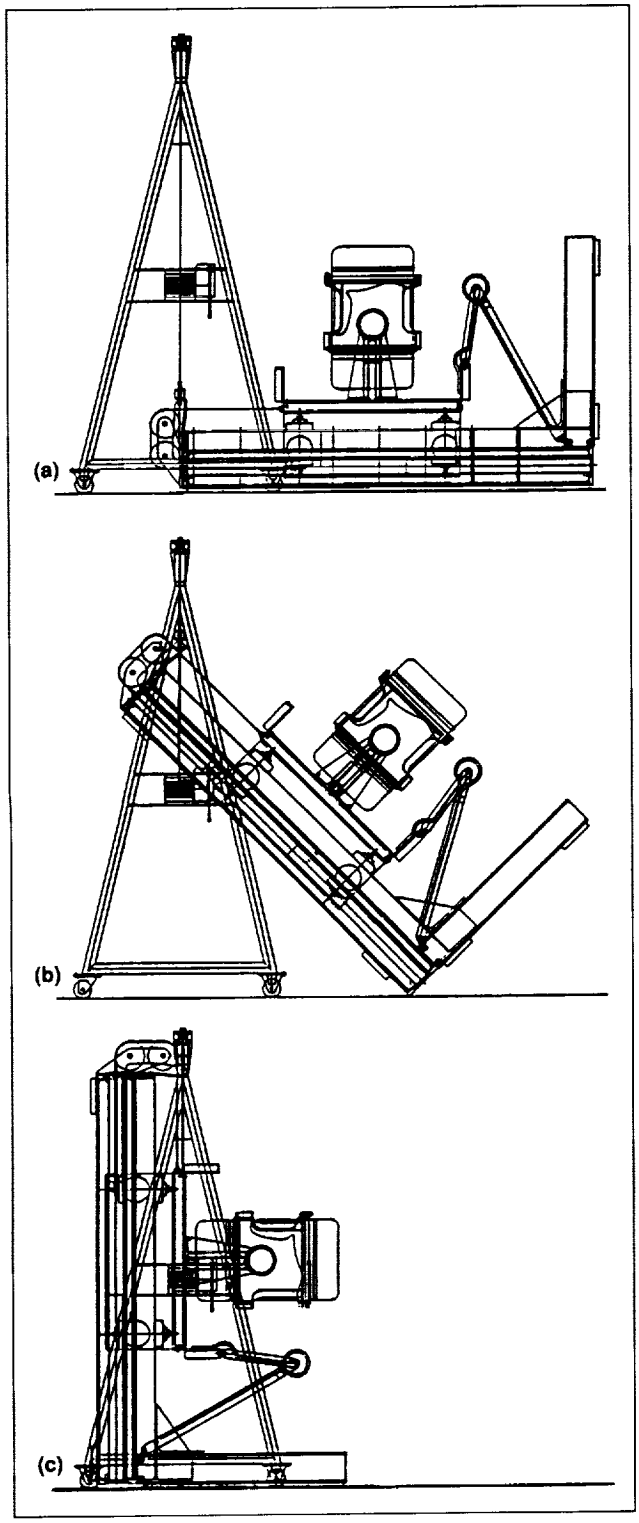

Vestibular sensors provide information on head position as well as on linear and angular motion in inertial space. Output from these biological linear and angular accelerometers is used by the brain to produce eye movements to compensate for head motions, stabilizing the eyes and vision in inertial space. Vestibular linear acceleration receptors (otoliths) play a critical role in control of eye movements during head pitch, roll, or linear motion. These receptors code position with regard to Earth gravity and translation. The exact eye-movement control mechanisms are not understood, especially how the sensors interact in the brain, how linear motion produces eye movements, and how linear motion is differentiated from head tilt by the brain. Brain mechanisms that use otolith output are affected by microgravity exposure resulting from the removal of Earth gravity effects. An objective of NASA's Biomedical Research Program is to understand how this system adapts to weightlessness and readapts to Earth gravity on return from space. To study the system, responses must be recorded during controlled, noise-free, linear head motion during spaceflight and during readaptation after return to Earth.

During the past year, a portable linear sled (PLS) for the biomedical research program was designed and fabricated (see figure). The PLS was designed to provide controlled linear motion parallel or orthogonal to Earth gravity. A modular approach was used to facilitate field assembly and disassembly; no piece weighs more than 600 pounds. Off-the-shelf air bearings support a carriage which contains a superstructure that enables subject reorientation with respect to the linear motion axis and to the delivery

Fig. 1. The portable linear sled (PLS). Hardware includes a hand-operated gantry which is shown reorienting the PLS track from an Earth-horizontal (a) to an Earth-vertical (c) position.

of angular rotations. The air bearings "float" on 6- by 12- by 96-inch ceramic rails polished to a tolerance of 0.003 inch. Controllable motion is supplied by a pulse-width modulated linear servometer with a programmable controller. After design, fabrication, and testing at Ames, the PLS was disassembled, transported to Russia, and reassembled for testing of rhesus monkey responses before and after a 14-day orbital flight. Preflight testing of 12 subjects has been completed, and the data are being analyzed. Postflight testing will take place in January 1993. Experimental results will be compared with the results of extensive background studies of rhesus and squirrel monkeys that have been conducted using sleds at Ames.

Ames-Moffett contact: D. Tomko
(415) 604-5723
Headquarters program office: OSSA

Comparison of a Microgravity Experiment and a Hypergravity Equivalent

Marilyn Vasques

The effects of microgravity and hypergravity (centrifugation) on living systems have been documented from various U.S. and Russian spaceflights and ground-based experiments. Previous studies have focused solely on either microgravity (0 G) or hypergravity (2 G). Different experimental conditions have precluded direct comparison of 0 G and hypergravity effects. The objective of our "Cosmos 2 G" study was to compare hypergravity results with microgravity results from a previous spaceflight mission (Cosmos 2044, 1989). The experiment conditions were duplicated to facilitate comparison. The same strain and number of rats, diet, feeding schedule, cage size, and other environmental conditions used on the Cosmos mission were used for the hypergravity study. Comparisons were made to determine which physiological systems are affected by alteration of gravity and whether the changes follow a gravitational-force continuum.

In a microgravity environment, the animals have access to the entire cage (three dimensions), whereas in a gravity environment they can use only the bottom of the cage, so it was necessary to determine whether or not this difference would result in a crowding effect which would nullify the comparison. In an initial study, rats that were housed either 10 per cage, as in the spaceflight mission, or five per cage were centrifuged for 14 days, the same length of time as the spaceflight mission. Growth rates of rats housed 10 per cage were then compared to those of rats housed only five per cage. No significant difference was found.

The Cosmos 2 G study was then conducted and tissue samples were collected in a manner similar to that of Cosmos 2044. Over 2000 samples were collected, preserved, and distributed, for analysis, to the same investigators as for the previous Russian mission. The tissue samples are now being analyzed. The body and tissue weights as well as blood chemistry data are presented here.

Although the rats from Cosmos 2 G and Cosmos 2044 were of the same strain (Wistar), the Cosmos 2 G rats had a much higher growth rate than the Russian rats. As a consequence, the rats were the same weight at the beginning of both studies although there was a significant difference in their ages (Cosmos 2044 rats were 107 days old, Cosmos 2 G rats, 60 days old). Both the Cosmos 2 G (hypergravity) and Cosmos 2044 (microgravity) studies had appropriate 1 G controls. The results are presented here as differences ($p < 0.05$) between the flight or centrifuged rats and their respective controls. Body weights of Cosmos 2044 (0 G) rats were unaffected, whereas hypergravity (2 G) inhibited growth (see first figure). Microgravity (0 G) had no effect on organ weights (per 100 g body weight) but 2 G increased the kidney, spleen, adrenal gland, and testis weights. The weights of eight hindlimb muscles increased in 2 G rats; three other muscles were

unchanged. In 0 G, four muscles had reduced weights and seven muscles were unchanged. The muscle that was most affected by microgravity, the soleus, was one of those that increased in weight as a result of 2 G (see second figure). Testosterone was unaffected by 2 G but was reduced 86% after 0 G. In both groups, thyroxine was decreased and corticosterone was unchanged.

The responses of tissue weights and plasma chemistry to gravitational force are not universal. In our study, different tissues responded to the altered force in different ways. Muscles that support the body against gravity on Earth responded to gravitational force in a linear fashion whereas other skeletal muscles responded only to 2 G. A concurrent study of muscle tissue response to microgravity, hypergravity, and simulated microgravity (hindlimb suspension) would be informative.

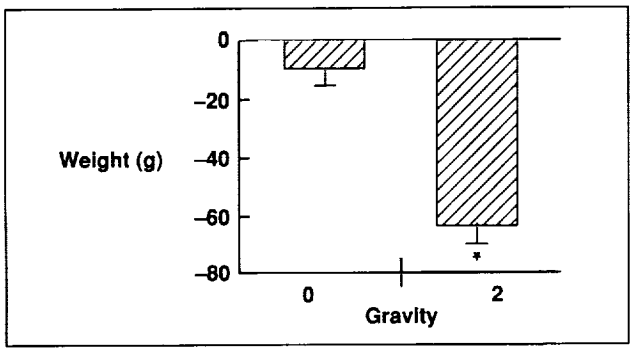

Fig. 1. Body weight of rats (difference from 1 G control).

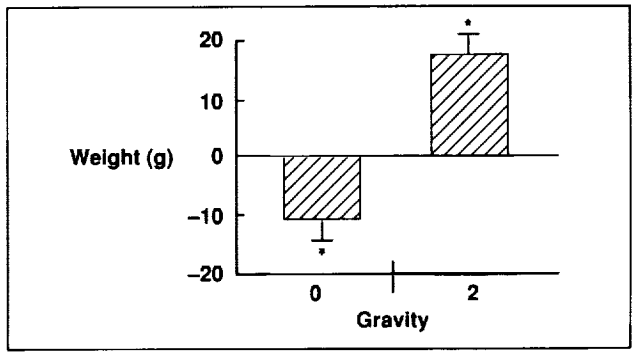

Fig. 2. Change in weight of soleus per 100 g body weight (difference from 1 G control).

Ames-Moffett contact: M. Vasques
(415) 604-6120
Headquarters program office: OSSA

An Exercise Device that Uses Self-Generated Lower-Body Negative Pressure

Donald E. Watenpaugh

Exercise against the footward force produced by lower-body negative pressure (LBNP) may provide a simple and inexpensive technique to simulate gravity during spaceflight. To allow the legs themselves to generate the negative pressure against which they work, a flexible cylinder around the lower body which is sealed at the waist expands and collapses longitudinally, but not radially (see figure). As the legs push footward to expand the cylinder, the air pressure in the cylinder decreases, increasing the force required to continue expanding the cylinder. In theory, a subject in microgravity expanding such a cylinder (radius 30 centimeters) from 75 to 100 centimeters in length generates 7763 newtons of force at the outer extent of expansion, and reduces the internal pressure 206 millimeters of mercury (mmHg). A 70-kilogram person "weighs" 686 newtons. In practice, the negative pressure and the resulting force achieved are limited by the user and by an adjustable valve that allows controlled airflow into the cylinder. An additional valve remains closed during cylinder expansion, but allows air to enter the cylinder during retraction. Shoulder straps and/or handles on top of the cylinder allow the subject to counteract the downward force exerted by the legs. The force produced depends on air inflow rate, cylinder radius, and length and rate of expansion. When the

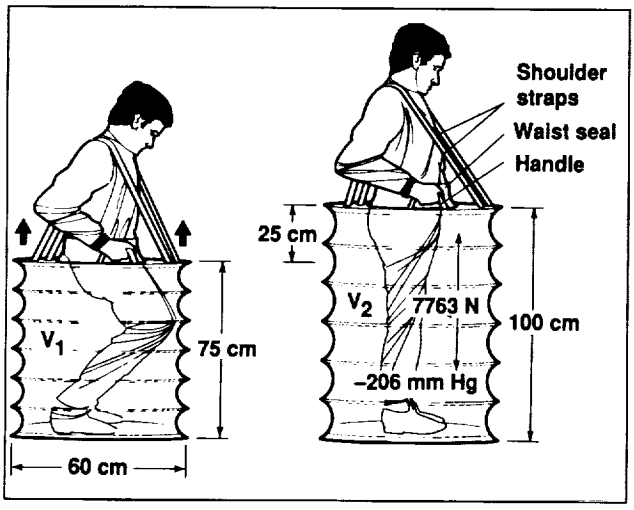

Fig. 1. Self-loading exercise device.

adjustable valve is nearly closed, exercise with this device is analogous to a leg press. When the valve is farther open, more rapid knee bends can be performed. With both types of exercise, workload increases as a result of increasing leg mechanical advantage.

Seven healthy subjects (weight 70.0 ± 5.0 kilograms (mean ± SE)) performed knee-bend exercise (analogous to repetitive concentric leg presses) at 19 cycles per minute for 5–6 minutes. Footward force was measured with load cells, cylinder pressure by a transducer, heart rate by electrocardiogram, and oxygen consumption by turbine volumetry and gas analysis. Maximum footward force at the peak of the exercise cycle averaged 1116 ± 87 newtons (114 ± 9 kilograms), and pressure within the cylinder concomitantly decreased 26 ± 3 mmHg below ambient pressure. Heart rate and oxygen consumption increased 75 ± 4 beats per minute and 26.3 ± 1.4 milliliters per kilogram per minute, respectively, from supine resting values. One subject (the strongest in the group) achieved 2958 newtons (302 kilograms) at maximal effort in the negative-pressure exerciser with the air inlet valve fully closed.

This self-loading exercise device has many features that make it attractive for use during spaceflight. First, it is safe: workload is controlled and limited entirely by the user, no potentially dangerous inertial forces are generated, and the maximum attainable LBNP levels (about 70 mmHg) are transient and user-dependent. Second, the device primarily strengthens the antigravity muscle groups of the legs and back in a manner similar to a standing leg press. These muscles are the most susceptible to microgravity-induced atrophy, and therefore are in greatest need of exercise during spaceflight. Also, spinal loading from this type of exercise may prove beneficial in alleviating back pain experienced by astronauts. Third, exercise within this device hypothetically elicits intermittent increases in lower-body vascular transmural pressures, and may effectively simulate the circulatory conditions of upright exercise on Earth by redistributing blood and body fluids from upper to lower body. Fourth, the self-generating LBNP exerciser provides a wide range of exercise rates and workloads simply by the user's adjusting the air inlet resistance. Fifth, the body is ventilated by the cycling of air in and out of the cylinder. Lack of convection in microgravity hypothetically reduces airflow over the skin during exercise. Sixth, the device requires no external power source: the user's movements generate the negative pressure against which they work, and force feedback could be provided by a simple aneroid pressure gauge.

Other advantages include ease of use, low vibration during free-floating use (minimizing impact on sensitive materials-science experiments), simplicity, low mass, collapsibility for stowage, and economy of construction. Modifications are planned which will permit eccentric as well as concentric exercise. Devices for the trunk and upper body could also employ self-generated pneumatic pressure differentials against which exercise could be obtained. The concept of exercising against self-generated pneumatic pressure differentials offers a novel and versatile means of exercising in microgravity. Athletes as well as astronauts could benefit from training with this simple system.

Ames-Moffett contact: D. Watenpaugh/A. Hargens
(415) 604-5747/5746
Headquarters program office: OSSA

Adaptation to Rearranged Sensory Environments

Robert B. Welch

An altered gravitational–inertial environment (e.g., microgravity) produces dramatic errors in vision, motor performance, and visuomotor coordination, as well as an abnormal gain in the vestibulo-ocular reflex and disturbed postural equilibrium and locomotion. Although reports from orbital missions suggest that astronauts are able to adjust to these difficulties in 1 to 2 days, it is important to understand the nature of the adaptive process by which this occurs. The current investigation aims to accomplish this goal, as well as to examine human adaptability to other forms of sensory rearrangement.

In our initial experiment on adaptation to altered gravity we exposed 10 human subjects to 2.0 G along the head-to-foot (z) body axis for 25–30 minutes in the Ames 20-G Centrifuge facility. Before, during, and after this period of hypergravity, subjects were tested on (1) perceived location of a visual target viewed in an otherwise dark setting and (2) accuracy in reaching for an unseen position in space. As expected, at the onset of 2 G_z, subjects perceived the target to be substantially higher than it actually was (the "elevator illusion"), and reached too low for the unseen position (the "muscle-loading effect").

For the remainder of the exposure period, subjects pointed at visual targets and either received visual feedback about their accuracy (the visual-feedback condition) or did not (the no-visual-feedback condition). The muscle-loading effect disappeared after several trials and was replaced by a tendency to reach too high. Of more interest than this proprioceptively based adaptation, however, was the finding that the elevator illusion gradually declined in strength over the course of the exposure period and that it was further attenuated by the presence of visual-error-corrective feedback. It was concluded that the elevator illusion is subject to both sensory habituation, from extended exposure to hypergravity, and adaptation, as the result of active, error-corrective interaction with the gravitationally distorted visual field.

We are particularly interested in the possibility that repeated alternation between exposure to hypergravity and "readaptation" to normal gravity will lead subjects to acquire separate adaptations to both environments. Thus, by means of this "dual adaptation," subjects would be able to make the transition between the two gravitational conditions with much less interference than they experienced at first. We hope to examine this question in our next centrifugation experiment.

In a second series of experiments, we are examining the possibility of dual adaptations by means of an "analog" experiment that involves a rearrangement of hand–eye coordination in a visual tracking task. Subjects are required to alternate between a normal tracking task and one that involves a 108-degree rotation between movements of the hand and movements of a visual cursor viewed on a video monitor. The results of four experiments confirm that dual adaptations can be produced in this situation and that the cues by which subjects distinguish between the two sensory environments include both warning signals, just before the transition, and visual feedback from their initial interactions with the new environment.

In still another series of experiments, we have found evidence of dual adaptation when subjects are required to adapt their target-pointing responses alternately to rightward and leftward optical displacement of the visual field. Even more significant was the discovery that subjects who have undergone this dual-adaptation training regimen acquire the ability to adapt more readily to a "new" prismatic displacement (i.e., one they have never seen before). We refer to this phenomenon as "adaptive generalization." We are currently examining the minimum number of trials and alternation cycles necessary to produce both dual adaptation and adaptive generalization.

The results of our investigations have improved our understanding of human perception and adaptability. They may have implications for the adaptation of pilots and astronauts to training simulators and for the transfer of this training to the real world.

Ames-Moffett contact: R. Welch
(415) 604-5749
Headquarters program office: OSSA

Monitoring the Ground Reaction Forces

Robert T. Whalen, Jason Quintana

Theoretical models and experimental studies of bone remodeling have identified three possible contributors to the bone modeling and remodeling stimulus: peak cyclic force levels (or tissue strain-energy density per load cycle), number of daily loading cycles, and loading (strain) rate. During daily activity the human body is subjected to a random external loading history supplied primarily by the ground reaction force (GRF). The GRF consists of body weight (BW) plus inertial forces (related to intensity of activity) that accelerate the body center of mass. We have hypothesized that monitoring the vertical component of the GRF (GRF_z) may provide a useful method of quantifying activity level in order to investigate the influence of mechanical forces on muscle and bone. We have developed instrumentation to monitor this vertical component of the GRF during normal daily activity.

The components of the force-measuring system are shown in the top part of the first figure. The system is composed of a capacitance insole force sensor and a battery-powered data processing and storage unit. RS232 communication transfers data to a workstation for display and further analysis. The combined dimensions of processor, memory, and signal conditioner are approximately 3 inches by 3 inches by 1 inch. The GRF is sampled at a frequency of 100 hertz to detect peak force levels and load rates during high-intensity activities such as running. Incoming GRF_z data are filtered in the time interval between sampling. The processing unit is designed to operate continuously for approximately two weeks without data retrieval or battery replacement.

The lower part of the first figure illustrates the filtering process applied to a 12-second GRF_z record of standing, walking, and jogging. The microprocessor continuously filters the digitized GRF_z for "significant" peaks (P = force level at the peak) and valleys (V = force level at the valley) in the force–time history, storing peaks and valleys that contribute to a force magnitude, $|P - V|$ or $|V - P|$, greater than a minimum selectable level (e.g., 0.2 BW in the figure). In addition, the processor continuously time-

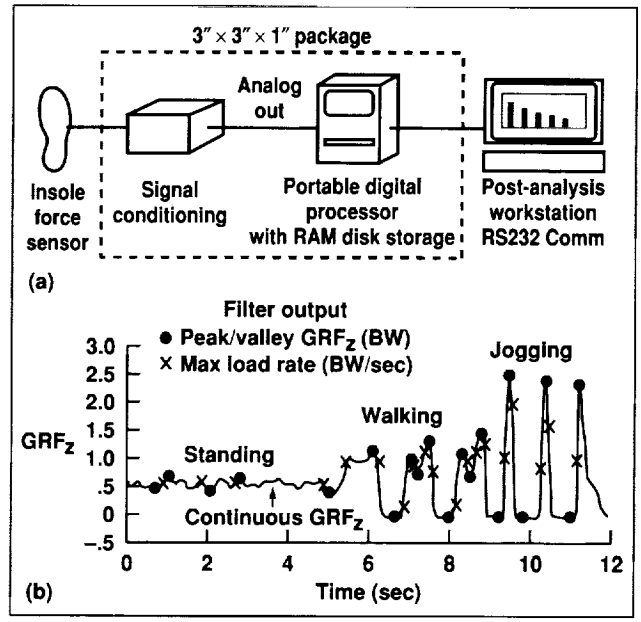

Fig. 1. (a) Insole force sensor and data acquisition system. (b) Continuous and filtered output record from the system.

differentiates the force and saves the maximum load rate between each significant peak and valley. The data logger also stores the time of occurrence of the significant event *and* the total daily duration at force levels partitioned into 0.1-BW intervals. On-board postprocessing sorts the loading cycles into a histogram organized according to cyclic range ($|P - V|$) and GRF_z loading-cycle offset.

We collected loading rate and loading history data (loading cycles and magnitudes) in a human subject during walking and jogging trials and during one 15-hour day without exercise. Loading of the body, e.g., during heel strike, produces positive loading rates (positive slope of the GRF_z–time history) whereas unloading, e.g., during pushoff, produces negative loading rates. Peak loading rates for walking and jogging were approximately 20 BW per second and 80 BW per second, respectively. Unloading rates

for walking and running were on the order of –10 BW per second and –25 BW per second. Data from a typical "nonexercising" day (second figure) revealed that, according to duration, the body was rarely loaded above approximately 1.0 BW (9 minutes or 1% of the nonresting day). However, approximately 41% of the daily loading cycles had a range of 1.0 BW or greater, whereas 45% had a range of 0.5 BW or less with a GRF_z offset of 0.7 BW.

We believe that long-term monitoring of GRF to obtain habitual individual loading histories may provide new insights into the role of repetitive mechanical loading on the modeling and remodeling response of bone. This method may also be used to evaluate exercise activities in space and to establish loading histories equivalent to those of activities on Earth.

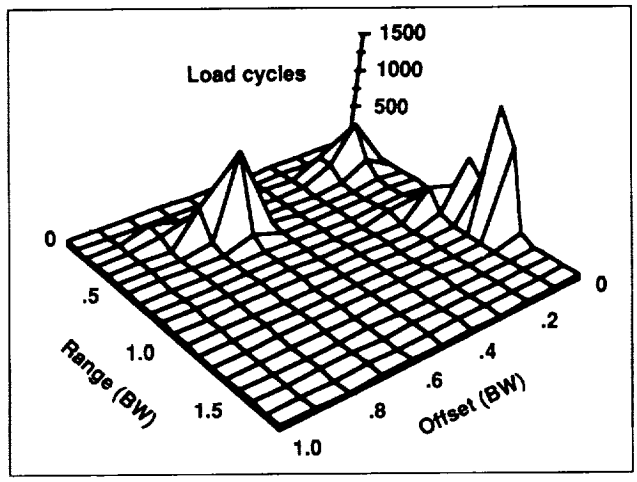

Fig. 2. Loading history for one 15-hour day without exercise.

Ames-Moffett contact: R. Whalen
(415) 604-3280
Headquarters pogram office: OSSA

Life Sciences Experiments Flown on STS-42 (IML-1)

Joellen Lashbrook, Charles M. Winget

With the flight of the space shuttle Discovery and Mission STS-42, the Ames Space Life Sciences Payloads Office (SLSPO) successfully completed an effort that began in 1978. The eight-day mission was the first flight of the International Microgravity Laboratory (IML-1), a unique experiment in international cooperation that involved more than 15 countries. The mission included 51 life sciences and materials experiments, and astronauts from the U.S., Canada, and Germany.

The SLSPO, as payload experiment developer, supported the successful integration and processing of two experiments flown in the Gravitational Plant Physiological Facility (GPPF): Phototropic Transients, referred to as FOTRAN (principal investigator (PI) D. G. Heathcote), and Gravity Threshold, referred to as GTHRES (A. H. Brown). Ames Research Center (ARC) also built hardware and supported three experiments flown on the European Biorack Facility: United States (US)-1 (G. A. Nelson), US-2 (C. V. Bruschi), and US-3 (P. J. Duke). Over 25,000 pieces of hardware were used for the flight.

During the flight, January 22–30, 1992, the experiment environmental parameters were maintained, hardware operated as designed, and all experimental flight objectives were achieved—some were exceeded. A preliminary evaluation of the postflight specimens was performed and it was determined that they were in excellent condition; thus a primary flight objective was achieved.

Flight operations were supported cooperatively by the Ames PIs, the European Space Agency, Ames Research Center, and Payload Operations Control Center Cadre teams. The progress of the experiments and the performance of Biorack and GPPF equipment were monitored at the Marshall Space Flight Center (MSFC) Science Operations Area and the Kennedy Space Center (KSC) Experiments Monitoring Room throughout the mission with two-shift, 24-hour coverage.

The monitoring of the flight activities at MSFC worked very well. The greater-than-expected plant growth during flight (due to precocious seed germination) was dealt with in a positive way by making use of extensive replanning capability. The use of downlink television images of the plants was critical in permitting the GPPF/ARC team to replan the mission and therefore obtain more than 100% of planned data return.

Post-flight operations included the recovery and processing of the flight specimens at Dryden for GPPF, US-1, and US-2, and at KSC for US-3 by the PI/ARC teams. Visual inspection of the flight hardware during deintegration at both recovery sites verified hardware integrity. All GPPF, US-1, US-2, and US-3 hardware functioned flawlessly.

Ames-Moffett contact: J. Lashbrook
(415) 604-5682
Headquarters program office: OSSA

Physiological Anatomical Rodent Experiments

Debra Reiss-Bubenheim

The Secondary Payloads program of Ames Research Center's Space Life Sciences Payloads Office successfully completed the first in a series of eight Physiological Anatomical Rodent Experiments (PARE). The experiment, PARE.01, was a middeck experiment using one animal enclosure module (AEM) which housed eight juvenile female rats. Flown on Space Transportation System 48 (STS-48) as a secondary payload for a 5-day mission, the experiment was designed to investigate the effects of microgravity exposure on juvenile rodent development. The principal investigator for the experiment was Mark B. Tischler.

Muscle atrophy is a serious detrimental effect of long-term spaceflight. Ground-based studies on rodents are routinely conducted using unweighting or muscle unloading techniques such as harness or tail-cast suspension models which elevate the animals' hind limbs above the cage floor. These studies have indicated that posterior hind-limb muscles, whose function depends on weight-bearing, are most responsive to unweighting. Among the so-called "antigravity muscles," the soleus is the most responsive and atrophies quickly when unweighted, while the other posterior muscles show slower deterioration. A problem with ground-based models is that the animals' hind limbs are still subjected to the ever-present pull of gravity, even though the hind limbs do not bear weight. Comparison of spaceflight results with suspension studies suggests that these models have some validity, but insufficient data and ground controls exist to allow valid comparison between the models and actual spaceflight conditions. This flight experiment was designed to provide data relevant to microgravity-induced muscle atrophy and muscle-wasting diseases. This study also provided the first data regarding changes in muscle mass in developing mammals as a consequence of spaceflight.

After the 5.4-day flight, the animals were received at the Dryden Flight Research Facility laboratory, 2 hours after the shuttle landing. After removal from the housing hardware, the animals were weighed and their muscles were excised. Approximately 7 weeks later, two additional groups of animals, housed in standard vivarium cages, were studied as a ground control for the flight group. The second group was tail-cast, hind-limb suspended.

Food and water consumption of the animals, as well as weight gain, were similar to those in previous AEM experiments. Food consumption was 15.6 grams/rat/day; water consumption was 12.5 milliliters/rat/day. Animals gained an average of 35.3 grams during the mission, or 5.6 grams per day. The flight animals gained a significantly greater percent of their body weight per day than the ground controls, although food and water consumption values were similar. The difference may be related to cage volume: the flight animals may have utilized fewer calories because of their smaller cages. Suspended animals gained weight more slowly than either the flight or nonsuspended ground control groups.

The posterior weight-bearing muscles of the hind limb were most affected. Of these, the soleus showed the most atrophy in both the flight and the suspended control animals. The results of this experiment indicate that the tail-cast hind-limb-suspension model of juvenile rats appears suitable for mimicking the effects of microgravity on developing hind-limb muscles.

Ames-Moffett contact: D. Reiss-Bubenheim
(415) 604-3605
Headquarters program office: OSSA

Frog Embryology and Autogenic Feedback Training Experiments on Spacelab-J

Greg Schmidt, Sally Ball

On September 12, 1992, the space shuttle Endeavour was launched on its second mission, carrying the Spacelab-J (SL-J) payload. The SL-J mission was the first major cooperative mission between NASA and the Japanese space agency NASDA, and included 35 experiments developed by NASDA. Two Ames experiments flew on SL-J: the Frog Embryology Experiment and the Autogenic Feedback Training Experiment.

The Frog Embryology Experiment was developed by principal investigator Ken Souza to investigate the effects of microgravity on egg fertilization and subsequent embryo development in the African clawed frog, *Xenopus laevis*. This experiment required three dedicated racks of Spacelab hardware, several stowage lockers, and space on the shuttle middeck for sample cooling. In addition to the general purpose work station (GPWS), the refrigerator/incubator module, and the refrigerator/freezer (versions of these had flown on previous missions), the Frog Embryology Experiment required the development of items of life sciences laboratory equipment as well as experiment-unique equipment. The Electronic Systems Branch was responsible for development and fabrication of the frog embryology unit (FEU), which housed the frogs in a moist, temperature-controlled environment for incubation of the developing embryos at both microgravity and 1 G (see figure).

Four female *Xenopus* were flown on SL-J, and after an in-flight fertilization test two frogs were chosen to provide eggs for the experiment. After fertilization, eggs from both micro-G and 1-G groups were fixed at the 2–4 cell, gastrula, neurula, and tadpole stages for later histological studies. During the mission, behavioral observations were made both on tadpoles from the eggs fertilized in space and on tadpoles from eggs fertilized immediately prior to the mission. In addition to the fixed embryos, approximately 150 live tadpoles were returned to Earth for behavior and maturation studies. All flight frogs were returned in perfect health.

The Autogenic Feedback Training Experiment (AFTE) was designed to investigate the effects of

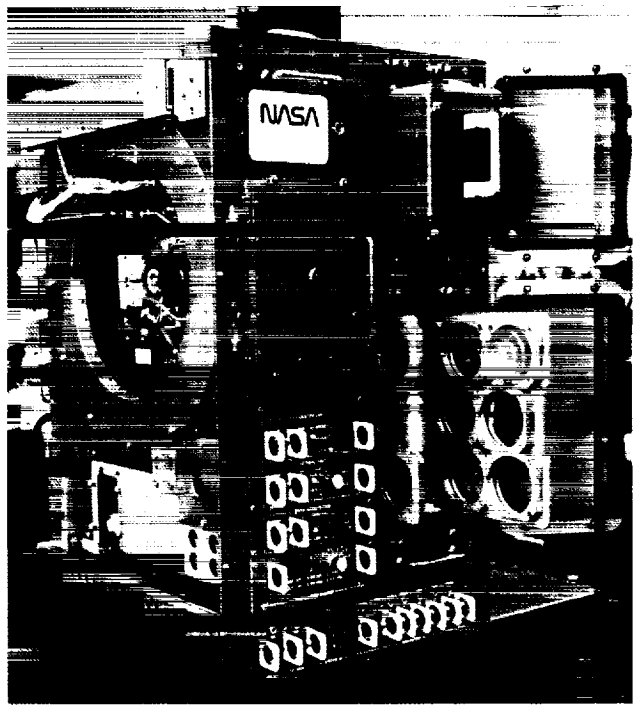

Fig. 1. Frog environmental unit.

autogenic therapy, a form of biofeedback training, on reducing the effects of space motion sickness. This experiment, originally flown on the SL-3 mission by principal investigator Patricia Cowings, is a multimission experiment, originally designed to be complete after 16 subjects were flown. The Autogenic Feedback System, designed and managed by the Electronic Systems Branch, was developed into a small, self-contained system, the AFS-2, which records electrocardiogram, respiration rate, skin conductance, blood volume pulse, triaxial accelerations, and temperature. Several of these parameters are displayed on a wrist display unit, which is used in-flight as a biofeedback aid.

Two of the SL-J flight crew participated in the AFTE, one as an experimental subject and one as a control. Two years before the flight, baseline data were collected on both crewmembers in resting,

ambulatory, and motion-sickness-provocative environments. The experimental subject then received 16 hours of AFT (this was repeated later because of mission delays), and data were again collected on motion sickness susceptibility. For the SL-J launch, both participating crewmembers wore the AFS-2 system in a modified configuration in order to record physiological parameters prior to and during launch, as well as during the critical period immediately after launch. The AFS-2 was also worn by the crew during the first three mission days, so that data were continuously recorded while the crew participated in the other flight experiments. The hardware functioned perfectly during the mission, and analysis of the flight data is ongoing.

Preliminary results of the Ames SL-J payload will be published soon. The high level of cooperation between the Japanese and the United States teams during this mission set the stage for future endeavors by our two space agencies.

Ames-Moffett contact: G. Schmidt
(415) 604-6455
Headquarters program office: OSSA

The Astrophysical Simulation and Analysis Facility

Louis J. Allamandola, Farid Salama, Scott A. Sandford, William Schutte, Robert Walker

In the Ames astrophysical simulation and analysis facility, experimental studies of materials produced under conditions similar to those in interstellar space are carried out to provide the fundamental data needed to design future space missions and to interpret the measurements made with existing NASA telescopes and satellites. The principal goals are to (1) discover the composition of such very different celestial objects as comets and some planets and their satellites and, with this information, deduce their evolutionary history and (2) describe the role their composition plays in determining these objects' physical and radiative properties. We are able to measure the ultraviolet, visible, and infrared spectroscopic properties of cosmic-material analogs at temperatures ranging from a few degrees above absolute zero to room temperature. By detailed comparisons of these spectral properties with astronomical spectra measured through telescopes, the composition of the astronomical objects is determined.

Recent contributions from our laboratories include the first measurement of the ultraviolet and visible spectroscopic properties of the polycyclic aromatic hydrocarbon (PAH) pyrene, isolated in neon in both the ionized and neutral forms. This information on a PAH that is truly isolated as in space has direct applications in several areas. As shown in the figure, the strongest band of ionized pyrene falls remarkably close to the famous 4430-angstrom unidentified interstellar absorption band. This 4430-angstrom band is one of about 50 interstellar bands that were discovered in the early part of this

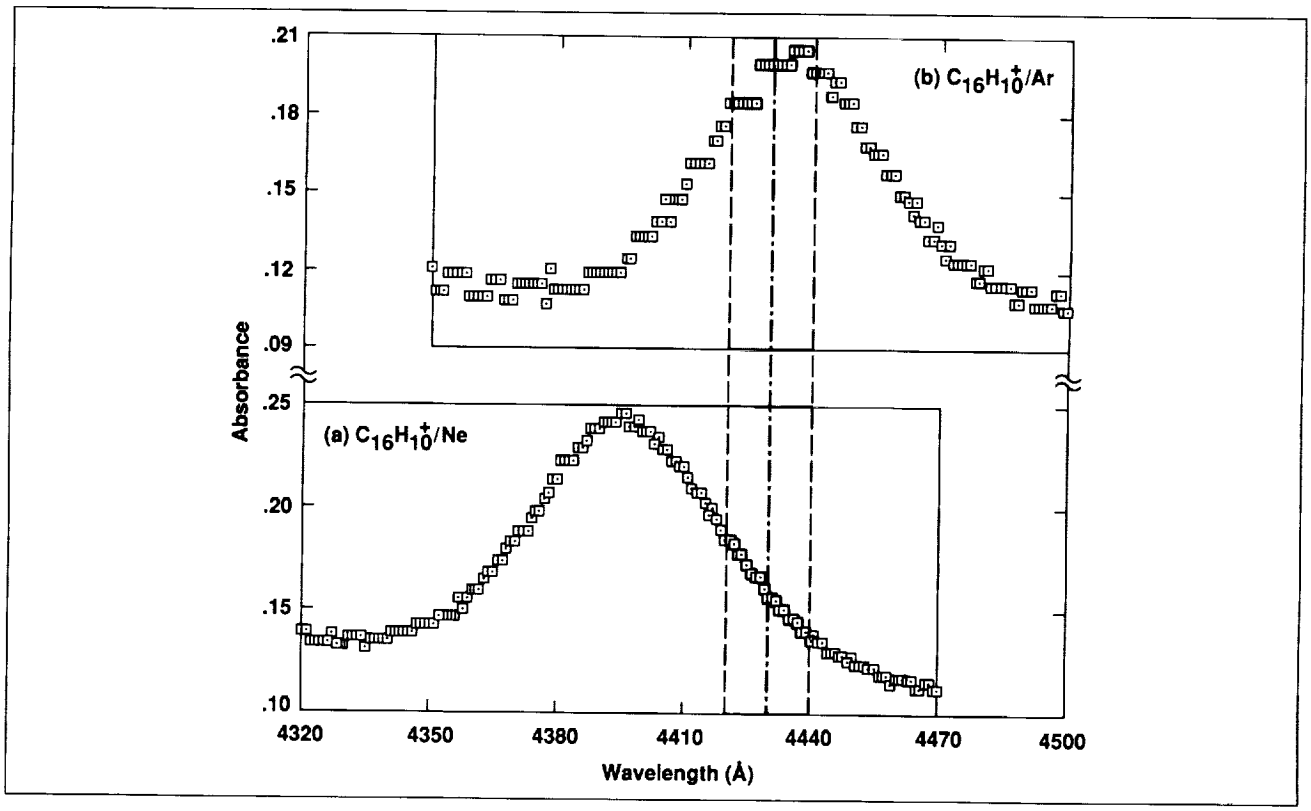

Fig. 1. Comparison of the pyrene ion ($C_{16}H_{10}$) band measured in argon (top) and neon (bottom), in the laboratory, with the position and width (dashed lines) of the well-known 4430-Å interstellar band. The remarkable match in position strongly suggests that a pyrene-like material is the long-sought-after carrier of the interstellar band.

century and which remain unidentified. The identification of the carriers of these bands has been called the classic problem in 20th century astrophysics. The good agreement between our pyrene spectrum and the 4430-angstrom band, which is the strongest and most well-known of the interstellar absorption bands, is an encouraging sign that interstellar PAHs are indeed the agents responsible for most of the unidentified interstellar bands. We previously reported that our spectrum of another PAH ion, the naphthalene ion, matched several of the weaker interstellar bands. This work has already had an impact on this field.

Other studies of interstellar, planetary, and cometary ices are under way. Our experimental studies of the reactions in interstellar/pre-cometary ice analogs has given insight into the chemical and physical nature of the processes that may occur in this complex material. For example, we have recently demonstrated that reactions between formaldehyde and other constituents of these ices can occur at temperatures as low as 40 kelvin. This surprising finding is important to our understanding of the processes that determine a comet's organic composition. It also sheds light on the nature of the organic materials that coat the grains of interstellar space, and that may eventually find their way into meteorites and interplanetary dust particles. This information is especially useful in setting instrumental criteria for the comet sample analysis mission now in the planning stages.

We have also made spectroscopic observations of the organic materials in dense interstellar molecular clouds. We have found that a diamond-like, carbon-rich material seems to be an important and ubiquitous organic component of these clouds, whereas paraffin-like material is the dominant refractory organic component in the diffuse, tenuous interstellar medium.

Ames-Moffett contact: L. Allamandola
(415) 604-6890
Headquarters program office: OSSA

The Outer Heliosphere and Termination Shock

Aaron Barnes

The expansion of the solar wind into the local interstellar medium creates a cavity called the heliosphere. It is generally believed that the wind changes abruptly from supersonic to subsonic flow, at some heliocentric distance within the range of 50–200 astronomical units (AU), via a shock wave, usually called the heliospheric termination shock. Pioneer 10, at present the most distant spacecraft from the Sun, is located at nearly 56 AU heliocentric distance, near the solar equatorial plane. It is possible that the spacecraft will encounter the termination shock within the next several years. The Ames Research Center (ARC) plasma analyzer aboard Pioneer 10 would be the primary instrument used in such a discovery.

We investigated the probable response of the ARC plasma analyzer to shocked heliospheric plasma. We found that, because of its wide spread in direction and energy, the shocked plasma would be detectable only in the two outermost sensors, which have large geometrical factor and long sampling time. But even if the solar wind signal should disappear completely, the termination shock is thought to be moving back and forth, and therefore the signal would almost certainly reappear days or weeks later as the termination shock moved outward past the spacecraft again. Several such encounters with the shock are likely, so the plasma analyzer would provide an unambiguous description of the shock encounters.

We have developed a self-consistent gas-dynamic model of the response of the termination shock to upstream variations in the solar wind in order to estimate the speed of the shock as it moves back and forth. We find that for typically observed variations in solar wind density the shock speed would be 50 to 200 kilometers per second, and a typical inward or outward excursion would be on the order of 1–10 AU.

The sunspot number has been declining since 1990. Through 1991 there were copious and frequent mass ejections from the solar corona, which eventually propagated into the outer heliosphere. The entire heliosphere exhibited frequent high speeds not observed during other phases of the solar cycle. The 1992 period has been quieter, and the heliosphere appears to be approaching conditions more typical of solar minimum.

Comparison of data from Pioneer 10 and 11 and Voyager 2 has been used to study the variation of solar wind temperature in the outer heliosphere. It appears that beyond about 20 AU the average temperature remains fairly constant as heliocentric distance increases. The observations also suggest that there is a systematic variation of temperature with celestial longitude. Both findings can be plausibly interpreted as indications of interaction between the heliosphere and the local interstellar medium.

Ames-Moffett contact: A. Barnes
(415) 604-5506
Headquarters program office: OSSA

The Venus Plasma Environment and the Inner Heliosphere

Aaron Barnes

The Pioneer Venus Orbiter spacecraft was inserted into a highly elliptical orbit about Venus in 1978. Since then, under the influence of solar gravity, the periapsis altitude has varied, increasing from less than 200 kilometers in 1978 to a maximum of over 2000 kilometers in 1986, and decreasing thereafter. In October 1992, periapsis decreased to the point that the spacecraft entered the planet's atmosphere and was destroyed, ending a period of almost 14 years of successful operation.

During this period, the Ames Research Center Plasma Analyzer aboard the spacecraft made extensive observations of the plasma in the environment of Venus. In addition, near-apoapsis observations provide the only solar wind data from a heliocentric distance of less than 1 astronomical unit for most of the mission.

In the past year we have concentrated on electron observations made from low-altitude periapses in the last years of the mission. Such observations are of special importance in assessing the role of electron precipitation in maintaining the planet's nightside ionosphere. Low-altitude periapsis data from early in the mission cannot be used, because at that time the spacecraft's radar was operating. The radar produced strong interference in the electron scans; this source of interference did not exist later in the mission. Our analysis shows no clear evidence of electron precipitation, although there is a suggestion of impact ionization from the atmosphere at the very lowest altitudes. At this stage we place a preliminary upper limit of (1) $\sim 6 \times 10^5$ electrons per square centimeter per second if the electrons are a collimated beam, and (2) $\sim 3 \times 10^8$ electrons per square centimeter per second per steradian if the electrons are distributed isotropically. These results suggest that electrons with less than 250 electrovolts of energy are not a significant contributor to nightside ionization.

Solar wind data from Pioneer Venus and the Earth orbiter IMP 8 were correlated to investigate the global morphology of the inner heliosphere within approximately 7 degrees of the solar equator. Synoptic maps of solar wind velocity, density, and other parameters were constructed for the period between 1983 and 1988, including the sunspot minimum in 1986. The strong latitude gradients characteristic of solar minimum were confirmed. Density and related parameters were found to be highest near the position of the interplanetary neutral sheet, the irregular moving boundary between the magnetic hemispheres of the solar wind.

Ames-Moffett contact: A. Barnes
(415) 604-5506
Headquarters program office: OSSA

Spectral Imaging of Astronomical Polycyclic Aromatic Hydrocarbon Sources

Jesse D. Bregman

Polycyclic aromatic hydrocarbon (PAH) molecules are among the most abundant molecular species in our galaxy, containing from 1% to 10% of all the carbon. They are observed via a series of infrared emission bands spread between 3 and 11 microns. Although the molecules are abundant, their identification was fairly recent, and there is only limited understanding of what factors determine the emission spectrum. Some researchers are not completely convinced that the observed emission features are from PAHs. To determine whether the emission is from PAHs, there are specific predictions about the behavior of the emission features which can be tested.

In collaboration with David Rank and Pasquale Temi of the Lick Observatory and the University of California at Santa Cruz, we developed two infrared cameras which we have used to image several PAH sources through narrow-band filters centered on the 3.3- and 11.3-micron emission features. The observations were made in collaboration with Scott Sandford and Doug Hudgins at Ames. In the PAH model, the two emission features studied are both from the same C–H bonds, although the 3.3-micron feature is primarily from small PAHs and the 11.3-micron feature is from large PAHs. Our images of the star-formation region NGC 1333 show that the 3.3-micron band peaks outside the region of the 11.3-micron emission, where the strength of the ultraviolet radiation from the central star is weak. Since small PAHs are more easily destroyed by high-energy ultraviolet photons than large PAHs, the observed distribution of these bands is understandable if there is a distribution of sizes of PAHs in NGC 1333, and the smallest PAHs do not survive close to the central star.

Similar observations of the preplanetary nebula HD44179 show an object that is centrally peaked and symmetrical at 3.3 microns but double-lobed at 11.3 microns. We interpret these observations as being due to a disk of material around the central star which is optically thick at 11.3 microns but optically thin at 3.3 microns. Laboratory measurements of absorption cross sections for PAHs show that the 11.3-micron absorption cross section is nine times greater than the 3.3-micron absorption cross section, consistent with PAHs being the source of the emission in this nebula.

The capabilities of the two infrared cameras have opened up a new area for our research. Spectral imaging is a powerful method for studying the emission from extended objects. We are currently analyzing images of the Orion Bar and comparing the PAH band strengths with models calculated by several investigators at Ames (Schutte, Allamandola, and Tielens). These data and models will provide, for the first time, the basis for a quantitative study of PAHs. The cameras are also being applied to other studies, including an examination of ice distribution in star-formation regions and the supernova rate in galaxies.

Ames-Moffett contact: J. Bregman
(415) 604-6136
Headquarters program office: OSSA

Telepresence for Planetary Exploration

Geoffrey Briggs, Carol Stoker

When human exploration of Mars begins in the first decades of the next century, the character of robotic spacecraft on the surface of Mars can change substantially from relatively simple semiautonomous machines to robots having virtually the full range of human capability. This transformation will be the result of powerful telepresence and virtual-environment technologies that are being developed at Ames Research Center and elsewhere in the Santa Clara Valley. Mobile robots will be teleoperated (through communication satellites circling Mars) by geologist astronauts from their Mars base through control systems that will link the robot to the operators' instinctive viewing (eye and head motions) and manipulation (arm and hand) capabilities. Through such systems the Mars astronauts will be able to extend their reach across the entire planet. As an example, the permanent south-polar cap of Mars can be explored by an astronaut located at a base closer to the equator. Such an experimental capability was demonstrated at Ames in December 1992 when, through a combination of satellite and land-line communication links, a small telepresence-controlled remotely operated vehicle (TROV) explored the ice-covered waters of McMurdo Sound in Antarctica.

The TROV has been under development at Ames for more than a year to continue studies of the ecology of the unique ice-covered lakes found in the Dry Valleys of Antarctica—regions that are the closest analog on Earth to conditions found on the frigid desert surface of Mars. Mars has no liquid water on its surface, only solid water ice at the north pole (the permanent southern cap is mostly dry ice—CO_2) and permafrost. In the distant past, however, there evidently was liquid water on Mars and, before it was finally all lost, there may well have been long-lived ice-covered lakes not unlike those of the Dry Valleys. The microbial life forms found in abundance at the bottom of Antarctica's frigid lakes are, therefore, of considerable interest to exobiologists at Ames who are seeking to understand the conditions under which life might have evolved on Mars and, also, where the most promising places might be to look for fossil or chemical evidence of ancient life. Diving in the Antarctic lakes is difficult, and the radius of operation of divers from a dive hole cut in the ice is limited. Remotely operated vehicles have already made a significant difference in what can be accomplished in the brief time available for exploration during the austral summer. The new TROV opens the window of opportunity even further.

After limited testing of the TROV off the Florida Keys in December 1991, the vehicle was further developed during the year. A single color camera is mounted on a servocontrolled platform. The camera has sufficient motor power to rapidly follow the head motions of the operator. The operator's vision display system was upgraded during the year to one that has an image, with superimposed navigation data, provided to each eye through a television projector and a fiberoptic bundle. Head motions are tracked by a magnetic device that is available commercially. A scientific payload (to measure oxygen levels and temperature) and a data recording system were also developed during the year; these systems were mounted on and inside the submersible vehicle so that, in addition to observing the distribution of microbial mats in the lake, the vehicle could be used for systematic mapping of chemical and physical properties. Testing of the system was conveniently carried out in the U.S. Navy swimming pool at Moffett Field and, later, in the clear waters of Lake Tahoe.

The TROV was shipped to the Antarctic in mid-August, to be followed by the study team in November—part of a continuing research program and, now, part of a joint NASA–National Science Foundation program to carry out mutually beneficial

research in Antarctica. The team, led by Robert Wharton of the University of Nevada's Desert Research Institute (DRI), included Carol Stoker (Ames), Dale Andersen (Lockheed), Don Barch (San Jose State University), and Scott Tyler (DRI). Wharton and colleagues operated the TROV under the ice at Lake Hoare as planned. The team also deployed a pair of solar arrays constructed by the NASA Lewis Research Center to power their camp (the TROV itself requires a powerful diesel generator). On return to McMurdo Base the TROV was used to demonstrate the potential of real-time control from the U.S. via a satellite hook-up that had been established by Mark Leon and colleagues of the Science Internet Office at Ames. Television images were returned via an Intelsat satellite relay, laser and microwave links, and fiber-optic ground segments. Commands were relayed to the Antarctic via a multisegment land-line system. With this two-way link, Butler Hine of the Information Sciences Division at Ames was able, from his robotics laboratory, to control the TROV's camera in real time while it was operating under the ice in McMurdo Sound; he used a head-mounted display system similar to that used by the researchers at Lake Hoare. This demonstration, the result of a last-minute opportunity, was accomplished one year earlier than planned.

Ames-Moffett contact: C. Stoker
(415) 604-6490
Headquarters program office: OSSA

Hypervelocity Impact Survivability Experiments for Carbonaceous Impactors

Ted E. Bunch

A small fraction of the craters in NASA's Long Duration Exposure Facility (LDEF) contain carbon-bearing residues. Few detailed investigations of carbonaceous impactors have been made, although the information contained within these impactors is vital to understanding their origin and significance. Two of the three crystalline forms of carbon—diamond and graphite—are known to occur in meteorites, and diamond occurs in the interstellar medium (ISM). Amorphous carbon and poorly crystallized graphite (PCG) form the bulk of the carbon inventories in carbonaceous chondrites. Many other organic compounds are also present, including polycyclic aromatic hydrocarbons (PAHs), which are also found in the ISM. All of these and yet other organic compounds may occur in comets. The possibility exists that the LDEF sampled carbonaceous particles from all of these environments. In addition, fullerene, the third form of carbon, was recently identified in an LDEF crater by means of single-laser-ionization mass spectrometry, although fullerenes have not yet been identified in meteorites or in the ISM.

In the attempt to characterize and interpret LDEF carbonaceous residues, several questions were addressed by experimentation: (1) Can carbon crystalline phases and organic compounds survive low-velocity (<6 kilometers per second (km/sec)) impact and if they do survive, what are their characteristics? (2) If they do not survive impact, what are their impact products? and (3) Were the fullerenes formed from other carbonaceous materials at impact or were they primary, i.e., did they survive impact?

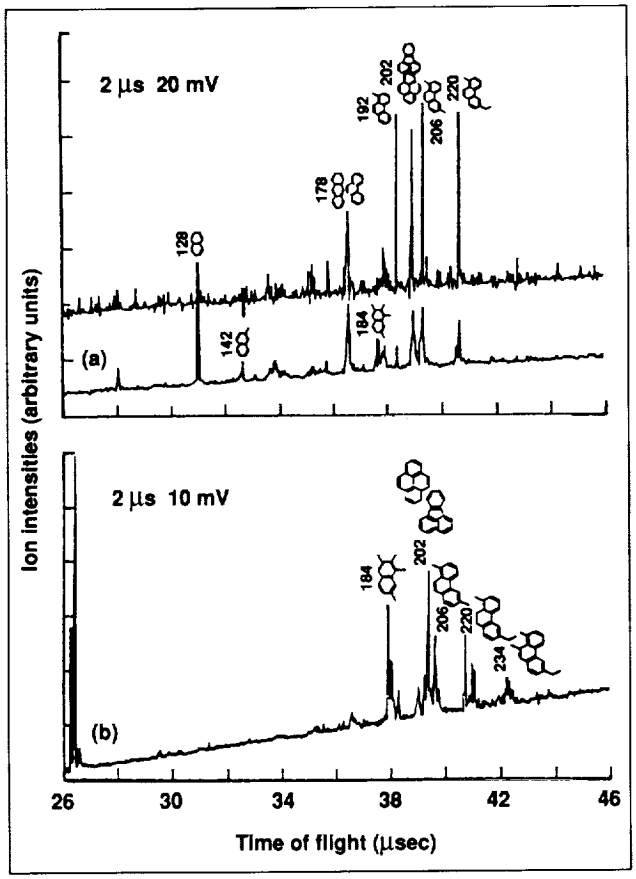

Fig. 1. (a) Laser desorption/multiphoton ionization time-of-flight mass spectrum of nonimpacted Murchison meteorite. Possible mass identifications are 128, naphthalene; 178, phenanthrene/anthracene; 192, methylphenanthrene; 202, fluoranthrene/pyrene; 206, C_{16}-alkylphenanthrene/C_{16}-alkylanthracene; and 220, C_{17}-alkylphenanthrene/C_{17}-alkylanthracene. (b) 100-shot averaged spectrum for the Murchison sample impacted at 5.9 km/sec. Possible mass identifications are 184, C_{14}-alkylnaphthalene; 202, fluoranthrene/pyrene; 206, C_{16}-alkylphenanthrene/C_{16}-alkylanthracene; and 220, C_{17}-alkylphenanthrene/C_{17}-alkylanthracene. Note the loss of the lowest-mass PAHs below mass 184.

Light-gas-gun hypervelocity experiments were conducted using the Ames Vertical Gun Facility.

In an analytical protocol that included field-emission scanning electron microscopy (SEM) imagery, SEM analyses, laser Raman spectroscopy, single and two-stage laser mass spectrometry, and laser-induced fluorescence (LIF) it was found that (1) diamonds did not survive impact at 4.8 km/sec, but were transformed into various forms of disordered graphite; (2) intact, well-ordered graphite impactors did survive impact at 5.9 km/sec, but were only found in the centers of the crater bottoms. The degree of impact-induced disorder in the graphite increased outward (walls, rims, ejecta); (3) phthalic acid crystals were destroyed on impact (at 4.2 km/sec), although a large proportion of phthalic acid molecules did survive impact; (4) fullerenes did not form as products of carbonaceous impactors (5.9–6.1 km/sec). Fullerene impactor molecules mostly survived impact at 5.9 km/sec; and (5) two Murchison meteorite samples (launched at 4.8 and 5.9 km/sec) showed preservation of some higher-mass PAHs compared with the nonimpacted sample (see figure). Each impactor type shows unique impactor residue morphologies produced at a given impact velocity.

We are performing additional impact experiments on survivability of carbonaceous impactors for use in LDEF impactor interpretation and also to possibly shed light on the survivability of carbonaceous materials delivered to the Earth by comets and other accreting bodies.

Ames-Moffett contact: T. Bunch
(415) 604-5909
Headquarters program office: OSSA/OAST

Particle–Gas Dynamics in the Protoplanetary Nebula

Jeffrey N. Cuzzi

Theoretical and observational studies have demonstrated that flattened disks of dust and gas form as a natural byproduct of stellar formation, and the global thermal and dynamical properties of these disks have been established. Many researchers believe that planets result from settling of particulates into a sufficiently flattened layer that gravitational instability may occur. Others believe that accretion must have been a much slower, step-by-step process. The physical and chemical properties of primitive meteorites provide clues to these processes. Our studies have focused on the formation environment of primitive bodies within a settled layer, carefully modeling the dynamical and radiative interactions of nebula gas and particulates. Our fluid dynamics group (Cuzzi, A. Dobrovolskis of U.C. Santa Cruz, and J. Champney of Synernet, Inc.) interacts closely with Ames investigators P. Cassen and T. Bunch.

In 1992, we utilized our Reynolds-averaged Navier–Stokes two-phase, compressible, viscous model in a one-dimensional configuration to model particle settling and diffusion near the midplane of a circumstellar nebula at a stage in which the particles had grown to tens or hundreds of centimeters. Considerable effort was given to realistic modeling of all relevant turbulent transport terms, and significant numerical difficulties were overcome. An effort was made to develop a relationship between eddy viscosity and turbulent kinetic energy in a rotating system; this relationship is not well covered in the literature. We ran models for a range of particle sizes between 10 centimeters and 1 meter, at nebula locations ranging from the Earth's location to Saturn's location. We also ran a set of models in a likely circumplanetary nebula, such as that within which a system of regular satellites might form. The results imply that gravitational instability is precluded in all of these systems, given the likely abundance of solid material in the early solar nebula. By the time particles grow sufficiently large to settle into a layer which is marginally gravitationally unstable, their mass is too large and their abundance too low to permit the strong energy dissipation that is required for these incipient instabilities to collapse directly to solid planetesimals. We have backed up these numerical results by theoretical studies.

The results define the radial drift velocities of forming objects. In regions where the particle density is low, the gas orbits at a slower rate than the particles because it is pressure supported. This causes a headwind or drag on the particles, which then spiral in toward the sun on time scales of hundreds to thousands of years in quiescent nebulae. This effect is greatly enhanced in certain active, if short-lived, stages of nebula evolution through which all solar-type systems are believed to pass repeatedly. During these stages, particles may be lost in less than a hundred years. However, we have found that the mass density of the particle layer near the midplane greatly exceeds that of the gas, and therefore, by drag forces, causes the gas to orbit more rapidly than it would in the absence of particles. The headwind incurred by the particles, and the inward drift that results, is thus reduced by as much as an order of magnitude very near the midplane. This occurrence might provide an important means of preserving solid objects during brief epochs of high nebula activity.

Ames-Moffett contact: J. Cuzzi/A. Dobrovolskis
(415) 604-6343/4194
Headquarters program office: OSSA

Planetary Ring Dynamics and Morphology

Jeffrey N. Cuzzi

Planetary rings as a class share many structural similarities, and presumably have similar controlling processes, but there are also great differences in structure and particle properties. From an understanding of the structure and dynamics of planetary rings, we hope to gain insight into how planets form from their own protoplanetary particle disks.

One process that should affect all ring systems is "ballistic transport" of material that is ejected after meteoroid bombardment of ring systems. The process is principally that of mixing the meteoroid mass with the icy ring particle mass, and redistributing both, to a degree that is determined by the properties of the ejection process, the surface mass density and optical depth (area fraction), and the typical particle size in the given ring region. In 1992, Cuzzi and Stanford student Paul Estrada modeled the implications of this process for the variation of ring particle albedo near the B-ring–C-ring boundary, where there is a factor-of-two shift in the particle brightness and color ratio. We implemented a radiative transfer model for the grainy regolith (porous surface region) of a single ring particle, to obtain the particle's reflectivity and subsequently that of the ring region in the geometry of the observations. This model requires only the wavelength-dependent refractive indices of the grains and an estimate of the degree of forward scattering of a typical grain, and is an improvement over commonly used models for regolith radiative transfer. The model naturally explains why the optically thin (C ring) and thick (B ring) regions have their respectively low and high particle albedos, and relates the albedo to an "exposure age" of the rings. We can reproduce the observed radial profiles of both ring brightness and ring color very closely given our hypothesis of extrinsic bombardment by primitive (cometary) material. We find that the rings must have had a small but significant amount (tenths of a percent by mass) of a reddish, possibly differentiated component such as an organic material or ferric iron compound. This compound must have been well mixed within the ring material at some initial time before the onset of extrinsic bombardment by primitive cometary material, which is known to be both highly absorbing and fairly colorless in the visual spectral range. By fitting the model results to the observed radial profiles of brightness and color, we can determine the efficiency with which extrinsic material remains unaltered by the high-velocity impact, thus removing one important unknown from the problem. Then, based on the currently estimated flux of interplanetary material at Saturn (from Pioneer 10 and 11 data), we can estimate the age of the rings as roughly 100–200 million years, much younger than the solar system. We plan to apply this technique to other regions within Saturn's rings. Our radiative transfer approach could possibly be applied to compositional evolution of satellite surfaces as well.

Ames-Moffett contact: J. Cuzzi
(415) 604-6343
Headquarters program office: OSSA

The Influence of Continental Evolution on the Rise of Oxygen in the Ancient Atmosphere

David J. Des Marais

It has long been recognized that plants and algae created the oxygen that makes up 20 percent of our atmosphere and sustains many forms of life. Before about 2 billion years ago, oxygen was a trace constituent of the atmosphere. The timing and magnitude of the oxygen increases that occurred, and the processes that controlled them, are not well understood.

When oxygen is produced during photosynthesis, organic matter is also produced for the sustenance and growth of algae and plants. Almost all of this organic matter is subsequently destroyed by the process of respiration, in which oxygen is consumed. However, some of the organic matter is buried in sediments such as those in river deltas, estuaries and swamps. This burial permits some of the photosynthetic oxygen to accumulate in the atmosphere. If it were possible to measure how rapidly organic matter had been buried during the Earth's history, it should be possible to deduce how rapidly oxygen accumulated in the ancient environment. An estimate of organic burial rates can be obtained when measurements of stable carbon isotopes in carbonates and organic matter in shales are evaluated, together with the history of the continents. H. Strauss (Ruhr Universität Bochum, Germany), R. Summons (Australian Geological Survey Organization, Canberra), J. Hayes (Indiana University), and I conducted such a study.

The inventory of organic matter in Earth's crust increased steadily between 2.5 and 0.6 billion years ago. This finding is consistent with the observation that atmospheric oxygen levels increased during this period. Furthermore, these increases occurred principally during periods when continents experienced rifts and collisions on a global scale. These events were accompanied by increased rates of erosion and sedimentation, which coincide with relatively rapid rates of organic burial. Thus the inventory of atmospheric oxygen has apparently been controlled by geological as well as biological factors.

Because oxygen is required by multicelled life forms such as plants and animals, its abundance and availability could have influenced the timing of their first appearance. Thus the evolution of life has apparently been controlled in part by the evolution of the planet and its continents. This principle should be kept in mind as we search for biospheres, either extinct or extant, on Mars and elsewhere in the cosmos.

Ames-Moffett contact: D. Des Marais/A. Tharpe
(415) 604-3220/6110
Headquarters program office: OSSA

A Gas Chromatographic Column for Storing Sample Profiles

Jean-Marie D. Dimandja, Jose R. Valentin, John B. Phillips

A technique was developed that is based on a sample storage column that preserves the true time profile of an analyte. A gas chromatography column is used to retrieve chemical information for a component of interest. The purpose of the storage column is not the separation of compounds, as in gas chromatography, but rather the selective retardation of a compound concentration profile with respect to time. Potential applications of this technique include the measurement of component profiles in planetary atmospheres where there is insufficient time for analysis during probe descent; the study of environmental substances in remote environments; the replacement of hygrometric instruments; and the improvement of certain medical analyses.

The main advantage of this storage system is its convenience for use in remote areas. The sample is accumulated for an appropriately long time, and then is read in as short a time as conveniently possible. The operation of the storage system can be compared to that of a tape recorder. In a tape recorder, sound (analogous to the concentration profile) is recorded onto a magnetic tape (analogous to the storage column) as a function of time. The signal is stored until it is convenient to play it back (readout time). The playback version of the signal is an accurate reproduction of the original signal.

The goal of the sample storage technique is to capture and store an analyte of interest over a period of time, and then analyze the sample profile later when it is convenient to do so or when the storage column is retrieved from its remote location. The storage column stores the sample continuously at a low temperature and then releases it more quickly at a high temperature.

The storage process can be divided into three distinct stages: the sampling stage, the storage stage, and the readout stage. During the sampling stage, the sample stream enters the column at a low temperature. During the storage stage, the gas flow is shut off. This stage includes the time during which the sample

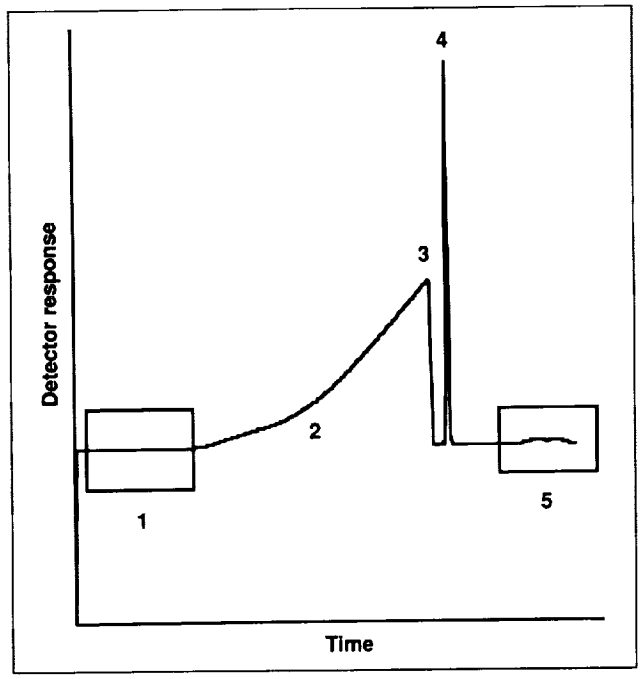

Fig. 1. A typical profile for storage and readout of octane. A sample profile was stored at 60°C and read out at 100°C. The sampling period (1) lasted 2400 seconds. The storage period (2), during which the flow was shut off, lasted 5400 seconds. The baseline drift is due to the flow being shut off on the sample line of the thermal conductivity detector while the reference line was left on. The sudden drop (3) corresponds to the moment when the flow was reopened. A small leak was present in the system, resulting in air entering the system during the storage period. The air peak (4) corresponds to the time it took for this accumulated air to reach the detector after the flow was reestablished in the storage column. Finally, the sample profile (5) eluted through the detector. Conditions such as sampling and readout temperature, sampling period, storage period, and readout period varied with different experiments.

profile is stored and the time it takes to increase the temperature of the column from the sampling temperature to the readout temperature (heating time). During the readout stage, the flow is reopened and the stored sample elutes to the detector at a high temperature. The sampling stage and the readout stage are isothermal processes.

The storage process is shown in the first figure. An injection pattern was input at the sampling temperature through the use of a software program that generated periodic pulses into the column. This injection pattern is a simulation of a changing stream in the sense that the periodic injections are events in time that are occurring in the sample profile. The injection valve is a convenient way to generate a, model changing sample stream. The injections should not be looked upon as samples taken from a stream but as the changing stream itself which flows directly into the column.

In one experiment, four injections were made during the sampling period. The flow through the column was then shut off and the temperature of the oven was raised to 130°C. This was done because it was easier to manually control one flow line instead of having to control both lines. The changing gas flow resulted in a detector baseline drift (marked as zone 2 in the first figure). Once the temperature had stabilized at the readout temperature of 130°C, the valve controlling the flow through the column was reopened. The detector readout of this response is shown in the second figure. The four injections, at 30°C, were done at 1550, 3100, 4650 and 6200 seconds. The injector alternates between 60- and 100-milliliter sample loops, thus providing sample peaks of alternating sizes. This pattern is clearly shown in the readout response in the second figure. The first and third peaks had areas equal to 4.06 and 4.10 (arbitrary units). The areas of peaks 2 and 4 were 6.34 and 6.59. This pattern of peak areas is significant because it corresponds to the two different sizes of sample loops

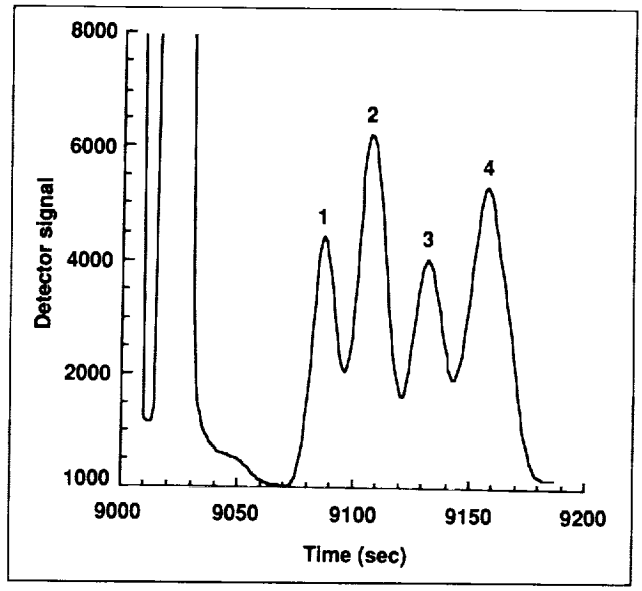

Fig. 2. Octane sample profile. The sampling time was 6200 seconds (at the sampling temperature of 30°C). The storage time was 2800 seconds. The storage temperature was the same as the sampling temperature to minimize the effects of diffusion during flow shutoff. The readout time was 200 seconds at the readout temperature of 130°C. The first and third peaks are from the 60-milliliter injection loop; the second and fourth peaks are from the 100-milliliter injection loop.

on the injection valve. The ratio of peaks 1 and 3 over peaks 2 and 4 is 0.63, which is consistent with the ratio of the loop sizes used.

Since the readout temperature is much higher than the storage temperature, sample profiles that had been collected over a period of a few hours could be detected in a matter of minutes.

Ames-Moffett contact: J. Valentin
(415) 604-5766
Headquarters program office: OSSA

Exploring the Solar System through Stellar Occultations

Edward W. Dunham

A stellar occultation occurs when an object in the solar system passes between an observer and a star. Earth-based observations of stellar occultations provide spatial resolution for objects in the outer solar system that is thousands of times better than that of traditional imaging observations. Since stellar occultations probe refraction and extinction by material between the occulted star and the observer, they may be used to establish the structure of the atmospheres and ring systems of solar system bodies at high spatial resolution.

The Voyager II flyby of Triton, the 1988 stellar occultation by Pluto, and the now-complete set of occultations and eclipses that involved Pluto and its satellite Charon have revolutionized our understanding of these small, remote objects. The stellar occultation technique may be used to provide further fundamental information about the cryogenic atmospheres of Pluto and Triton. Examples of such uses include monitoring the density of the tenuous atmospheres of these objects to search for seasonal variations, determining whether an absorbing atmospheric haze is present near Pluto's surface, and completing the temperature profile of Triton's atmosphere derived from the Voyager II radio and ultraviolet spectrometer occultation experiments.

In order to realize the promise of these upcoming events, the focus of work this year was on development of improved instrumentation and occultation prediction procedures. A large-format charge-coupled device (CCD) camera system that will be used for both occultation observations and prediction astrometry is nearly complete; a portable CCD photometer system to allow high-quality observations from remote sites is also nearly complete; a near-infrared-array camera system suitable for occultation work has been developed at Lick Observatory by K. Gilmore and D. Rank; astrometric test data were obtained with the Crossley telescope at Lick Observatory; and astrometric data analysis procedures are being developed.

The occultation prediction methods used so far have been labor intensive and have not provided sufficiently accurate predictions early enough to allow efficient observing plans to be made. A new astrometric procedure is being developed that promises to eliminate these difficulties. The astrometric tests carried out this year showed that the scatter in individual position measurements was about a third of the apparent angular radius of Pluto and Triton (0.02 arcseconds) indicating that the required precision for occultation predictions is present. An instability in the apparent star positions, probably caused by atmospheric distortions, limits the accuracy to about 1.5 times the apparent radius of these objects (0.09 arcseconds). However, repeated observations of the area of sky around the star to be occulted allows construction of an accurate set of "guidepost" stars well before the occultation. When the occulting object enters this field of stars, the position instability can be removed by means of the previously determined positions of the "guidepost" stars.

The CCD instrumentation and astrometric data-analysis procedures described here will be completed in the first half of 1993 and will be applied to Triton and Pluto occultations that will occur in the latter half of the year. The results of these occultation observations will significantly improve our understanding of these remote objects.

Ames-Moffett contact: E. Dunham
(415) 604-5523
Headquarters program office: OSSA

Mars Site Selection for Exobiology Studies

Jack Farmer, David J. Des Marais

Major goals of exobiology in Mars exploration are (1) to determine whether a biosphere exists on Mars, or has existed in the past; (2) to define the nature of early Mars environments (especially those regarded as favorable for the development of life); and (3) to understand the geochemistry of the biogenic elements (carbon, nitrogen, oxygen, sulfur, and phosphorus, with an emphasis on organic compounds). To achieve these goals, exobiology studies during future Mars explorations must include a systematic search for organic compounds, water and/or biologically important minerals, a fossil record, and extant life. The identification of landing sites on Mars that offer the best potential for meeting the objectives of exobiology has a high priority in the planning of future missions.

In collaboration with colleagues at Arizona State University, and using Viking Orbiter data, we have been developing objective methods for selecting high-priority sites for exobiology studies on Mars. Perhaps the most immediate need is to target sites for high-resolution orbital imaging during the Mars Observer and the Russian Mars 94 and Mars 96 missions. High-resolution imaging will contribute significantly to the identification of landing sites for exobiology studies.

Preliminary work has focused on a survey of sites listed in NASA's Mars Landing Site Catalog. Localities were screened for geological features considered to be indicative of major water or water-related environments (i.e., lake, stream, spring, and periglacial) using Viking Mars Chart prints (scale 1:2 million) and Mars Transverse Mercator maps (scale 1:500,000). Sites of interest for exobiology studies were further evaluated using Viking Orbiter images, referenced in the Mars Landing Site Catalog. Diagnostic geological features were assigned scores based on three subjectively weighted factors: the visibility of the feature on the image, the uniqueness of the feature–process relationship, and the perceived importance of the feature in relationship to the objectives of exobiology. Scores were summed independently for each of the primary geological environments (stream, lake, spring, and periglacial), and priorities were determined by comparing total scores. High-priority sites were subsequently described in detail using mosaicked digital image models (resolution 231 meters per pixel), along with the highest-resolution Viking Orbiter images available from the Image Retrieval and Processing System (40–250 meters per pixel).

Of the 83 sites evaluated from the 1990 edition of the Mars Landing Site Catalog, 12 were given a high priority for exobiology studies. Descriptions of these sites were updated and expanded for inclusion in the new edition of the site catalog. In addition, we evaluated five high-priority sites from the literature, sixteen sites proposed for the Mars Environmental Survey (MESUR), and the Viking lander sites. Future objectives are to continue to refine our site-selection methodology while broadening the scope of site selection for exobiology studies to encompass a systematic global reconnaissance of Mars.

Ames-Moffett contact: J. Farmer
(415) 604-5748
Headquarters program office: OSSA

Gas-Grain Simulation Facility Conceptual Design

Mark L. Fonda, Judith L. Huntington

The Gas-Grain Simulation Facility (GGSF) is being designed to study the effects that weak forces, such as van der waals force, coulomb force, and surface tension, as well as other physical and chemical phenomena, may have on the behavior and characteristics of clouds of small grains or particles (submicron to millimeter size) suspended in various controlled environments. A broad set of experiments (outlined during a NASA Ames workshop and in a recent survey) forms the basis for the scientific and technical (S&T) requirements summarized in the table. Based on the S&T requirements, trade-off analyses were performed and a common grouping of functional requirements was established. Possible technical approaches were identified and evaluated to form the GGSF conceptual design.

The GGSF system provides a broad range of capabilities that satisfy most of the S&T requirements. It consists of several subsystems configured within a Space Station Freedom international standard payload rack (ISPR) and includes four interchangeable chambers (one of these chambers is shown in the first figure). The four chambers accommodate the following pressures, temperatures, and experiment volumes:

Chamber	Volume (liters)	Pressure (bar)	Temperature (K)
Large-volume	67	10^{-6}–1	150–400
Low-temp.	4.2	10^{-6}–3	60–400
High-temp.	8.2	10^{-6}–1	300–1,200
High-vacuum	4.2	10^{-10}–1	60–400

Table 1. Summary of scientific and technical requirements

Chamber pressure	10^{-10} to 3 bars; goal is to reach 11 bars
Chamber temperature	10 to 1,200 kelvin; goal is to reach 4 kelvin
Chamber volume	1 cubic centimeter to several hundred liters; various geometries
Particulate type	Liquid aerosols, solid powder dispersions, soots from combustion, high-temperature condensates (nucleation of metal and silicate vapors), low-temperature condensates (ices of water, ammonia, methane, or CO_2), single liquid droplet, single or few particles, particulates generated in situ by UV radiation
Particulate size	10 nanometers to 3 centimeters
Particulate concentration	A single particle to 10^{10} particles per cubic centimeter
Gases required	Air, N_2, He, H_2, Ar, O_2, Xe, H_2O, CO_2, CO, NH_3, CH_4, etc.
Diagnostics required	In-line optical systems and off-line sample analysis, including measurements of grain strength, mass, density, charge, and geometry; grain size distribution, number density, optical properties (index of refraction, emission and absorption spectra); imaging; particle kinematic parameters before and after a collision
Experiment duration	Seconds (collisions) to weeks (aerobiology experiments)

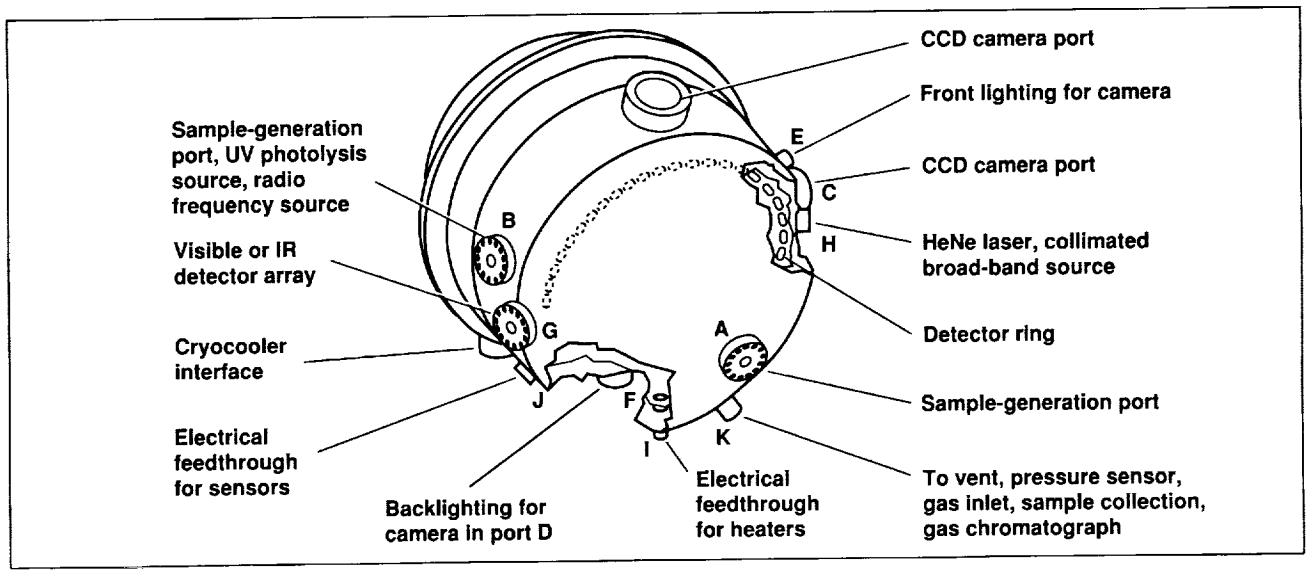

Fig. 1. Experiment chamber concept.

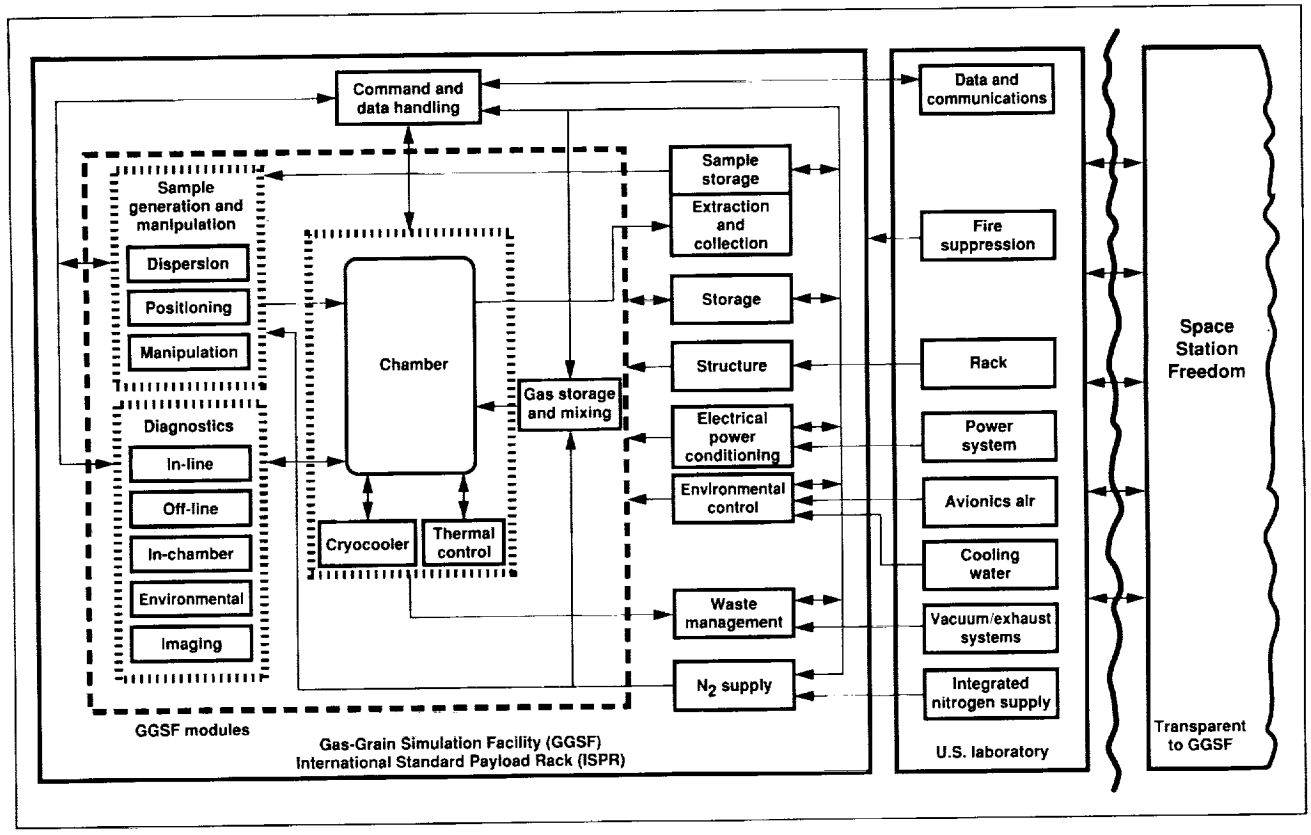

Fig. 2. Block diagram of GGSF system.

Maintenance and housekeeping subsystems of the GGSF provide command and data handling, electrical power distribution, waste management, and experiment storage. In addition, a variety of assemblies for sample generation and handling, diagnostics, and gas storage and mixing are included. The second figure is a block diagram of the system.

This GGSF conceptual design is a first attempt at providing a research facility to accommodate the S&T requirements necessary for a wide variety of experiments. The next step in facility development will be to review the design with the scientific community to further clarify the S&T requirements and to identify any shortcomings.

Ames-Moffett contact: M. Fonda
(415) 604-5744
Headquarters program office: OSSA

Particle Generation for the Gas-Grain Simulation Facility

Mark L. Fonda, Judith L. Huntington, Kenji Nishioka

A particle-generation system concept for the Gas-Grain Simulation Facility (GGSF) is undergoing tests in a laboratory (breadboard) version. The GGSF, a multidisciplinary research facility being developed at Ames Research Center for Space Station Freedom, will serve a broad range of scientific investigators, including exobiologists investigating the origin, evolution, and distribution of life in the universe; planetary scientists investigating dust storms on Mars; astrophysicists investigating the optical properties of interstellar dust clouds; and terrestrial scientists investigating the role of suspended particulates in climatic and air-pollution studies. Wide ranges of particulate compositions, sizes, and concentrations are required for these investigations. For example, particles derived from geological material such as dusts, high-temperature condensates of metals, silicates, and other compounds are needed; smokes and liquid and ice particles also would be included. A particle-generation system concept that will meet many of these requirements is being developed and tested. This system will provide a mechanism to suspend clouds of particles of predictable and repeatable characteristics. The complete system will include bulk sample holders and generation and dispersion devices interfaced with the GGSF experiment chamber.

Current work is focused on the requirements for solid-particle generation, simulating, for example, dust in terrestrial or planetary atmospheres or in interstellar space. A multidisciplinary group of experiments, discussed during a NASA Ames workshop, led to a set of requirements for this effort, which are summarized in the table.

Table 1. Science and technical requirements for solid-particle generation

Particulate type	Geological material including basalt, quartz, and pyroclastic minerals, carbon and silicates, metal oxides, soots from combustion, high-temperature condensates (nucleation of metal and silicate vapors), low-temperature condensates (ices of water, ammonia, methane, and CO_2).
Particulate size	10 nanometers to 3 centimeters
Particulate concentration	A single particle to 10^{10} particles per cubic centimeter

As well as the generator concept now being tested, which is based on a device previously used in studies of pulverized coal, several existing laboratory and commercial generator designs were evaluated, including fluidized beds and mechanical feeders. These were rejected because they did not meet the requirement for an efficient device that would function in either Earth-gravity or low-gravity environments. The design and testing efforts are addressing gravity dependencies of the complete system, which is shown in schematic form in the figure, and deagglomeration efficiency of the generator while the system is operating with a representative range of bulk powder samples. Initial test data indicate that deagglomeration is efficient for test particles greater than a few micrometers in size. The effects of electric charges are being evaluated, and an effort is being made to achieve uniform distributions of particles in the experiment chamber. Future plans include testing the generator system using a range of powders,

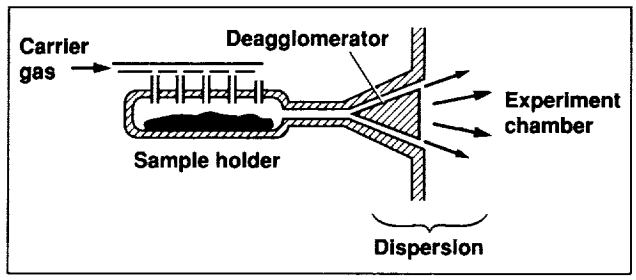

Fig. 1. Solid-particle generation system.

including size-classified terrestrial mineral dusts. Flight-test opportunities are being investigated for evaluations of low-gravity operation when the Earth-gravity laboratory testing is completed.

Ames-Moffett contact: M. Fonda
(415) 604-5744
Headquarters program office: OSSA

Electrical Conductivity of Planetary Interiors

Friedemann Freund

The deeper regions of planets, including Earth, are accessible only through remote measurements. One way to learn more about the layering of the Earth's crust and underlying mantle is to probe the electrical conductivity as a function of depth. Paramount to the interpretation of the data thus obtained is an understanding of the electrical conductivity of the various rocks and of the fluids that these rocks may contain, mainly water and carbon dioxide. Fluids can exist in the pore space in their commonly known forms, as saline solutions or gas or superheated steam. In this case their contributions to the conductivity are relatively well understood. However, the same fluids can also enter the structures of the various constituent minerals. In this case their influence on the electrical conductivity is much more subtle.

Strong evidence exists that a certain type of electrical charge carrier has been entirely overlooked in spite of decades of intense laboratory studies. The charge carriers in question are defect electrons in the oxygen sublattice of oxide and silicate minerals, also described as O^- states. They derive from small concentrations of fluid components that are structurally incorporated into the minerals. Tightly coupled at low temperatures, these O^- become mobile in a temperature window of 500°C–800°C; this window is of great geophysical interest because it comprises the

temperatures believed to prevail in most regions of the Earth's lower continental crust and at the contact between its crust and upper mantle.

There are two main reasons why the oxygen defect electrons have not been recognized before. First, because they have a strong propensity for the surface of any sample, the O^- have long been misinterpreted as being caused by surface contamination. Second, because they are oxidizing radicals, the O^- react across a sample surface with reduced gases and are thus easily annihilated in the course of an experiment unless special precautions are taken.

A new technique for measuring electrical charge carriers has been perfected over the past two years, with support from the Department of Energy. The technique, charge distribution analysis (CDA), has been endorsed by the National Institute of Standards and Technology as a new method for measuring previously unmeasurable fundamental properties of materials. CDA allows detection of charge carriers such as the elusive oxygen defect electrons in any solids, even in minerals that, because of their complex chemistry and structure, are not amenable to other diagnostically powerful measurements; e.g., those relating to magnetic and optical properties.

To prove the presence of the elusive oxygen-based charge carriers and to characterize them more fully, independent physical measurements were performed on magnesium oxide crystals, which serve as a model for more complex natural minerals. The experiments were selected to take advantage of the different theoretically predictable physical expressions of the O^- charge carriers. One of these features is that the O^- will be diamagnetic as long as they remain tightly coupled, but must become paramagnetic as their bond loosens. Using intrinsically diamagnetic magnesium oxide crystals, the appearance of the paramagnetic signature was detected. This measurement provided the first unambiguous confirmation of the presence of the oxygen defect electrons.

Another predictable feature is that, when the oxygen defect electrons decouple and start to spread out as mobile charge carriers, they will decrease the mean electron density in the valence band. This decrease in electron density has two important consequences: (1) a slight decrease in the bond strength between ions and (2) an increase in the polarizability of the remaining valence electrons. The decrease in bond strength leads to an anomalously high thermal expansion. The increase in the polarizability leads to an anomalously low refractive index. Both measurements have been successfully completed on magnesium oxide crystals, and thus this series of fundamental studies is complete.

As a result of these independent confirmations of CDA findings that were obtained earlier, the project now enters a new phase in which we can use CDA more confidently to study the chemically and structurally more complex natural minerals that make up the rocks. Several representative minerals have been surveyed, including feldspars from the Earth's lower crust and garnets from highly metamorphic rocks, plus olivine, which is the dominant mineral in the upper mantle. The results indicate that oxygen defect electrons are pervasive in all these minerals. It is therefore anticipated that their presence will have a profound effect on the electrical-conductivity profiles of the rocks deep in the crust of the Earth and possibly in the upper mantle.

Ames-Moffett contact: F. Freund
(415) 604-5183
Headquarters program office: OSSA

Calculation of C_2 and C_2^- Opacity Sources

David Goorvitch

The presence of C_2 bands is a primary distinguishing characteristic of carbon stars. A carbon star is usually defined as a star with C_2 absorption bands. The observation of weak C_2 bands can potentially reveal the physical properties of a carbon star because these bands will contain many lines that are not expected to be saturated. The presence of C_2 bands in carbon stellar spectra has led several observers to look for the related molecule C_2^-, the negative ion of C_2.

Several new opacity sources are being calculated for C_2 and C_2^-. These new opacity sources are important in interpreting stellar spectra. To be able to calculate the opacity of a species, several physical parameters must be known. These parameters include the abundance of the species and its intrinsic molecular parameters. The intrinsic molecular parameters needed are energy levels of the upper and lower states of a transition; an electronic dipole moment function; a Höln–London factor that describes the coupling of the angular momenta; the Franck–Condon factor for the band, which describes the overlap of the vibrational transition wavefunctions; and the partition function as a function of temperature. The Franck–Condon factor is unity for nonelectronic transitions.

Intrinsic molecular parameters have been calculated or observed for the $B^1\Delta_g$ to $A^1\Pi_u$ and the $B'^1\Sigma^+_g$ to $A^1\Pi_u$ transitions of C_2 and the $A^2\Pi_u$ to $X^2\Sigma^+_g$ transitions of C_2^-. Using the parameters reported in the literature, line lists for transitions in these bands are calculated. These bands have band heads in the infrared region of the spectrum. Line lists are presented that give the following information: the transition frequency, the lower term energy, the gf factor (a temperature-independent line strength), the Höln–London factor, the line strength calculated at 3,000 kelvin, the upper and lower vibrational numbers, the transition type, the angular momentum quantum number, and the symmetry classification of the lower state.

Ames-Moffett contact: D. Goorvitch
(415) 604-5502
Headquarters program office: OSSA

ATP Synthesis in the Extreme Halophiles

Lawrence I. Hochstein

The membrane-bound ATPase from the Archaebacterium *Halobacterium* (*Hb.*) *saccharovorum* (A-ATPase) was previously shown in this laboratory to be structurally unrelated to the ubiquitous ATP synthase complex (F-ATPase) found in bacteria, plants, and animals. In addition, enzyme activity is repressed by nitrate and N-ethylmaleimide but is unaffected by sodium azide. This behavior is uncharacteristic of F-type ATPases but is similar to the response of a class of ATPases found in eukaryotic cells, the so-called vacuolar ATPases (V-ATPases), which do not synthesize ATP. The similarity of the amino acid sequences of V- and F-type ATPases suggests that they originated from an ancestral ATPase that had vacuole-like properties but was able to synthesize ATP. Subsequently, the amino acid sequences of several archaebacterial ATPases were shown to resemble those of V-type ATPases. These relationships led others to propose that all proton-translocating ATPases originated from an ancestral enzyme that had the characteristics of a V-type ATPase. Implicit in this notion is that the V-type A-ATPases synthesize ATP, a hypothesis for which there is no evidence.

We have carried out a series of experiments designed to ascertain if ATP synthesis in *Hb. saccharovorum* is caused by the A-ATPase we previously described. The rationale was that, if this V-like ATPase synthesized ATP, agents that inhibit its activity (nitrate and N-ethylmaleimide) should inhibit ATP synthesis, whereas sodium azide, which does not affect A-ATPases, should not. The following chart summarizes our experiments. The symbols (+) and (–) indicate whether the agents do or do not inhibit ATP synthesis, respectively; the symbol (!!) indicates that the levels of ATP are greater than in the control.

Inhibitor	ATP synthesis	Type of ATPase A	V	F
N-ethylmaleimide	(!!)	+	+	–
Nitrate	–	+	+	–
Azide	+	–	–	+

This pattern is inconsistent with the operation of a V-type ATPase and suggests the presence of two ATPases—one synthetic, the other hydrolytic.

We propose that ATP synthesis in *Hb. saccharovorum* is catalyzed by the ubiquitous F-type ATPase and not the V-type enzyme. This is the first demonstration that such an enzyme occurs in the Archaebacteria. We have examined seven other extreme halophiles: *Hb. salinarium*, *Hb. vallismortis*, *Haloferax mediterranei*, *Haloferax denitrificans*, *Haloarcula californiae*, and *Haloarcula hispanicum*, and in every case we observed similar results. This suggests that our original observation with *Hb. saccharovorum* is not uniquely associated with this organism and that an F-type ATPase may be operative in other Archaebacteria.

Ames-Moffett contact: L. Hochstein
(415) 604-5938
Headquarters program office: OSSA

The Center for Star Formation

David Hollenbach, Patrick Cassen

The Center for Star Formation Studies, a consortium of scientists from Ames Research Center and the Astronomy Departments of the University of California at Berkeley and Santa Cruz, conducts a coordinated program of theoretical research on star and planet formation. The Center supports postdoctoral fellows, senior visitors, and students; meets regularly at Ames to exchange ideas and to present informal seminars on current research; hosts visits of outside scientists; and conducts a week-long workshop on selected aspects of star formation each summer.

The Star Formation Summer Workshop in 1992 was held at the University of California at Berkeley (U.C. Berkeley), and included, in addition to the Center scientists, about 60 astrophysicists from around the world. The main topics discussed included the fragmentation and collapse of molecular clouds, the origin of protostellar winds, and the effect of winds and stellar radiation on the circumstellar environment.

The main focus of work in 1992 was the collapse of dense cores to form low-mass protostars and their protoplanetary disks, and the evolution of these disks until planets are formed and the disks are dispersed. F. Shu and D. Galli of U.C. Berkeley showed that magnetic fields in the clouds collapsing to form a low-mass star cause the material to initially collapse to a disk-like configuration whose extent is perhaps 20 times the size of the solar system. The gas and dust then falls nearly radially inward until it hits the orbiting protoplanetary disk. The accretion shock formed at this interface has been modeled by D. Hollenbach and D. Neufeld (Johns Hopkins University) and is predicted to be luminous in the infrared transitions of vibrationally excited CO. P. Bodenheimer and W. Kley of U.C. Santa Cruz have also modeled the spectra from the protostar, disk, and collapsing cloud.

In the protoplanetary disk, the dust may settle toward the midplane, where it coagulates to much larger objects called planetesimals. J. Cuzzi and T. Dobrovolskis studied how turbulence in the disk affects this coagulation process, and D. Lin (U.C. Santa Cruz) has shown how the planetesimals collide and merge to form terrestrial planets and the cores of the giant gaseous planets such as Jupiter and Saturn. Once the cores become as massive as 15 to 20 times the Earth's mass, they can gravitationally attract the surrounding gas in the disk and grow to become large planets. F. Shu, D. Johnstone (U.C. Berkeley), and D. Hollenbach showed how the ultraviolet radiation from the early sun may have evaporated the disk gas beyond Saturn in a relatively short time. This may explain why Uranus and Neptune, which have core masses similar to those of Jupiter and Saturn, have so small a mass of gas surrounding their cores.

These theoretical models have been used to interpret observational data from such NASA facilities as the Infrared Telescope Facility (IRTF), the Kuiper Airborne Observatory (KAO), and the Infrared Astronomical Observatory (IRAS), as well as from numerous ground-based radio and optical telescopes. In addition, they have been used to determine requirements for proposed future missions such as the Stratospheric Observatory for Infrared Astronomy (SOFIA) and the Space Infrared Telescope Facility (SIRTF).

Ames-Moffett contact: D. Hollenbach
(415) 604-4164
Headquarters program office: OSSA

Facultative Anoxygenic Cyanobacteria

Linda L. Jahnke, Elaine Munoz

Microbial ecosystems are perhaps nearly as ancient as life itself, having existed on Earth for at least 3.5 billion years. Modern cyanobacterial mats provide an opportunity both to study the dynamic interactions between organisms that have taken place in such communities throughout this period and to view microbial evolution within the context of global change. The transition from an anoxic, sulfide-dominated environment to an oxygen-rich one must have occurred as part of the early evolution of the biosphere. Such processes still occur in modern microbial mats within the light–dark metabolism shifts associated with the diurnal cycle. Study of the associated organisms can provide insights into the evolutionary transitions that must have occurred during this period of the Earth's history.

Photosynthesis first evolved as an anoxygenic process, with sulfide serving as a potential source of reducing material in much the same way as water does in modern-plant-type oxygenic photosynthesis (see figure). Anoxygenic photosynthesis is characteristic of a number of phototrophic bacteria associated with microbial mats; these bacteria are obligate anaerobes, reflecting their ancient microbial niche. The predominant mat-forming phototrophs, however, are the cyanobacteria. These bacteria evolved the potential for oxygenic photosynthesis and are responsible for development of our modern oxygen-dominated biosphere. Two filamentous cyanobacteria have been isolated from a laminated microbial mat found in a hypersaline pond located in Guerrero Negro, Baja California Sur, Mexico. The morphology of the filaments (trichomes) indicates that one is an *Oscillatoria* and the other is a *Pseudanabaena*. Rapid rates of sulfate reduction during both night and day result in consistently high levels of sulfide in these mats. Sulfide is normally inhibitory to oxygenic

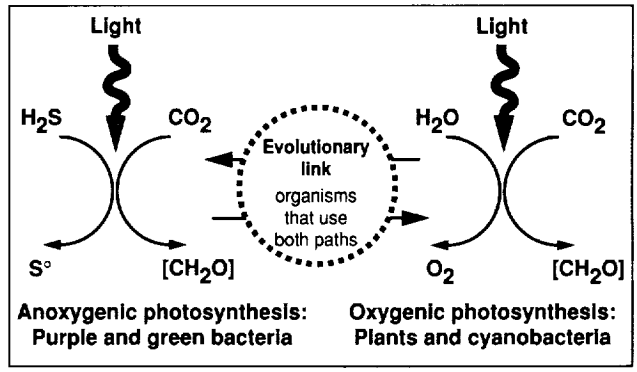

Fig. 1. Evolution of microbial photosynthesis.

photosynthesis, but these bacteria have maintained what may be ancient strategies to deal with this sulfide-dominated environment. Both organisms are capable of anoxygenic photosynthesis in the presence of sulfide, and of oxygenic photosynthesis in its absence. In the *Oscillatoria*, both oxygenic and anoxygenic photosynthesis can occur simultaneously in the presence of relatively high levels of sulfide. Analysis of the membrane lipids of these two cyanobacteria indicate that they probably use an anaerobic mechanism for the synthesis of unsaturated fatty acids rather than the more highly evolved, oxidative mechanism that is normally characteristic of cyanobacteria. The use of the anaerobic mechanism allows these cyanobacteria to deal with a sulfide-rich environment and provides a model for microbial evolution.

Ames-Moffett contact: L. Jahnke
(415) 604-3221
Headquarters program office: OSSA

Prebiotic Polymerization Models

Anastassia Kanavarioti, Sherwood Chang

In 1952, Watson and Crick made the revolutionary discovery that self-replication of nucleic acids is based on specific recognition between pairs of nucleotide building blocks: guanine–cytosine (GC) and adenine–uracil (AU). During formation of a new strand of nucleic acid from a strand acting as a template, C in the parent directs the incorporation of G in the complementary daughter strand, G directs the incorporation of C, A directs the incorporation of U, and U directs the incorporation of A. This complementarity occurs in the absence of enzymes or other catalysts and provides the basis for template chemistry. Thus enzyme-free, template-directed polymerization has been studied as a prebiotic model for the formation of ribonucleic acid (RNA).

We have been studying the polymerization of G nucleotides in the presence of the complementary C polymer, poly(C), which acts as the template. The reaction products, G polymers of length n = 2 to 20 (see figure), are separated and quantified using high-performance liquid chromatography. By measuring the time-dependent growth of each G polymer, we were able to calculate second-order rate constants of elongation, $k_{elongation}$. This analysis provides a rate constant for every step of the polymerization, and thus allows quantitative comparisons between experiments performed under different conditions.

Perhaps the most intriguing discovery was that $k_{elongation}$ increases with decreasing poly(C) template concentration. Many experiments had indicated that template-directed reactions required solutions saturated with the template compound and mononucleotide. This requirement detracted from the model because saturation concentrations were implausible in the prebiotic environment. With a better understanding of the reaction mechanisms gained in our past work, we sought and found evidence that even minute amounts of the template compound can direct and catalyze the synthesis of G polymers. Most important, the G products formed in the presence of lesser amounts of template compound are, in some cases, longer than those produced in the presence of excess poly(C). The fact that a high degree of template-directed polymerization can be

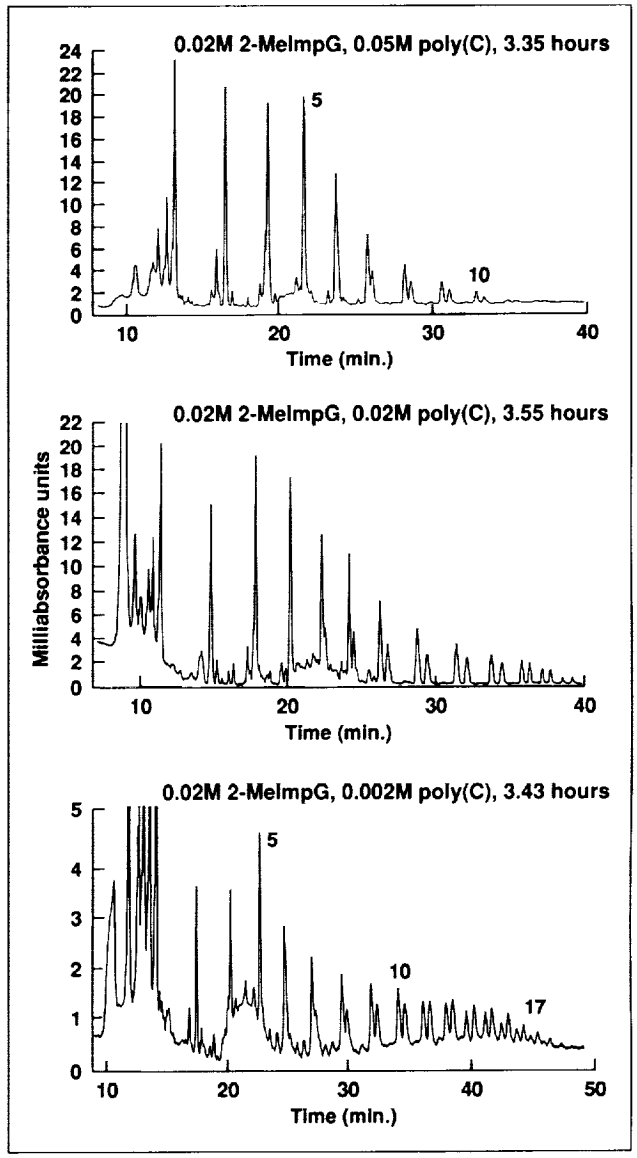

Fig. 1. Polymer elution profiles from high-performance liquid chromatography: effect of template concentration on yield and length of oligomeric products in the template-directed polymerization of 0.02-molar 2-methyl ImpG (the numbers 5, 10, and 17 on the peaks indicate length of G polymers in monomer units). For each polymer length there is more than one isomeric product, as indicated by multiple peaks.

achieved while using traces of template compound is of great importance in the development of chemical models for the origin of life.

The figure shows the product distribution from the reaction of a 20-millimolar concentration of the mononucleotide 2-methyl ImpG (2-MeImpG) in the presence of different concentrations of poly(C) after approximately 3.5 hours. With 0.05-molar poly(C), G-10mers (polymers up to 10 units long) are detected (top); with 0.02-molar poly(C), G-14mers are visible (middle); and with only 0.002-molar poly(C), G-17mers are present in the sample. This is consistent with the observation that the longest products are formed in the presence of the least amount of template compound.

Apparently, G mononucleotides take part in two types of interactions: they associate with the template by hydrogen bonding with C, and they self-associate by stacking among themselves while on the template. Hence the reacting molecules form a stable complex, and the energy that is usually required to bring reactants together is diminished. In addition, when the concentration of the mononucleotide is equal to or higher than the concentration of the template (template concentration is measured in C units, to make it comparable to G), then the template is completely covered and polymerization becomes very efficient. To a first approximation, the probability for a specific site on the template to be occupied by a stable G reaction complex is higher the larger the G/C ratio. This is why the longest products are observed with 0.002-molar poly(C). However, the yield in terms of total monomer incorporated into polymers diminishes substantially with 0.002-molar template.

The results of this GC system cannot yet be generalized to other nucleotide pairs. It is likely that a template-directed reaction based on other nucleotides may behave differently, because of differences in hydrogen-bonding strength or stacking behavior. Whether or not template chemistry was actually a precursor of the biosynthesis of RNA remains unclear. Many more reactions need to be investigated before the principles and the limitations of template chemistry for the origin of molecular self-replication are understood.

Ames-Moffett contact: A. Kanavarioti
(415) 604-3226
Headquarters program office: OSSA

A GC–IMS for the In Situ Analysis of Extraterrestrial Environments

Daniel R. Kojiro, Glenn C. Carle

Flight instrumentation for analyzing extraterrestrial environments must often perform under severely restricted conditions. Although the ability to detect and identify a multitude of chemical species over vast concentration ranges is a primary requirement, emphasis is also placed on minimizing the size, weight, and energy consumption of the instruments. To fulfill the analytical needs of extraterrestrial missions, highly sensitive analytical techniques and instrumentation must continually be investigated and developed. Although the gas chromatograph (GC) has been successfully utilized for several exobiological missions, future missions require increased analytical capabilities. In particular, sample identification by the GC detector, independent of GC retention time, would be a powerful analytical improvement. Because the ion mobility spectrometer (IMS) is a pressure instrument and is therefore easily interfaced with the GC with minimal additional power requirements, the development of a GC–IMS for the analysis of extraterrestrial environments shows great potential.

The Titan Aerosol and Gas Experiment (TAGEX) (see first figure) was proposed to analyze the atmosphere of Saturn's moon Titan. TAGEX would collect and analyze gas and aerosols, using a GC–IMS, as it descended through Titan's atmosphere. It was anticipated that such an analysis would involve the detection and quantitation of at least 15 atmospheric gas components. Concentrations of many of the compounds of interest were expected to be below 1 part

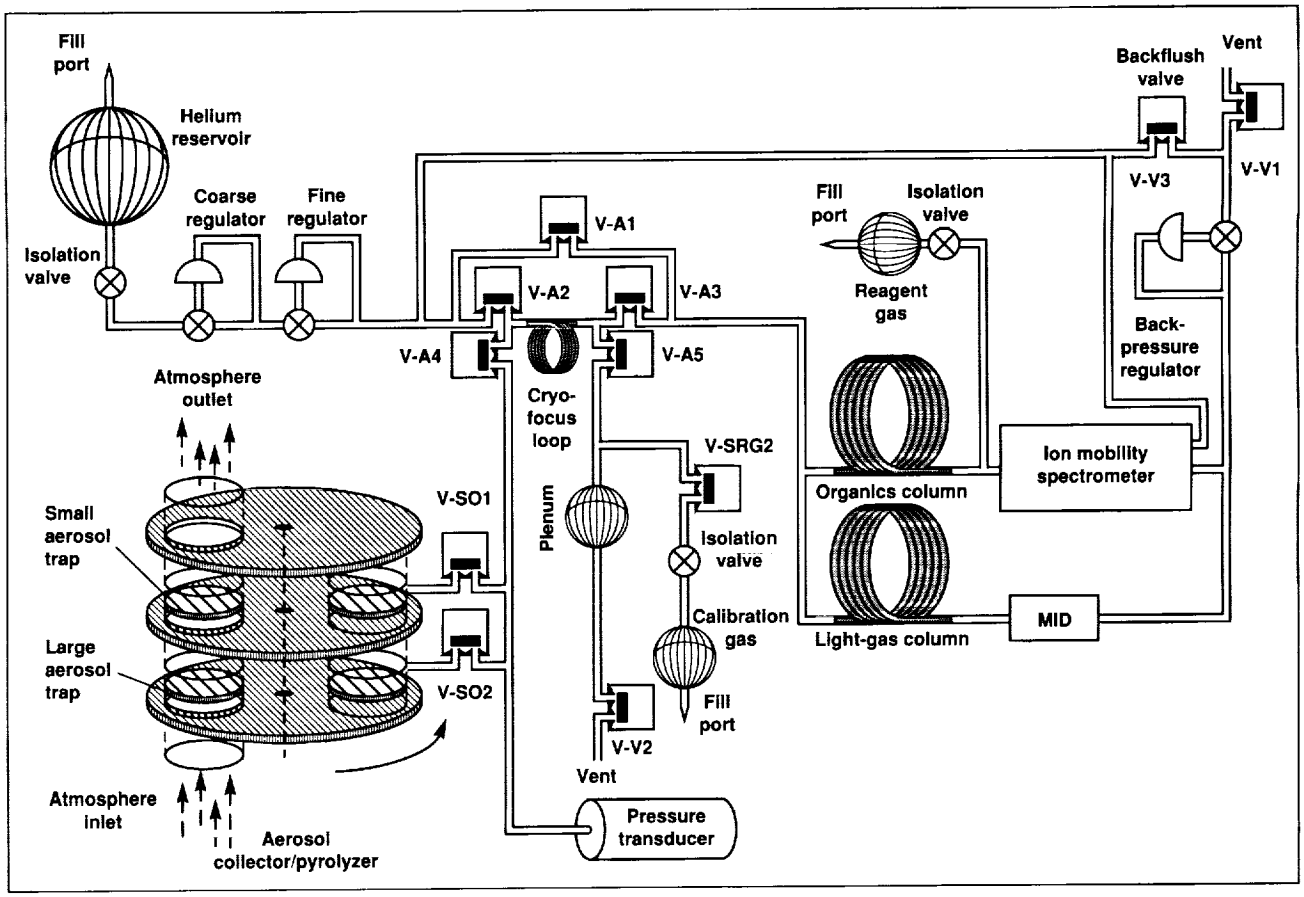

Fig. 1. TAGEX gas-flow diagram.

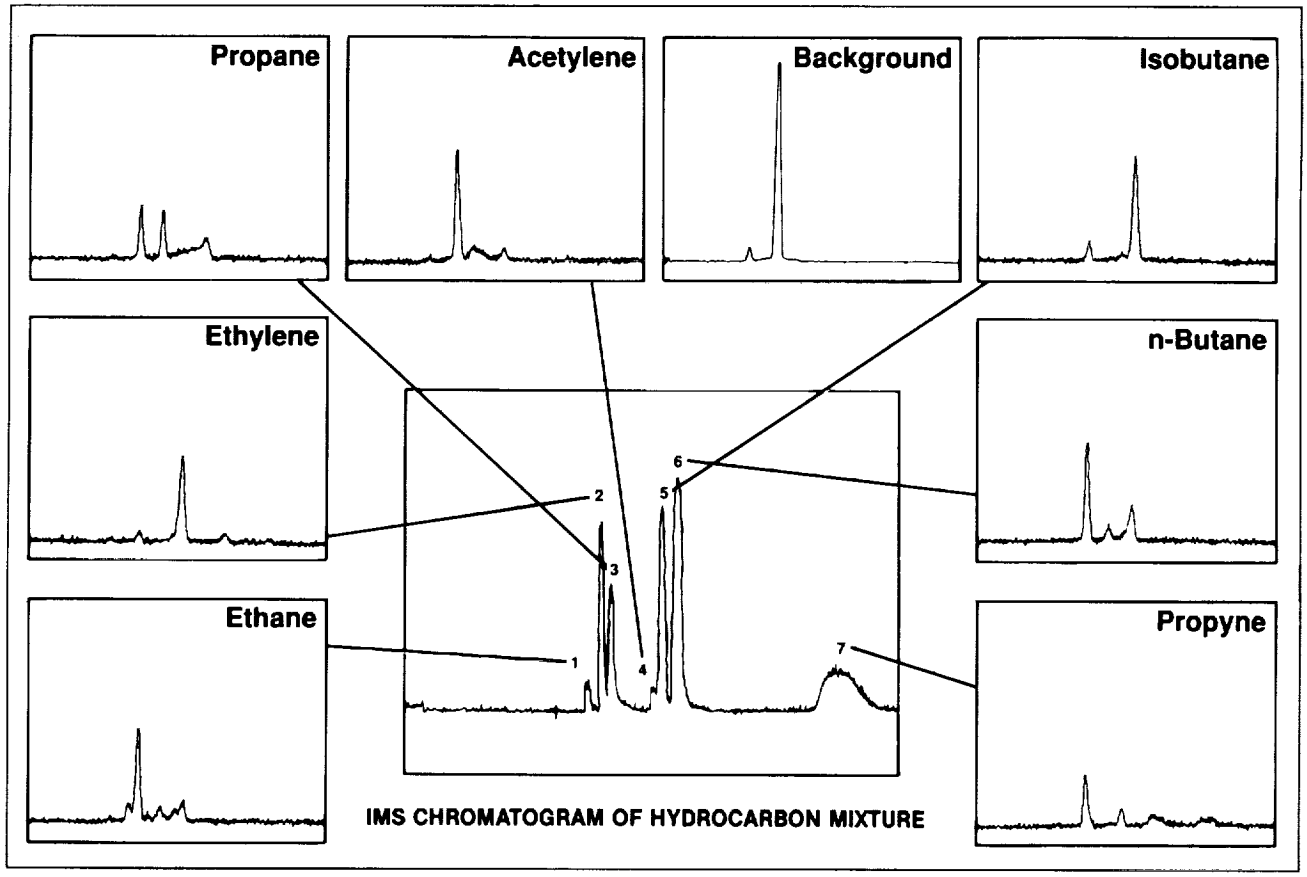

Fig. 2. GC–IMS chromatogram of alkane mixture, surrounded by identifying IMS spectra of each separated component.

per million. The components of the aerosols, collected and pyrolyzed, would add many more organic molecules to be determined.

The GC consisted of a light-gas column and an organics column. Each column had a modulated-voltage metastable ionization detector for detection of eluting components. In addition, the organics column also had an IMS for sample identification. The IMS consisted of a reaction region of 5 centimeters and a drift region of 5 centimeters with a diameter of 2 centimeters. The limited resources, space, and weight allowed for this type of flight instrument necessitated the use of one gas as both carrier and drift gas. Helium is the usual carrier gas for this type of gas chromatography. More important, however, was the use of metastable ionization detectors (MIDs). Since an MID was used on each column and requires helium in order to function at its most sensitive level, it was essential that the one carrier/drift gas be ultra-high-purity helium.

Of particular concern for the TAGEX IMS was the mission requirement of determining the abundance of light hydrocarbons down to concentrations of less than one part per million. The TAGEX IMS, using helium with water removed to below part-per-billion levels, was able to detect and produce identifying spectra of simple alkanes at concentrations not previously dealt with by IMS (see second figure).

Although the TAGEX GC–IMS was developed specifically to fulfill the analytical requirements of the Cassini mission to Saturn, it is representative of what is needed for all space-probe-type missions. Future missions present opportunities for similar research efforts to develop analytical instrumentation incorporating IMS.

Ames-Moffett contact: D. Kojiro
(415) 604-5364
Headquarters program office: OSSA

The Search for Interstellar Molecules in Carbonaceous Meteorites

Narcinda R. Lerner

Many classes of organic compounds exist in carbonaceous meteorites. Their origins are poorly understood. These compounds could have originated in the solar nebula, the parent body, or the interstellar medium.

Evidence for their origin in the interstellar medium is the presence of anomalous deuterium/hydrogen (D/H) ratios. Anomalous D/H ratios have been observed in amino acids, carboxylic acids, and kerogenous organic matter obtained from carbonaceous meteorites. To date, all measurements of D/H isotope ratios have been made at the compound class level; there are no data at the compound level. Such data are needed in order to develop a mechanism for the formation of these compounds.

Mechanisms for the formation of compounds can be inferred from D/H ratios measured in meteoritic organic compounds by comparing D–H exchange in laboratory simulation of postulated synthetic routes to compound formation. The overall objective of this project is to obtain data that will reveal the deuterium and hydrogen distribution in organic compounds found on meteorites as a function of molecular structure and to relate the D/H ratios to possible synthetic pathways originating with deuterium-enriched molecules formed in the interstellar medium.

We have investigated the Strecker synthesis, $RR'CO + NH_3 + HCN + H_2O \rightarrow RR'C(NH_2)CO_2H$, which has been suggested as a possible route on the meteorite parent body for the synthesis of deuterium-enriched amino acids found on the Murchison meteorite. A requirement of this mechanism is that the excess deuterium of deuterium-enriched interstellar aldehyde and ketone precursors be retained in the product amino acids. The carbonyl compounds we used in this simulated synthesis were formaldehyde ($R = R' = D$), expected to yield glycine (GLY); acetaldehyde ($R = D$, $R' = CD_3$), expected to yield alanine (ALA); and acetone ($R = R' = CD_3$), expected to yield α-amino isobutyric acid (AIBA).

The Strecker synthesis has been carried out in aqueous solution (H_2O) alone and in aqueous solutions containing dust from the Allende meteorite or dust from the Murchison meteorite. The major products obtained in the Strecker synthesis were the expected compounds ALA, GLY, and AIBA. Unexpected products obtained were imino dicarboxylic acids: imino diacetic acid (IDA) and imino acetic propionic acid (IPA). The deuterium retention of these compounds is 50% to 98%, with variations in retentivity depending on the amino acid and the reaction conditions. Clearly, parent-body Strecker syntheses of amino acids from interstellar precursors can account for the deuterium enrichment observed in meteoritic amino acids.

The deuterium retention during the Strecker synthesis is sufficiently high that these results could be used in conjunction with the measured D/H ratios of amino acids on meteorites to set limits on the D/H ratios of the putative interstellar precursors. The deuterium-retention data suggest that a D/H ratio of 10^{-3} occurred in the interstellar formaldehyde which is thought to be precursive to the Murchison amino acid, glycine. D/H ratios of up to 0.1 have been observed in interstellar organic compounds, whereas the ratio in the nearby galaxy is 2×10^{-5}. However, the imino dicarboxylic acids have not been observed in meteorites. If the Strecker synthesis is the route for amino acids in meteorites, a reasonable explanation must be found for the absence of the imino dicarboxylic acids.

Ames-Moffett contact: N. Lerner
(415) 604-6941
Headquarters program office: OSSA

Exobiology Experiments for the In Situ Analysis of the Martian Surface

Rocco Mancinelli, Lisa White

Little is known about the mineralogy of the Martian surface material. Several techniques have been suggested as candidates for the in situ identification of the Martian surface material. The most promising of these techniques include differential thermal analysis (DTA) coupled with gas chromatography (GC), and differential scanning calorimetry (DSC) coupled with either mass spectrometry (MS) or GC. Our studies have shown that differential thermal analysis coupled with gas chromatography (DTA/GC) is a more appropriate analytical technique than DSC/MS or DSC/GC to identify the mineralogy of the Martian surface material *in situ*. DTA/GC can be regarded as an advancement from pyrolytic GC analyses that have been successfully flown on previous missions but must have supplied only limited mineralogical information.

Coupling DTA with GC enables the researcher to identify and quantify gases that evolve during the heating process (e.g., organics, CO_2, H_2O), and to correlate the thermal events on the DTA with the specific gases evolved during that event. Samples can then be characterized, and distinction can be made among a variety of mineral classes (e.g., clays, zeolites, and silicates), degrees of hydration, and salts (CO_3^{2-}, NO_3^-, etc.).

The development of a prototype flight instrument is based on criteria defined using laboratory equipment. To define the flight experiment, laboratory analyses were conducted using a Dupont model-1600 high-temperature DTA oven equipped with a model-910 cell base. Typically, 30 milligrams of sample were analyzed and 30 milligrams of Al_2O_3 served as the reference. The chamber was sealed, and the analysis was performed under a vacuum. The system is controlled by a Sun Sparc II workstation. The interface between the DTA and the GC consists of a stainless steel tube, equipped with pressure sensors, leading to the GC sampling valve. If gas evolves during the heating process, it is sensed by the pressure sensors, which then trigger a valve that allows the gas to be expanded from the oven chamber into a GC sample loop for GC analysis. The Sun Sparc II then automatically injects the sample onto the GC column and resets the system for another event.

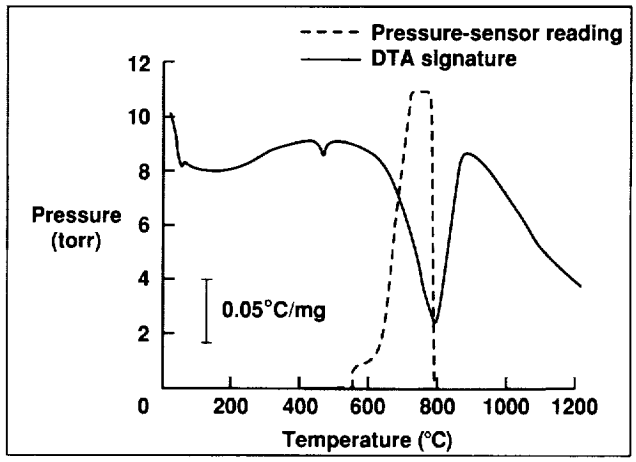

Fig. 1. DTA signature and concomitant pressure-sensor readings for the analysis of an evaporite from Yellowstone National Park, Wyoming.

When a gas evolves during a thermophysical event, the temperature is recorded such that the evolved gas is temperature-stamped so that it can be associated with a specific thermal event to the nearest degree. For example, the analysis of an evaporite collected from Yellowstone National Park, Wyoming, reveals that at ~800°C, an endotherm occurs that is associated with the release of a gas (see figure), identified as CO_2. The sample-identification software yields an identification of the sample and the probability of its accuracy. For this analysis the sample was identified as aragonite and calcite with a probability of 99%.

Because it has been suggested that clays may be an important component of the surface of Mars, their identification during in situ experiments will be important. We have previously shown that the DTA signatures for montmorillonite and kaolinite can be easily distinguished by their dehydroxylation

exotherms (550°C for kaolinite and 700°C for montmorillonite) and high-temperature transition exotherms (970°C for montmorillonite and 1,020°C for kaolinite). The difference in the high-temperature transition is critical in distinguishing a variety of clays from one another using the DTA. In addition, we have shown that various oxides of iron associated with the iron-enriched montmorillonite can be distinguished from one another.

Ames-Moffett contact: R. Mancinelli
(415) 604-6165
Headquarters program office: OSSA

Structure of Simple Membrane–Water Interfaces

Andrzej Pohorille, Michael A. Wilson

The structure and functions of the earliest ancestors of contemporary cells are focal points in studies of the origin of life. Probably the first cell-like structures were vesicles: closed, spheroid structures with aqueous medium trapped inside. The walls of vesicles, which resemble closely the membranes of contemporary cells, are built of chain molecules composed of charged or polar head groups and long oily tails. These molecules are arranged in bilayers such that the polar groups always point toward water and the oily tails form the interior of the bilayer.

A large number of essential cellular processes, such as capture and transduction of energy, sequestering of organic material, and synthesis of new molecules, occur at the interfaces between water and membranes. The selectivity and dynamics of these processes are largely determined by the structural and electrical properties of the interface. Recently, we have studied these properties in large-scale computer simulations using the molecular dynamics method. This method yields a detailed and accurate microscopic description of a molecular system that is often not available experimentally.

The membrane studied was composed of glycerol 1-monooleate (GMO). Glycerol forms the polar head group, and the oily tail contains 18 carbon atoms. The density distributions of different components of the water–membrane system are shown in the figure. All head groups are located in two narrow regions at the interfaces with water. The membrane interior, formed by the tails, is fluid, with chain disorder increasing toward the center of the bilayer. These results are in agreement with X-ray and neutron scattering data from related bilayers. The width of the membrane is not constant, but fluctuates in time and space. Occasional thinning defects in the membrane may have a significant influence on rates of passive transport of small molecules across membranes.

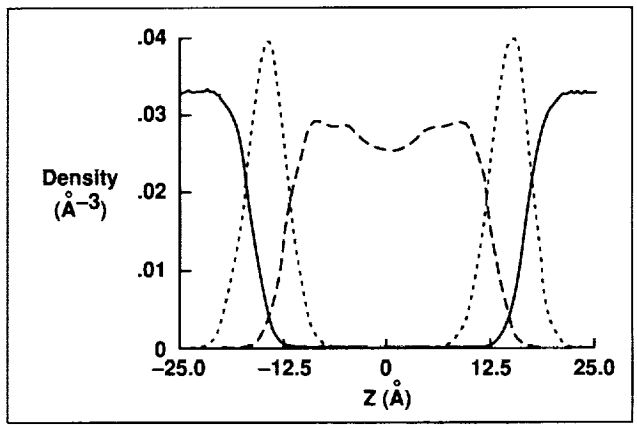

Fig. 1. Density profiles of water (solid line), GMO head groups (dotted line), and GMO tail groups (dashed line) perpendicular to the water–GMO bilayer interface (Z direction). The origin represents the center of mass of the bilayer.

As can be seen in the figure, water penetrates the head-group region but not the oily interior of the membrane. Water molecules near the interface are oriented by dipoles of the head groups. The resulting electrostatic potential across the interface has been found to be markedly larger than that across the water–oil interface.

Our simulations provide unique molecular-level information about membrane–water interfaces. They show that membranes are flexible, continuously fluctuating structures. Their head groups strongly organize interfacial water molecules, which, in turn, contribute to the electrostatic potential across the interface. All these properties influence basic processes of protobiological interest, such as transport of ions, protons, electrons, and nutrients across membranes, and simple interfacial catalysis. We plan to study these processes in detail.

Ames-Moffett contact: A. Pohorille
(415) 604-5759
Headquarters program office: OSSA

A Titan Simulation Chamber

Shelly Pope

The surface of Titan is obscured from view by a global haze layer composed of photochemically produced aerosols. Knowledge of the chemical and physical properties of the aerosols is critical in understanding the important role the aerosols play in controlling both the amount of sunlight that reaches the surface of Titan and the thermal emission. To increase our understanding of the aerosols, researchers have simulated the atmosphere of Titan in laboratory chambers. Aerosol particles are produced when the various gas mixtures relevant to Titan's atmosphere are exposed to ultraviolet light. The particles are collected and then examined using a scanning electron microscope. Shelly Pope has designed and built a chamber that can produce aerosols in a similar way; this chamber also can cool the simulated atmosphere to temperatures appropriate to those of Titan's aerosol-forming region. The goal of this work is to investigate experimentally the size, shape, and cohesiveness of simulated Titan aerosols formed at cold temperatures.

The chamber can be cooled to approximately 170 kelvin using liquid nitrogen; the temperature of the gas at the top and bottom of the chamber is monitored with thermocouple sensors. Glass microscope slides serve as a collection surface for the aerosols. One slide is placed at the bottom of the chamber in a horizontal orientation and another in a vertical orientation. The vertical slide is designed to address the question of selective particle loss to the walls of the chamber; this is one of the "wall effects" that distinguish what happens in laboratory simulations from what happens in actual planetary atmospheres.

In a related effort, Pope and Tom Scattergood (State University of New York at Stony Brook) conducted two Titan aerosol experiments in support of the descent imager/spectral radiometer (DISR). This instrument is slated to fly on the Huygens Probe into Titan's atmosphere as part of NASA's Cassini mission to Saturn, and is being developed by Martin Tomasko's group at the University of Arizona. Tomasko and the Martin Marietta Corporation engineers who are building the DISR wanted to assess the effect of particles on the windows of the instrument. We supplied them with glass slides coated with some simulated Titan aerosols so that they could gauge the effect of the particles on the window transmission.

Ames-Moffett contact: S. Pope
(415) 604-6538
Headquarters program office: OSSA

The New Ames Mid-Infrared Astronomical Camera

Thomas L. Roellig

A new infrared camera has been developed at Ames Research Center for observations from ground-based telescopes. The heart of the camera is a Hughes 58- by 62-pixel arsenic-doped silicon detector array that has the spectral sensitivity range to allow observations in both the 10- and 20-micron atmospheric windows. Three discrete 8% filters at 18, 20, and 22 microns, as well as a 3% circular variable filter covering the 7.5–14-micron atmospheric window, define the spectral resolution. A polarimeter using a cold-wire grid polarizer in combination with a warm, rotating half-wave plate has also been built into the camera, giving polarimetric capability over the complete spectral range of the camera. A flexible optical design and a dedicated guider/mounting box allow camera operation with any major telescope that has a focal ratio within the range of 17 to 45. The camera is still undergoing development, but was used on an engineering observing run with the Mt. Lemmon 60-inch telescope for a week in November 1992 by a group including M. McKelvey and F. Witteborn at Ames, T. Gustavson (Caltech.), and L. Yuen and R. Cooper (both of Orion TechnoScience).

The Ames mid-infrared camera was found to meet all of its designed sensitivity performance goals during the tests at Mt. Lemmon. On the 60-inch Mt. Lemmon telescope, the camera sensitivity was found to be 0.62 Janskys/pixel in one minute of telescope observing time, which translates into a point-source sensitivity of 0.41 Janskys in one minute of telescope observing time. With this telescope, each camera pixel corresponded to a square 0.73 arc-seconds wide on the sky, which gave a total camera field of view of 42 by 45 arc-seconds. Two images that the camera took during the engineering run are shown in the figure. They are images of the planetary nebula NGC 7027 at two wavelengths, with higher flux levels indicated by progressively redder colors and lower flux levels indicated by progressively bluer colors. In these images, north is toward the top and east is toward the left. The infrared image size of NGC 7027 is approximately 15 by 12 arc-seconds in both pictures. The new mid-infrared camera clearly

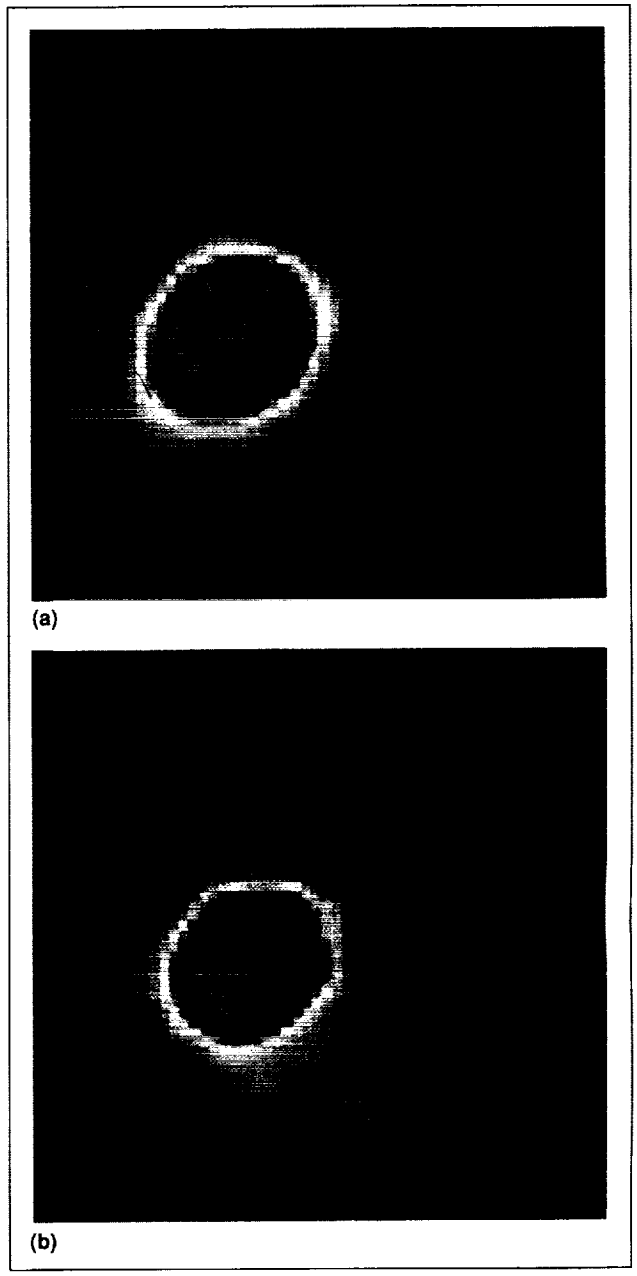

Fig. 1. Images of NGC 7027 from the Ames mid-infrared camera. (a) Measured at 11.4 microns with a 0.33-micron spectral bandwidth; (b) measured at 10.4 microns with a 0.33-micron spectral bandwidth. (See color plate 13 in Appendix)

shows the two-lobed structure of NGC 7027 in the infrared. The images also show that the shape of the object does not change between 10.4 and 11.4 microns. This is important, because the 10.4-micron flux arises solely from thermal emission from warm dust grains, whereas the 11.4-micron flux also has a component arising from a line-emission feature centered at 11.4 microns.

Now that the camera is working well, additional engineering test observations on the Mt. Lemmon telescope will be used to verify the performance of its polarimetry capabilities. Future plans also include using the Ames infrared camera with larger telescopes on Mauna Kea in Hawaii, to study interacting galaxies and particle shells around stars.

Ames-Moffett contact: T. Roellig
(415) 604-6426
Headquarters program office: OSSA

Diode Laser Spectroscopy of $^{12}C/^{13}C$ and $^{16}O/^{18}O$

Todd Sauke, Joe Becker

We are developing a stable-isotope laser spectrometer (SILS) that employs high-resolution, tunable diode lasers to measure ratios of stable isotopes of carbon and oxygen in carbon dioxide obtained from soil and rock samples. The goal is to develop an instrument for analysis of planetary soils on possible near-term Mars missions such as the Mars environmental survey (MESUR) or the Mars Rover sample return mission (MRSR).

The present spectrometer has the extended capability of measuring isotopic ratios of $^{18}O/^{16}O$ in CO_2 in addition to $^{13}C/^{12}C$. Appropriate spectral absorption lines have been identified for these measurements; initial results for the oxygen isotope indicate an accuracy of better than 1%, and the results for carbon have improved to better than 0.4%. Efforts to further improve accuracy have resulted in the development of a technique for automatic real-time removal of instrumental drift from signal-averaged absorption spectra. The method involves "locking" on a strong absorption feature and digitally shifting each individual spectral scan to eliminate detected drifts before the scan is added to previously acquired scans. By minimizing spectral drifts during signal averaging, the spectrometer's instrument response function (IRF) can be reduced in width and made more reproducible, allowing its effects to be modeled and successfully taken into account during data analysis.

A new technique has been developed to measure the IRF of the stable isotope laser spectrometer which provides a direct and independent measure that can be used to verify previous estimates of the IRF. These improvements will lead to better line-shape determinations and higher accuracy of measured isotopic ratios. The data-analysis software has been improved to include the effects of the instrument response in modeling and fitting of the data. The residual (difference between data and fit) has been substantially reduced. This advance promises to reduce systematic errors in data analysis. Further improvements have made the data-analysis peak-fitting software more robust against the deleterious effects of baseline drifts and the presence of small, extraneous absorption peaks.

Preliminary measurements of ^{12}C and ^{13}C diffusion in magnesium oxide, a model crystal, indicate that the SILS, even in its present state of development, can measure isotopic ratios with sufficient accuracy to provide information of importance to geologists and planetary scientists.

Ames-Moffett contact: T. Sauke
(415) 604-3213
Headquarters program office: OSSA

Analysis Techniques and the Search for Life on Mars

Debbie Schwartz, Rocco Mancinelli, Lisa White

To address the critical question of whether life could have arisen on Mars, two analytical approaches can be taken—first, in situ sample analysis, performed either remotely or by humans during a mission, or, second, laboratory analysis of samples returned to Earth. In the near term, it appears that missions to Mars will be uncrewed and of the MESUR (Mars environmental survey) class, capable of remote in situ analyses only. In light of these expectations, we have concentrated our efforts on defining an experiment that will allow us to gain, during MESUR-class missions, information pertinent to exobiology and to the question of the origin of life on Mars. Given current mission constraints on mass, power, and volume, planned exobiology experiments can be performed using only analytical techniques, such as electron microscopy, X-ray fluorescence, X-ray diffraction, α-proton backscatter, γ-ray spectrometry, differential thermal analysis, differential scanning calorimetry, pyrolysis gas chromatography, mass spectrometry, and specific element detectors.

In order to define an in situ exobiology experiment for Mars, laboratory studies must be performed. Two test samples that contained components of interest to exobiologists were prepared. The first sample consisted of 1% bovine serum albumin (BSA) in palagonite. BSA was chosen because it is a semidefined, amorphous, complex organic material. Palagonite, a hydrated devitrification product of basaltic glass, was selected because it is a possible analog of Martian surface material. The second test sample consisted of a mixture of palagonite, clays, carbonates, evaporites, and iron oxides. The clays chosen have at one time or another been used as analogs of at least some portion of the Martian surface material. The carbonates were selected because the possibility exists that carbonates were a sink for the dense carbon dioxide atmosphere postulated to have existed on early Mars. A variety of carbonates were selected to ensure that the technique chosen would differentiate between minerals that have similar (or the same) chemical compositions but different crystallographic structures. Evaporitic salts were chosen as constituents of the test sample because they may be minor components of the Martian surface material. The magnetic iron-oxide minerals magnetite and maghemite were selected because iron is an elemental constituent of the Martian surface material and is thought to exist as an oxide. A variety of techniques were employed to analyze these two samples. It was determined that a combination of X-ray diffraction and differential thermal analysis coupled with gas chromatography provides the best insight into the chemistry, mineralogy, and geological history of the samples.

Ames-Moffett contact: D. Schwartz
(415) 604-3668
Headquarters program office: OSSA

Column Development for Gas Chromatographs

Thomas Shen

Exobiology has been, and continues to be, a subject of interest to NASA. The examination of extraterrestrial bodies, e.g., planets, moons, comets, and planetary dust, for the presence of the compounds and elements necessary for the development of life is therefore the focus of much effort. From our knowledge of life on Earth, we know that water and ammonia are of critical importance to the development of life. Gas chromatography is a technique that can be used for the analysis of water and ammonia; good separation columns, however, are difficult to find. Although several liquid-coated columns have been used for this application, they can not be used in coordination with highly sensitive detectors such as the ion mobility spectrometer (IMS) or metastable ionization detector (MID) because of bleeding problems. For these reasons, Ames Research Center is developing low- or no-bleed columns for use in gas chromatography.

In addition, current commercial columns separate water and ammonia through temperature programming. In flight missions, an isothermal condition is preferred. Under isothermal conditions, most of the commercial columns either do not give good separation or have high tailing problems. Recently, several porous-layer open-tube (PLOT) columns were developed for water/ammonia separation. In this report, the size effect and solubility effect of water and ammonia separation are described.

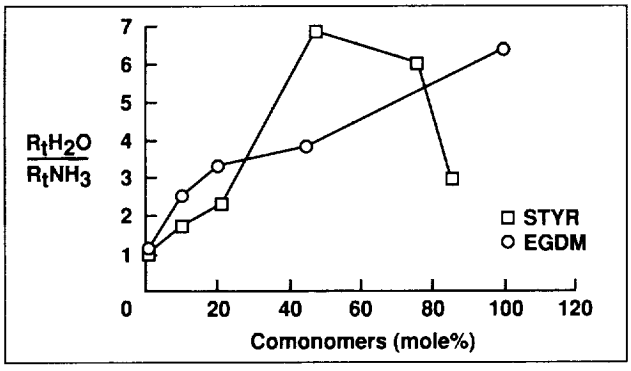

Fig. 1. Effect of mole% of comonomers in divinylbenzene copolymer columns for water/ammonia (H_2O/NH_3) separation.

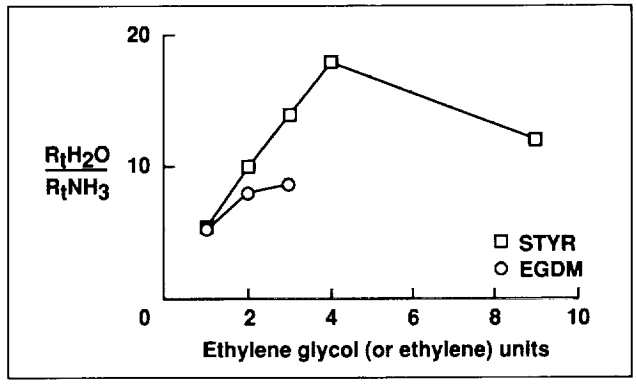

Fig. 2. Effect of chain length between methacrylol groups on water/ammonia separation.

Several divinylbenzene copolymer and dimethacrylate homopolymer PLOT columns for the separation of water and ammonia were investigated using in situ polymerization methods developed in our laboratory. The results indicate that (1) increasing the amount of comonomers, ethylene glycol dimethacrylate (EGDM) or styrene (STYR), in the divinylbenzene copolymers increases the relative retention time (R_t) between water and ammonia (see first figure); (2) increasing the chain length between the methacrylol groups in dimethacrylate monomers increases the separation of water and ammonia, e.g., homopolymer triethylene glycol methacrylate gives better separation of water/ammonia than diethylene glycol dimethacrylate and ethylene glycol dimethacrylate (see second figure). These results suggest that size effect is important in water and ammonia separation; and (3) an ethylene glycol chain between methacrylol groups in dimethacrylate homopolymer also gives better separation than an ethylene chain, e.g., triethylene glycol dimethacrylate separating water and ammonia is better than 1,6-hexamethylene dimethacrylate (see second figure).

Ames-Moffett contact: T. Shen
(415) 604-5769
Headquarters program office: OSSA

Computer Model of Microgravity Aerosols

David Stratton

Both NASA and the European Space Agency are planning aerosol experiments to be performed in microgravity. Examples are the Gas-Grain Simulation Facility (GGSF), in development at Ames, and the Columbus (precursor flights) protoplanetesimal dust aggregation experiment (CODAG), being developed in Germany. The low-acceleration environment expands the definition of aerosol by extending the range of particle sizes that can be suspended in a gas for a reasonable period of time, and enables new research, such as the study of fractal aggregates that are unstable in an Earth-gravity environment. A major difficulty in such experimentation is inherent in the small size of the aerosol-experiment chamber (compared to those used on Earth) necessitated by the high cost of space flight. The smaller the chamber, the greater the impact of diffusion on the experiment. The spatial inhomogeneity brought on by diffusion of aerosol particles to the chamber walls influences particle coagulation rates, so particle size spectra will also be spatially inhomogeneous. This spatial variation in particle size spectra further modifies the diffusion rates. The diffusion and coagulation of aerosol particles in a chamber are closely related and shape the aerosol in a complex way. A better understanding of these effects could greatly improve development of effective microgravity aerosol experiments and interpretation of the data collected from them.

A computer model of coagulation and diffusion in a closed volume has been developed to better understand this complex physical system. By studying the relationships between coagulation rates, diffusion, and the size and shape of the experiment volume, it may be possible to compensate for wall effects by one or more of the following methods:

1. Designing experiments in which wall effects will be minimal;
2. Estimating the degree to which experiment data are influenced by wall effects;
3. Providing a theoretical basis for extrapolating to the unbounded case from experimental data.

The program was written in C, allowing portability to other platforms, and is running on an Apple Macintosh computer, making it accessible to a wide audience of potential GGSF experimenters. The experiment volume is a rectangular box with user-selected size, shape, and spatial resolution. A broad range in particle sizes is accommodated by a particle-size binning technique.

The model indicates that after ten days, an initially homogeneous aerosol of micron-sized particles will develop spatial inhomogeneity such that the outer 50% of the volume will have particle concentrations 5% less than the inner 50%. In contrast, an initially homogeneous aerosol of nanometer-sized particles will develop the same level of inhomogeneity in less than 100 seconds. Spatial variations in concentration and size spectrum will introduce uncertainty in several types of aerosol characterization measurements:

1. Measurements of average values along a line through the volume (such as optical extinction measurements) will have the least uncertainty;
2. Measurements that average over the entire experiment volume (such as a condensation nuclei counter processing the entire volume in a destructive measurement) will be more uncertain;
3. Uncertainty for measurements made on a small sample of the aerosol removed from the experiment chamber is even greater.

Future enhancements of this model will include an algorithm to introduce the effects for convective mixing and gravitational settling, to relate the model to a ground-based experiment. Future versions will also allow for agglomerates that are not compact spheres, e.g., fractal aggregates. More realistic aerosol injection models will also be developed.

Ames-Moffett contact: D. Stratton
(415) 604-4204
Headquarters program office: OSSA

Absolute Airborne Infrared Spectroscopy

Fred C. Witteborn, Martin Cohen, Diane H. Wooden

Infrared spectra of astronomical objects are usually obtained by determining the ratio of the spectrum of the object and that of a bright, standard star whose spectrum is assumed to be known. Now that some programs—such as planet surface mineralogy, the Infrared Space Observatory (ISO), and the Midcourse Space Experiment (MSX)—demand accuracies of 2% or better, it has been necessary to recalibrate bright, standard stars in the 3–30-micron range with improved accuracy and higher spectral resolution. Old assumptions of blackbody behavior of hot stars in this spectral range must be abandoned in favor of sophisticated models of stellar atmospheres that include effects of absorption lines and wavelength-dependent opacity. Even the brightest hot, standard stars are quite faint beyond 20 microns, so asteroids are often proposed as infrared standards. Asteroids change in brightness and their spectral properties must also be modeled, but these models are based on information quite different from the stellar models. Thus there are two independent ways of calibrating the standards. What if they give different answers? A direct, physical approach to absolute calibration of the standards is to compare the stellar and asteroid spectra to spectra of an on-board blackbody cavity. All of these approaches are being employed using the high-efficiency, infrared faint object grating spectrometer (HIFOGS) on the Kuiper Airborne Observatory (KAO).

A few KAO flights devoted to standards have already been made. The data from these, from ground-based 8–13-micron data and from earlier flights in which ratios of various bright stars were obtained in the 3–9-micron spectral range, have been reported in two articles in the Astronomical Journal (1992). These papers illustrate the effect of carbon monoxide and silicon oxide absorption on spectra of K and early M stars (temperature range 5,000 kelvin down to 3,500 kelvin). They are calibrated on the stellar atmospheric model of Sirius (a 10,000-kelvin main sequence star) calculated by Kurucz. His models are believed to be accurate because they explain all features seen in the ultraviolet and in the observed depths of hydrogen-absorption lines in the visible spectrum.

Preliminary comparisons of the spectra of α Tau and the asteroid Vesta in the 3–26-micron range have been made on the KAO. These require additional data to improve signal-to-noise ratios. They also raise the question of our understanding of mineralogical features in asteroid IR spectra.

A direct comparison of a stellar spectrum to that of a nearby blackbody cavity would seem to be the most reliable method of spectral calibration. Unfortunately, the terrestrial atmospheric absorption and the telescope optical absorptions no longer automatically cancel out as they do when astronomical objects are compared through similar air masses. Furthermore, because of nonuniform detector/detector-optics response, one must be certain that radiation from the cavity arrives at the same parts of the detectors as does radiation from the stars. Preliminary measurements from the KAO in May 1992 are still being analyzed. Improvements in the technique are being incorporated to simplify both the taking and analysis of data in the more extensive measurements to be made in April 1993. A specially developed blackbody cavity with accurate thermometry and designed to provide emissivity of 0.995–0.999 throughout the 3–30-micron range has been ordered and will serve as a laboratory standard.

While much work remains to be done, the HIFOGS/KAO stellar calibrations using the Kurucz model of the Sirius spectrum have produced the best spectral standards available for astronomical work in the 5–14-micron range. Further work will expand the number of standard stars, the wavelength coverage, and the level of confidence.

Ames-Moffett contact: F. Witteborn
(415) 604-5520
Headquarters program office: OSSA

The Galileo Probe Mission to Jupiter

Richard E. Young

Galileo is the first planetary mission designed to conduct extended observations of one of the giant outer planets, in this case Jupiter, and is the first mission to directly sample the atmosphere of one of the giant planets.

The spacecraft consists of an orbiter and an atmospheric entry probe. The orbiter will conduct an extensive (approximately 10 orbits during a 22-month period) survey of the Jovian system, including the planet, its satellites, and its magnetosphere. The entry probe will directly sample the composition, structure, and meteorological state of Jupiter's atmosphere. The spacecraft was launched October 18, 1989, aboard the space shuttle Atlantis and will encounter Jupiter on December 7, 1995. During the trip to Jupiter, Galileo will make scientific observations of Venus and the Earth–moon system and will obtain the first close-up views ever of an asteroid.

The atmospheric entry probe represents one of the most difficult and demanding aspects of Galileo. The probe was designed and built by Hughes Aircraft under the supervision of Ames Research Center. At encounter with Jupiter, the probe's speed relative to the Jovian atmosphere exceeds 100,000 miles per hour; peak deceleration due to atmospheric entry is equivalent to 350 G. Bow shock temperature is 28,000°F, and two-thirds of the heat shield ablates during deceleration to Mach 1. The probe carries six scientific instruments and will measure atmospheric winds, composition, structure, radiative heating distribution, aerosol distribution, helium abundance, and lightning frequency and intensity.

On November 20, 1992, the first in-flight mission sequence test (MST) was conducted. This test cycles the probe system and scientific instruments through a complete command and function sequence corresponding to the actual mission. Because the high-gain antenna is still not deployed, and may not be before the Jupiter encounter, it is possible that this test, which was conducted as part of the overall mission sequence for the second Earth gravity assist to the spacecraft, may be the last complete test of the probe before encounter on December 7, 1995. Preliminary analyses of the data from the test indicate nominal readings. In addition to the MST, an abbreviated systems function test (ASFT) was conducted on December 2. Its purpose was to test the command sequence for an abbreviated probe-systems test, which will be done several months before the probe's release from the orbiter on July 10, 1995. A full test cannot be done without the high-gain antenna; hence the need for an abbreviated test procedure. Both tests showed that the probe systems and scientific instruments were functioning normally, and therefore a complete and successful probe mission at Jupiter is expected.

Ames-Moffett contact: R. Young
(415) 604-5521
Headquarters program office: OSSA

Gravity Waves in the Venus Atmosphere

Richard E. Young, Howard Houben

Several studies indicate that internal gravity waves of synoptic scale or smaller could be a significant presence in the Venus atmosphere. In addition, there are convincing observations from the VEGA Venus balloon mission that gravity waves generated by surface topography reach cloud levels with significant amplitude, and that gravity waves generated by other means are ubiquitous as well. Gravity waves are thought to play a critical role in the maintenance of the observed atmospheric superrotation.

A computer code is being used to simulate 2-D gravity waves in the atmosphere of Venus. The code accounts for all nonlinear interactions in the equations of motion and can therefore examine the effects that gravity waves have on the atmosphere.

During the last year we have continued the gravity-wave computations begun the previous year and have extended the cases considered to include large-amplitude wave forcing near the Venus surface due to winds flowing over surface topography. These most recent simulations account for the feedback of the gravity waves on the surface wind; hence the surface forcing itself depends on the amplitude of the waves. The results from these latest calculations show that waves generated near the surface can reach large amplitudes above cloud levels (more than 55-kilometer altitude), having clear signatures in the circulation pattern. At still higher levels (more than 100 kilometers) the waves appear to reach large enough amplitude that they break, depending on forcing amplitude, vertical energy propagation speed or group velocity, and damping time scales above the clouds. In regions where gravity waves break, wave energy and momentum are deposited, and turbulence-like motions can result. The computed waves also develop complex flow patterns well below the region where they are likely to break as the result of finite-amplitude wave–wave interactions. The result is that waves that have considerably shorter horizontal wavelengths than that associated with the forcing near the surface become apparent well below cloud levels. Another interesting feature of the finite-amplitude waves is that, unlike small-amplitude waves, the correlation of wave vertical velocity with wave temperature fluctuation is significant in certain regions, one of which is the middle cloud layer convective region. Such a nonzero correlation is usually interpreted in terms of turbulence or convection and is typically used to distinguish such types of motions from waves. Thus, the large-amplitude waves produce a significant heat flux and cannot be distinguished from purely turbulent motions on this basis.

Further simulations treating gravity waves generated by other mechanisms, such as a convective surface boundary layer, are being carried out and will indicate how important such waves are for the maintenance of the atmospheric superrotation.

Ames-Moffett contact: R. Young
(415) 604-5521
Headquarters program office: OSSA

Simulation of the El Chichon and Mt. Pinatubo Volcanic Aerosol Clouds in the Stratosphere

Richard E. Young, Howard Houben, Brian Toon

The importance of dynamical, chemical, and aerosol microphysical processes occurring in the Earth's stratosphere has been emphasized with the discovery of the Antarctic ozone hole. Major NASA programs, such as the Upper Atmosphere Research program, the NASA Ames aircraft expeditions to the Antarctic in 1987 and the Arctic during the winter of 1988–1989, and various Earth-orbiting satellite programs such as the Upper Atmosphere Research Satellite program, have as a principal goal the study of the climatology of the stratosphere. NASA has also initiated the Volcano Climate Interaction program to assess the effects of major volcanic eruptions on the Earth's climate. A unique set of opportunities to better understand stratospheric transport and aerosol microphysical processes, as well as climatic effects of volcanic aerosols, occurred when the El Chichon volcano erupted in April 1982, injecting about 10 million tons of aerosol particles into the stratosphere, and when the even larger eruption of Mt. Pinatubo occurred in June 1991. A comprehensive climatology of the subsequent dispersal of the volcanic clouds, gathered from aircraft, satellite, and ground-based observations, has been and is being compiled for the years immediately following the eruptions. We are numerically simulating the behavior of the volcanic clouds and comparing the results to observed cloud climatology. In this way we can assess and improve our theoretical understanding of transport and aerosol microphysical processes in the stratosphere.

The procedure is to calculate winds in the stratosphere with a 3-D global circulation model, and then to input these winds to an aerosol transport model which then computes the transport, accounting for sedimentation, chemistry, and coagulation of aerosol particles. In the interactive mode, the two models work together simultaneously: the aerosol transport model provides new cloud distribution properties, which are then used by the circulation model to determine wind and temperature fields. In the passive tracer mode, which is being used initially, there is no feedback allowed from the presence of the volcanic aerosols.

Observed characteristics of the dispersion of the volcanic clouds are fairly well represented in passive tracer simulations, in which the feedbacks of the volcanic aerosols on stratospheric wind and temperature fields are neglected. Such observed characteristics as time to circle the globe near the latitude of the eruption (about 3 weeks) and direction of cloud movement (westward) are seen in the simulations, as is the confinement of the cloud to tropical latitudes. The figure illustrates the computed Pinatubo cloud (total column) at 21 days after the eruption. The most serious deficiency of the passive tracer calculations seems to be that the Pinatubo cloud's center of mass is about 5–7 degrees north of the equator rather than at, or slightly south of, the equator, as observed. Radiative heating of the aerosol cloud itself is thought to be important, and this effect is now being incorporated into the model calculations to see if the cloud's center of mass will then move farther south.

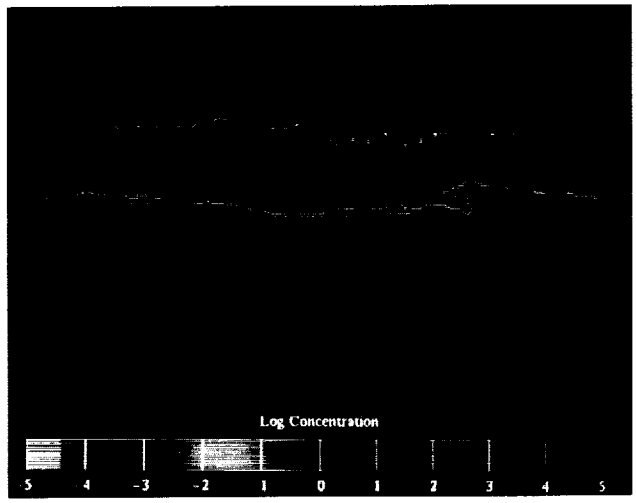

Fig. 1. Simulated Mt. Pinatubo volcanic cloud after 21 days. The cloud has just completed one circumnavigation of the globe and is confined to the tropics. Dotted lines represent latitude in 15-degree increments. (See color plate 14 in Appendix)

Ames-Moffett contact: R. Young
(415) 604-5521
Headquarters program office: OSSA

The Tunguska Event of 1908

Kevin Zahnle

On June 30, 1908, a meteorite exploded about 10 kilometers above the Siberian taiga with the energy of a 15-megaton thermonuclear bomb. The event is known as the Tunguska explosion, because it occurred about 50 kilometers north of the Podkammenaya Tunguska River. The force of the explosion flattened the forest over a 2,000-square-kilometer region. The blast wave excited an earthquake equivalent to Richter magnitude 5. According to contemporary newspaper reports, local tribesmen and townspeople, most of them farther than 250 kilometers from the explosion site, were amazed and terrified; many expected the world to end. Probably because of the extremely low population density of Siberia, no one was killed. Although it is clear that the Tunguska explosion was caused by Earth's encounter with a wayward celestial object, no expedition—there have been several—has unearthed a single proven fragment of meteoritic material.

The nature of the Tunguska event excited remarkable speculations, many fueled by the failure of the meteor to leave any fingerprints. Antimatter (then known as "contraterrane matter") was suggested as early as 1940, refuted in 1949, and suggested again in 1966. The hypothesis fails because the needed nugget of antimatter would be so small that atmospheric drag would halt it 50 kilometers above the surface, far too high in the atmosphere to account for the Tunguska treefall. A tiny cosmic black hole piercing the Earth was suggested in 1973. This idea fails because it predicts a comparable exit hole. Barographic records prove that Tunguska was singular. Perhaps inevitably, even the explosion of a doomed UFO has been advanced, on the grounds that only an intelligent agent could pilot a course that could satisfy all the eyewitness accounts.

Comets, which are less dense and more easily vaporized than asteroids, have dominated the more serious press. Yet excesses still occur. In the late 1970s an extremely low density comet (density less than 0.01 gram per cubic centimeter, i.e., denser than air but less dense than freshly fallen snow) became popular in the scientific literature.

We show that Tunguska was caused by the disruption of an ordinary dense, stony asteroid by aerodynamic forces. We (Kevin Zahnle; Christopher Chyba, at NASA Goddard Space Flight Center; and Paul Thomas, at the University of Wisconsin at Eau Claire) conceptualize the asteroid as a cylinder moving along its axis of symmetry. As the asteroid descends into the atmosphere, a ram pressure of order ρv^2, where ρ is the density of air and v the object's velocity, buffets its leading face. The sides and rear are subject to much weaker pressures. When the aerodynamic stresses exceed the asteroid's native strength, the asteroid fragments. For a strong, stony object this occurs about 20 kilometers above the ground. If the fragments cannot relieve the building stress by moving out of the way, they, too, in turn, fragment; there results a pulverized mass of rubble. The rubble behaves like a fluid. The aerodynamic pressure at the front becomes a pressure that spreads the gravel bank sideways. The volume of the asteroid is preserved as the cylinder is pressed into a squatter version of itself. As the asteroid spreads, its effective cross section increases and it intercepts more air, and it is through sweeping up air that the swarm of fragments halts in the atmosphere. The final catastrophic flattening takes less than a second. Thus the asteroid can be regarded as truly exploding.

We find that a comet with a kinetic energy equivalent to a 15-megaton bomb would be too easily ablated, too weak, and not dense enough to penetrate to within 25 kilometers of the ground. An iron asteroid, by contrast, would be too strong and dense; it would reach the ground and leave a substantial crater. The famous meteor crater in Arizona was produced by a 15-megaton explosion. A strong, stony asteroid, of density 3.5 grams per cubic centimeter, velocity 15 kilometers per second, and diameter 60 meters would produce an explosion of that size. Tunguska is the reasonable result of a 60-meter-diameter stony asteroid striking the Earth.

Ames-Moffett contact: K. Zahnle
(415) 604-3148
Headquarters program office: OSSA

Post-Stall Envelope Expansion of the X-31 Enhanced Fighter Maneuverability Airplane

John T. Bosworth, Jeffrey E. Bauer, Patricia C. Seamount

Post-stall maneuvering capability has been shown to provide significant tactical advantages in close-in-combat simulation studies. Although dome-to-dome simulation provides one tool to assess tactics, in-flight demonstration is required for a more realistic demonstration of the merits of post-stall maneuverability.

The X-31 experimental research aircraft (see figure) was designed to demonstrate enhanced fighter maneuverability in the post-stall flight regime. The aircraft is equipped with three thrust-vectoring paddles that provide yaw and pitch vectoring to augment aerodynamic control at extreme angles of attack. The full-authority digital flight-control system is designed to provide controlled flight up to a 70-degree angle of attack.

An international flight-test team composed of NASA, Rockwell, DASA, the German government, and the U.S. Air Force and Navy is currently expanding the flight envelope to the airplane's full maneuvering limits. Real-time monitoring of the aircraft, control surface motion, and internal flight-control system variables is required to ensure a safe envelope clearance. An easily programmable color graphics display capability is used to provide flexible display formats to ensure quick, clear interpretation of critical safety parameters. This capability can be quickly adapted to focus the monitoring on specific mission requirements.

In addition to real-time monitoring, the aircraft response is recorded and compared to that of a simulation model. The recorded pilot inputs from flight can be used to drive the full six-degree-of-freedom nonlinear simulation. Discrepancies in behavior are quickly highlighted by these comparisons. If required, flight-control-system behavior can be further investigated by using control-system feedbacks as well as pilot commands, recorded from flight, to drive a FORTRAN control law model in an open-loop fashion. This allows for an in-depth analysis of the inner workings of a complex multiple-input, multiple-output control system without overtaxing the on-board data measuring and recording system.

To investigate sensitivity to aerodynamic variations and to match flight-test results, the X-31

Fig. 1. X-31 research aircraft.

nonlinear simulation is programmed to accept data files that contain perturbations to selected aerodynamic stability derivatives. This allows for rapid incorporation of results from the flight test into a full six-degree-of-freedom nonlinear simulation. This capability, coupled with the ability to compare simulation results directly with flight-test results, allows for quick modi-fications to the aerodynamic data base for analysis purposes.

Complex motions of the aircraft are analyzed by differentiating the flight measured body-axis angular rates and decomposing them into inertial, kinematic, gyroscopic, thrust-vectoring, and aerodynamic components. In addition, a visual playback is reconstructed using a graphic model to provide a clearer picture of the sometimes complex aircraft motions.

With these flight-test techniques, the aircraft flight envelope has been cleared to 1-G flight at a 70-degree angle of attack. Full-stick bank-to-banks and velocity vector rolls have also been performed. Continued envelope expansion will include accelerated entry into the post-stall region. Upon conclusion of the envelope-expansion flight-test phase, the X-31 experimental aircraft will go on to investigate the merits of post-stall maneuvering capability as they apply to the close-in-combat arena.

Ames-Dryden contact: J. Bosworth
(805) 258-3792
Headquarters program office: OAST

Parameter Identification for Highly Augmented Aircraft

Albion H Bowers, Brent R. Cobleigh

Accurate mathematical models of high-performance aircraft are very important since they are used for control system design and refinement, flight software checkout, flight-test maneuver design, pilot training, military utility simulation studies, etc. To update the wind-tunnel-derived models, parameter-identification derivative (PID) methods are used to estimate the stability and control derivatives from flight-test maneuvers. Typically, these maneuvers consist of stick and/or rudder inputs applied by the pilot at a specific flight condition. The preferred input for PID has traditionally been a square wave doublet, since it excites the aircraft over a broad frequency range and is easy for the pilot to perform. It can be shown that the maximum attainable accuracy of the parameter estimates is directly related to the quality of the input.

Unfortunately, the complex control systems that are allowing controlled flight at high angles of attack also degrade the pilot stick as a suitable input source for PID. This is because the pilot input is manipulated to obtain coordinated flight, a by-product of which typically causes several control surfaces to move as a linear combination. This linear dependence prevents the effectiveness of control surfaces from being estimated independently.

The F-18 High Angle of Attack Research Vehicle is being used to demonstrate a technique to improve PID inputs for high-angle-of-attack estimation. The technique uses an on-board excitation system (OBES) to send inputs directly to the individual control surfaces, one at a time, during a PID maneuver. The predefined inputs are programmed into the flight software and selected by the pilot from a digital display in the cockpit. The system is mechanized such that the inputs are added to the basic pilot commands. To maintain a reasonable level of flight safety, the control-system rate limits and feedbacks are left on during the maneuver. Suitable input magnitudes and timing are refined in the simulator.

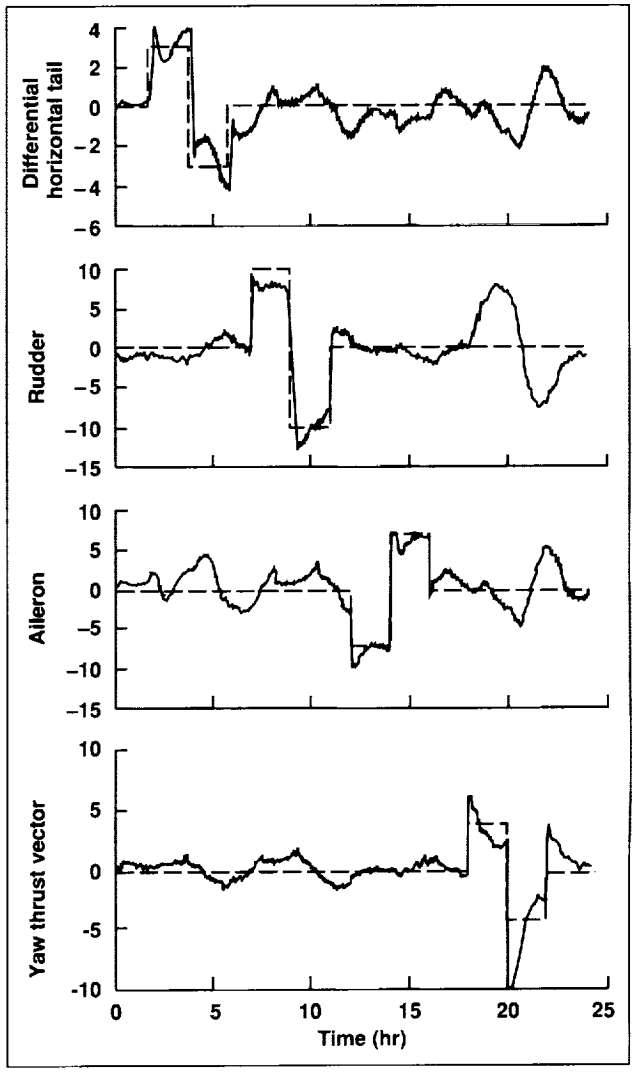

Fig. 1. Comparison of programmed inputs and actual flight-test time histories.

A typical 40-degree-angle-of-attack OBES lateral maneuver is shown in the figure, where the differential horizontal tail, rudder, aileron, and thrust vectoring are all excited with doublets. This maneuver was successfully demonstrated in September 1992. The figure illustrates that, even with the feedbacks on, the control surfaces are moved independently. In addition to providing better data, the OBES technique was found to be a more efficient user of flight time. To date, lateral and longitudinal demonstration maneuvers have been flown up to an angle of attack of 60 degrees with good results. A complete evaluation flight of this technique is scheduled for mid-1993.

Ames-Dryden contact: A. Bowers
(805) 258-3716
Headquarters program office: OAST

Actuator Modeling for High-Angle-of-Attack Aeroservoelasticity

Martin J. Brenner

The validity of an aeroservoelastic model depends not only on the dynamic modeling of its components but also on the coupling between these components. Airframe, aerodynamics, actuation, and the control system must be accurate over a desirable frequency range. Actuator responses are customarily represented with low-order transfer functions matched to actuator test data, and control-surface stiffness against the airframe is often modeled as a linear spring. More realistic predictions of airframe/actuation coupling are needed for the more demanding tasks of modern control systems. In particular, for agility enhancement at high angle of attack and low dynamic pressure, structural integration characteristics such as hinge moments and effective actuator stiffness and damping between the airframe and control surface are expected to be prominent. Therefore, considering the physical properties of actuation and its installation on the airframe, detailed actuator models which consider the physical, electrical, and mechanical elements of actuation are desired for more accuracy to keep up with advances in structural, aerodynamic, and control-system modeling.

The F/A-18 aileron actuator installation and corresponding control system with servovalve and ram-position feedbacks is used to illustrate modeling effects. Dynamic coupling occurs as a result of aerodynamic loads (aerodynamic hinge moment), structural modes, and piston motion relative to the main ram assembly. Hydraulic systems supply pressure to the servovalve, which in turn activates the piston. The servovalve and ram electrical feedbacks maintain coordination and adequate stability. A linear model is derived by neglecting such characteristics as hysteresis, friction, and limits. Ground vibration test (GVT) data were used to investigate the differences in accuracy between linear aeroservoelastic analyses, in which the actuators are modeled as low-order (LOM) transfer functions, and analyses with the high-order (HOM) actuation modeling, which include the critical coupling mechanisms. The first figure compares the model responses with test data for the response of a sensor feedback due to rudder actuator command.

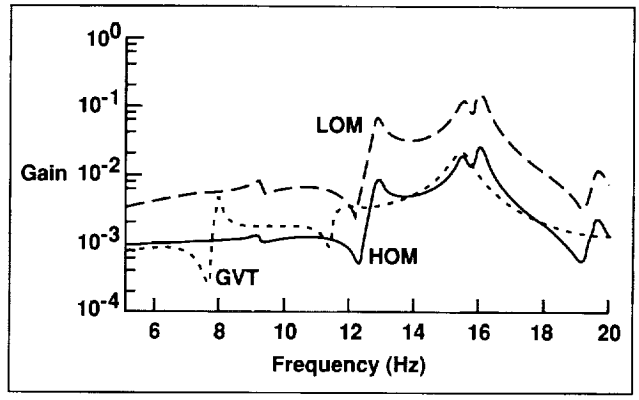

Fig. 1. Open-loop frequency response comparisons between analytical servoelastic models using high-order (HOM) and low-order (LOM) actuators, and ground-vibration test results (GVT).

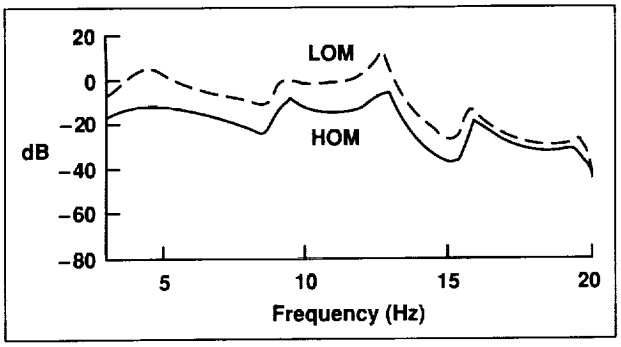

Fig. 2. F/A-18 HARV TVCS RFCS loop gains for lateral control loop computed using HOM and LOM actuator models and without unsteady aerodynamics at a high-angle-of-attack flight condition.

Clearly, the high-order models more accurately represent the aircraft dynamics.

The differences between the models can also be significant for stability analyses. Loop gains from the lateral control loop of the F/A-18 High Angle of Attack Research Vehicle (HARV) with a thrust vectoring control system (TVCS) and research flight control system (RFCS) are shown in the second figure for a high-angle-of attack flight condition. As can be seen, discrepancies in stability estimates between models using low-order actuation and those with high-order actuators can be extremely significant.

Detailed modeling of actuator hydraulic and electromechanical properties is important for any aeroservoelastic analysis regardless of flight condition, but the coupling mechanisms between actuation and structural dynamics are more pronounced with the decreased dynamic pressure characteristic of sustained high-angle-of-attack flight. Stability predictions may be unreliable when low-order actuation is used in the aeroservoelastic model since all the coupling mechanisms are not properly represented.

Ames-Dryden contact: M. Brenner
(805) 258-3793
Headquarters program office: OAST

Landing Systems Research Aircraft Capabilities

Vincent Chacon, John Carter, Darlene Mosser-Kerner

The Landing Systems Research Aircraft (LSRA) was conceived for testing Space Shuttle Orbiter landing gear and tires. Tires and landing-gear components for the Orbiter operate under higher loads and higher speeds than most commercial aircraft tires, and anomalous landing-gear results have been observed on several Orbiter landings. Limited instrumentation and the undesirability of taking any risks with the Orbiter make the Orbiter itself a poor candidate for conducting landing-gear tests. The LSRA was developed by NASA as a suitable testbed to provide a versatile capability for controlling test-gear vertical load, tire-slip angle, forward velocity, and landing surface to simulate actual landings, as shown in the figure. Although the project was funded for landing-gear tests for the Space Shuttle Orbiter, care has been taken to ensure that the LSRA retains a generic capability.

The centerline keel of the Convair 990 has been removed to create a large, unobstructed bay for the installation of a candidate test gear. The bay measures 7 feet long by 6.5 feet wide, and test gear up to 8.5 feet high can be accommodated. A generic test-gear pallet provides an adaptable mounting surface for candidate landing gear. A complete landing gear may be attached to the pallet, or a steerable fixture may be used to test a single tire and/or brake assembly.

Control of the test gear is attained by a test conductor and on-board computers. The test conductor is responsible for initiating and monitoring the test. Once started, the computers use preprogrammed

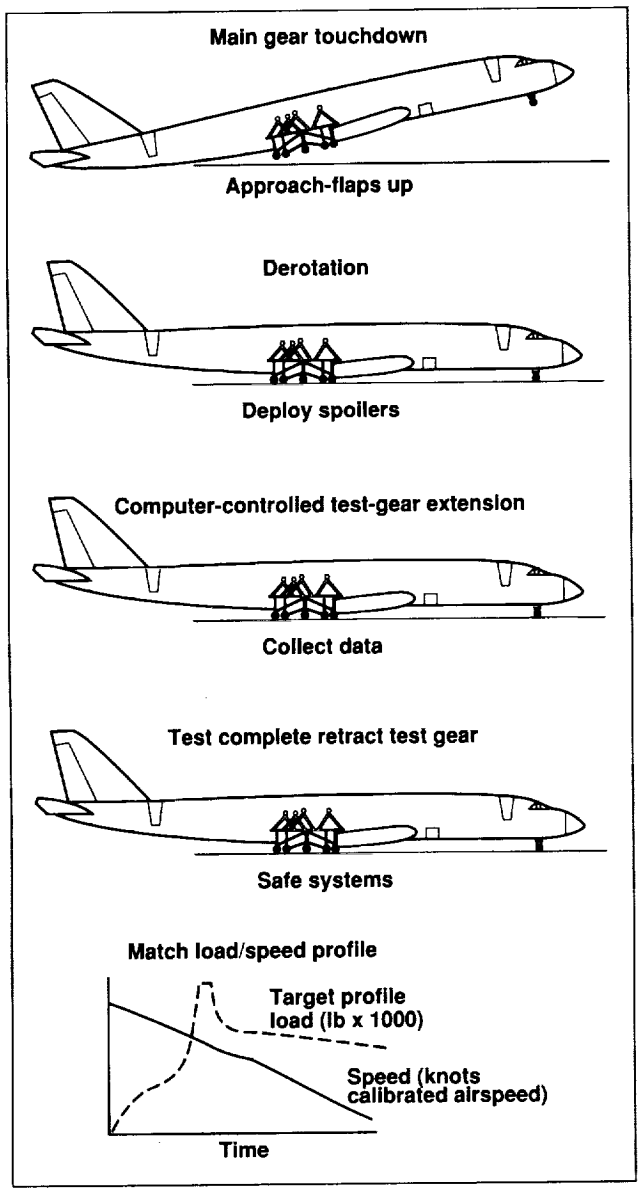

Fig. 1. Overview and capabilities of the LSRA.

profiles to generate commands for vertical load, tire-slip angle, and desired velocity. Load modulation is achieved by commanding a powerful hydraulic system to lower or raise the test gear. This action transfers total aircraft download between the Convair main gear and the test gear. Steering commands are computed using a measured aircraft drift angle to develop true tire-slip angle. The computer can also be programmed to output other analog and discrete signals for brake control and pilot information. A hydraulic source for test gear brakes is also available from the on-board hydraulic system.

The LSRA can generate up to 250,000 pounds of vertical load on a test gear using pallet extensions of up to 66 inches. Extension rates of up to 15 inches per second are achievable, giving the LSRA the ability to approximate moderate touchdown sink rates. With an average landing gear, full loads can be achieved in approximately 3.5 seconds after touchdown. The single tire steerable fixture is capable of sustaining 150,000 pounds of vertical load.

A large rotary actuator mounted on the steerable fixture will rotate the test tire between ±20 degrees of steering angle. This allows tire-slip angles of about ±17 degrees. Maximum rates of 35 degrees per second are possible. The actuator provides 380,000 inch-pounds of torque and is computer controlled to maintain tire-slip accuracies to within a quarter of a degree.

Using requalified main-gear tires and newly designed nose-gear tires, the basic aircraft can land at speeds up to 230 knots. Speed profiles during tests are maintained by the pilot using normal thrust reversers and brakes. A special computer-driven "on-speed" indicator has been added to the cockpit to facilitate this task.

To record test data and ensure flight safety, the aircraft and its test systems are heavily instrumented. Measurements for the test gear include vertical load, side force, drag force, tire pressure and temperature, axle accelerations, and brake pressures. All parameters are collected by a data-recording console that supports both on-board recording and telemetry to a ground station. On-board computers also allow self-contained data analysis for operation at remote sites.

Both hardware and software detectors have been built into the systems to detect anomalous test conditions. These have been linked to a special "updrive" system that will raise the test pallet if activated. Water deluge has been provided for both test gear and Convair main gear in the event of an unexpected tire or brake fire. In addition, a special brake-misting system has been installed to cool the brakes during high-deceleration tests.

Initial test plans for the LSRA will generate both tire force and wear information using several different test tires and failure modes and effects for two types of landing gear. The measurement of lakebed rolling friction and its correlation to lakebed conditions will also be determined. Testing will be conducted at both Edwards Air Force Base and Kennedy Space Center. Testing at Edwards will include landings both on concrete and on lakebed runways.

Ames-Dryden contact: V. Chacon
(805) 258-3791
Headquarters program office: OAST

Airborne Research System Architecture

Vince Chacon

The Airborne Research Test System (ARTS) is a powerful, general-purpose aircraft computer system that provides users, such as engineers and researchers, with the capability to rapidly develop and deploy experimental avionic and research systems. The ARTS can monitor aircraft data and present these data as engineering-unit information to resident research-and-development applications performing computationally intensive tasks while in flight. An overview is shown in the figure.

The ARTS is an "open system" in that it provides general-purpose functions and capabilities supporting specific applications and experiments. Computer programs written on workstations are incorporated with the ARTS and operated in flight with little or no modifications to the original application programs. The ARTS workstation environment can simultaneously support a variety of computer languages, such as C, FORTRAN, and Ada. In addition, the ARTS can host a wide variety of hardware compatible with the VME computer bus.

The ARTS is implemented using a two-level architecture. The lower level contains input/output (I/O) interfaces to flight hardware and processors, while the upper level supports a standard UNIX workstation environment. The lower level provides functions that are common to all airborne computer systems. Common functions include hardware interfaces to aircraft, avionic, and telemetry systems; data acquisition, storage, and retrieval capabilities; support functions such as autonomous boot, operation, and built-in test; and operator interfaces to the cockpit and ground support systems. The upper level provides an environment familiar to those who use UNIX workstation programming environments. The user has access to aircraft data that are provided by the low-level I/O devices through a dual-port memory by reflective memory. With the ARTS, the user can update and modify test applications software without affecting the low-level I/O interfaces to the flight hardware. The advantage of using an "open system" approach is that it will allow users unfamiliar with aircraft electronic systems, or users with limited financial resources, to flight test their software and ideas as opposed to merely simulating the flight environment on their workstations.

In addition to flight hardware, ARTS provides a generic solution to systems development. A typical avionic system requires a laboratory to support hardware/software development, operation, and maintenance. These systems are developed ad hoc and, as such, require large amounts of time and money. ARTS provides a general-purpose development environment which is based on "off-the-shelf" workstations and operating systems. This limits the effort required for developing and deploying an experimental avionic system to obtaining the software and hardware that is unique to the project—the ARTS provides the bases for the overall system.

ARTS hardware is based on recent advances in computer technology that have produced small, powerful, and inexpensive computer systems with the same or better capabilities and reliability than larger

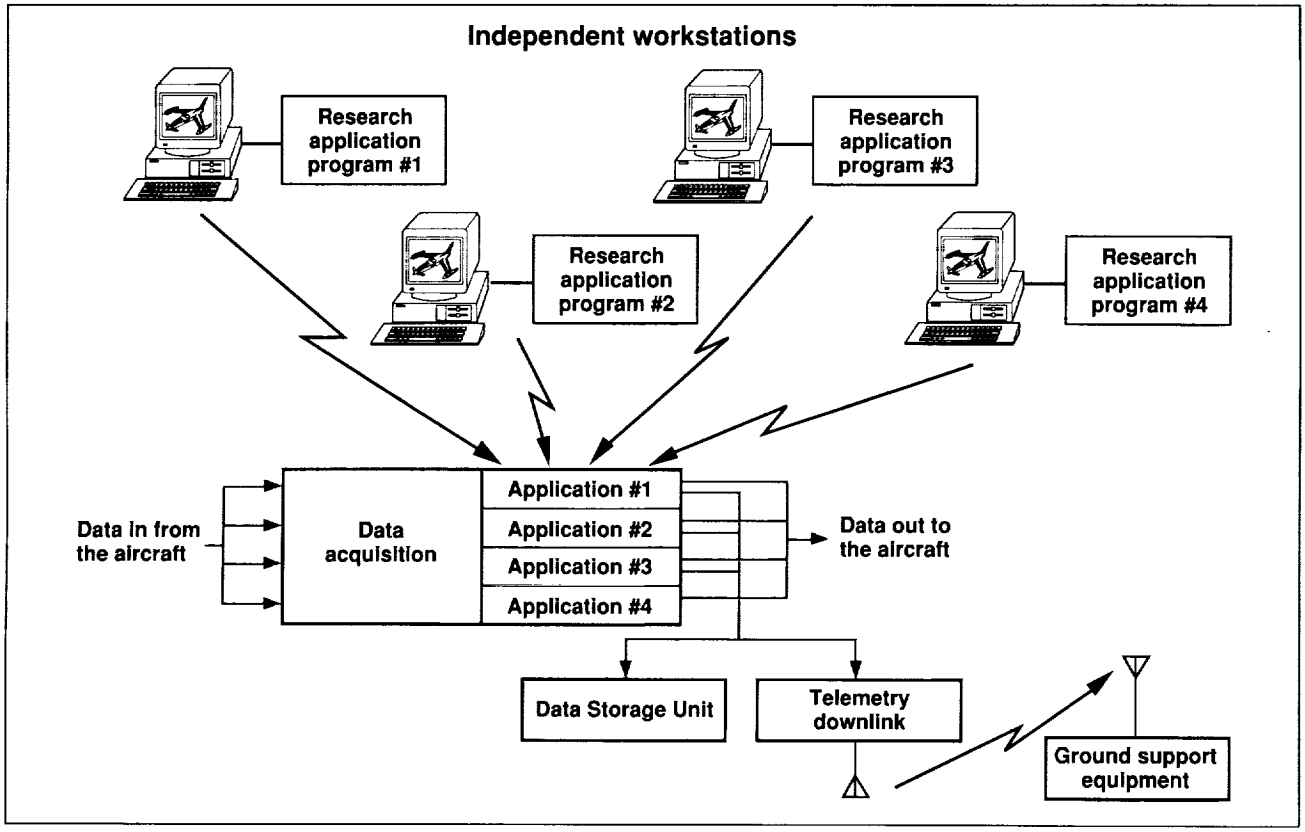

Fig. 1. Overview of the ARTS concept.

systems now in use. As a result of this technology, it is feasible and practical to install powerful, general-purpose computer systems aboard flight vehicles. Since the ARTS is constructed of commercially available, industrial-grade components, the cost of the system is significantly less than the cost of similar military-grade systems. The quality, ruggedness, and availability of industrial-grade components have improved to the point where they satisfy noncritical flight requirements. Given the variety of industrial-grade components available, the system can be constructed without internal hardware development of board-level components. If, however, a high-reliability version of an ARTS system is needed, it can be implemented using functionally compatible, commercially available military-grade versions of the industrial-grade components.

The ARTS will allow numerous cutting-edge concepts from the theoretical and academic community to be used in the operation of aerospace systems.

Ames-Dryden contact: V. Chacon
(805) 258-3791
Headquarters program office: OAST

C-4.

Flying-Qualities Investigation of the Long-Period Dynamics of a Generic Hypersonic Vehicle

Timothy H. Cox

Although recently published flying-qualities standards addressing long-term dynamics are adequate for subsonic and transonic flight, they are deficient for hypersonic flight. A divergent "height" mode that results from density gradients in the upper atmosphere exists in the hypersonic flight regime. Current flying-qualities standards do not address the effects of height modes. The phugoid mode is potentially more unstable in the hypersonic flight regime, with altitude and speed excursions much more pronounced than in the subsonic regime. These considerations warrant investigation of the impact of long-period dynamics on the flying qualities of a hypersonic vehicle.

The Technical University of Munich and the Ames-Dryden Flight Research Facility are collaborating to investigate this issue. The goal of this investigation is to define acceptable levels of height- and phugoid-mode instabilities using a generic, unclassified hypersonic vehicle simulation.

Preliminary results have been obtained by modifying the aerodynamic derivatives CM_γ and CD_v in a linearized model of a generic hypersonic vehicle. These modifications resulted in various aperiodic phugoid- and height-mode instabilities. Short-period, dutch-roll, roll, and spiral modes were designed to be satisfactory with no need for improvement. The model included a simple, conventional control system with pitch-rate feedback. The control system assumed perfect actuators and no filters.

Two Ames-Dryden research pilots flew a fixed-base, real-time simulator at Mach 10. The pilots evaluated the instabilities using two maneuvers: steady, level turn and vertical plane altitude change. Results are summarized in the figure. This figure illustrates the average pilot flying qualities rating for each maneuver versus the time to double amplitude. Four regions of flying qualities are defined: "satisfactory performance without improvement" (level 1), "acceptable performance with tolerable pilot workload" (level 2), "unacceptable" (level 3), and "uncontrollable." Two items are noteworthy:

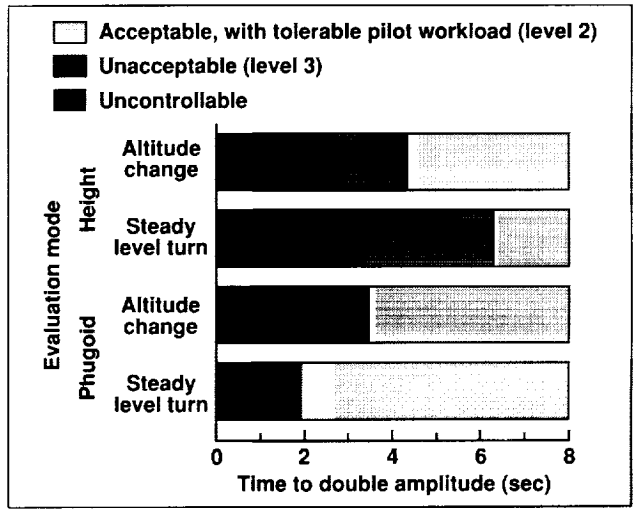

Fig. 1. Regions of phugoid- and height-mode instability for the steady, level turn and vertical plane altitude change maneuvers.

1. For the phugoid evaluation, the level 2/level 3 border was not definable because of control-surface deflection limits of the vehicle. The time to double amplitude of the "uncontrollable" border indicates the highest level of instability tested before control-surface deflection limits were reached. Metrics were measured to determine the pilot's ability to perform the task and the pilot's workload in performing the task. These metrics show only small degradations up to the "uncontrollable" border. This indicates that even shorter time to double amplitudes may be acceptable as long as control-system authority and control power are adequate.

2. Inconclusive information was obtained on the "satisfactory without improvement" region (level 1) for both modes. In general, the least unstable test cases were rated as level 2. Pilot comments indicate that other factors besides the phugoid- and height-mode instabilities are driving the vehicle to be rated as level 2.

These results indicate preliminary level-2 and level-3 regions of height and phugoid instabilities. Continued studies are anticipated to define the influence of pilot learning curve, displays, and oscillatory phugoid roots. Evaluations of the phugoid- and height-mode instabilities during an ascending turn will be added. A rate command attitude hold control system with an integrator in the forward loop will also be investigated.

Ames-Dryden contact: T. Cox
(805) 258-2126
Headquarters program office: OAST

In-Flight Structural Deflection Measurement Technology Transferred to Industry

V. Michael DeAngelis, William A. Lokos

In the early 1970s, NASA sponsored the development of the Highly Maneuverable Aircraft Technology (HiMAT) Remotely Piloted Research Vehicle (RPRV), which incorporated the first aeroelastically tailored graphite/epoxy composite wing for a flight vehicle. To evaluate the performance of the aeroelastically tailored structure, a direct measurement of the structural deflections was required. In 1976 NASA and the Grumman Aerospace Corporation began to develop the electro-optical Flight Deflection Measurement System (FDMS). The first system was tailored to fit the subscale HiMAT RPRV and was matured to a reliable and accurate flight system through a joint NASA and Grumman effort involving extensive ground testing and flight testing. The FDMS performed flawlessly throughout the HiMAT RPRV flight-test program and provided invaluable deflection data needed to evaluate the aeroelastic tailoring of the wing and canard. An unprecedented amount of deflection data was generated on only 12 flights of the HIMAT RPRV.

A system diagram for the electro-optical FDMS is shown in the first figure. The targets, which are mounted on a deforming surface such as a wing, consist of light-emitting diodes (LEDs) that are turned on and off sequentially beginning with target 1 and ending with target 48. Sequencing through the 48 LED targets takes 240 milliseconds, producing a sampling rate of 4 samples per second for each target. Light from the target LED passes through the cylindrical lens of the receiver and is focused as a line on a light-sensitive diode array mounted at the lens focal point. An electrical signal proportional to the point at which

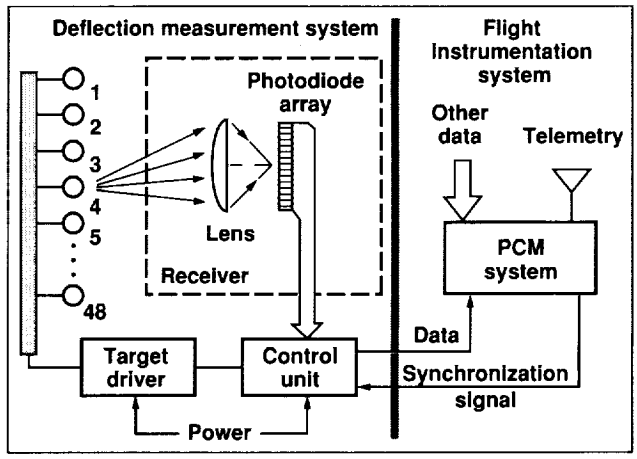

Fig. 1. Electro-optical FDMS system diagram.

the target light encounters the diode array is relayed to the control unit by the receiver. The control unit, which contains the logic necessary to operate the FDMS, also serves as an interface between that system and the pulse code modulation (PCM) data-recording system. The FDMS is synchronized by using the PCM system frame pulse. Data are sent to the recording system as two 10-bit digital words. One word contains target identification and error messages. The other word contains the corresponding target position information. Once the data are acquired by the PCM system, they are transmitted to a ground station for recording, displaying in real time, or both.

NASA developed the software programs needed to manage the FDMS data and worked with Grumman

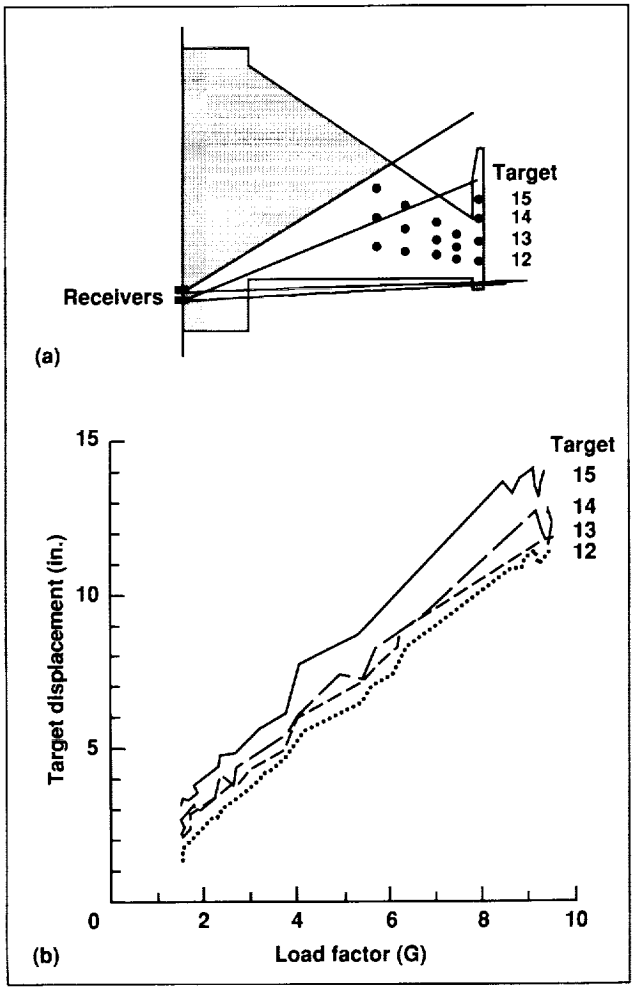

Fig. 2. FDMS application for F-16 wing deflection measurement. (a) Target and receiver locations; (b) wingtip deflections for a 9-G maneuver.

Aerospace Corporation to improve and expand the capability of the system. Development of second- and third-generation systems continued for about 10 years. Since the HiMAT RPRV program, the X-29A Forward Swept Wing and AFTI/F-111 Mission Adaptive Wing programs have used the FDMS.

In 1990 General Dynamics committed to use the electro-optical FDMS for an F-16 flight-test program. General Dynamics procured a complete system from Grumman Aerospace Corporation and installed it on the F-16 airplane with assistance from NASA engineers. NASA also provided a NASA-designed target calibration fixture and NASA-developed software for data acquisition and analysis. The F-16 airplane has undergone extensive flight testing during 1992, completing more than 100 flights without a single system failure. The second figure shows how two receivers were used to measure 16 targets installed on the F-16 wing panel. The figure also shows deflection data obtained from a 9-G wind-up-turn maneuver performed during a system-checkout flight.

Ames-Dryden contact: V. DeAngelis
(805) 258-3921
Headquarters program office: OAST

Engine Exhaust Characteristics in Support of Acoustic Testing

Kimberly Ennix, L. Dean Webb

Environmental issues are a continuing concern for designers of new transport aircraft. To meet the strict noise requirements of Federal Aviation Regulation, part 36, stage III, Community Noise Standards, designers need to improve their understanding of engine noise levels and sources. To understand the acoustical characteristics of engines of future transport airplanes, designers must study the aircraft noise sources and update the noise-prediction codes. The aeronautics industry often uses the Aircraft Noise Prediction Program (ANOPP) for noise prediction. This computer program has a wide range of noise-prediction modules that can be upgraded to assess advanced engine and aerodynamic concepts for reducing noise. However, ANOPP is semiempirical and does not include a large amount of flight data generated with engines operating at high nozzle pressure ratios (NPRs) or at speeds above Mach 0.3.

To obtain a high-quality noise data base, the Dryden Flight Research Facility (DFRF) and Langley Research Center (LaRC) conducted a joint study of the subsonic climb noise acoustics using aircraft with engines operating at high NPRs and flight speeds above Mach 0.3. The flight tests were conducted using an F-18 (with the F404-GE-400 engine) and an F-16 XL (with the F110-GE-129 engine) aircraft because their engines can simulate exhaust characteristics of future transports.

The flight study consisted of a series of flights over microphone arrays. The flight tests were flown over Rogers Lake (dry) adjacent to DFRF. At an elevation of 2300 feet, this dry lakebed provides a flat, interference-free area for acoustic testing. LaRC personnel set up analog and digital microphone arrays on the lakebed. The first figure shows the array placement on the lakebed. This consisted of 28 microphones placed along the "fly-by" line. Using the ground track and distance displayed in the control room, the pilots were guided over the acoustic array. There were 120 recorded flyovers.

To establish baseline acoustic levels under static conditions, additional tests were conducted on both aircraft on the thrust stand pad at the Air Force Flight Test Center in Edwards, California. The throttle setting

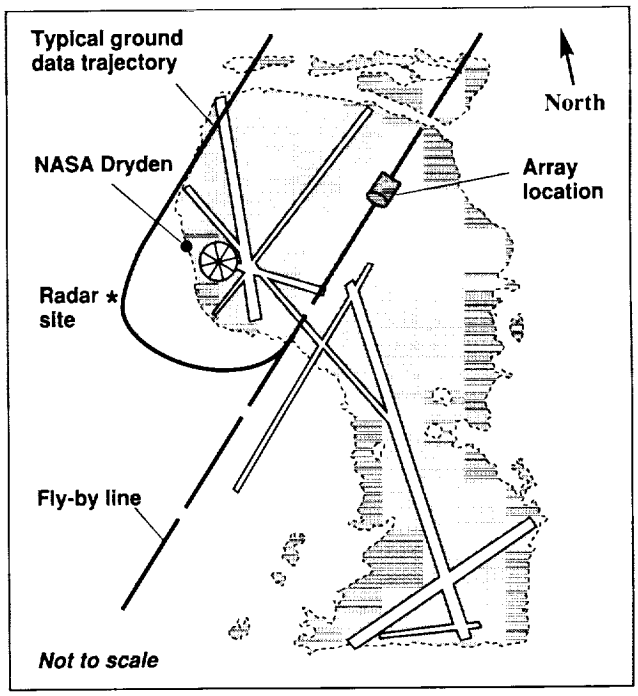

Fig. 1. Ground-tracking and array layout at Rogers Lake (dry), Edwards, California.

was varied between idle and intermediate power. Microphones were placed in an arc at a predetermined distance from the tailpipe of these aircraft.

The flight tests were conducted in two segments: subsonic climb and ANOPP validation. The flight matrix for the climb segment consisted of level flyovers at various Mach numbers to simulate points along an optimum climb profile. Altitudes varied from 3,800 to 32,500 feet with speeds from Mach 0.3 to Mach 0.95. To maximize NPR, a power setting of intermediate (maximum nonafterburning) was used. The ANOPP evaluation segment was flown at a constant altitude of 3,800 feet (1,500 feet above the ground) with speeds from Mach 0.3 to Mach 0.95. Power settings varied according to what was required to maintain steady flight at any given speed.

Dryden operated two engine-performance codes and was responsible for reducing the engine data to

provide the jet characteristic values that LaRC combined with the acoustics measurements. The codes were the F404-GE-400 in-flight thrust performance code and the F110-GE-129 steady-state code. Data obtained from the engine during the flight and ground tests included compressor speed and discharge pressure, fan speed, fuel flow, inlet and gas temperatures, and turbine discharge pressure. Measured engine data obtained from the flight tests do not directly give the values of nozzle-exit Mach and velocity (M_9 and V_9) and fully expanded exit Mach and velocity (M_{jet} and V_{jet}) needed for ANOPP. The measured engine data were input into the engine performance codes, which were modified to calculate the desired values for M_9, V_9, M_{jet}, and V_{jet}.

The second figure shows a comparison of V_9 and V_{jet} for the ground tests for both aircraft for varying throttle settings. The V_9 varied from 1,400 to 2,000 feet per second for the F-16 XL and from 1,800 to 2,800 feet per second for the F-18. By determining V_{jet} and V_9, LaRC can update the ANOPP prediction code. With real quantitative flight data available, the updates will result in higher-fidelity predictive codes for use on future aircraft-design studies.

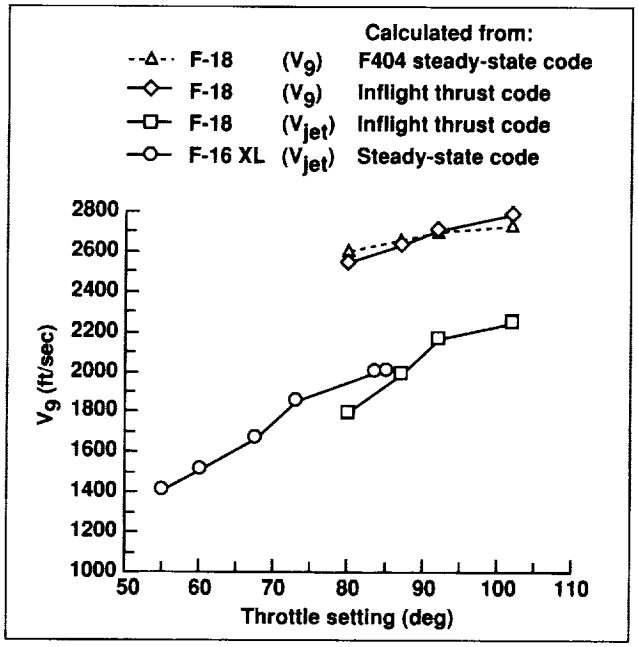

Fig. 2. Acoustic jet velocity characteristics of F-16 XL ship #2 and F-18 from static ground test.

Ames-Dryden contact: K. Ennix
(805) 258-2479
Headquarters program office: OAST

F-18 Forebody Boundary-Layer Transition-Strip Study

David F. Fisher

Recent flight tests at high angles of attack on the F-18 High Angle of Attack Research Vehicle (HARV) have shown that the state of the boundary layer on the forebody can have a large effect on the forebody pressure distributions, boundary-layer separation characteristics, and aircraft yawing moments. Extensive pressure distribution data have been obtained on the F-18 HARV with and without 1/8-inch-wide longitudinal boundary-layer transition strips using #36 Carborundum grit. Both symmetric and asymmetric transition strips were tested. The symmetric transition strips extended longitudinally from the radome apex to the leading edge of the leading-edge extensions at a circumferential angle of 80 degrees from the bottom centerline. The asymmetric transition strip was limited to the radome only and was located on the left side at a circumferential angle of ±65 degrees from the bottom centerline.

Previous surface-flow-visualization flight tests on the F-18 HARV showed significant laminar flow on the forebody at angle of attack (α) ≈ 47 degrees. It is thought that if there were different states of the boundary layer (laminar vs. turbulent) on opposite sides of the forebody, significant yawing moments could result because of different separation characteristics. The surface flow visualization did not detect significant differences in the boundary-layer transition at $\alpha \approx 47$ degrees, and no yawing moment at this angle of attack was noted. However at $\alpha \geq 60$ degrees, asymmetries were noted in the forebody pressure distributions and the aircraft did develop a significant nose yawing moment. Circumferential pressure distributions for $\alpha \approx 70$ degrees at fuselage station 142 with and without the longitudinal transition strips are shown in the first figure. The locations of the orifices are shown in the figure inset. Significant differences in the pressure levels between the right and left sides can be seen in the pressure distribution for the clean configuration; these differences result in large side forces. For example, note the difference in pressure level from $\theta = 60$ to $\theta = 120$ degrees compared to that from $\theta = 120$ to $\theta = 240$ degrees. The asymmetries were significantly reduced with the use of the symmetric longitudinal transition strips. Forebody pressures for angles of attack from 15 to 70 degrees were integrated and forebody yawing moments were determined. The forebody yawing moments for the symmetric and asymmetric longitudinal transition strips as well as for the clean configuration are shown in the second figure. The symmetric transition strips

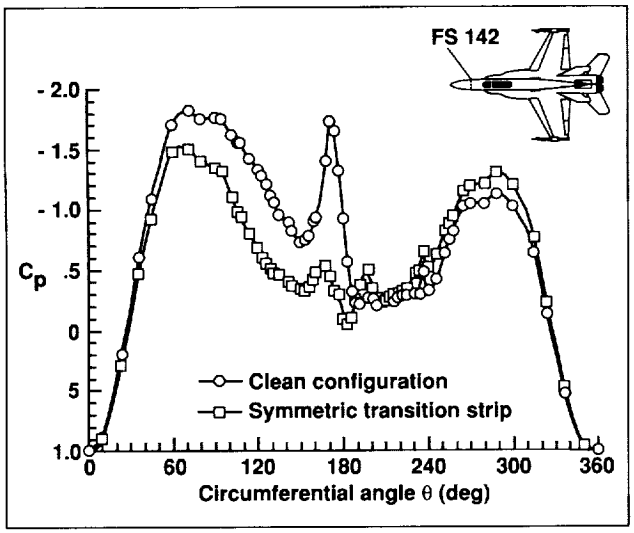

Fig. 1. Forebody pressure distributions at fuselage station 142 with and without longitudinal transition strips, α = 70 degrees.

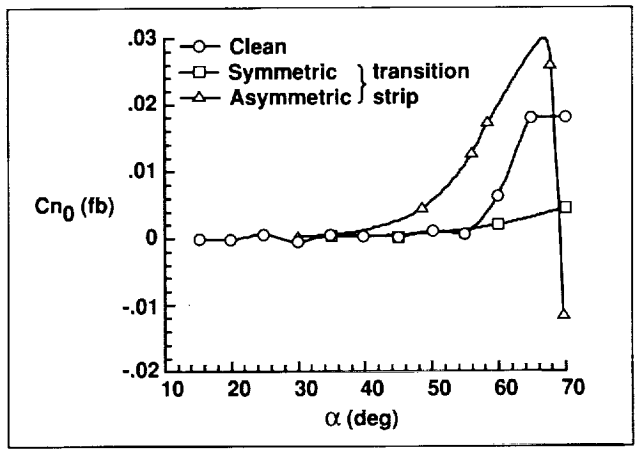

Fig. 2. F-18 HARV forebody yawing moments (Cn_0(fb)) with and without longitudinal transition strips.

reduced the natural yaw asymmetry of the clean configuration by more than 70%. The asymmetric transition strip appeared to cause the natural asymmetries to occur at a lower angle of attack; these asymmetries were larger than those for the clean configuration. At the highest angle of attack with the asymmetric transition strip, the yawing moment abruptly changed direction.

Ames-Dryden contact: D. Fisher
(805) 258-3705
Headquarters program office: OAST

Development of a Modal State Monitor

Lawrence C. Freudinger

Improved techniques for observing the vibration characteristics of aircraft are being developed at the Ames-Dryden Flight Research Facility in collaboration with the Structural Dynamics Research Laboratory at the University of Cincinnati. A tool called the Modal State Monitor will be used to implement on-line estimation schemes and to significantly automate ground and flight testing of research aircraft. This tool will replace the less efficient off-line test techniques now in use.

Ground-based and in-flight vibration tests (experimental modal analysis) are required with new or modified aircraft to ensure that the aircraft is safe to fly. These tests measure the effects of aerodynamic forces and control-system forces on the airframe's vibrational characteristics. Failure to understand these phenomena can result in catastrophic loss of the aircraft. As aerospace vehicles get more complex, so do the tests required to evaluate these systems.

The Modal State Monitor is a research tool for developing new testing methodologies that will enable the test engineer to understand the meaning of his measurements much faster. This tool will reduce the time and cost of testing and increase confidence in the decisions that are based on these measurements.

The Modal State Monitor allows the user to move all data analysis and data post-processing into the measurement cycle. Multiple processors allow distributed processing at variable update rates. Prototyping new applications is accomplished using a high-level programming language for linear algebra.

One of the monitor's unique features is its ability to specify general coordinate transformations for the raw data before any other processing. This is a powerful feature that will be used to map sensor arrays to fewer and more useful channels of information. Vibration parameter estimates are passed to the post-processing computer, which at this time is limited to on-line plotting of the results.

Near-term goals of the research necessarily involve development of advanced parameter-estimation algorithms and post-processing techniques. Ultimately, these functions will be performed on board the aircraft, thus providing the basis for the design of very intelligent airborne systems for health monitoring and vibration control.

Ames-Dryden contact: L. Freudinger
(805) 258-3542
Headquarters program office: OAST

Performance-Seeking Control Flight Results

John Orme

Performance-Seeking Control (PSC) is a model-based, adaptive algorithm that performs real-time optimization of the propulsion system during quasi-steady-state operation. Optimal trims determined by PSC are sent to the engine and inlet. The algorithm identifies off-nominal engine performance with a Kalman filter to adjust a propulsion-system model to more accurately reflect the flight article. The PSC optimization logic employs a linear programming technique to optimize an integrated system model. The PSC system includes three optimization modes: (1) minimum fuel at constant thrust, (2) maximum thrust, and (3) minimum turbine-inlet temperature at constant thrust. During subsonic flight, PSC optimizes the engine only; at supersonic conditions, PSC additionally optimizes the inlets and stabilator.

Subsonically, PSC has been demonstrated to produce the desired results for all three modes: up to 15% increases in thrust, temperature reductions exceeding 100°R, and up to 2% savings in specific fuel consumption. Supersonically, the PSC can be expected to attain performance improvements equal to or greater than those achieved subsonically, especially in the minimum-fuel mode. Initial flight tests have shown thrust increases of 9%, fuel savings of 8%, and reduction in turbine temperatures of as much as 85°F.

Time histories are shown in the first figure for an acceleration with the maximum thrust mode from Mach 0.5 to Mach 0.95. At this subsonic condition, there was an approximate 10% increase in thrust and 10% decrease in acceleration time. Thrust was increased primarily by using excess fan stall margin and by operating at higher turbine temperatures. Similar thrust increases have been obtained supersonically. One implication of such thrust increases is clear: fighters will gain an advantage in acceleration performance.

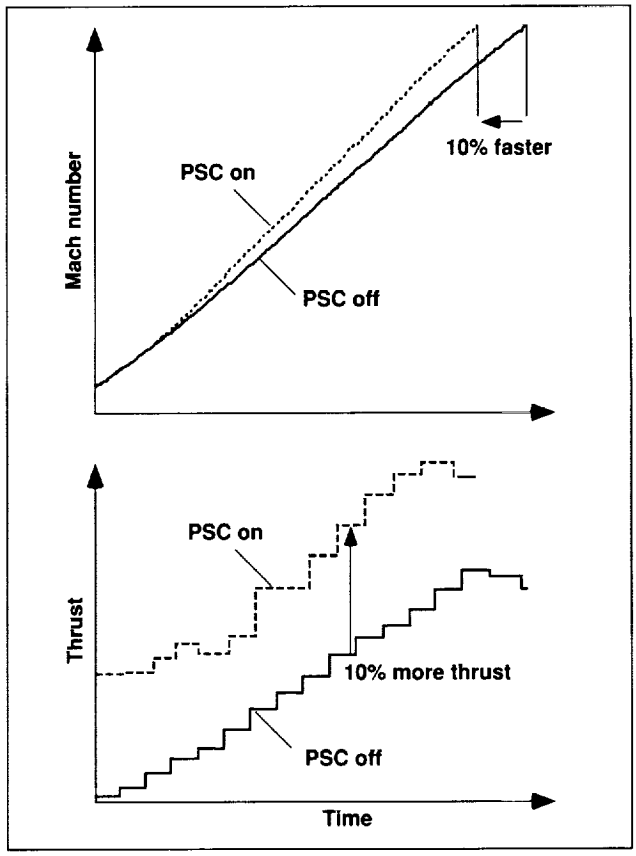

Fig. 1. PSC maximum-thrust mode.

In addition to the increased aircraft performance available from PSC, as in the maximum-thrust mode, the two other PSC modes provide improved engine efficiency. The minimum-fuel and minimum-turbine-inlet-temperature modes seek to improve efficiency by controlling the inlets and engine to reduce drag and lessen the amount of required thrust. Minimum-turbine-inlet-temperature-mode time histories are

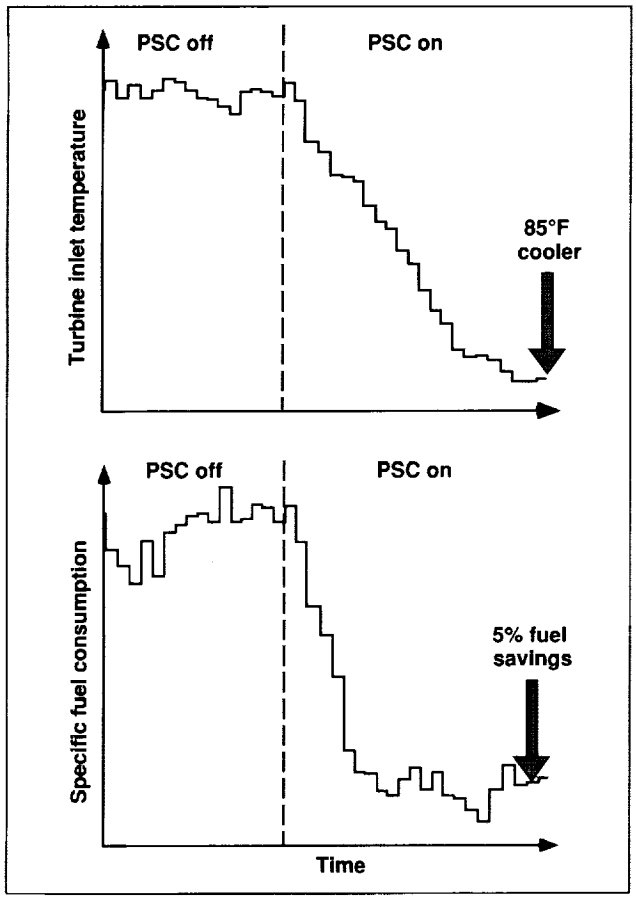

Fig. 2. PSC minimum-temperature mode.

shown in the second figure for a cruise test at Mach 1.8 at 45,000 feet. In addition to the substantial reductions in turbine-inlet temperature of approximately 85°F, a 5% savings in specific fuel consumption was observed. Improved operating efficiency was achieved through reductions of total aircraft drag; drag contributions of the inlet, engine, and stabilator were all reduced. Engine life could be significantly increased with temperature reductions of this magnitude. The increased fuel efficiency could mean extended range or reduced takeoff gross weight.

The application of optimal real-time control technology, such as PSC, to the integrated engine/airframe system promises to produce a wealth of benefits. Development and implementation of this dual-use technology will serve both military and commercial interests by maximizing fuel efficiency, maximizing thrust, and extending engine life.

Ames-Dryden contact: J. Orme
(805) 258-3683
Headquarters program office: OAST

Real-Time Thrust Method for High Angle of Attack Engine Performance Evaluations

Ronald J. Ray, Andrew Yuhas

A real-time thrust method (RTTM) was implemented on the F-18 High Angle of Attack Research Vehicle (HARV) to evaluate engine thrust loss due to extreme aircraft maneuvering. The method was chosen because of its unique ability to inherently account for inlet distortion without the need of sophisticated inlet-pressure instrumentation. Because the F-18 HARV utilizes a thrust-vectoring system (TVS), the RTTM is useful in evaluating TVS performance, supports parameter-identification derivative determination, and is used to assess the thrust estimator used in the TVS control software. Preliminary results show a bias of up to 9% in the thrust estimator when RTTM values for both engines are compared.

The RTTM has been previously evaluated by NASA on the F100 and J85 engines and found to have the real-time advantages of minimal instrumentation and computational requirements. The method was originally developed for and applied to the F404-GE-400 engine on the X-29A using ground-test data obtained during extensive test-cell calibration of the engine for thrust. The X-29A used the algorithm successfully for a real-time evaluation of aircraft performance.

The gross-thrust algorithm calculates thrust based on a one-dimensional isentropic flow analysis in the engine afterburner section and exhaust nozzle. The algorithm requires gas-pressure measurements from three afterburner locations, as well as free-stream static pressure. The afterburner pressures include the turbine-exhaust total pressure and the afterburner entrance and exit static pressures. Calibration coefficients were determined during thrust calibration of the X-29A's flight-test engine at Lewis Research Center. A ±1.8% thrust accuracy was achieved. The algorithm was modified for application to the F-18 HARV to account for the removal of the divergent nozzle section. Because the RTTM determines mass flow in the engine afterburner section, where the gas flow is well mixed, inlet flow distortion effects are minimized.

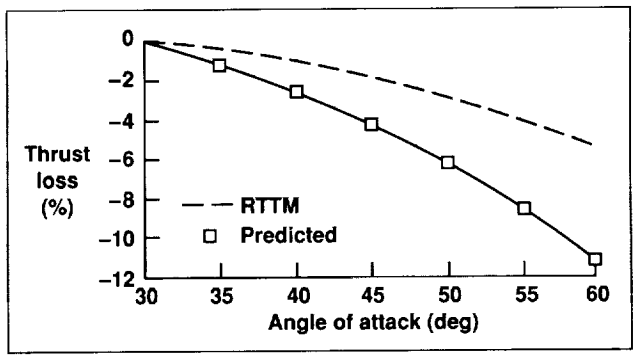

Fig. 1. F-18 HARV thrust loss with increasing angle of attack.

An evaluation of F-18 HARV maneuvers indicate a significant amount of thrust is lost at high angles of attack. For example, the RTTM data at maximum power, 20,000 feet, shows an 11% reduction in gross thrust for maneuvering from a 30-degree to a 60-degree angle of attack. For this same condition, the engine performance prediction model estimates only a 5% reduction. This is a significant discrepancy since the prediction code is used in aircraft simulators and design applications. Similar results were found at military power settings. Results from this study will be useful in improving engine model performance, simulations, and the thrust-vectoring design data base.

Ames-Dryden contact: R. Ray
(805) 258-4687
Headquarters program office: OAST

An Improved Task for Flying-Qualities Assessment of Aircraft

Mary F. Shafer

To accurately assess the flying qualities of an aircraft requires a high-gain, precise, repeatable, and well defined task. This task must be performed consistently by all pilots involved in the test program and must have clearly defined levels of satisfactory and acceptable performance. The task must be safely performable. It is also desirable for the task to be realistic, resembling one that might be encountered in operational flying.

To provide such a task, a ground-deployed system was developed and tested at the Ames-Dryden Flight Research Facility. This system, the Adaptable Target Lighting Array System (ATLAS), is based on the German Ground Attack Test Equipment (GRATE). These systems provide a flying-qualities task, emulating the ground-attack task with ground-deployed, lighted targets. These targets light in an unpredictable sequence, and the pilot has to aim the aircraft at whichever target is lighted. The nine targets are usually arranged in a loose diamond with one target in the center. The diamond array is about 300 meters by 100 meters. The targets can be arranged in a variety of patterns, providing flexibility to assess specific axes or to vary airspeed.

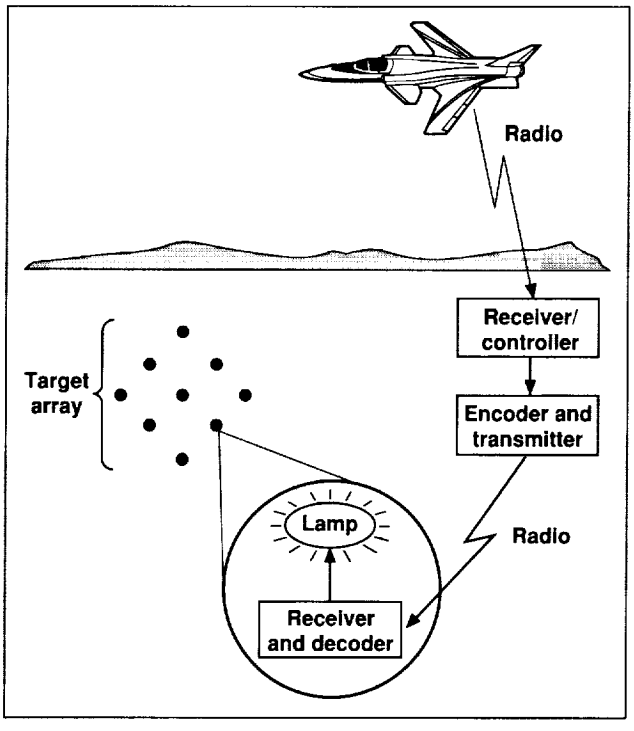

Fig. 1. ATLAS system.

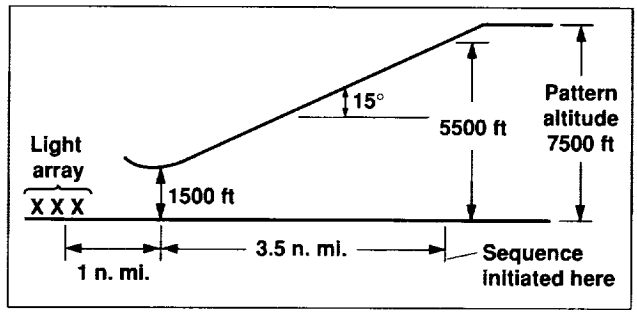

Fig. 2. ATLAS task profile.

A block diagram of ATLAS is shown in the first figure. ATLAS is a stand-alone, ground-based system that consists of a receiver/controller; an encoder and transmitter; and nine targets, each consisting of a receiver, a decoder, and a target lamp. The task is initiated when the pilot turns the system on using the aircraft radio. All of the target lamps light simultaneously for five seconds to allow the pilot to acquire the target array and set up the run. The encoder then transmits the identifier of a specific target from the preprogrammed sequence. When the target decoder receives its identifier it turns the target lamp on. The pilot then points the aircraft at the lighted target, using the gunsight or head-up display (HUD) reticle. After a preset time interval, a new target is designated and the pilot again changes aim point. This continues until the preprogrammed sequence ends. At this time all of the target lamps again light simultaneously for two seconds to indicate to the pilot that the task is complete. The task profile is shown in the second figure.

Three flight-test programs were used to assess the suitability of ATLAS. The first program used the U.S. Air Force NT-33A Variable Stability Aircraft to establish that ATLAS provided a task suitable for use in flying-qualities research. An HUD tracking task was used for comparison. The second program used the

X-29A Forward Swept Wing aircraft to demonstrate that the ATLAS task was suitable for assessing the flying qualities of a specific experimental aircraft. In this program, the ground-attack task was used for comparison. In the third evaluation, two flights were flown by U.S. Air Force pilots in F-15 Eagles. Again, the ground-attack task was used for comparison.

Pilots who flew the ATLAS task found it highly satisfactory. The pilot cannot anticipate the sequence, and precognitive behavior does not occur. The test pilots all preferred ATLAS to a variety of other tasks for flying-qualities assessment, saying that the task was safe, well defined, and consistent. They have recommended that it become a standard for flying-qualities evaluations.

Although this task resembles the ground-attack task, it is a more general task and is suitable for use with all aircraft, not just attack aircraft. However, the resemblance to the ground-attack task provides realism and reduces, to a certain extent, the training required by the pilot.

ATLAS is suitable both for assessing the flying qualities of a specific type of aircraft (i.e., specification compliance) and for carrying out general flying-qualities research (i.e., using variable-stability aircraft).

Ames-Dryden contact: M. Shafer
(805) 258-3735
Headquarters program office: OAST

Spacecraft Autoland Project

Alex Sim, James Murray, Dale Reed

Many NASA programs are studying techniques for returning humans and cargo from low Earth orbit. The Assured Crew Return Vehicle will be used to return humans and cargo from Space Station Freedom. The Space Exploration Initiative (SEI) is also looking at techniques to transport crewmembers and experiments to the planetary surface. Elements of SEI include the Lunar Transportation System and the Mars Environmental Survey. The Personal Launch System and Lifesat missions will also return crewmembers and biological experiments from low Earth orbit. Vehicle configurations to accomplish these tasks have not been finalized. For a capsule vehicle, all of the above-named missions could benefit from the use of a deployable precision landing system.

A joint program between Johnson Space Center and the Dryden Flight Research Facility was initiated to develop a deployable precision landing system. The program is of limited scope and is funded through discretionary sources. Phase 1 of the program consists of the operational demonstration of a model spacecraft flown under a ram-air parachute. Autonomous flight will be demonstrated from 10,000 feet to a precision landing into the wind and at a predetermined site. The global positioning system (GPS) will be used for navigation.

As a generic spacecraft capsule, the flattened biconic wedge was chosen for the flight vehicle. It is 4 feet long and weighs 140 pounds. The wedge has capability for both manual radio ground control and autonomous flight. It contains a radio uplink, servos, a flight-control computer, a GPS receiver, and a data recorder. A sonar altimeter is used to sense terminal altitude; higher altitudes are sensed using a conventional pressure transducer. A magnetometer is used in conjunction with the GPS system for better navigation in the presence of wind. The wedge is flown under a personnel-qualified ram-air parachute (see first figure). A custom harness was adapted between the vehicle and the parachute.

Phase-1 accomplishments include manual and autonomous flight from a 4,000-foot altitude. With only light winds, the autonomous control mode has been validated including flight to a point, holding pattern, final turn into the wind, flare, and precision landing (see second figure). The control algorithms for moderate winds are still being developed. Other

ongoing Phase-1 tasks include formal documentation of the results.

In Phase 1, a relatively large parachute was chosen to provide a margin of safety while the landing-flare techniques were being refined. Although the large parachute did prove to be a wise initial choice, it yielded a wing loading near 0.5, whereas a full-scale spacecraft is projected to have a wing loading near 2.0. In Phase 2, the primary task will be to evaluate a smaller parachute that has a wing loading of 2.0, and successful landing demonstrations will be the main objective.

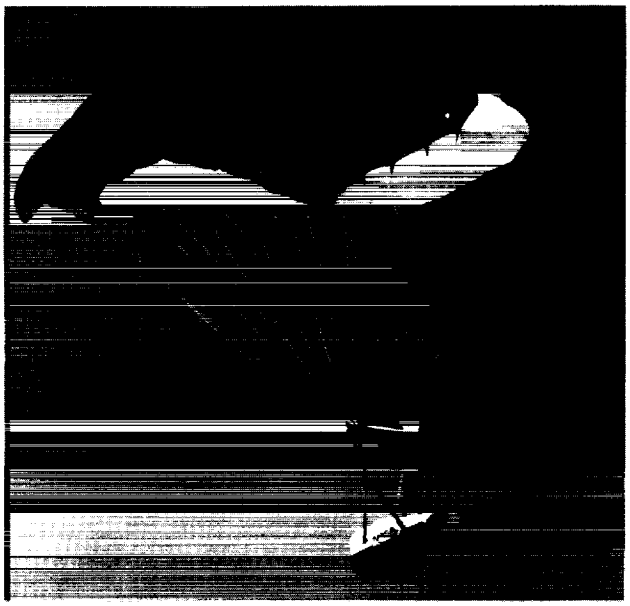

Fig. 1. Spacecraft autoland wedge vehicle.

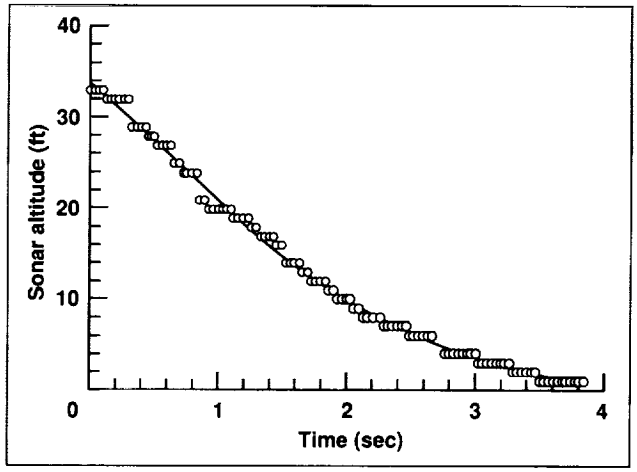

Fig. 2. Wedge landing in the automatic control mode.

The flare retraction of the parachute trailing edge by means of a servo, as in Phase 1, will be difficult to incorporate into a full-sized spacecraft because of weight and power requirements. Servos will still be used for turns, as only small control inputs are required. Another Phase-2 task will be to evaluate alternate landing-flare techniques. These include stored energy devices, gravity flare, and possible leading-edge extensions.

Ames-Dryden contact: A. Sim
(805) 258-3714
Headquarters program office: OAST

Flutter Excitation System Research and Flight-Test Results

Lura E. Vernon

Modern high-performance aircraft use thin, low-drag airfoils designed for maximum aerodynamic efficiency. This has often resulted in more flexible and flutter-prone wings. In addition, the use of high-gain, digital flight-control systems can result in an adverse interaction with the aircraft structural modes and cause aeroservoelastic instabilities. The desired flight envelope for new and modified research aircraft is usually verified to be free of these instabilities through flight flutter testing. Flutter testing consists of three basic tasks: the first is to excite the structure of the airplane by means of an excitation system; the second is to measure the resulting structural response with accelerometers; the third is to analyze the data to determine structural stability at subcritical airspeeds.

Most airborne structural excitation systems are quite expensive and difficult to install. In addition, their high power requirements pose serious aircraft-system integration problems. As a consequence, use of natural turbulence for excitation is often resorted to, often with mixed results. Experience has shown that without proper excitation, an impending instability may not be detected.

An experimental exciter has been designed and built by Dynamic Engineering, Inc. This exciter is an airfoil with a rotating, slotted cylinder attached to the trailing edge. A series of flight tests have been conducted at an altitude of 30,000 feet on the F-16XL airplane. The exciter was tested over a speed range of Mach 0.6–1.7. The flight tests were designed to determine the excitation frequency bandwidth, and the force levels over this speed regime. The resulting data were compared to random atmospheric-turbulence-response data.

The structural-response data obtained with the exciter were significantly better than those obtained with random atmospheric turbulence. The vane and rotating cylinder assembly excited all of the expected modes of the aircraft in a frequency bandwidth of 5–35 hertz at adequate force levels (see part (a) of figure). The atmospheric turbulence excited only the first symmetric wing-bending mode (see part (b) of figure). The importance of this result is that the critical flutter mode for this airplane was not excited by atmospheric turbulence.

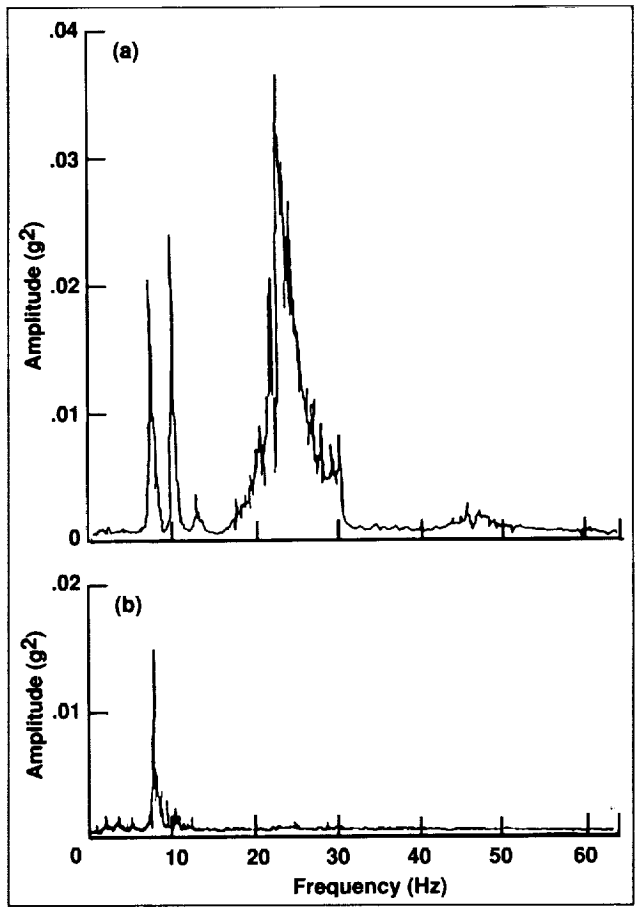

Fig. 1. Comparison of excitation of the left-wing aft accelerometer at Mach 0.9 and 30,000 feet. (a) Exciter sweep; (b) random turbulence.

Overall, the relatively simple installation requirements, precise excitation control, low power requirements, and high output-force levels over a large frequency range are all aspects that qualify this exciter as a viable solution for safer, more effective flight flutter testing.

Ames-Dryden contact: L. Vernon
(805) 258-2337
Headquarters program office: OAST

A Novel Control-Surface Free-Play Measurement Technique and Its Application to the X-31 Aircraft

Leonard S. Voelker

Ordinarily, measurement of aircraft control-surface free play is a straightforward task performed at infrequent intervals by a long-established procedure. The test is usually performed by applying known external loads, incrementally or slowly varying, to the control surface in question and measuring the deflections produced. Free play is determined from the resulting load-deflection plots. For these tests the aircraft's flight-control system, including hydraulic pressure and feedback controls, is activated to hold the hydraulic actuator steady without drift. The fundamental assumption is that all free play stems only from the hinge and linkage bearings. The X-31 high-angle-of-attack flight research program provided a challenging exception to this assumption.

The two X-31 aircraft have 17 control surfaces each, most with dual linear-stroke hydraulic actuators. The aircraft are equipped with high-bandwidth flight controls and are flown for extended periods in a severe buffet environment. This has resulted in a very rapid growth of free play on many of the control surfaces in a short amount of flight time, and in the need for frequent free-play testing. Surprisingly, the source of most of this free-play growth was found to be internal to the hydraulic actuators themselves rather than the bearings. These actuators have two-piece piston-head/piston-rod assemblies. Under the severe dynamic loads encountered, the joint between the head and rod tended to loosen up far more rapidly than anticipated. This looseness thwarted attempts to measure free play by the standard procedure, since loads applied to the control surface resulted in piston rod movement and feedback commands that separately moved the piston head. But without the feedback commands the actuators would drift hard over. An initial solution to this problem was to apply a "hydraulic lock" on each actuator tested. The frequent testing caused extensive, time-consuming maintenance of the hydraulic system and risked eventual contamination of the fluid or damage to the hydraulic fittings.

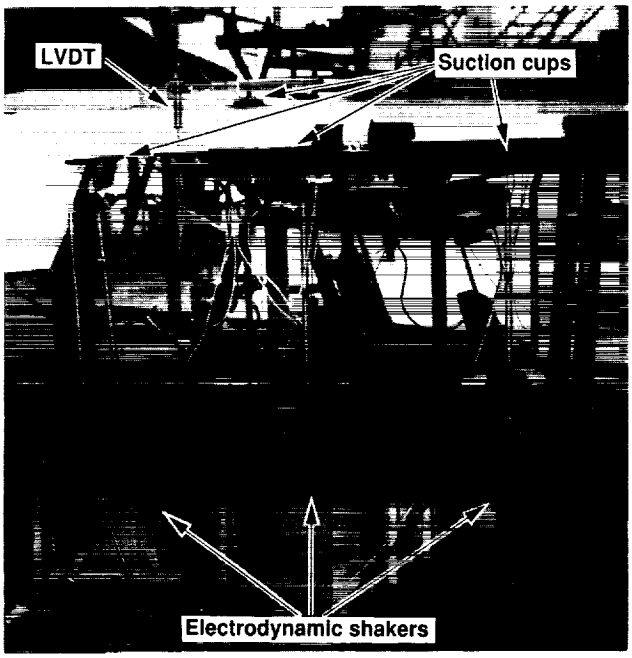

Fig. 1. Typical free-play test setup.

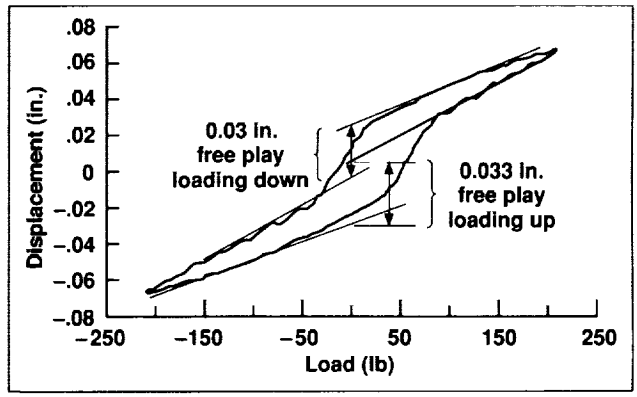

Fig. 2. Typical load-deflection plot.

An alternative testing procedure was developed which did not require the hydraulic locks, was much faster, and provided more accurate data. The basic assumption was that if the loads applied to control surfaces were cycled just fast enough, trapped hydraulic fluid would be able to hold the piston heads sufficiently steady without the need for hydraulic pressurization. Without pressurization, there was no need for feedback control to prevent actuator drift.

Electrodynamic shakers instrumented with force transducers provided measured, oscillating external loads to the control surfaces (see first figure). Linear variable-differential transformers measured the control-surface deflections. A computer was used to control the shakers and automatically acquire the test data necessary for load-deflection plots. Suction cups and a vacuum pump were used to quickly attach the shakers and instrumentation to the aircraft for the many test setups. The method worked well for all control surfaces except the trailing-edge flaps.

The actuators for these surfaces were equipped with small hydraulic bypass orifices to reduce the force fight between the dual actuators. However, these orifices allowed some piston head movement during testing. The solution for these cases was to pressurize the hydraulic system but prevent actuator drift by using a very slow-acting servoamplifier for feedback.

A typical load-deflection plot, shown in the second figure, illustrates how free play was obtained from the data.

Overall, this method provides a quick and accurate means of measuring control-surface free play on even the most complex flight-control systems.

Ames-Dryden contact: L. Voelker
(805) 258-3709
Headquarters program office: OAST

Application of a Flush Airdata Sensing System to a Wing Leading Edge

Stephen A. Whitmore, Timothy R. Moes

Airmass reference data for flight vehicles—traditionally referred to as airdata—always have been critical measurement parameters for the flight-test community. Historically, airdata measurements were performed using intrusive booms that extend away from the aircraft to minimize local flow-field effects. Pitot-static probes were traditionally used to measure airspeed and altitude, and mechanical vanes were used to measure angles of attack and sideslip. Specialized requirements such as stealth, hypersonic flight, and high-angle-of-attack flight have, however, made the use of conventional intrusive airdata-measurement systems highly undesirable.

As a means of circumventing the difficulties encountered with intrusive systems, the flush airdata sensing (FADS) system was developed. In the FADS system, airdata are inferred from nonintrusive surface-pressure measurements. Several FADS demonstration programs have been flight tested in the past. In all cases, the pressures were measured at the nose of the aircraft. Unfortunately, installation of FADS sensors and the associated electronics at the nosetip complicates the design and operation of an aircraft radar, a critical feature of most high-performance aircraft.

This research demonstrated the feasibility of locating a FADS system on the leading edge of a wing. The test was conducted in the Dryden low-speed wind tunnel on an unswept two-dimensional wing with a symmetrical airfoil. The airdata quantities measured included angle of attack, dynamic pressure, and ambient pressure.

The aerodynamic model, which relates the measured pressure data to the desired airdata quantities, was developed from incompressible potential flow around a cylinder and included calibration parameters that were empirically adjusted from tunnel-test results. Nine pressures were located on the leading edge of the airfoil, as shown in the first figure. The pressure at the i^{th} port was estimated by the aerodynamic model to be

$$P_i = \theta_\infty[\cos^2(\theta_i) + e \sin^2(\theta_i)] + p_\infty$$

where θ_∞ is the free-stream dynamic pressure, p_∞ is the free-stream static pressure, θ is the total-flow incidence angle at pressure port i, and e is an empirically determined calibration parameter.

As can be seen, the aerodynamic model is nonlinear and therefore cannot be directly inverted to

give airdata as a function of the measured pressures. Thus an iterative least-squares regression was used to obtain the airdata estimation. The regression was overdetermined since nine pressure measurements were available to obtain the three airdata parameters. The major benefit of the overdetermined system was to minimize the effects of any small errors in the pressure measurements.

The sensor was calibrated as a function of airspeed and angle of attack. The second figure shows the FADS-estimated angle of attack and stagnation pressure plotted against the reference angle of attack and stagnation pressure. The standard deviation

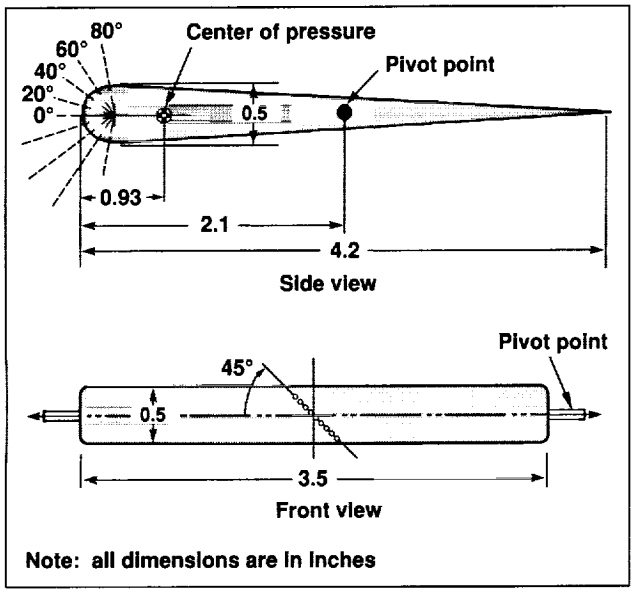

Fig. 1. Schematic of FADS test wing.

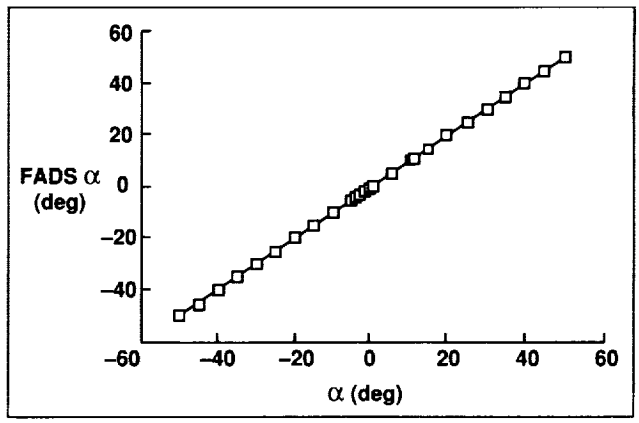

Fig. 2. FADS performance evaluation.

between the FADS-estimated and the reference angle of attack is approximately 0.25 degrees. The standard deviation between the FADS-estimated and the reference stagnation pressure is approximately 0.8 pound per square foot.

Proposed follow-on work includes testing swept wings. With FADS pressure ports on both wings of a swept configuration, it is suspected that angle of sideslip can also be identified. Dynamic wind tunnel tests are also planned to investigate the effects of unsteady aerodynamics on the FADS aerodynamic model.

Ames-Dryden contact: S. Whitmore
(805) 258-2002
Headquarters program office: OAST

Effects of Bleed-Air Extraction on Thrust Levels of the F404-GE-400 Turbofan Engine

Andrew Yuhas, Ronald J. Ray

A ground test was performed to determine the effects of compressor bleed-flow extraction on the performance of the General Electric F404-GE-400 engine, a two-spool, low-bypass axial-flow turbofan with afterburner. The engines were installed in the F/A-18 High Angle of Attack Research Vehicle at the Dryden Flight Research Facility. A specialized bleed ducting system was installed on the aircraft to control and measure engine-bleed airflow while the aircraft was tied down to a thrust-measuring stand. The test was conducted on each engine and at various power settings up to maximum afterburning. The bleed-air extraction levels analyzed included flow rates above the manufacturer's specified maximum.

The measured relationship between thrust and bleed-flow extraction was shown to be essentially linear at all power settings, with an increase in bleed flow causing a corresponding decrease in thrust. The measured thrust loss above the manufacturer's maximum-specification bleed-flow limit showed the same linear relationship as that predicted below the limit. The figure shows a comparison of percent thrust loss for each pound per second of bleed extraction between the measured characteristics and the F404-GE-400 aerothermal engine performance-simulation estimation. The estimation was within 0.5% of measured thrust losses for large increases in bleed-flow rate. At military power, a 1% increase in bleed airflow caused a 2% loss in thrust. The percent

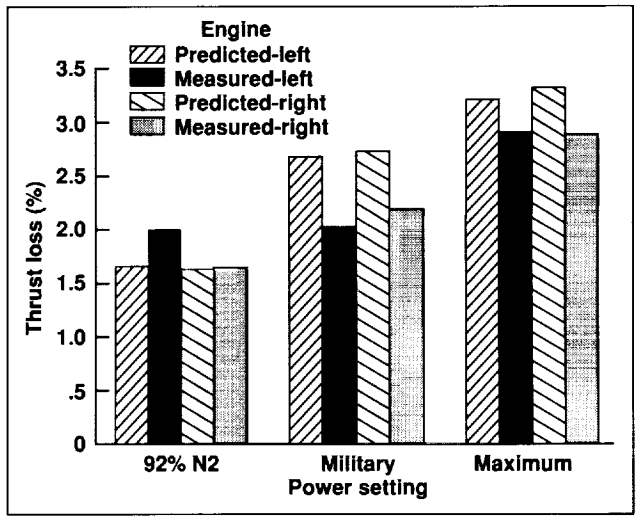

Fig. 1. Percentage thrust loss per lb/sec of bleed extraction.

thrust loss for a given bleed setting increased with higher power settings. The results support the use of the manufacturer's model for predicting in-flight performance loss due to bleed extraction.

Ames-Dryden contact: A. Yuhas
(805) 258-2312
Headquarters program office: OAST

The color plates in this appendix correspond to black and white photographs in the text. Each caption provides the location of the corresponding photograph.

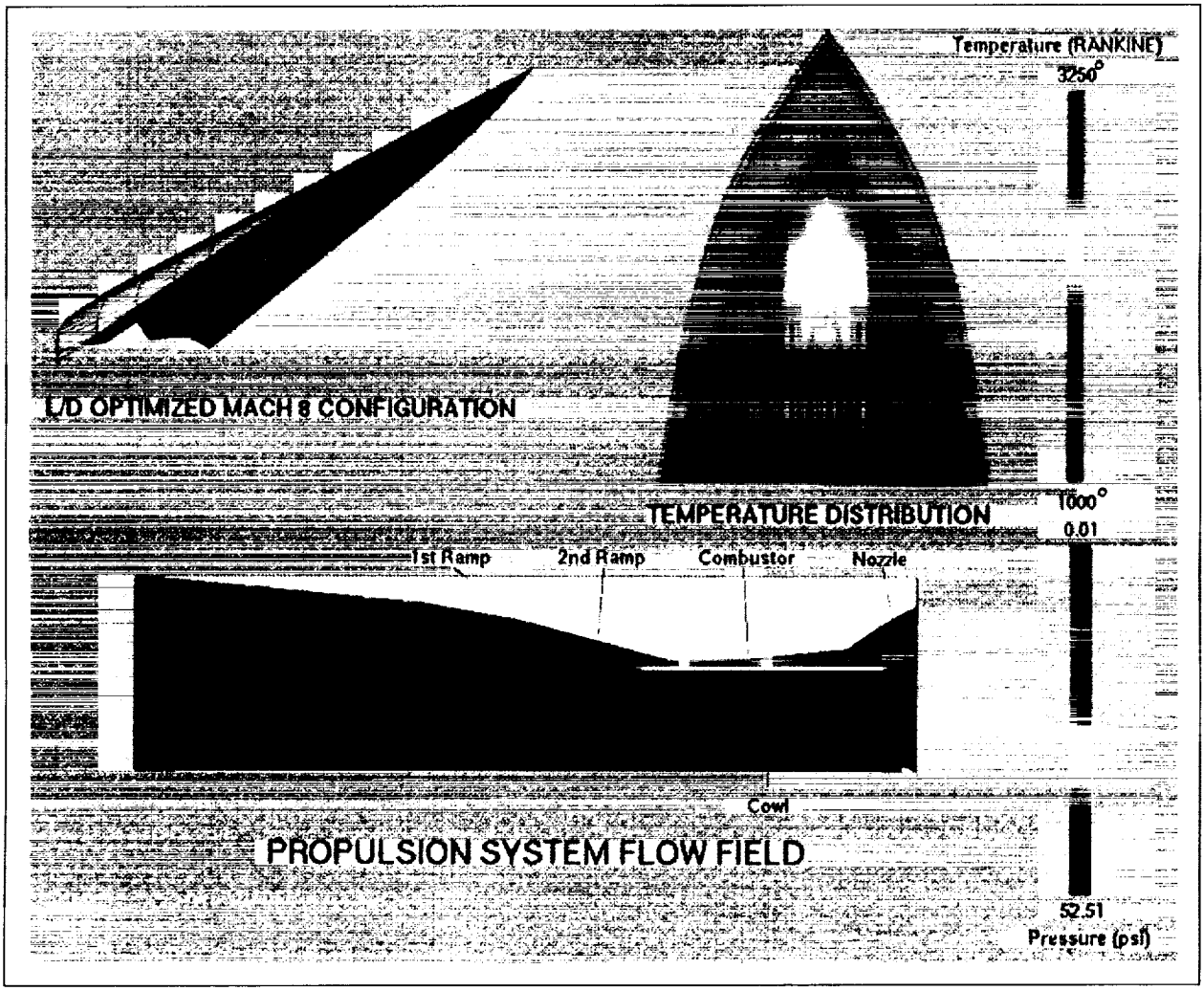

Color plate 1. Optimized Mach 8 waverider configuration, surface temperature distribution, and nose-to-tail flow field. (fig. 1, page 2)

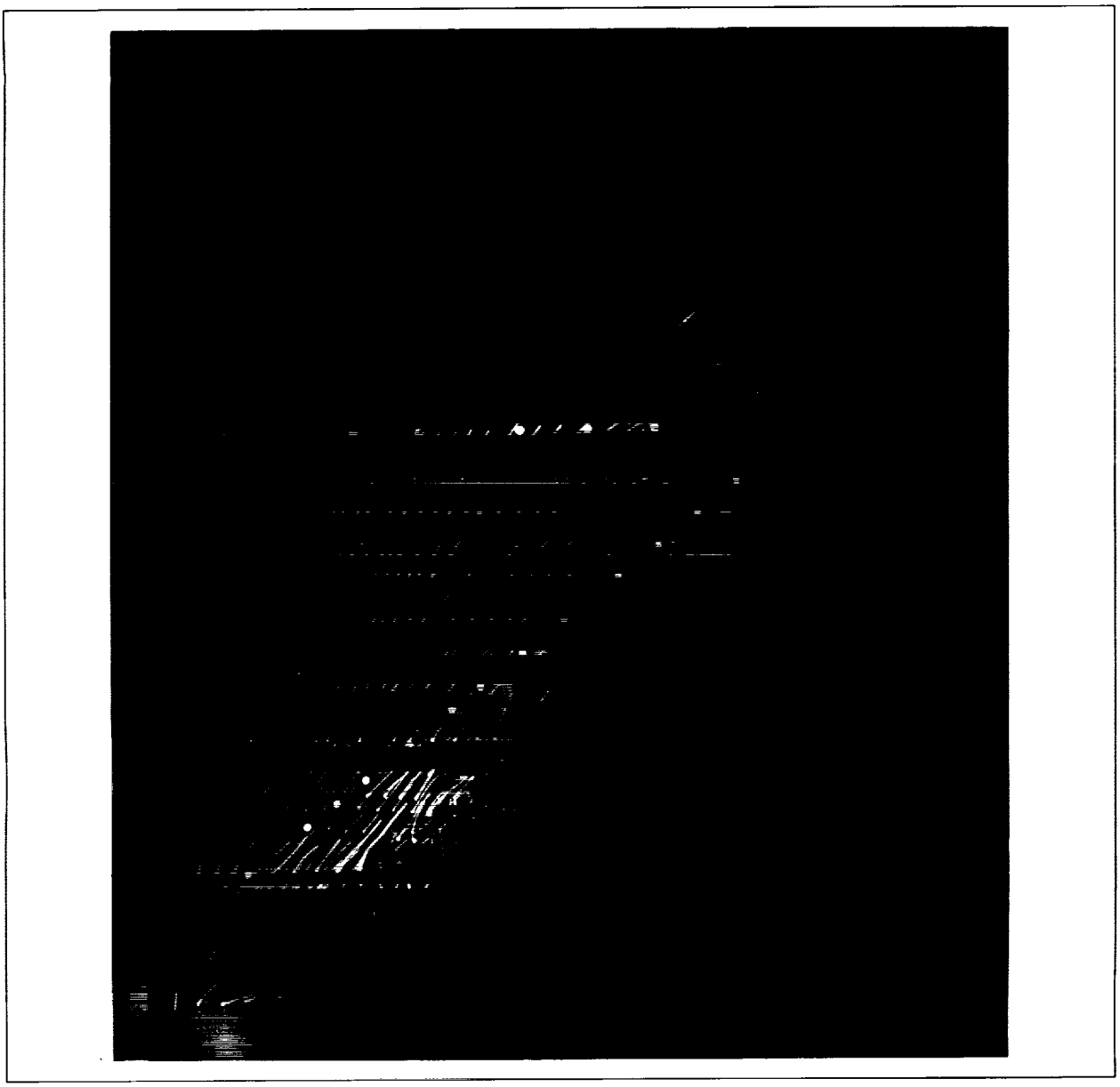

Color plate 2. Oil flow on the semispan wing model. (fig. 2, page 22)

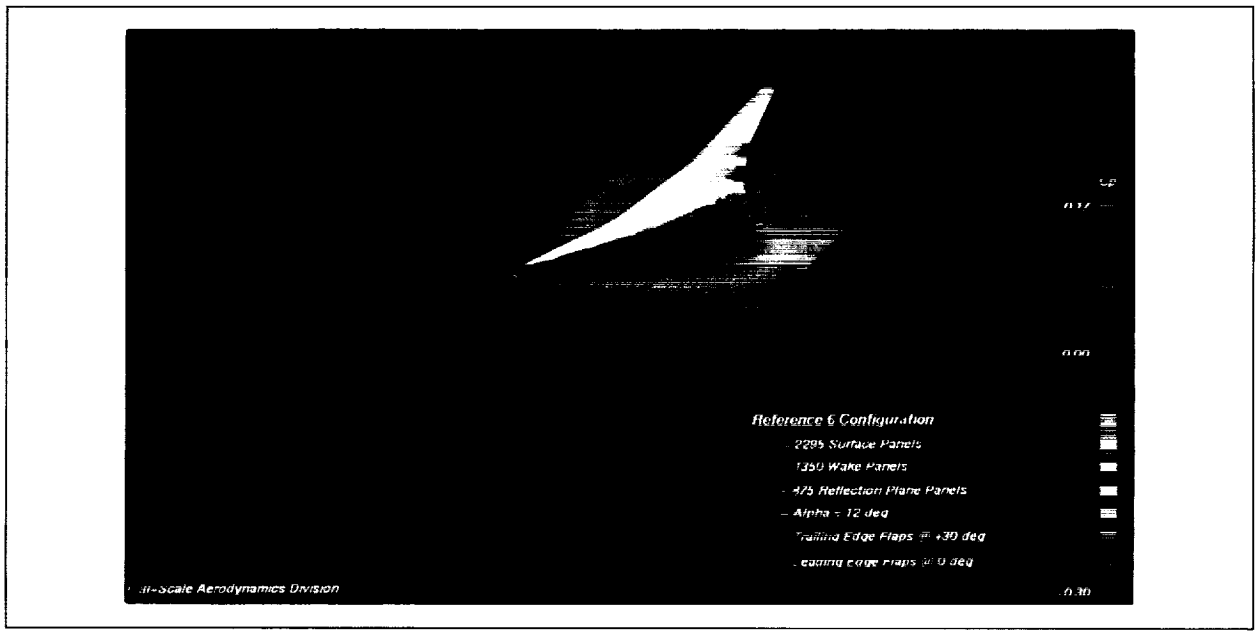

Color plate 3. PMARC code predictions of the static pressures on the HEAT symmetry plane. (fig. 2, page 35)

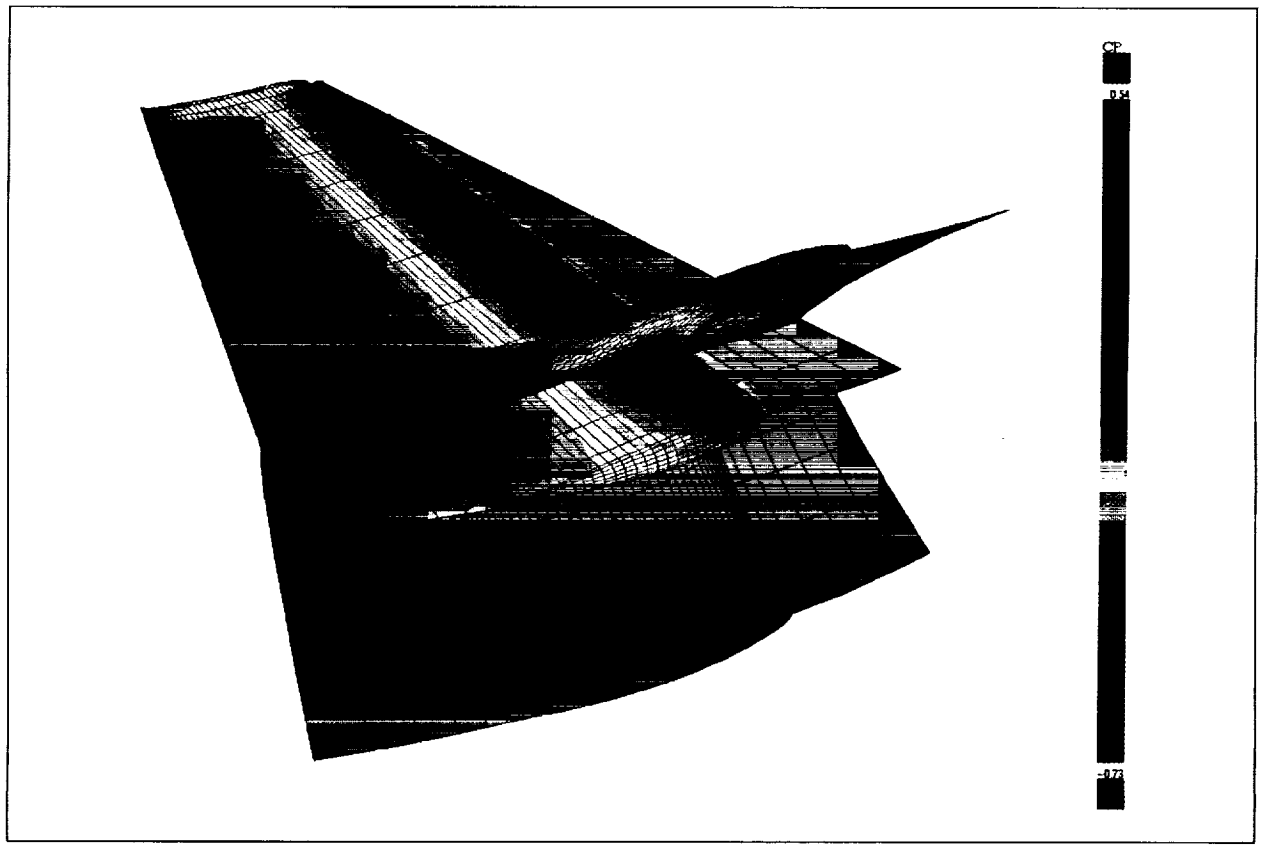

Color plate 4. Computed pressure contours for the flow field of a hovering two-bladed rotor. (fig. 2, page 38)

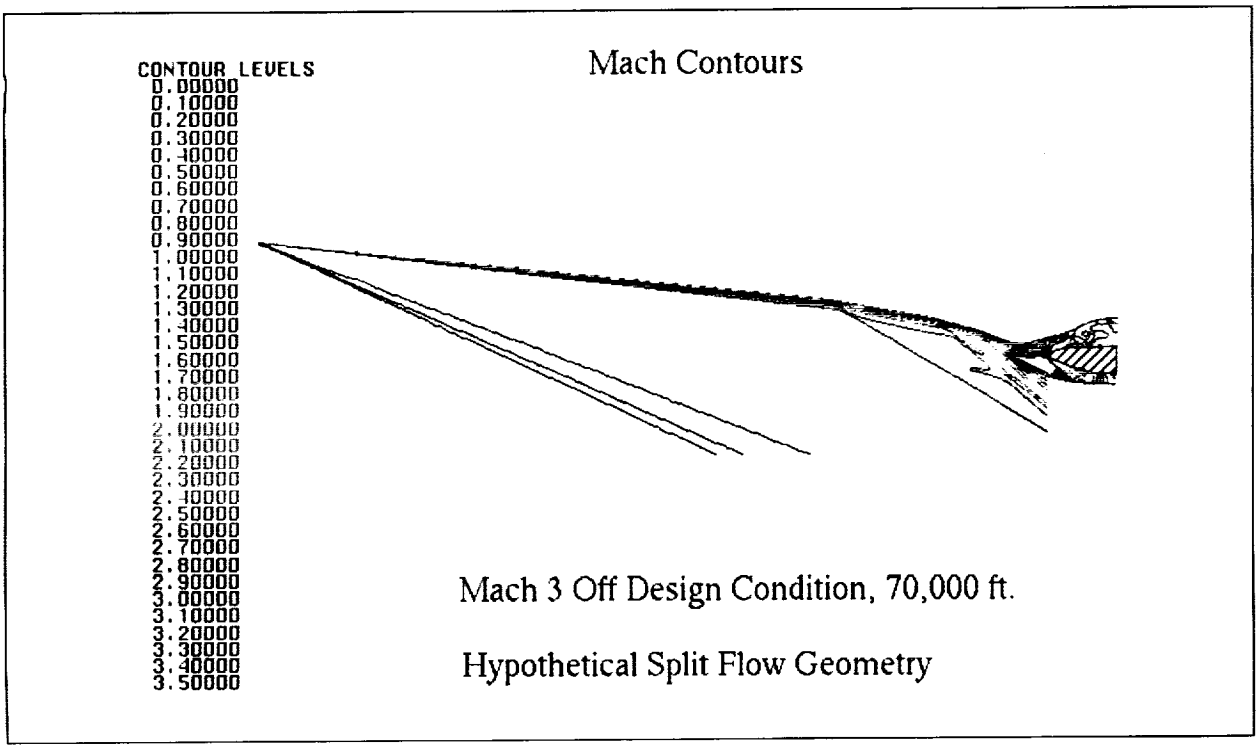

Color plate 5. Mach number contours for the entire forebody/inlet flow field. (fig. 1, page 118)

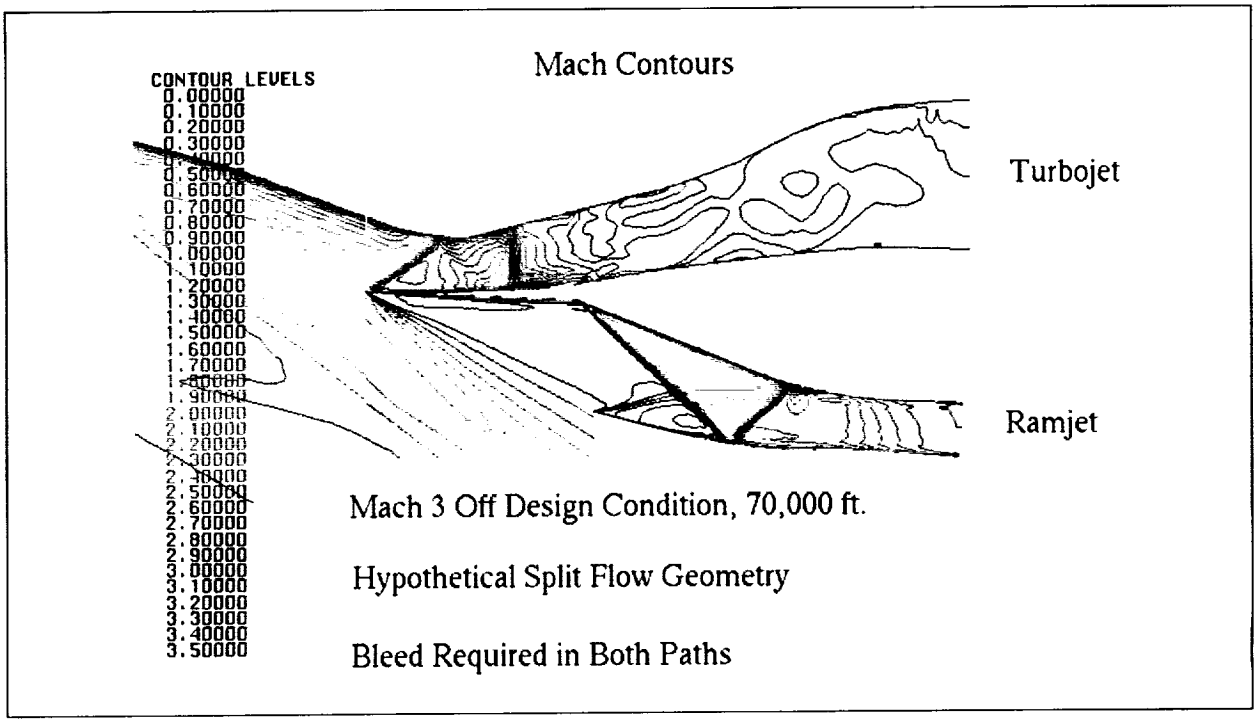

Color plate 6. Detailed Mach number contours in the turbojet and ramjet ducts. (fig. 2, page 119

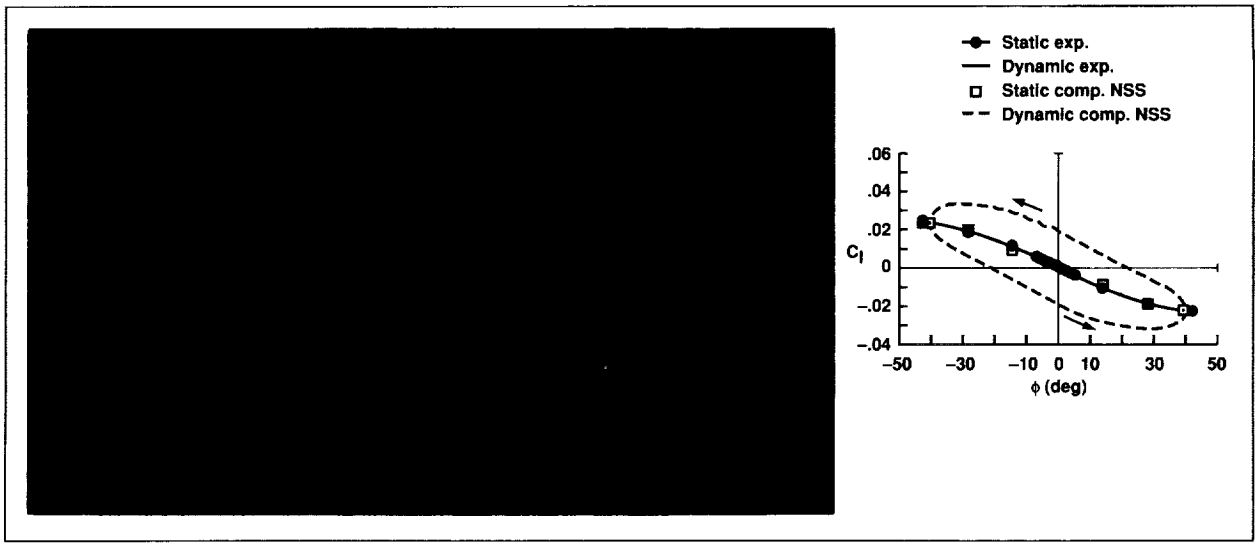

Color plate 7. Visualization of dynamic roll vortices and comparison of static and dynamic rolling moment coefficients. (fig. 2, page 122)

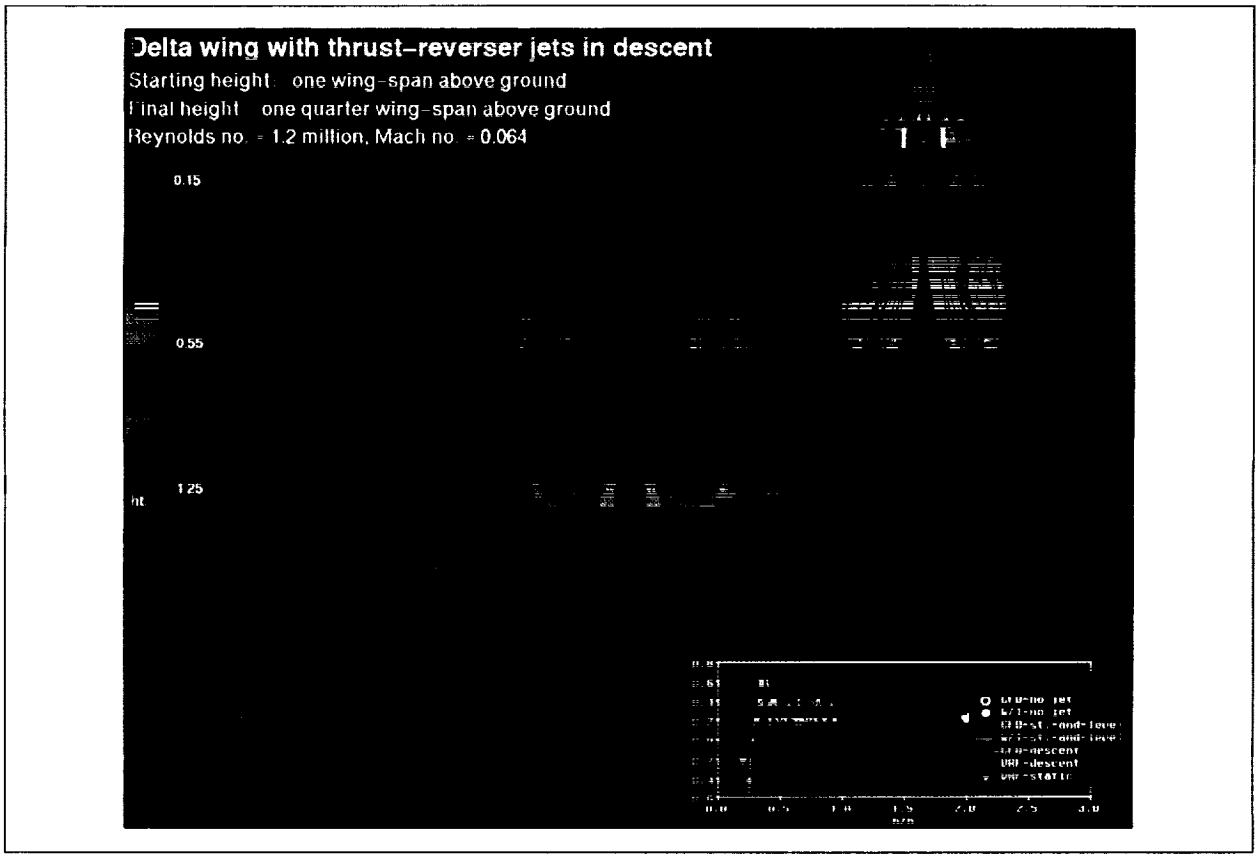

Color plate 8. A delta-wing aircraft descent simulation. (fig. 1, page 125)

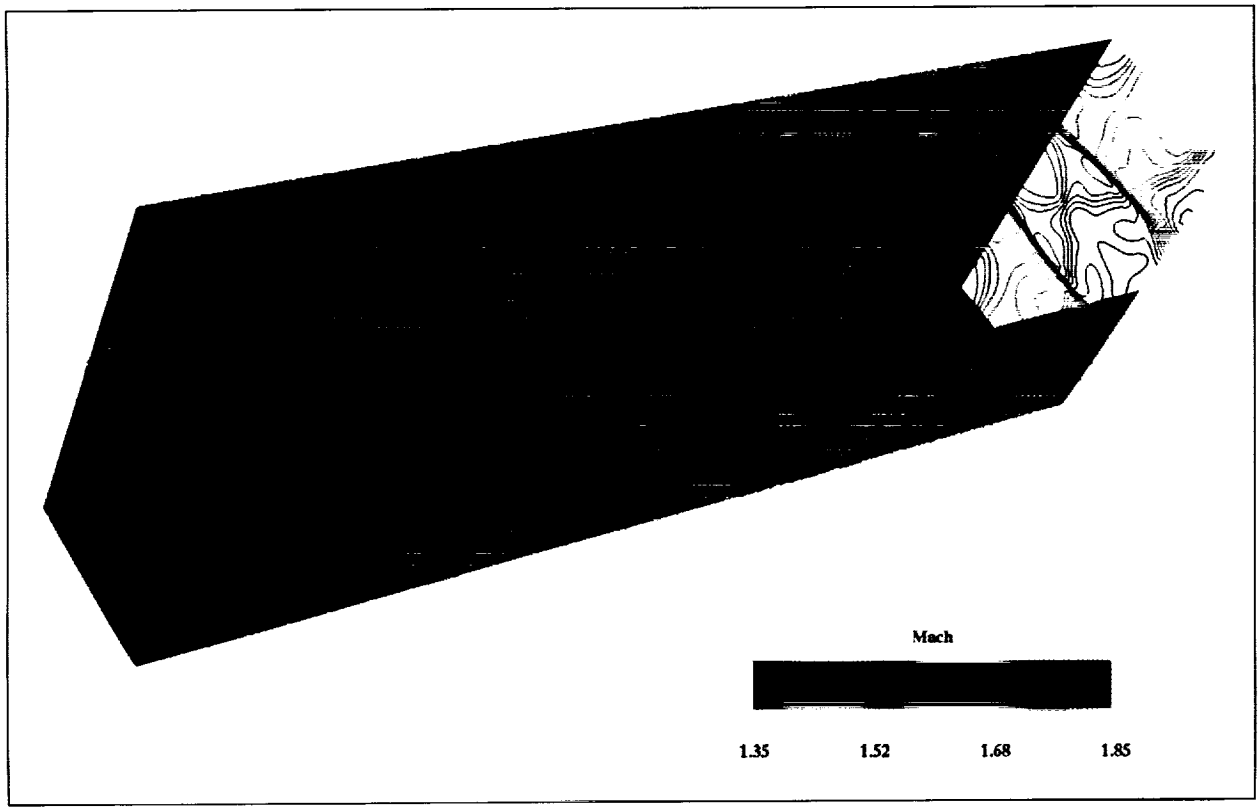

Color plate 9. Computed shock waves on a test model at Mach 1.6 in the Laminar Flow Supersonic Wind Tunnel. (fig. 1, page 132)

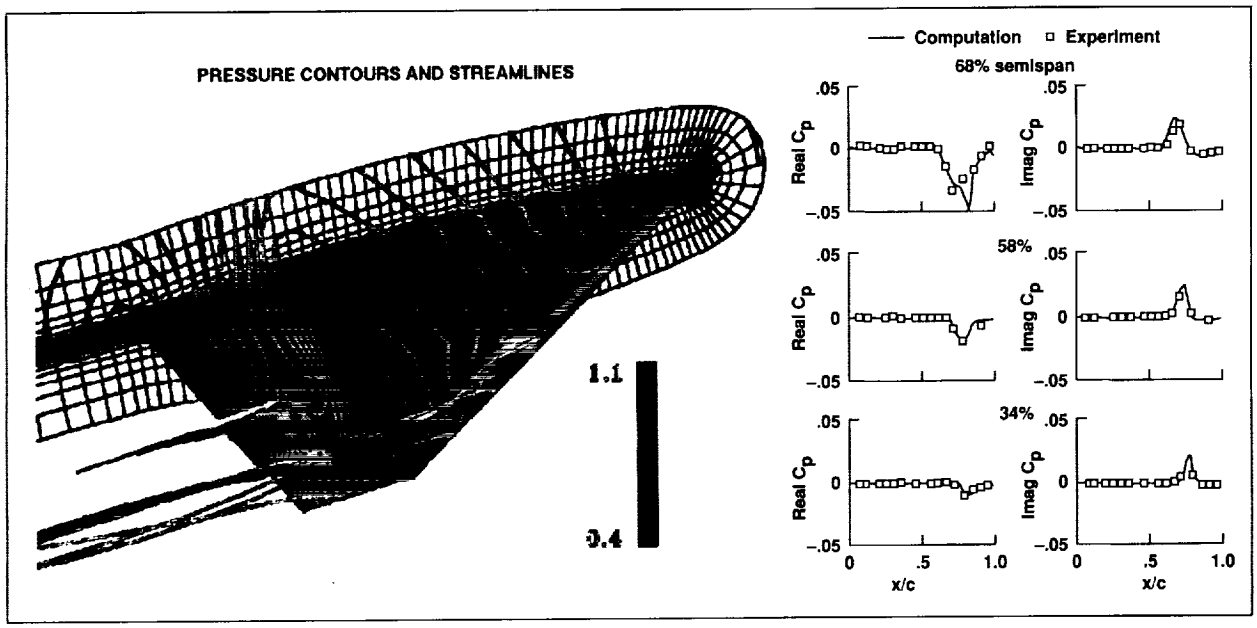

Color plate 10. Navier–Stokes computation on a clipped delta wing with oscillating control surface. Left: Pressure contours and instantaneous streamlines. Right: Comparison of unsteady pressures. (fig. 1, page 136)

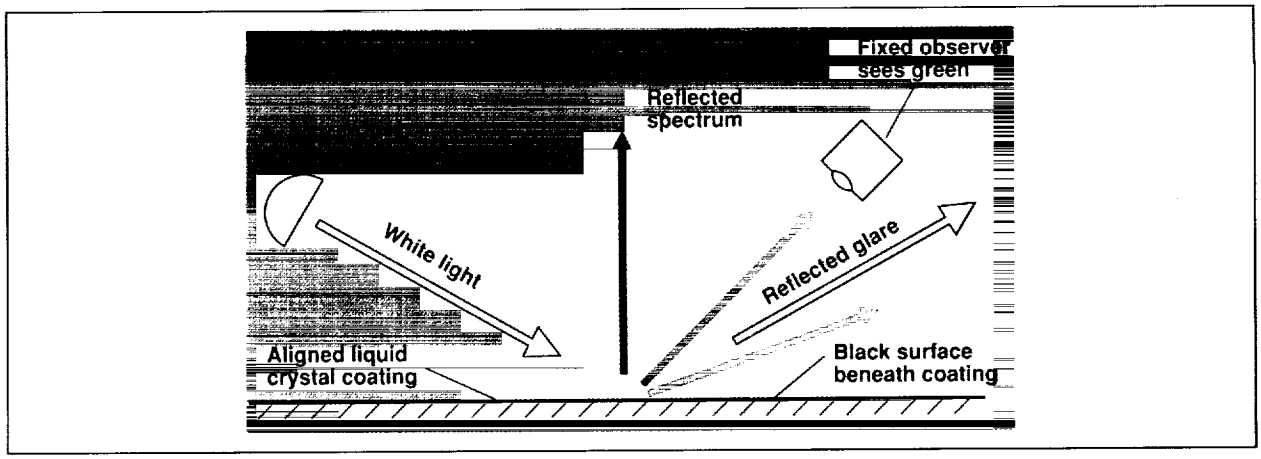

Color plate 11. Liquid-crystal reflected spectrum. (fig. 1, page 137)

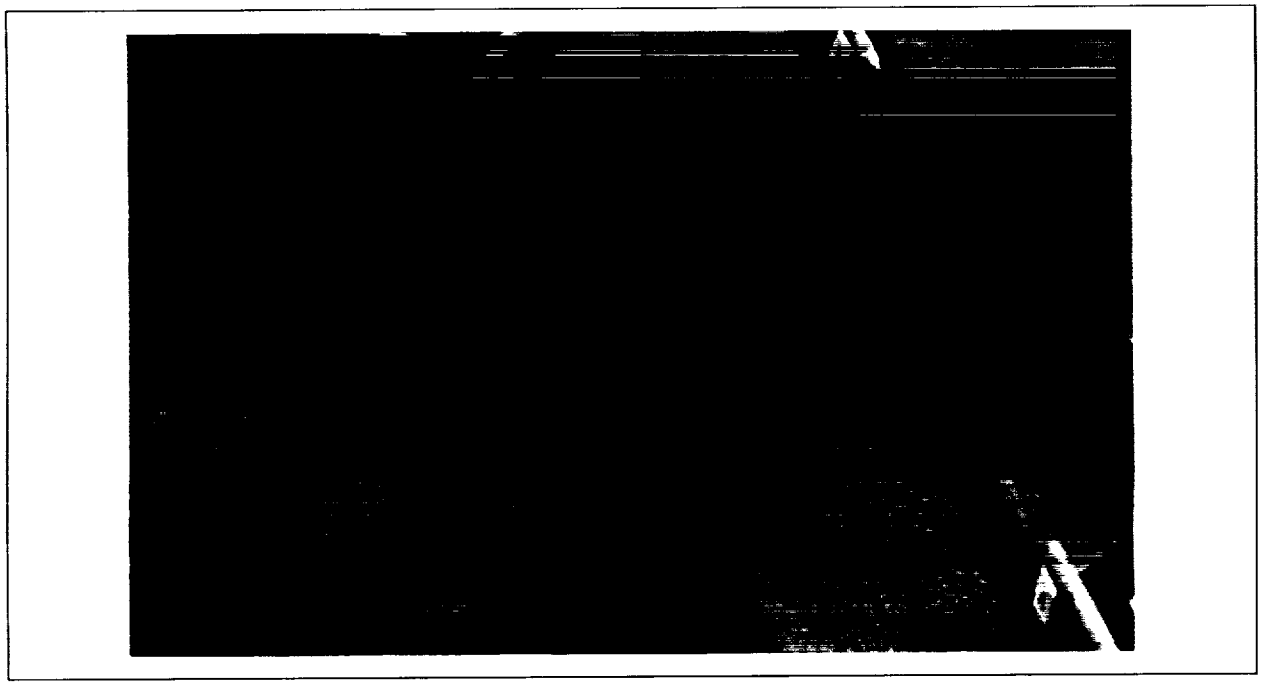

Color plate 12. Color patterns induced by equal-strength, opposite-direction tangential jets flowing side by side. (fig.2 , page 137)

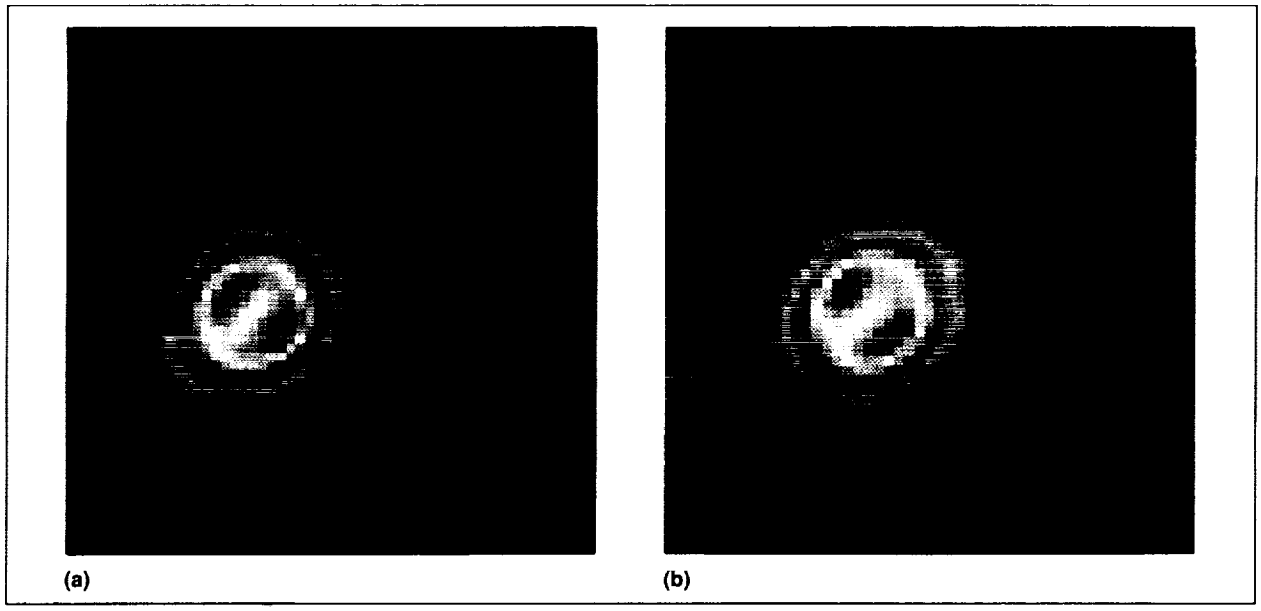

Color plate 13. Images of NGC 7027 from the Ames mid-infrared camera. (a) Measured at 11.4 microns with a 0.33-micron spectral bandwidth; (b) measured at 10.4 microns with a 0.33-micron spectral bandwidth. (fig. 1, page 258)

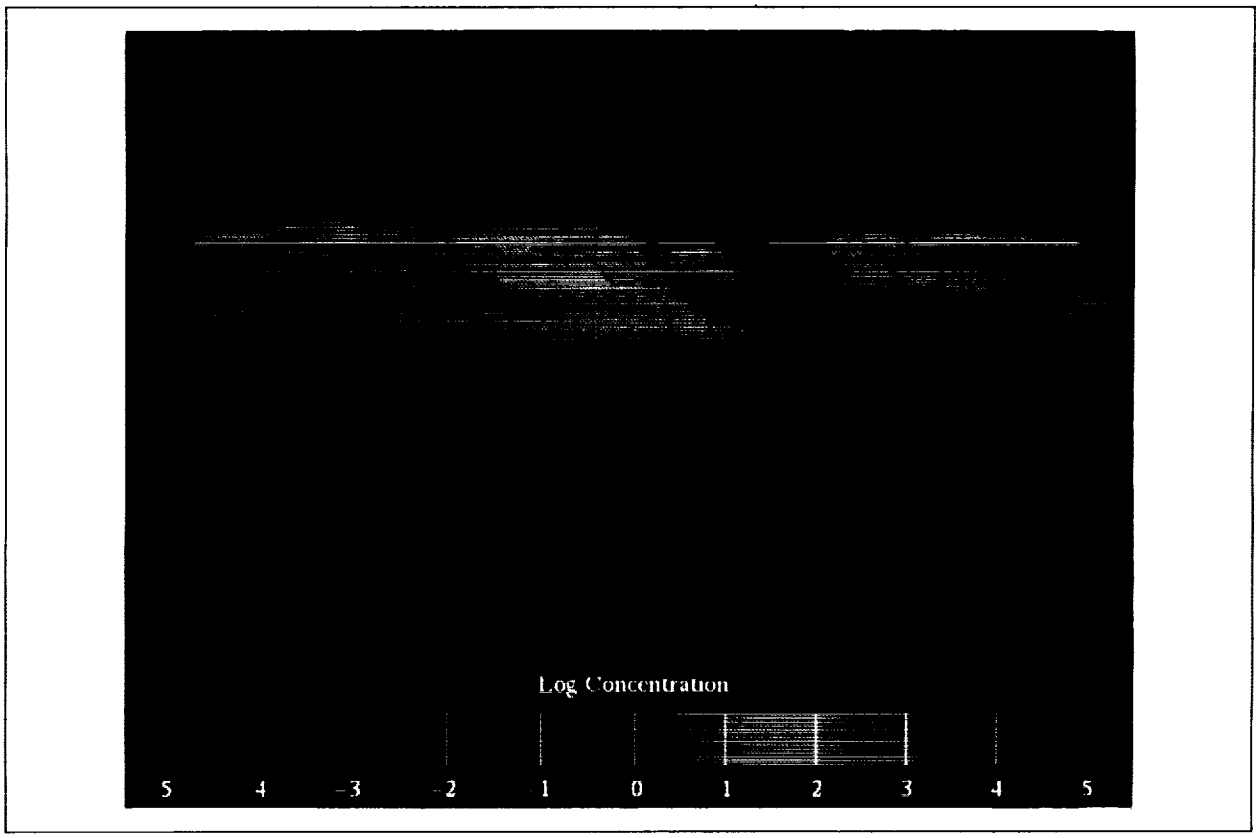

Color plate 14. Simulated Mt. Pinatubo volcanic cloud after 21 days. The cloud has just completed one circumnavigation of the globe and is confined to the tropics. Dotted lines represent latitude in 15-degree increments. (fig. 1, page 266)

REPORT DOCUMENTATION PAGE

Form Approved
OMB No. 0704-0188

1. AGENCY USE ONLY *(Leave blank)*	2. REPORT DATE	3. REPORT TYPE AND DATES COVERED
	November 1993	Technical Memorandum – Fiscal Year 1992

4. TITLE AND SUBTITLE

Research and Technology 1992

5. FUNDING NUMBERS

6. AUTHOR(S)

Ames-Moffett and Ames-Dryden investigators

7. PERFORMING ORGANIZATION NAME(S) AND ADDRESS(ES)

Ames Research Center
Moffett Field, CA 94035-1000

8. PERFORMING ORGANIZATION REPORT NUMBER

A-93030

9. SPONSORING/MONITORING AGENCY NAME(S) AND ADDRESS(ES)

National Aeronautics and Space Administration
Washington, DC 20546-0001

10. SPONSORING/MONITORING AGENCY REPORT NUMBER

NASA TM-103996

11. SUPPLEMENTARY NOTES

Point of Contact: John T. Howe, Chief Scientist, Ames Research Center, MS 200-1B, Moffett Field, CA 94035-1000; (415) 604-5500 or the contact person(s) at the end of each article

12a. DISTRIBUTION/AVAILABILITY STATEMENT

Unclassified – Unlimited
Subject Category 99

12b. DISTRIBUTION CODE

13. ABSTRACT ***(Maximum 200 words)***

Selected research and technology activities at Ames Research Center, including the Moffett Field site and the Dryden Flight Research Facility, are summarized. These activities exemplify the Center's varied and productive research efforts for 1992.

14. SUBJECT TERMS

Aeronautics, Space technology, Space sciences, Earth sciences, Life sciences, Computer science, Research and technology

15. NUMBER OF PAGES

320

16. PRICE CODE

A14

17. SECURITY CLASSIFICATION OF REPORT	18. SECURITY CLASSIFICATION OF THIS PAGE	19. SECURITY CLASSIFICATION OF ABSTRACT	20. LIMITATION OF ABSTRACT
Unclassified	Unclassified		

U.S. GOVERNMENT PRINTING OFFICE: 1993--583-716

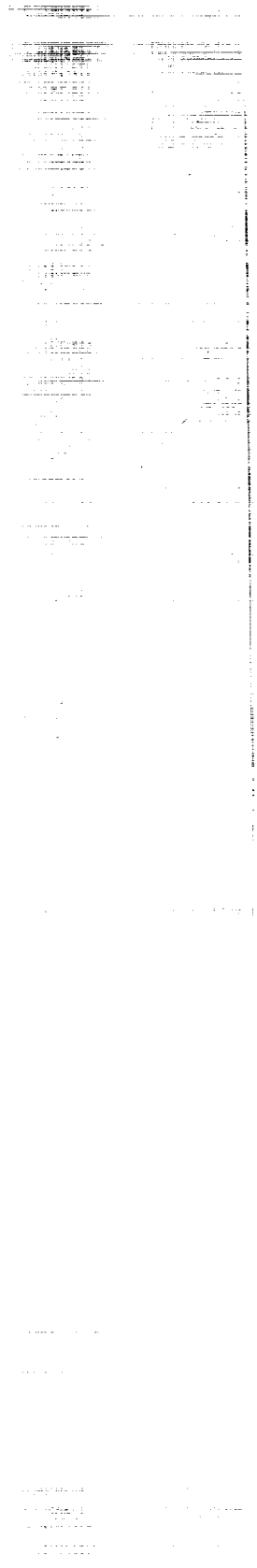

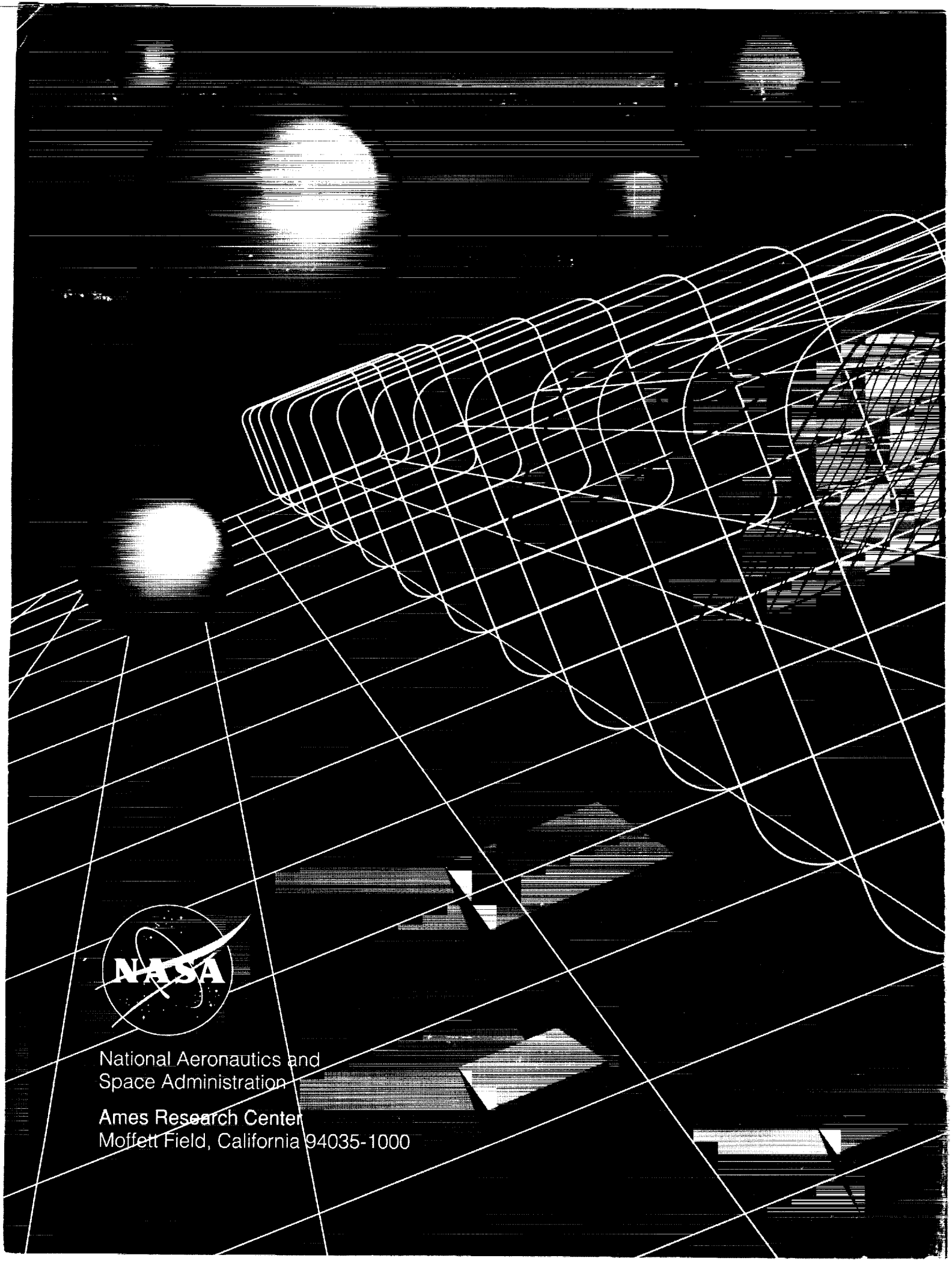

National Aeronautics and
Space Administration

Ames Research Center
Moffett Field, California 94035-1000